STRUCTURAL ASSESSMENT OF D-REGIONS AFFECTED BY ALKALI-SILICA REACTION/DELAYED ETTRINGITE FORMATION

A Dissertation

by

SHIH-HSIANG LIU

Submitted to the Office of Graduate Studies of
Texas A&M University
in partial fulfillment of the requirements for the degree of

DOCTOR OF PHILOSOPHY

Approved by:

Chair of Committee,	Joseph M. Bracci
Committee Members,	John B. Mander
	Stefan Hurlebaus
	Harry A. Hogan
Head of Department,	John M. Niedzwecki

December 2012

Major Subject: Civil Engineering

ABSTRACT

A combined experimental and analytical program was conducted to investigate the effects of Alkali-Silica Reaction (ASR) and Delayed Ettringite Formation (DEF) on D-regions in reinforced concrete (RC) bridge bents. Four large-scale RC specimens, which represent cantilever and straddle bents in Texas bridges in each specimen, were constructed. The first specimen represented the unexposed control specimen, while the other three were conditioned in the field with supplemental watering to promote ASR/DEF and served as the exposed specimens. The control and two exposed specimens with various levels of ASR/DEF, after eight months and two years of field conditioning, were load tested to failure. The last specimen remains in field with additional exposure to promote ASR/DEF and will be load tested in future studies.

The width and length of preload-induced cracks and developing cracks that initiated in the exposed specimens and grew over time, indicating concrete expansion due to ASR/DEF mechanisms, were measured. Petrographic analysis results of concrete cores extracted from the exposed specimens after their load testing confirmed the formation of ASR gel and minimum accumulation of ettringite. The structural testing results showed that the failure mechanism in all three tested specimens was due to a brittle shear failure in the beam-column joint. However, slightly greater stiffness, strength, and ductility were observed in the exposed specimens as a result of the activation of the reinforcing steel in the specimens due to the expansion of the concrete primarily from ASR, which effectively prestressed and confined the core concrete.

Sectional analysis and Strut-and-Tie Modeling (STM) of the experimental specimens were applied. Three-dimensional nonlinear Finite Element Analyses (FEA) were also conducted to numerically simulate the overall structural performance, internal response, and out-of-plane behavior of the experimental specimens. The effects of varying constitutive relations of the concrete in tension on models of the specimens were compared with the measured experimental response. A method to mimic ASR/DEF effects on exposed specimens was proposed and incorporated into the FEA approach. As a result, forces that prestress and confine the core concrete were effectively applied through the reinforcing steel prior to subsequent structural loading. The three-dimensional FEA approach was able to simulate the out-of-plane behavior of the beam-column joint and the proposed method yielded comparable results with the measured overall and internal behavior of specimens.

This dissertation is dedicated to my family.

My father Han-Shan, for his belief in my potential and his life advice and support.

My mother Kuei-Hsun, for bringing me into the world and her unconditional love.

My sister Hui-Chen, for her genuine caring and her company while growing up.

For encouragement from my family.

With all my sincere Love and Gratitude.

ACKNOWLEDGEMENTS

I would like to express my most sincere gratitude to my advisor, Dr. Joseph M. Bracci, for granting me the opportunity to prove myself as a structural engineer and for his professional support and advice in many aspects throughout this study. His dedicated mentorship and warm friendship will be forever appreciated and this positive teacher student relationship will be always memorable.

I also would like to express my genuine appreciation to Dr. John B. Mander for his active support and profound guidance throughout this study and for his marvelous teaching style. My sincere thanks also go to Dr. Stefan Hurlebaus for his vivacious role and for awarding me the opportunity to serve as a teaching assistant for his class. I would also like to thank Dr. Harry A. Hogan for serving on my committee and for his review of this dissertation.

My sincere thanks go to my research colleagues, Reece Scott and Michael Wilson, for their contribution in the experimental program. I am truly grateful to them for sharing experiences in the laboratory and for their hard work during the construction and structural testing of the specimen. The unique experiences of working with them in the laboratory will be always cherished. I would also like to thank my research colleague, Madhu Karthik, for his help and support during the exposure phase of the experimental specimens. His friendship will always be cherished.

Special thanks also go to Jason Zidek and Marcus Schniers for their support and help during the structural testing and exposure phase in the experimental program. My

appreciation is also extended to Brandon Cochran, Jack Soape, Jordan Main, Kenneth Anton, and Reid Dumas for their physical help in the laboratory. The experiences of working with these fellows will be forever appreciated.

Special thanks also go to Dr. Peter B. Keating and Mr. Matthew Potter of the Zachry Department of Civil Engineering High-Bay Structural and Materials Laboratory at Texas A&M University for their technical assistance during the construction and structural testing of the large-scale specimens.

I would also like to express my appreciation to Mr. Edward Morgan for spending his precious time on the petrographic analyses of the concrete cores taken from the experimental specimens.

My appreciation is also extended to my office mates, Alex Pagnotta, Kathleen Eck, Ramesh Kumar, and Armin Tabandeh, for sharing laughs and for their willingness to listen to me. Their friendships will be forever cherished.

Special thanks also go to Ms. Maria Medrano for her kindheartedness and help throughout the duration of this study.

Funding for this study was provided by the Texas Department of Transportation (TxDOT) (Project 0-5997) and the Federal Highway Administration through the Texas Transportation Institute. The support is gratefully acknowledged.

The Texas A&M Supercomputing Facility is also acknowledged for providing computing resources useful in conducting this research.

NOMENCLATURE

AASHTO	American Association of State Highway and Transportation Officials
ACI	American Concrete Institute
ASR	Alkali-Silica Reaction
CFT	Compression Field Theory
C-S-H	Calcium Silicate Hydrate
DEF	Delayed Ettringite Formation
DEMEC	Demountable Mechanical (Point/Gage)
ERW	Electrical Resistive Wiring
FEA	Finite Element Analysis
HCP	Hydrated Cement Paste
KM	Type KM Concrete Gage
LRFD	Load and Resistance Factor Design
LVDT	Linear Variable Differential Transformer
MCFT	Modified Compression Field Theory
PCD	Premature Concrete Deterioration
PEX	Cross-Linked Polyethylene
RC	Reinforced Concrete
RH	Relative Humidity
SG	Strain Gage

SP	String Potentiometer
SSD	Saturated Surface Dry
STM	Strut-and-Tie Modeling
TxDOT	Texas Department of Transportation

TABLE OF CONTENTS

Page

LIST OF FIGURES

Page

LIST OF TABLES

Page

CHAPTER I

INTRODUCTION

1.1 RESEARCH MOTIVATION

It is widely known that a significant amount of reinforced concrete (RC) structures over the world have experienced premature concrete deterioration (PCD) due to a variety of material degrading mechanisms including Alkali-Silica Reaction (ASR) and Delayed Ettringite Formation (DEF). Over the past two decades, a large number of RC bridges have been planned, designed and constructed by the Texas Department of Transportation (TxDOT) to accommodate the growing population in Texas. To satisfy the growing traffic demands in metropolitan areas, the size of bridge structures has become significantly larger and large concrete placements can result higher concrete curing temperatures. In addition, it is believed that high early strength cement has been used by some contractors to fulfill aggressive construction schedules. Early set cement also leads to higher concrete curing temperatures and provides more essential elements involved in chemical reactions of ASR and DEF. Furthermore, the use of reactive aggregates, along with high alkali contents and moisture, leads to ASR. Such practices and concrete material constituents can lead to later concrete cracking and deterioration of modern bridge structures.

For large structural elements, the behavior of deep beams and disturbed regions, so-called D-regions, in structural systems may not be accurately described using sectional analysis. The approach of strut-and-tie modeling (STM) for design of

reinforced and prestressed concrete elements prone to shear deformations has been used by TxDOT and implemented in the *AASHTO LRFD Bridge Design Specifications* and *ACI 318 Building Code Requirements for Structural Concrete*. However, the adequacy of this method and yet the structural performance for large structural elements, including RC bridge bents, affected by ASR and DEF are currently unknown. It is believed that ASR and DEF reduce the elastic modulus and tensile strength of the concrete much more than compressive strength. How much these reductions affect the overall force-deformation behavior in large structural elements both physically and computationally is not clear yet. Moreover, the out-of-plane behavior of D-regions for both sound and ASR/DEF affected RC structures cannot be described by strut-and-tie modeling or other two-dimensional simulation techniques.

This research specifically aims to identify the adequacy of D-regions in RC bridge bents undergoing varying levels of ASR and DEF mechanisms using a combined experimental and analytical program. The conventional design code-based analysis tends to underestimate the ultimate strength and leads to local element failure rather than system failure (e.g., brittle shear failure). Out-of-plane behavior is neglected and cannot be addressed in such analysis approaches. In an attempt to address these issues, a three-dimensional nonlinear finite element analysis (FEA) approach to model structural performance and simulate the ASR/DEF effects on D-regions in RC bridge bents was also conducted.

1.2 RESEARCH OBJECTIVES

To achieve the structural assessment of D-regions affected by premature concrete deterioration due to ASR and DEF, the objectives of this study were as follows:

1) Conduct an experimental program which includes the construction of large scale RC bridge bent specimens; the exposure of these specimens to supplemental water for accelerating concrete expansion due to ASR/DEF mechanisms; the observations of cracking and expansion at the surface concrete, mid-depth core concrete strains and reinforcing steel strains; and the structural testing of the control and the exposed specimens with varying levels of ASR/DEF.
2) Perform an analytical program which consists of conventional code-based analyses and three-dimensional nonlinear finite element analyses of the experimental specimens. Conventional code-based methods including sectional analysis and strut-and-tie modeling were applied to estimate the strength capacity of the control specimen. To visualize out-of-plane behavior and to mimic ASR/DEF expansion, a three-dimensional nonlinear finite element modeling approach was utilized. The experimental and analytical results were then compared for further examination.

1.3 SCOPE OF WORK

The following outlines the contents of this dissertation and underscores the scope of this research. Chapter II reviews the mechanisms of ASR/DEF premature concrete deterioration, the related damage in D-regions of RC bridge bents, and the current computational modeling techniques for D-regions. Chapter III outlines the design and

detailing of the experimental specimens, the construction of these specimens, the curing of the concrete, and the internal instrumentation for each specimen. Chapter IV summarizes the external instrumentation for monitoring ASR/DEF expansion, the pre-loading setup, the specimen exposure condition, and the setup of supplemental watering system. Visual observations of concrete surface cracking and measurements of surface concrete strains, internal concrete strains, and reinforcing steel strains of the exposed specimens over time are presented. The petrographic analysis results of cores extracted from specimens after structural testing are also documented. The control and two exposed specimens were tested to failure and the results are compared. Chapter V presents the results of the concrete cylinder testing, the experimental setup of structural testing, the loading history, the load-deformation behavior, and the failure assessment for the tested specimens. Chapter VI presents the strength estimates for the control specimen using sectional analysis and strut-and-tie modeling methods. Chapter VII focuses on a three-dimensional nonlinear finite element analysis approach to simulate the force-deformation behavior and out-of-plane behavior of the control and two tested exposed specimens. The effect of concrete tension stiffening on structural performance is examined by incorporating different concrete tensile constitutive relations from literature. Moreover, concrete expansion due to ASR/DEF mechanisms is achieved by applying various levels of concrete expansion along the depth in numerical models. Chapter VIII summarizes the key findings of this research, major conclusions from these findings, and recommendations for future study.

CHAPTER II

BACKGROUND

2.1 OVERVIEW

This chapter presents an overview of the past studies on ASR and DEF as mechanisms of premature concrete deterioration (PCD) and the effects of concrete expansion as a result of PCD damage. Damage caused by ASR/DEF in RC bridge structures in Texas is then discussed. Subsequently, various code-based analyses and modeling approaches to simulate structural performance of disturbed regions, commonly referred to as D-regions, in RC bridge bents are summarized. A series of nonlinear finite element studies of RC structures and the available constitutive modeling techniques for RC members, namely concrete and reinforcing steel, are also described.

2.2 PREMATURE CONCRETE DETERIORATION MECHANISMS

ASR and DEF are potentially damaging mechanisms that can lead to premature concrete deterioration (PCD). Researchers have reported that high alkali cement and reactive forms of silica in aggregates with sufficient moisture can promote the formation of ASR (Bauer et al. 2006; Folliard et al. 2006; Bracci et al. 2012; Mander et al. 2012). Furthermore, it has been reported that cracking and deterioration from ASR can lead to later formation of ettringite (DEF), when concrete curing temperature exceeded 148 to 160 ˚F (64 to 71 ˚C) along with subsequent supplemental moisture, which can result in further damage (Thomas 2001; Bauer et al. 2006; Folliard et al. 2006; Burgher et al. 2008; Bracci et al. 2012; Mander et al. 2012). Nevertheless, some researchers asserted

that DEF is not a consequence of ASR (Hime and Marusin 1999). This section provides a brief review of the literature or past studies on ASR and DEF mechanisms and the effects of internal expansion on RC structures due to such mechanisms.

2.2.1 Alkali-Silica Reaction (ASR)

Alkali-silica reaction was first recognized as concrete failure resulting from combinations of certain mineral constituents in aggregates and high alkali cement in the early 1940s (Stanton 1940). There have been significant studies on ASR over the past decades and it is currently well-known that high alkali contents in cement when used with reactive siliceous aggregates in concrete can result in ASR, particularly when exposed to moisture (Hobbs 1984; Swamy and Al-Asali 1988; Poole 1992; Multon et al. 2005; Bauer et al. 2006; Folliard et al. 2006; Multon and Toutlemonde 2010; Bracci et al. 2012; Mander et al. 2012). ASR results in the formation of expansive products that generally form around the aggregates, termed ASR gel, which in turn leads to cracking of the concrete.

ASR is one of the most serious serviceability concerns of concrete structures over the world (Folliard et al. 2006). It has been well documented that the conditions for ASR to occur include reactive silica form in the aggregates, sufficient alkali hydroxides in the pore solution ($[Na^+]$, $[K^+]$, and $[OH^-]$), and sufficient moisture available in the hardened concrete (Folliard et al. 2006; Bracci et al. 2012; Mander et al. 2012). For ASR once the three conditions are met, the reaction between the reactive silica and the alkalis produce expansive products primarily around the aggregates, namely ASR gel. When exposed to sufficient moisture, ASR gel expands over time which can lead to

cracking of the concrete. However, as the alkalis and reactive silica are consumed with time, the ASR process stops unless these constituents are provided from external sources (Folliard et al. 2006). Mohammed et al. (2003) reported that expansion due to ASR can be divided into three periods, namely, the incubation period, the cracking period, and the stabilized period. This theory has been supported by experimental program results from the literature (Hobbs 1984; Swamy and Al-Asali 1988; Swamy and Al-Asali 1989; Ahmed et al. 1998; Fan and Hanson 1998a; Ahmed et al. 1999a; Bérubé et al. 2002; Mohammed et al. 2003; Multon et al. 2005; Folliard et al. 2006; Giaccio et al. 2008; Giaccio et al. 2009; Multon and Toutlemonde 2010).

Courtier (1990) and Deschenes et al. (2009) pointed out that the surface cracking due to ASR results from differential expansion between the core and the surface concrete. As leaching of the alkalis and surface drying reduce the alkali content in the surface layer, the amount of ASR gel is reduced. As a result, this leads to reduced expansion in the cover concrete and results in differential expansion between the surface and the interior. Moreover, Bérubé et al. (2002) pointed out that the exposure conditions of concrete greatly affect the development of surface cracking. Although wetting and drying reduced surface expansion of concrete cylinders, compared with those stored under constant humidity, it promoted surface cracking which can later introduce more moisture into the concrete. Jensen (2003) reported that the relative humidity was significantly greater on the concrete faces normally exposed to rain water in an existing structure in Norway. It is believed that the ASR expansion is more prominent when the relative humidity exceeded 80% (Poole 1992; Jensen 2003). In addition, Multon and

Toutlemonde (2010) reported that late moisture exposure was able to promote large ASR expansion, if the maximum potential expansion not reached, even after a certain period (14 months) of drying. This correspondingly indicates the importance of applying sealers on ASR-affected concrete that can potentially stop further expansion (Bérubé et al. 2002; Jensen 2003; Williams and Choudhuri 2010).

As the ASR gel starts to form, tensile stresses develop in the concrete because of swelling pressures exerting along the interface of the hydrated cement paste (HCP) and aggregates which are sufficient to initiate micro-cracking. The expansion may induce widespread cracking in the HCP and therefore diminish the strength of concrete (Poole 1992; Swamy 1992). Additionally, Jensen (2003) pointed out that ASR-damaged concrete underwent cracking in both the HCP and aggregates. The amount of cracking in both aggregates and HCP was determined through micro structural analyses. Several past studies have shown evidence of the phenomenon of cracking in both HCP and aggregates in ASR-damaged concrete (Giaccio et al. 2008; Deschenes et al. 2009; Bracci et al. 2012). Since shear capacity partly relies on the nature of the aggregate interlock, cracking in aggregates may potentially influence shear capacity and further affect the durability of structures in service.

Depending on exposure conditions, reinforcement details, and the amount of alkali content and reactive aggregates, ASR-induced expansion can vary significantly. Hobbs (1984) measured overall expansion approaching 0.35% in unreinforced concrete prisms with high alkali content subjected to accelerated exposure condition. Fan and Hanson (1998a) recorded 0.4% expansion in plain concrete but reduced expansion,

0.35% and 0.2% in transverse and longitudinal directions, respectively, in reinforced concrete prisms when 0.54% steel reinforcement ratio was added in longitudinal direction. Although added reinforcement reduced the amount of concrete expansion by 50%, the overall expansion caused a strain of 0.002 in reinforcing steel which is close to yielding of the steel. Furthermore, Mohammed et al. (2003) investigated the effect of various restraint conditions of different reinforcement layouts in concrete prisms on ASR-induced expansion. It was observed that transverse expansion reduced more than 50% when 0.85% smooth bars were added in longitudinal direction but no significant effect on longitudinal expansion was noted. For existing structures, a maximum strain of 0.005 (0.5%) was measured in Australian concrete bridges due to ASR after 12 years from construction (Carse and Dux 1990). It was also reported that some concrete structures in Australia expanded at intense rates even at age of 10 years.

2.2.2 Delayed Ettringite Formation (DEF)

Delayed ettringite formation was first termed in the literature to examine the development of secondary ettringite in heat-treated concrete in the 1980s (Heinz and Ludwig 1987). DEF is most common in precast concrete elements as a consequence of heat treatment during production (Folliard et al. 2006). However, due to the modern need for the large size bridge structures, higher curing temperature as a result of large cast-in-place concrete placements can also promote DEF. Over time, it has been found that large volume concrete placement can lead to high heat generation at the center during concrete hydration (Petrov et al. 2006). This process can cause cracking due to thermal gradients and later age DEF-induced cracking (Hobbs 1999; Thomas 2001;

Bauer et al. 2006; Folliard et al. 2006; Burgher et al. 2008; Deschenes et al. 2009; Bracci et al. 2012; Mander et al. 2012). Normally, ettringite forms in fresh concrete after the high heat condition during initial concrete curing. The reformation of ettringite, commonly known as DEF, can lead to later concrete expansion and cracking. It has been well documented that DEF develops as a result of high temperatures at an early age in concrete ranges from 148 to 160 ˚F (64 to 71 ˚C) (Kelham 1996; Odler and Chen 1996; Scrivener and Lewis 1997; Hobbs 1999; Thomas 2001; Pavoine and Divet 2003; Bauer et al. 2006; Folliard et al. 2006; Petrov et al. 2006; Burgher et al. 2008).

Ettringite forms at an early age of hydration regardless of curing temperature (Famy and Taylor 2001). DEF may take place at later ages once the concrete curing temperature reaches the threshold temperature. The sulfate, typically from gypsum in the cement, is consumed while reacting with the calcium aluminates in the presence of calcium hydroxide to form ettringite. Once this reaction completes, that is, the sulfate is depleted, the calcium aluminates react with the already formed ettringite to produce calcium monosulfoaluminate or monosulfate (Folliard et al. 2006). If later sulfates are introduced from either external sources or internal sources, the monosulfate can revert to ettringite, commonly referred to as DEF. When subjected to early high heat, sulfate and aluminate ions can physically become attached to the calcium silicate hydrate (C-S-H) being trapped and may release later from the C-S-H to react with monosulfate, producing DEF (Heinz and Ludwig 1987). With sufficient moisture, ettringite can absorb water and expand with time, causing expansive forces and concrete cracking. Many researchers have thus concluded that concrete exposed to high temperatures

during hydration with subsequent moisture can potentially cause DEF to form (Fu et al. 1994; Kelham 1996; Scrivener and Lewis 1997; Hobbs 1999; Thomas 2001; Pavoine and Divet 2003; Bauer et al. 2006; Folliard et al. 2006; Petrov et al. 2006; Burgher et al. 2008).

Although it usually takes longer for DEF to occur than for ASR in field structures, the overall expansion induced by DEF can significantly exceed that by ASR. Many researchers have investigated the effect of aggregate composition, curing temperature, and exposure condition on the amount of DEF-induced expansion in small samples. Grattan-Bellew et al. (1998) observed a maximum of 0.4% of DEF-induced expansion over a period of 65 days storage in lime water. Hobbs (1999) measured that the expansion caused by DEF can reach 2.5% after 5 years by using local aggregates. Barbarulo et al. (2005) found that late thermal treatment can trigger more DEF expansion even after stored at room temperature for 1 year. A maximum of 3.5% overall expansion and more than 65% of additional growth were recorded. Moreover, Bouzabata et al. (2012) reported that the storage conditions can greatly influence both ASR and DEF expansion, although the critical amount of moisture for DEF to arise was higher than that for ASR.

In general, it is believed that structures first exhibit cracking due to ASR and then DEF. While ASR initiates at the interface of the HCP and aggregates introducing tensile stress and resulting in cracking, DEF typically occurs at void locations in the HCP and then causes internal stresses (Folliard et al. 2006; Burgher et al. 2008). Although ASR and DEF initiate in different areas, both mechanisms can lead to cracking of the HCP

and aggregates. From the point of view of structural integrity, both ASR and DEF can cause cracking of the concrete and potentially affect structural performance even though they are different concrete deterioration mechanisms (Bauer et al. 2006; Folliard et al. 2006; Deschenes et al. 2009).

2.2.3 Effects of Internal Expansive Forces on Material Properties and Structural Performance

Mechanical properties of materials are essential characteristics required by structural engineers for either design or analysis purposes. Once concrete deterioration occurs, the material properties can alter such that structural performance based on initial design may consequently change. It is well-known that ASR and DEF cause internal expansion and lead to cracking of the concrete. Many researchers have been dedicated to explore the effects of ASR/DEF-induced expansion on concrete material properties and structural performance. Table 2-1 summarizes a few studies that have reported the influence of internal expansive forces on concrete material properties in terms of the compressive strength, tensile strength, elastic modulus, and dynamic modulus on small samples. In general, most concrete material properties were reduced when ASR/DEF was present. Relatively few studies found that internal expansion increased or slightly changed the compressive strength of concrete. Table 2-2 highlights the results on how ASR affects the structural performance such as the flexural capacity, shear capacity, bearing capacity, bond strength, and fatigue life duration. Some studies found beneficial effects of ASR on shear capacity of reinforced concrete specimens and led to increase fatigue duration as a consequence.

Table 2-1 Effects of Internal Expansive Forces on Concrete Material Properties (Adapted from Bracci et al. [2012])

Author(s)	Material Properties of Concrete			
	Comp. Strength	Tensile Strength	Elastic Modulus	Dynamic Modulus
(Hobbs 1986)[1]	⇩	⇩	⇩	
(Swamy and Al-Asali 1988)	⇩	⇩	⇩	⇩
(Chana and Korobokis 1991)	⇩	⇩	⇩	
(Chana and Korobokis 1992)	⇩	⇩	⇩	
(Fan and Hanson 1998b)	⇩	⇩		⇩
(Ahmed et al. 1999a and 1999b)	⇩	⇩	⇩	
(Monette et al. 2002)	⇧	⇩	⇩	⇩
(Zhang et al. 2002)				⇩
(Mohammed et al. 2003)	⇩		⇩	
(Multon et al. 2005)	⇔	⇔	⇩	
(Giaccio et al. 2008)	⇩ & ⇔[2]	⇩ & ⇔[2]	⇩	

⇩: reduction; ⇧: increase; ⇔: minimal change

1. Tests were carried out on affected and sound concrete cubes.
2. Samples with reactive aggregates exhibited lower strength values. Samples with slow reactive aggregates showed no significant difference.

However, the results from the above-cited studies were mainly obtained from the tests of small-scale specimens. Structures in the field generally have much more complex reinforcement details, loading conditions, and exposure conditions which may lead to varying structural behavior. A substantial amount of research on various structural performances of ASR/DEF-affected RC structures has been conducted. Deschenes et al. (2009) constructed six large-scale RC bent cap specimens to investigate the effects of ASR/DEF on structures prone to shear and no substantially deleterious effects of ASR/DEF were observed on shear capacity after 1 year exposure. Moreover,

Bracci et al. (2012) studied the effects of ASR/DEF on the performance of lap splices in large-scale columns and no detrimental structural effects were observed after 3 year exposure. The ASR/DEF-induced cracks were mainly oriented in the directions of the tension field under compressive loading that mimicked in-service gravity loading. Giaccio et al. (2009) observed a similar ASR-induced crack pattern in small-scale specimens under axial compressive loading. The density of cracks was measured and the results showed that loaded specimens experienced 40% reduction of cracks compared to unloaded specimens. Bae et al. (2007) noted that wrapping carbon fiber-reinforced polymer around ASR/DEF-damaged structures can limit later expansion and potentially reduce the detrimental effects due to ASR/DEF.

Table 2-2 Effects of Internal Expansive Forces on Structural Performance (Adapted from Bracci et al. [2012])

Author(s)	Structural Performance				
	Flexural Capacity	Shear Capacity	Bearing Capacity	Bond Strength	Fatigue Life
(Swamy and Al-Asali 1989)	⇩				
(Chana and Korobokis 1991)		⇩ & ⇧[1]			
(Chana and Korobokis 1992)	⇩ & ⇔[2]	⇩	⇩	⇩	
(Ahmed et al. 1998)		⇧			⇧
(Fan and Hanson 1998b)	⇔				
(Ahmed et al. 1999a)	⇩			⇩	⇩
(Ahmed et al. 1999b)			⇩		
(Monette et al. 2002)	⇔				

⇩: reduction; ⇧: increase; ⇔: minimal change

1. Samples without links except 1 group (average values) exhibited lower values. Samples with links showed scattered results. Samples with either straight or bent ends exhibited lower values.
2. Only an approximately ± 4% of difference was observed in bent-up bar tests.

In addition, Courtier (1990) proposed a general method to evaluate the effects of restraint provided by reinforcement leading to reactive stress in the concrete. A schematic linear superposition of stresses induced by loading and ASR in the concrete and reinforcing steel was provided. However, the linear relation between load-induced and ASR-induced stresses was not clearly demonstrated yet. Multon et al. (2005) examined the structural behavior and measured longitudinal and transverse concrete expansion due to ASR in RC beams over 14 months. It was found that the effect of the reinforcement on ASR-induced expansion was substantial. Compared with plain concrete specimens, reinforcement in longitudinal direction decreased the ASR-induced expansion while local stirrups had little effect on transverse expansion. Mohammed et al. (2003) also presented comparable results showing that the strain at the surface was reduced in the restraint direction. That is, the restraint provided by reinforcing steel can reduce the surface strain in the corresponding direction. It was also reported that the closer the reinforcing steel was to the surface, the less surface strain was observed. However, the more surface strain was reduced, the more strain was exerted in reinforcing steel.

In Japan, researchers have presented fracture of reinforcing steel caused by ASR expansion in existing RC structures constructed in the 1980s (Kubo et al. 2003; Torii et al. 2009). It is believed that fracture of steel bars at the bends was induced by the change of mechanical properties during the bending process and the tensile stress in steel bars resulting from the effect of restraining ASR-induced expansion. Fracture of steel bars at the bends will raise serviceability concerns of structures (Inoue et al. 2012).

Additionally, ASR-induced cracking in the surface can permit future moisture ingress. Habuchi and Torii (2012) found that the alkali content that promoted ASR gel to form can suppress corrosion of reinforcing steel. Nevertheless, once the alkali content is consumed, that is, ASR formation is finished, the previously existing cracks in the surface can introduce more future moisture, resulting in potential corrosion of steel bars.

2.3 ASR/DEF DAMAGE IN D-REGIONS OF RC BRIDGE BENTS

The aim of this research is to investigate the effects of ASR/DEF on structural performance with particular reference to so-called disturbed regions, commonly referred to as D-regions. Figure 2-1 shows two typical RC bridge bent caps in Texas that are showing signs of ASR/DEF distress in their D-regions. Typically, ASR/DEF-induced cracking initially develops in the tension field of the concrete due to gravity loading. The cantilever bent on I–10 in San Antonio, Texas, shown in Figure 2-1a, exhibits flexural cracking in the column and diagonal shear cracking in the beam-column joint and bent regions. The straddle bent on I–45 and Beltway 8 in Houston, Texas, shown in Figure 2-1b, exhibits diagonal cracks in the beam and beam-column joint. These cracks exist mostly in the D-regions where both flexural and shear demands are high. Although cracks, typically hairline cracks, are expected in such zones in RC structures under gravity load, such cracks permit future moisture ingress and can promote later development of ASR/DEF, leading to deterioration of the structures.

(a) Cantilever Bent (San Antonio, TX)

(b) Straddle Bent (Houston, TX)

Figure 2-1 Cracking in Typical Bent Cap Structures

2.4 ANALYSIS FOR D-REGIONS OF RC BRIDGE BENTS

The strength of the D-regions in RC structures can be determined using various analytical techniques. Some of these techniques are adopted by design codes and often have slightly different design criteria. This section provides a review of the design codes or past studies on diverse analysis approaches that are applicable to this study. In the beginning, sectional analysis and strut-and-tie modeling (STM) approaches based on the provisions in the AASHTO LRFD (2010) and ACI 318-08 (2008) are cited. A recommendation of limiting compressive stress at the face of a node proposed by Birrcher et al. (2009) is also reviewed. Furthermore, a brief review of the compatibility-based STM technique that is capable of capturing nonlinear response of RC D-regions is provided. Lastly, a series of past studies of nonlinear finite element modeling of RC structures and the available constitutive models used within are summarized.

2.4.1 Sectional Analysis

This section includes the provisions in AASHTO LRFD (2010) and ACI 318-08 (2008) for determining the flexural and shear capacities of a RC section. For flexural analysis of the structural testing configurations in this research, as described in the next chapter, the nominal flexural capacity of the given RC section is divided by the distance from the application point of the load to the nearest inflexion point to derive the nominal loading capability. For the shear capacity, both the methods provided in AASHTO LRFD (2010) and ACI 318-08 (2008) are cited. The nominal shear strength is attributed to both the aggregate interlock of concrete and the shear resistance of transverse reinforcement steel.

2.4.1.1 Flexural Analysis

The flexural analysis of RC sections is based on the assumptions of strain compatibility where plane sections remain plane, the equivalent methods where elastic-perfectly plastic constitutive models are used for steel and the Whitney stress block is used for concrete, and equilibrium of internal and external forces.

The nominal moment strength for a singly reinforced rectangular concrete section, M_n^s, can be derived by:

$$M_n^s = C_c\left(d - \frac{a}{2}\right) \tag{2-1}$$

where $C_c = 0.85 f_c^{'} ba$ is the concrete compression force based on the Whitney Stress block approximation; $f_c^{'}$ is the concrete compressive strength; b is the width of the section; d is the distance from the extreme compression fiber to the centroid of the tension steel; $a = \beta_1 c$ is the depth of the equivalent rectangular stress block; c is the neutral axis depth derived through the equilibrium of the concrete compression force and the tension force in steel, given as:

$$0.85 f_c^{'} b \beta_1 c = A_s f_y \tag{2-2}$$

in which A_s is the area of the tension reinforcement; f_y is the yield strength of the tension reinforcement; β_1 is the equivalent rectangular stress block parameter defined as:

$$0.65 \le \beta_1 = 0.85 - 0.05\left(f_c^{'}(ksi) - 4\right) \le 0.85 \tag{2-3}$$

When compression steel is provided, the nominal moment strength of a doubly RC section, M_n^d, can be obtained by performing an iterative solution for the neutral axis depth c and can be derived by:

$$M_n^d = C_c\left(d - \frac{a}{2}\right) + C_s\left(d - d'\right) \tag{2-4}$$

where $C_s = A_s'\left(f_s' - 0.85 f_c'\right)$ is the equivalent force in the compression steel; A_s' is the area of the compression steel; f_s' is the stress in the compression steel; d' is the distance from the extreme compression fiber to the centroid of the compression steel.

Given the structural testing configuration, the applied loading to develop flexural capacity can be determined by:

$$V_n^f = \frac{M_n}{L} \tag{2-5}$$

where L is the distance from the loading point to the critical section for flexure.

The general strength design criterion for RC structures is as follows:

$$\phi M_n \geq M_u \tag{2-6}$$

where ϕ is the strength reduction factor, taken as 0.9 for flexural analysis; M_u is the factored demand moment.

2.4.1.2 Shear Strength

The nominal shear resistance by a RC beam section is attributed to the shear forces carried by the concrete and by the transverse reinforcement (ACI Committee 318 2008). Therefore, the nominal shear strength of a RC section, V_n, can be computed by:

$$V_n = V_c + V_s \tag{2-7}$$

where V_c is the nominal shear strength provided by concrete; V_s is the nominal shear strength provided by transverse reinforcement.

Based on the provisions of ACI 318-08 (2008) for RC members subject to only flexure moments and shear forces, V_c is defined by:

$$V_c = 2\lambda\sqrt{f_c^{'}(psi)}b_w d \tag{2-8}$$

where $\lambda = 1.0$ for normal weight concrete; b_w is the web width of the section.

The shear resistance by the transverse reinforcement, V_s, is given by:

$$V_s = \frac{A_v f_{yt} d}{s} \tag{2-9}$$

where A_v is the area of the transverse reinforcement within a given spacing s; f_{yt} is the yield strength of the transverse reinforcement.

The nominal shear strength defined by AASHTO LRFD (2010) includes the additional effect of a prestressing force:

$$V_n = V_c + V_s + V_p \tag{2-10}$$

where V_p is the component of the shear force carried by prestressing tendons.

The definitions of shear strength provided by concrete V_c and steel V_s in AASHTO LRFD (2010) differ from ACI 318-08 (2008), as follows:

$$V_c = 0.0316\beta\sqrt{f_c^{'}(ksi)}b_v d_v \tag{2-11}$$

$$V_s = \frac{A_v f_y d_v \cot\theta}{s} \tag{2-12}$$

where b_v is the web width across shear plane; d_v is the distance between the resultants of the tensile and compressive forces; f_y is the yield strength of the transverse reinforcement; β is the factor indicating the ability of diagonally cracked concrete to transmit tensile and shear forces; θ is the angle of inclination of diagonal compressive stresses.

Based on the provisions of AASHTO LRFD (2010), values of $\beta = 2.0$ and $\theta = 45°$ can be used for nonprestressed RC sections, which in turn yields to Eqs. (2-8) and (2-9) as provided in ACI 318-08 (2008).

For sections containing the minimum amount of shear reinforcement as specified in AASHTO LRFD (2010), β is determined by:

$$\beta = \frac{4.8}{(1+750\varepsilon_s)} \tag{2-13}$$

where ε_s is the net longitudinal strain at the centroid of tensile reinforcement.

For sections do not contain the minimum amount of shear reinforcement, β is determined by:

$$\beta = \frac{4.8}{(1+750\varepsilon_s)} \frac{51}{(39+s_{xe})} \tag{2-14}$$

where s_{xe} is the crack spacing parameter, as defined as:

$$12.0(in.) \le s_{xe} = s_x \frac{1.38}{a_g + 0.63} \le 80.0(in.) \tag{2-15}$$

where a_g is the maximum aggregate size; s_x is the lesser of d_v and the maximum distance between layers of longitudinal crack control reinforcement.

The net longitudinal strain at the centroid of tensile reinforcement is specified as:

$$\varepsilon_s = \frac{\left(\frac{|M_u|}{d_v} + 0.5N_u + |V_u - V_p| - A_{ps} f_{po} \right)}{E_s A_s + E_p A_{ps}} \tag{2-16}$$

where $|M_u|$ is the factored moment; N_u is the factored axial force; V_u is the factored shear force; V_p is the component of shear force carried by prestressing tendons; A_{ps} is the area of prestressing steel on the flexural tension side; $f_{po} = 0.7 f_{pu}$ for both pre-tensioned and post-tensioned members where f_{pu} is the ultimate stress of prestressing steel; E_s and E_p are elastic moduli of reinforcing steel and prestressing steel; A_s and A_{ps} are the areas of reinforcing steel and restressing steel.

Whether sections contain the minimum amount of shear reinforcement, θ is computed by:

$$\theta = 29 + 3500\varepsilon_s \tag{2-17}$$

The general shear strength requirement is defined as:

$$\phi V_n \ge V_u \tag{2-18}$$

in which ϕ taken as 0.75 in ACI 318-08 (2008) and 0.90 in AASHTO LRFD (2010) for normal weight concrete.

The sectional analysis method is commonly used for design of elements where the structural performance is dominated by a specific cause, that is, flexure or shear. The interactions among these individual effects are neglected and the behavior is considered separately. This approach may not be applicable in the assessment of D-regions where the assumptions of beam theory are not valid.

2.4.2 Strut-and-Tie Modeling

A comprehensive review on the developments of truss modeling approaches was presented by ASCE-ACI Committee 445 (1998). Truss models were first used in the design and analysis of RC beams in the early 1900s. The basic concept was that a RC beam could be idealized as a truss formed by a combination of top concrete compression chords, bottom steel tension ties, and inclined diagonal concrete struts at 45 degrees with respect to the longitudinal axis of the beam, after such beams cracked in the diagonal tension field due to loading. This approach led to the development of strut-and-tie modeling (STM), which applies consistent force equilibrium and ultimate material strength requirements for the design of D-regions in RC structures (Marti 1985; Schlaich et al. 1987). Since tensile and compressive forces could be carried by the truss members, the interaction of flexure and shear was thus considered. However, the truss models neglect the tensile strength of concrete and thus underestimate the overall strength of structure (ASCE-ACI Committee 445 1998).

As stated in AASHTO LRFD (2010) and Appendix A in ACI 318-08 (2008), STM can be applied to design structural concrete members, especially in D-regions such as deep beams, corbels, and anchorage zones for post-tensioned tendons. A graphical

truss model based on the elastic stress directions consisting of tension ties, compressive struts, and nodal zones has to be first constructed at the beginning of the design process. There is no unique truss model for a particular structure such that it is highly depended on the experience and choices of the designers. The internal forces of all members in the idealized truss model are then calculated using equilibrium. With regard to the truss members, struts represent concrete that carries compressive loads, while ties represent the steel reinforcement that carries tensile loads. The intersection of struts and ties forms nodes or nodal zones. In general, the label "C" represents compression struts while "T" represents tension ties. Depending on the combination of struts and/or ties at the intersections, there are four types of nodes, denoted as CCC node, CCT node, CTT node, and TTT node (Schlaich et al. 1987). The required width of struts, ties, and the geometry of nodal zones are then calculated and thus the required reinforcement can be determined. In general, members should be chosen and proportioned such that the failure mechanism initiates by yielding of the main longitudinal reinforcement (Marti 1985; Schlaich et al. 1987).

The load carried by a truss member must be less than the capacity of such member as follows:

$$\phi F_n \geq F_u \tag{2-19}$$

where F_n is the nominal strength of a given truss member; F_u is the factored force acting in such member; ϕ is the strength reduction factor, taken as 0.70 in AASHTO LRFD (2010) and 0.75 in ACI 318-08 (2008).

The nominal strength of a member, F_n, is defined as:

$$F_n = f_{ce} A_m \tag{2-20}$$

where f_{ce} is the effective strength of a given member; A_m is either the cross-sectional area of a strut or a tie, or the area of the face of a nodal zone.

2.4.2.1 Strength of Struts

According to ACI 318-08 (2008), the effective compressive strength of the concrete for a given strut, f_{ce}^{s}, is defined as follows:

$$f_{ce}^{s} = 0.85 \beta_s f_c^{'} \tag{2-21}$$

The factor β_s is taken as 1.0 for struts with uniform cross-sectional areas. For a given bottle-shaped strut, β_s is taken as 0.75 if the reinforcement crossing the strut satisfies the following:

$$\sum \frac{A_s^i}{b_s s_i} \sin \alpha_i \geq 0.003 \tag{2-22}$$

where A_s^i is the total area of the reinforcement at spacing s_i in the i-th layer crossing the strut at an angle α_i with respect to the axis of the strut; b_s is the width of the strut. Otherwise, β_s is specified as 0.60λ, where λ is defined in Section 2.4.1.

Based on AASHTO LRFD (2010), the limiting compressive stress in the strut is taken as:

$$f_{ce}^{s} = \frac{f_c^{'}}{0.8 + 170\varepsilon_1} \leq 0.85 f_c^{'} \tag{2-23}$$

in which ε_1 is the principal tensile strain, given by:

$$\varepsilon_1 = \varepsilon_s + (\varepsilon_s + 0.002)\cot^2 \alpha_s \tag{2-24}$$

where ε_s is the tensile strain in the direction of the tension tie; α_s is the smallest angle between the compressive strut and adjoining tension ties.

2.4.2.2 Strength of Ties

The effective strength of a given tie is taken as the area times the yield strength of the main reinforcement for non-prestressed concrete structures. In addition, the strength effects of prestressing tendons are considered in both ACI 318-08 (2008) and AASHTO LRFD (2010), which is beyond the scope of this study.

2.4.2.3 Strength of Nodes

As per ACI 318-08 (2008), the effective compressive strength of a concrete nodal zone, f_{ce}^n, is given as:

$$f_{ce}^n = 0.85\beta_n f_c' \tag{2-25}$$

where $\beta_n = 1.0$ for a given node bounded by struts or bearing areas, that is, CCC node; $\beta_n = 0.8$ when a node is intersected by one tie, namely, CCT node; $\beta_n = 0.6$ when two or more ties intersect at a given node, referred to as CTT or TTT node.

In accordance with AASHTO LRFD (2010), f_{ce}^n is taken as $0.85 f_c'$ for a CCC node, $0.75 f_c'$ for a CCT node, and $0.65 f_c'$ for either a CTT or TTT node.

Birrcher et al. (2009) provided a review of the code provisions according to AASHTO LRFD (2010) and ACI 318-08 (2008). An efficiency factor, ν, that is the ratio of the effective strength of a member to its ultimate material strength, was presented, as follows:

$$f_{ce} = \nu f_c^{'} \tag{2-26}$$

The effective compressive strength of a strut was presented as the efficiency of the strut-to-node interface in a node intersected by such strut. Thus, only the nominal strength of the nodes in a given truss model was considered. Based on the anchorage condition and loading condition of a given node, the node faces can be categorized as back face and bearing face. Each face of a single node can be subjected to various efficiency factors with respect to the type of such node face and the chosen design codes. Furthermore, a STM design method was proposed based on current design codes and experimental results of tested RC deep beams (Birrcher et al. 2009).

In summary, the efficiency factors and reduction factors in accordance with different design methods for a CCC node are listed in Table 2-3. Tables 2-4 and 2-5 show the efficiency factors and reduction factors per different design methods for a CCT node and a CTT node, respectively. According to Birrcher et al. (2009), the back face and exterior face of a CTT node are not critical, if reinforcing steel bars are anchored appropriately.

Table 2-3 Efficiency Factors and Reduction Factors for a CCC Node (Adapted from Birrcher et al. [2009])

Node Face	Design Method	Efficiency Factor ν	Reduction Factor ϕ
Back Face	AASHTO LRFD	0.85	0.70
	ACI 318-08	$0.85 \cdot 1 = 0.85$	0.75
	Birrcher et al.	0.85	n/a
Bearing Face	AASHTO LRFD	0.85	0.70
	ACI 318-08	$0.85 \cdot 1 = 0.85$	0.75
	Birrcher et al.	0.85	n/a
Strut-Node Interface	AASHTO LRFD	0.85	0.70
	ACI 318-08	$0.85 \cdot 0.75 = 0.64$, if Eq. (2-22) satisfies; otherwise, $0.85 \cdot 0.60 = 0.51$	0.75
	Birrcher et al.	$0.45 \le 0.85 - f_c'(ksi)/20 \le 0.65$	n/a

Barton et al. (1991) conducted an experimental study on RC dapped beams to examine the feasibility of utilizing STM on such structures. It was found that STM is efficient to design the details of dapped beams. Moreover, isolated CCT and CTT nodes of such dapped beams were tested to investigate the behavior of such nodes in STM. Some cover splitting failures at the U-shaped transverse steel bars were observed in the tests of CTT nodes. The confining pressure against the concrete produced by the transverse bars towards the out-of-plane direction caused spalling and subsequent splitting failure. This underlined the importance of the effect of confining reinforcement in a CTT node and the significance of detailing such node as a three-dimensional element (Birrcher et al. 2009). Furthermore, it was found that the transverse

reinforcement in a CCT node could restrain the cracks, which in turn prevented the anchorage failure.

Table 2-4 Efficiency Factors and Reduction Factors for a CCT Node (Adapted from Birrcher et al. [2009])

Node Face	Design Method	Efficiency Factor ν	Reduction Factor ϕ
Back Face	AASHTO LRFD	0.75	0.70
	ACI 318-08	$0.85 \cdot 0.8 = 0.68$	0.75
	Birrcher et al.	0.70	n/a
Bearing Face	AASHTO LRFD	0.75	0.70
	ACI 318-08	$0.85 \cdot 0.8 = 0.68$	0.75
	Birrcher et al.	0.70	n/a
Strut-Node Interface	AASHTO LRFD	$\frac{1}{0.8 + 170\varepsilon_1} \le 0.85$	0.70
	ACI 318-08	$0.85 \cdot 0.75 = 0.64$, if Eq. (2-22) satisfies; otherwise, $0.85 \cdot 0.60 = 0.51$	0.75
	Birrcher et al.	$0.45 \le 0.85 - f_c^{'}(ksi)/20 \le 0.65$	n/a

The STM is a force-based approach assuming a lower bound solution of an idealized plastic truss that satisfies consistent force equilibrium and ultimate material strength requirements (Marti 1985; Schlaich et al. 1987). This method provides a simple tool for design of the D-regions in RC structures. However, the compatibility of deformation and constitutive material relations of RC members, namely, concrete and steel, are not employed in this process. Thus, the eventual failure mode and overall

force-deformation behavior are uncertain by means of STM. In addition, the conventional STM approach is restricted to in-plane structural problems (Marti 1985). The behavior along the depth of structure is unclear and can be overlooked by means of such process.

Table 2-5 Efficiency Factors and Reduction Factors for a CTT Node (Adapted from Birrcher et al. [2009])

Node Face	Design Method	Efficiency Factor ν	Reduction Factor ϕ
Back Face	AASHTO LRFD	0.65	0.70
	ACI 318-08	$0.85 \cdot 0.6 = 0.51$	0.75
	Birrcher et al.	n/a	n/a
Exterior Face	AASHTO LRFD	0.65	0.70
	ACI 318-08	$0.85 \cdot 0.6 = 0.51$	0.75
	Birrcher et al.	n/a	n/a
Strut-Node Interface	AASHTO LRFD	$\frac{1}{0.8 + 170\varepsilon_1} \leq 0.85$	0.70
	ACI 318-08	$0.85 \cdot 0.75 = 0.64$, if Eq. (2-22) satisfies; otherwise, $0.85 \cdot 0.60 = 0.51$	0.75
	Birrcher et al.	$0.45 \leq 0.85 - f_c'(ksi)/20 \leq 0.65$	n/a

2.4.3 Compatibility Strut-and-Tie Modeling

The shear resistance in RC structural elements can be modeled as a combination of truss and arch action (Park and Paulay 1975). Shear resistance by truss action is provided by the transverse reinforcement, while arch action is composed of a

compressive field in a diagonal concrete strut. A compatibility-based strut-and-tie modeling technique, referred to as C-STM, consisting of truss and arch actions, was developed by Scott et al. (2012a and 2012b) and extended by Mander et al. (2012). The compatibility of deformation is achieved by constraining truss and arch response in parallel to one another. In contrast to conventional STM, a truss model consisting of tension chords, compression chords, compression struts, and transverse hoops is determined based on two-point Gauss Truss (Kim and Mander 1999 and 2007). Subsequently, an elastic axial rigidity to simulate individual response of concrete and steel is assigned to each member. The nonlinear material constitutive relation is then applied to define the strength and to mimic nonlinear behavior of each member. Thus, the overall force-deformation response of the structure and the mode of failure can be predicted. In addition, this approach is capable of capturing the internal behavior since each member retains an elastic axial rigidity and a corresponding constitutive stress-strain relationship. Although this method can yield fairly accurate overall nonlinear structural behavior, the out-of-plane behavior is neglected, that is, the formation of truss and arch action along the depth cannot be clearly visualized.

2.4.4 Nonlinear Finite Element Analysis

The finite element analysis (FEA), based on the concepts of stiffness matrix, is a numerical technique to derive approximate solutions for complex systems and has been used in engineering branches over past decades. To solve such problems, two common tools have been adopted by researchers and engineers, that is, script-based programing languages and commercial finite element packages with graphical user interface. Over

time, sophisticated commercial finite element packages have been developed and numerous aspects of engineering techniques have been deliberately incorporated. Moreover, most commercial packages have been advanced to allow user-coded subroutines to be included for particular field problems. However, an overcomplicated model may lower the computer efficiency. Thus, in general, researchers and engineers simplify the finite element models, based on various assumptions, to simulate the engineering problems, reducing the computing time.

Reinforced concrete, composed of concrete and steel, is one of the most broadly used building materials in modern bridge structures. Over time, FEA has been used to assess the structural performance of such structures. A simplified bi-linear constitutive relation of steel has been widely used in this approach (Figure 2-2).

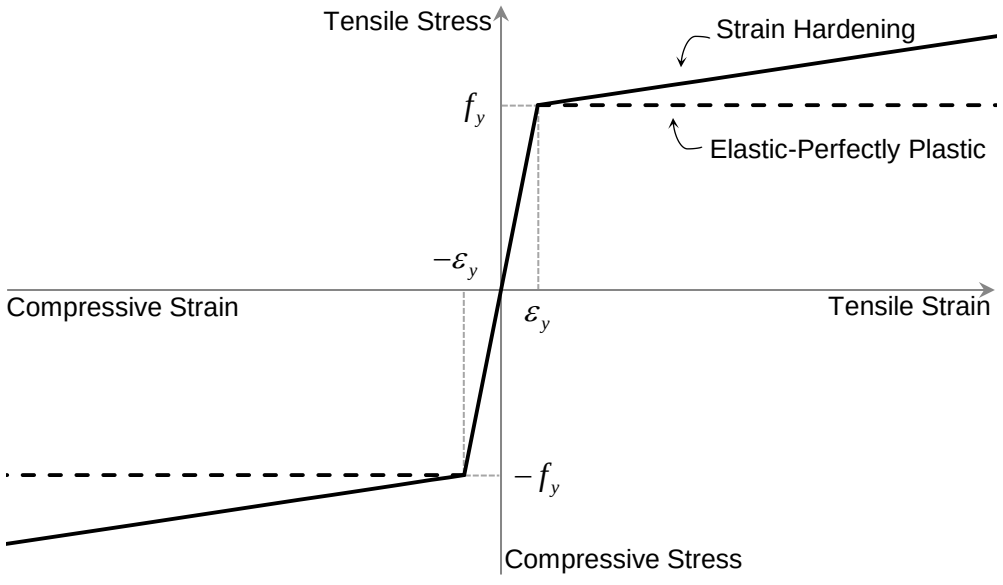

Figure 2-2 Idealized Stress-Strain Relation of Reinforcing Steel

However, due to the heterogeneity nature of concrete, that is, different behavior when concrete subjected to tension and compression, to mimic its behavior becomes challenging. The sudden drop in tensile strength after concrete cracking and the nonlinear behavior near peak compressive strength can cause singularity in formation of stiffness matrix (Figure 2-3).

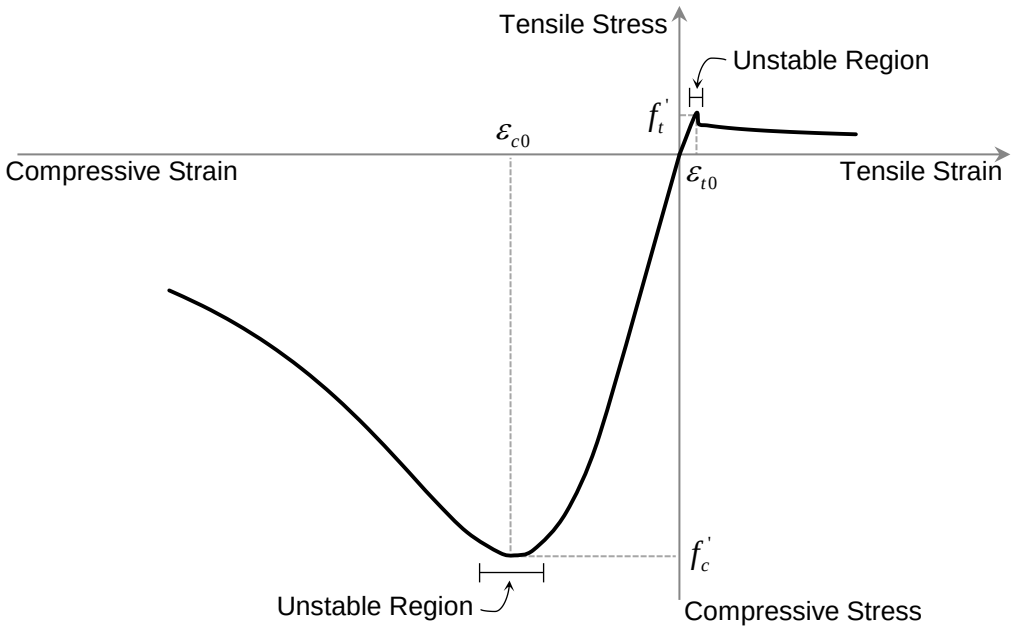

Figure 2-3 Typical Stress-Strain Relation for Concrete

This section presents a review of past studies on the constitutive modeling of concrete including the behavior under uniaxial compression, the compression softening effect, the tension stiffening in cracked concrete, and the confinement effect due to lateral stresses. Moreover, past research on RC structures using nonlinear FEA is

discussed. Lastly, a brief review of studies on mimicking ASR/DEF expansion effects on RC structures is provided.

2.4.4.1 Concrete in Uniaxial Compression

Popovics (1973) proposed an empirical equation of stress-strain relation of concrete subjected to uniaxial compression, as follows:

$$f_c = f_c^{'} \frac{n\left(\varepsilon_c / \varepsilon_c^{'}\right)}{n-1+\left(\varepsilon_c / \varepsilon_c^{'}\right)^n} \tag{2-27}$$

in which

$$n = \frac{E_c}{E_c - E_{\sec}} \tag{2-28}$$

where f_c is the compressive stress in concrete; ε_c is the corresponding strain; $\varepsilon_c^{'}$ is the strain corresponding to $f_c^{'}$; E_c is the initial elastic modulus of concrete; $E_{\sec} = f_c^{'} / \varepsilon_c^{'}$.

This equation has been found to work well for most concrete and has been used to develop more sophisticated expressions for concrete behavior. Based on this equation, Mander et al. (1988) developed a theoretical model to describe the behavior of confined concrete. The confinement effect is discussed in a later section.

2.4.4.2 Compression Softening

A theoretical model, based on equilibrium, compatibility and constitutive relationships, to predict the post-cracking behavior of RC members in torsion was developed by Mitchell and Collins (1974). Collins (1978) extended the theory to be capable of describing the behavior of post-cracking RC members in shear. This theory,

for both models of RC in torsion and shear, is well-accepted as the Compression Field Theory (CFT). However, the tensile stresses orthogonal to the compression field in cracked concrete, that is, stresses in the tension field, were neglected. Thus, this model is prone to overestimate the deformation and to underestimate the strength of a given RC structure (Duthinh and Carino 1996). Vecchio and Collins (1986) proposed a model for panel elements, that is, rectangular RC elements subjected to in-plane shear and axial stresses, based on the assumptions of CFT and incorporated the contribution of tensile stresses in cracked concrete, known as the Modified Compression Field Theory (MCFT). An average stress-strain relation of concrete based on experimental observations was proposed as follows:

$$f_{c2} = f_{c2\max}\left[2\left(\frac{\varepsilon_2}{\varepsilon_c^{'}}\right)-\left(\frac{\varepsilon_2}{\varepsilon_c^{'}}\right)^2\right] \tag{2-29}$$

where

$$\frac{f_{c2\max}}{f_c^{'}} = \frac{1}{0.8-0.34\,\varepsilon_1/\varepsilon_c^{'}} \le 1.0 \tag{2-30}$$

in which f_{c2} is the principal compressive stress in concrete; $f_{c2\max}$ is the compressive strength of concrete; ε_2 is the principal compressive strain in concrete; ε_1 is the principal tensile strain in concrete. Note that all variables are positive in tension and negative in compression.

In general, $\varepsilon_c^{'}$, the strain corresponding to the compressive strength of concrete, is taken as 0.002. Thus, Eq. (2-30) yields to:

$$\frac{f_{c2\max}}{f_c'} = \frac{1}{0.8+170\varepsilon_1} \le 1.0 \tag{2-31}$$

In other words, the tensile strain orthogonal to the compression field can reduce the compressive strength of the concrete, which is so-called compression softening in cracked concrete (Figure 2-4).

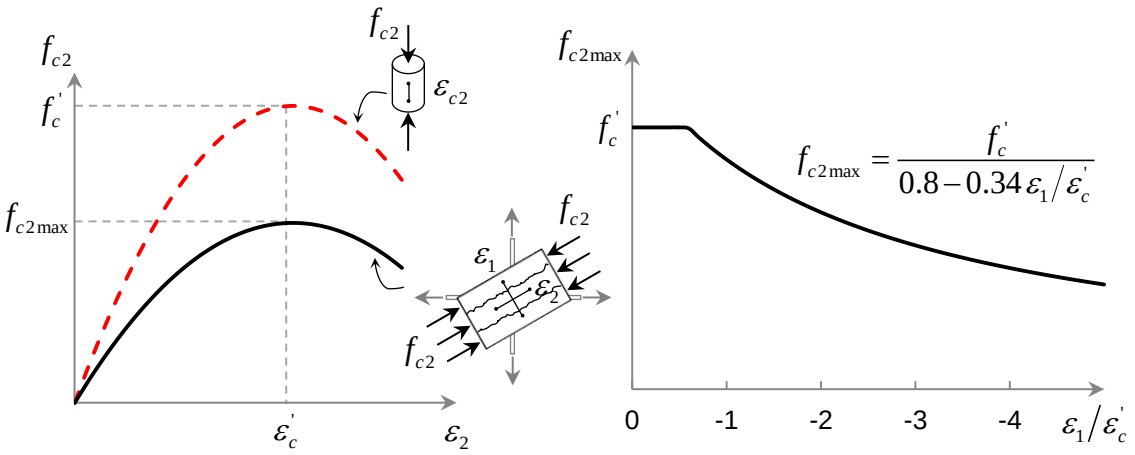

Figure 2-4 Compression Softening in Cracked Concrete (Adapted from Vecchio and Collins [1986])

2.4.4.3 Tension Stiffening

In general, tension stiffening refers to the contribution of concrete between the cracks in cracked RC members. As aforementioned, the MCFT takes into account the tensile stresses in concrete after cracking. Based on the experimental test results of panel elements reinforced with welded wire mesh, Vecchio and Collins (1986) suggested an average tensile stress-strain relation between cracks (Figure 2-5), as follows:

$$f_{c1} = E_c \varepsilon_1 \qquad \text{when} \quad \varepsilon_1 \le \varepsilon_{cr} \tag{2-32}$$

$$f_{c1} = \frac{f_{cr}}{1+\sqrt{200\varepsilon_1}} \quad \text{when} \quad \varepsilon_1 > \varepsilon_{cr} \tag{2-33}$$

where f_{c1} is the principal tensile stress in concrete; E_c is the modulus of elasticity of concrete; f_{cr} is the tensile strength of concrete ($f_t^{'}$).

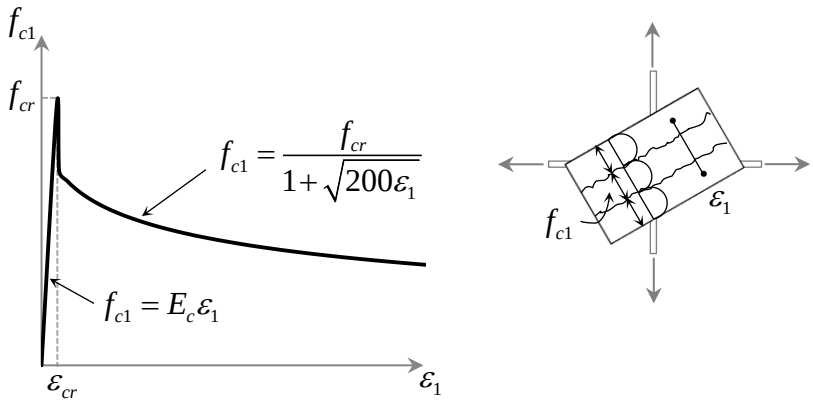

Figure 2-5 Tension Stiffening in Cracked Concrete
(Adapted from Vecchio and Collins [1986])

Based on the experimental results of large shell element tests, Collins and Mitchell (1987) modified the post-cracking tensile stress-strain relation, as follows:

$$f_{c1} = \frac{\alpha_1 \alpha_2 f_{cr}}{1+\sqrt{500\varepsilon_1}} \quad \text{when} \quad \varepsilon_1 > \varepsilon_{cr} \tag{2-34}$$

where $\alpha_1 = 1.0$ for deformed reinforcing steel bars; $\alpha_2 = 1.0$ for monotonic loading.

In Japan, Okamura et al. (1985) proposed an equation to describe the behavior of cracked concrete in tension, as follows:

$$f_{c1} = f_{cr}\left(\frac{\varepsilon_{cr}}{\varepsilon_1}\right)^{c} \tag{2-35}$$

where $c = 0.4$ for deformed bars; $c = 0.2$ for welded wire meshes.

Figure 2-6 compares the aforesaid available tension stiffening equations from past studies, that is, Eqs. (2-33), (2-34) and (2-35).

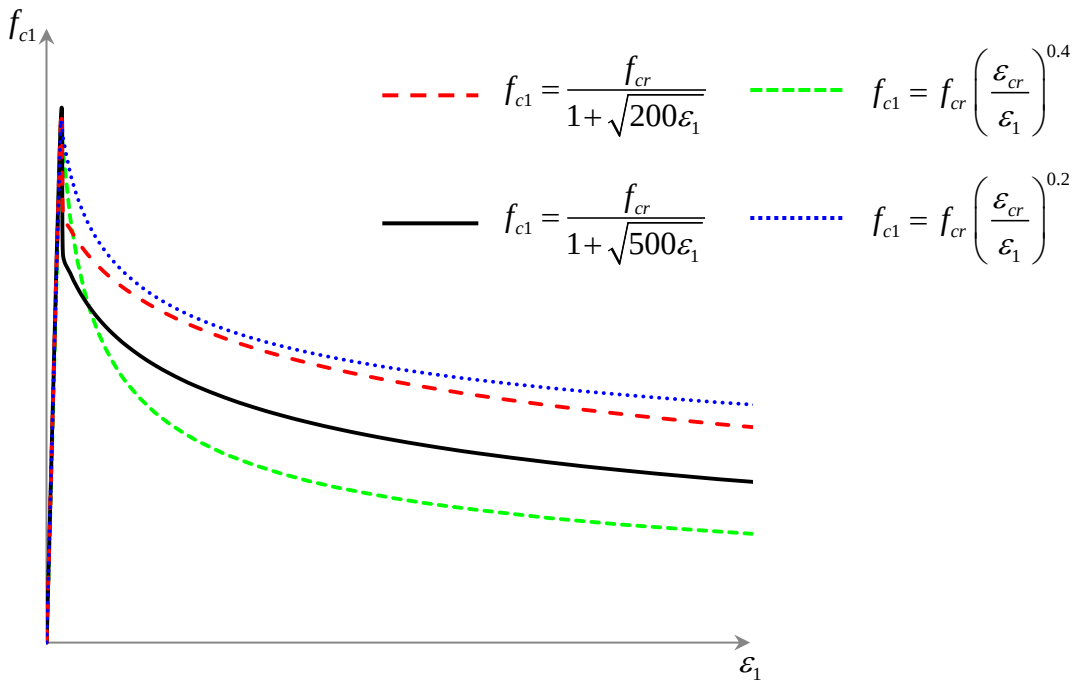

Figure 2-6 Comparison of Tension Stiffening Equations from Literature

2.4.4.4 Confinement Effect

Kupfer et al. (1969) conducted an experimental program of concrete plate tests to investigate the behavior of concrete subjected to biaxial stress combinations, that is, biaxial compression, compression-tension, and biaxial tension. Under identical biaxial

compression, a 16% increase in compressive strength was observed, compared to that under uniaxial compression. Based on the experimental results, an envelope of concrete strength, also referred to as yield surface, under biaxial stresses was then determined (Figure 2-7).

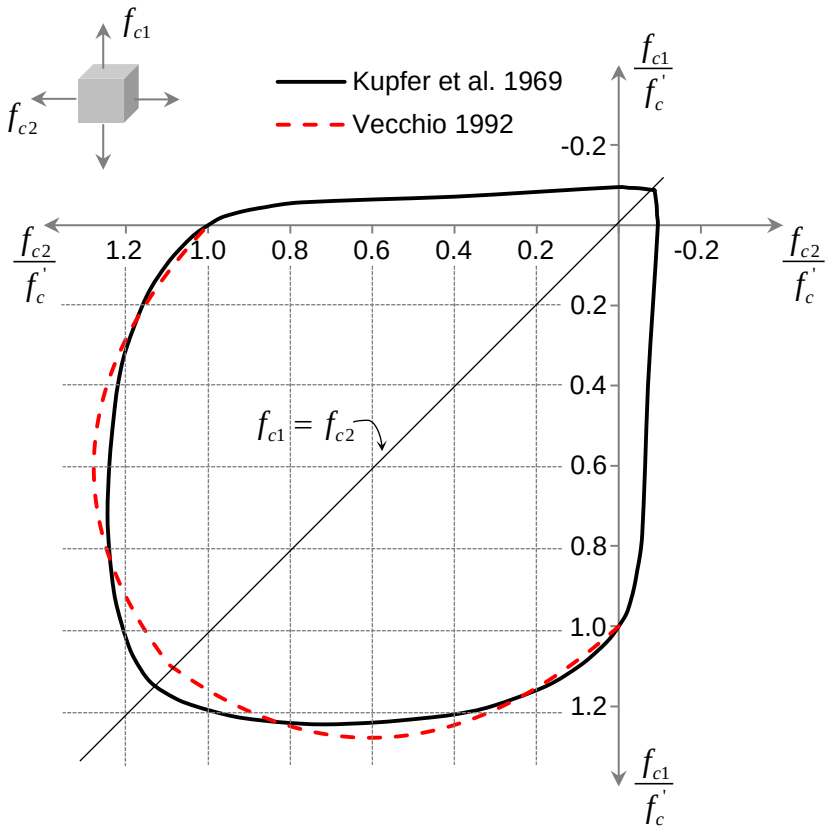

Figure 2-7 Typical Behavior of Concrete under Biaxial Stresses (Adapted from Kupfer et al. [1969])

Vecchio (1992) took into account Poisson effect and proposed an equation of strength enhancement factor, K_c, for concrete under biaxial compression. The

compressive strength of confined concrete, $f_{cc}^{'}$, and the strain at maximum concrete stress, $\varepsilon_{cc}^{'}$, were defined as:

$$f_{cc}^{'} = K_c f_c^{'} \tag{2-36}$$

$$\varepsilon_{cc}^{'} = K_c \varepsilon_c^{'} \tag{2-37}$$

where the strength enhancement factor, K_c, was given as:

$$K_c = 1 + 0.92\left(\frac{-f_{c1}}{f_c^{'}}\right) - 0.76\left(\frac{-f_{c1}}{f_c^{'}}\right)^2 \tag{2-38}$$

The curve based on Eqs. (2-36) and (2-38) is shown in Figure 2-7 as well.

Mander et al. (1988) quantified the area of effectively confined concrete core for circular and rectangular in RC structures and proposed a confinement effectiveness coefficient, k_e, given by:

$$k_e = \frac{A_e}{A_{cc}} \tag{2-39}$$

where A_e is the area of effectively confined concrete core; A_{cc} is the area of core within center line of transverse confining steel excluding area of longitudinal steel.

The effective lateral confining stress, $f_l^{'}$, was then defined as:

$$f_l^{'} = \frac{1}{2} k_e \rho_s f_{yh} \tag{2-40}$$

where ρ_s is the ratio of volume of transverse confining steel to volume of confined concrete core; f_{yh} is the yield strength of transverse confining steel.

Based on the assumption of equal effective lateral confining stresses, Mander et al. (1988) derived the confined compressive strength by:

$$f_{cc}^{'} = f_{c}^{'}\left(-1.254+2.254\sqrt{1+\frac{7.94\,f_{l}^{'}}{f_{c}^{'}}}-2\frac{f_{l}^{'}}{f_{c}^{'}}\right) \tag{2-41}$$

The increase of ductility due to confinement effect was also defined, as follows:

$$\varepsilon_{cc}^{'} = \varepsilon_{c}^{'}\left[1+5\left(\frac{f_{cc}^{'}}{f_{c}^{'}}-1\right)\right] \tag{2-42}$$

Figure 2-8 shows the typical stress-strain curves of unconfined and confined concrete.

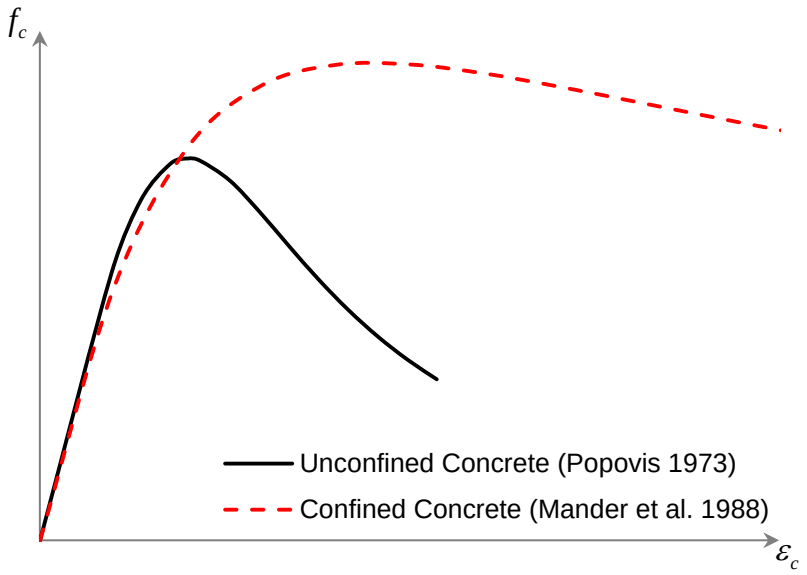

Figure 2-8 Typical Stress-Strain Curves of Unconfined and Confined Concrete

2.4.4.5 Modeling RC Structures

The nature of complexities in RC structures has made the modeling process to simulate the behavior in such structures laborious over past several decades. Over time, the development of concrete constitutive modeling and nonlinear solution techniques has made such analysis feasible. However, many characteristics of RC behavior, as mentioned in previous sections, cause the analysis to be rather complicated. Thus, reasonably accurate solutions for physical RC structures can result in excessive computational costs. In general, certain assumptions of the structural members, such as constitutive relations of concrete, and the structure itself, such as model geometry, are incorporated to compensate the computing costs. Nevertheless, if used inappropriately, this can result in overlooking certain crucial structural characteristics.

Cook and Mitchell (1988) used a self-developed finite element program to predict the behavior of D-regions in RC structures, such as a double-sided corbel and a rectangular dapped beam. The expressions of compression softening and tension stiffening of concrete proposed by Vecchio and Collins (1986) in MCFT were incorporated within two-dimensional plane stresses elements, representing concrete. It was found that nonlinear FEA yielded more accurate strength predictions than STM. However, the reinforcement was assumed to be smeared uniformly in this program (Cook 1987).

Fafitis and Won (1994) decomposed strain into volumetric and deviatoric components and proposed a three-dimensional constitutive equation of concrete based on incrementally linear elastic. Nonetheless, this suggested equation was simplified and

implemented into a two-dimensional FEA approach to analyze some deep beams. Salem (2002) presented a micro truss model for RC design, especially for D-regions. This two-dimensional approach was similar with the finite element approach since the structure was uniformly divided into nodes that were connected by truss elements, representing both concrete and reinforcing steel. Although constitutive models of concrete in uniaxial compression and tension were utilized, the interaction among them, that is, biaxial stresses, were not considered. Powanusorn (2003) and Powanusorn and Bracci (2006) proposed an analytical model, based on the assumptions of MCFT, to take into account the confinement effect due to transverse reinforcement in shear-dominated RC bent caps. This model was incorporated into a commercial package, Abaqus, by user-coded script programing and was verified with experimental test results by Young et al. (2002). However, the transverse reinforcement was smeared into a two-dimensional model in an average reinforcement ratio manner.

Pagnoni et al. (1992) presented a bounding surface model of concrete that took into account damage representation based on the yield surface concept. The propagation of cracks was illustrated through damage patterns. Although three-dimensional brick elements were used to model a RC deep beam and a prestressed concrete reactor vessel, modeling the reinforcing steel and prestressing strands were unclear. Claeson (1998) proposed a constitutive model for concrete and incorporated it into Abaqus through a user-coded subroutine to investigate the performance of confined concrete columns. A three-dimensional finite element model was constructed and the longitudinal reinforcement was modeled using certain built-in features in Abaqus. However, this

built-in feature treated reinforcement as a smeared layer that resulted in strengthening the concrete in the chosen direction. That is, it was solely applicable for uniaxial reinforcement. The confinement effect was therefore achieved by assigning different stress-strain relations to the core and cover concrete. As a result, the behavior of reinforcing steel was left unclear. Similarly, Dere and Dede (2011) used a smeared option in an alternative finite element package ANSYS to model straight steel bars in both beam and column sections of a RC frame. The effect of confinement was taken into account through applying a confined concrete material model rather than creating elements for transverse reinforcement.

In summary, to reduce possible computational costs, assumptions are generally adopted to achieve certain objectives of studies on RC structures using FEA approach. However, appropriate choices of assumptions must be made to avoid overlooking certain characteristics of a given RC structure.

2.4.4.6 ASR/DEF Expansion

Over past several years, there has been a significant amount of research on how to simulate the effect of ASR/DEF expansion in concrete at varying scales, such as microscopic models, material models and structure models (Seignol and Godart 2012). Mimicking the structural behavior of concrete affected by ASR/DEF mechanisms has proven difficult as a result of the nature of random parameters of the chemical processes (Farage et al. 2004). In general, such expansion in concrete can be modeled through applying an equivalent thermal load or by incorporating an empirical model. Dunant and Scrivener (2010) applied a pseudo-thermal expansion to the aggregates, serving as

the source of ASR expansion, in an artificial temperature field. The ASR-induced expansion was modeled as homogeneous aggregate expansion, gel rim expansion around the aggregates, and gel pockets expansion in the aggregates. As a result, cracking in HCP as well as splitting in aggregates were effectively generated using this modeling technique. Ulm et al. (2000) proposed a numerical model of ASR expansion as a function of time based on the results of an extensive experimental test program, as follows:

$$\varepsilon_{ASR}(t) = \varepsilon_{ASR}(\infty)\frac{1-\exp(-t/\tau_C)}{1+\exp(-t/\tau_C+\tau_L/\tau_C)} \tag{2-43}$$

where $\varepsilon_{ASR}(t)$ is the ASR-induced expansion over a given period of time t; $\varepsilon_{ASR}(\infty)$ is the swelling potential of ASR; τ_L is the latency time, corresponding to the inflexion point; τ_C is the characteristic time, defined as the intersection of the tangent at τ_L with the swelling potential $\varepsilon_{ASR}(\infty)$, as shown in Figure 2-9.

Furthermore, Ulm et al. (2000) developed a one-dimensional chemoelastic model to take into account the swelling pressure due to ASR expansion. The swelling pressure was paired with an elastic material behavior of the HCP to create an artificial spring device model in parallel. Two-dimensional analyses of a concrete gravity dam and a bridge box girder were then conducted through combining the empirical equation, that is, Eq. (2-43), and the chemoelastic model to examine the effect of ASR expansion over a period of time.

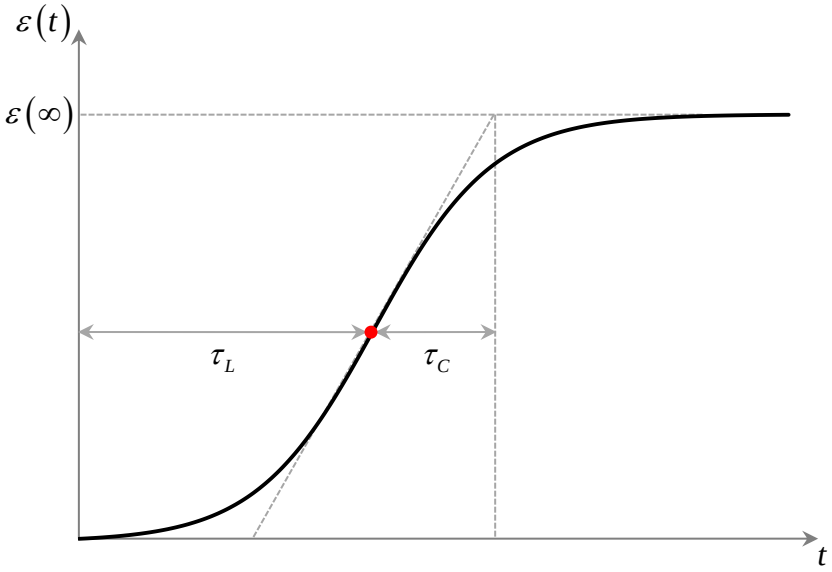

Figure 2-9 Definitions of Latency Time τ_L and Characteristic Time τ_C in a Typical Expansion Curve

Seignol et al. (2012) discussed the similarities between the numerical modeling of the behavior of structures affected by ASR and DEF. For both mechanisms, concrete is subjected to expansive forces over time, resulting in cracking of the HCP and aggregates, as mentioned in Section 2.2. To take into account the ability of continuous growth of DEF in a later age, the expression of ASR expansion over a given time, namely, Eq. (2-43), can be adapted, as follows:

$$\varepsilon_{DEF}(t) = \varepsilon_{DEF}(\infty)\frac{1-\exp(-t/\tau_C)}{1+\exp(-t/\tau_C+\tau_L/\tau_C)}\left(1-\frac{\phi}{\delta+t}\right) \tag{2-44}$$

where $\varepsilon_{DEF}(t)$ is the DEF-induced expansion over a given period of time t; $\varepsilon_{DEF}(\infty)$ is the swelling potential of DEF; ϕ and δ are two corrective durations, where $0<\phi<\delta$, to adjust the end of the DEF expansion curve, as shown in Figure 2-10.

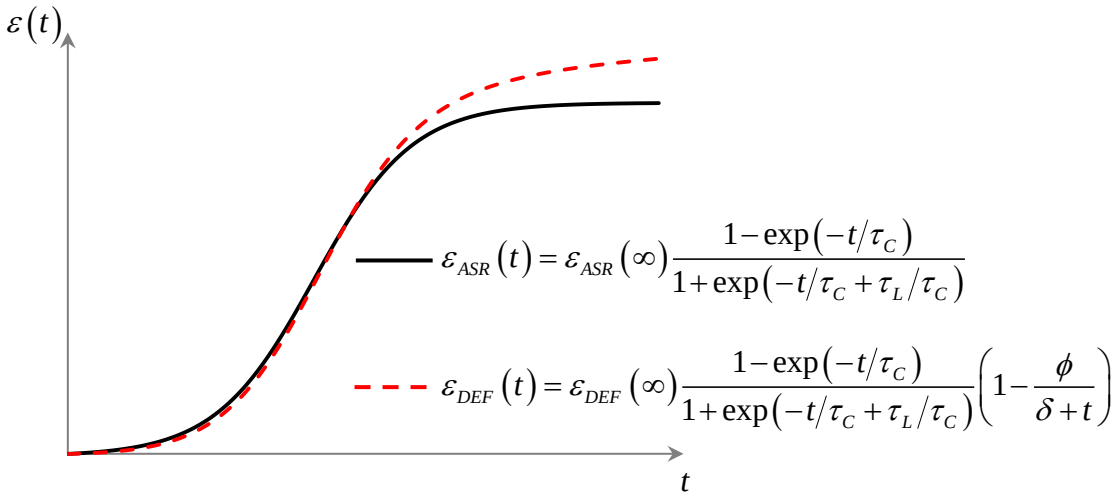

Figure 2-10 Comparison of Typical ASR and DEF Expansion Curves

CHAPTER III

EXPERIMENTAL PROGRAM — SPECIMEN DESIGN AND CONSTRUCTION

3.1 OVERVIEW

In recent years, a significant number of RC bridge structures have been exposed to premature concrete deterioration due to ASR and DEF. The primary objective of this study is to determine the strength and overall behavior of D-regions that are influenced by ASR/DEF. Thus, the structural performance of large-scale RC specimens designed to represent two typical bridge bents in Texas was experimentally examined. Moreover, the effect of premature concrete deterioration due to evolving ASR/DEF was investigated on large-scale specimens. The following sections present the development of these large-scale specimens to be structurally tested in this study.

3.2 REPRESENTATIVE PROTOTYPES

As discussed in Chapter II, some RC bridge bent caps in Texas have shown signs of ASR or DEF distress in their D-regions. As shown in Figure 3-1, two bridge bents were selected as the basis for designing the specimens to be tested in this study based on current bridge structures in Texas. Cantilever bents, as shown in Figure 3-1a, are typically designed with minimum compression steel in the bent caps based on bending theory or STM design methods. Therefore, a similar singly reinforced bent cap is considered in the specimen design. Straddle bents, as shown in Figure 3-1b, typically have both tension and compression steel in the bent caps to accommodate the alternating negative and positive moments along the bent caps. The bottom reinforcement needed

for positive moment at the mid-span region of the bent caps is normally terminated within the beam-column joint region. This leads to a doubly reinforced bent cap section where the amounts of tension and compression steel can be similar.

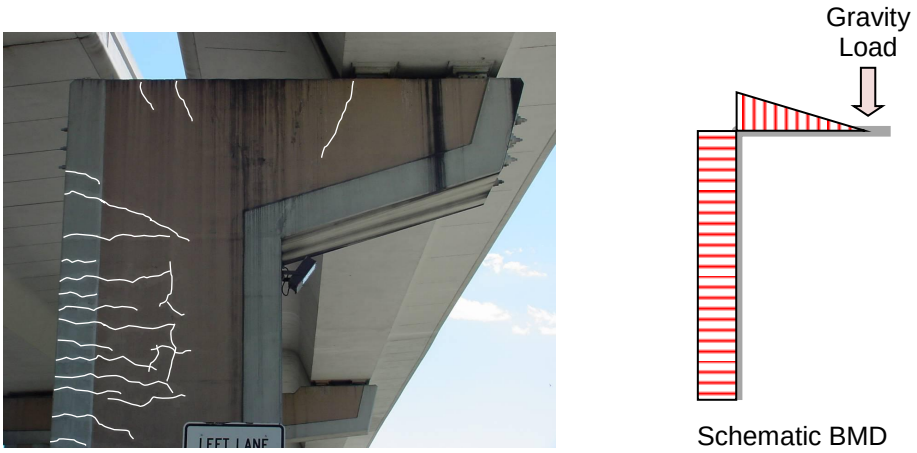

(a) Cantilever Bent (San Antonio, TX)

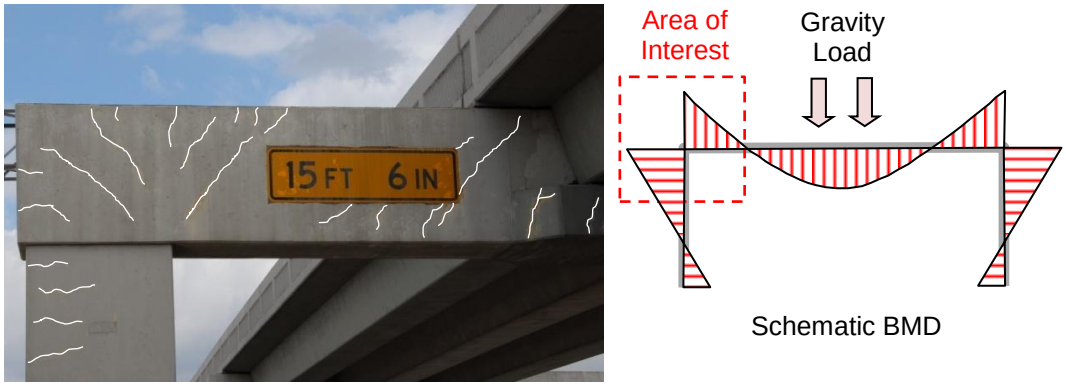

(b) Straddle Bent (Houston, TX)

Figure 3-1 Prototype Reinforced Concrete Bridge Bents

3.3 SPECIMEN DEVELOPMENT

This section presents the development of the experimental specimens in this study including the specimen design, the reinforcement detailing, the concrete mix design used to accelerate ASR/DEF mechanisms, the heating system for raising concrete curing temperatures to promote DEF, and the internal instrumentation to monitor internal behavior of the reinforcing steel and core concrete.

3.3.1 Specimen Design and Detailing

The experimental specimens in this study were designed as C-shaped sub-assemblages consisting of two D-regions (Figure 3-2). Four specimens were constructed with the same design. While one of these specimens represented the control, the other three were employed to investigate the influence of ASR/DEF. The C-shaped specimens had a constant cross-section, 24 inches (610 mm) wide by 36 inches (915 mm) deep. The only deviation from symmetry was the varying compression steel in the bent caps. Due to their large size, an essential feature was to ensure the specimens could be structurally tested using a self-reacting system as shown in Figure 3-2a. This test setup provided an axis of symmetry at the specimen's centerline. Considering the prototype structures shown in Figure 3-2b, the scale factor for the specimens in this study was approximately 50% to 75% of full-scale structures.

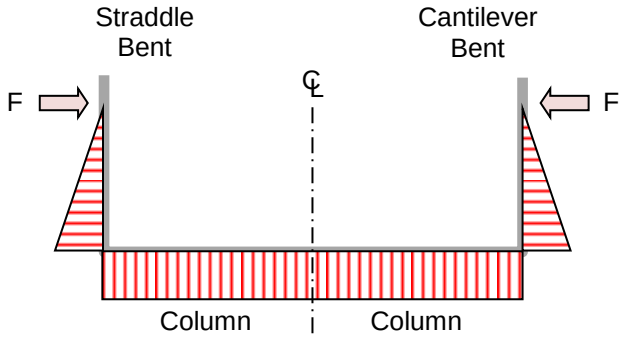

(a) Experimental Specimen Development

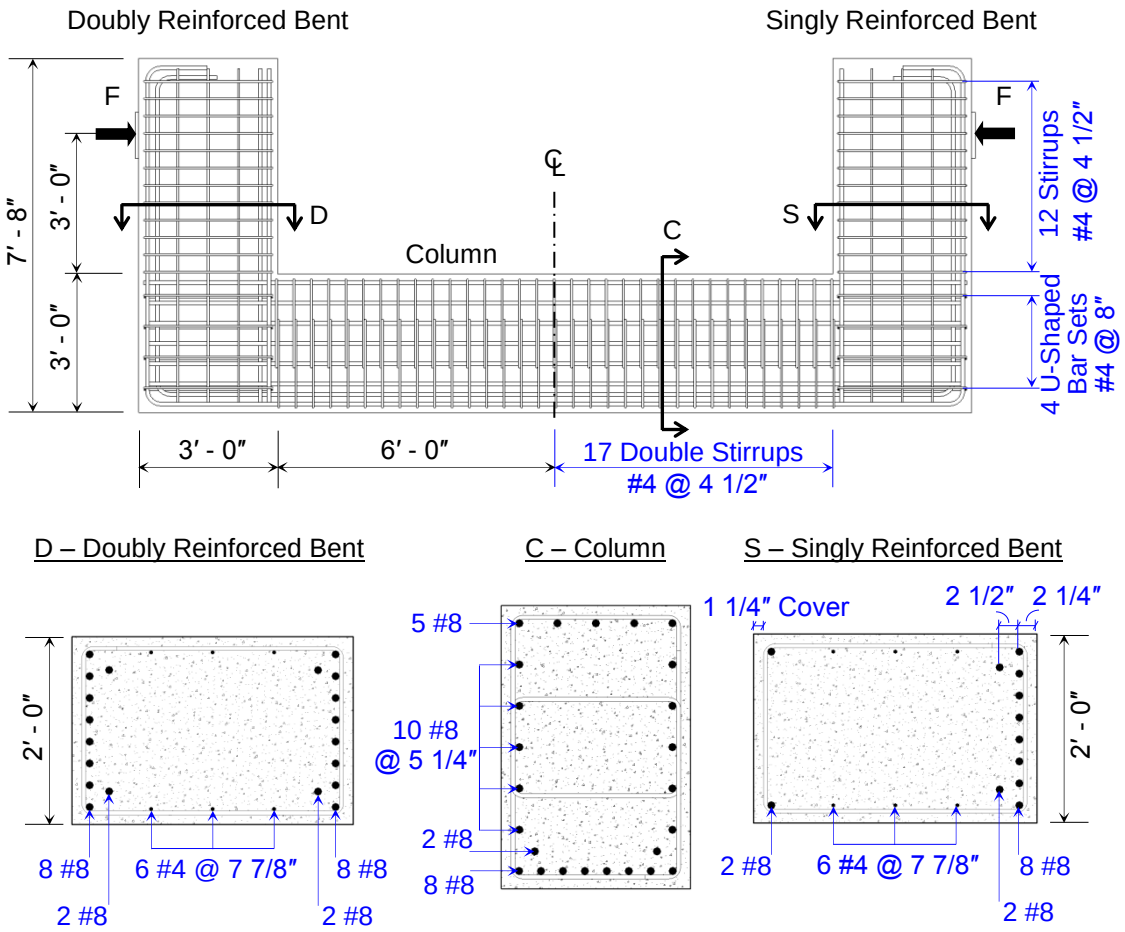

(b) Reinforcement Detailing

Figure 3-2 Experimental Specimen

Figure 3-2b presents the dimensions and reinforcement detailing of the C-shaped specimens. The longitudinal reinforcement, scaled to represent the cantilever and straddle bents, consisted of ten #8 bars (1.0 inch/25 mm diameter) running continuously on the tension side of the specimen and hooked at the end of each bent. The singly reinforced bent cap section (S) had only two #8 bars on the compression side. These bars are necessary and required for construction purposes in order to tie the transverse steel and form an enclosed cage. The doubly reinforced bent cap section (D) had ten #8 bars in both the tension and compression sides of the bent.

The longitudinal side face reinforcement along the bent cap consisted of three sets of equally spaced #4 bars (0.5 inch/13 mm diameter) as typical in past construction. The transverse reinforcement in bent caps consisted of closed #4 stirrups with a spacing of 4.5 inches (114 mm) starting at the column face. The longitudinal column reinforcement, in addition to the ten #8 bars used in the tension side, consisted of five sets of equally spaced #8 bars throughout the mid-region of the column section and five #8 bars along the compression side. The transverse column reinforcement consisted of equally spaced overlapping #4 hoops with a spacing of 4.5 inches (114 mm). The beam-column joint was reinforced with four #4 U-shaped bar sets spliced in the bent face at 8 inches (203 mm) spacing.

3.3.2 Specimen Construction and Curing

For the construction of each specimen, the concrete mix used in this study was designed for a target compressive strength of 5000 psi (34.5 MPa). Table 3-1 summarizes the mix proportions of the concrete used. Type III cement with a high alkali

content from Lehigh Cement in Evansville, PA was used in order to more aggressively promote both ASR and DEF deterioration mechanisms in the concrete. Siliceous reactive coarse gravel aggregate with a maximum size of 1 inch (25 mm) from Hanson Aggregate in Garwood, TX was mixed with reactive fine aggregate from Wright Materials in Robstown, TX. Sodium hydroxide (NaOH) solution with a target density in the specimens of 5.7 lb/yd^3 (3.4 kg/m^3) was added to further provide alkalis and accelerate ASR/DEF formation. The water/cement ratio for the concrete mix was w/c=0.48.

Table 3-1 Concrete Mix Proportions

Composition	Saturated Surface Dry (SSD) Weight unit: lb/yd^3 (kg/m^3)
Cement	752 (446)
Coarse Aggregate	1350 (801)
Fine Aggregate	1439 (854)
Water	361 (214)
Sodium Hydroxide (NaOH)	5.7 (3.4)

To promote the development of DEF in the concrete, the specimens were heated using electrical resistive wiring (ERW) to maintain concrete curing temperatures above 170 ˚F (77 ˚C) for at least two days, as shown in Figure 3-3. Each side of the formwork was insulated to maintain the internal curing temperature and supplemental heat. The ERW was pre-installed in the top and bottom faces of formwork and covered with stainless steel. In addition, to create a more uniform heat distribution, ERW was fed through cross-linked polyethylene (PEX) tubes located in the middle of specimen width.

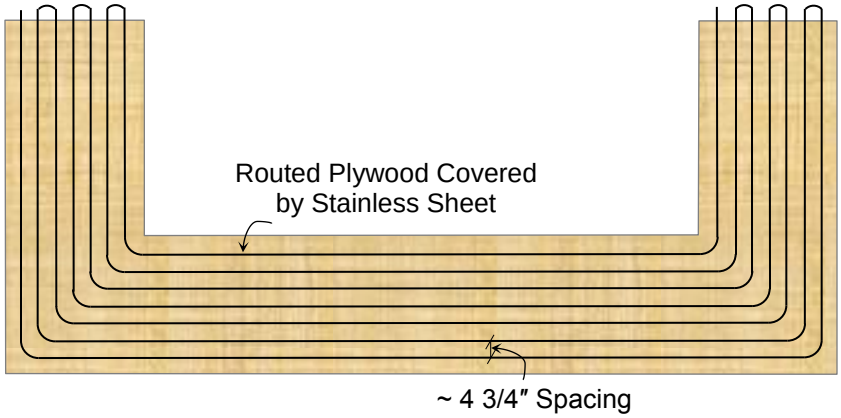

(a) Layout of ERW for Top and Bottom Faces of Formwork

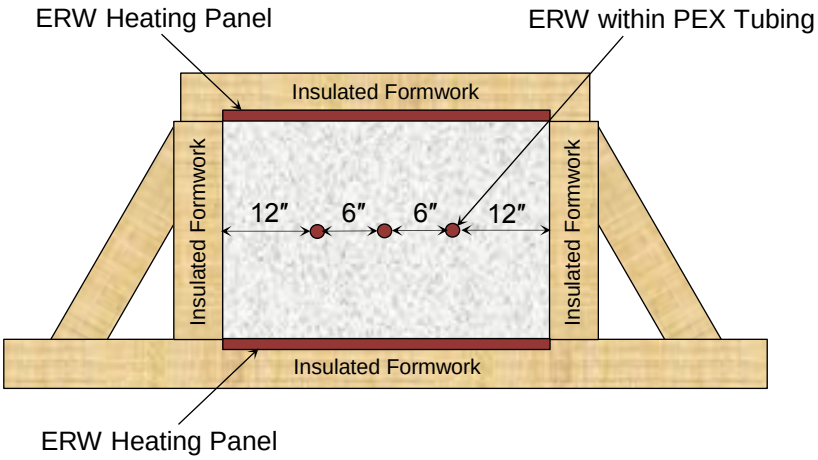

(b) Cross-Sectional View of ERW Layout

(c) ERW Panels in Position

Figure 3-3 Heating Arrangement Using Electrical Resistive Wiring (ERW)

In order to ensure that the curing temperature was above 170 ˚F and maintained for at least two days, 32 type T thermocouples manufactured by OMEGA Engineering, Inc. were embedded in each specimen to monitor the curing temperature and to actively control the ERW using a feedback loop (Figure 3-4). Figure 3-5 shows the typical curing temperature history at various locations in the concrete.

3.3.3 Internal Instrumentation

To measure the strain in the specimen's reinforcing steel, 2-element 90-degree, type UFCA-5-11 strain gages, produced by Tokyo Sokki Kenkyujo Co. Ltd. (TML), were attached to selected critical reinforcement locations for each specimen. To ensure that the strain gages were able to function properly after concrete casting and several potential years of environmental exposure conditions, a technique to attach strain gages to the reinforcing steel was carefully studied, experimentally tested, and eventually developed, as described below.

First, the ribs of the reinforcing steel at the designated locations for the strain gages were ground down with an electric grinder and carefully sanded with 200-grit sandpaper to create a 4-inch (102-mm) long smooth surface to mount the strain gage (Figure 3-6a). Vishay CSM-2 degreaser was then used to clean the smoothed surface areas. Subsequently, 400-grit extra fine sandpaper was used along with Vishay M-Prep Conditioner A to further smooth and clean the surface areas, followed by the application of Vishay M-Prep Neutralizer 5A to neutralize the residual acid content in Vishay M-Prep Conditioner A on the surface areas.

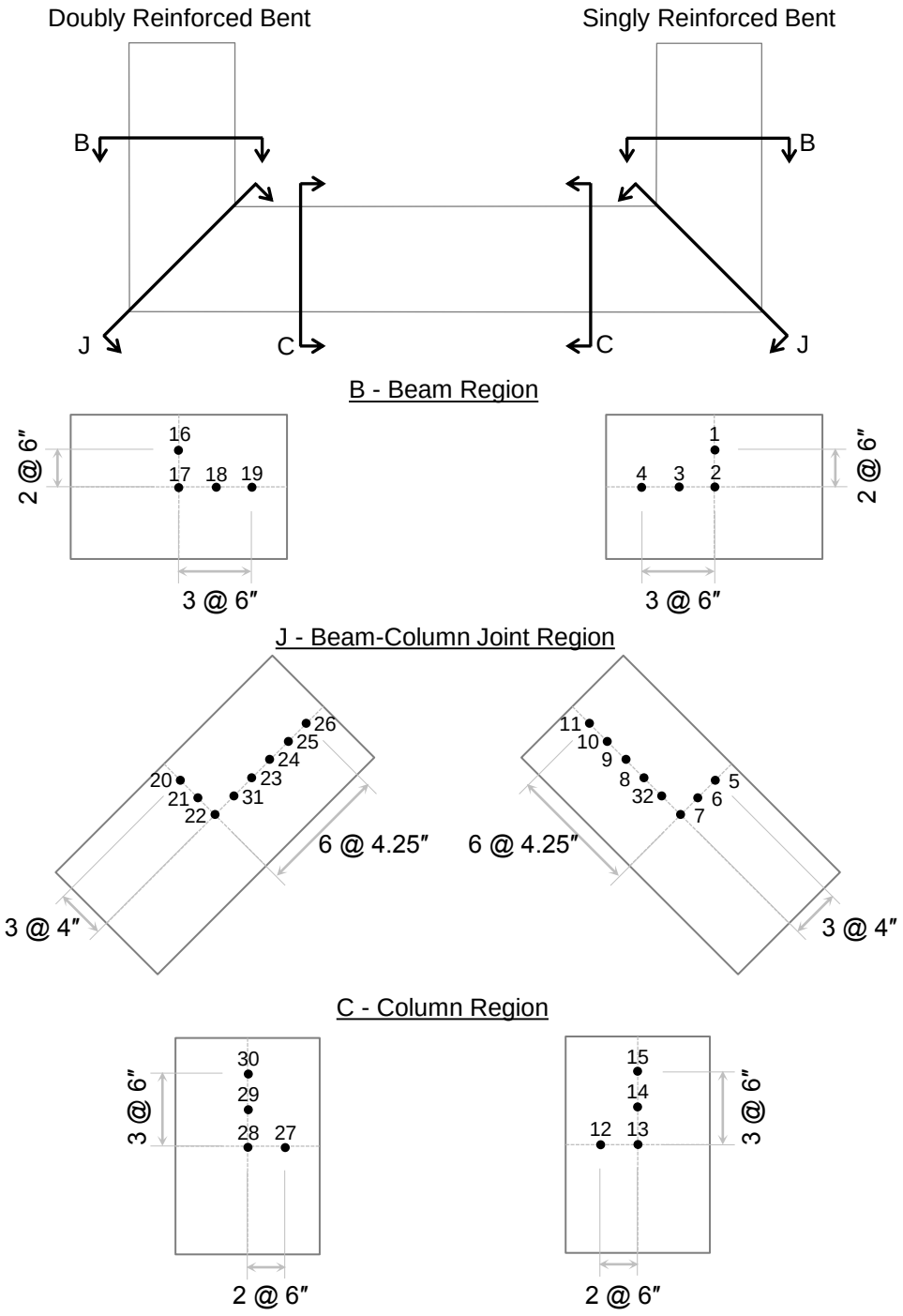

Figure 3-4 Thermocouple Locations

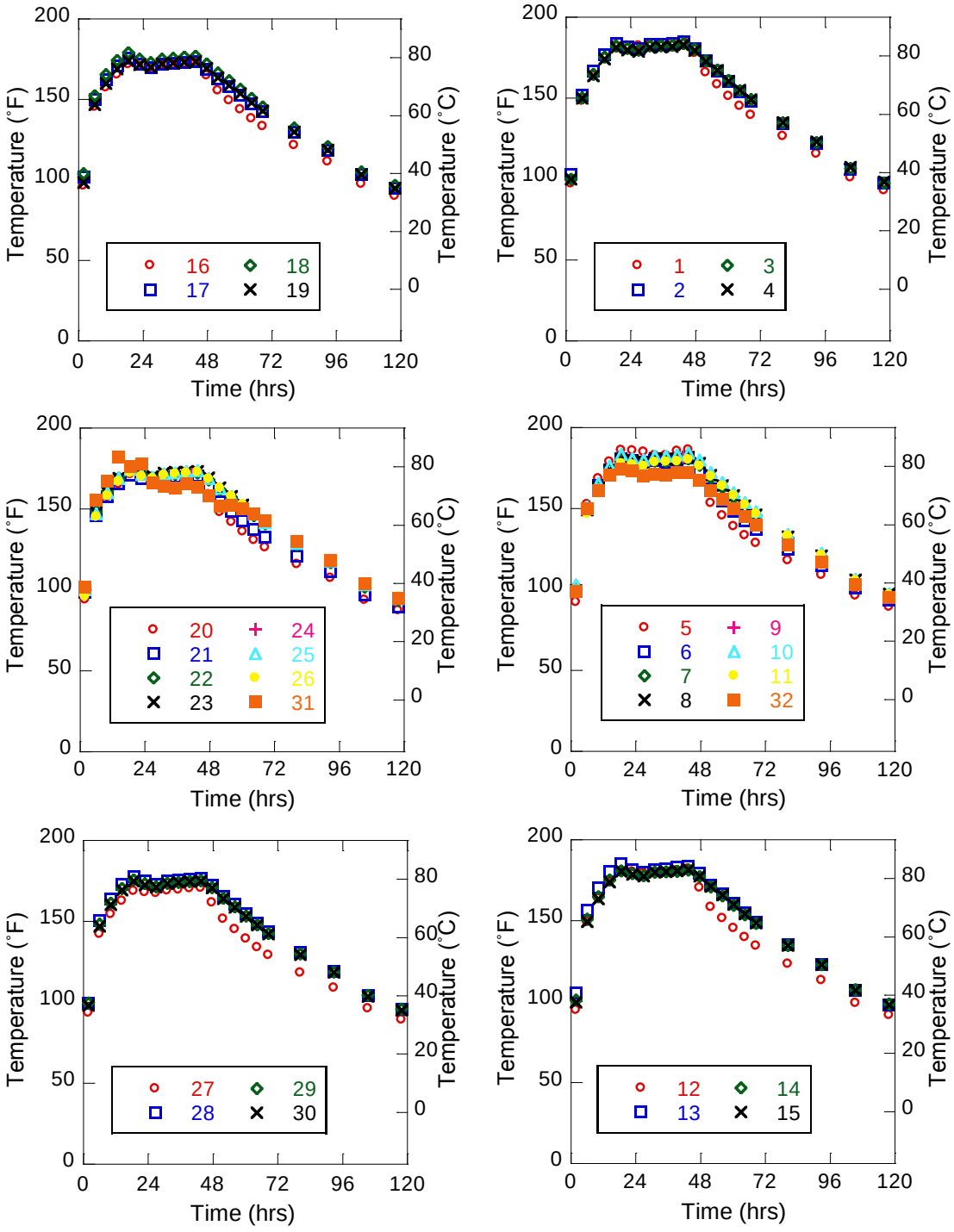

Figure 3-5 Typical Curing Temperature History

After the surface areas at the designated locations were cleaned, the strain gages were glued to the reinforcing steel using Vishay M-Bond GA-2 adhesive (Figure 3-6b). Teflon wires were used to create two half-bridge connections and Vishay TEC-1 Tetra-Etch was applied on the end of the wires, serving as the treatment agent for Teflon surface. Each wired strain gage, as shown in Figure 3-6c, was then checked using Vishay P3 Strain Indicator to ensure that the gage was functional.

(a) Grinding Procedure

(b) Glued Strain Gage

(c) Wired Strain Gage

(d) First Coating

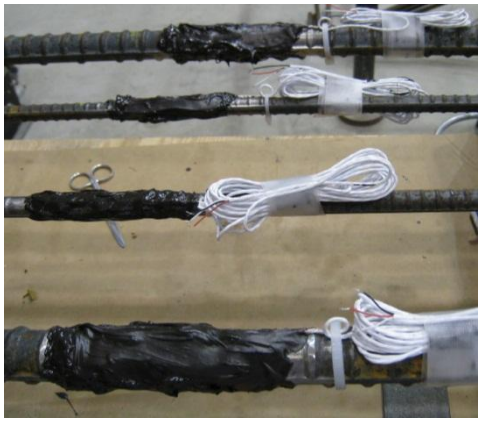

(e) Second Coating

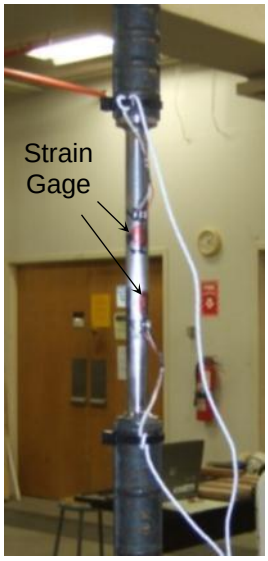

(f) Uniaxial Tension Test

Figure 3-6 Application of Strain Gages

To extend the durability of the strain gages, two layers of protective coatings were applied to cover the wired gages. Vishay M-Bond GA-2 and Vishay M-Coat J were applied as the first and second coatings, respectively, covering around the perimeter of each 4-inch (102-mm) long spot (Figure 3-6d and e). As shown in Figure 3-6f, a uniaxial tension test of a milled #8 steel bar, with two strain gages glued on smoothed surface using the same adhesive agent, was conducted to examine the durability of the glue. The results showed that the yield strength of the steel was about 65 ksi (448 MPa). Moreover, the glued strain gage could sustain a 0.02 strain, which was about nine times larger than the yield strain.

Figure 3-7 shows the selected critical locations of the reinforcing steel for the strain gages (SG). In total, 48 strain gages for the control specimen, referred to as Specimen 1, and 52 strain gages for the other three specimens, respectively referred to as Specimens 2, 3 and 4, were attached to the reinforcing steel at the designated locations. The recorded data in the specimen exposure phase and the structural testing phase are discussed in the later chapters.

Furthermore, in order to measure the strain in the core concrete, 12 concrete gages, type KM-100BT strain transducers, manufactured by Tokyo Sokki Kenkyujo Co. Ltd. (TML), were embedded in the core concrete. Figure 3-8 presents the locations of the concrete gages (KM). Three concrete gages were grouped and placed at the mid-depth of each STM compression strut, oriented in the three perpendicular directions (Figure 3-8). The recorded internal strains in the core concrete in the specimen exposure phase and the structural testing phase are presented in the later chapters.

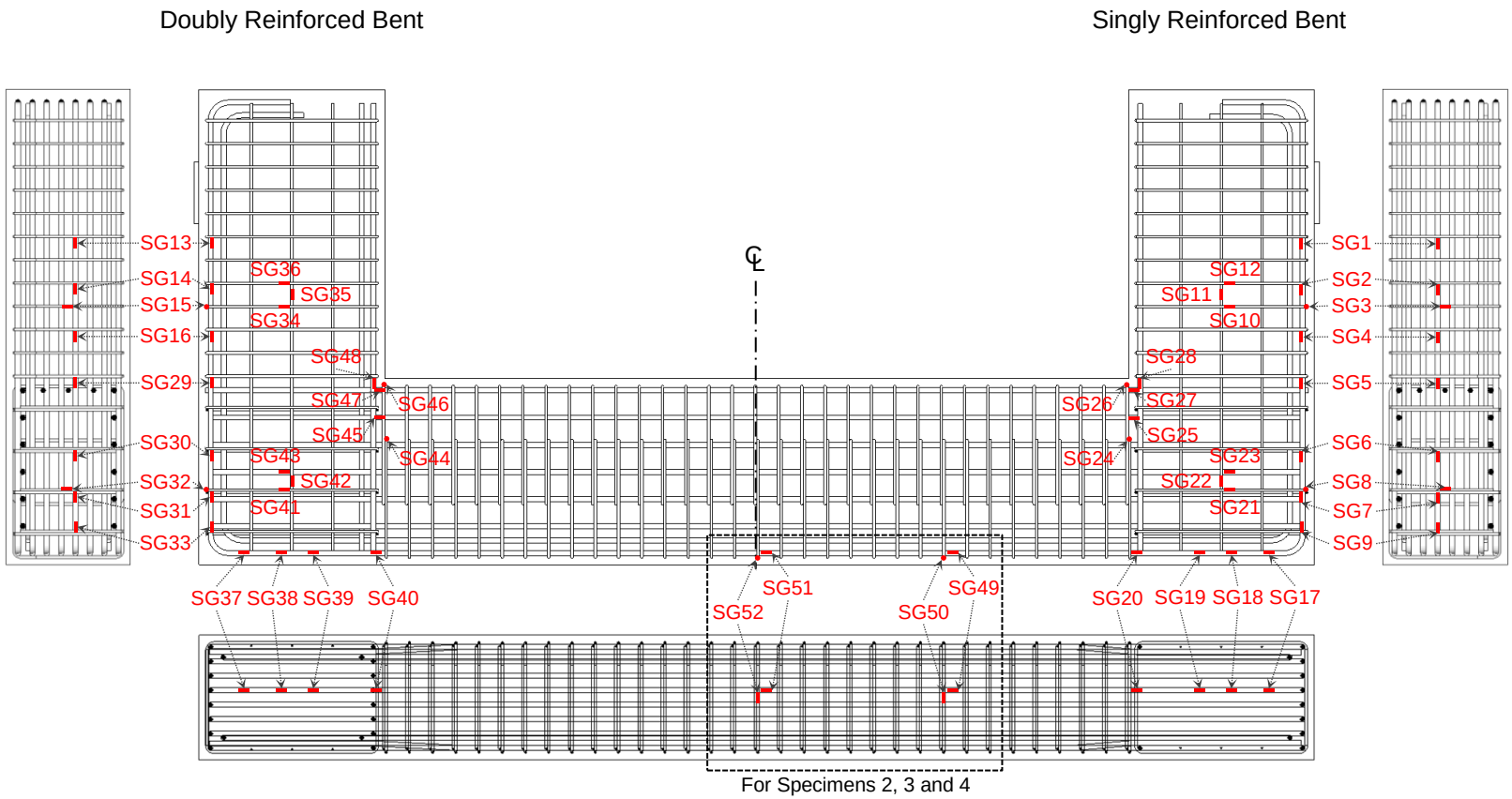

Figure 3-7 Strain Gage Locations

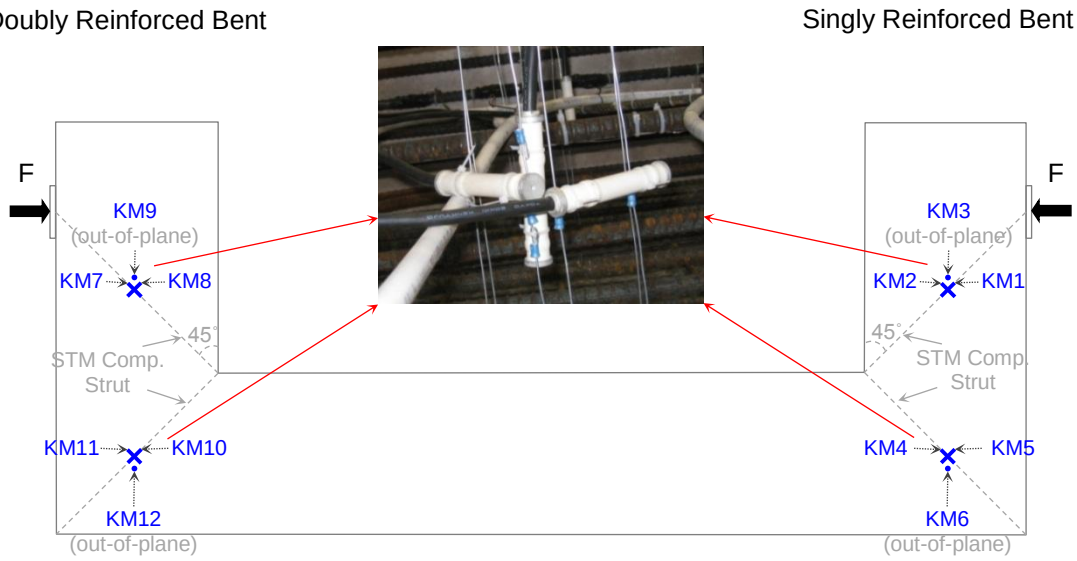

Figure 3-8 Concrete Gage Locations

3.4 SUMMARY

This chapter describes the design, construction and curing methods used for the four specimens in the experimental program. By combining high reactive aggregates along with high alkali Type III cement and a mix dosage of sodium hydroxide solution, four large-scale RC specimens representative of bridge bents with D-regions in Texas were constructed. The specimens were heated to maintain concrete curing temperatures above 170 ˚F (77 ˚C) for at least two days. The construction of the formwork and specimen fabrication process lasted from July 2008 to March 2009. After construction, one specimen was stored in the climate controlled laboratory without supplemental water serving as the control specimen, referred to as Specimen 1, and the other three specimens, referred to as Specimens 2, 3 and 4, were later transported to the Texas A&M University Riverside Campus for the exposure phase. The specimen exposure phase is presented in the following chapter.

CHAPTER IV

EXPERIMENTAL PROGRAM — SPECIMEN EXPOSURE PHASE

4.1 OVERVIEW

As discussed in Chapter III, three of the four constructed specimens, Specimens 2, 3 and 4, were first preloaded to simulate gravity load conditions of field structures and then transported to the Texas A&M University Riverside Campus for their exposure phase. This chapter presents the external instrumentation for monitoring concrete surface expansion during the exposure phase, the pre-loading setup to mimic the in-service gravity load effect, the specimen exposure conditions, and the setup of supplemental watering system for specimen's exposure phase. Visual observations of cracking, surface concrete strains, internal concrete strains, and reinforcing steel strains of these specimens over time are documented. The petrographic analysis results of cores extracted from specimens after structural testing are also presented.

4.2 DEVELOPMENT OF EXPOSURE PHASE OF SPECIMENS

This section highlights the development of the exposure phase of Specimens 2, 3 and 4. The external instrumentation for concrete surface strain measurements, the setup for pre-loading application, the specimen exposure conditions in field, and the supplemental watering system for these specimens are described as follows.

4.2.1 External Instrumentation

After specimen construction, 130 demountable mechanical (DEMEC) points were installed in the concrete surface of Specimens 2, 3 and 4, creating a grid of 218 measurements between two adjacent DEMEC points. Each DEMEC point was composed of a brass insert and a measurement tip manufactured by ELE International. In accordance with the grid of DEMEC points, 7/16 inch (11.1 mm) holes were drilled 7/8 inch (22.2 mm) deep into the specimens (Figure 4-1a). Subsequently, a low-creep epoxy was used to permanently hold the brass inserts in the concrete holes (Figure 4-1b). Then, the measurement tip was fixed to each brass insert (Figure 4-1c and d).

(a) Hole-Drilling Procedure

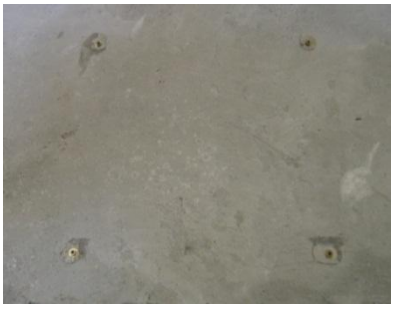

(b) Glued Brass Inserts

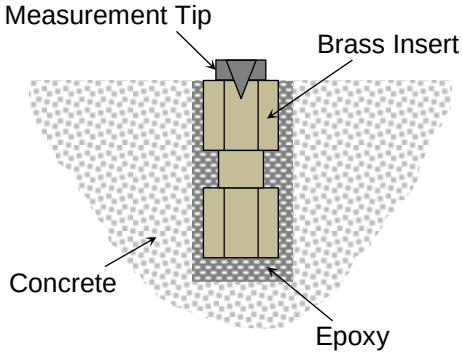

(c) Schematic DEMEC Point

(d) Installed DEMEC Point

Figure 4-1 Installation of DEMEC Points

As discussed in Section 3.3.1, Figure 4-2 depicts the beam, column, and beam-column joint regions of the experimental specimens according to the design of the C-shaped sub-assemblages that consisted of two D-regions in each specimen. Figure 4-3 shows the labels of each concrete surface that consisted of DEMEC points, and Figure 4-4 presents the layout of DEMEC points for each face of the specimen. On the side face (SF) of the specimen, the grid was typically spaced at 10 1/2 inches (267 mm). For the out-of-plane faces, that is, the column face (CF), the beam face on the tension side (BFT), and the beam face on the compression side (BFC), the DEMEC points were typically spaced at 10 1/2 inches (267 mm) in the longitudinal direction and 9 3/4 inches (248 mm) in the out-of-plane direction.

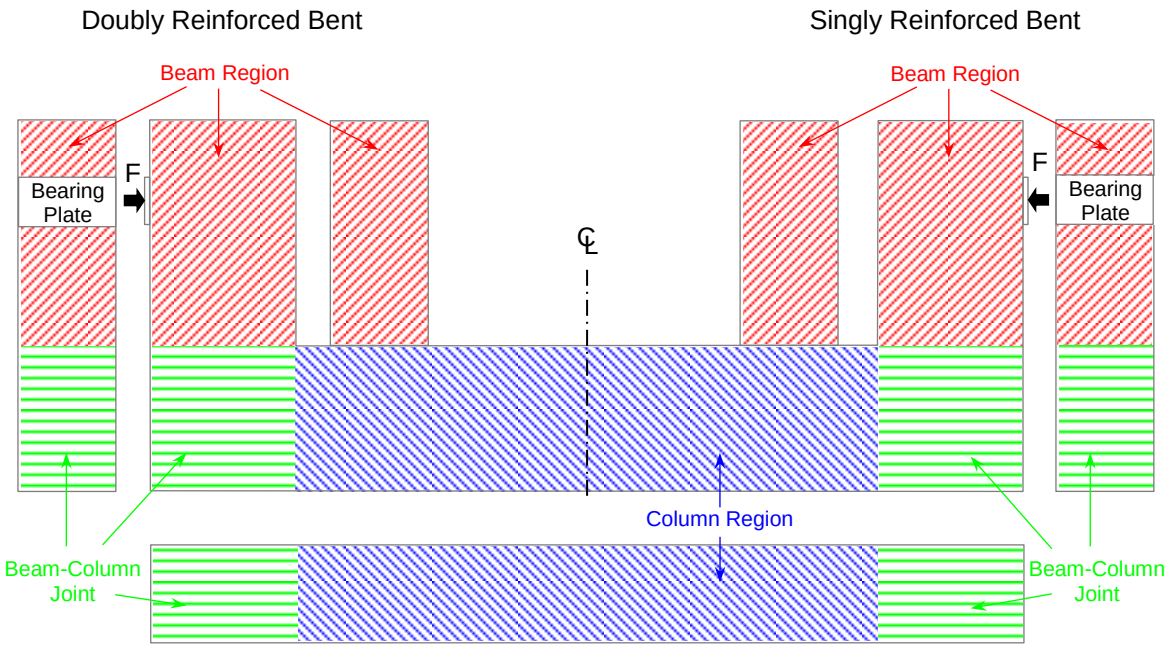

Figure 4-2 Layout of Beam, Column and Beam-Column Joint Regions

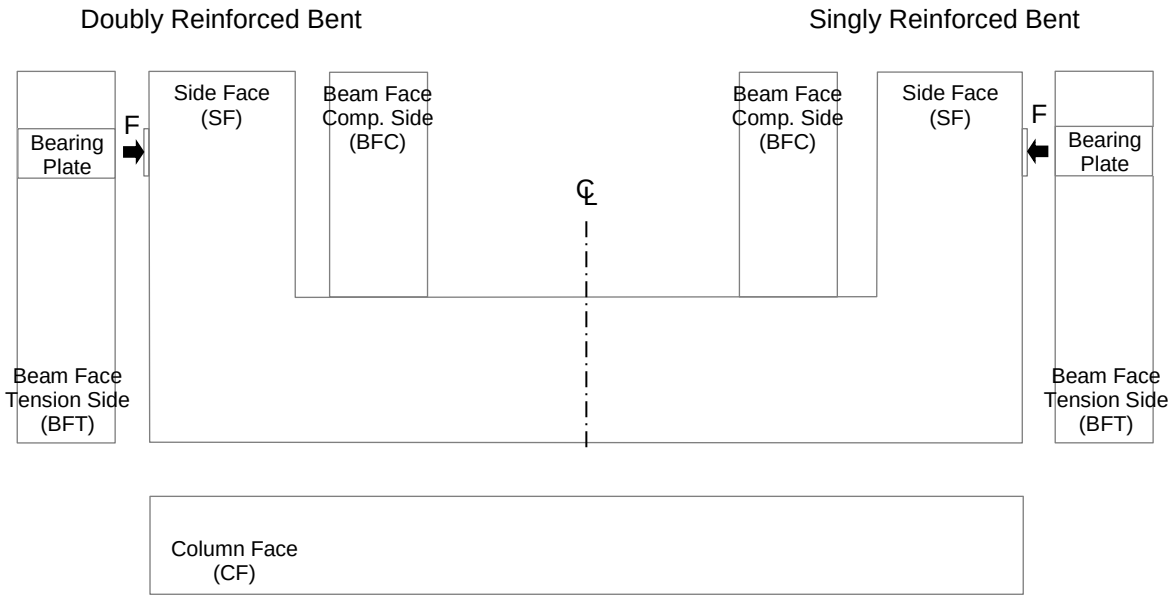

Figure 4-3 Labels of Each Concrete Surface with DEMEC points

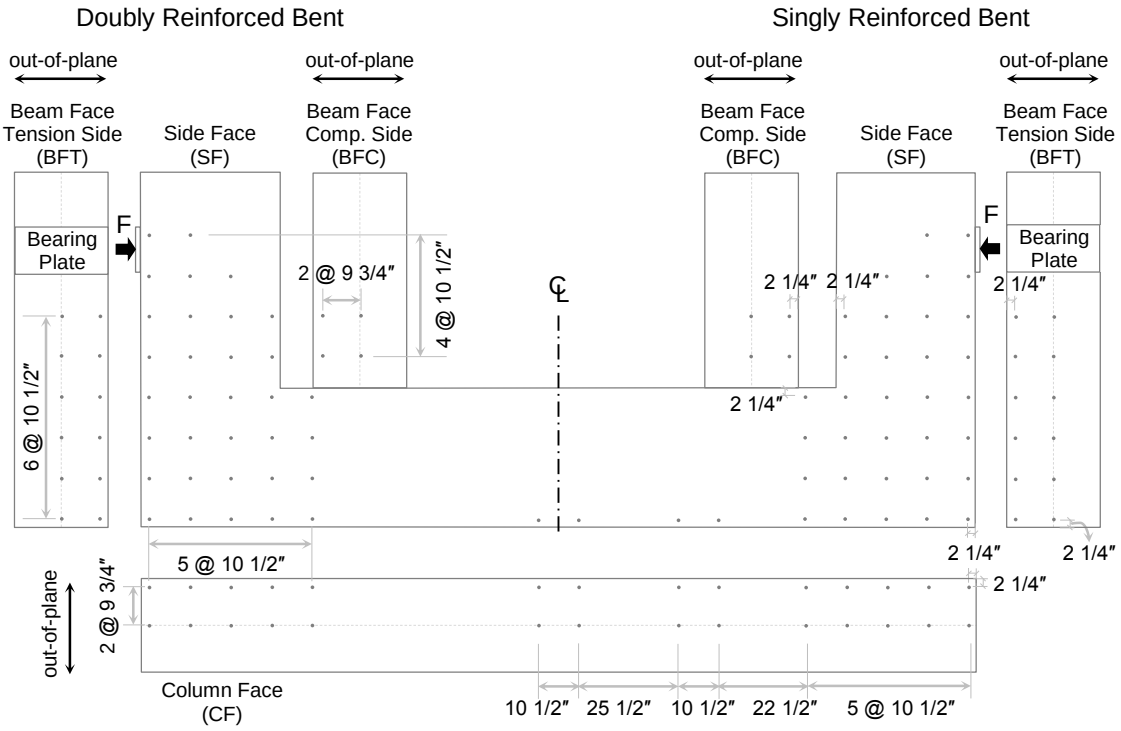

Figure 4-4 Layout of DEMEC Points

Once the installation was completed, a Mitutoyo 551-224-10 digimatic caliper with a LCD display resolution of 0.0005 inches (12.7 μm) and an accuracy of ± 0.002 inches (0.05 mm) for measurements up to 18 inches (457 mm) was used to measure the initial lengths of two adjacent DEMEC points. This value was later used for strain calculations as the initial length prior to specimen's exposure phase.

Figure 4-5 through Figure 4-7 present the layout of the DEMEC measurements (DM). These measurements were grouped by their directions and locations, namely, longitudinal readings in the beam and column, transverse readings in the beam and column, diagonal readings in the beam and beam-column joint, beam direction readings in the beam-column joint, column direction readings in the beam-column joint, and out-of-plane readings in the beam-column joint.

The concrete surface strain for each measurement DM according to Figure 4-5 through Figure 4-7, $\varepsilon_{DM}(t)$, over a given period of time t, is defined by:

$$\varepsilon_{DM}(t) = \frac{l_{DM}(t) - l_{DM}(0)}{l_{DM}(0)} \tag{4-1}$$

where $l_{DM}(t)$ is the measured length using the same Mitutoyo caliper at a given period of time t; $l_{DM}(0)$ is the initial length that was measured after the installation of the DEMEC points prior to specimen exposure.

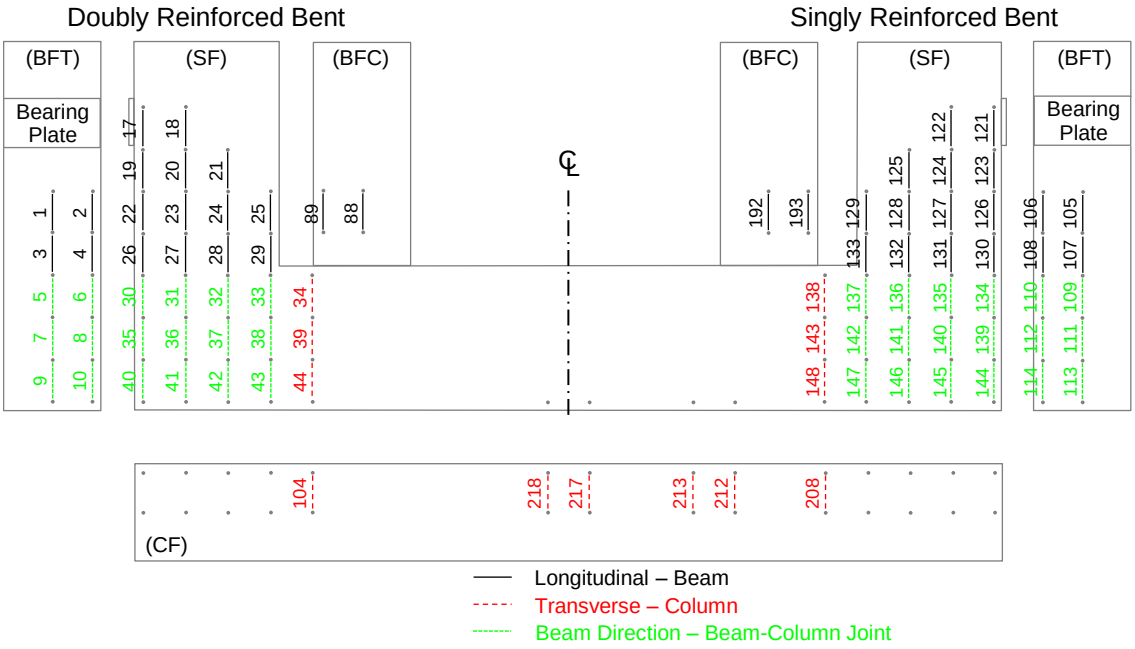

Figure 4-5 Layout of DEMEC Measurements (DM): Longitudinal Readings in Beam, Transverse Readings in Column, and Beam Direction Readings in Beam-Column Joint

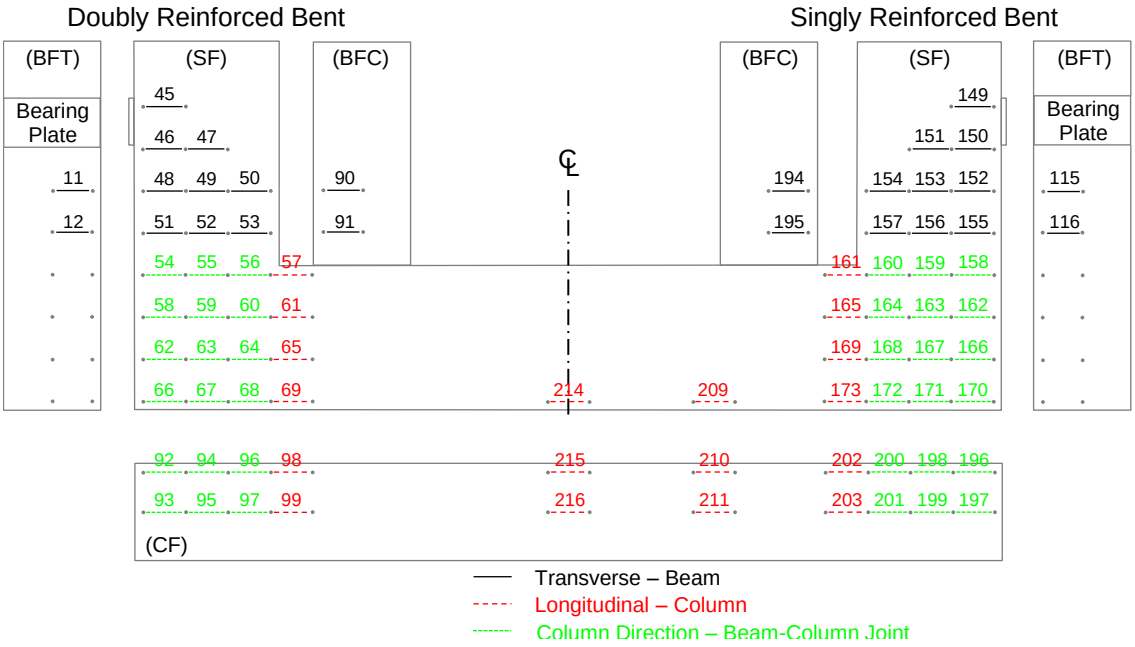

Figure 4-6 Layout of DEMEC Measurements (DM): Transverse Readings in Beam, Longitudinal Readings in Column, and Column Direction Readings in Beam-Colum Joint

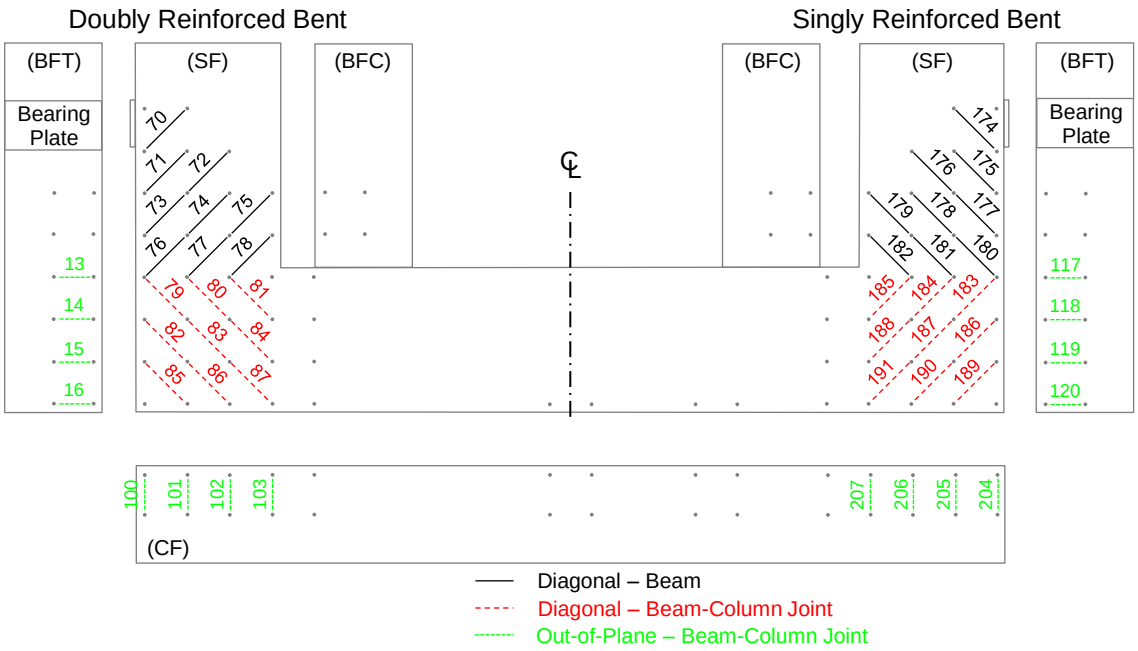

Figure 4-7 Layout of DEMEC Measurements (DM): Diagonal Readings in Beam, Diagonal Readings in Beam-Column Joint, and Out-of-Plane Readings in Beam-Column Joint

Figure 4-8 shows the critical average concrete surface strains from DEMEC measurements in the beam region. The average critical longitudinal concrete surface strains over time at different depths (L1 through L4) are compared and discussed in the later section. Moreover, the average critical transverse concrete surface strains over time (T1 through T3) were calculated and compared with the average longitudinal concrete surface strains. Figure 4-9 depicts the average diagonal concrete surface strains over time at different sections (D1 through D3), while Figure 4-10 presents the average concrete surface strains in the beam-direction (B1 and B2), column direction (C1 and C2), and out-of-plane direction (O1 and O2) over time in the beam-column joint. These strains are compared and discussed in the later section as well.

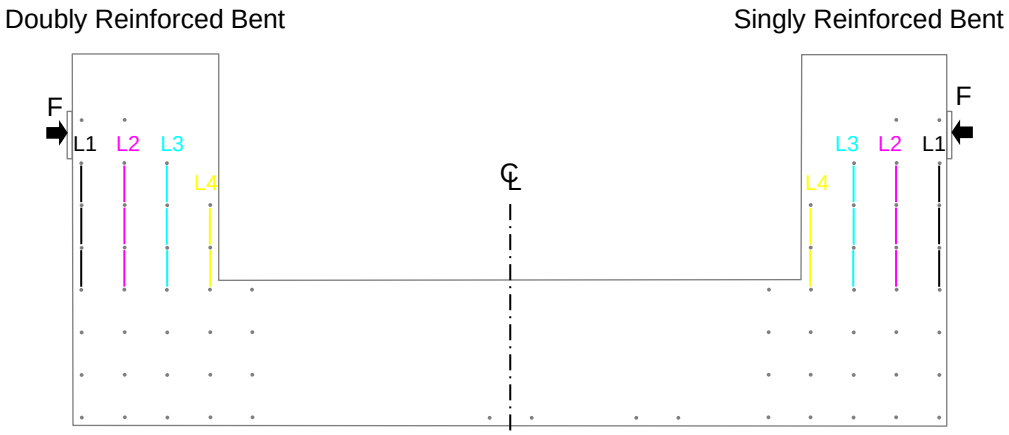

(a) Longitudinal Average Concrete Surface Strains

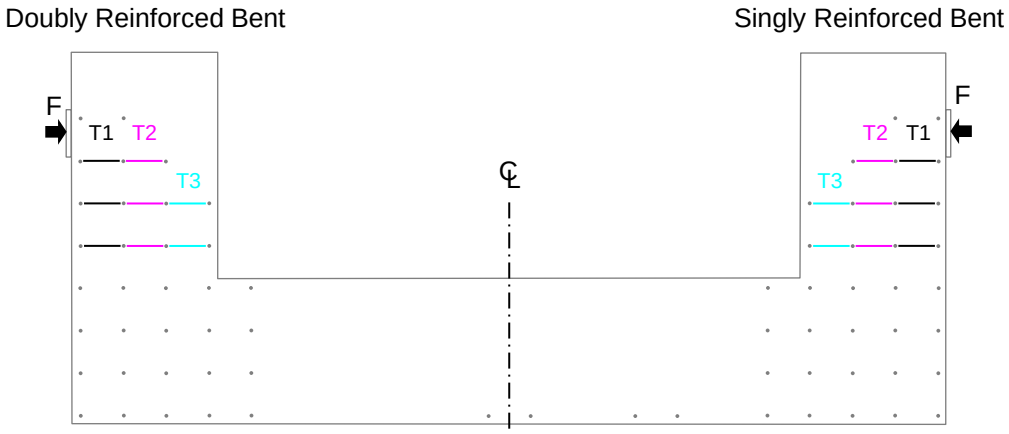

(b) Transverse Average Concrete Surface Strains

Figure 4-8 Critical Average Longitudinal and Transverse Concrete Surface Strains at Different Depths in Beam Regions

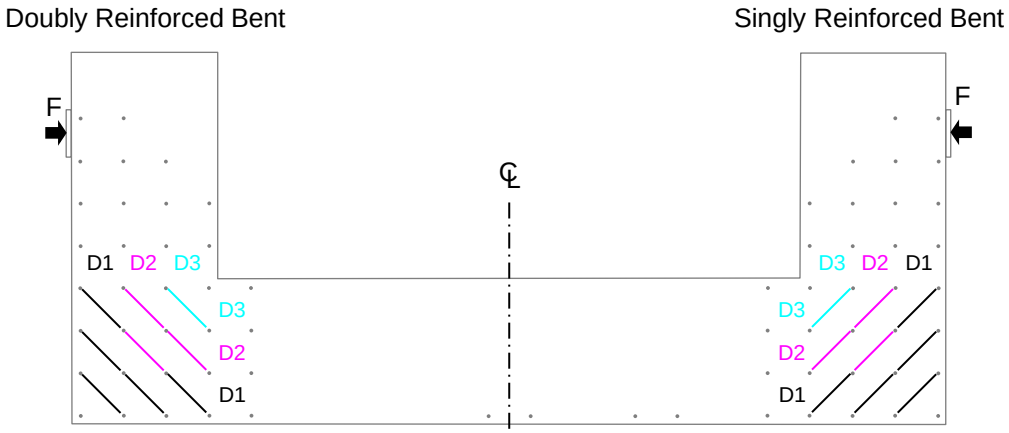

Figure 4-9 Average Diagonal Concrete Surface Strains at Different Sections in Beam-Column Joints

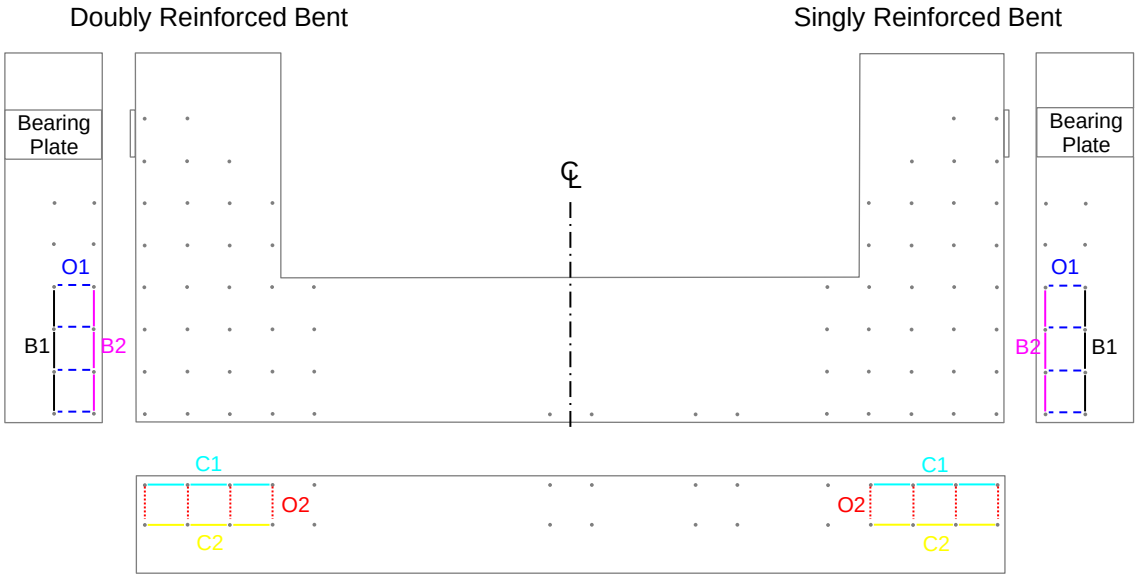

Figure 4-10 Average Concrete Surface Strains in Beam-Direction, Column-Direction, and Out-of-Plane Direction in Beam-Column Joints

4.2.2 Pre-Loading Setup

Figure 4-11 shows the application of the pre-loading applied to Specimens 2, 3 and 4. Two 1 1/4 inches (32 mm) high tensile alloy steel bars, DYWIDAG Prestressing Steel THREADBARs®, were located at a distance of 3 feet (0.91 m) from the column face with two groups of paired S 12 × 31.8 header beams to create an equal and opposite load condition for each bent (Figure 4-11). A 600-kip (2669-kN) capacity actuator was connected with a load cell to record the force exerted on the system during the pre-loading application. DYWIDAG couplers were used to extend the Threadbars for the setup during the loading and the hex nuts were then tightened to maintain the load. Moreover, strain gages were placed on the Threadbars to monitor the applied prestress force. The total force exerted on the specimen was calculated using the recorded Threadbar strains, concurrently providing a reference during the pre-loading application and giving future tendency of remaining prestress force over time during the exposure phase. This operation was undertaken in the laboratory and the actuator was removed once the pre-loading application was completed.

Pre-loading was gradually increased up to a load of about 215 kips (956 kN) when hairline diagonal cracking in the beam regions was observed. The load (determined to be about 40% of the specimen's capacity during the structural load testing) was secured into the specimen to simulate the gravity loading effects of such bents, which typically induced minor flexural cracking in field structures. Losses of prestress forces due to end anchoring were observed immediately after preloading. Figure 4-12 shows the remaining prestressing forces in each specimen after the initial

anchorage losses according to the Threadbar strain gage readings were approximately 200 kips (890 kN).

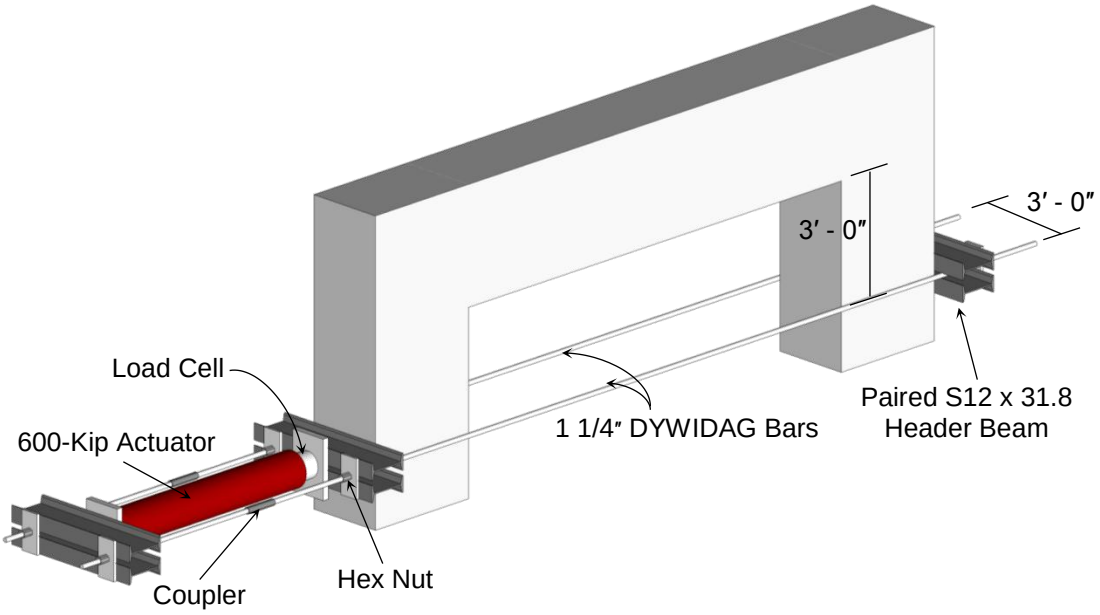

Figure 4-11 Pre-Loading Application

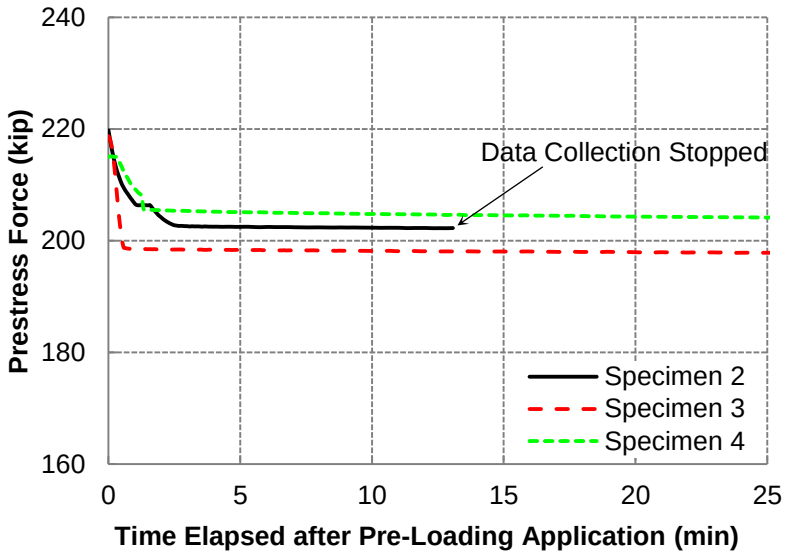

Figure 4-12 Initial Losses of Prestress Forces

The crack pattern induced by the prestress load prior to any field exposure is shown in Figure 4-13. The prestress load which is eccentric to the column centerline created a bending moment that resulted in initial flexural cracking in the column and beam regions. As the load increased, cracking developed diagonally in the beam from the loading point to the inside corner of the beam-column joint and diagonally in the beam-column joint. According to a crack comparator card, the observed cracks were merely hairline and less than 0.005 inches (0.13 mm) in width. Thus, once the specimens were exposed to field, these initial cracks potentially permitted later moisture ingress which can lead to the formation of ASR/DEF. Figure 4-14 shows the main longitudinal tension steel strains induced by prestress load were less than 0.0009, which was about 40% of steel yield strain. Note that some strain gages failed before the pre-loading application.

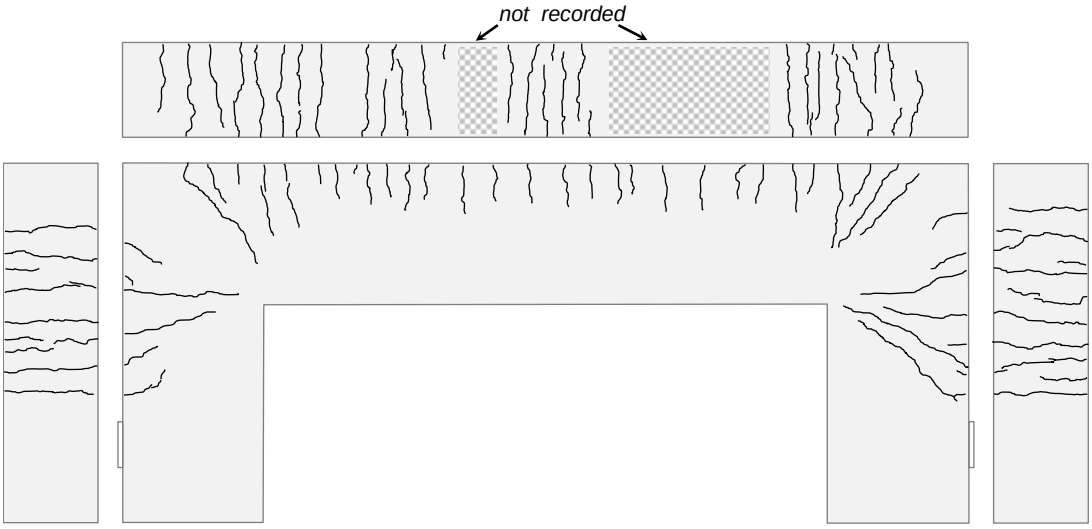

Figure 4-13 Typical Crack Pattern Induced by Pre-Loading

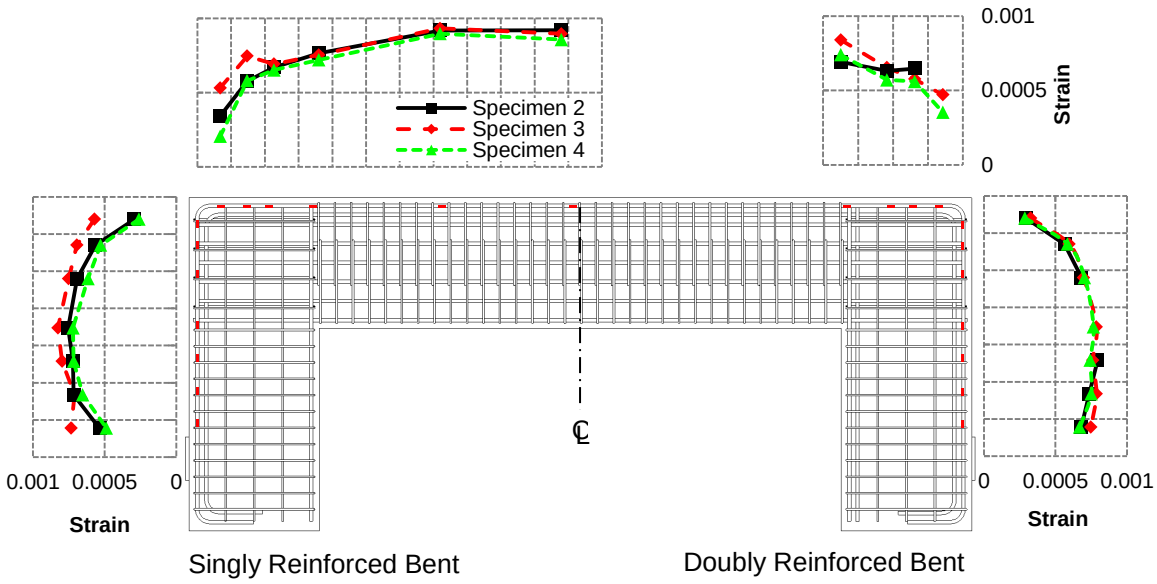

Figure 4-14 Longitudinal Tension Steel Strains Induced by Pre-Loading

4.2.3 Specimen Exposure Condition

Shortly after the application of pre-loading, Specimens 2, 3 and 4 were transported and placed at the Texas A&M University Riverside Campus for the exposure phase. Figure 4-15 shows the recorded daily average high and average low temperatures, and Figure 4-16 presents the monthly precipitation throughout the three-year period from May 2009 to August 2012 for Bryan, TX according to Weather Underground (2012). The average high temperature exceeded 80 ˚F (26.7 ˚C) from about April to October.

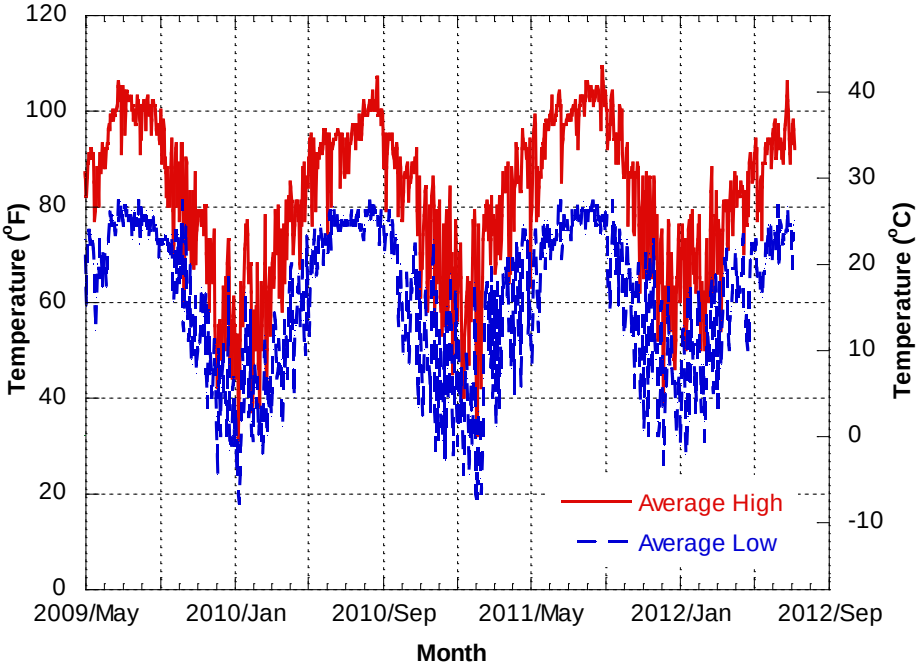

Figure 4-15 Daily Temperatures during Exposure Phase (Weather Underground 2012)

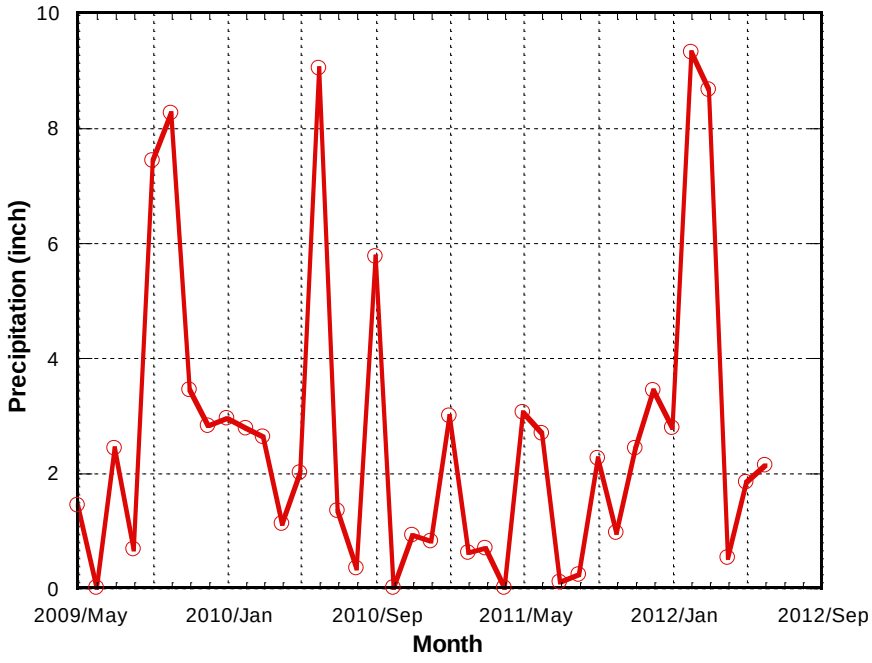

Figure 4-16 Monthly Precipitation during Exposure Phase (Weather Underground 2012)

4.2.4 Supplemental Watering System

Figure 4-17 shows the setup of the supplemental watering system and field conditions for Specimens 2, 3 and 4 during their exposure phase. To provide sufficient moisture to accelerate the formation of ASR/DEF, a sprinkler system that applied water for 15 minutes four times a day was built. As shown in Figure 4-17a, five sprinklers were installed to ensure uniform watering coverage. The specimens were placed at a clear space of approximately 6 feet (1.83 m) to ensure watering coverage of each face of each specimen (Figure 4-17b).

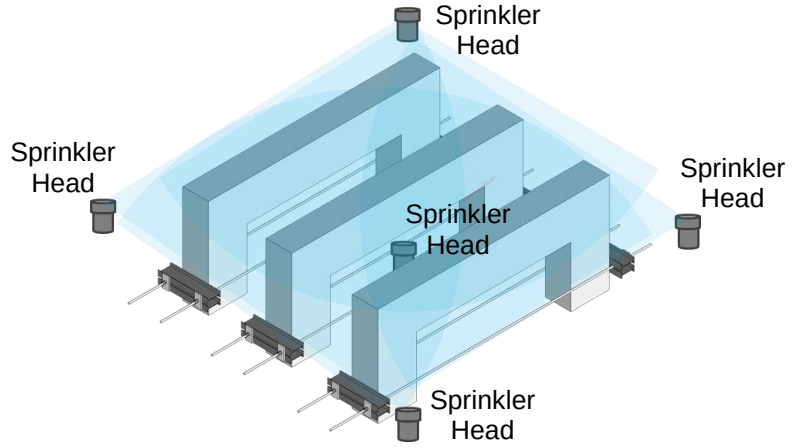

(a) Coverage of Supplemental Watering System

(b) Specimens Exposed to Field Conditions

Figure 4-17 Field Conditions for the Exposure Phase Specimens

4.2.5 Summary of Exposure Phase Specimen Development

Table 4-1 summarizes concrete casting date, age when applying pre-loading, age when utilizing supplemental watering system in the field, and age when shipping specimen back to the structural testing laboratory for each exposure phase specimen. The application of pre-loading for each exposure phase specimen was completed in one day. Shortly after the shipment to the field, the supplemental watering system was constructed and the watering regime was applied. The prestress assembly was removed shortly before specimens were transported back to the laboratory for structural load testing. Specimens 2 and 4 were shipped back after eight-month and two-year exposure, respectively. Specimen 3 exhibited more concrete expansion than Specimen 4 after two years of exposure and remains at the exposure site for future structural testing.

Table 4-1 Summary of Exposure Phase Specimen Development

Specimen	Concrete Casting	Laboratory	Field	Laboratory	Laboratory
		Prestress Applied	Supplemental Watering Applied	Transported to Lab with Prestress Removed	Structural Load Testing
		Age (days)			
2	01/13/2009	97	112	364	499
3	02/13/2009	66	81	remains in field	n/a
4	03/06/2009	45	60	808	888

∗ The concrete casting of Specimen 1 was completed on November 24th, 2008 and the structural load testing of Specimen 1 started on December 21st, 2009.

† The application of pre-loading was completed 15 days prior to the exposure phase.

4.3 VISUAL OBSERVATION

As aforementioned, the prestress loads were applied to the specimens to emulate the gravity load effects that led to the development of cracks as depicted in Figure 4-13. These load-induced cracks and new cracking due to ASR/DEF grew in length and width over time. Figure 4-18 through Figure 4-20 present the crack patterns over time for the exposed specimens. Longitudinal cracks (parallel to the longitudinal steel in the beam and column regions) were first recorded on the tension side of the beam and column faces after 76 days of exposure, with a largest crack width of 0.009 inches (0.23 mm) at the outside corner of the beam-column joint. After a 129-day exposure, white residues were first noticed on the concrete surface (Figure 4-21). Moreover, new longitudinal cracks were observed on the side face (SF) with a largest crack width of 0.010 inches (0.25 mm) and some map cracking due to ASR/DEF was also noticed, merging with prestress load-induced cracks. The largest existing longitudinal crack at the outside corner of the beam-column joint was measured as 0.025 inches (0.64 mm) and 0.050 inches (1.27 mm) in width after 150-day and 192-day exposure, respectively. More excessive map cracking and longitudinal cracks on the compression side of the main elevation face were observed after 406-day exposure. The maximum crack width of the longitudinal cracks on the column face was greater than 0.060 inches (1.52 mm), while 0.050 inches (1.27 mm) was measured as the largest longitudinal crack width on the main elevation face.

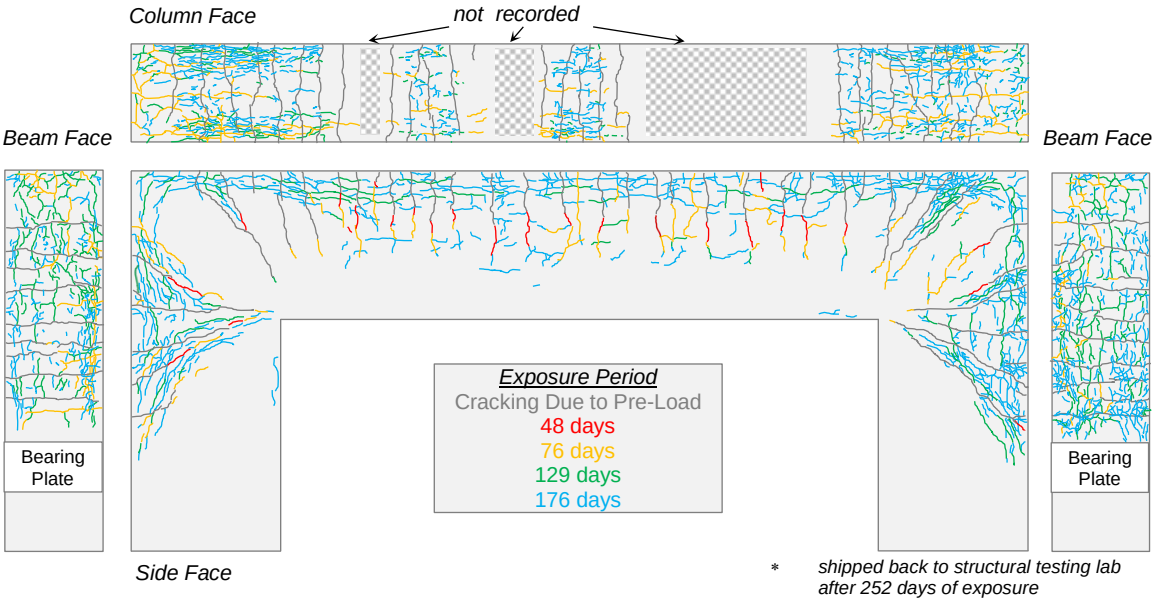

(a) Overall Crack Pattern

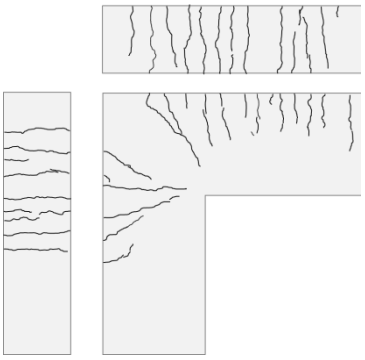

(b) 48 Days of Exposure

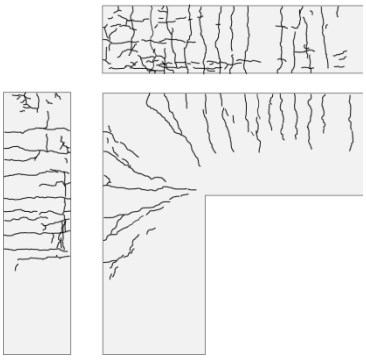

(c) 76 Days of Exposure

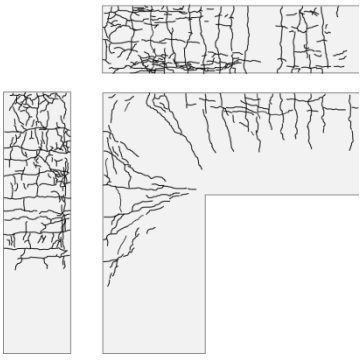

(d) 129 Days of Exposure

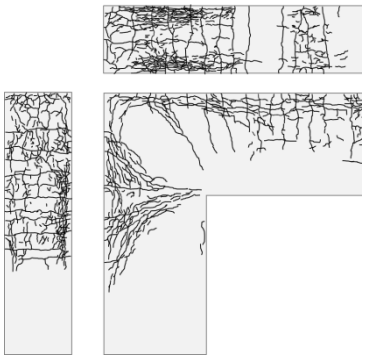

(e) 176 Days of Exposure

Figure 4-18 Crack Pattern over Time – Specimen 2

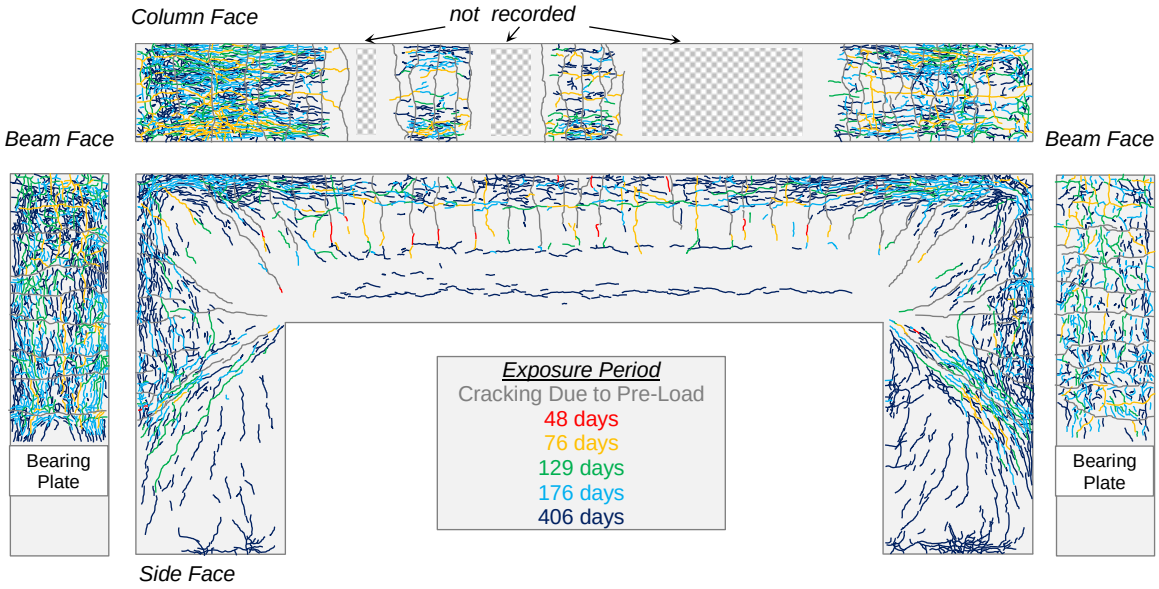

(a) Overall Crack Pattern

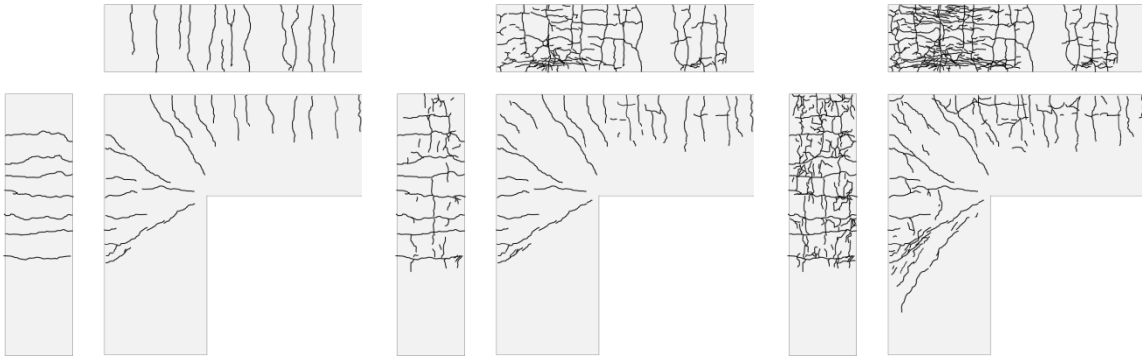

(b) 48 Days of Exposure *(c) 76 Days of Exposure* *(d) 129 Days of Exposure*

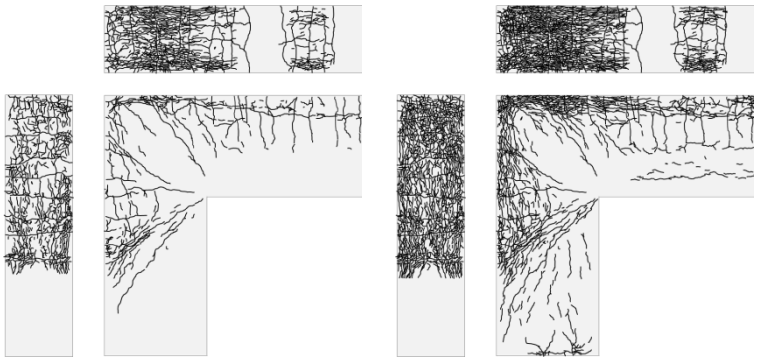

(e) 176 Days of Exposure *(f) 406 Days of Exposure*

Figure 4-19 Crack Pattern over Time – Specimen 3

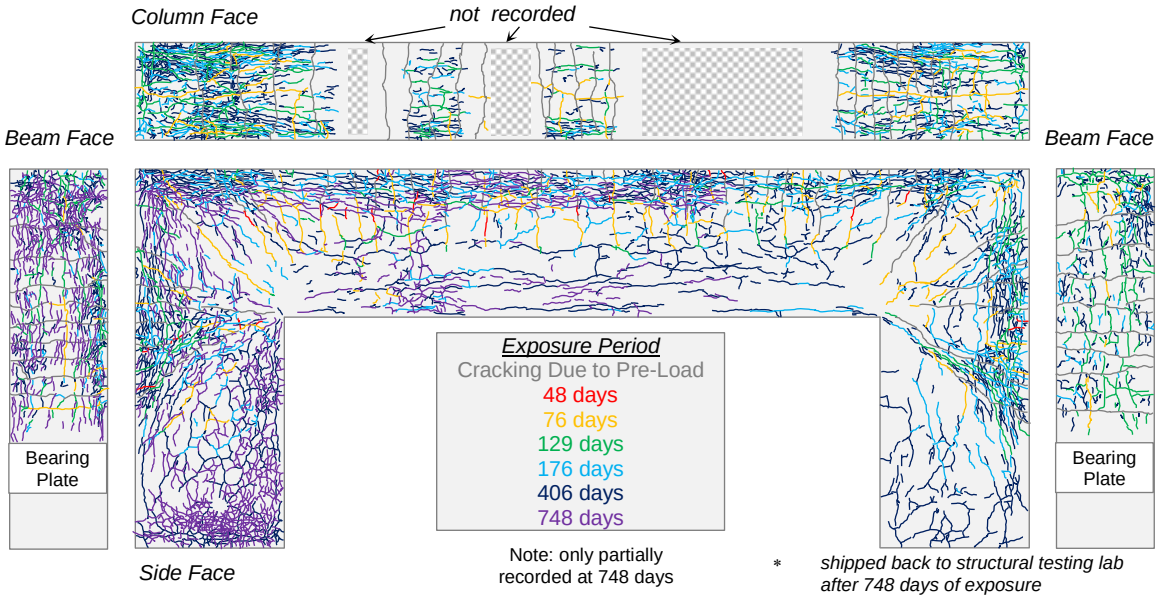

(a) Overall Crack Pattern

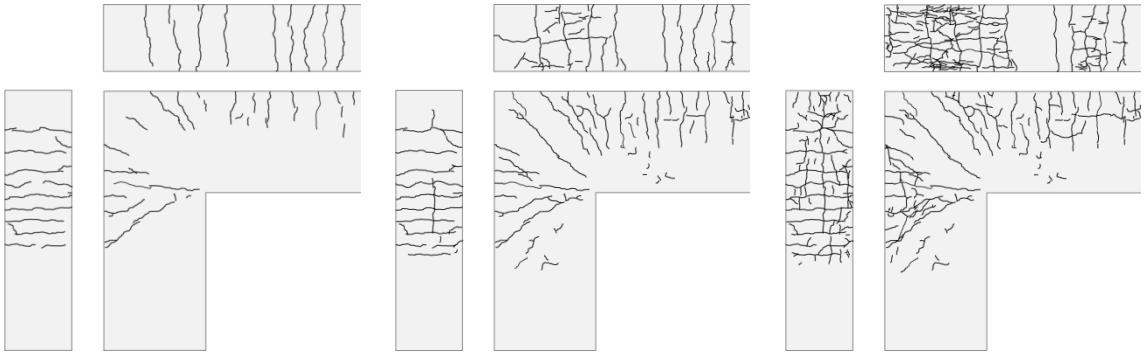

(b) 48 Days of Exposure *(c) 76 Days of Exposure* *(d) 129 Days of Exposure*

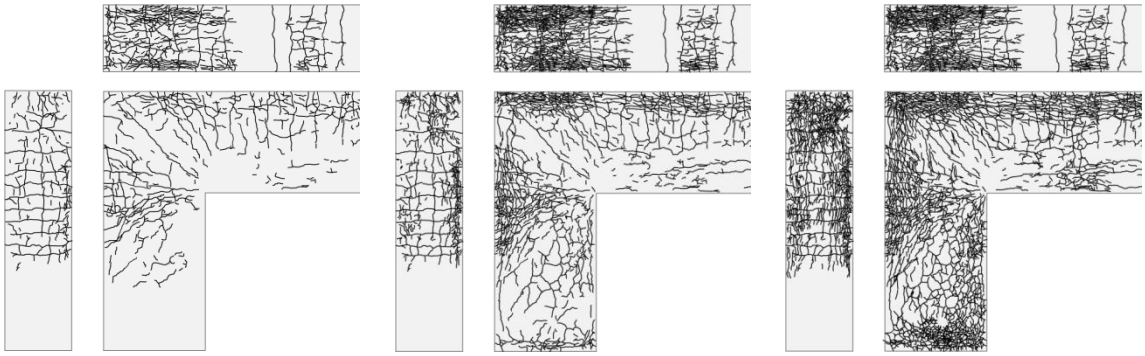

(e) 176 Days of Exposure *(f) 406 Days of Exposure* *(g) 748 Days of Exposure*

Figure 4-20 Crack Pattern over Time – Specimen 4

(a) Side Face (Specimen 3) *(b) Column Face (Specimen 2)*

Figure 4-21 White Residues Leached from Cracks

The maximum crack width at the outside corner of the beam-column joints for Specimen 2 after 252 days of exposure was recorded as 0.03 inches (0.76 mm). A significant amount of cracks were observed after 748-day exposure (Specimen 4, [Figure 4-20] and Specimen 3, [Figure 4-22]). The maximum cracks at the outside corner of the beam-column joints were measured as 0.5 inches (12.7 mm) and 0.25 inches (6.35 mm) in width for Specimens 3 and 4, respectively (Figure 4-23). Moreover, the largest longitudinal crack width on the side face (SF) in the beam-column joint region near the column face (CF) was greater than 0.060 inches (1.52 mm). For Specimen 3, the crack at the outer corner of the beam-column joint, as shown in Figure 4-23a, had a width of approximately 0.85 inches (21.6 mm) and 0.95 inches (24.1 mm) after 1108-day and 1150-day exposure, respectively.

The prestress load-induced cracks, however, grew less aggressively than later-initiated longitudinal cracks and map cracking. Figure 4-24 summarizes the measured

crack widths of major load-induced cracks in the beam, beam-column joint and column regions for each exposed specimen. After 748 days of exposure, a maximum crack width of 0.035 inches (0.89 mm) was observed in the beam region of Specimen 3, which was only 7 % of the largest crack width at the outside corner of the beam-column joint in the singly reinforced bent. Evidently, this is due to the absence of the reinforcing steel in the out-of-plane direction on the column face in the beam-column joint to restrain the ASR/DEF expansion, causing excessive cracking parallel to the longitudinal reinforcing steel on the column face of the beam-column joint region (Figure 4-25a). Thus, it is proposed that U-shaped reinforcing steel bars should be also used in the direction perpendicular to the existing U-shaped steel bars in the beam-column joint regions (Figure 4-25b). These additional U-shaped steel bars can not only restrain the ASR/DEF expansion in the out-of-plane direction, but also provide shear resistance in the joint region. The beneficial effects of the application of additional U-shaped reinforcing steel bars are also discussed in the later chapters.

In addition to the growth of prestress load-induced cracks, new longitudinal cracks due to ASR/DEF were observed over time. Therefore, it is postulated that debonding may take place and cause redistribution of forces along the longitudinal steel in the beam and column regions, leading to the development of the new longitudinal cracks. Moreover, as a consequence of the orientation of the exposed specimens in the field and the setup of supplemental watering system, water tended to saturate the tension side where the existing load-induced cracks located. This provided sufficient water as a constituent to promote ASR/DEF, leading to excessive cracking.

Figure 4-22 Crack Pattern of Specimen 3 after 748 Days of Exposure

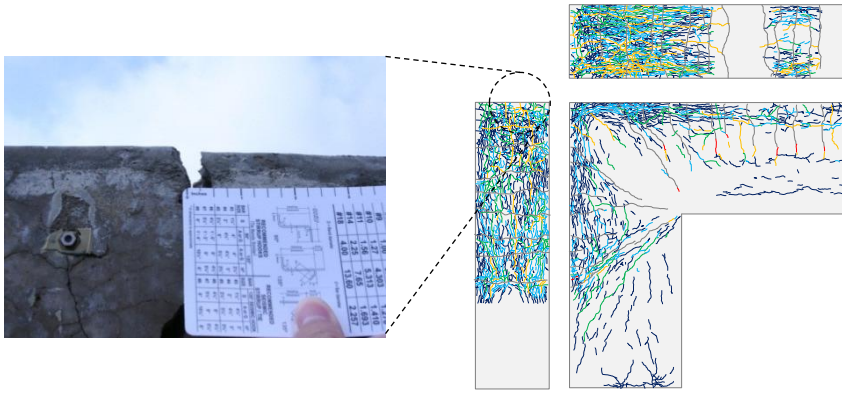

(a) Specimen 3

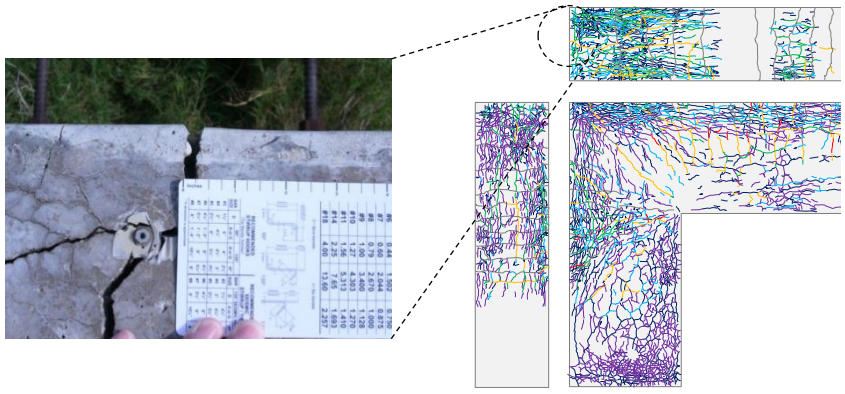

(b) Specimen 4

Figure 4-23 Largest Cracks after 748 Days of Exposure

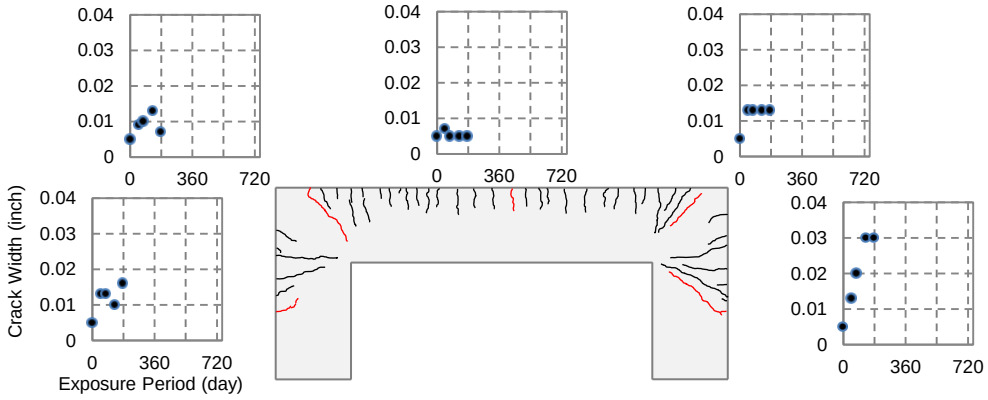

(a) Specimen 2

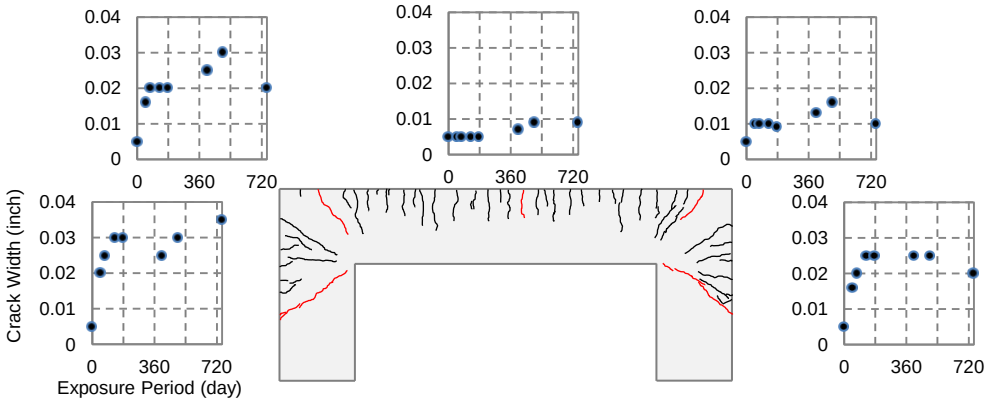

(b) Specimen 3

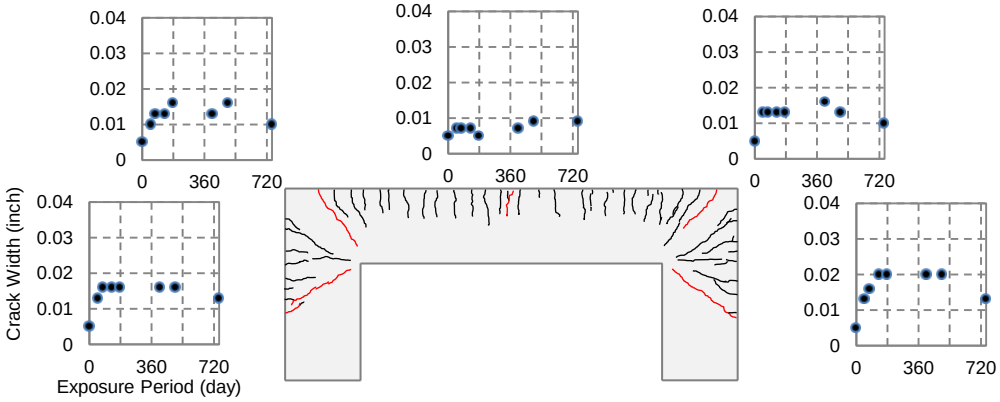

(c) Specimen 4

Figure 4-24 Widths of Major Load-Induced Cracks (in red) over Time

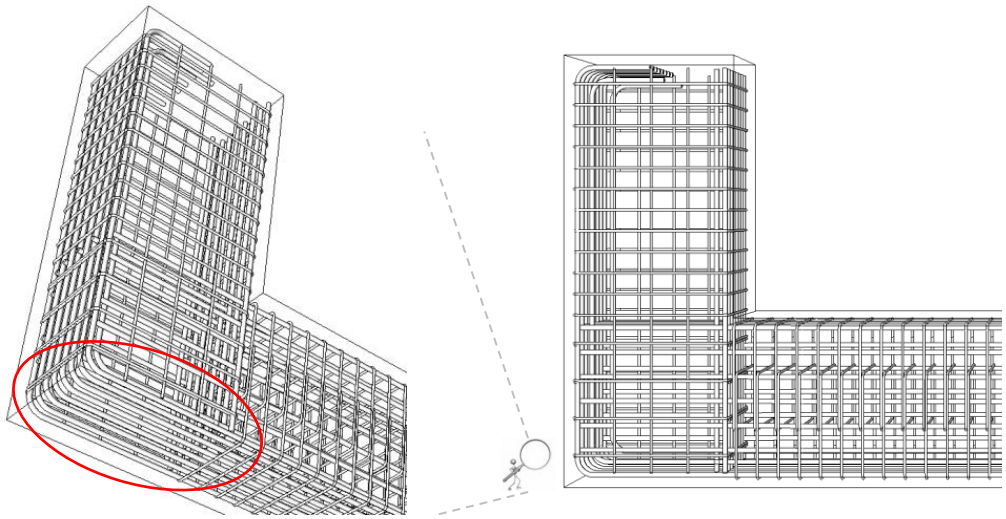

(a) Original Reinforcing Steel Detail of Beam-Column Joint

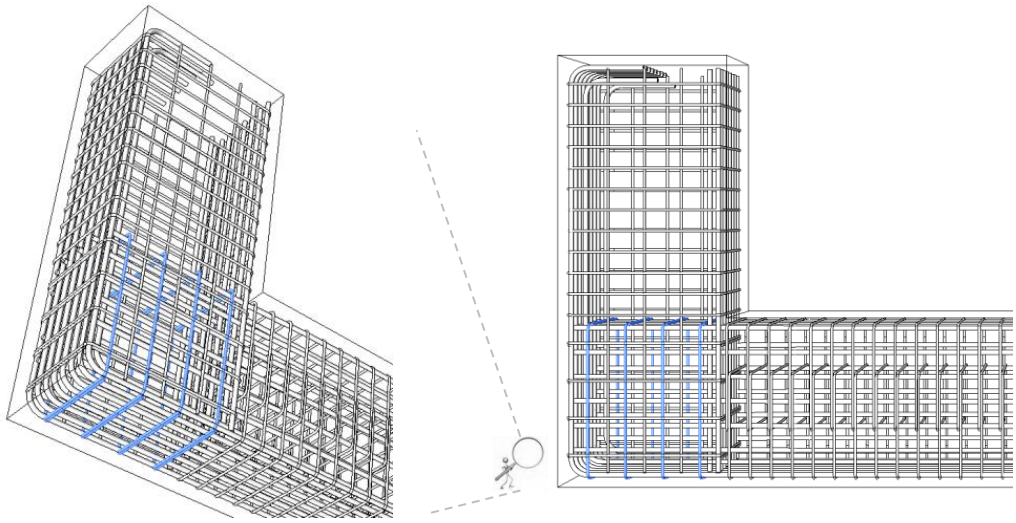

(b) Proposed Additional U-shaped Reinforcing Steel Bars in Beam-Column Joint

Figure 4-25 Original and Proposed Reinforcing Steel Detail of Beam-Column Joint

4.4 SURFACE CONCRETE STRAIN

Prior to the exposure phase, the surface concrete strains were first calculated using DEMEC measurements taken after the application of pre-loading. These strains in each direction were within the range of the tension and compression yield strains of reinforcing steel (±0.0022). After the specimens were transported to the field, the measurements were taken approximately every two weeks (15 days) for the first seven months, every four weeks (30 days) for the next seven months, and every seven weeks (50 days) afterwards.

Figures 4-26 and 4-27 present the progression of longitudinal surface concrete strains in the beam regions for each exposed specimen. The prestress load-induced longitudinal surface concrete strains on the tension side were greater than those on the compression side. After the first two months (60 days) of exposure, some minor expansion was observed. These longitudinal strains in the beam regions were typically less than 0.004 after the first 15 months (450 days) of exposure and gradually developed over time.

Figures 4-28 and 4-29 show the transverse surface concrete strains in the beam regions for each exposed specimen over time. After six months (180 days) of exposure, strains greater than 0.004 were observed in some measurements across the prestress load-induced cracks in the beam regions. It was observed that these strains increased over time and reached 0.016 and 0.020 after 24-month (720 days) and 40-month (1200 days) exposure, respectively.

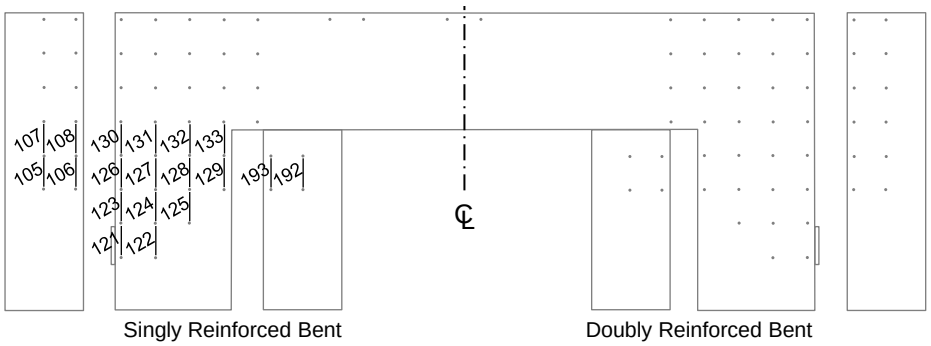

(a) DEMEC Measurements

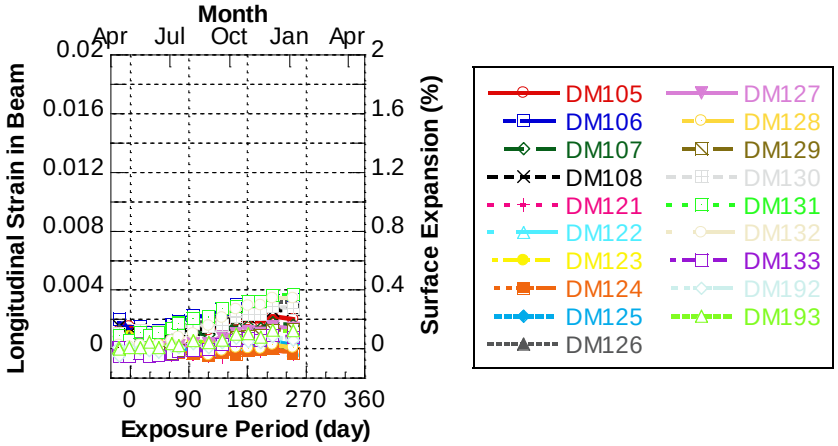

(b) Specimen 2

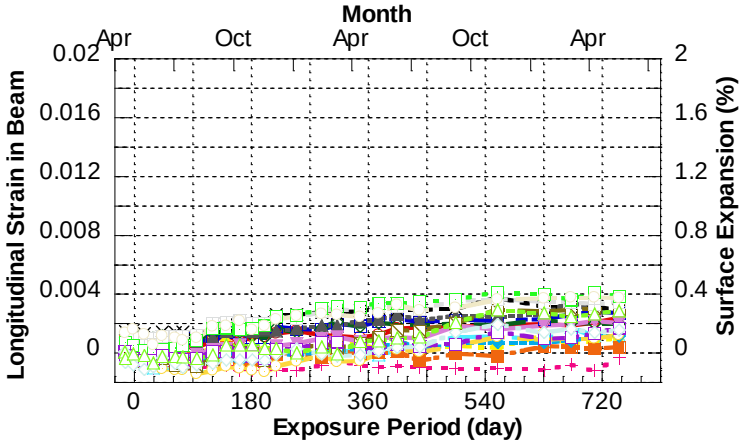

(c) Specimen 4

Figure 4-26 Longitudinal Surface Concrete Strains in Beam Region of Singly Reinforced Bent

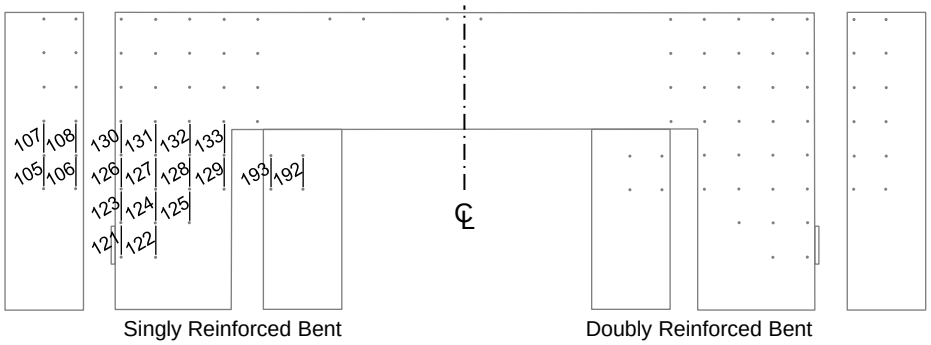

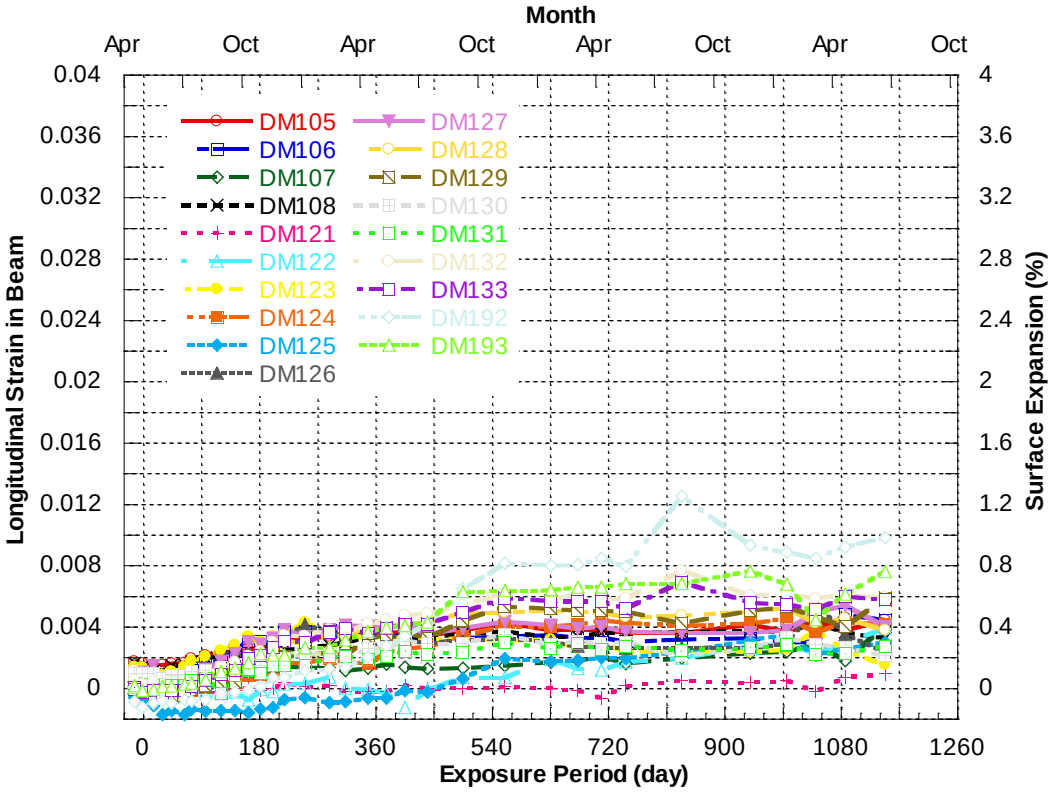

(d) Specimen 3

Figure 4-26 Longitudinal Surface Concrete Strains in Beam Region of Singly Reinforced Bent (Continued)

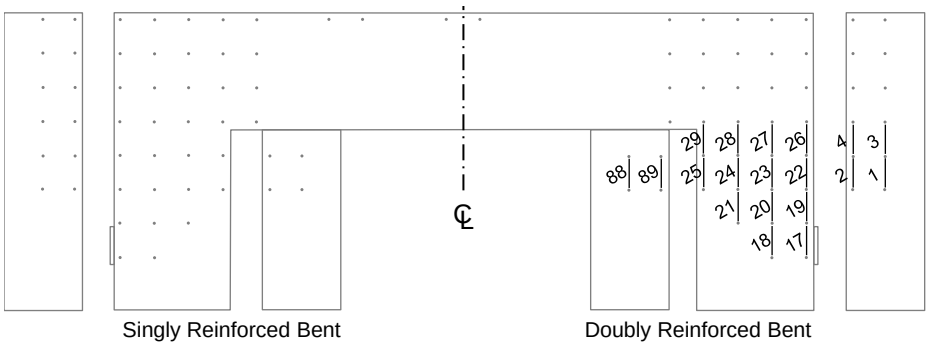

(a) DEMEC Measurements

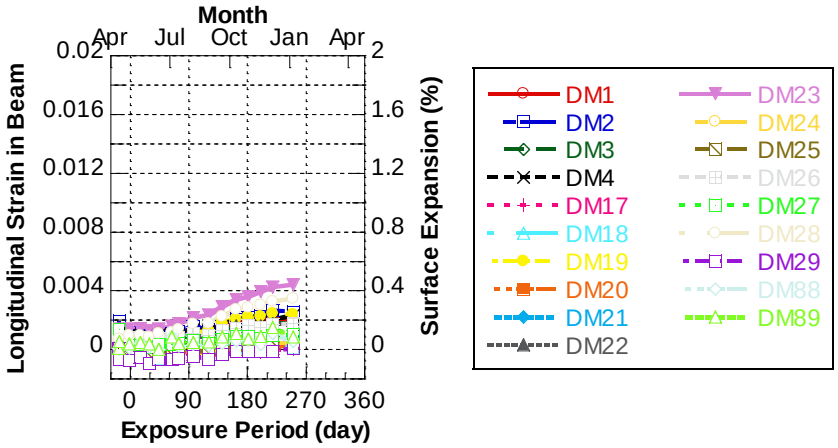

(b) Specimen 2

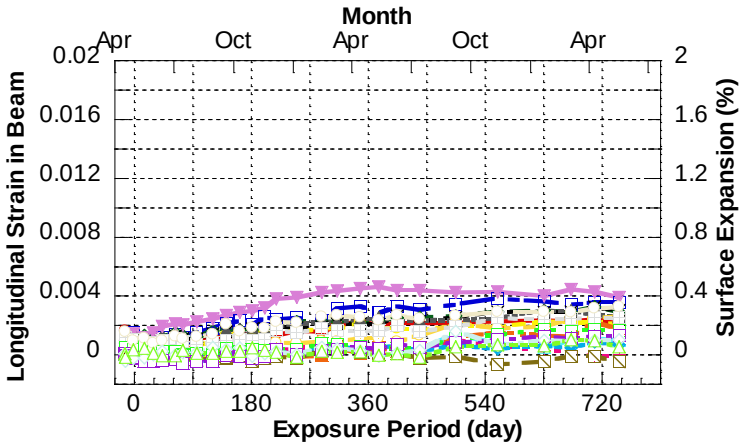

(c) Specimen 4

Figure 4-27 Longitudinal Surface Concrete Strains in Beam Region of Doubly Reinforced Bent

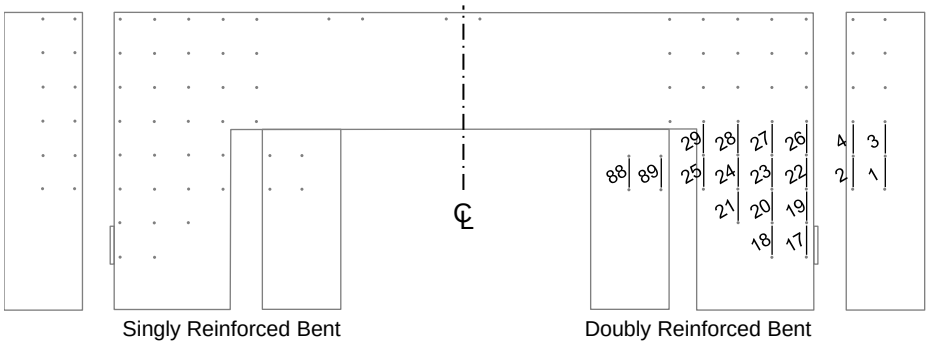

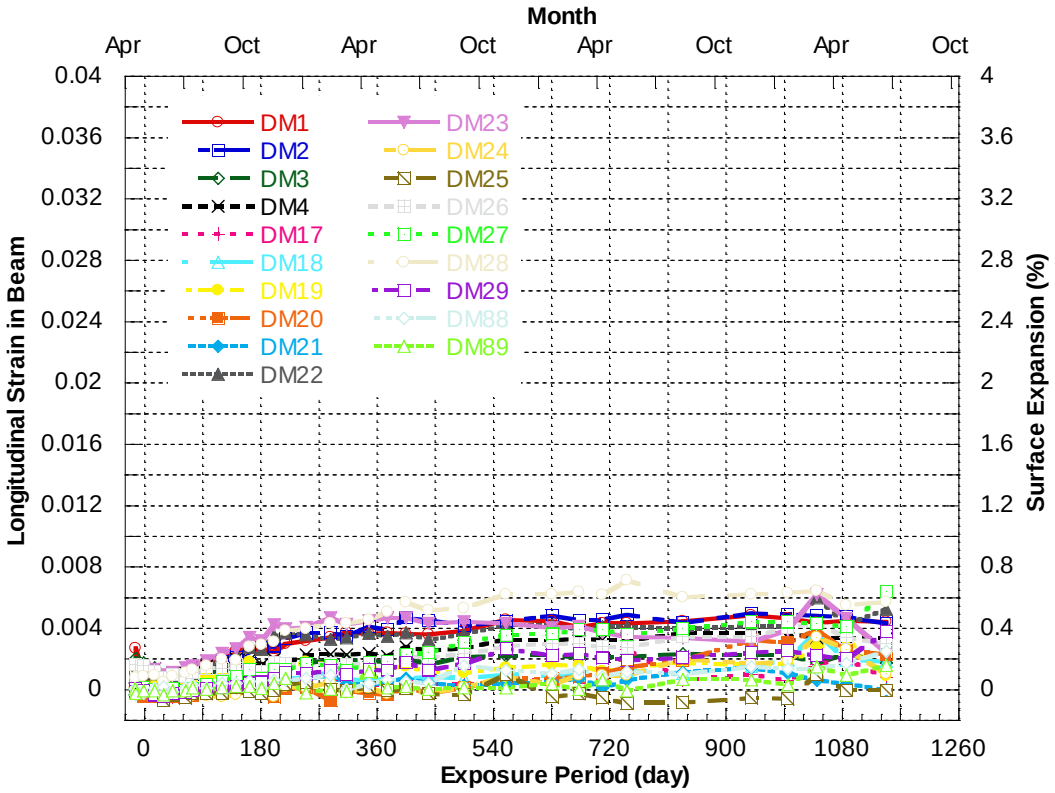

(d) Specimen 3

Figure 4-27 Longitudinal Surface Concrete Strains in Beam Region of Doubly Reinforced Bent (Continued)

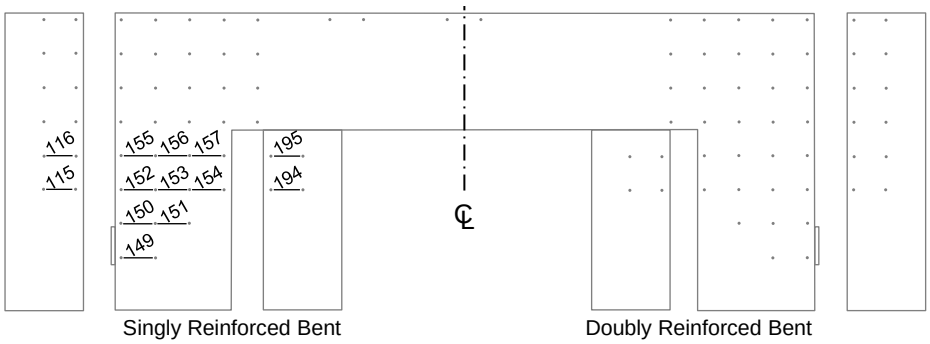

(a) DEMEC Measurements

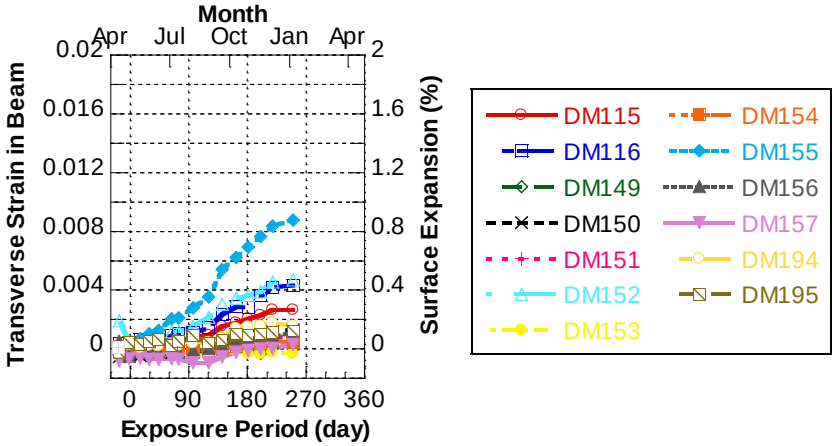

(b) Specimen 2

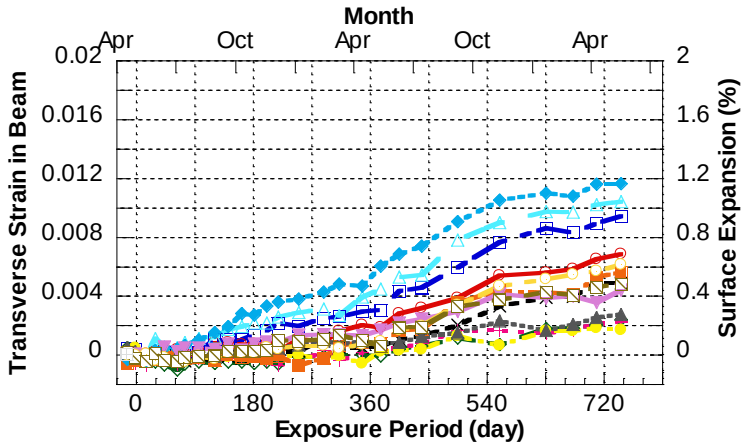

(c) Specimen 4

Figure 4-28 Transverse Surface Concrete Strains in Beam Region of Singly Reinforced Bent

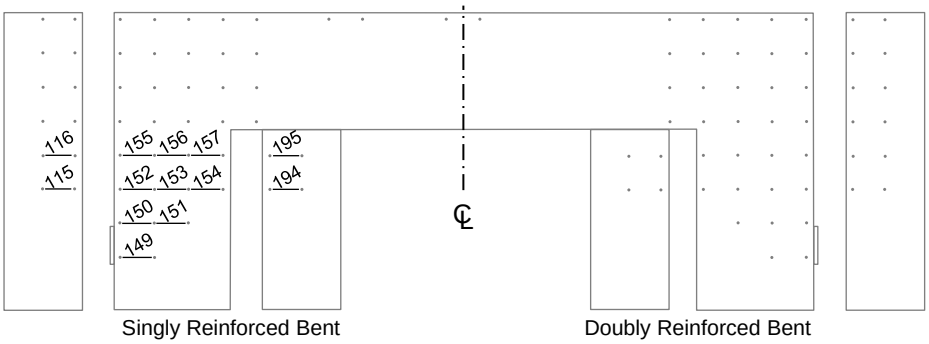

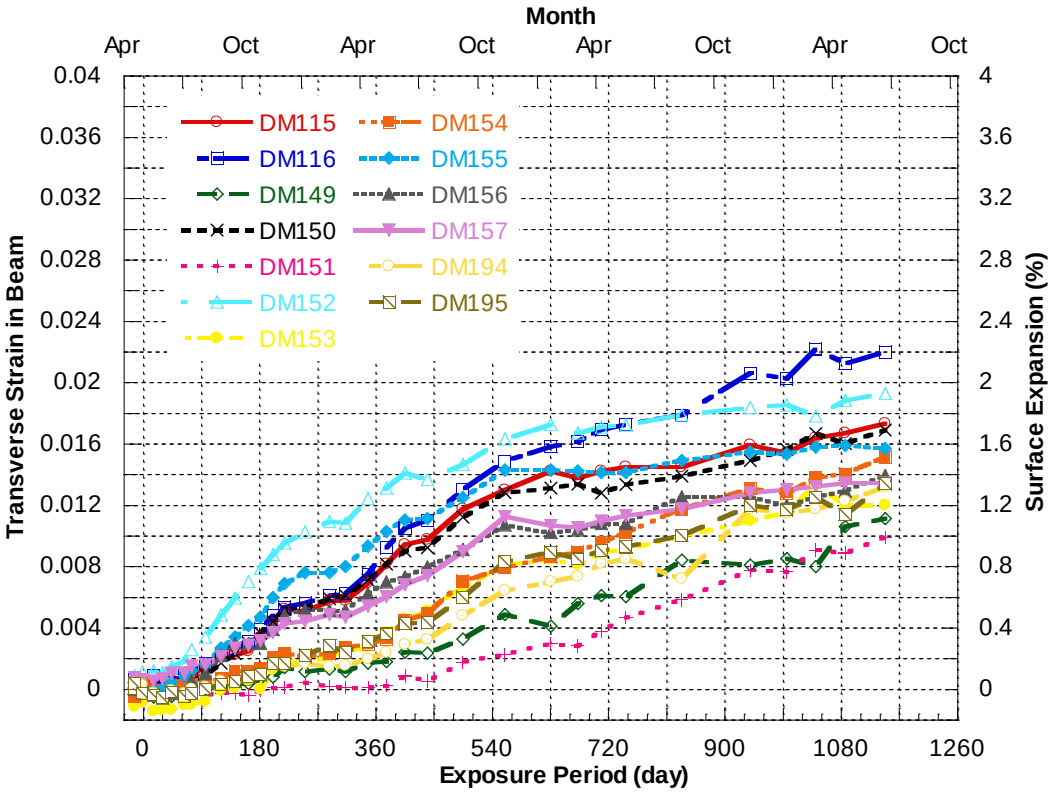

(d) Specimen 3

Figure 4-28 Transverse Surface Concrete Strains in Beam Region of Singly Reinforced Bent (Continued)

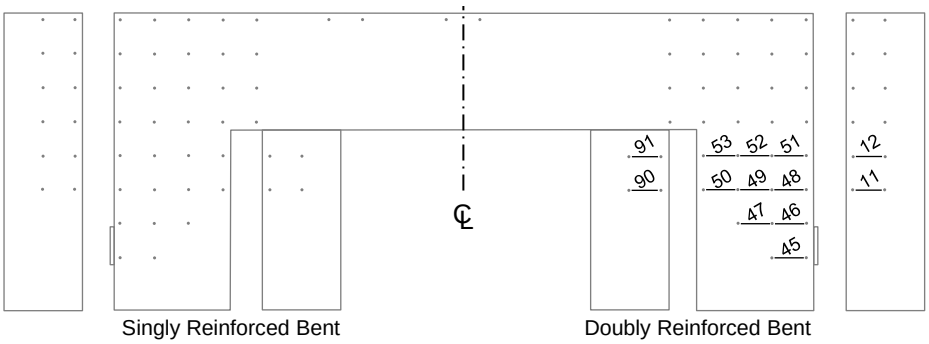

(a) DEMEC Measurements

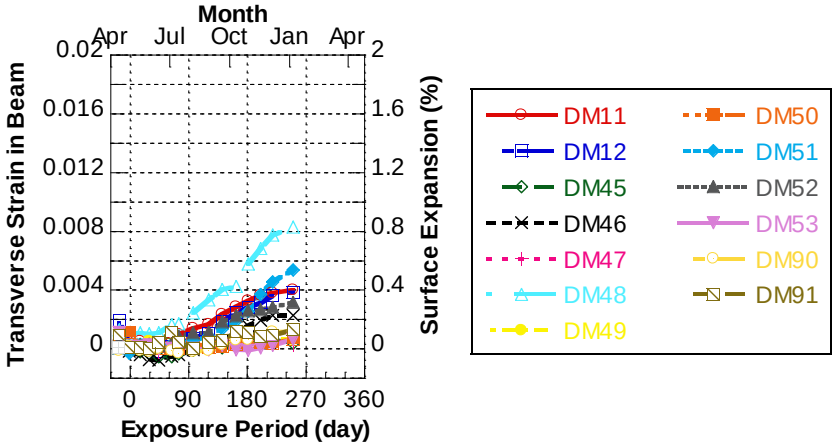

(b) Specimen 2

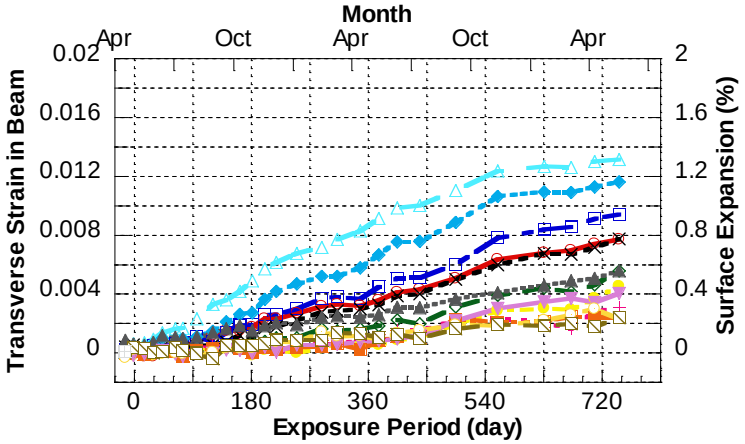

(c) Specimen 4

Figure 4-29 Transverse Surface Concrete Strains in Beam Region of Doubly Reinforced Bent

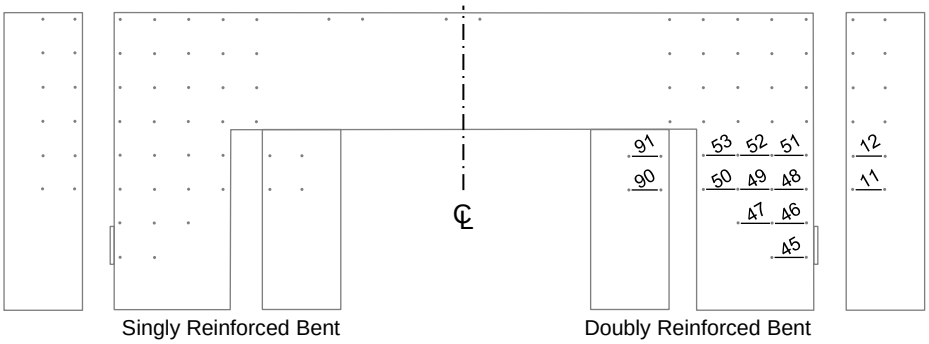

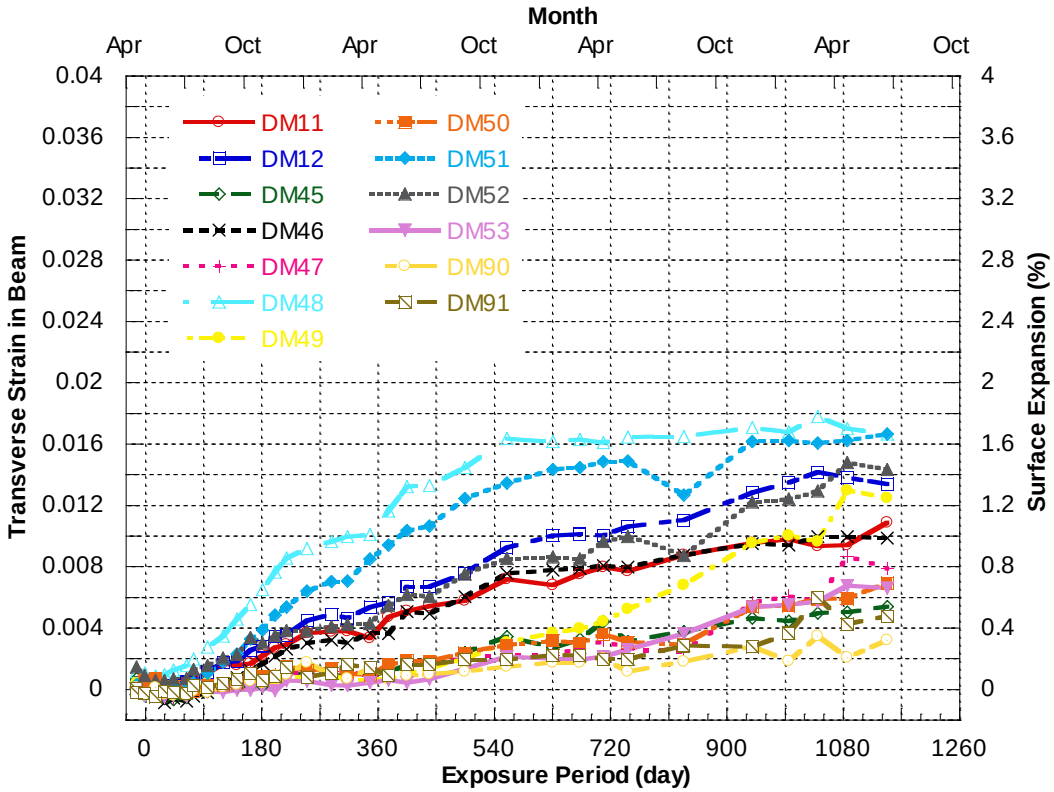

(d) Specimen 3

Figure 4-29 Transverse Surface Concrete Strains in Beam Region of Doubly Reinforced Bent (Continued)

A significantly higher expansion rate was observed in the transverse direction than in the longitudinal direction in the beam regions (Figure 4-26 through Figure 4-29). In addition, a higher surface expansion rate was observed during the warmer months from April to October. Thus, based on the recorded temperatures by Weather Underground (2012), it may be inferred that the development of ASR/DEF accelerated once temperatures exceeded 80 ˚F (26.7 ˚C).

Figures 4-30 and 4-31 present the longitudinal and transverse surface concrete strains in the column during the exposure phase. Minor surface expansion in the longitudinal direction was observed in the column after 24 months (720 days) of exposure. Some surface strains gradually developed and reached 0.004 after 40 months (1200 days) of exposure. However, more surface expansion in the transverse direction was observed over time owing to the growth of some new longitudinal cracks across these measurements, as discussed in the previous section. Some transverse surface strains on the column face (DMs 208 and 212) were greater than 0.012 after 18 months (540 days) of exposure and reached 0.024 after 40 months (1200 days) of exposure, which were ten times greater than the yield strain of reinforcing steel.

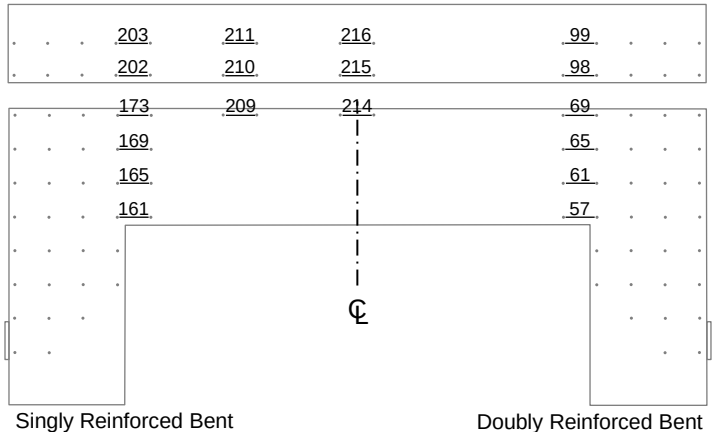

(a) DEMEC Measurements

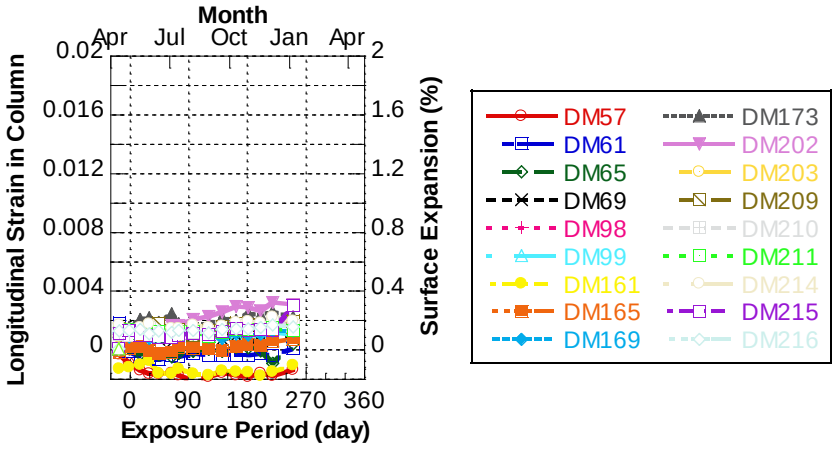

(b) Specimen 2

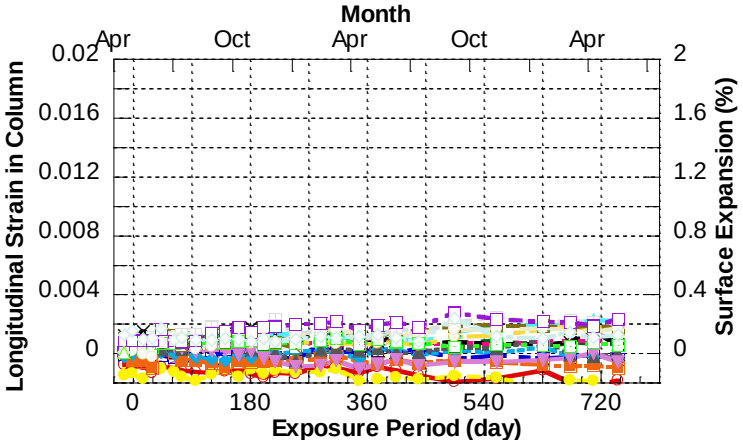

(c) Specimen 4

Figure 4-30 Longitudinal Surface Concrete Strains in Column Region

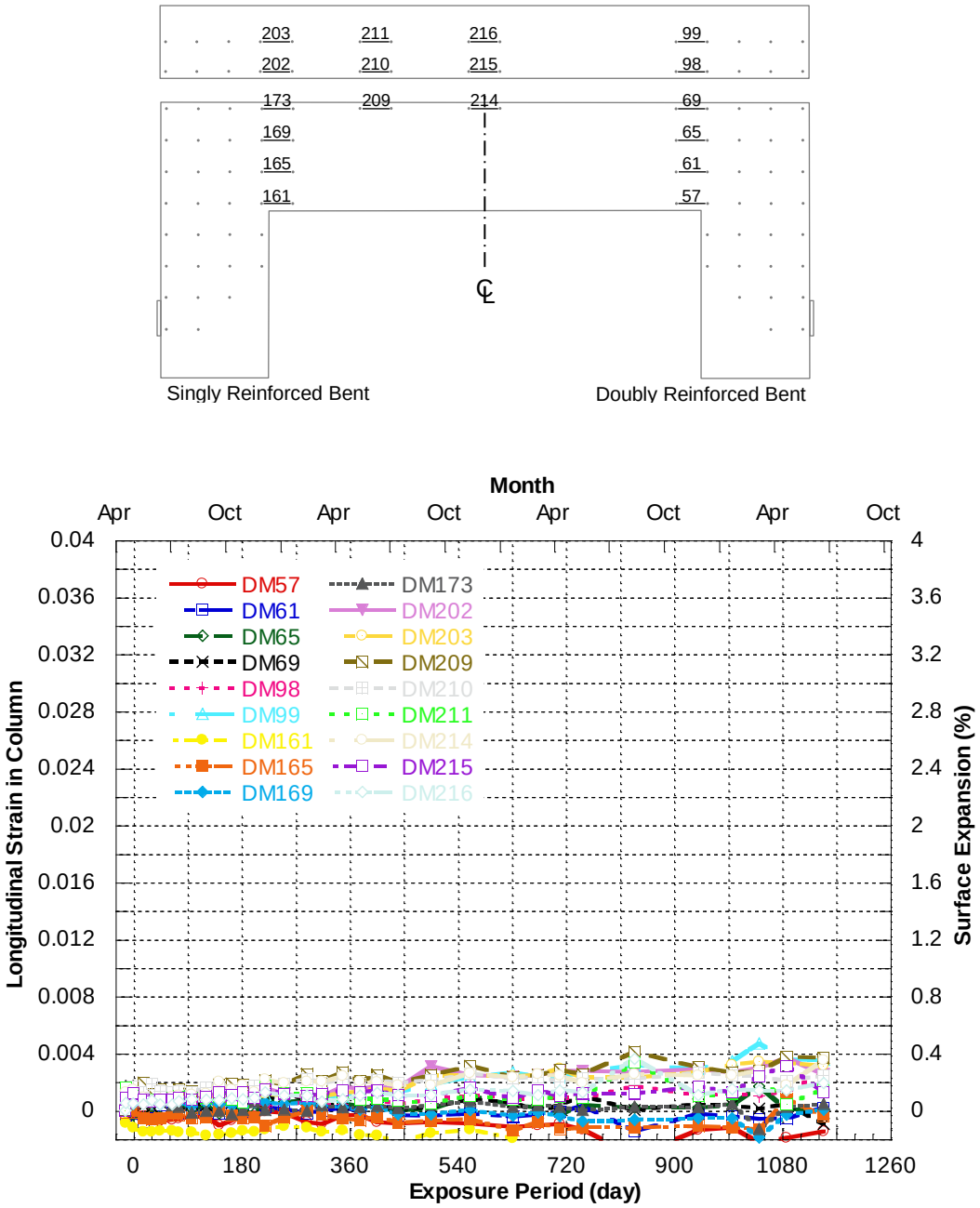

(d) Specimen 3

Figure 4-30 Longitudinal Surface Concrete Strains in Column Region (Continued)

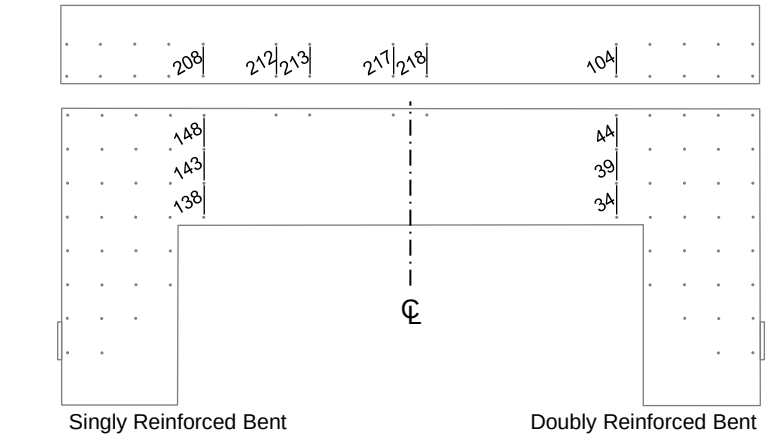

(a) DEMEC Measurements

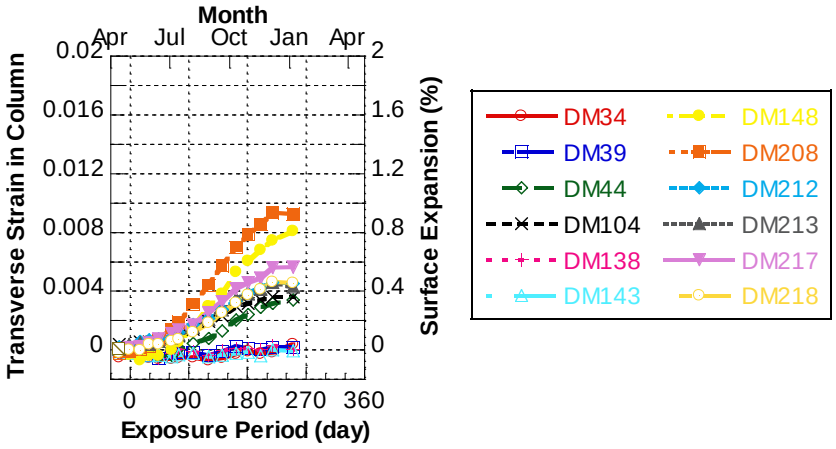

(b) Specimen 2

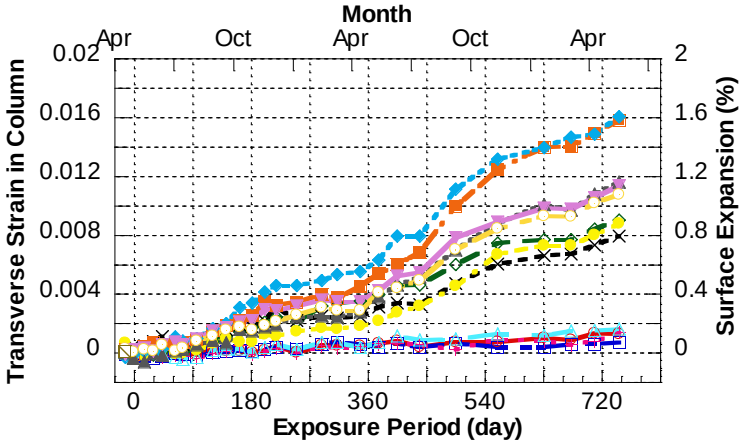

(c) Specimen 4

Figure 4-31 Transverse Surface Concrete Strains in Column Region

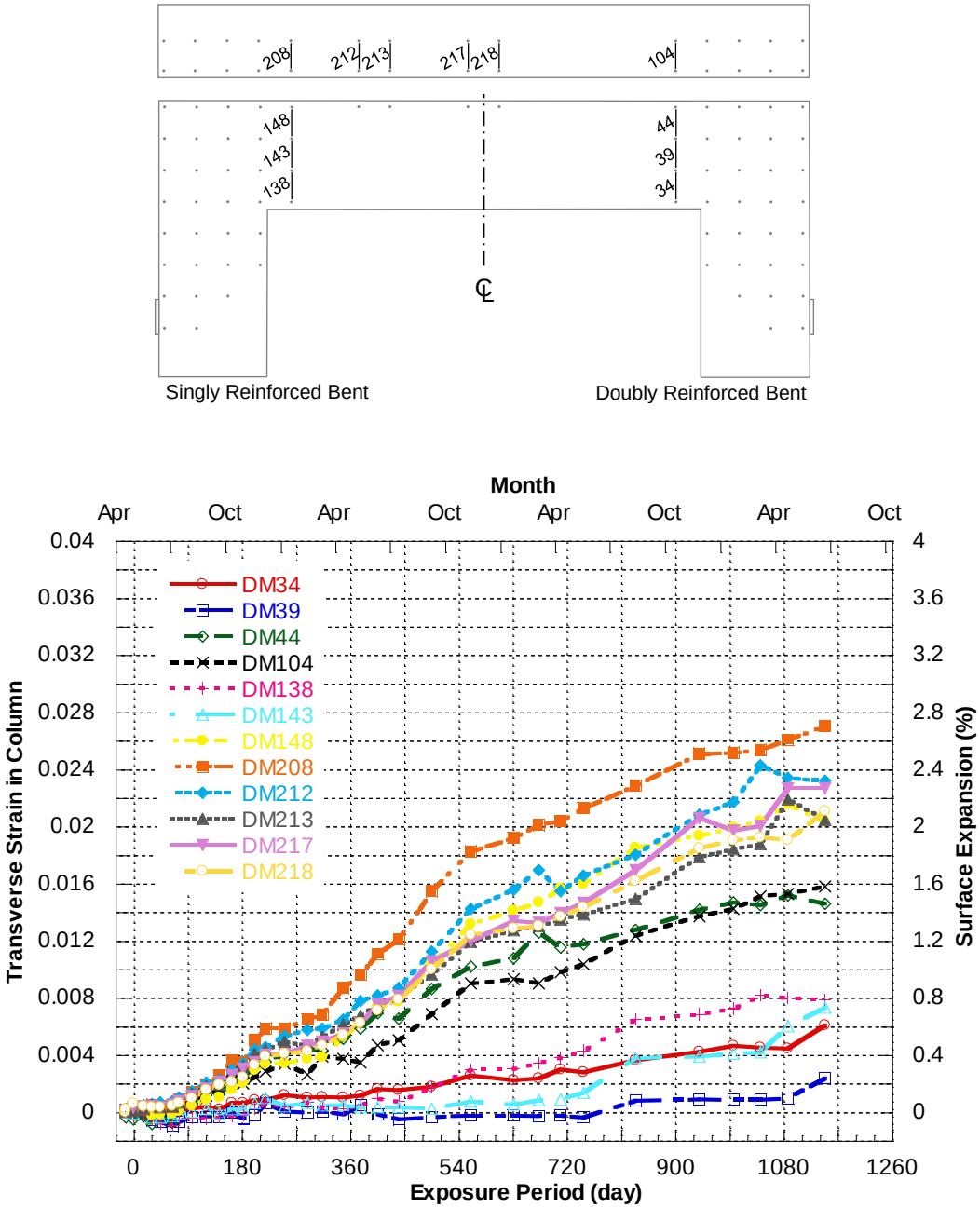

(d) Specimen 3

Figure 4-31 Transverse Surface Concrete Strains in Column Region (Continued)

Figures 4-32 and 4-33 depict the diagonal surface concrete strains in the beam regions over time. Due to the excessive cracking on the tension side of the beam regions, the diagonal strains cross the major cracks (DMs 177 and 73), which potentially permitted early moisture ingress due to the cracks caused by the pre-load, exhibited more expansion over time and reached 0.010 and 0.014 after 24 months (720days) and 40 months (1200 days) of exposure, respectively.

Figures 4-34 and 4-35 present the diagonal surface concrete strains in the beam-column joints over time. More surface concrete expansion was observed in the regions close to the column face (DMs 189-191 and 85-87), that is, nearby the top side as per the specimens' orientation during the exposure phase. The prompted wetting and drying effects during the warmer months from April to October caused cracking on the top side, as per the orientation of the specimens in field, and the cracks expanded over time. In the singly reinforced bent of Specimen 3, these strains approached 0.016 and 0.024 after 24 months (720days) and 40 months (1200 days) of exposure, respectively.

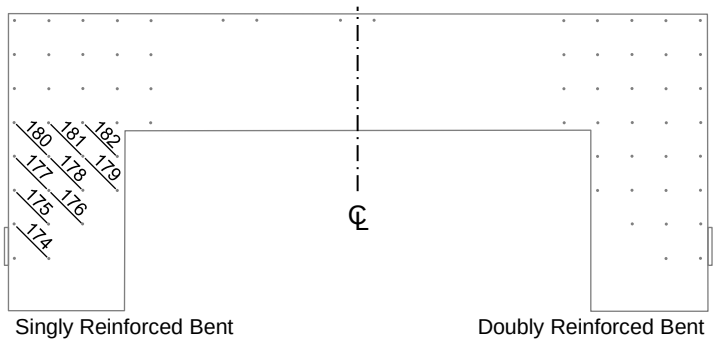

(a) DEMEC Measurements

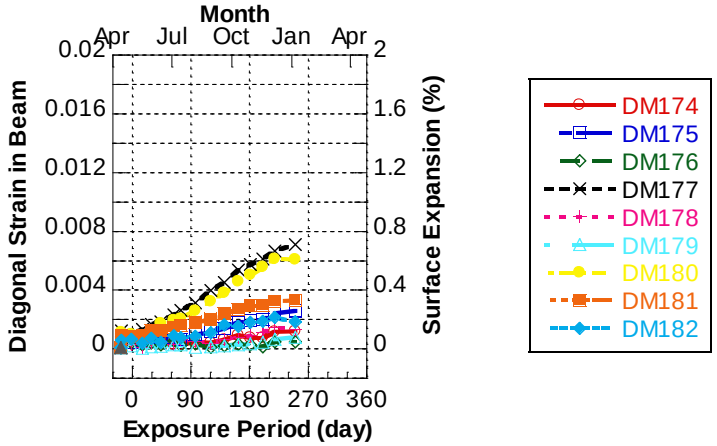

(b) Specimen 2

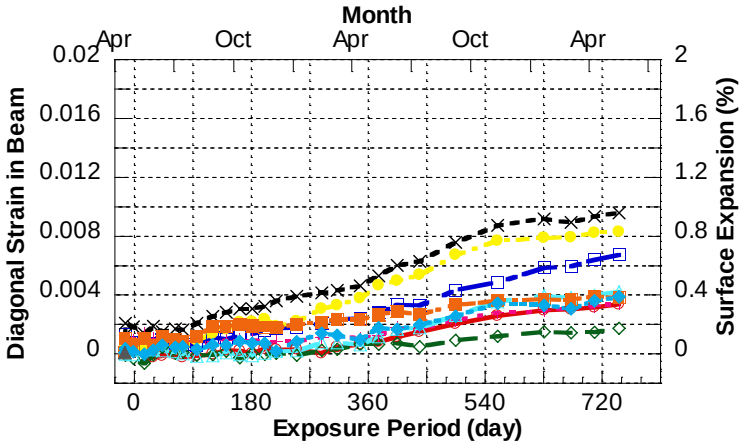

(c) Specimen 4

Figure 4-32 Diagonal Surface Concrete Strains in Beam Region of Singly Reinforced Bent

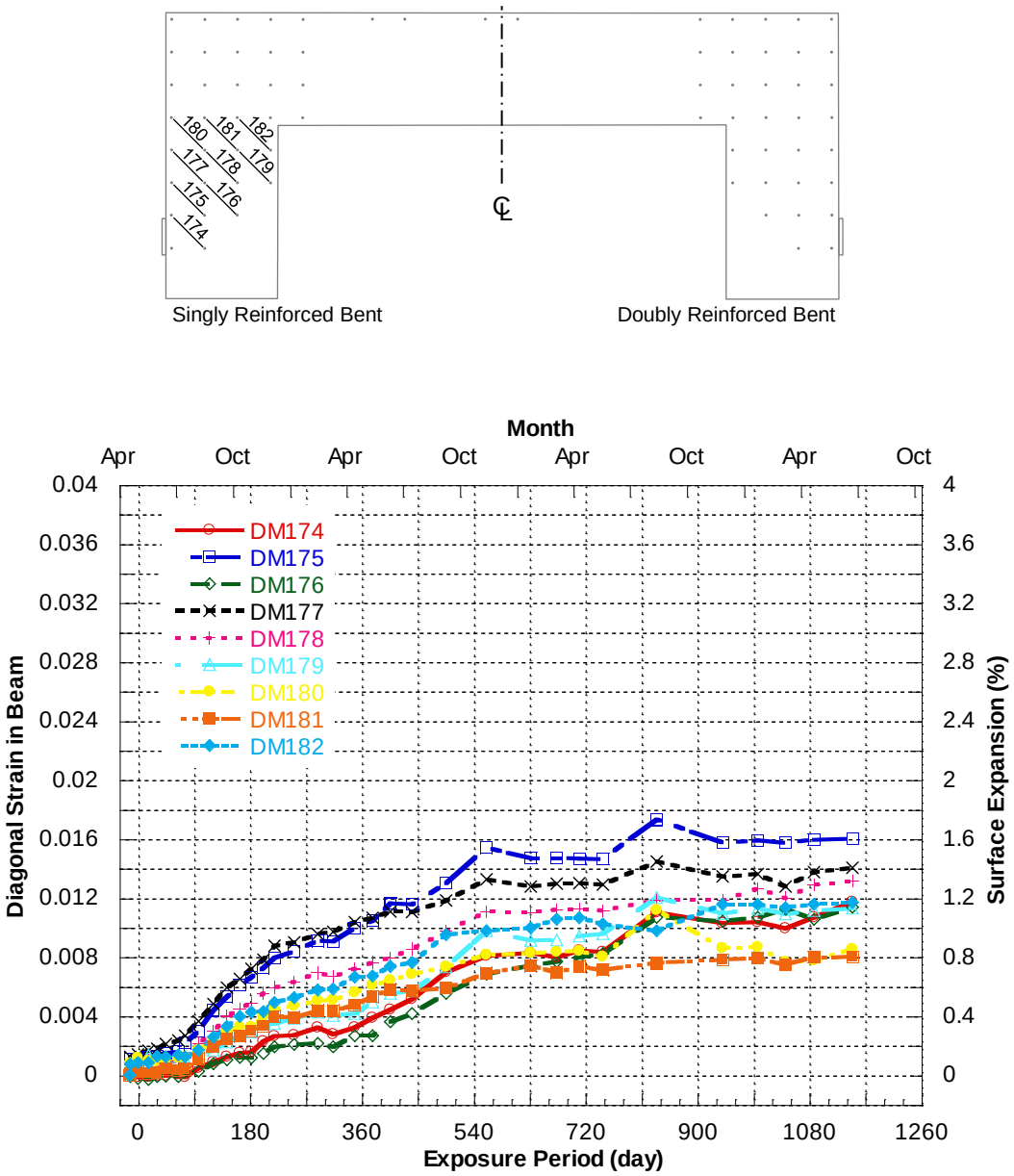

(d) Specimen 3

Figure 4-32 Diagonal Surface Concrete Strains in Beam Region of Singly Reinforced Bent (Continued)

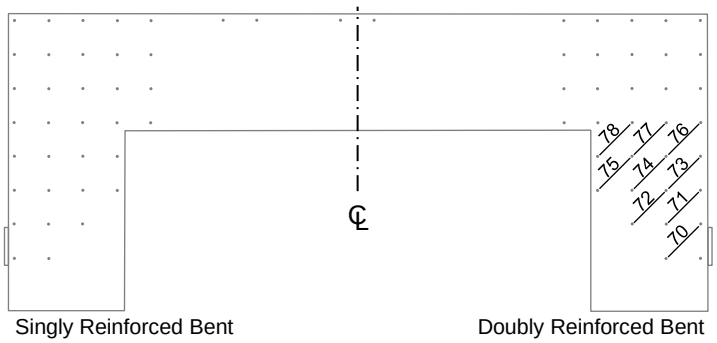

(a) DEMEC Measurements

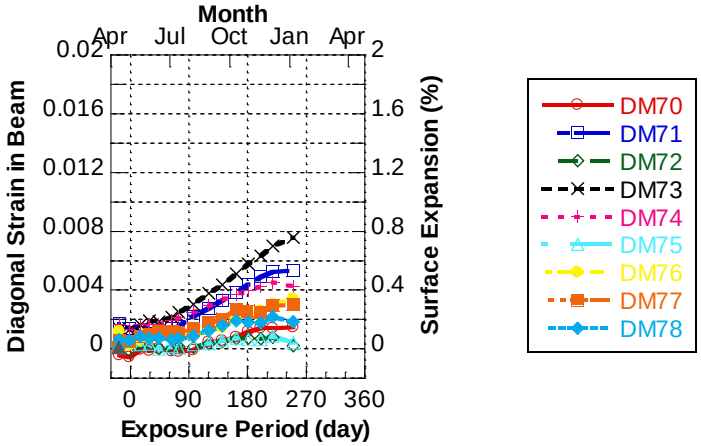

(b) Specimen 2

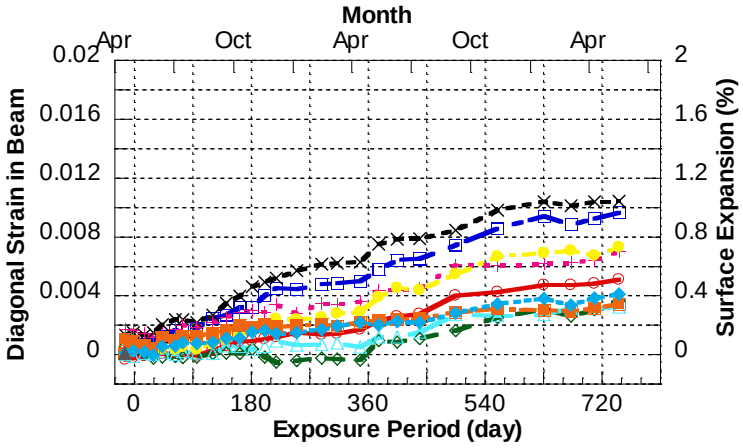

(c) Specimen 4

Figure 4-33 Diagonal Surface Concrete Strains in Beam Region of Doubly Reinforced Bent

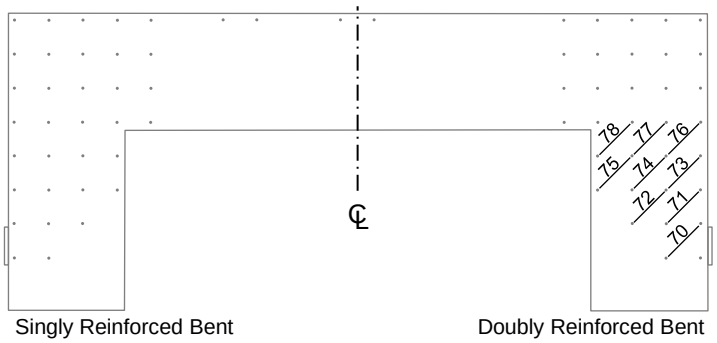

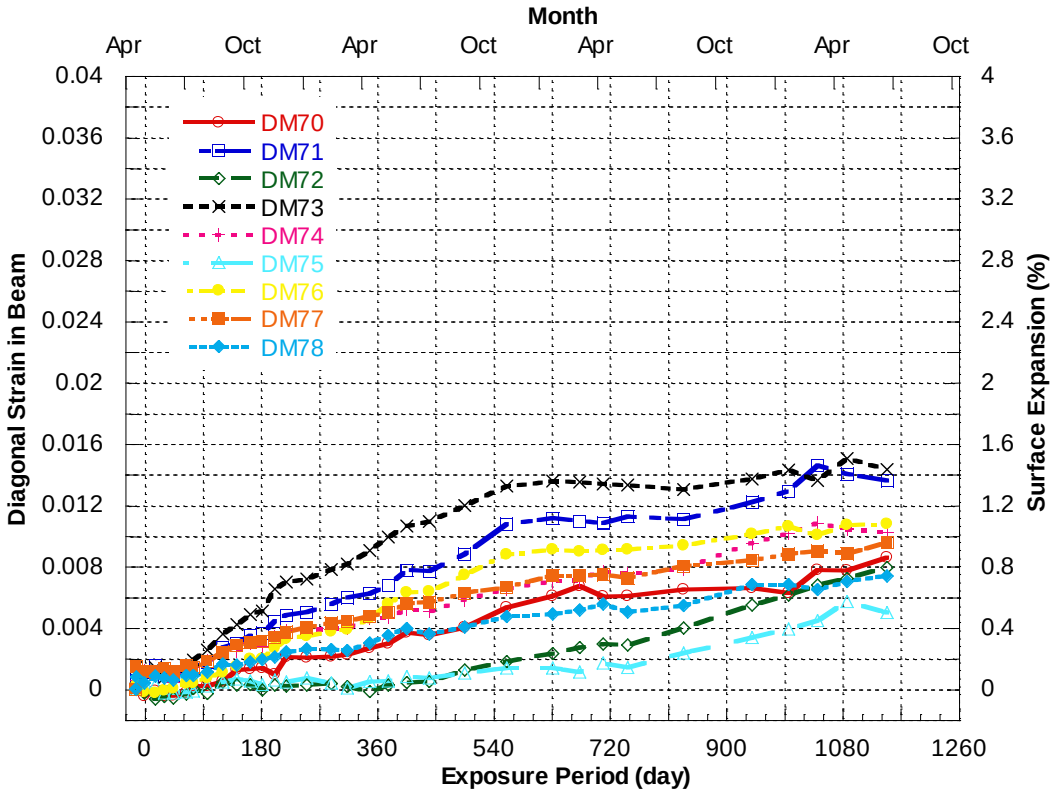

(d) Specimen 3

Figure 4-33 Diagonal Surface Concrete Strains in Beam Region of Doubly Reinforced Bent (Continued)

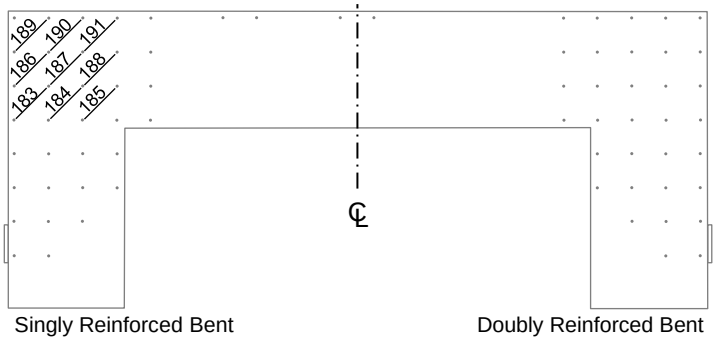

(a) DEMEC Measurements

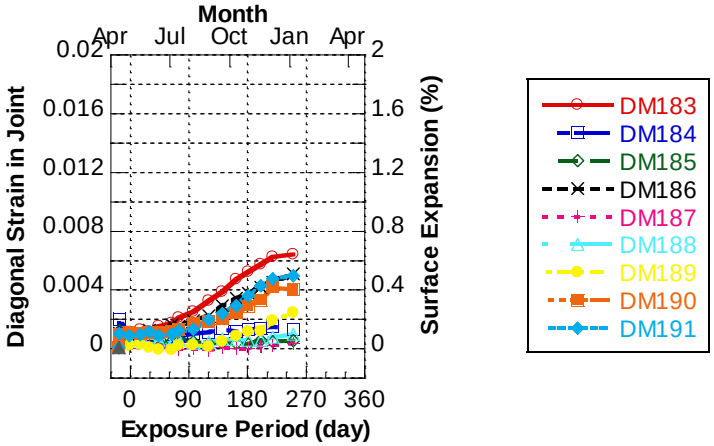

(b) Specimen 2

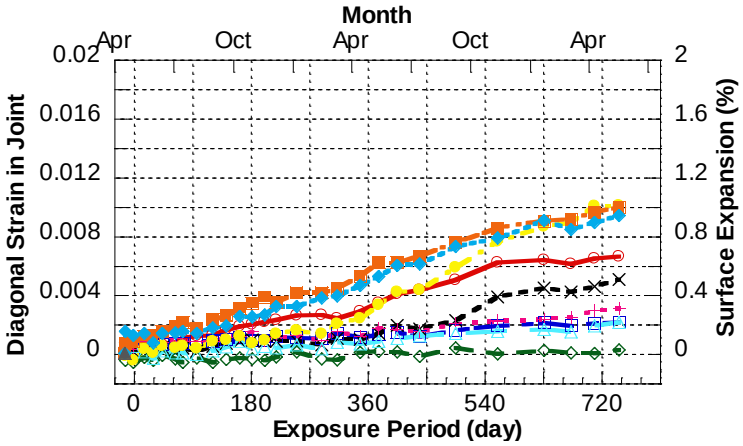

(c) Specimen 4

Figure 4-34 Diagonal Surface Concrete Strains in Beam-Column Joint of Singly Reinforced Bent

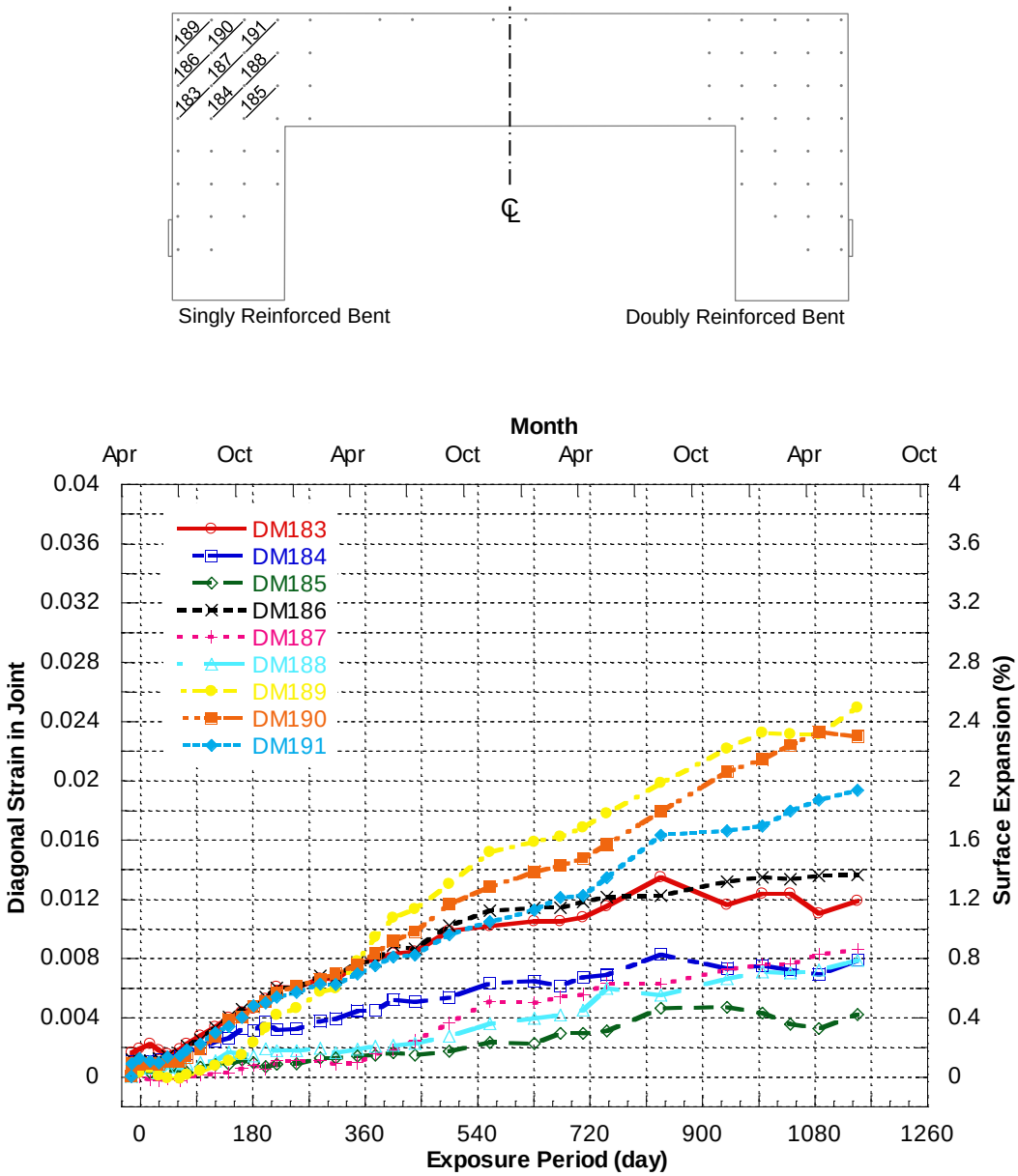

(d) Specimen 3

Figure 4-34 Diagonal Surface Concrete Strains in Beam-Column Joint of Singly Reinforced Bent (Continued)

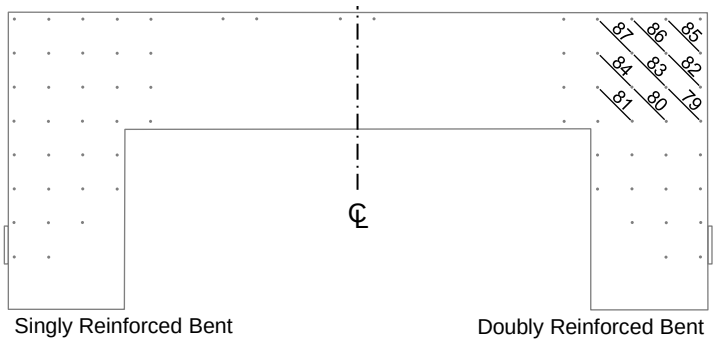

(a) DEMEC Measurements

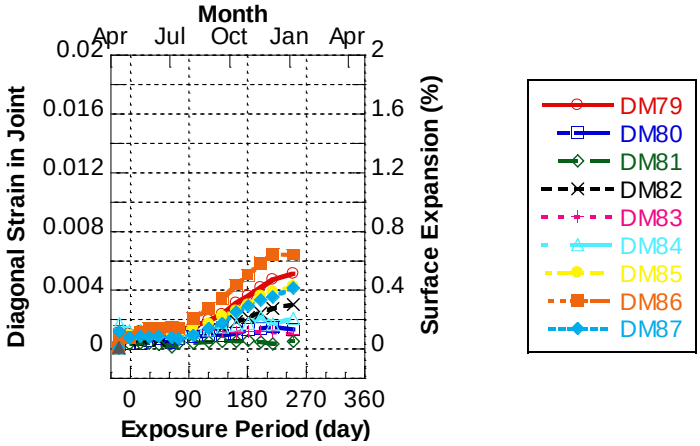

(b) Specimen 2

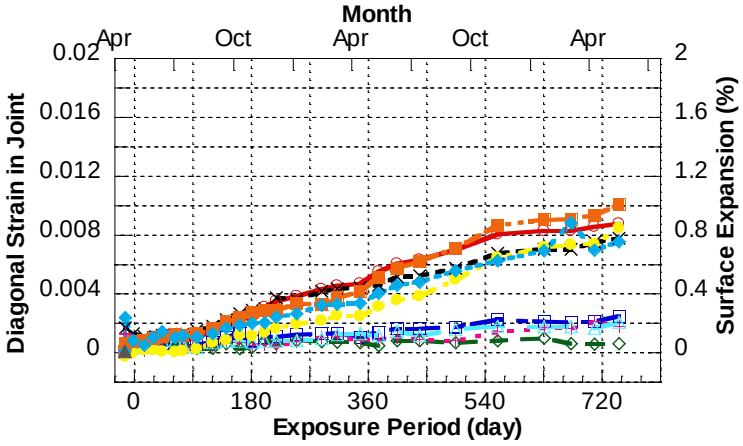

(c) Specimen 4

Figure 4-35 Diagonal Surface Concrete Strains in Beam-Column Joint of Doubly Reinforced Bent

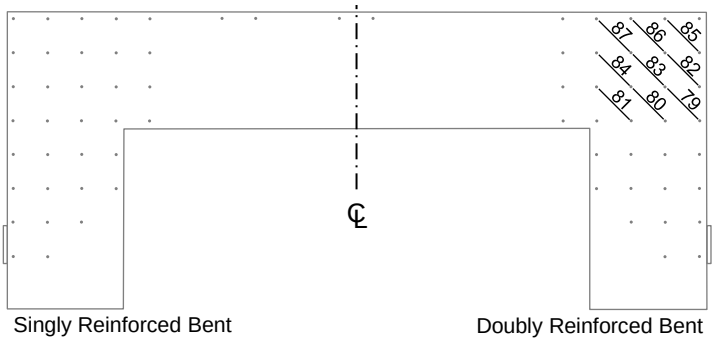

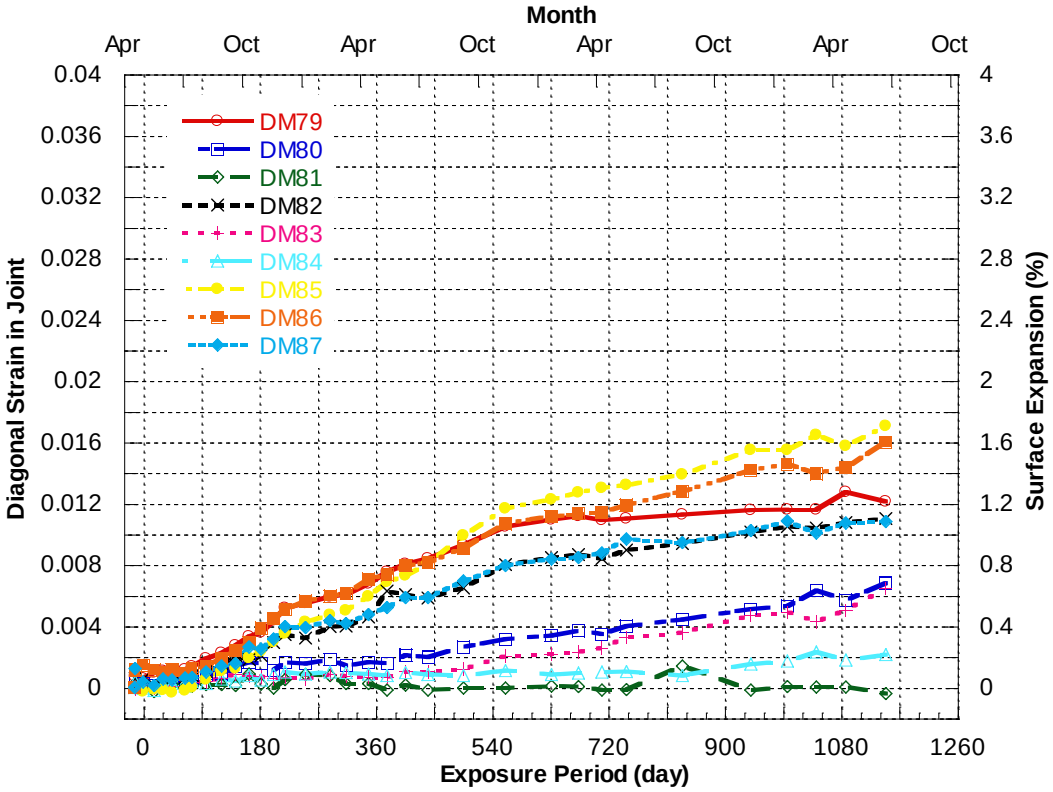

(d) Specimen 3

Figure 4-35 Diagonal Surface Concrete Strains in Beam-Column Joint of Doubly Reinforced Bent (Continued)

Figures 4-36 and 4-37 show the beam direction strains in the beam-column joints during the exposure phase. As aforementioned, new cracks on the tension side were observed after first several months of exposure and grew in width and length over time. The strains close to the top side (DMs 113-114, 144-147, 9-10 and 40-43), as per the orientation of the specimens in the field, significantly developed and exhibited a higher expansion rate after 3 months (90 days) of exposure. In the singly reinforced bent of Specimen 3, some beam direction strains in the beam-column joints reached 0.020 after 24 months (720 days) of exposure and approached 0.036 after 40 months (1200 days) of exposure. Figures 4-38 and 4-39 present the column direction strains in the beam-column joints. Similarly, the tension side exhibited a higher expansion rate than the compression side. However, these strains grew less aggressively compared to the column direction strains in the beam-column joints.

Figures 4-40 and 4-41 depict the progression of the out-of-plane strains in the beam-column joints over time. As shown in Figure 4-23, cracks crossing the out-of-plane DEMEC measurements were observed in the beam-column joint regions. The out-of-plane strains at the outside corner of the joints significantly expanded after the first 2 months (60 days) and exhibited a higher expansion rate from April to October. For the singly reinforced bent of Specimen 3, some out-of-plane strains in the beam-column joints reached 0.020 and 0.040 after 12-month (360 days) and 18-month (540 days) exposure, respectively. Furthermore, due to the significant expansion of the large crack at the outside corner of the joint, some strains were greater than 0.100 after 40-month (1200 days) exposure.

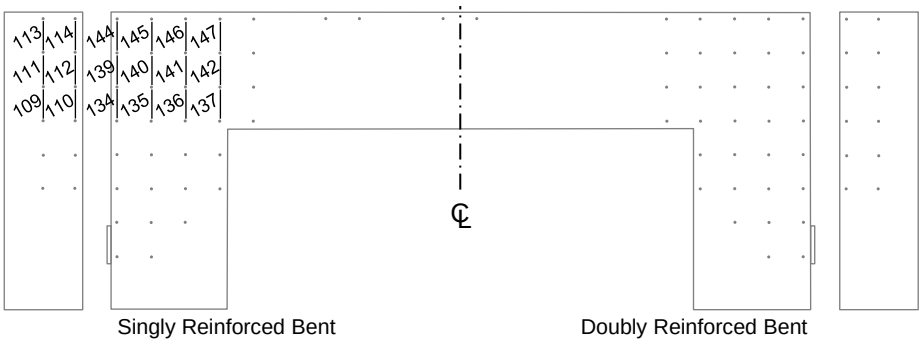

(a) DEMEC Measurements

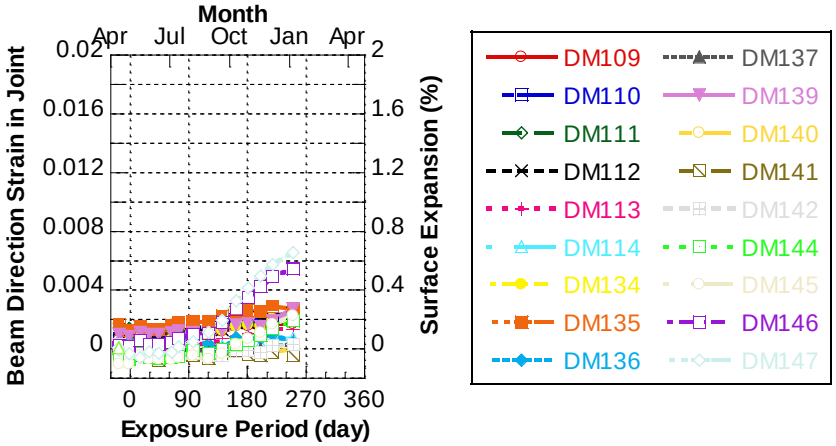

(b) Specimen 2

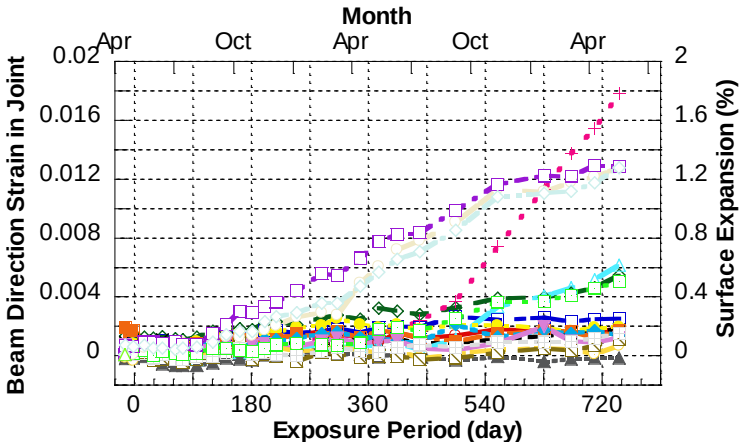

(c) Specimen 4

Figure 4-36 Beam Direction Surface Concrete Strains in Beam-Column Joint of Singly Reinforced Bent

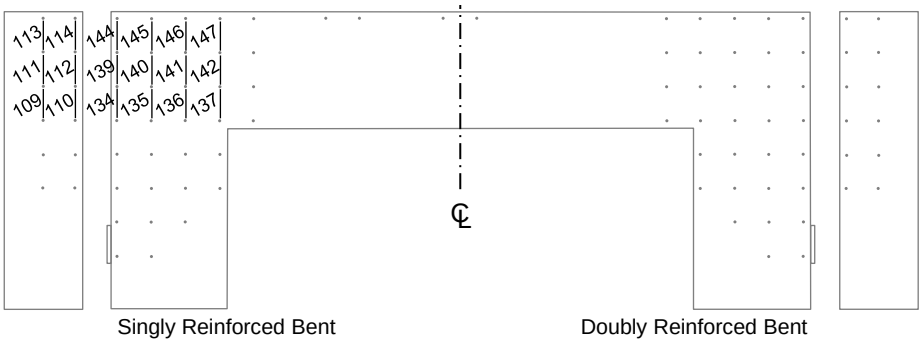

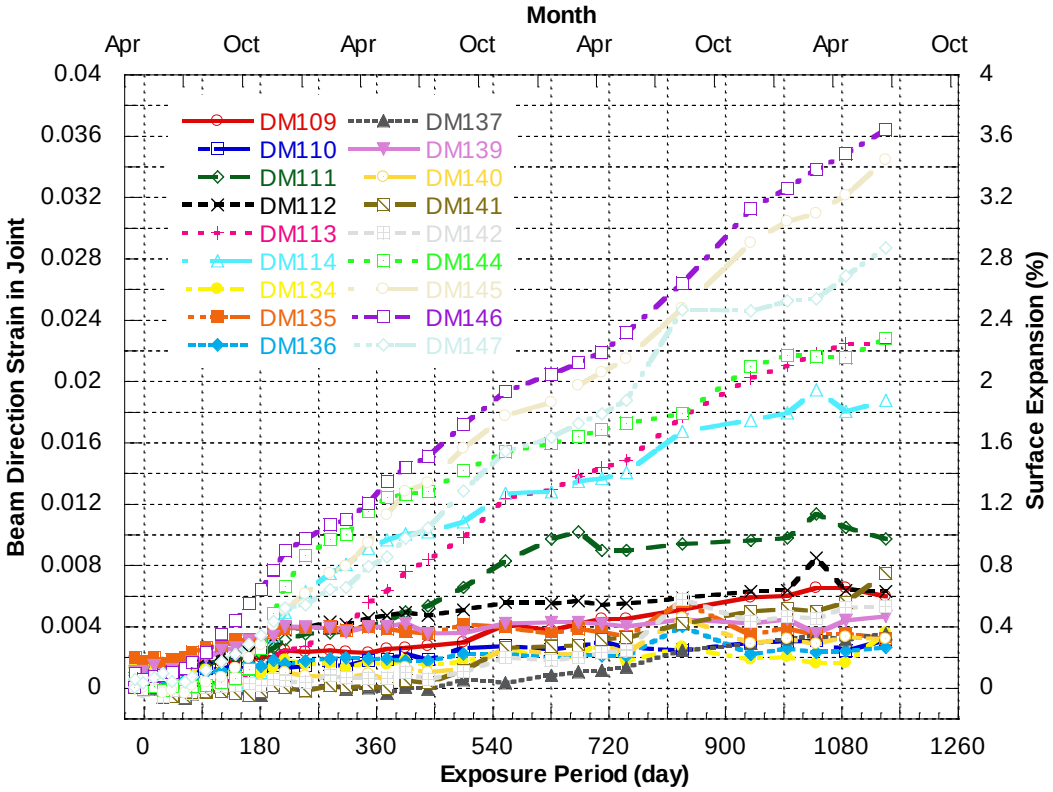

(d) Specimen 3

Figure 4-36 Beam Direction Surface Concrete Strains in Beam-Column Joint of Singly Reinforced Bent (Continued)

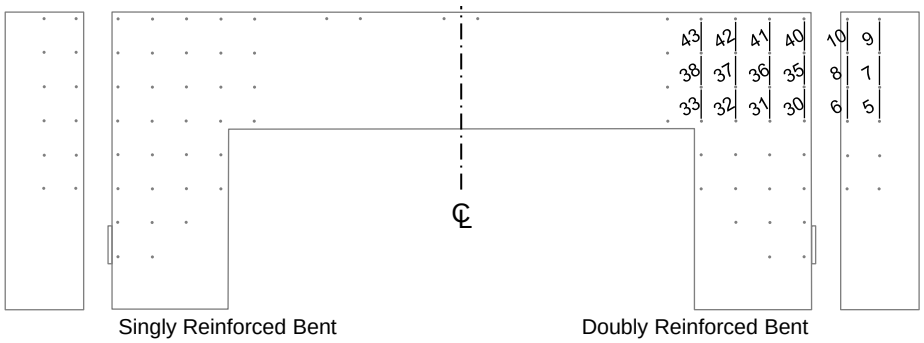

(a) DEMEC Measurements

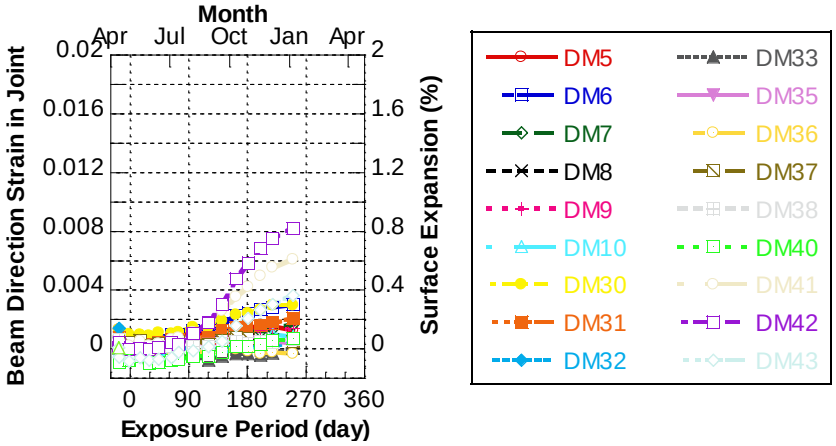

(b) Specimen 2

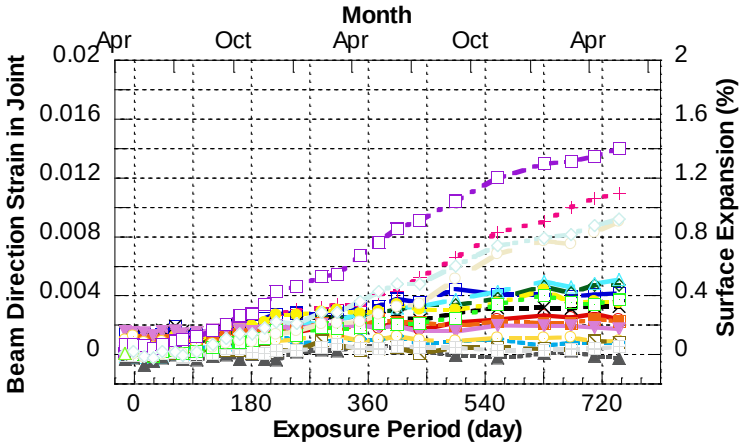

(c) Specimen 4

Figure 4-37 Beam Direction Surface Concrete Strains in Beam-Column Joint of Doubly Reinforced Bent

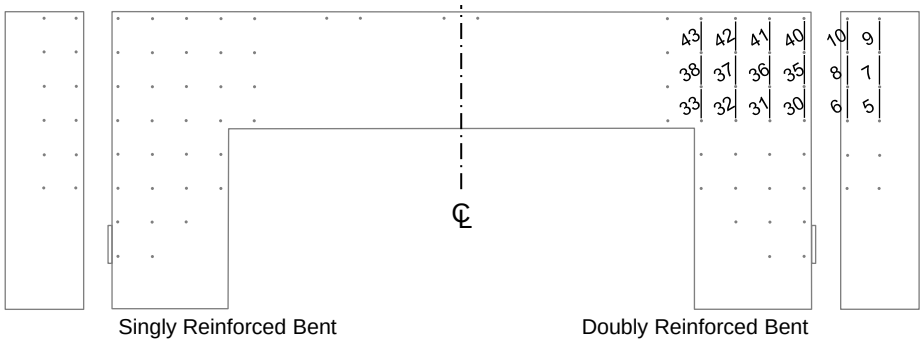

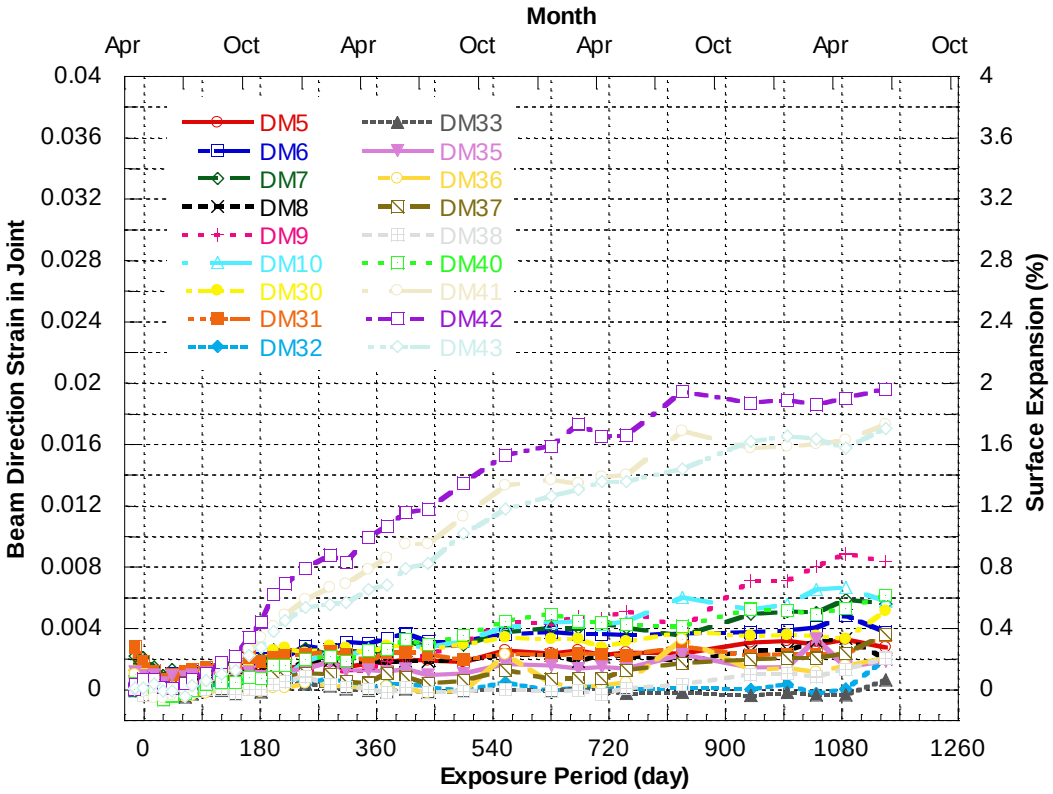

(d) Specimen 3

Figure 4-37 Beam Direction Surface Concrete Strains in Beam-Column Joint of Doubly Reinforced Bent (Continued)

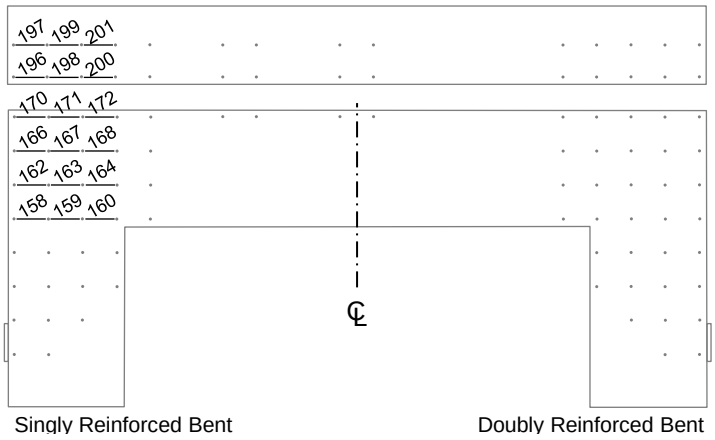

(a) DEMEC Measurements

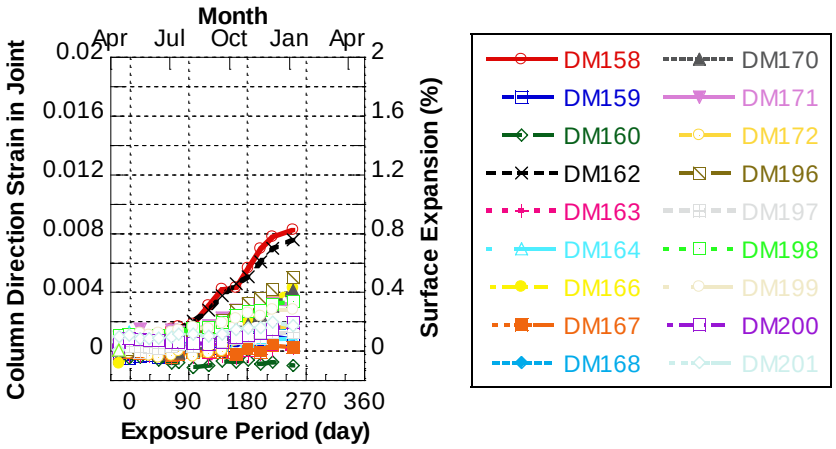

(b) Specimen 2

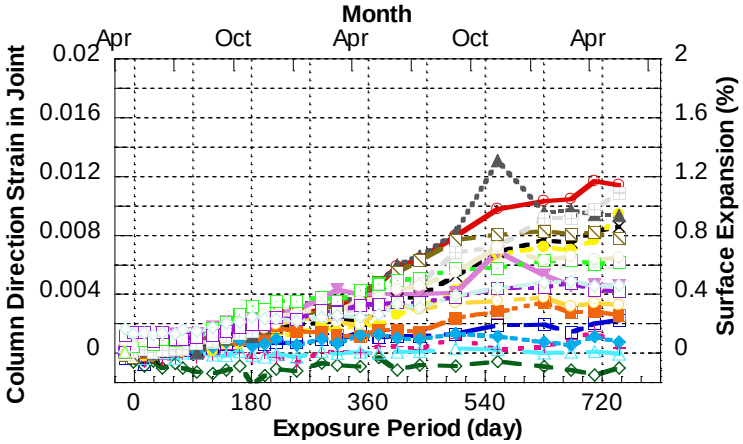

(c) Specimen 4

Figure 4-38 Column Direction Surface Concrete Strains in Beam-Column Joint of Singly Reinforced Bent

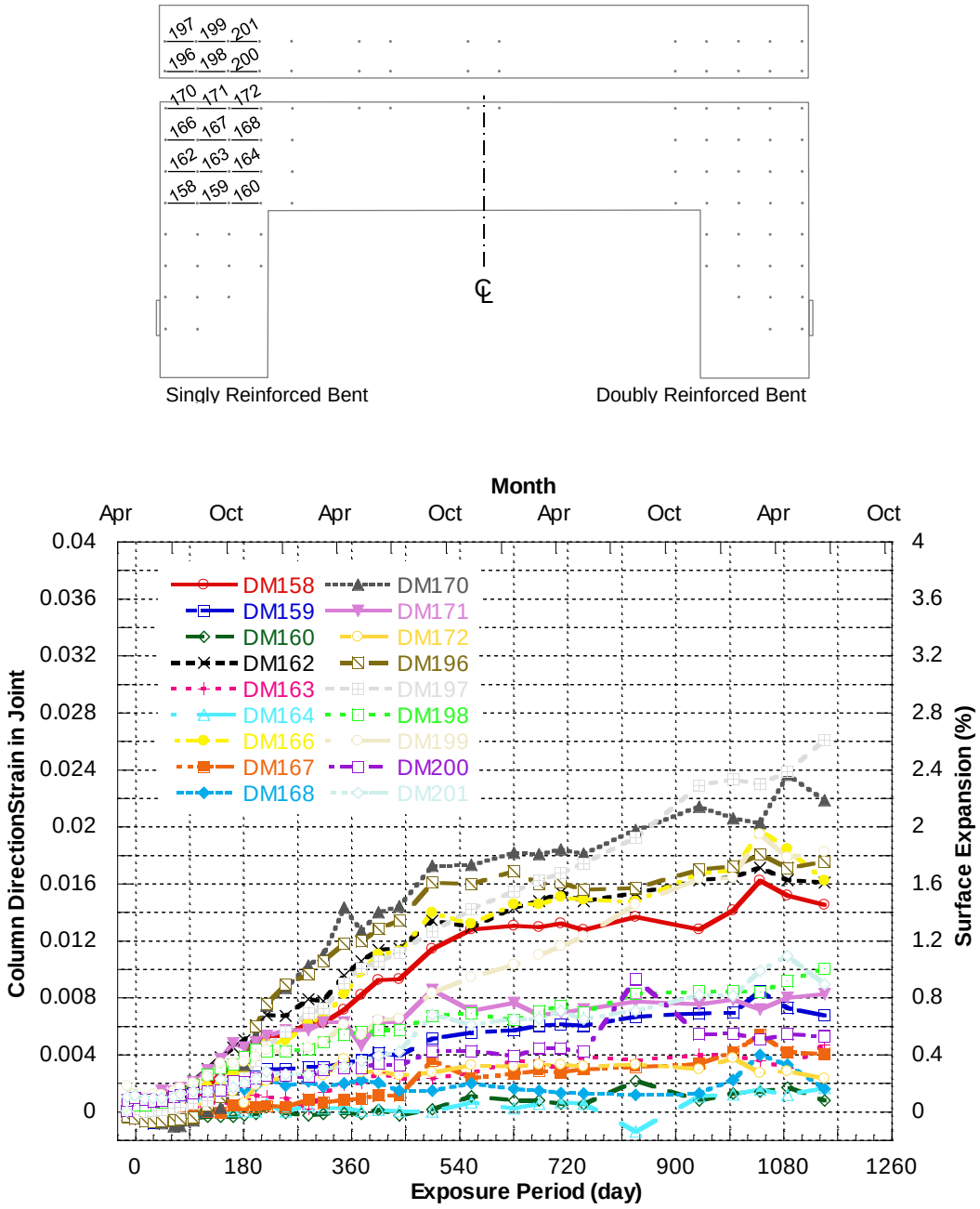

(d) Specimen 3

Figure 4-38 Column Direction Surface Concrete Strains in Beam-Column Joint of Singly Reinforced Bent (Continued)

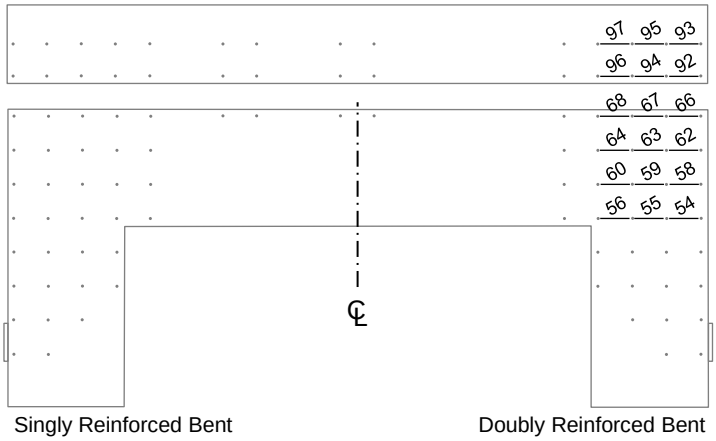

(a) DEMEC Measurements

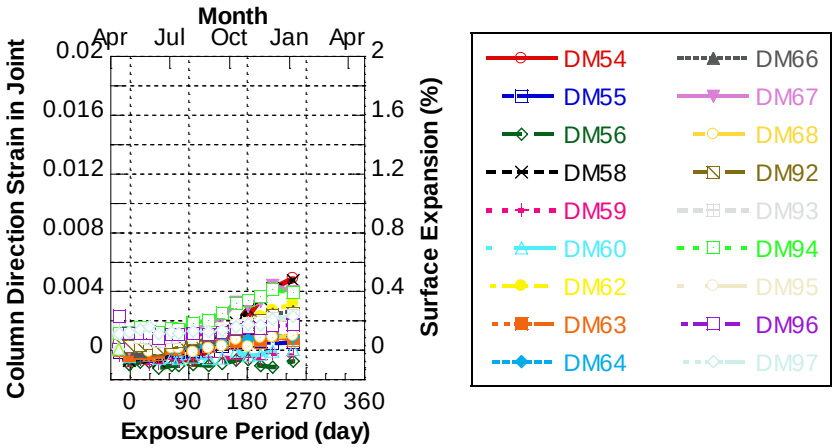

(b) Specimen 2

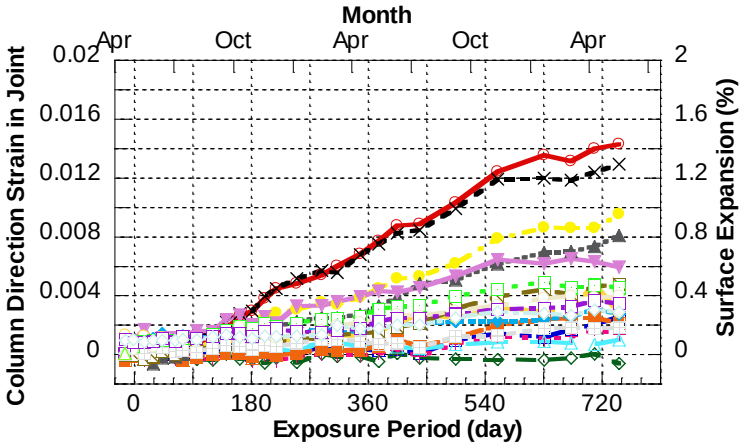

(c) Specimen 4

Figure 4-39 Column Direction Surface Concrete Strains in Beam-Column Joint of Doubly Reinforced Bent

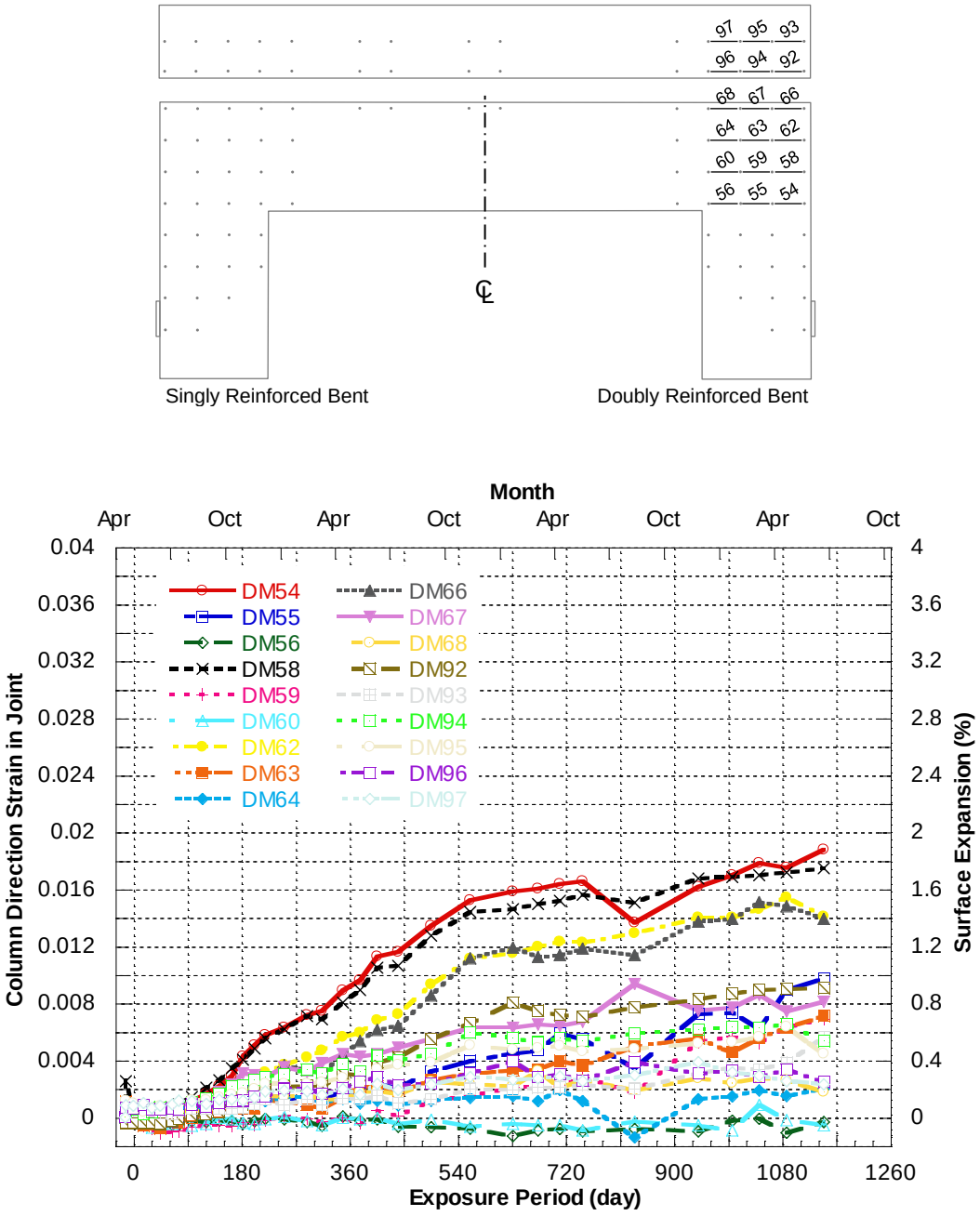

(d) Specimen 3

Figure 4-39 Column Direction Surface Concrete Strains in Beam-Column Joint of Doubly Reinforced Bent

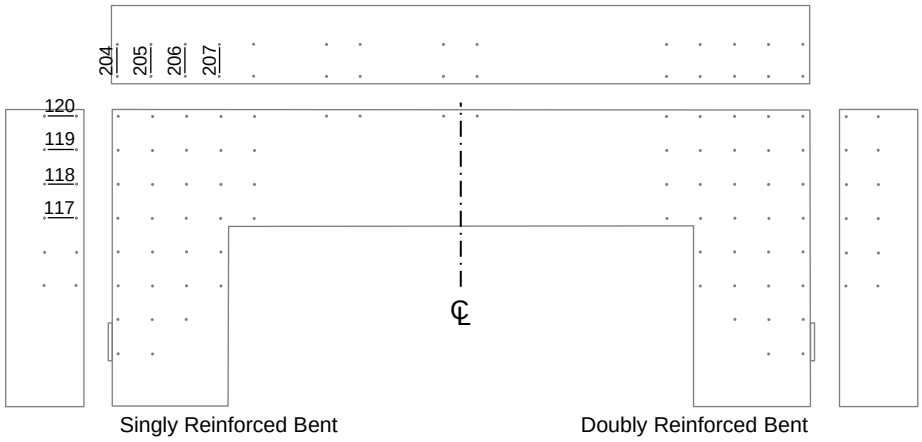

(a) DEMEC Measurements

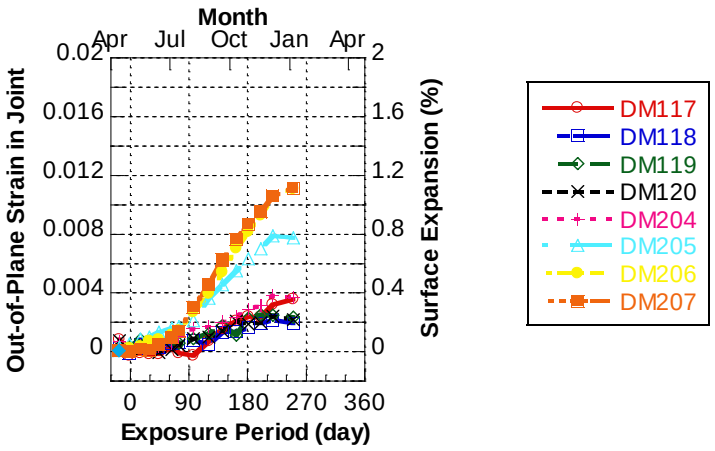

(b) Specimen 2

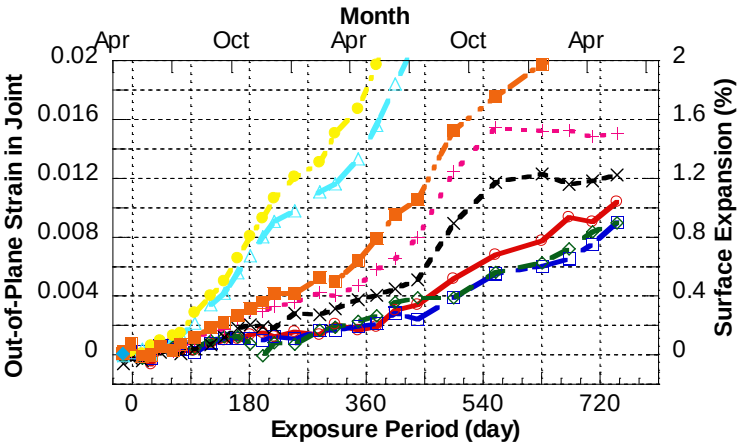

(c) Specimen 4

Figure 4-40 Out-of-Plane Surface Concrete Strains in Beam-Column Joint of Singly Reinforced Bent

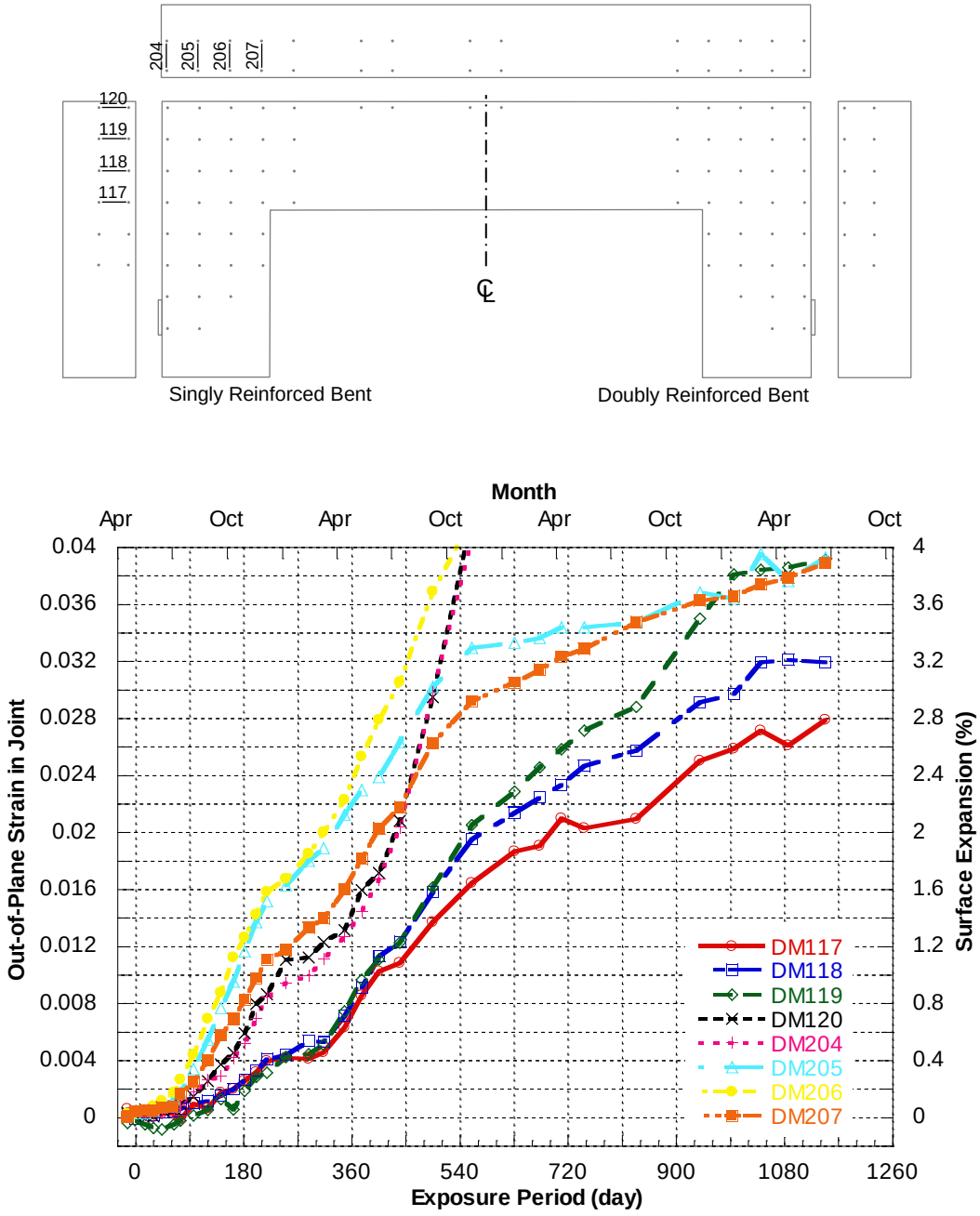

(d) Specimen 3

Figure 4-40 Out-of-Plane Surface Concrete Strains in Beam-Column Joint of Singly Reinforced Bent (Continued)

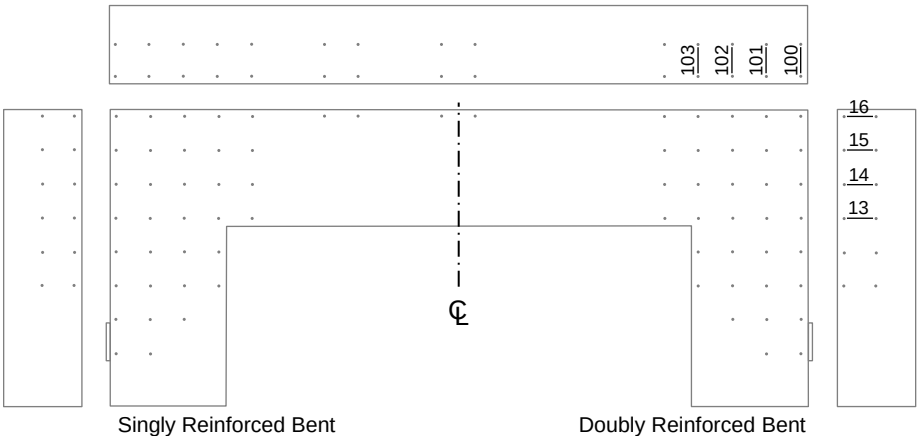

(a) DEMEC Measurements

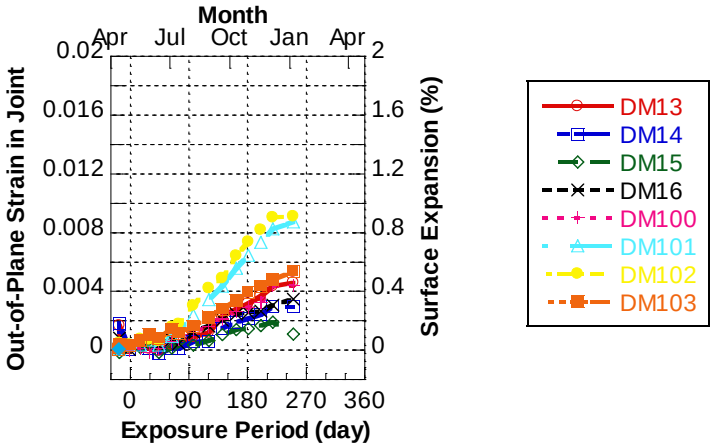

(b) Specimen 2

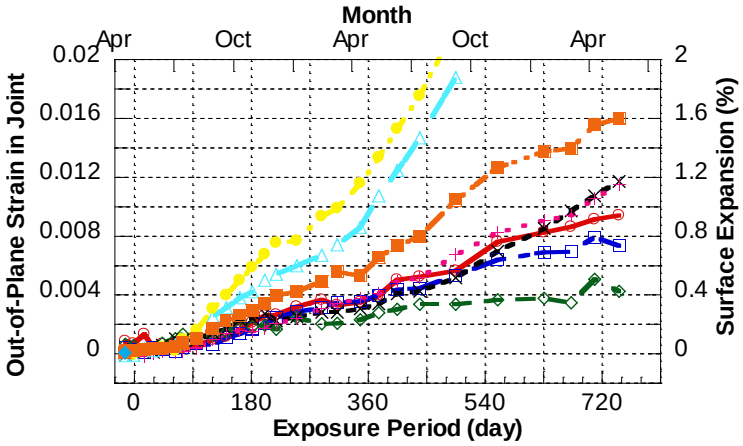

(c) Specimen 4

Figure 4-41 Out-of-Plane Surface Concrete Strains in Beam-Column Joint of Doubly Reinforced Bent

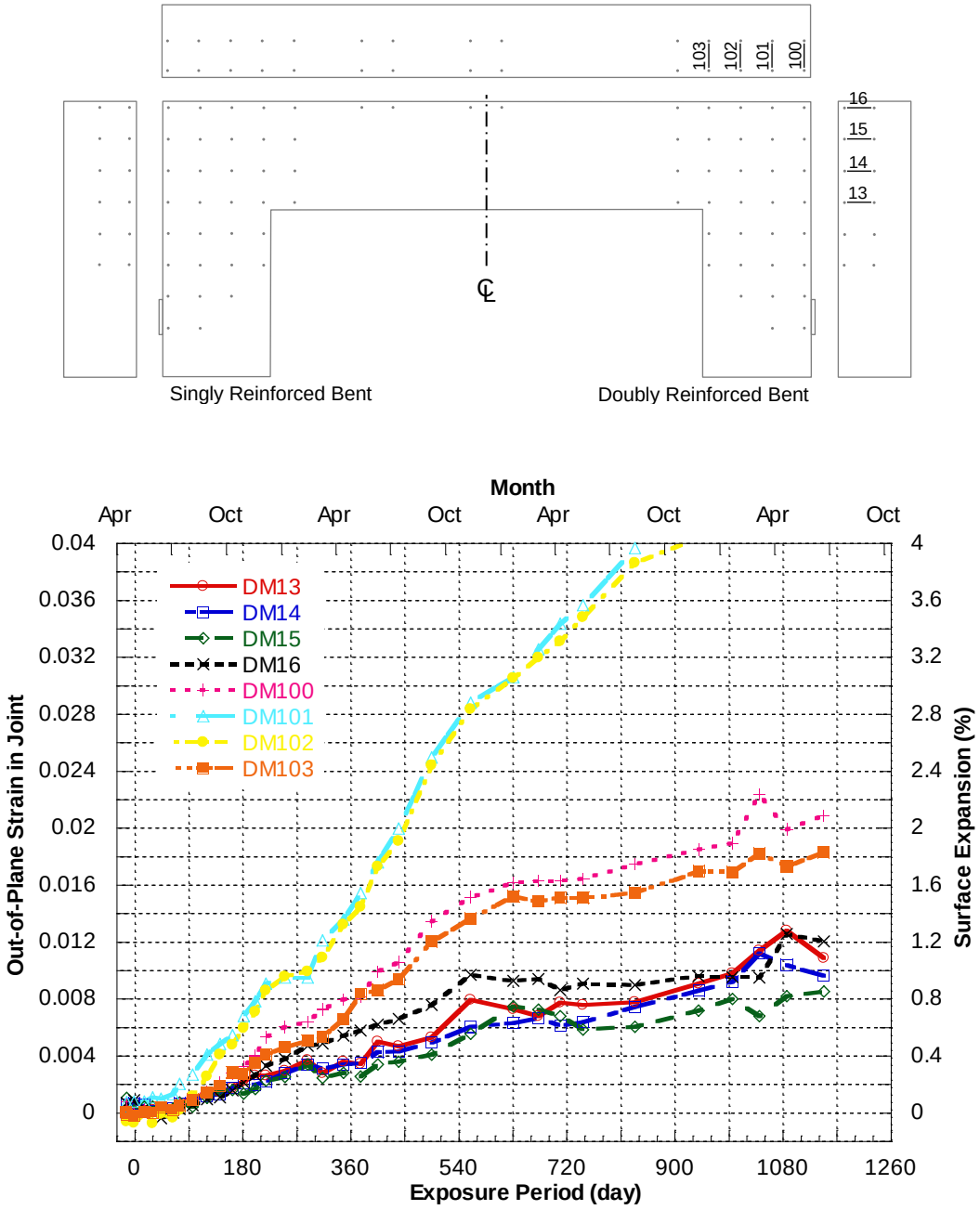

(d) Specimen 3

Figure 4-41 Out-of-Plane Surface Concrete Strains in Beam-Column Joint of Doubly Reinforced Bent (Continued)

Higher expansion rates were observed during the warmer months from April to October. The wetting and drying mechanism was prompted during these months as well, causing surface concrete cracking and allowing moisture ingress. From the observed results, the development of ASR/DEF accelerated once temperatures exceed 80 ˚F (26.7 ˚C) (Figure 4-15). As the high heat plus the wetting and drying effect subsided over the non-summer months, the expansion rate declined.

As per the orientation of the specimens in the field, water tended to saturate the top side of the specimen. Along with the prompted wetting and drying effect during the summer months, a significant amount of cracks developed and essentially permitted more moisture ingress, leading to more excessive cracking. From the observed out-of-plane and column direction strains on the top side of the beam-column joints, as shown in Figure 4-38 through Figure 4-41, it was validated that the greater amount of reinforcement was influential in restraining the column direction surface concrete expansion (Figure 3-2). As discussed in the previous section, it is proposed that U-shaped reinforcing steel bars should be also used in the direction perpendicular to the existing U-shaped steel bars in the beam-column joint regions (Figure 4-25). These additional U-shaped steel bars can not only restrain the ASR/DEF expansion in the out-of-plane direction on the column face (CF) in the beam-column joint region, but also provide shear resistance in the joint region. The beneficial effects of the application of additional U-shaped reinforcing steel bars on the provision of shear resistance in the beam-column joint region are discussed in the later chapters.

4.5 INTERNAL CONCRETE STRAINS

Figures 4-42 and 4-43 present the mid-depth core concrete strains in the three perpendicular directions over time. After the application of the pre-loading, compression strains were observed in the STM compression struts (KMs 1, 4, 7 and 10) and some strains greater than 0.002 were observed in the directions perpendicular to the STM compression struts in the beam regions (KM2 of Specimen 3 and KM8 of Specimen 2). Note that some gages failed (stopped reading) due to the development of ASR/DEF during the exposure phase and some faulty readings, that is, scattered patterns of readings, may have been recorded.

In general, the concrete strains in the STM compression struts, except for KM4 of Specimen 3, remained in compression and varied little over time. However, the concrete strains perpendicular to the STM compression struts (KMs 2, 5, 8 and 11) and the out-of-plane concrete strains (KMs 3, 6, 9 and 12) reached 0.001 after the first summer (April through October). In addition, these strains in Specimen 3 developed at a higher rate and exceeded 0.003 after 6 months (180 days) of exposure. In the out-of-plane direction, however, the concrete expanded significantly during the second summer and reached over 0.005 after 24-month (720 days) exposure. It was observed that the core concrete tended to expand more across the width of the specimens. That is, the transverse hoops in the beam regions and the U-shaped steel bars in the beam-column joints provided relatively little restraint against ASR/DEF expansion over time. The proposed additional U-shaped reinforcing steel bars perpendicular to the existing U-shaped steel bars can provide more constraint in the beam-column joint (Figure 4-25).

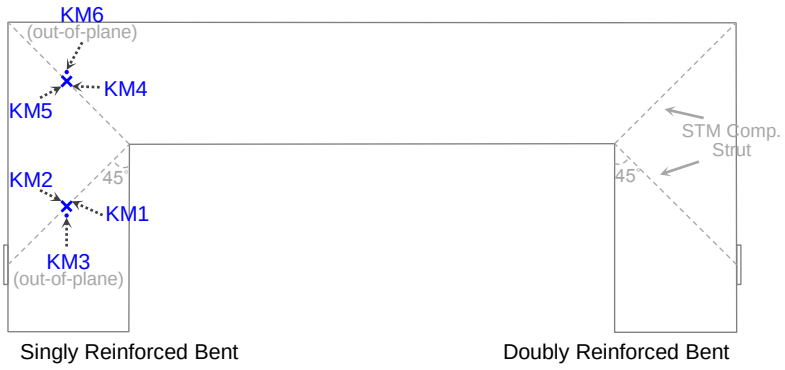

(a) Orientations of Concrete Gages at Mid-Depth

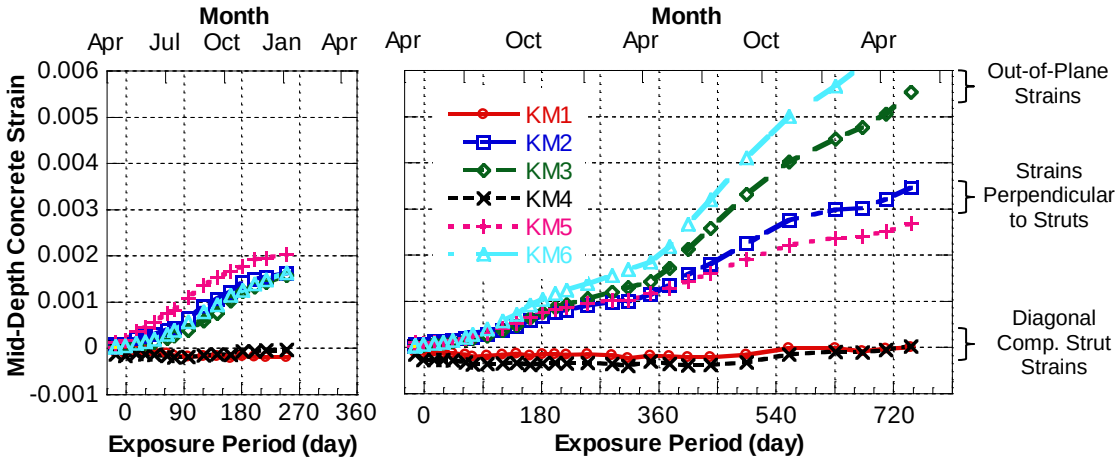

(b) Specimen 2 *(c) Specimen 4*

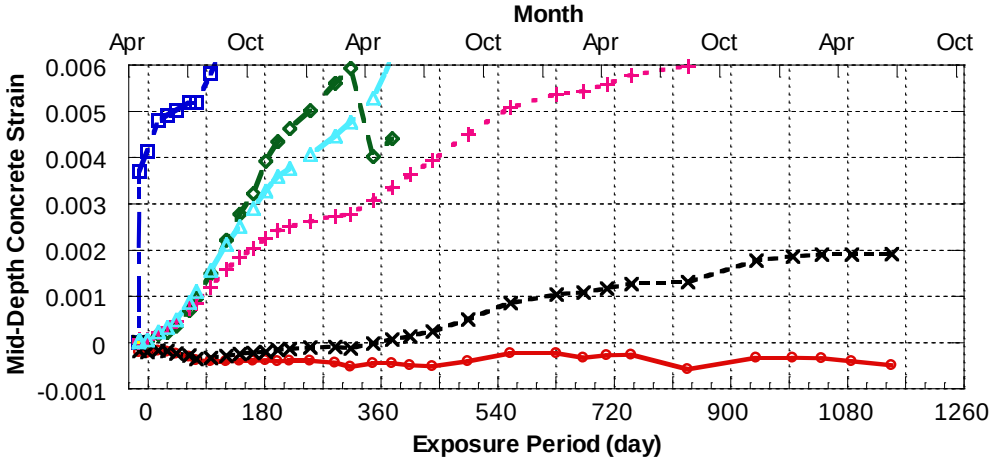

(d) Specimen 3

Figure 4-42 Mid-Depth Concrete Strains of Singly Reinforced Bent

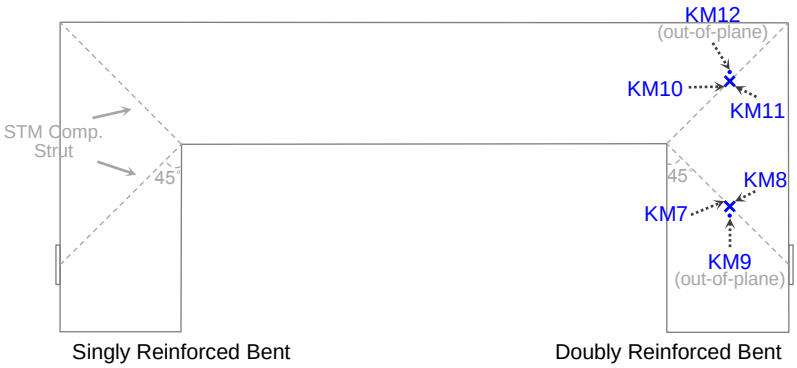

(a) Orientations of Concrete Gages at Mid-Depth

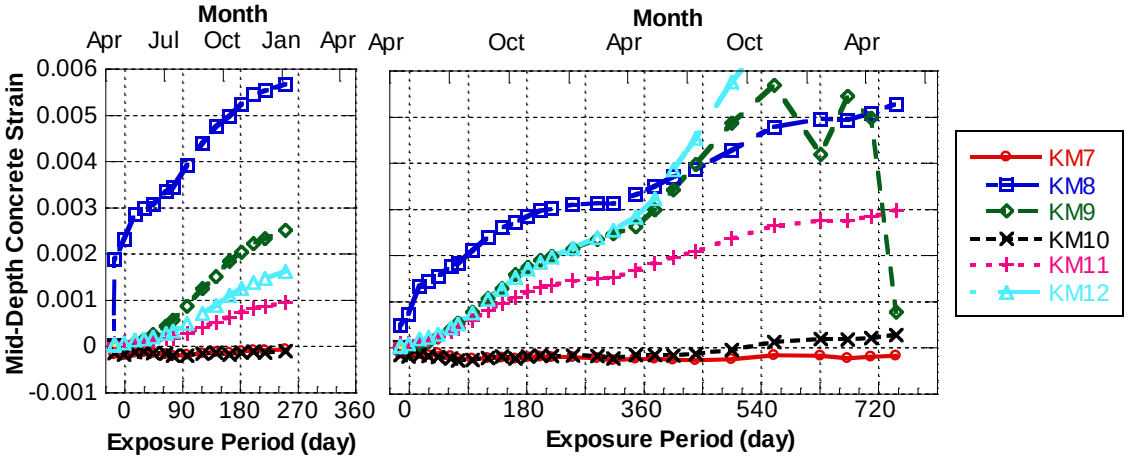

(b) Specimen 2 *(c) Specimen 4*

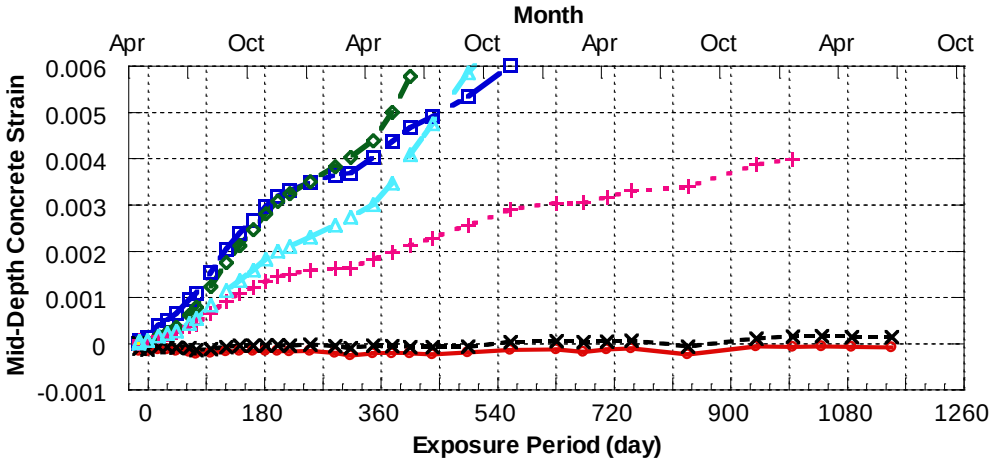

(d) Specimen 3

Figure 4-43 Mid-Depth Concrete Strains of Doubly Reinforced Bent

4.6 REINFORCING STEEL STRAINS

Figures 4-44 and 4-45 show the longitudinal reinforcing steel strains in the beam regions over time. Note that some strain gages failed (stopped reading) after concrete casting, pre-loading application, and during the exposure phase. Once the prestress was applied, the strains in the longitudinal tension steel in the beam regions were within the range of 0.0005 to 0.0008 in tension (22 to 36% of reinforcing steel tension yield strain) before the specimens were transported to the field. These strains gradually increased to over 0.001 in tension (45% of reinforcing steel tension yield strain) primarily due to ASR in the first nine months (270 days) during the subsequent exposure phase. In the following period, some compression strains were recorded and the gage readings scattered over time. This could be caused by the development of faulty gages over time from the ASR/DEF expansion.

Comparable results were observed in the longitudinal reinforcing steel in the column region (Figure 4-46). The strains in the longitudinal tension steel in the column region ranged from 0.0005 to 0.001 in tension (22 to 45% of reinforcing steel tension yield strain) after the pre-loading application and gradually developed to over 0.0012 in tension (54% of reinforcing steel tension yield strain) primarily due to ASR after nine months (270 days) of exposure. Some scattered gage readings were also recorded in the subsequent period, due to the development of faulty gages as a result of the ASR/DEF expansion over time.

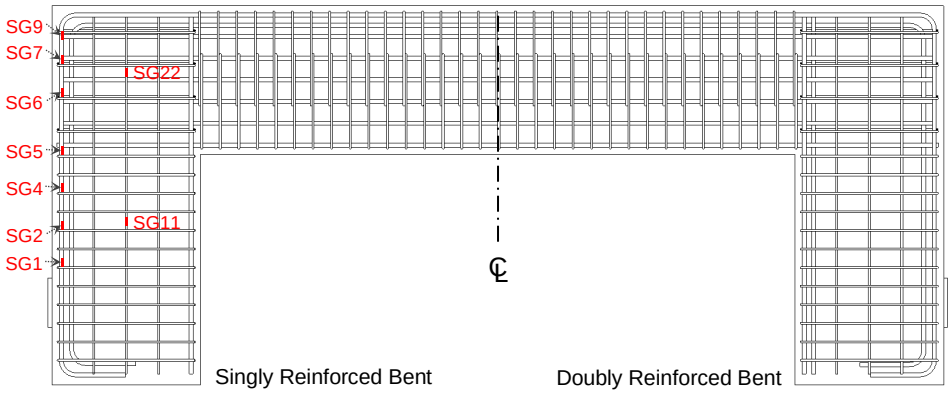

(a) Locations of Strain Gages Attached to Reinforcing Steel

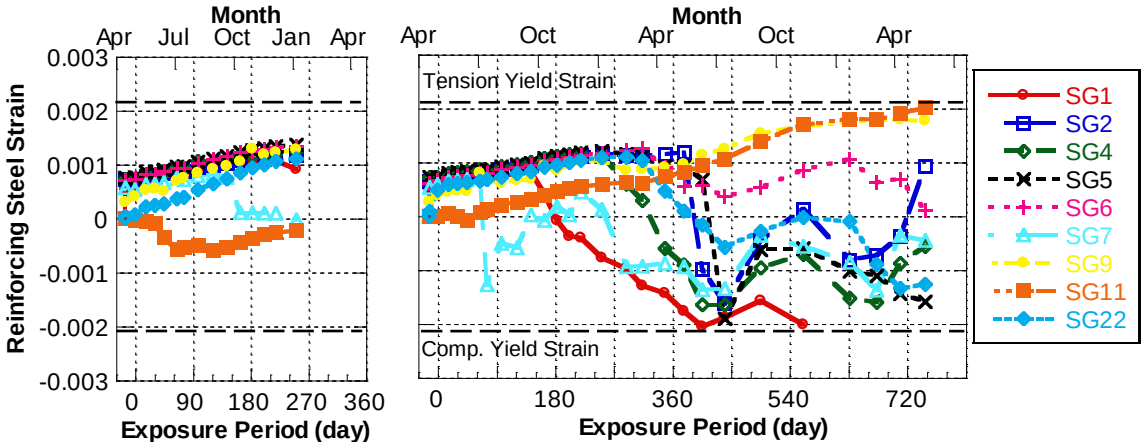

(b) Specimen 2

(c) Specimen 4

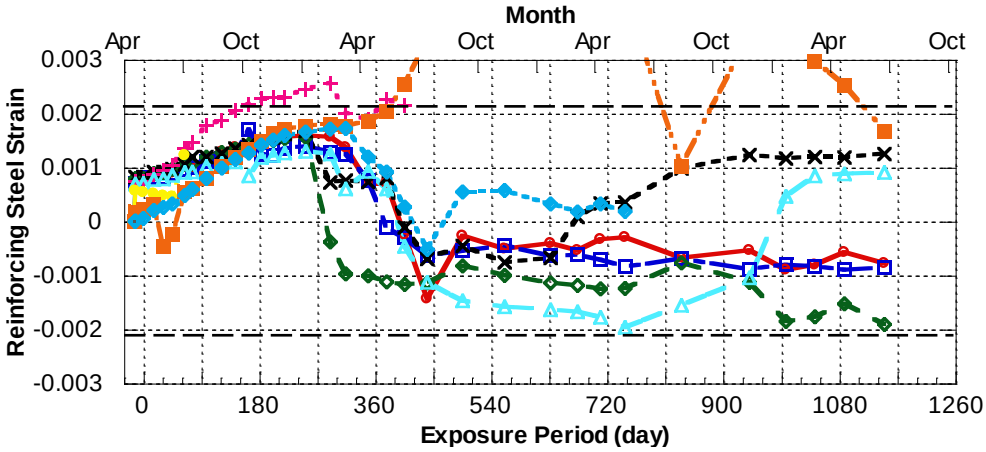

(d) Specimen 3

Figure 4-44 Longitudinal Reinforcing Steel Strains in Beam Region of Singly Reinforced Bent

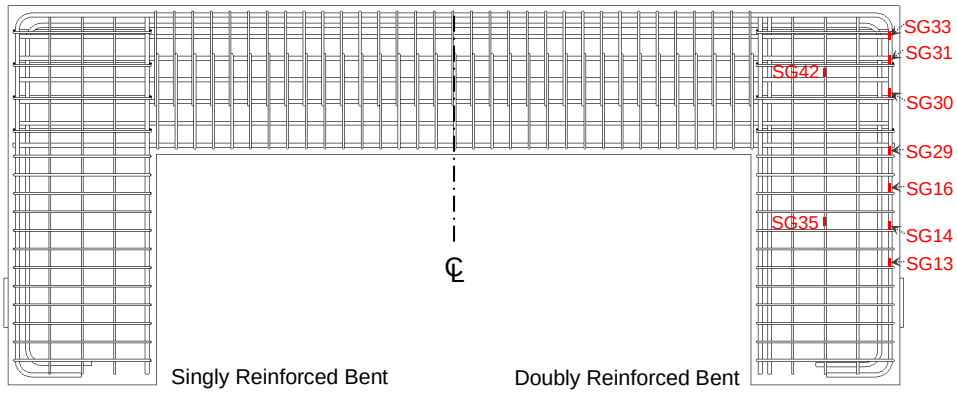

(a) Locations of Strain Gages Attached to Reinforcing Steel

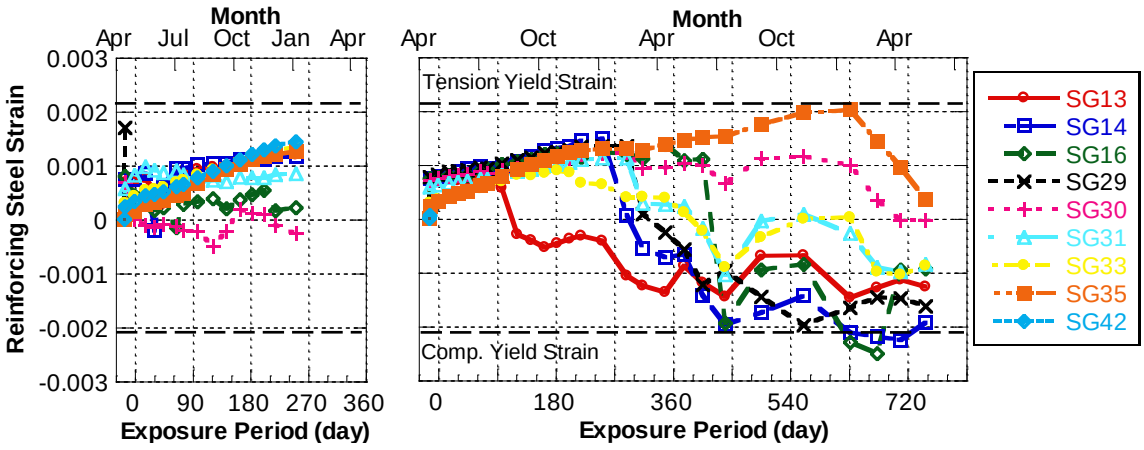

(b) Specimen 2

(c) Specimen 4

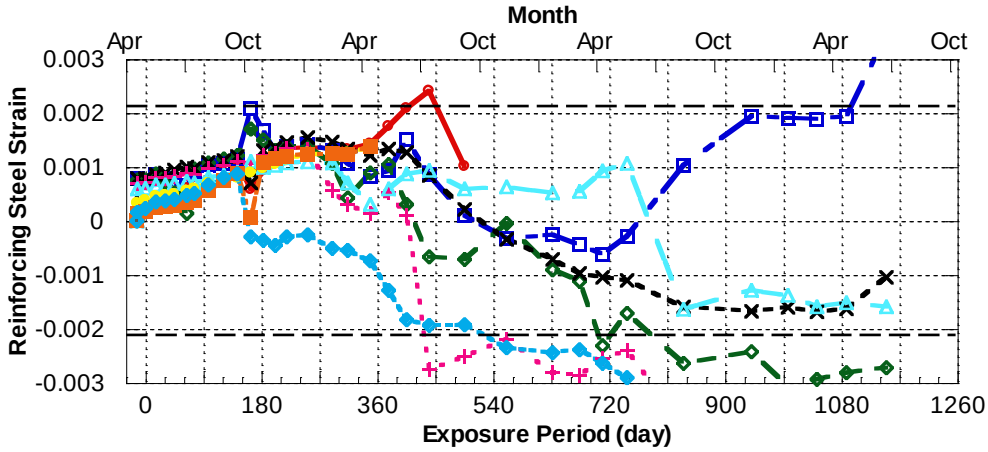

(d) Specimen 3

Figure 4-45 Longitudinal Reinforcing Steel Strains in Beam Region of Doubly Reinforced Bent

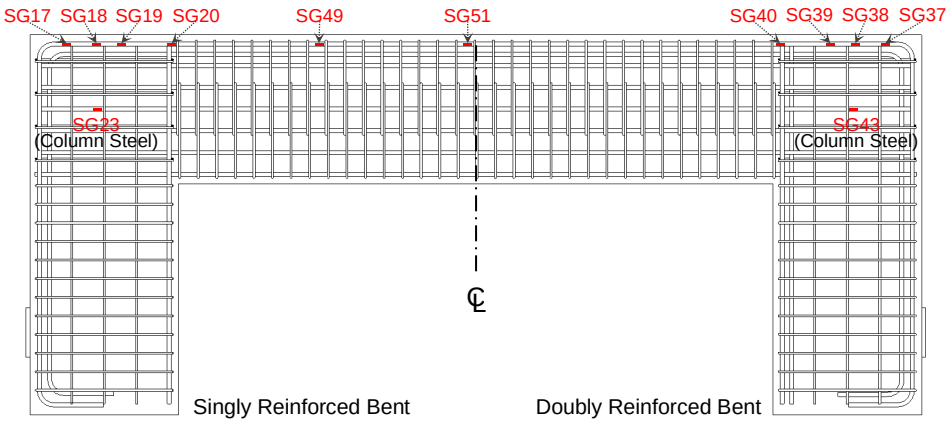

(a) Locations of Strain Gages Attached to Reinforcing Steel

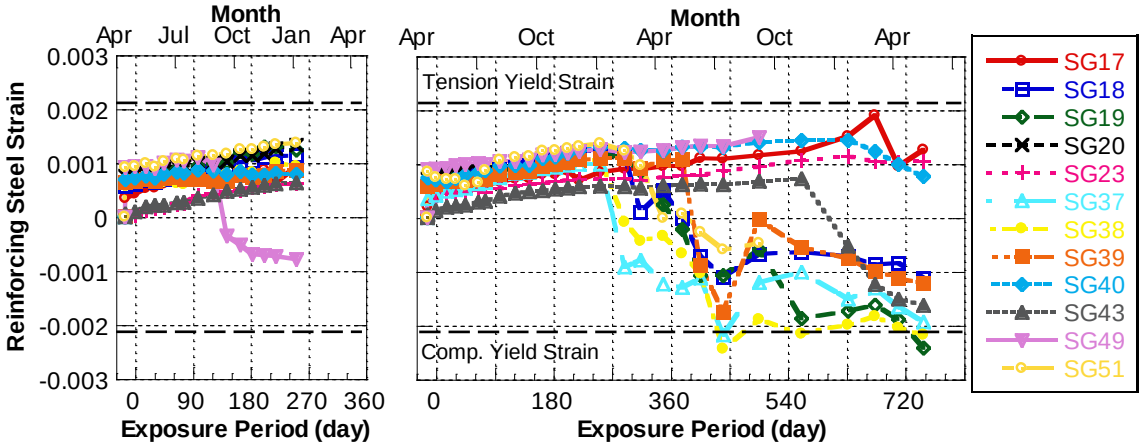

(b) Specimen 2

(c) Specimen 4

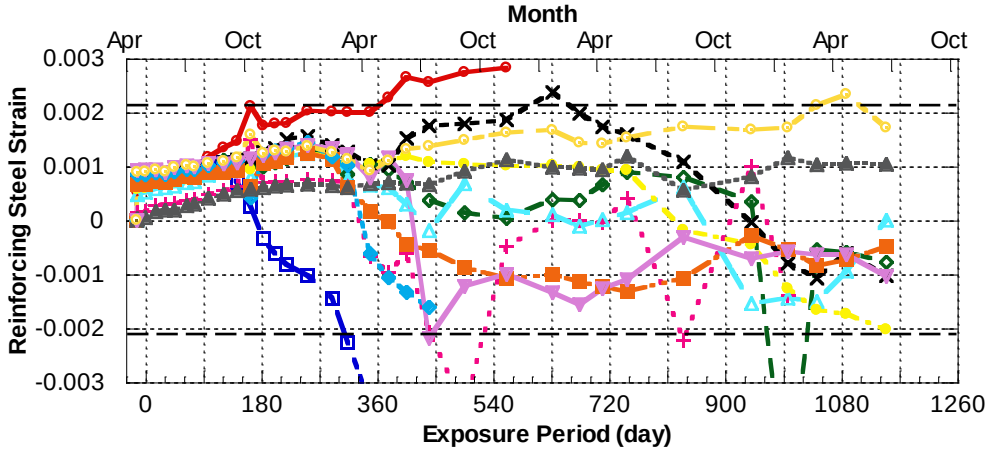

(d) Specimen 3

Figure 4-46 Longitudinal Reinforcing Steel Strains in Column Region

Figures 4-47 and 4-48 present the strains in the transverse hoops in the beam regions and the U-shaped steel bars in the joint regions during the exposure phase. Minor strains in these steel bars were observed from the pre-loading application, except for SG10 in Specimen 3 and SG34 in Specimens 2 and 4. Although some scattered readings were recorded, the strains in some transverse hoops and U-shaped steel bars gradually increased during the summer months and reached the tension yield strain. It is evident that the ASR/DEF expansion introduced some confining effect to core concrete and caused the hoop steel and U-shaped bars to yield.

Strains in the compression reinforcement in the beam and column near the inside corner of the joint region (STM CCC node) were -0.0005 in compression after pre-loading was applied (Figure 4-49). Over time, these strains changed from compression to tension and reached 0.001 due to the ASR/DEF expansion, which potentially stretched the reinforcing steel provided by the bond between concrete and reinforcing steel. This also confirms the prestressing effect of the concrete from the contributions of the longitudinal reinforcing steel.

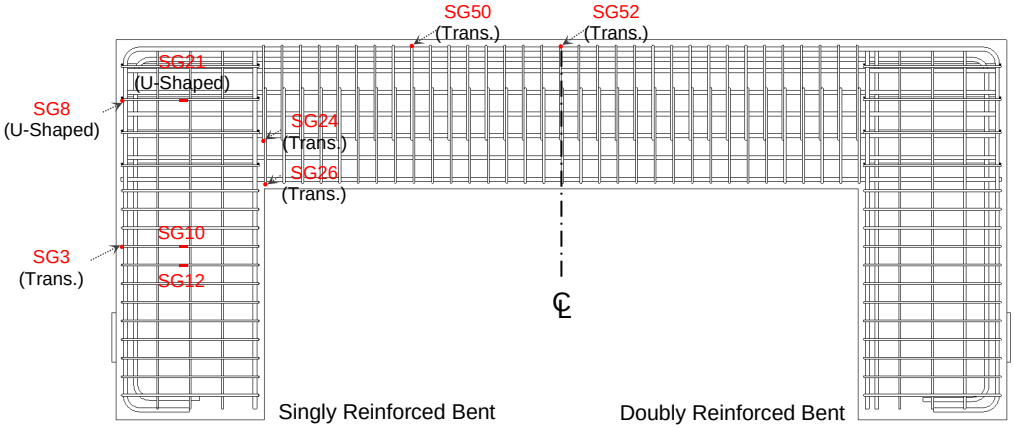

(a) Locations of Strain Gages Attached to Reinforcing Steel

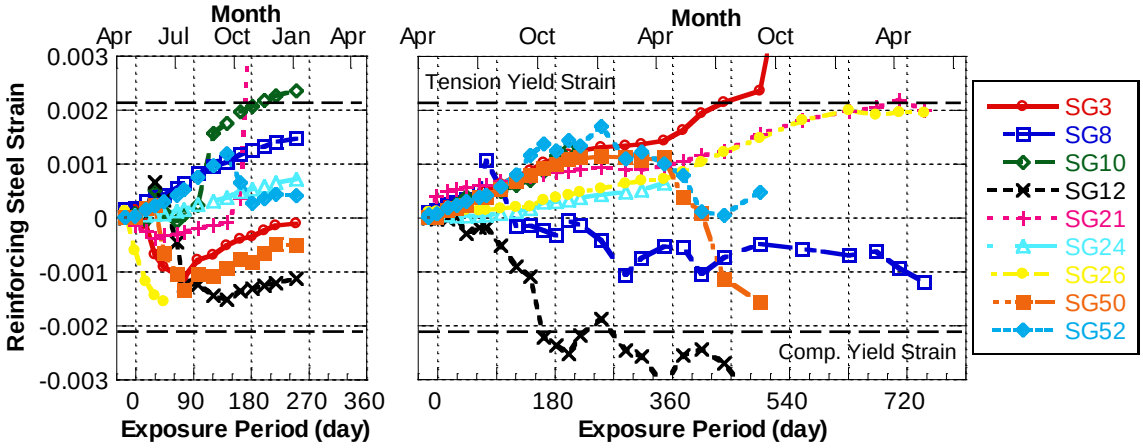

(b) Specimen 2

(c) Specimen 4

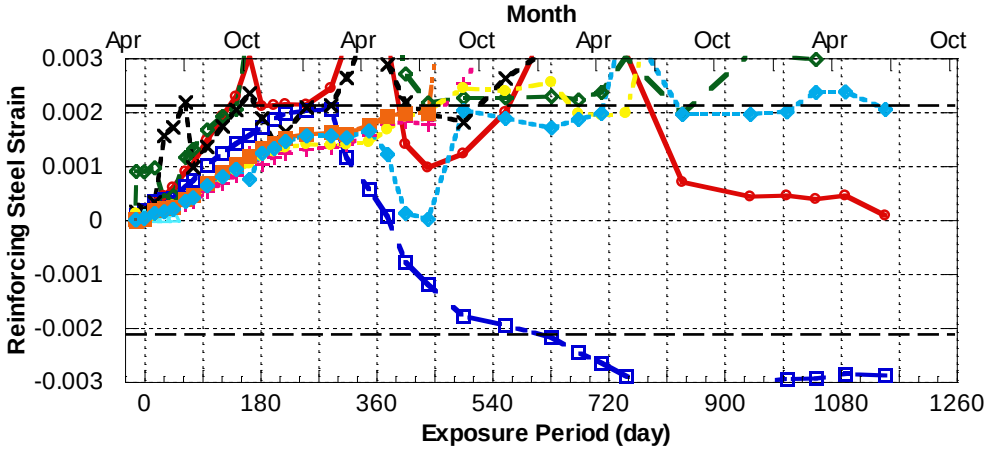

(d) Specimen 3

Figure 4-47 Strains in Transverse Steel and U-Shaped Steel Bar of Singly Reinforced Bent

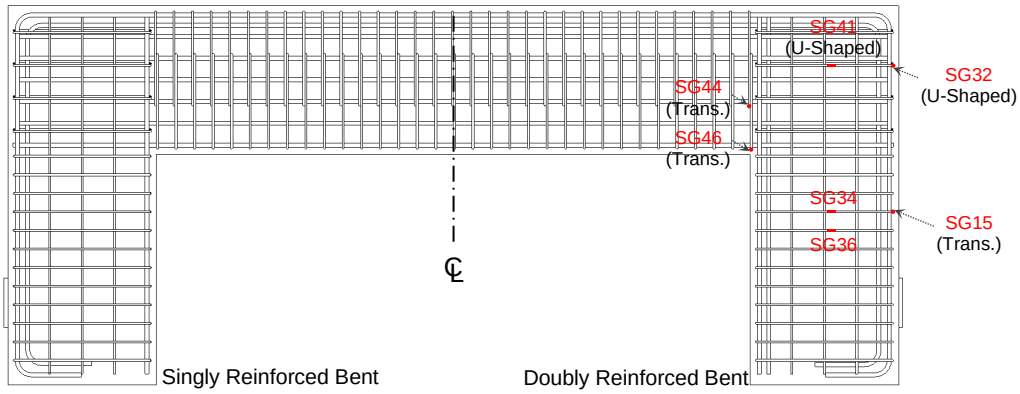

(a) Locations of Strain Gages Attached to Reinforcing Steel

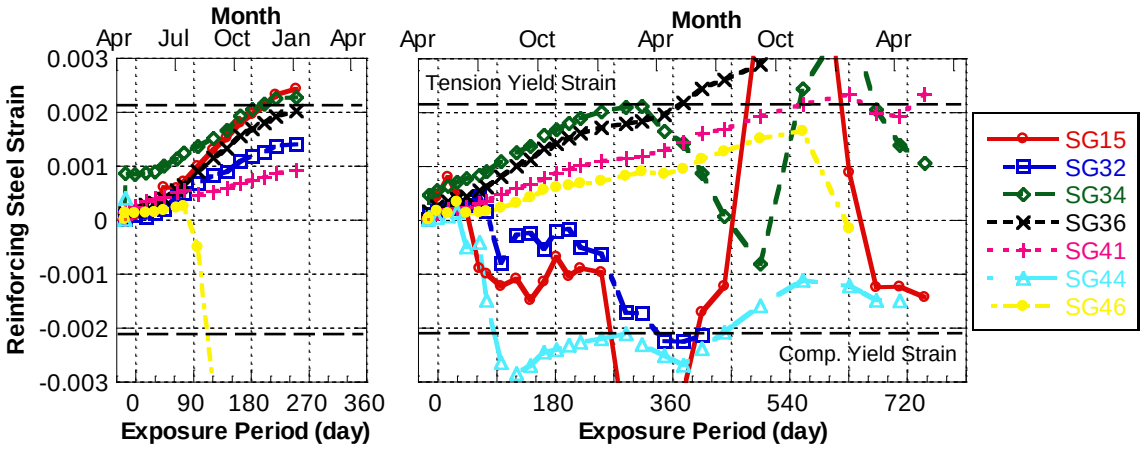

(b) Specimen 2

(c) Specimen 4

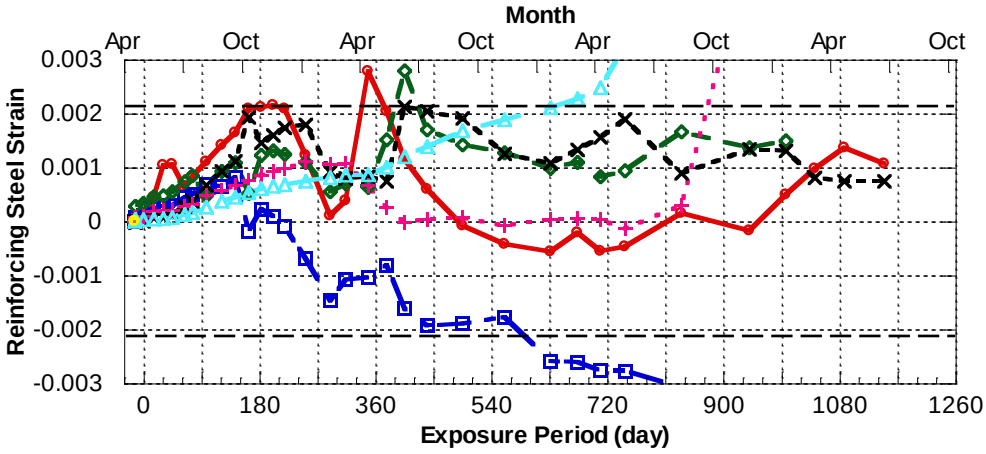

(d) Specimen 3

Figure 4-48 Strains in Transverse Steel and U-Shaped Steel Bar of Doubly Reinforced Bent

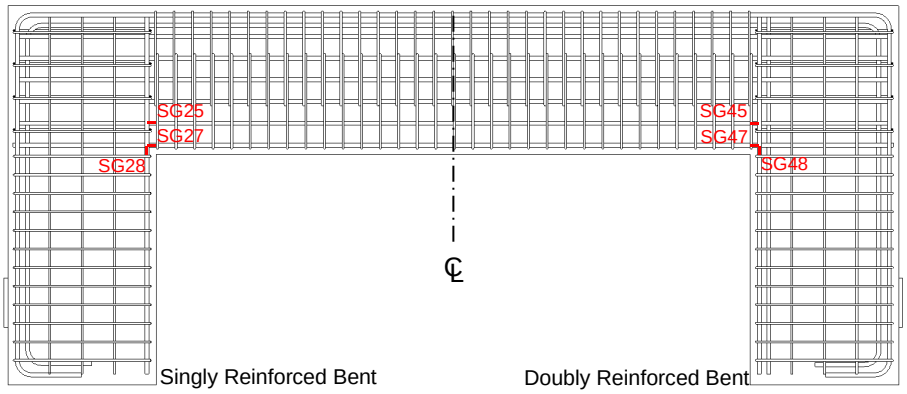

(a) Locations of Strain Gages Attached to Reinforcing Steel

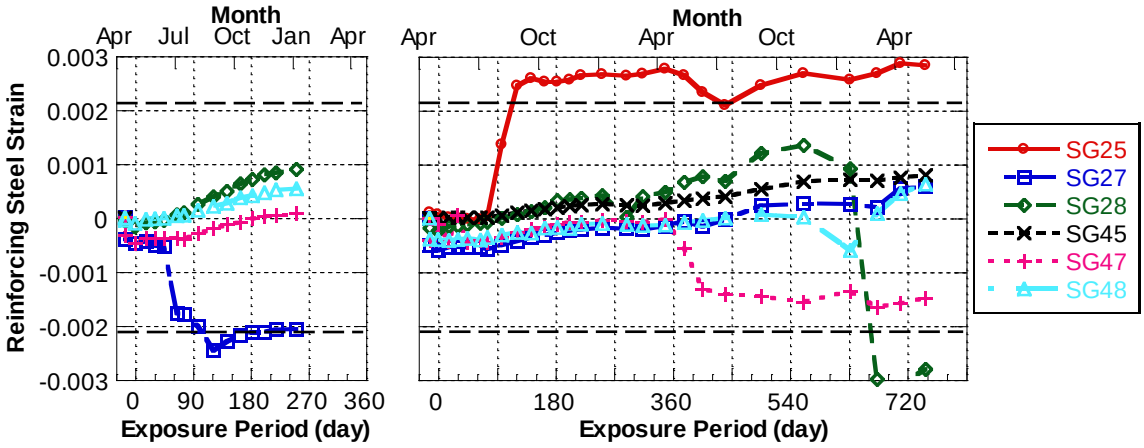

(b) Specimen 2 *(c) Specimen 4*

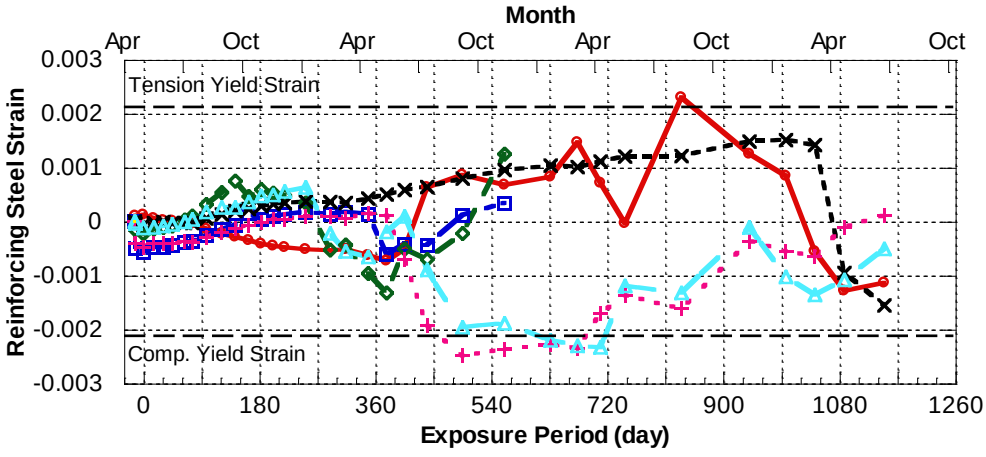

(d) Specimen 3

Figure 4-49 Reinforcing Steel Strains in Compression Zone

4.7 PETROGRAPHIC ANALYSIS RESULTS

A series of concrete cores were extracted from Specimens 1, 2 and 4 following their structural testing to examine if ASR/DEF was evident in the specimens. Multiple 4-inch (102 mm) diameter concrete cores of varying depths were taken using a Hilti DD 200 coring machine along with diamond core bits. Some 6-inch (152 mm) diameter concrete cores were also extracted from Specimen 2. These cores were drilled through longitudinal or transverse reinforcement, near locations with mild or no cracking, near locations with large cracks or severe map cracking, and near locations with white residues on the surface. Petrographic analyses of these cores were then conducted independently by TxDOT personnel. Appendixes A, B and C show three petrographic analysis reports for Specimens 1, 2 and 4, respectively.

For Specimen 1 (the unexposed specimen), it was reported that some ASR gel was observed in the coarse and fine aggregates but the amount was sparse (Figure 4-50). The gel had not absorbed much water since Specimen 1 was stored in the climate controlled laboratory without supplemental water after the construction. Therefore, it was evident that exposure conditions greatly affect the development of ASR/DEF, as discussed in Section 2.2.

Figure 4-51a depicts the locations of the cores extracted from Specimen 2. Note that Specimen 2 was shipped back to the structural testing laboratory after 252 days of exposure in the field. It was reported that the surface cracks with a maximum width of 0.016 inches (0.41 mm) were traced from the surface to a depth of 2.5 inches (64 mm) (Figure 4-51b and c). Figure 4-51d shows that ASR gel was observed in air voids

adjacent to reactive aggregates and the aggregates showed signs of distress due to the ASR expansion. It was reported that ASR was the primary cause for the distress of aggregates in Specimen 2 and the ASR-distressed level was reported as moderate to high stages of ASR formation. Moreover, minor accumulation of ettringite was observed within air voids and cracks (Figure 4-51d). In addition, ettringite was noted at the interface of aggregates and cement paste and as coating around the reinforcing steel bars (Figure 4-51e). Although the ettringite formation within some of the cores was observed, there was not enough evidence to confirm that DEF caused the distress.

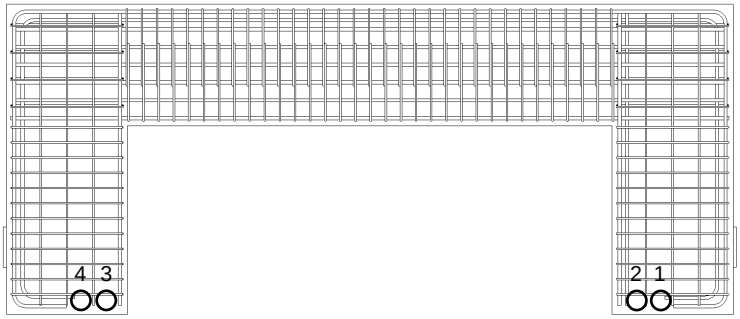

(a) Core Locations

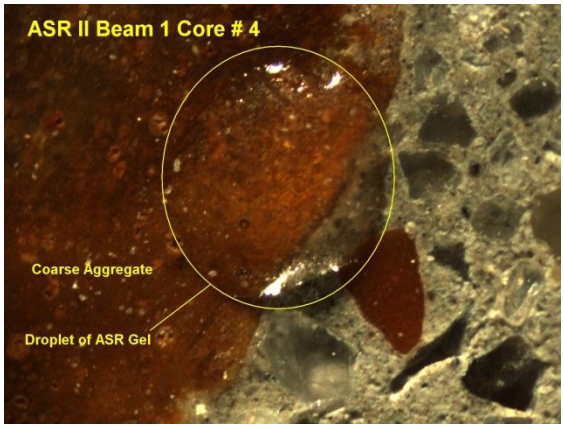

(b) Sparse ASR gel in Coarse Aggregate

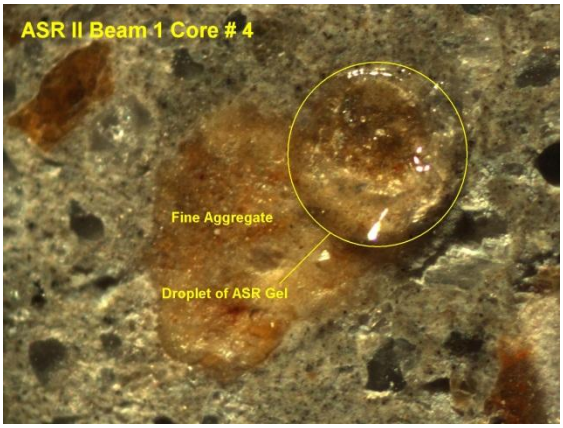

(c) Sparse ASR gel in Fine Aggregate

Figure 4-50 Petrographic Analysis Results of Cores Extracted from Specimen 1

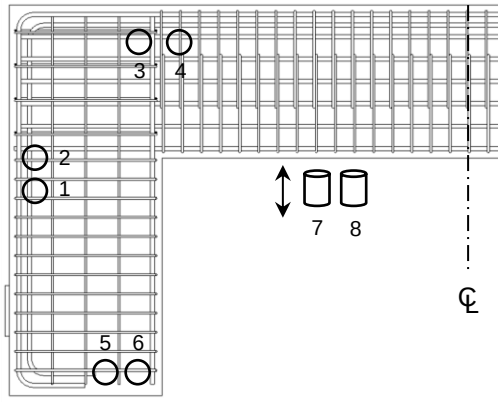

(a) Core Locations

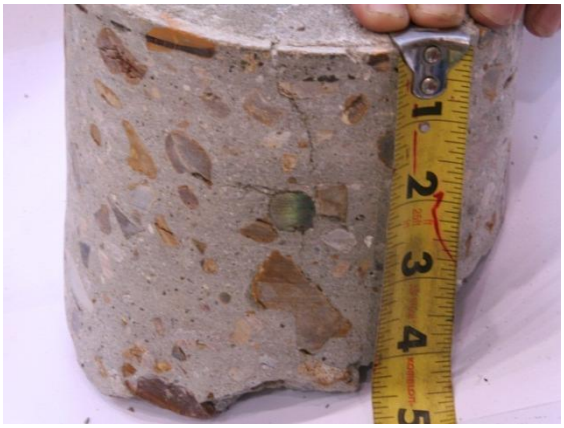

(b) Crack from Surface to Reinforcing Steel (Core 1)

(c) Crack from surface to Reinforcing Steel (Core 2)

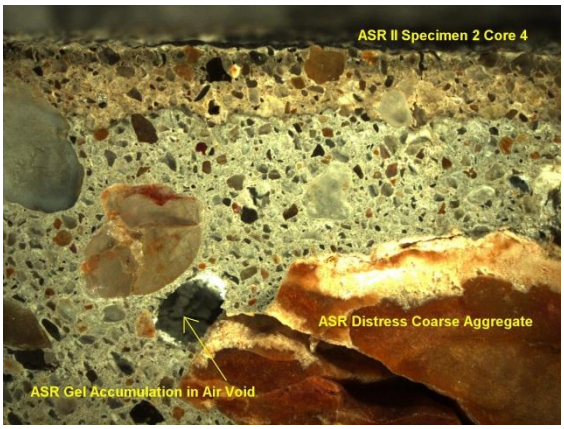

(d) ASR Gel Accumulation in Air Void and ASR Distressed Coarse Aggregate

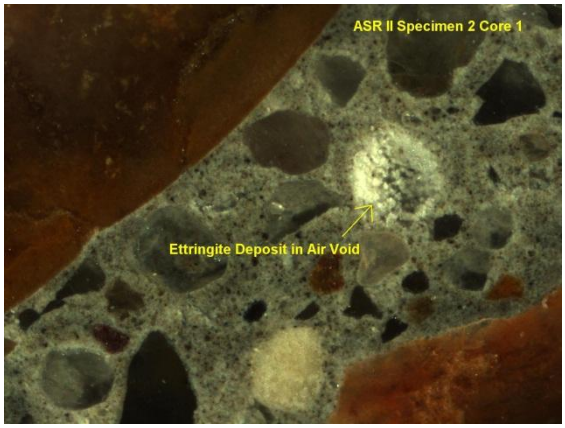

(e) Accumulation of Ettringite in Air Void

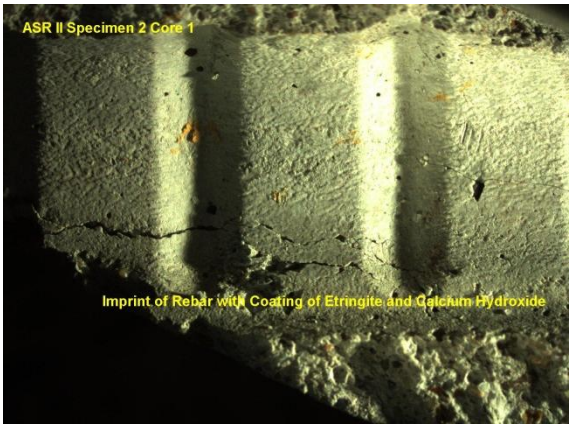

(f) Imprint of Reinforcing Steel with Accumulation of Ettringite

Figure 4-51 Petrographic Analysis Results of Cores Extracted from Specimen 2

Figure 4-52a shows the locations of the cores extracted from Specimen 4. Note that Specimen 4 was transported back to the structural testing lab after 748 days of exposure in the field. It was reported that the surface crack width was up to 0.12 inches (3 mm). In addition, some cracks were traced from the surface and intersected reinforcing steel bars at a depth of 1 5/8 inches (41 mm). Figure 4-52b through d show that ASR gel was observed in air voids near reactive aggregates and some of these aggregates showed signed of distress due to the ASR expansion. Fluorescent image also evidenced the sign of ASR-induced distress in aggregates (Figure 4-52e). It was reported that ASR was the primary cause for the distress of aggregates in Specimen 4 and the ASR-distressed level was reported as high to extensive stages of ASR formation. In addition, it was also reported that the accumulation of ASR gel around the reinforcing steel bars indicated debonding occurred between the cement paste and reinforcing steel bars. Moreover, ettringite was observed within air voids, cracks, the interface of aggregates and cement paste, and as coating around the reinforcing steel bars (Figure 4-52f). However, it was reported that the distribution of ettringite was not consistent with DEF.

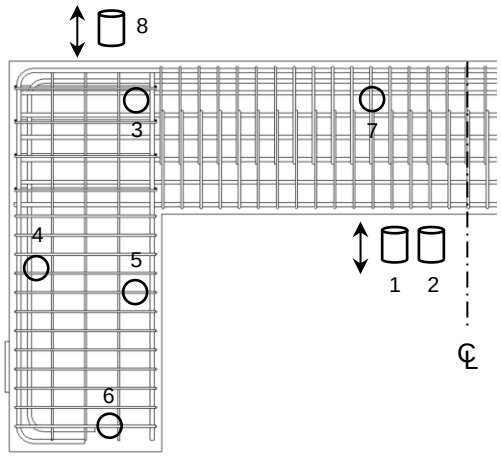

(a) Core Locations

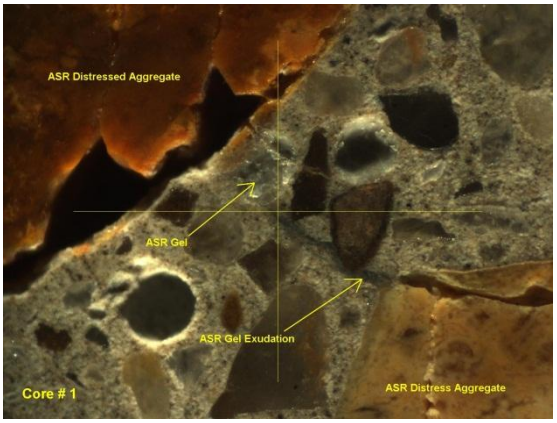

(b) ASR Gel Accumulation in Air Void and ASR Distressed Coarse Aggregate (Core 1)

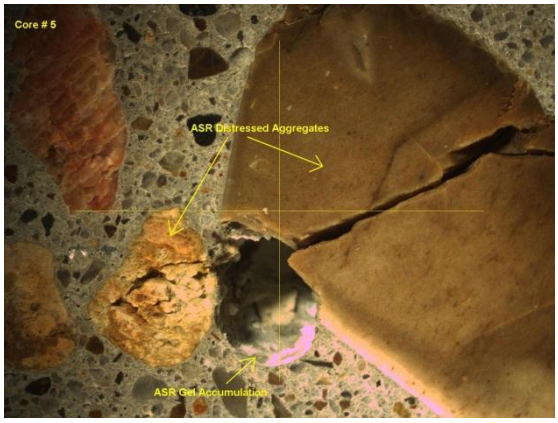

(c) ASR Gel Accumulation in Air Void and ASR Distressed Coarse Aggregate (Core 5)

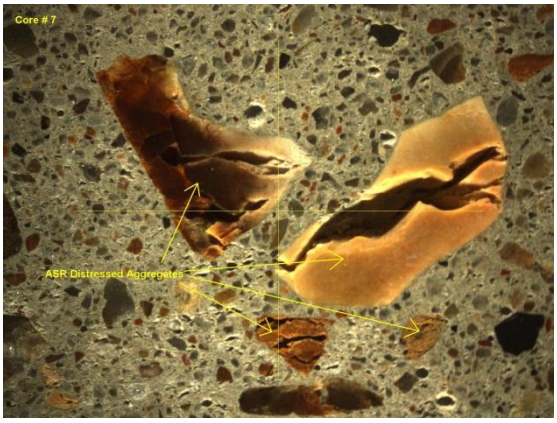

(d) ASR Distressed Coarse Aggregate (Core 7)

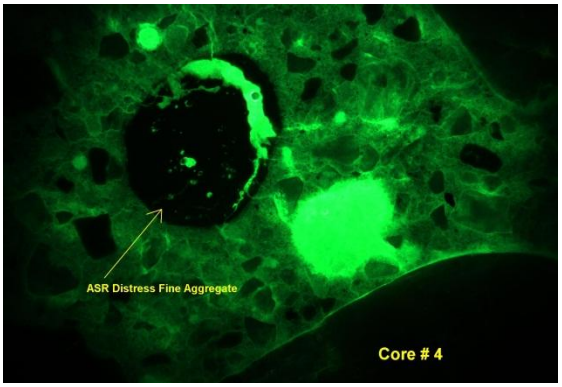

(e) Fluorescent Image of Fine Network of ASR-Induced Cracking

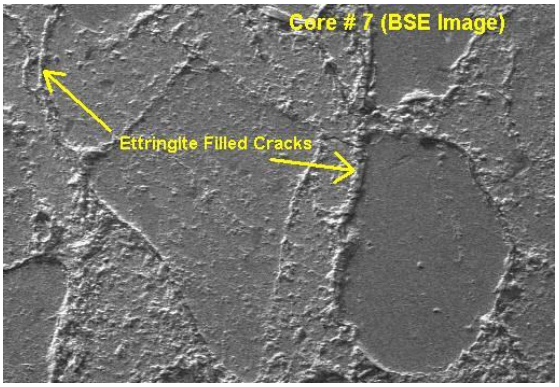

(f) Ettringite Filled in Cracks (Core 7)

Figure 4-52 Petrographic Analysis Results of Cores Extracted from Specimen 4

4.8 DISCUSSION

Figures 4-53 and 4-54 present the average longitudinal surface concrete strains at different depths in the beam regions for each exposed specimens. In general, the average longitudinal surface concrete strain on the tension side (L1) was greater than that on the compression side (L4) after prestress applied. Over time, the average longitudinal strain on the compression side gradually increased and was about three times as large as that on the tension side in the singly reinforced bent of Specimen 3 (Figure 4-53d). However, in the doubly reinforced bent, the longitudinal strain on the compression side was merely 61% of that on the tension side (Figure 4-54d). Moreover, only 31% of longitudinal strain on the compression side was observed in the doubly reinforced bent compared to that in the singly reinforced bent. This may infer that the amount of compression steel plays a significant role of restraining concrete expansion due to ASR/DEF.

Figures 4-55 and 4-56 show the average transverse surface concrete strains at different depths in the beam regions. Due to the later-initiated longitudinal cracks and excessive map cracking on the tension side, as discussed in Section 4.3, the average transverse strain on the tension side (T1) grew at a higher rate than that on the compression side and exceeded 0.010 in Specimens 3 and 4 after 12 months (360 days) and 21 months (630 days) of exposure, respectively. For Specimen 3, the ratios of the transverse strain on the tension side to that on the compression side was 1.2 and 2.1 in the singly and doubly reinforced bent, respectively.

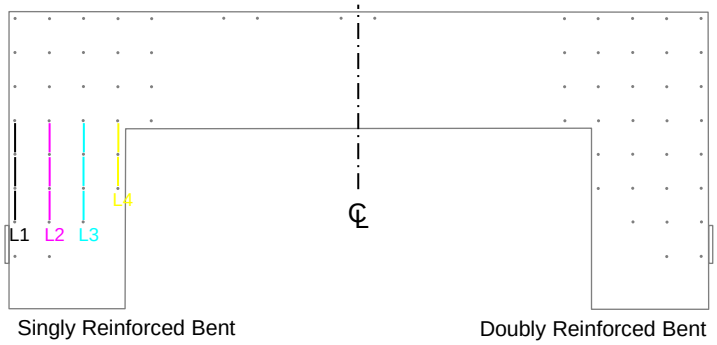

(a) Average Longitudinal Surface Concrete Strains at Different Depths (L1 through L4)

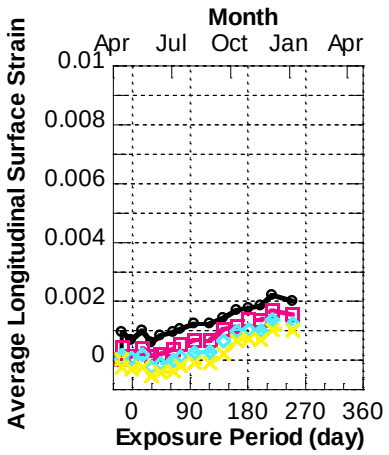

(b) Specimen 2

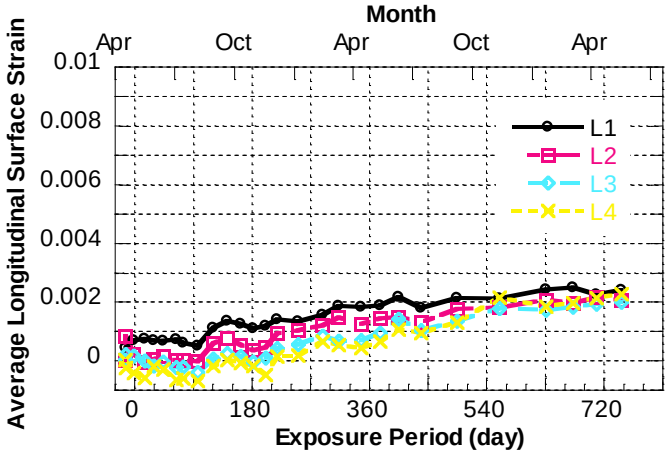

(c) Specimen 4

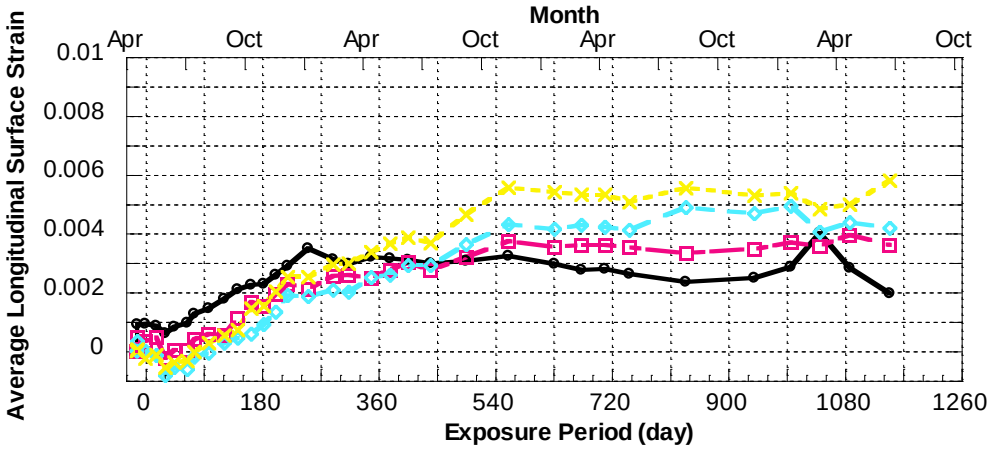

(d) Specimen 3

Figure 4-53 Average Longitudinal Surface Concrete Strains in Beam Region of Singly Reinforced Bent

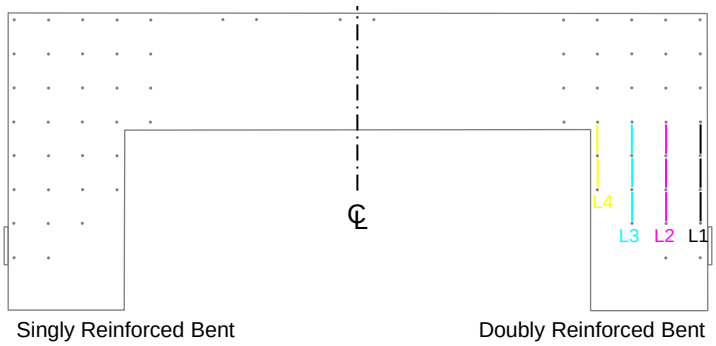

(a) Average Longitudinal Surface Concrete Strains at Different Depths (L1 through L4)

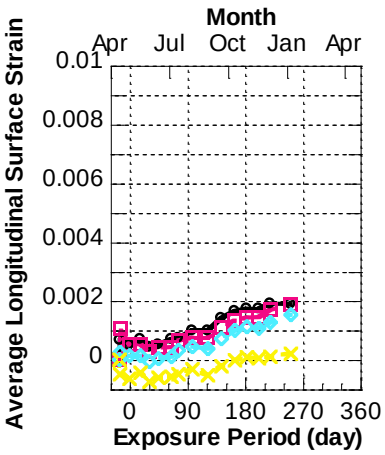

(b) Specimen 2

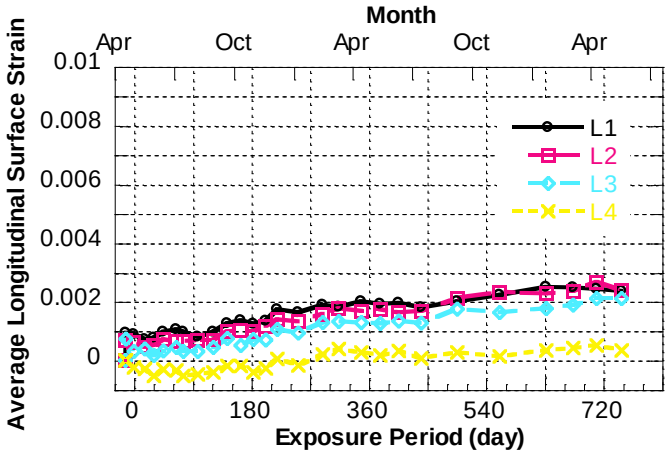

(c) Specimen 4

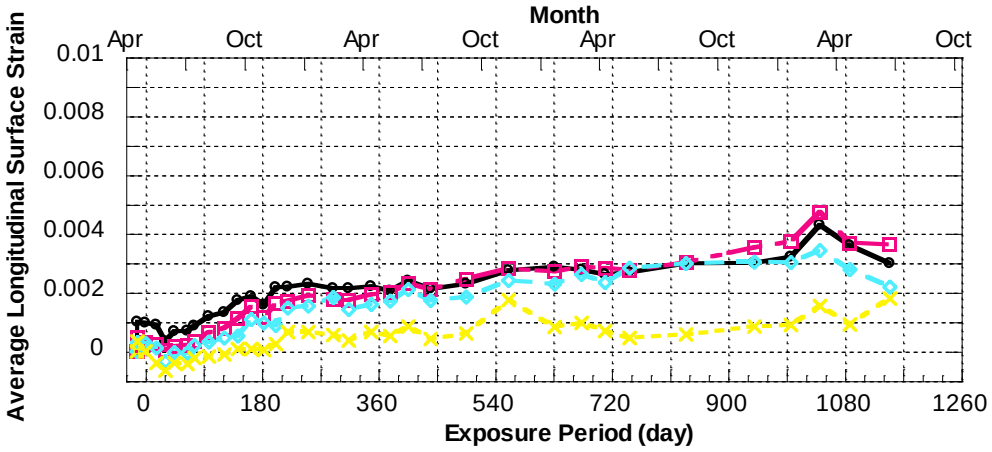

(d) Specimen 3

Figure 4-54 Average Longitudinal Surface Concrete Strains in Beam Region of Doubly Reinforced Bent

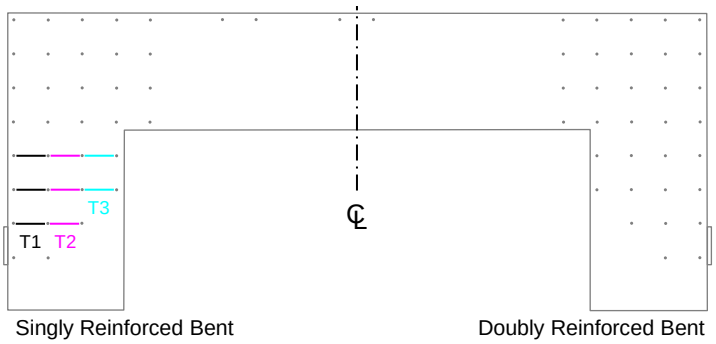

(a) Average Transverse Surface Concrete Strains at Different Depths (T1 through T3)

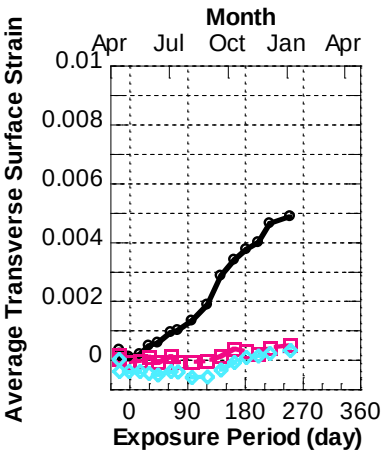

(b) Specimen 2

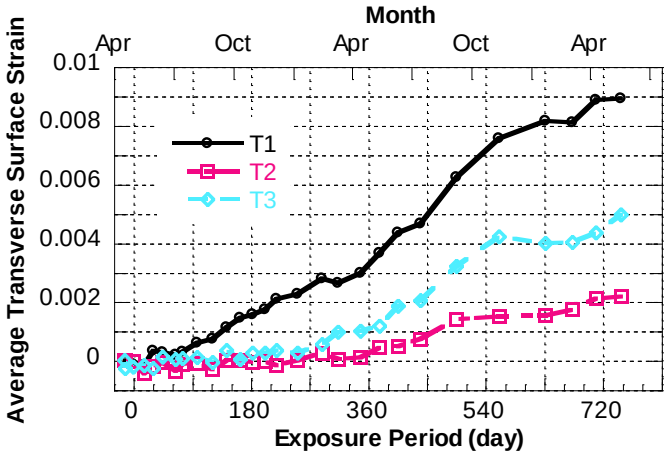

(c) Specimen 4

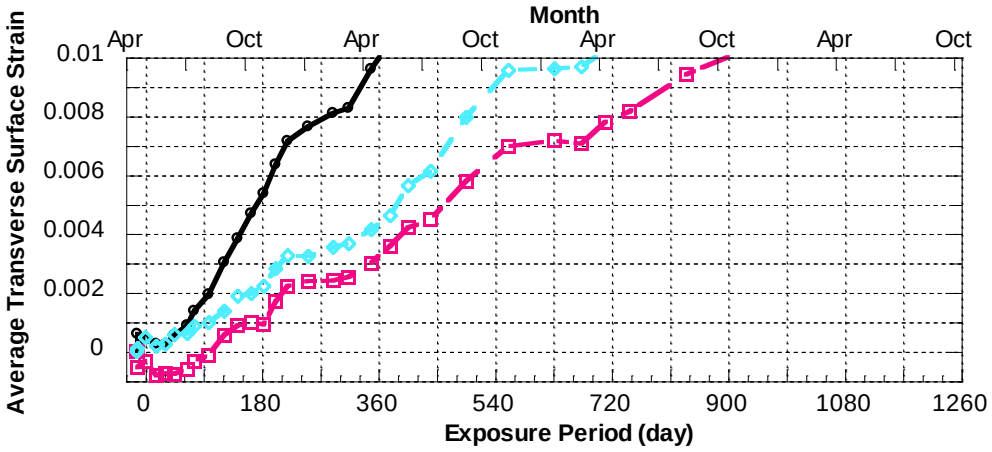

(d) Specimen 3

Figure 4-55 Average Transverse Surface Concrete Strains in Beam Region of Singly Reinforced Bent

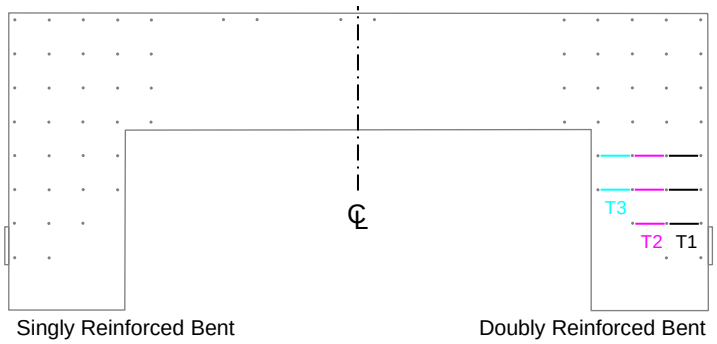

(a) Average Transverse Surface Concrete Strains at Different Depths (T1 through T3)

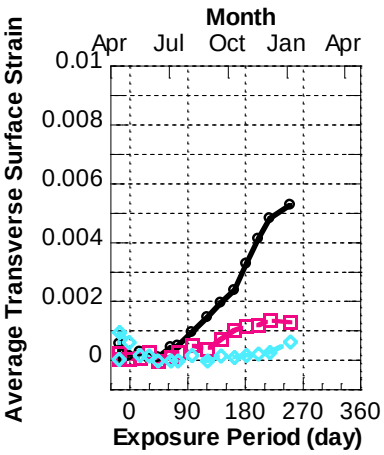

(b) Specimen 2

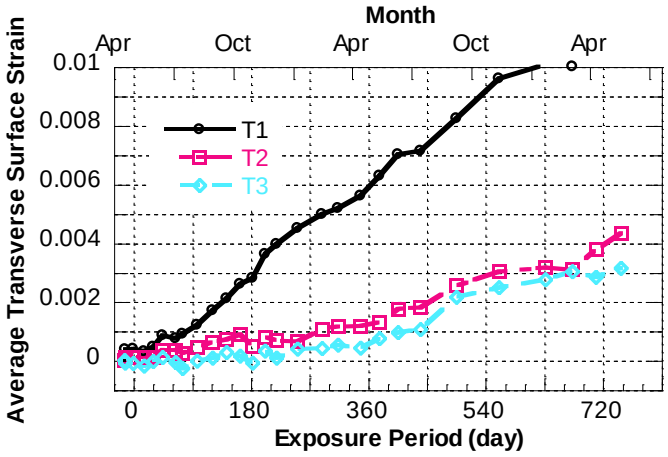

(c) Specimen 4

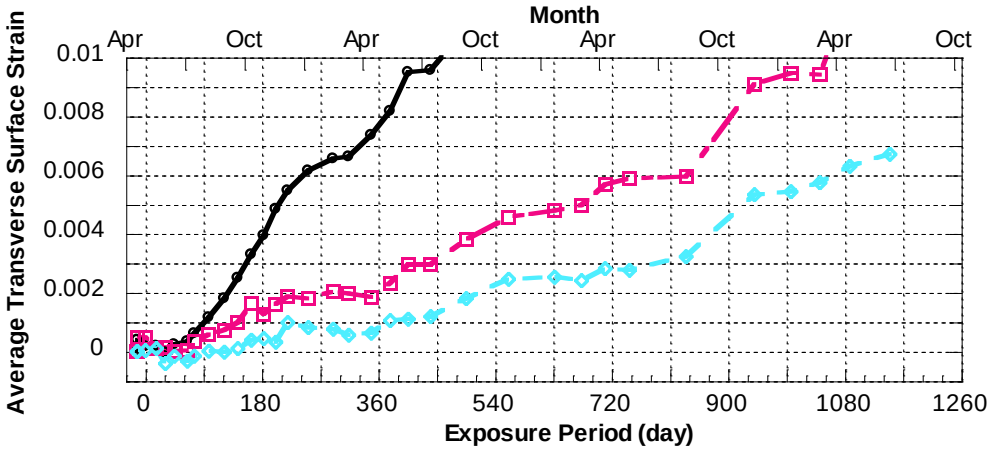

(d) Specimen 3

Figure 4-56 Average Transverse Surface Concrete Strains in Beam Region of Doubly Reinforced Bent

Figure 4-57 presents the progression of the ratios of the average transverse strain to the average longitudinal strain on the tension side in the beam regions, that is, $T1/Avg(L1, L2)$. It was found that the transverse strain grew much aggressively and the expansion rate was five times as large as that of the longitudinal strain in the beam regions after 40 months (1200 days) of exposure.

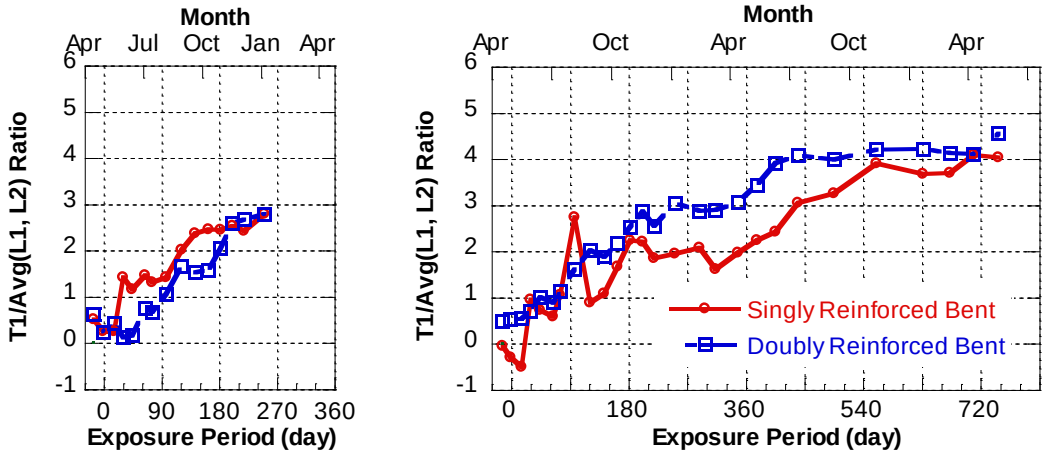

(b) Specimen 2

(c) Specimen 4

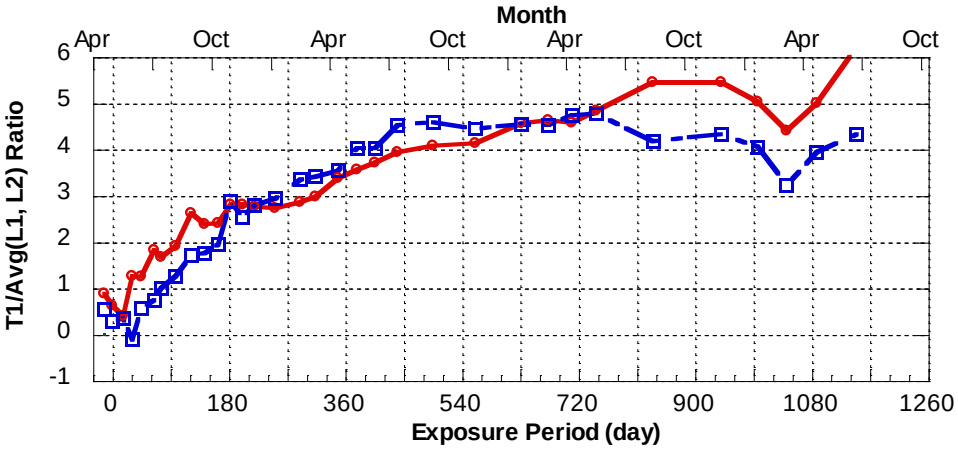

(d) Specimen 3

Figure 4-57 Average Transverse Strain to Average Longitudinal Strain Ratios

Figures 4-58 and 4-59 show the average diagonal surface concrete strains in the beam-column joints. The average strain on the tension side, denoted as D1, exhibited more expansion over time as due to the later-initiated cracks and map cracking in these locations. The results showed that these strains were about four times greater than the other average diagonal strains (D2 and D3) in the beam-column joints.

Figures 4-60 and 4-61 present the average of beam-direction surface concrete strains (B1 and B2) and out-of-plane surface concrete strain (O1) on the beam face of the beam-column joint regions. In general, strains developed at a higher rate in out-of-plane direction. Figure 4-62 shows the ratios of the average out-of-plane strain to the average beam-direction strain in such regions, that is, $O1/Avg(B1,B2)$. The results showed that the expansion rate in out-of-plane direction was twice as large as that in beam direction. Note that large cracks were observed in the beam-column joint of the singly reinforced bent in Specimen 3 as discussed in Section 4.3 and the ratio was calculated as 4.8 after 40 months (1200 days) of exposure.

Figures 4-63 and 4-64 present the average of column-direction surface concrete strains (C1 and C2) and out-of-plane surface concrete strain (O2) on the column face of the beam-column joint regions. Similarly, the results showed that strain significantly developed in the out-of-plane direction and reached 0.008 after nine-month (270 days) of exposure. Figure 4-65 shows the ratios of the average out-of-plane strain to the average column-direction strain in these region, namely, $O2/Avg(C1,C2)$. As a result of the development of large cracks at the outside corner of the beam-column joints, the ratio of

Specimen 3 exceeded 6 after 24 months (720 days) exposure and was calculated as 6.9 after 40 months (1200 days) of exposure.

Figures 4-66 and 4-67 compare the surface and internal strains at mid-depth of the STM strut in the beam regions. In general, the core concrete strains corresponded to the surface concrete strains in the beam regions. However, the reinforcing steel strains showed some random patterns after 9-month (270 days) exposure due to the possibility of the development of faulty gages induced by ASR/DEF, as discussed in Section 4.6. In the beam regions, the average reinforcing steel strain after such exposure period was 35%, 43% and 88% of the surface concrete strain for Specimens 2, 3 and 4. Figures 4-68 and 4-69 compare the surface and internal strains at mid-depth of the STM strut in the beam-column joint. Similarly, the results showed that the core concrete strains approximately matched the surface concrete strains. In the beam-column joints, the average reinforcing steel strain after 9-month (270 days) exposure was 193%, 106% and 93% of the surface concrete strain for Specimens 2, 3 and 4.

After the first two-month exposure, the specimens subsequently expanded at a higher rate during warmer months. Table 4-2 summarizes the surface expansion rate from DM191 measurements, where the later-initiated longitudinal crack located on main elevation, during the summer and non-summer months. The ratios of the average expansion rate during summer months to non-summer months ranged from 0.98 to 1.71. From the observed results, it may infer that ASR/DEF accelerated from April to October when the temperatures exceeded 80 ˚F (26.7 ˚C) (Figure 4-15).

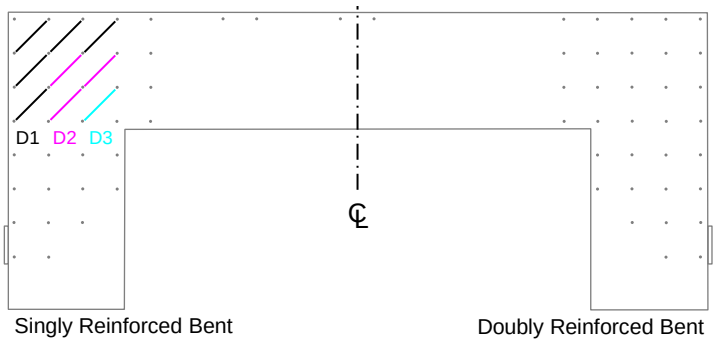

(a) Average Diagonal Surface Concrete Strains (D1 through D3)

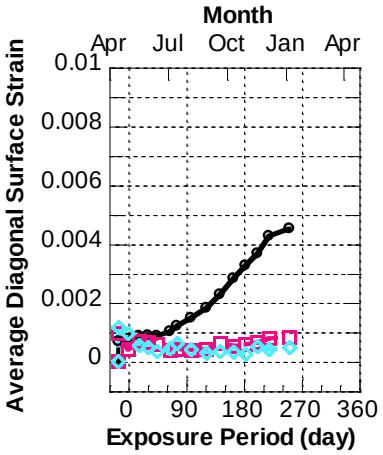

(b) Specimen 2

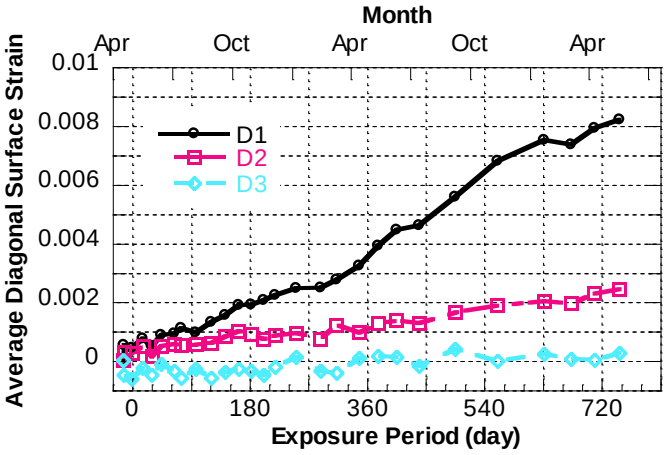

(c) Specimen 4

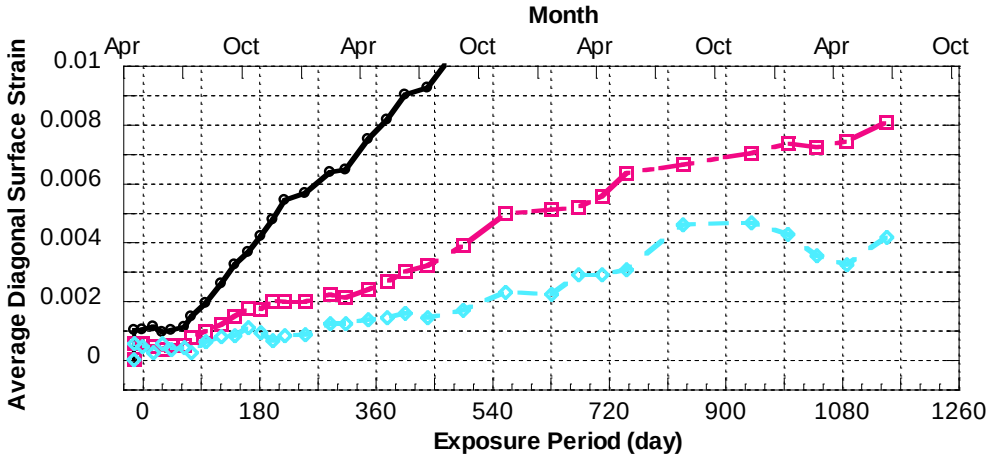

(d) Specimen 3

Figure 4-58 Average Diagonal Surface Concrete Strains in Beam-Column Joint of Singly Reinforced Bent

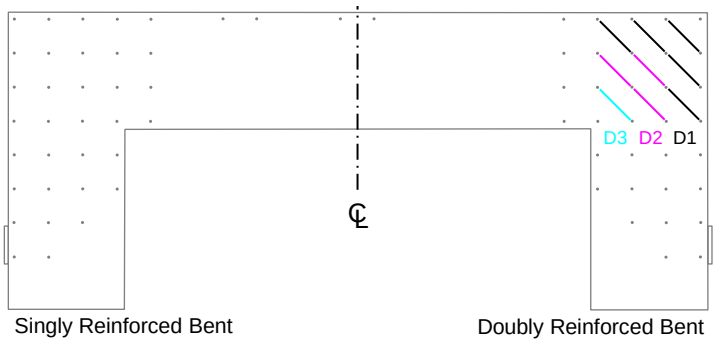

(a) Average Diagonal Surface Concrete Strains (D1 through D3)

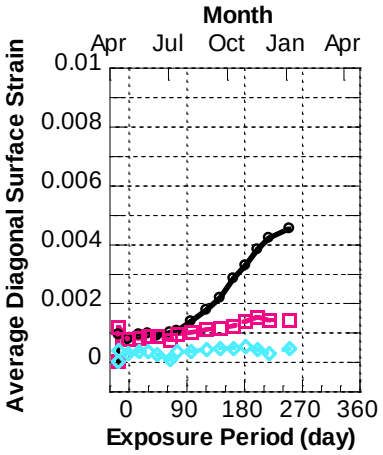

(b) Specimen 2

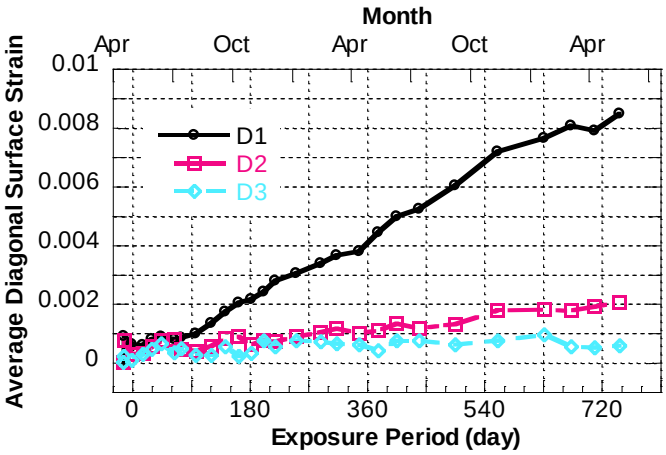

(c) Specimen 4

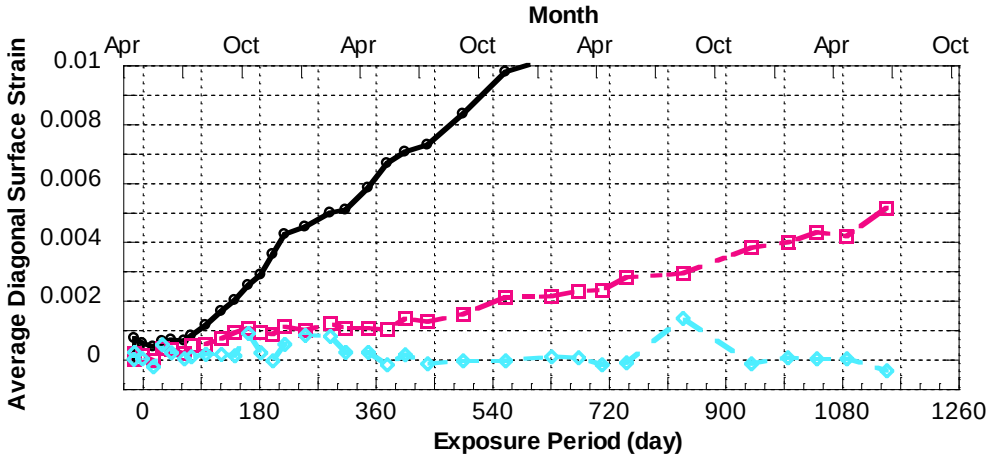

(d) Specimen 3

Figure 4-59 Average Diagonal Surface Concrete Strains in Beam-Column Joint of Doubly Reinforced Bent

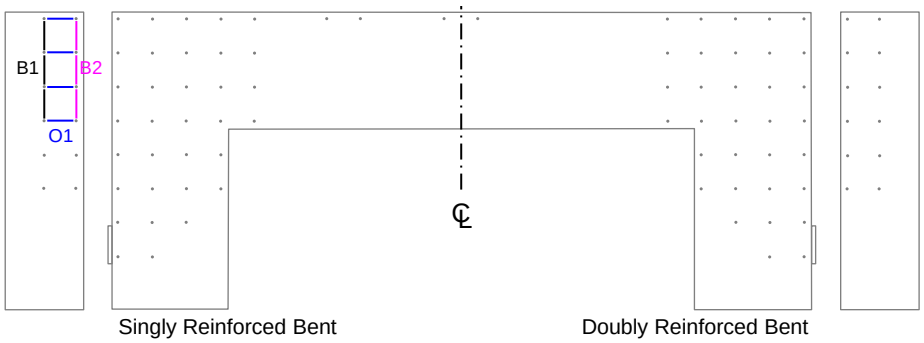

(a) Average Beam Face Strains (B1, B2 and O1)

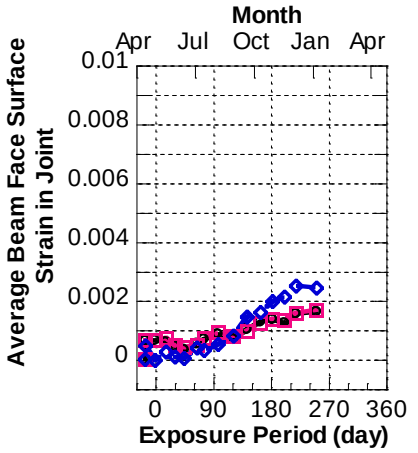

(b) Specimen 2

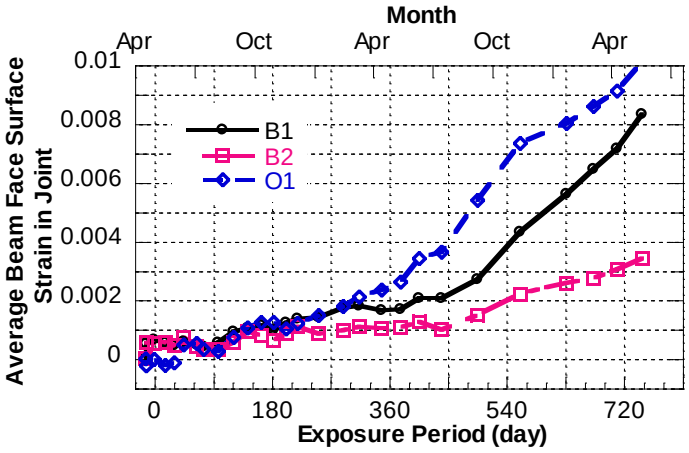

(c) Specimen 4

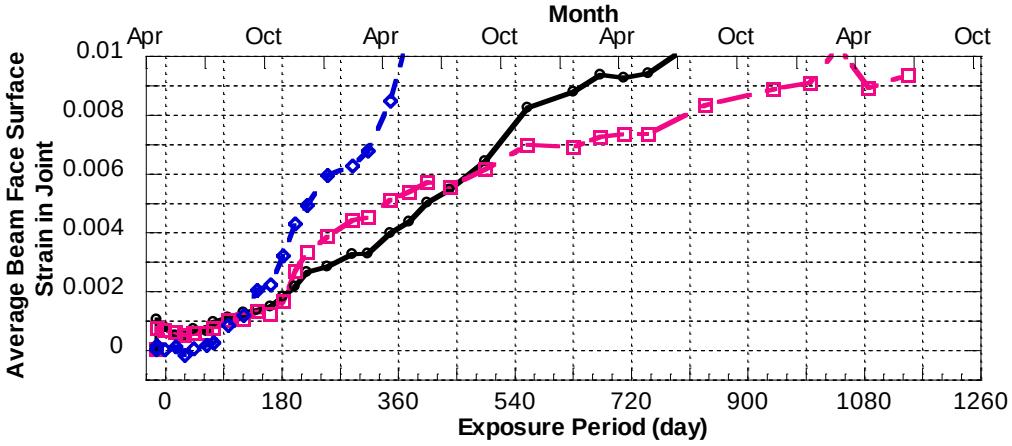

(d) Specimen 3

Figure 4-60 Average Beam Face Strains in Beam-Column Joint of Singly Reinforced Bent

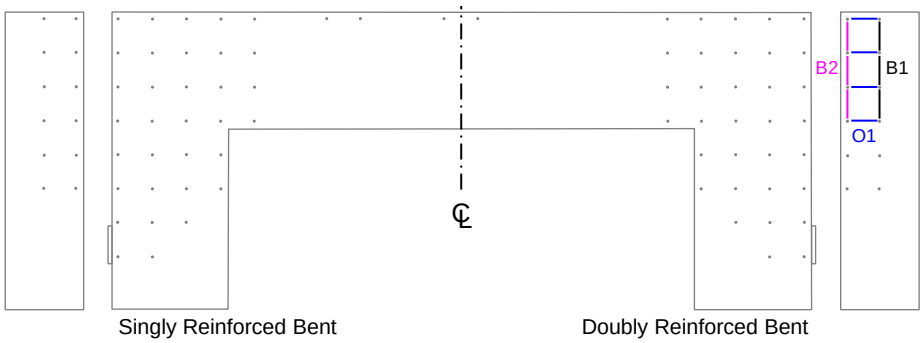

(a) Average Beam Face Strains (B1, B2 and O1)

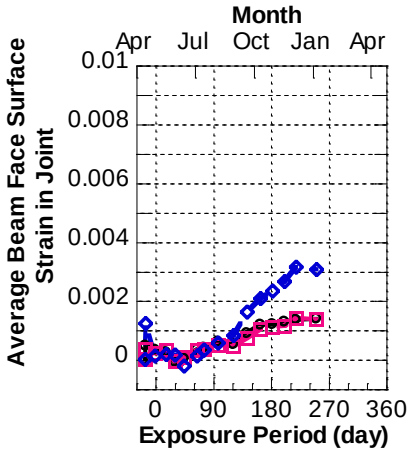

(b) Specimen 2

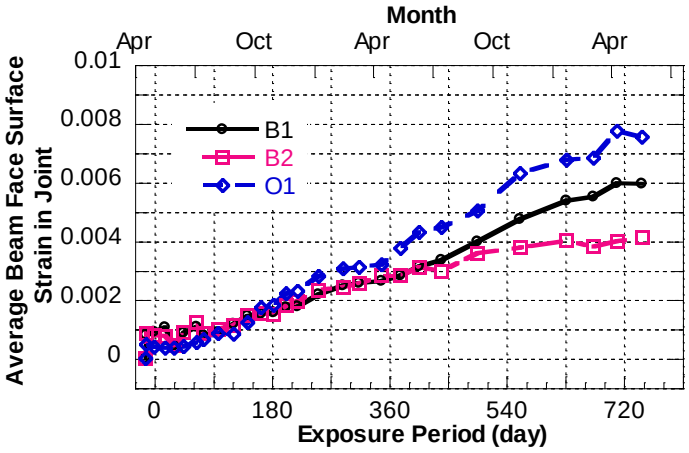

(c) Specimen 4

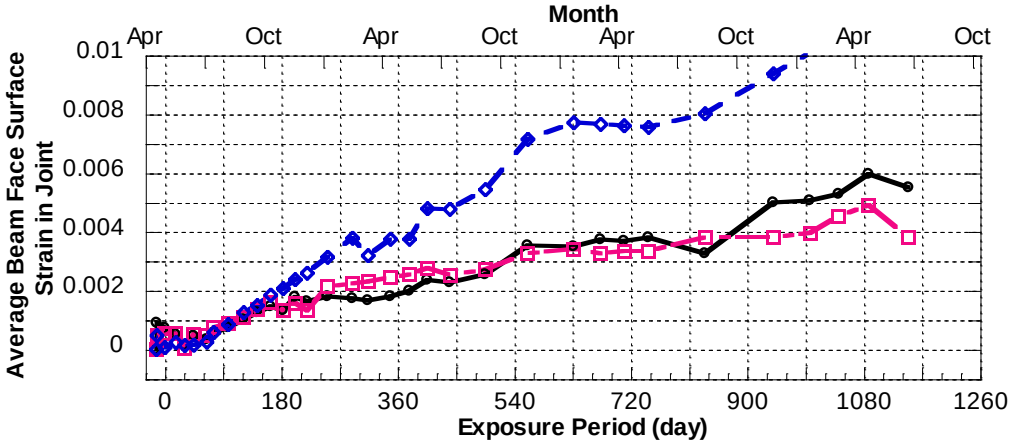

(d) Specimen 3

Figure 4-61 Average Beam Face Strains in Beam-Column Joint of Doubly Reinforced Bent

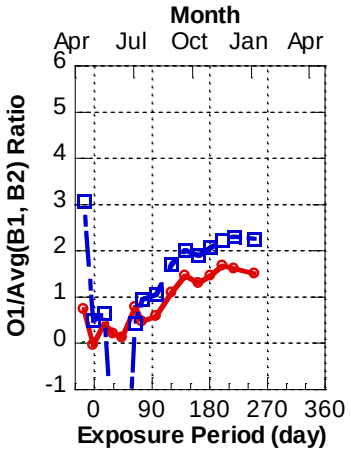

(b) Specimen 2

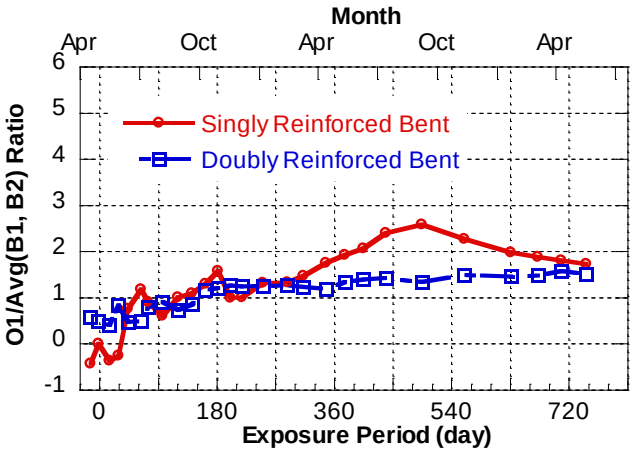

(c) Specimen 4

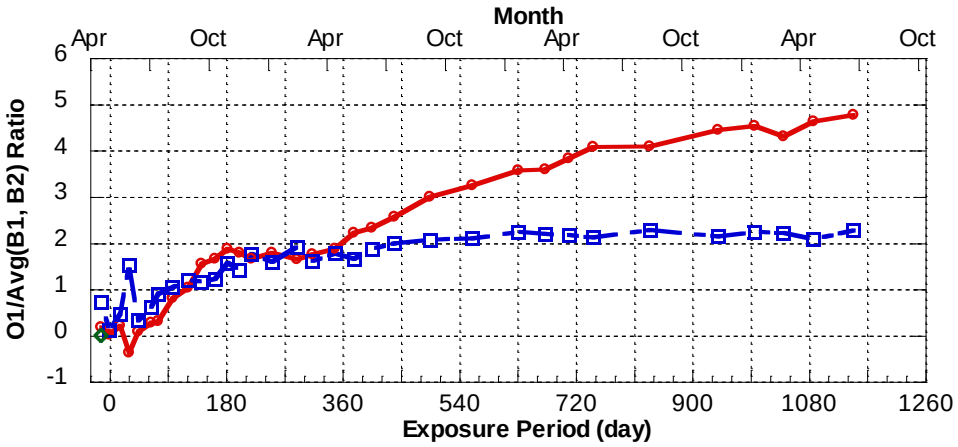

(d) Specimen 3

Figure 4-62 Average Out-of-Plane Strain to Average Beam-Direction Strain Ratios

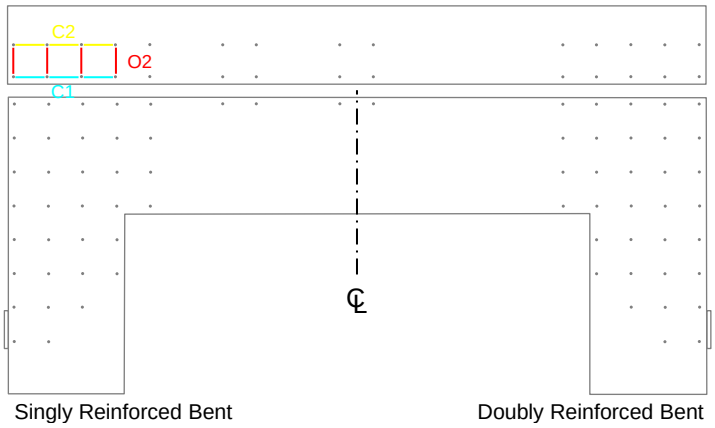

(a) Average Column Face Strains (C1, C2 and O2)

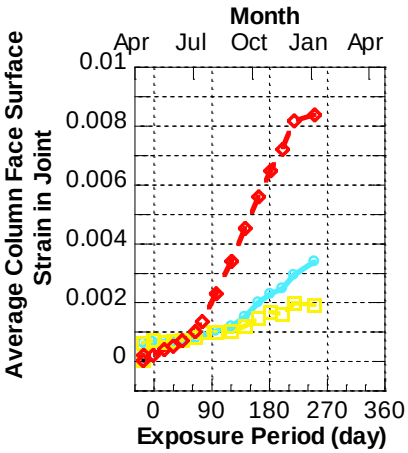

(b) Specimen 2

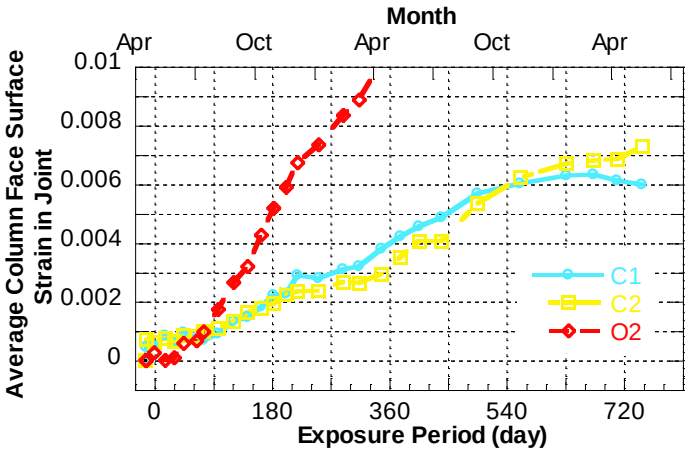

(c) Specimen 4

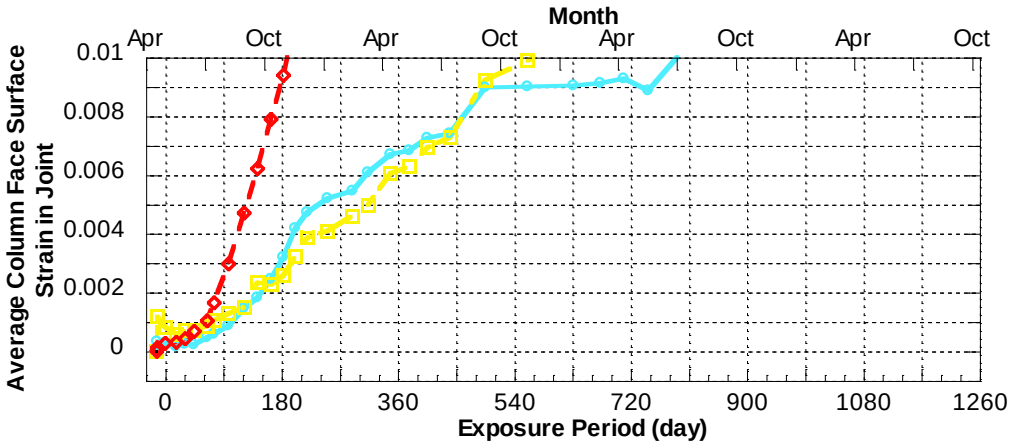

(d) Specimen 3

Figure 4-63 Average Column Face Strains in Beam-Column Joint of Singly Reinforced Bent

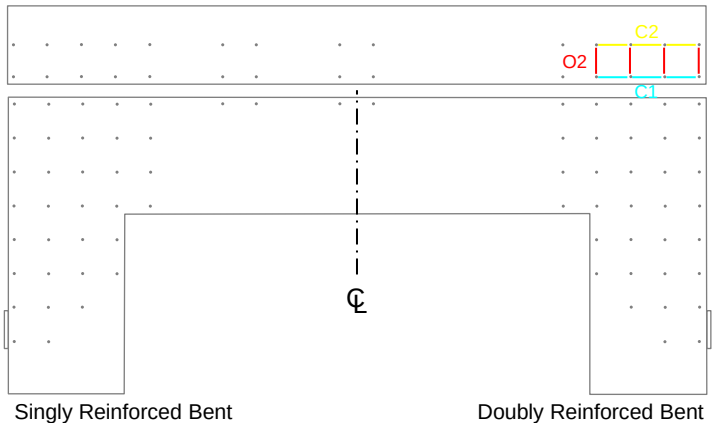

(a) Average Column Face Strains (C1, C2 and O2)

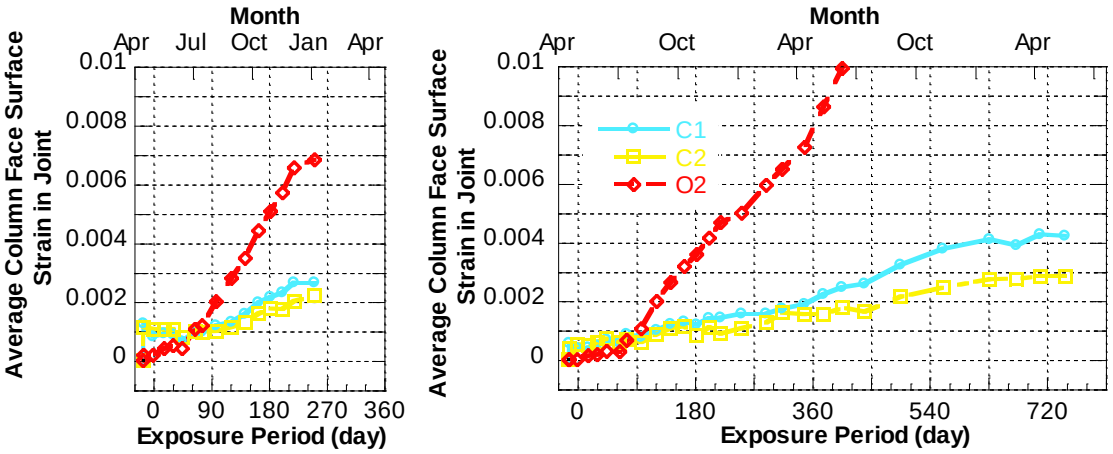

(b) Specimen 2

(c) Specimen 4

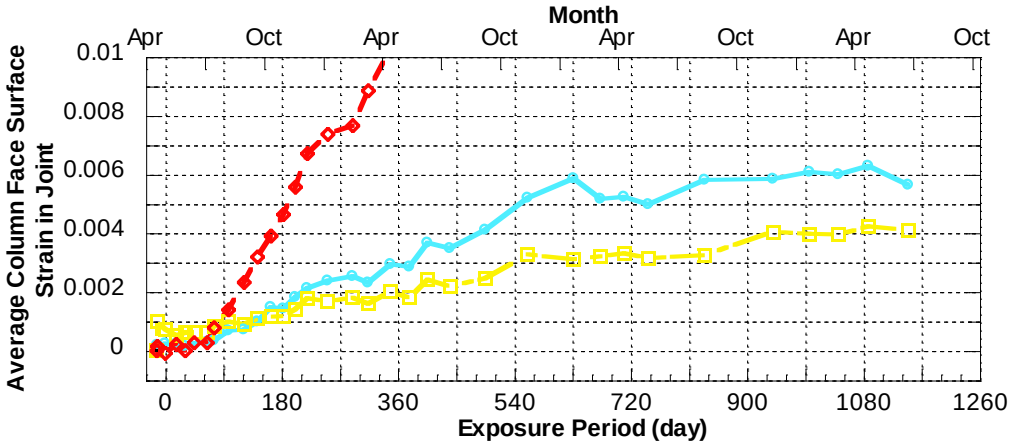

(d) Specimen 3

Figure 4-64 Average Column Face Strains in Beam-Column Joint of Doubly Reinforced Bent

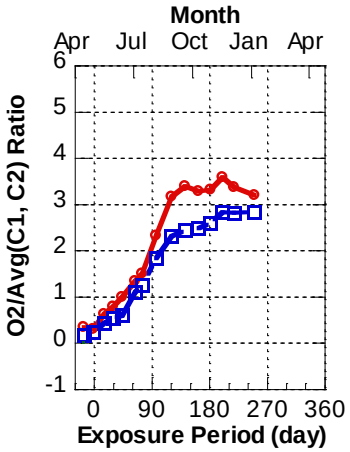

(b) Specimen 2

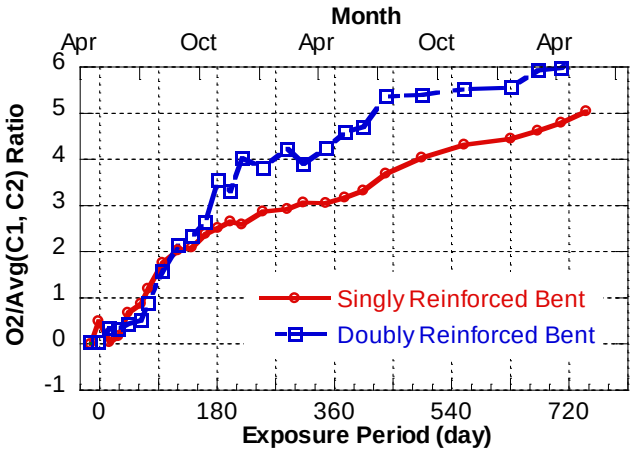

(c) Specimen 4

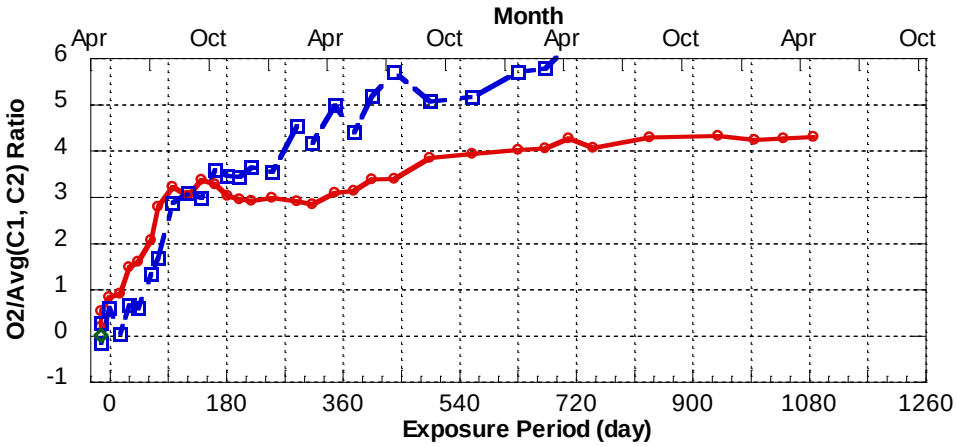

(d) Specimen 3

Figure 4-65 Average Out-of-Plane Strain to Average Column-Direction Strain Ratios

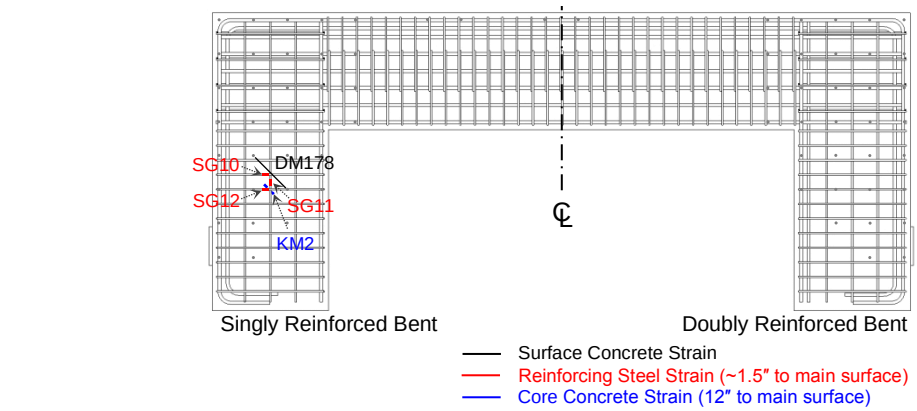

(a) External Measurement and Internal Instrumentation at Mid-Depth

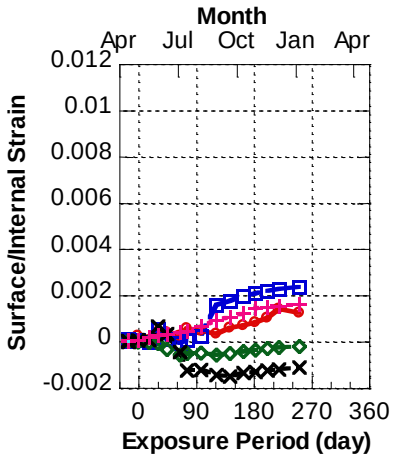

(b) Specimen 2

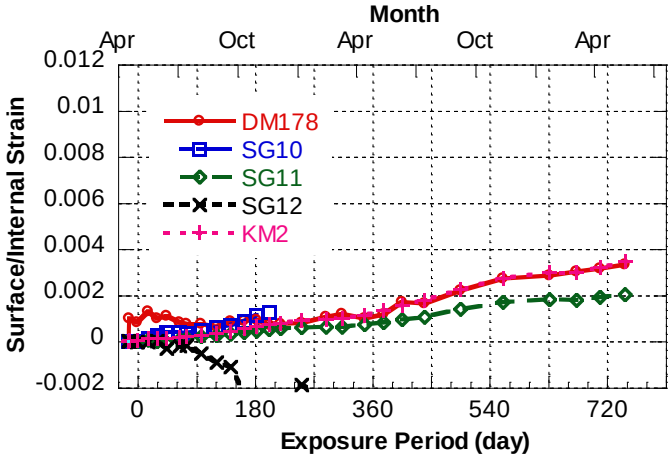

(c) Specimen 4

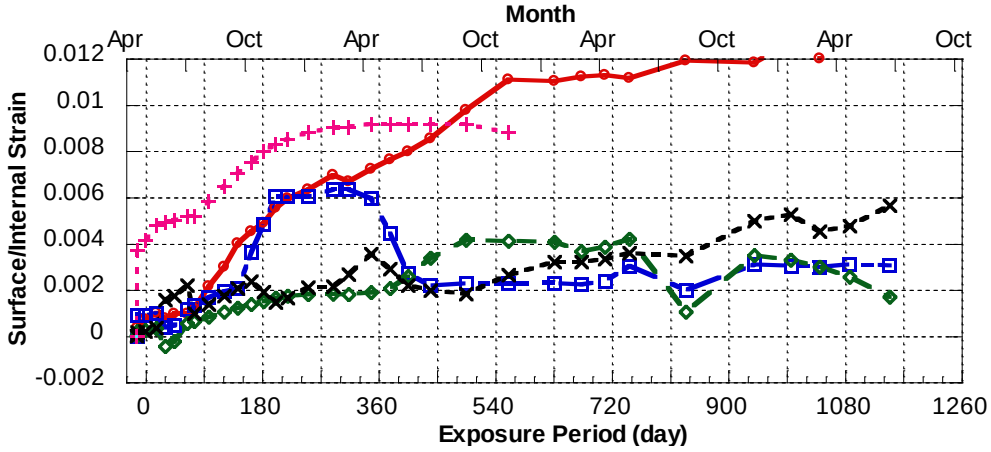

(d) Specimen 3

Figure 4-66 Comparison of Surface and Internal Strains at Mid-Depth in Beam Region of Singly Reinforced Bent

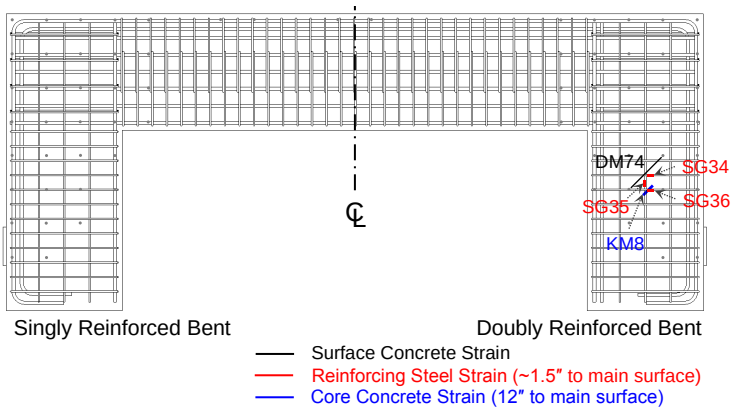

(a) External Measurement and Internal Instrumentation at Mid-Depth

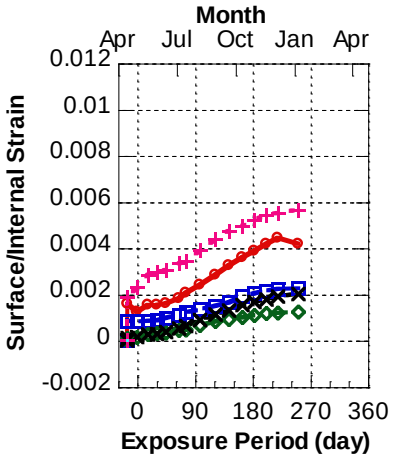

(b) Specimen 2

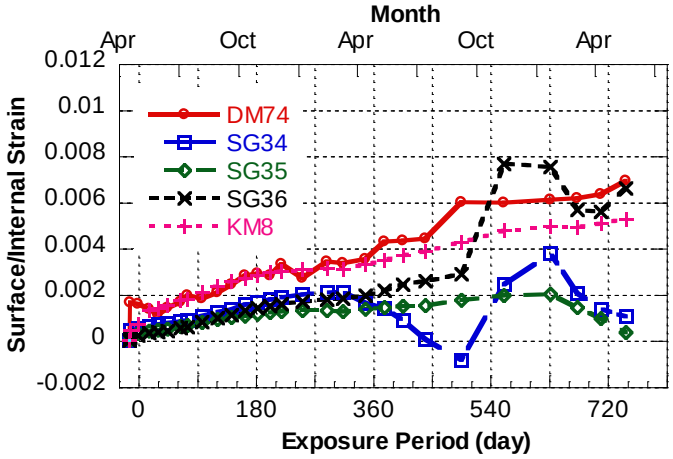

(c) Specimen 4

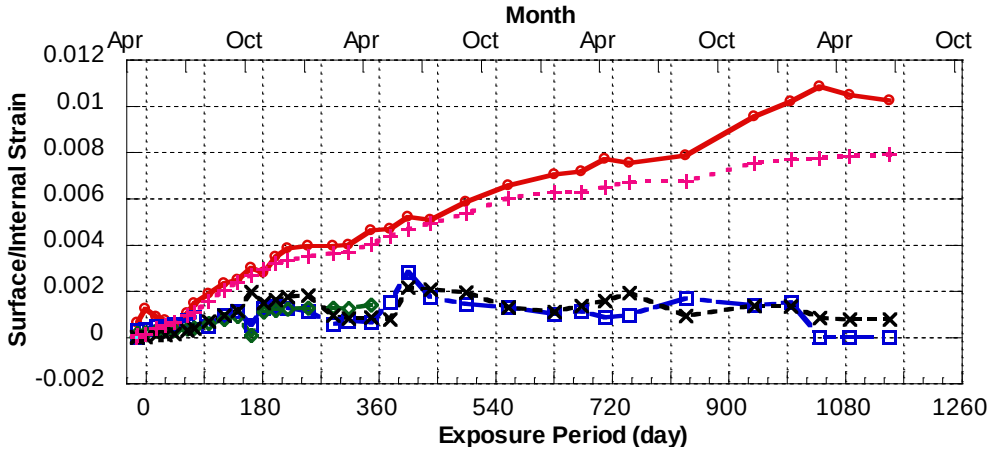

(d) Specimen 3

Figure 4-67 Comparison of Surface and Internal Strains at Mid-Depth in Beam Region of Doubly Reinforced Bent

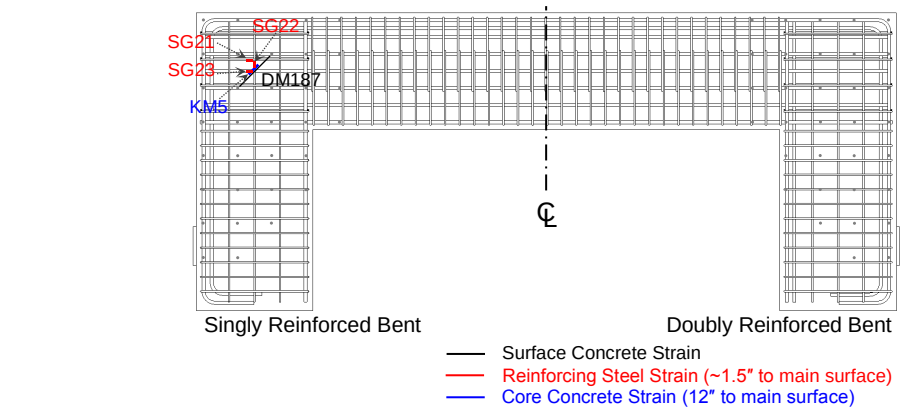

(a) External Measurement and Internal Instrumentation at Mid-Depth

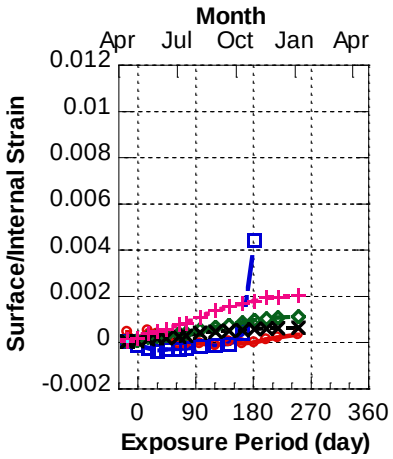

(b) Specimen 2

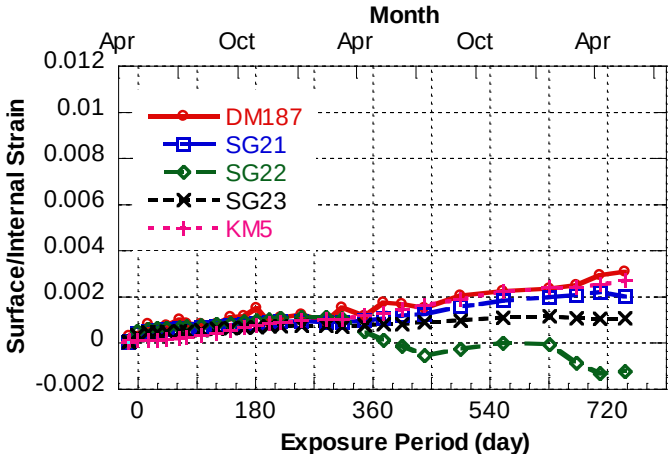

(c) Specimen 4

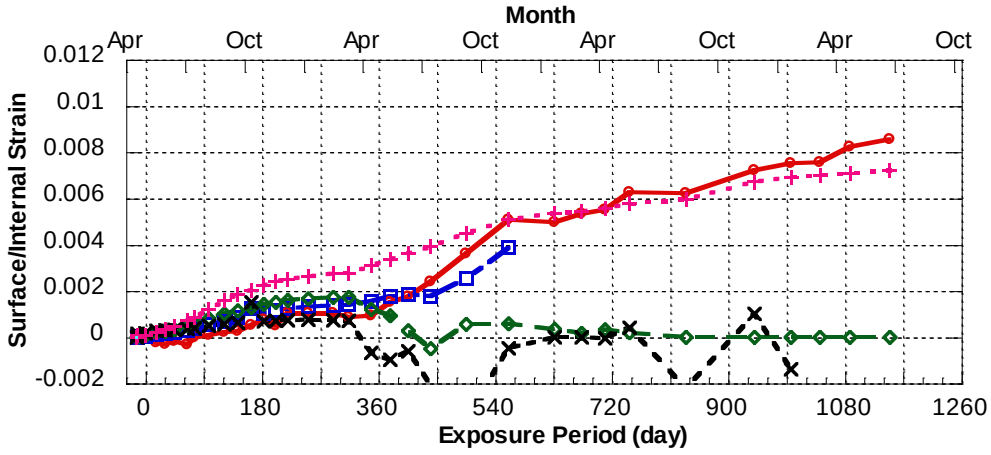

(d) Specimen 3

Figure 4-68 Comparison of Surface and Internal Strains at Mid-Depth in Beam-Column Joint of Singly Reinforced Bent

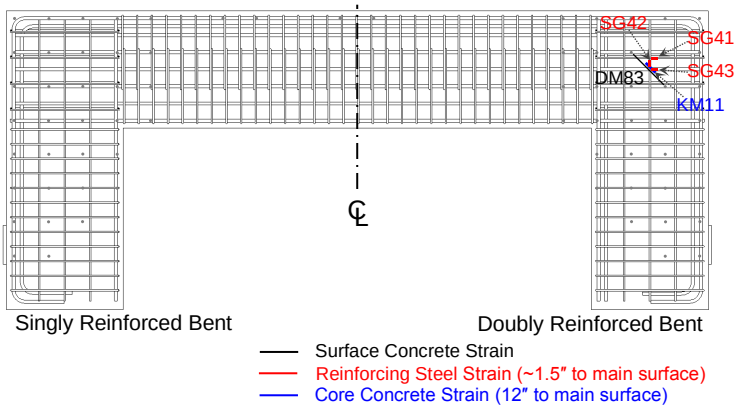

(a) External Measurement and Internal Instrumentation at Mid-Depth

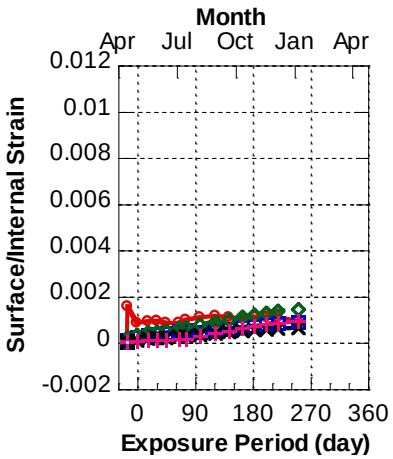

(b) Specimen 2

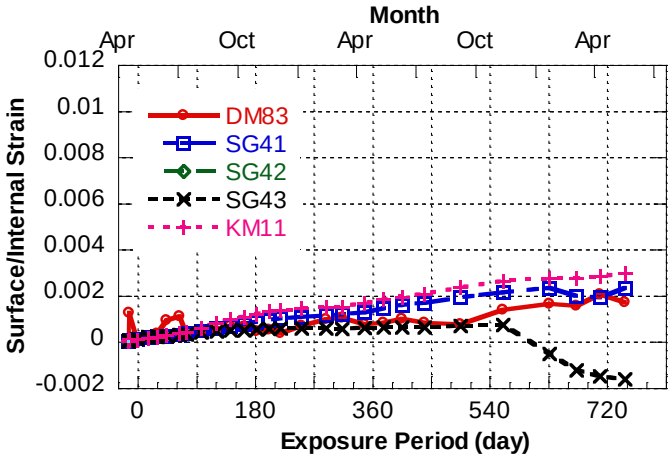

(c) Specimen 4

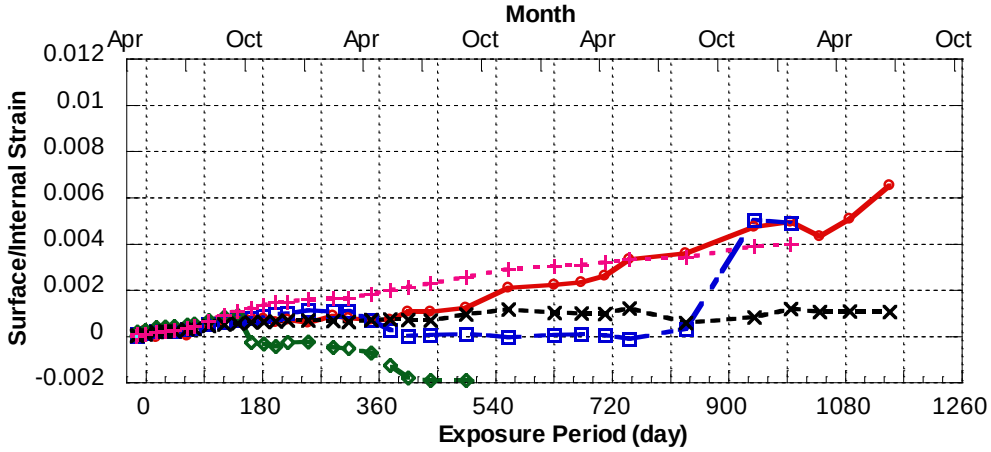

(d) Specimen 3

Figure 4-69 Comparison of Surface and Internal Strains at Mid-Depth in Beam-Column Joint of Doubly Reinforced Bent

Table 4-2 Expansion Rate of Surface Concrete Strain over Time (DM191)

Specimen	Surface Concrete Strain Growth per Month						
	Jul, 09 | Oct, 09	Nov, 09 | Mar, 10	Apr, 09 | Oct, 10	Nov, 10 | Mar, 11	Apr, 11 | Oct, 11	Nov, 11 | Mar, 12	Apr, 12 | Aug, 12
2	0.00059	0.00060	n/a	n/a	n/a	n/a	n/a
	Summer/Non-Summer Expansion Ratio = 0.98						
3	0.00078	0.00033	0.00054	0.00043	0.00097	0.00039	0.00033
	Average Summer/Non-Summer Expansion Ratio = 1.71						
4	0.00034	0.00033	0.00054	0.00016	0.00037	n/a	n/a
	Average Summer/Non-Summer Expansion Ratio = 1.70						

A hypothesis that attempts to explain the performance of structures affected by ASR/DEF is shown in Figure 4-70. After construction, subsequent construction and/or structural loading may cause cracking mostly on the surface and in the cover region (Figure 4-70a). Although the cracks were minor in terms of width and depth, these cracks may allow future moisture ingress. If active aggregates are present in the concrete mix or if the curing temperature was high, there is the possibility of the development of either ASR and/or DEF in such structures (Figure 4-70b).

Once cracking has formed in the cover region, a pathway for moisture penetration is formed, leading to the possibility of ASR/DEF formation in both cover and core concrete (Figure 4-70c). ASR/DEF formation leads to expansive strains and caused further cracking in the cover concrete. In the core concrete, expansive strains induce tension forces on the reinforcing steel (Figure 4-70d). These forces tend to restrain ASR/DEF expansion due to the provision of a passive confining action. It is

postulated that this beneficial confining effect offsets the deleterious effects induced by ASR/DEF. Although significant cracking develop on the surface due to ASR/DEF, the structural performance in terms of the strength of the structure may not be significantly impaired. This hypothesis is examined further through physical structural testing and finite element analysis (FEA), as discussed in the later chapters.

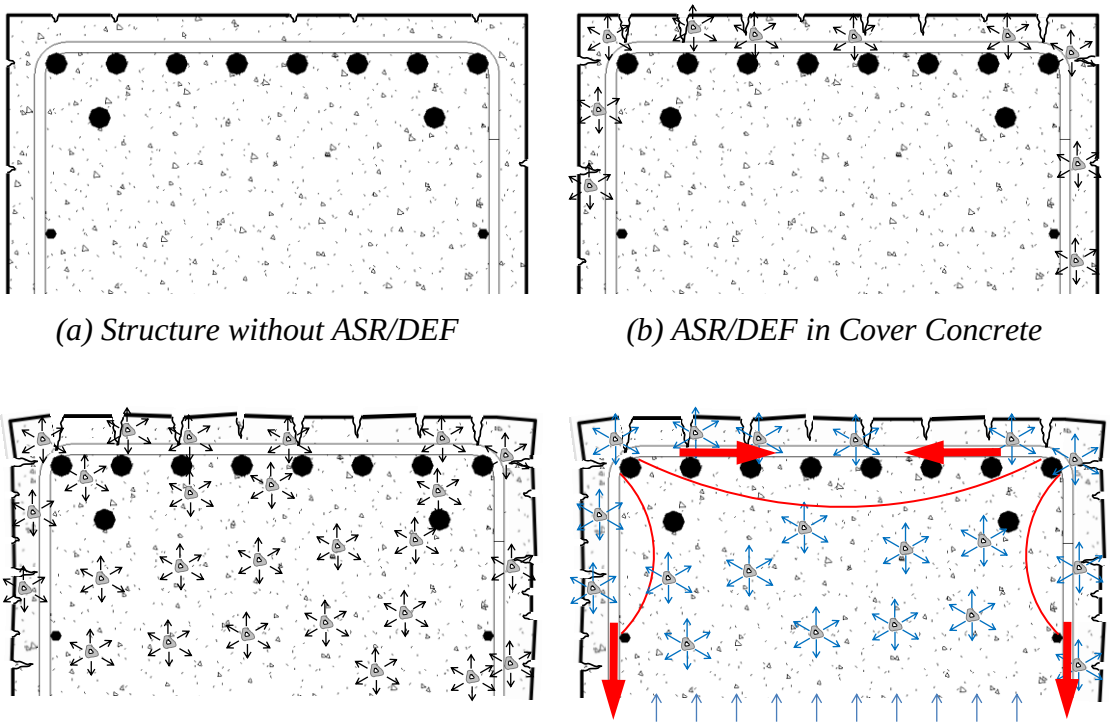

(a) Structure without ASR/DEF *(b) ASR/DEF in Cover Concrete*

(c) ASR/DEF in Cover and Core Concrete *(d) Partially Confined Due to ASR/DEF*

Figure 4-70 Structural Performance with ASR/DEF Expansion

4.9 SUMMARY AND CONCLUSIONS

In summary, three C-shaped specimens were loaded via an external prestressing assembly to emulate the gravity effects of the entire bridge bent and then transported to the Texas A&M University Riverside Campus for the exposure phase. Specimens 2 and 4 were exposed to outdoor weather conditions in Bryan, TX for eight months (252 days) and two years (748 days), respectively. Specimen 3 remains in the field and has been exposed to outdoor weather conditions over 40 months (1200 days). Supplemental water was provided for 15 minutes, four times a day to create wetting and drying cycles so as to accelerate ASR/DEF mechanisms. External surface and internal instrumentation measurements were recorded throughout the exposure phase, providing significant information and evidence of the expansion induced by ASR/DEF. Petrographic analysis results of the cores extracted from the specimens after their structural load testing showed that ASR was the primary cause of the distress in aggregates. Although accumulation of ettringite was observed, there was not enough evidence to confirm that DEF caused the distress.

The key findings from the exposure phase of the experimental program are as follows:

- The three exposure phase specimens have successfully developed significant premature concrete deterioration primarily due to ASR.
- Over 40 months (1200 days) of exposure, considerable growth of the load-induced cracks and numerous new cracks were observed. Load-induced cracks gradually increased in width and then stabilized. Subsequently, map cracking

and cracks parallel to longitudinal reinforcing steel bars developed and grew significantly over time. The largest cracks in terms of crack width were observed at the outside corner of the beam-column joints and the crack width reached 0.03, 0.25, and 0.95 inches (0.76, 6.35, and 24.1 mm) in Specimens 2, 4, and 3 after 252-day, 748-day, and 1150-day exposure, respectively.

- The amount of compression steel significantly influenced the ASR/DEF expansion on the compression side of the beam regions. The longitudinal surface concrete strain on the compression side in the doubly reinforced bent was only 31% of that in the singly reinforced bent of Specimen 3 over 40 months (1200 days) of exposure.
- The tension field induced by prestress load played a significant role in the later growth and initiation of ASR/DEF-induced cracking. Numerous new cracks were observed on the tension side after 129-day exposure. The ratios of the transverse surface concrete strain on the tension side to that on the compression side was 1.2 and 2.1 in the singly and doubly reinforced bent of Specimen 3, respectively. Moreover, the diagonal surface concrete strain on the tension side in the beam-column joints was four times as large as those on the compression side in the beam-column joints due to the excessive cracking in these locations.
- The transverse surface concrete strain was about five times larger than the longitudinal surface concrete strain on the tension side of the beam regions due to the longitudinal restraint provided by the larger amount of longitudinal tension reinforcement.

- The out-of-plane surface concrete strain on the beam/column face in the beam-column joints developed at a higher rate than that in the direction parallel to the main longitudinal reinforcing steel as a consequence of less/none reinforcement restraint provided in the out-of-plane direction (four sets of spliced U-shaped bars on the beam face and none on the column face). After 40 months (1200 days) of exposure, the ratio of the out-of-plane strain to the beam/column direction strain in the beam-column joints of Specimen 3 was 4.8 and 6.9 on the beam and column face, respectively. The proposed additional U-shaped reinforcing steel bars perpendicular to the existing U-shaped steel bars would have helped constrain out-of-plane expansion.
- The measured core concrete strains at the mid-depth of the STM struts approximately matched the diagonal concrete surface strains. For Specimens 2, 3 and 4, the reinforcing steel strains in the cover regions exhibited 35%, 43% and 88% in the beam regions and 193%, 106% and 93% in the beam-column joints of the surface concrete strain after 9-month (270 days) exposure. The measured reinforcing steel strains showed some random patterns due to the possible development of faulty gages after nine months of exposure.
- Although some scattered reinforcing steel strains were recorded, the strains in some transverse hoops and U-shaped steel bars gradually increased during the summer months and reached the tension yield strain. It is evident that the ASR/DEF expansion introduced some confining effect to core concrete and caused the hoop steel and U-shaped bars to yield.

- Longitudinal compression steel strains of -0.0005 were recorded in the compression zone once the pre-loading was applied. Over time, these strains changed from compression to tension and reached 0.001 due to the ASR/DEF expansion, which potentially stretched the reinforcing steel provided by the bond between concrete and reinforcing steel. Moreover, the strains in the longitudinal tension steel gradually developed and reached 0.0012 after nine months (270 days) of exposure, although some scattered readings were recorded afterwards. This indicated that the longitudinal steel bars on both sides of the section were stretched, allowing prestress forces to be effectively applied onto the core concrete.
- The specimens expanded at a higher rate during the warmer months (April through October). The ratio of the surface concrete expansion rate in the beam-column joint where the later-initiated large crack located (DM191) during the summer months to that during the non-summer months ranged from 0.98 to 1.71. It may infer that ASR/DEF expansion accelerated when the temperatures exceeded 80 ˚F (26.7 ˚C).

CHAPTER V

EXPERIMENTAL PROGRAM — STRUCTURAL LOAD TESTING

5.1 OVERVIEW

As discussed in Chapter III and Chapter IV, four large-scale RC specimens representative of bridge bents with D-regions in Texas were constructed. After construction, one specimen was stored in the climate controlled laboratory without supplemental water serving as the control specimen, and the other three specimens were loaded to mimic the in-service gravity load effect and later transported to the Texas A&M University Riverside Campus for their exposure phase.

The control (Specimen 1) and two exposed specimens (Specimens 2 and 4) with various levels of ASR/DEF, after eight months and two years field exposure, respectively, were tested to failure. This chapter presents the concrete material properties for each tested specimen, the experimental test setup, the external instrumentation for structural testing, the testing procedure including loading history, the specimen behavior during structural load testing, and the failure assessment for each specimen.

5.2 CONCRETE MATERIAL STRENGTH TESTING

During the construction of each specimen, standard 4-inch by 8-inch (102-mm by 203-mm) cylinders were also made from the same concrete mix according to ASTM Standard C31 (2007). Thus, concrete compressive strength data of cylinder tests as per ASTM Standard C39 (2007) and tensile strength data of cylinder tests as per ASTM

Standard C496 (2007) could be determined. Half of these cylinders were stored in a curing room at 73.4 ˚F (23.0 ˚C) and with 100% relative humidity (RH), and the other half were stored at the same location and condition as the specimens. Cylinders were tested for 28-day compressive strengths as specified in ASTM Standard C39 (2007). Concrete tensile strengths were obtained using two test methods: embedded bar tensile test (t), where a 0.5-inch diameter threaded rod of high strength steel was embedded in a 3-inch by 3-inch by 36-inch (76-mm by 76-mm by 914-mm) prism of the same concrete mix of each specimen; and splitting tensile test (s-t) as per ASTM Standard C496 (2007). To determine the material strength at the time of specimen structural load testing, samples were also tested around the same time. Table 5-1 summarizes the age of the tested specimens at their structural load testing. Although the same concrete mix design was used throughout this research as discussed in Section 3.3.2, the concrete casting of each specimen was conducted separately with different batches of concrete mix (Table 5-1).

Table 5-1 Specimen Age at Structural Load Testing

Specimen	Concrete Casting	Laboratory	Laboratory
		Transported to Lab with Prestress Removed	Structural Load Testing
		Age (days)	
1	11/24/2008	n/a	392
2	01/13/2009	364 (after 8-month exposure)	499
4	03/06/2009	808 (after 2-year exposure)	888

The individual test results and average of concrete compressive and tensile strengths at 28 days and at the time of structural load testing for Specimens 1, 2 and 4 are presented in Tables 5-2 and 5-3. Note that in Tables 5-2 and 5-3, "Curing Room" means that samples were stored in a wet room as aforementioned; "Lab" means that samples were stored adjacent to the specimen (Specimen 1) in the climate controlled structural testing laboratory without supplemental water; "Field" means that samples were stored adjacent to the exposed specimens (Specimens 2 and 4) at the Texas A&M University Riverside Campus.

Table 5-2 Concrete Cylinder Compressive Strengths

Specimen	28-Day Strength, ksi (MPa)				Strength at Time of Structural Testing, ksi (MPa)			
	Curing Room		Lab		Curing Room		Lab/Field	
	Test	Avg.	Test	Avg.	Test	Avg.	Test	Avg.
1	4.9 5.1	5.0 (34.5)	4.1 4.3 4.6	4.3 (29.6)	4.8 5.0 5.1	5.0 (34.5)	5.1 5.4 5.9 5.5 5.3	5.4 (37.2)
2	4.6 4.8 4.6	4.7 (32.4)	n/a		5.3 5.7 5.9 5.5 5.4	5.6 (38.6)	1.4 4.1 1.5	2.3* (15.9)
4	5.0 4.6 4.7	4.8 (33.1)	n/a		4.0 4.8 3.3	4.0 (27.6)	n/a	

* Unreliable data

Note that the exposed specimens, cylinders and prisms were transported to the field no less than two months after the construction (Table 4-1). Therefore, the 28-day field concrete strengths for Specimens 2 and 4 were not determined. The compressive strength of Specimen 2 from the test results of field cylinders at the time of structural load testing varied from 1.4 ksi (9.7 MPa) to 4.1 ksi (28.3 MPa), resulting in an unreliable indication of the compressive strength. The field concrete cylinders under exterior weather conditions and supplemental watering exhibited significant cracking due to ASR/DEF effects compared to those stored in the curing room, as show in Figure 5-1. The highly cracked cylinders of Specimen 2 led to scattered test results of the concrete compressive strengths. Thus, the compressive strength was considered to be invalid and therefore field cylinders of Specimen 4 were not tested at the time of its structural load testing. Also, due to the lack of sufficient cylinders and prisms, the tensile strength at the time of testing of Specimens 2 and 4 were not determined. However, due to the severely cracked state of the field samples, it was presumed that the tensile strength at the time of structural load testing was significantly less than the 28-day tensile strengths of the samples stored in the curing room.

Table 5-3 Concrete Tensile Strengths
(t: embedded bar tensile test; s-t: splitting tensile test)

Specimen		28-Day Strength, ksi (MPa)				Strength at Time of Structural Testing, ksi (MPa)			
		Curing Room		Lab		Curing Room		Lab/Field	
		Test	Avg.	Test	Avg.	Test	Avg.	Test	Avg.
1	t	n/a		0.39 0.46	0.43 (2.96)	0.41 0.32	0.37 (2.55)	0.19 0.14	0.17 (1.17)
	s-t	0.64 0.65	0.65 (4.48)	0.65 0.65	0.65 (4.48)	0.63 0.58	0.61 (4.21)	0.54 0.60	0.57 (3.93)
2	t	0.46 0.45	0.46 (3.17)	n/a		n/a		n/a	
	s-t	0.65 0.63	0.64 (4.41)	n/a		n/a		n/a	
4	t	0.49 0.48	0.49 (3.39)	n/a		n/a		n/a	
	s-t	0.51 0.58 0.51	0.53 (3.65)	n/a		n/a		n/a	

(a) Concrete Cylinder in Curing Room (with Hairline Cracking)

(b) Field Concrete Cylinder

Figure 5-1 Comparison of Cured and Field Cylinders (Specimen 4)

5.3 EXPERIMENTAL TEST SETUP

The experimental test setup for the C-shaped specimens was designed to be a self-reacting system. The specimens concurrently represented two bridge bent types, with potentially two comparative results obtained from one sub-assemblage test. Figure 5-2 shows a detailed plan and elevation of the experimental test setup for Specimens 1 and 2. For experimental convenience, the specimens were oriented so that the column was placed horizontally, while the cantilevered beams were oriented vertically. The column was seated on two hinge supports located at a distance of 1.5 feet (0.46 m) from the inside beam face. Equal and opposite loads were applied to the beams at a distance of 3 feet (0.91 m) from the inside column face using two 220-kip (979-kN) MTS model

244.51S actuators placed in parallel. The actuators were connected to header beams using 1 3/8 inches (35 mm) diameter high strength DYWIDAG Threadbars, and were operated in displacement control using a servo hydraulic system. A third actuator, operated in force control, was placed between the two 220-kip (979-kN) actuators and maintained at 100 kips (445 kN) in order to provide a total capacity of 540 kips (2402 kN).

For Specimen 1, in order to maximize the results of the experimental investigation, the beam on one end of the specimen was strengthened using external post-tensioning, as shown in Figure 5-2. This was done to prevent yielding of the longitudinal reinforcing steel in the beam region and minimize cracking in the beam and beam-column joint region, thus focusing the other end of the specimen as the test subject area. In this way, two tests were performed on Specimen 1 as discussed in subsequent sections. As shown in Figure 5-2, the strengthening consisted of two 1 3/8 inches (35 mm) high strength DYWIDAG Threadbars, eccentrically positioned 12 inches (0.30 m) from the beam centerline toward the tension steel and post-tensioned to a total axial load of 300 kips (1334 kN).

For Specimen 2, the same experimental setup was applied but no strengthening was provided. Thus, only a single test was conducted primarily because of the unknown specimen damage due to the ASR/DEF effects. As the test setup for Specimen 1, two 220-kip (979-kN) MTS actuators were placed in parallel and operated in displacement control, while the third actuator was operated in force control and maintained at a load of 100 kips (445 kN) providing a total capacity of 540 kips (2402 kN).

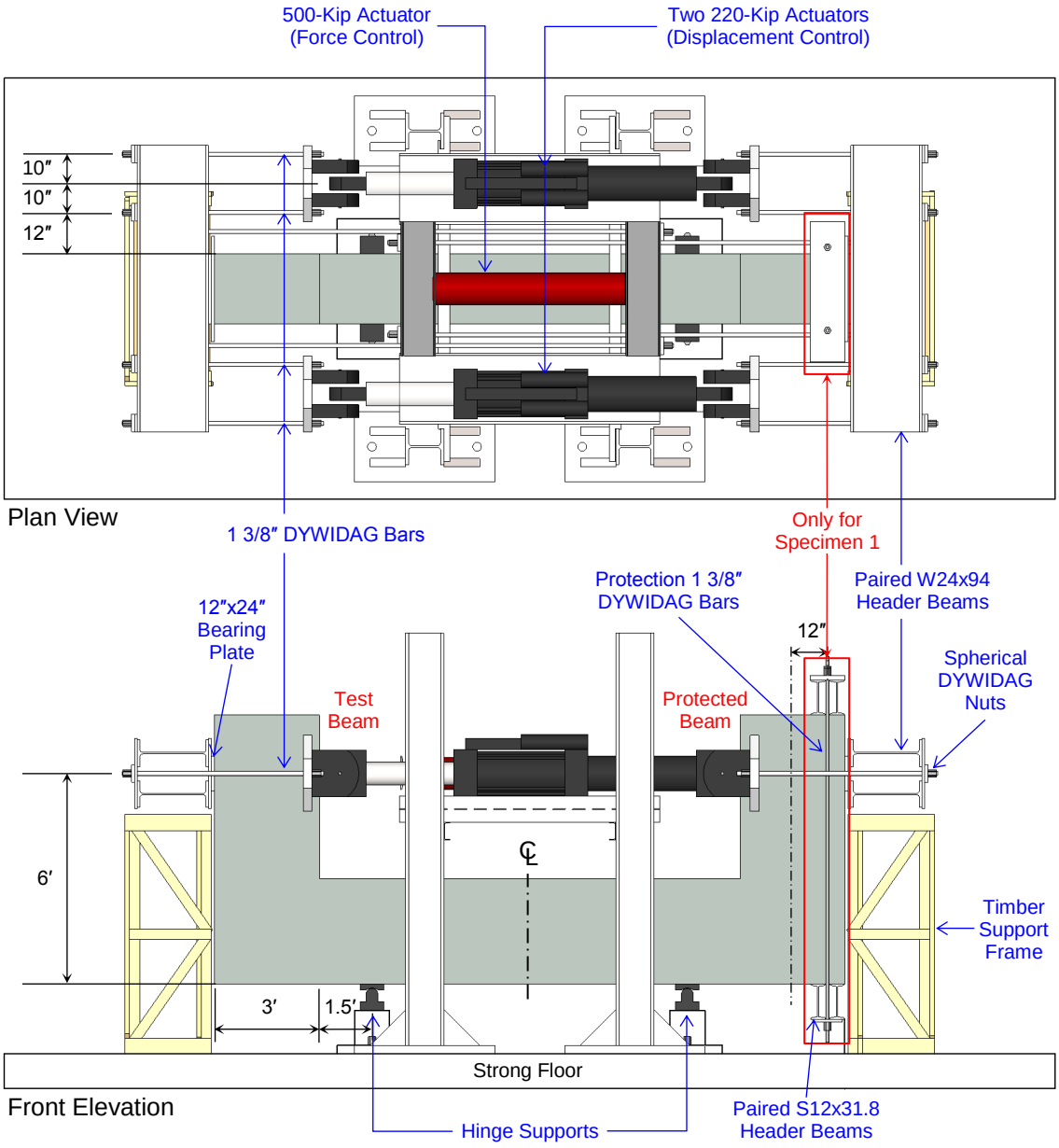

Figure 5-2 Experimental Setup for Specimens 1 and 2

In order to simplify the test setup, Specimen 4 was tested with only one 220-kip (979-kN) MTS actuator in displacement control. Figure 5-3 presents the plan and elevation of the experimental test setup for Specimen 4. The specimen was oriented the same as in the previous test setup where the column was placed on two hinge supports, and the beams were oriented vertically. One 220-kip (979-kN) MTS model 224.51S actuator was placed at one side of the specimen with a distance of 22 inches (0.56 m) from the surface of the specimen to the centerline of the actuator. Three 1 1/4 inches (32 mm) high strength DYWIDAG Threadbars were aligned vertically with a distance of 8 inches (0.20 m) from the surface of the specimen to the centerline of the bars. A roller support was used on one side of the specimen to create a leverage mechanism. The setup takes advantage of using one actuator with 2.7-to-1 mechanical lever mechanism to create a total capacity of 594 kips (2642 kN)). Similar to Specimen 2, by considering the uncertainty of the ASR/DEF effects, only one test was performed to investigate the ultimate strength and behavior of the specimen.

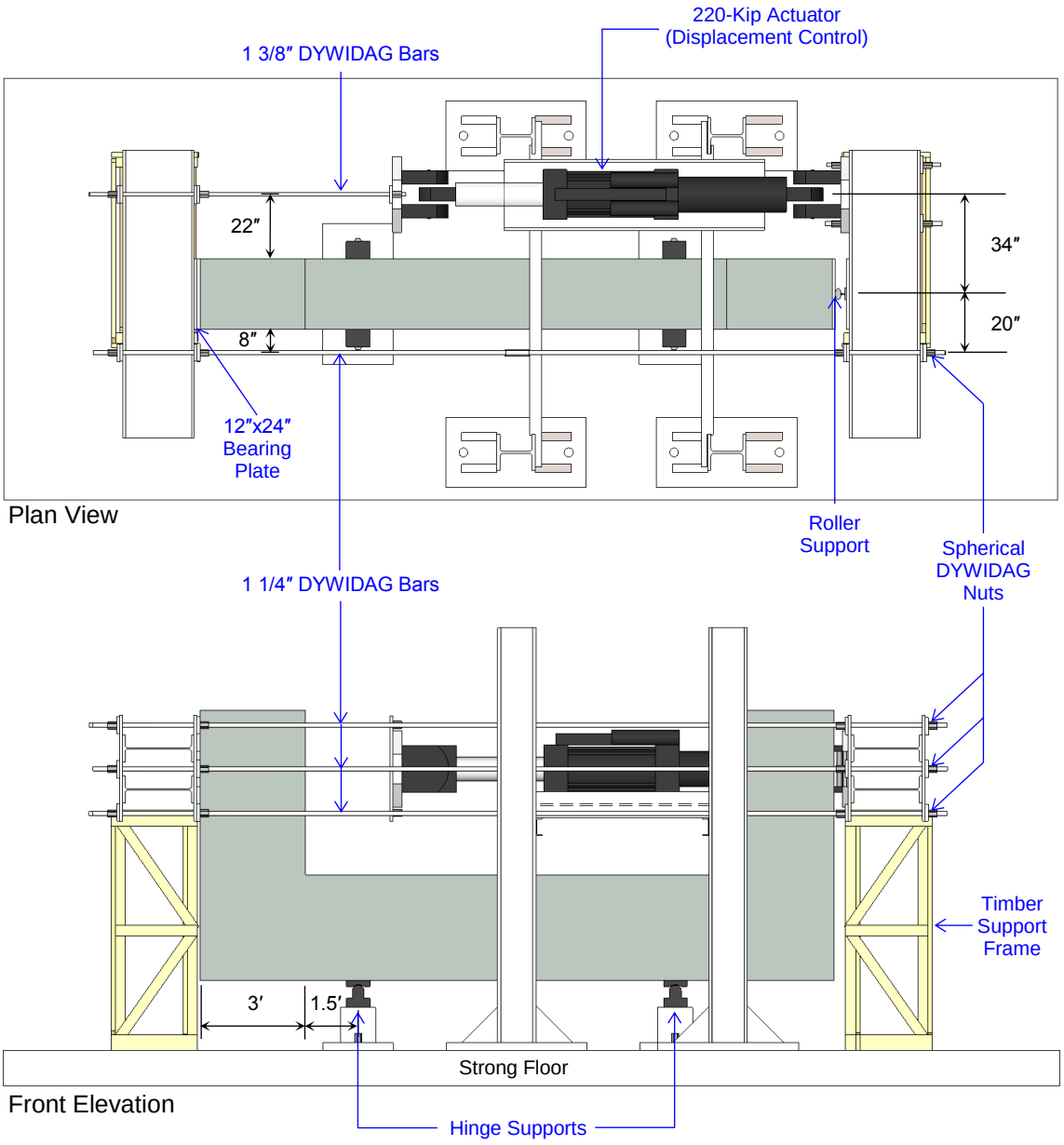

Figure 5-3 Experimental Setup for Specimen 4

5.4 EXPERIMENTAL INSTRUMENTATION

Figure 5-4 shows the external instrumentation layout used to obtain experimental displacement measurements. Specimens were externally instrumented using linear variable differential transformer (LVDTs) and string potentiometers (SPs). Since only a single test was conducted for Specimens 2 and 4, their external instrumentation layout (Figure 5-4c) was different from Specimen 1 (Figure 5-4a) due to the amount of the available instrumentation.

The global displacements at the applied loading points on the specimens were measured from string potentiometers that were connected from a rigid external column to the specimen above and below the header beam on each end, and an average of the measured displacements on each end was used. Experimental deformations associated with the STM and truss modeling were measured using LVDTs mounted to aluminum truss members that were rigidly connected to the specimen between selected nodal points (Scott, 2010). Each nodal point had an embedded DEMEC brass insert securely attached into the specimen. Aluminum truss members with pin-slotted end connections attached to two DEMEC brass inserts and LVDT, denoted as LV, were attached to measure the relative deformations between two nodal points. For Specimen 1, this consisted of ten members with six nodal points for the tested end and four members with four nodal points for the protected end (Figure 5-4a and b). For Specimens 2 and 4, both ends had six members and six nodal points (Figure 5-4c and d). Inferred principal tensile strains perpendicular to the STM struts were measured using four LVDTs

mounted perpendicular to the anticipated crack angles (55˚ and 45˚ in the beam and beam-column joint, respectively) with a 9 inches (0.23 m) gage length.

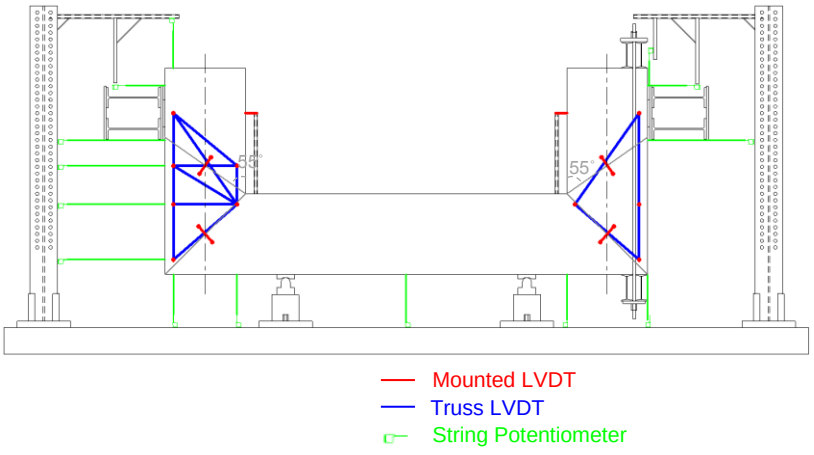

(a) Experimental Instrumentation Layout for Specimen 1

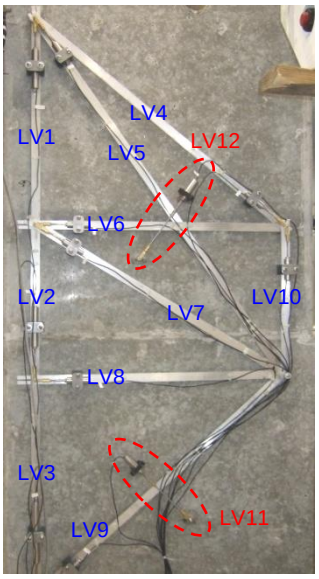

(b) Truss LVDT Setup for Specimen 1

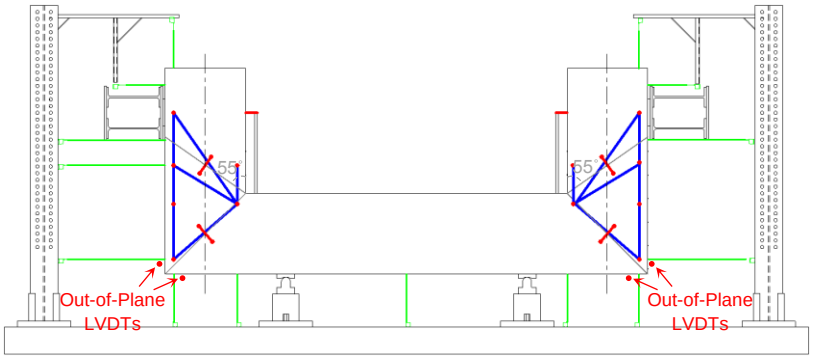

(c) Experimental Instrumentation Layout for Specimens 2 and 4

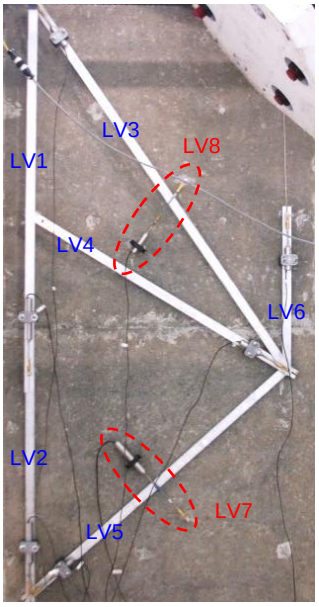

(d) Truss LVDT Setup for Specimens 2 and 4

Figure 5-4 Experimental Instrumentation Layout

5.5 EXPERIMENTAL TESTING PROCEDURE

As aforementioned, two tests were conducted for Specimen 1 in order to individually assess the performance of each D-region through effective strengthening using external post-tensioning on one end of the specimen, as depicted in Figure 5-5 through Figure 5-7.

For Specimen 1, Test 1 focused on the performance of the singly reinforced beam region of the specimen, where the doubly reinforced beam region was protected using external post-tensioning. The specimen was gradually loaded at 0.001 inch/sec (25 μm/sec) to about 200 kips (890 kN) and held for approximately two hours to record crack orientations and width measurements (Figure 5-5). Then, the specimen was completely unloaded in order to record structural response during in-service load level reversals. The specimen was reloaded at 0.002 inch/sec (50 μm/sec) to about the specimen's yield point at 440 kips (1957 kN), which was the maximum loading of the test setup at that point, and subsequently unloaded (Figure 5-6).

Test 2 focused on the pre-cracked performance of the doubly reinforced beam region until the ultimate failure load, where the singly reinforced beam region was strengthened via the application of external post-tensioning (Figure 5-7). A third actuator operated in force control was implemented in the test setup to increase the maximum loading capacity. As discussed in Section 5.3, the third actuator was first loaded in force control and maintained at 100 kips (445kN). Then the 220-kip (979-kN) MTS actuators, enabling a total capacity of 540 kips (2402 kN), were loaded in displacement control at 0.002 inch/sec (50 μm/sec) until specimen's failure.

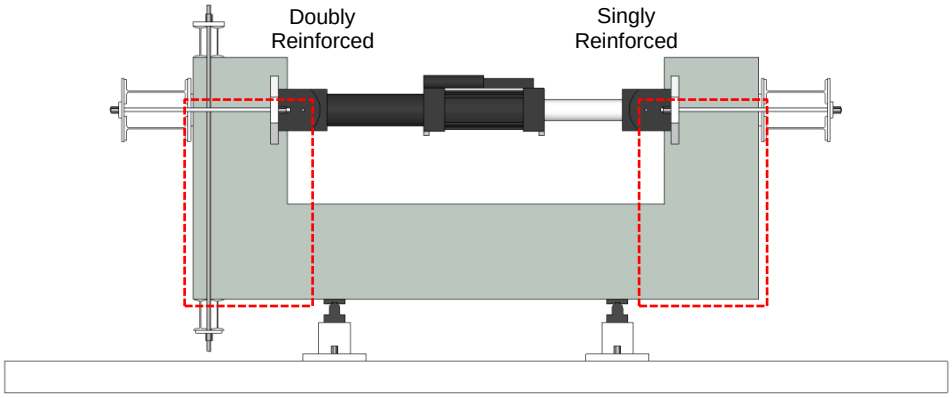

(a) Doubly Reinforced Beam Region

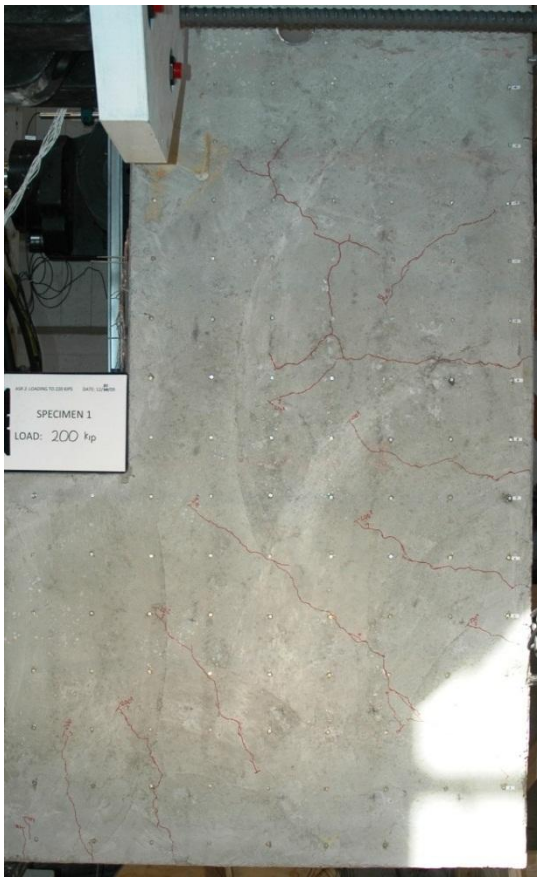

(b) Singly Reinforced Beam Region

Figure 5-5 Test 1 of Specimen 1 – In-Service Load at 200 Kips

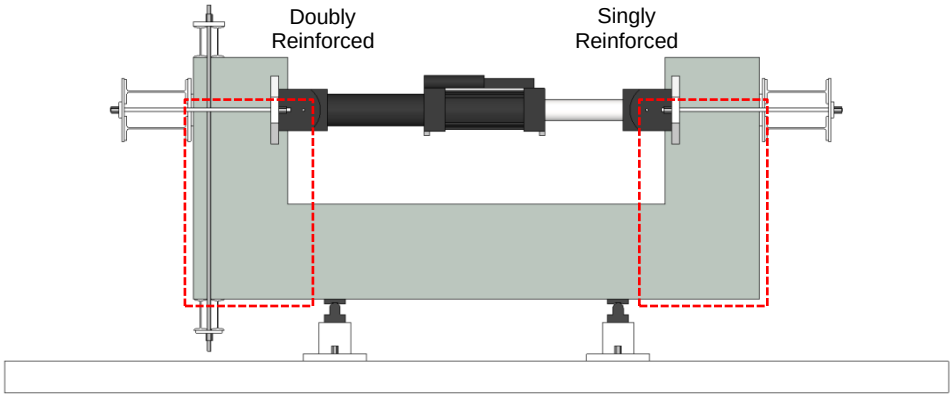

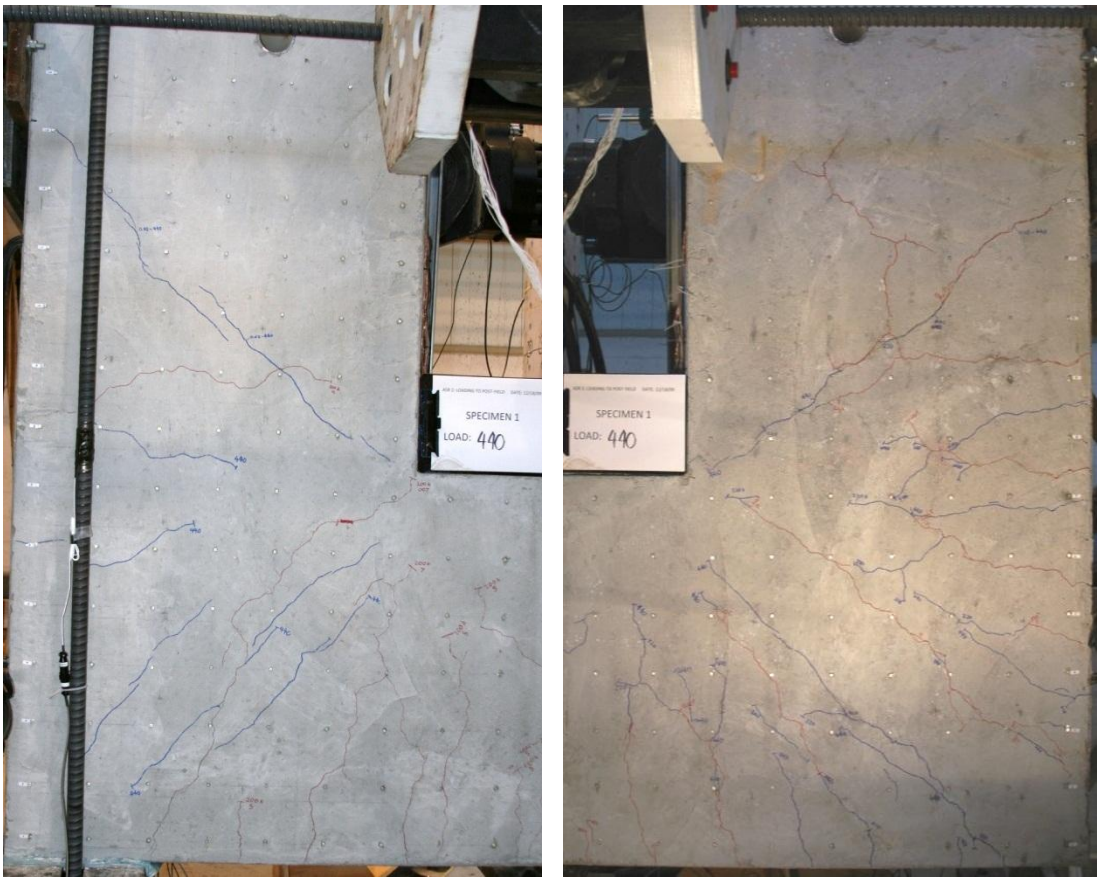

(a) Doubly Reinforced Beam Region *(b) Singly Reinforced Beam Region*

Figure 5-6 Test 1 of Specimen 1 – Yield Load at 440 Kips

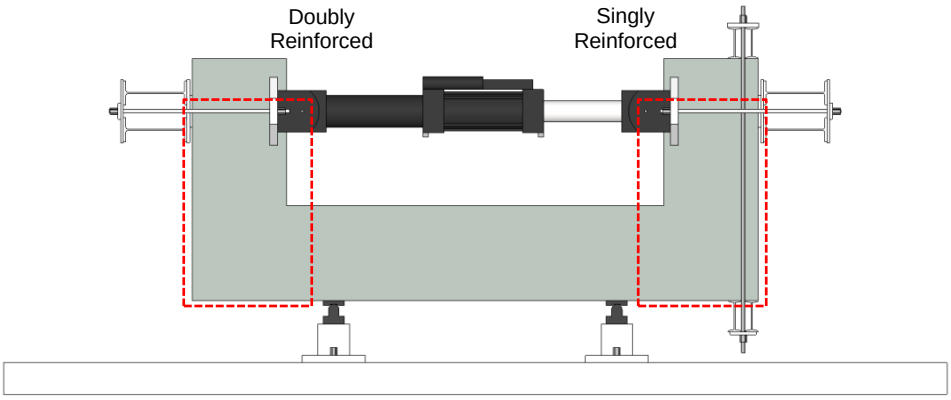

(a) Doubly Reinforced Beam Region

(b) Singly Reinforced Beam Region

Figure 5-7 Test 2 of Specimen 1 – Ultimate Load at 474 Kips

Since the ASR/DEF effects on the exposed specimen's structural performance were unclear before the structural load testing, only one test was conducted for each exposed specimen, that is, Specimens 2 and 4. As discussed in Section 5.3, the test setup for Specimen 2 consisted of two 220-kip (979-kN) MTS model 224.51S actuators operated in displacement control, and a third actuator operated in force control and maintained at 100 kips (445 kN) to create a total capacity of 540 kips (2402 kN). For Specimen 4, only one 220-kip (979-kN) MTS model 224.51S actuator was used to create a total capacity of 594 kips (2642 kN) through the leverage mechanism.

Figure 5-8 through Figure 5-10 show the critical areas of both ends of Specimen 2 at particular load levels during the test. The specimen was gradually loaded at 0.001 inch/sec (25 μm/sec) to 200 kips (890 kN) and held for crack width measurements (Figure 5-8). Subsequently, the specimen was loaded at 0.002 inch/sec (50 μm/sec) to 400 kips (1779 kN) without unloading and held for visual investigations (Figure 5-9), and then loaded to failure (Figure 5-10). Note that map cracking was previously observed during the specimen's exposure period prior to the structural load testing.

Figure 5-11 through Figure 5-13 present the critical areas of both ends of Specimen 4 at particular load levels during the experimental testing. Similar with Specimen 2, severe map cracking was observed during the specimen's exposure phase prior to the structural load testing. Specimen 4 was gradually loaded at 0.001 inch/sec (25 μm/sec) to 450 kips (2002 kN) using the leverage mechanism and the test was stopped due to lack of mechanism travel. Following unloading and some adjustments of the test setup, the specimen was reloaded to ultimate failure.

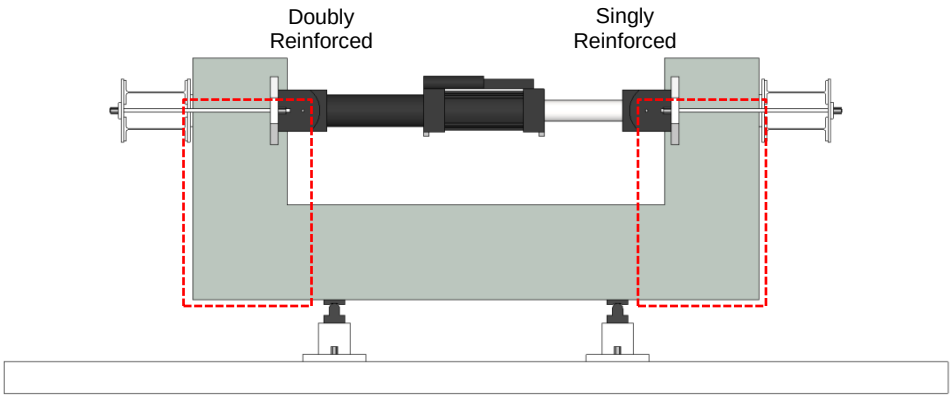

(a) Doubly Reinforced Beam Region

(b) Singly Reinforced Beam Region

Figure 5-8 Test of Specimen 2 – In-Service Load at 200 Kips

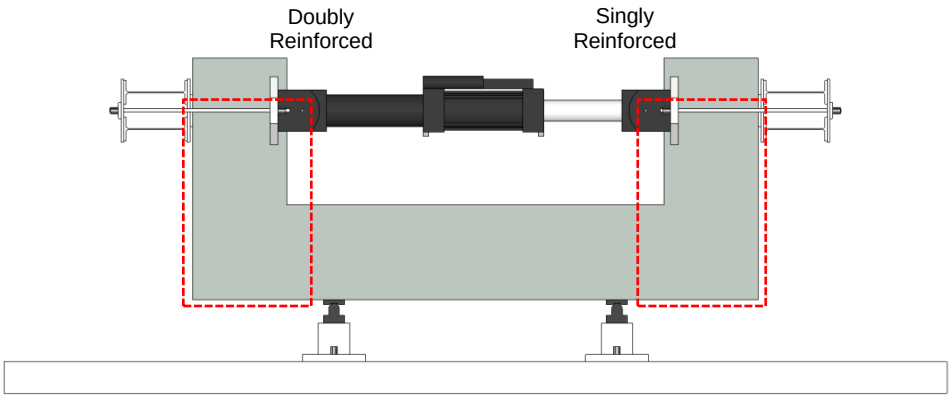

(a) Doubly Reinforced Beam Region

(b) Singly Reinforced Beam Region

Figure 5-9 Test of Specimen 2 – Load at 400 Kips

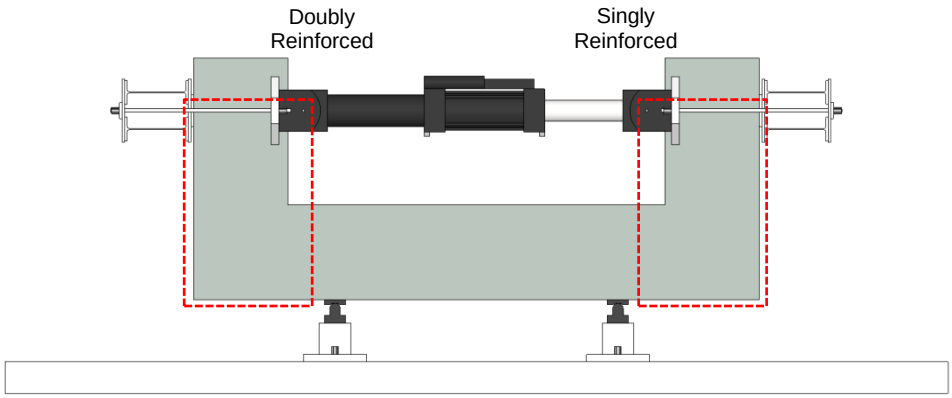

(a) Doubly Reinforced Beam Region

(b) Singly Reinforced Beam Region

Figure 5-10 Test of Specimen 2 – Ultimate Load at 500 Kips

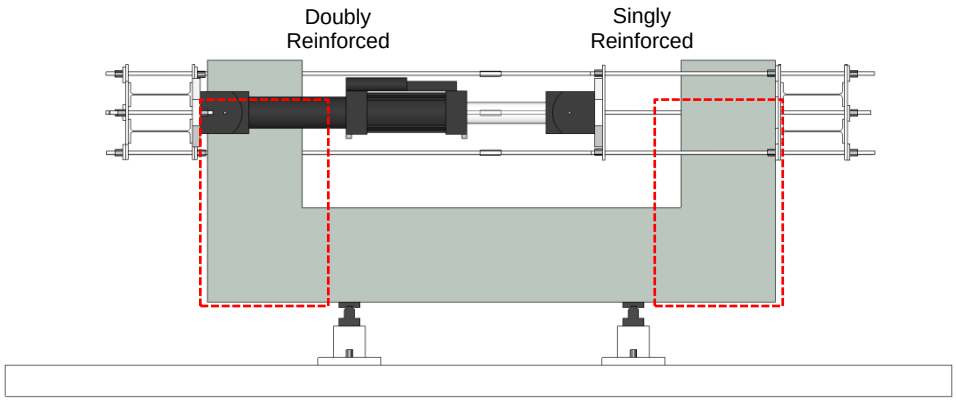

(a) Doubly Reinforced Beam Region

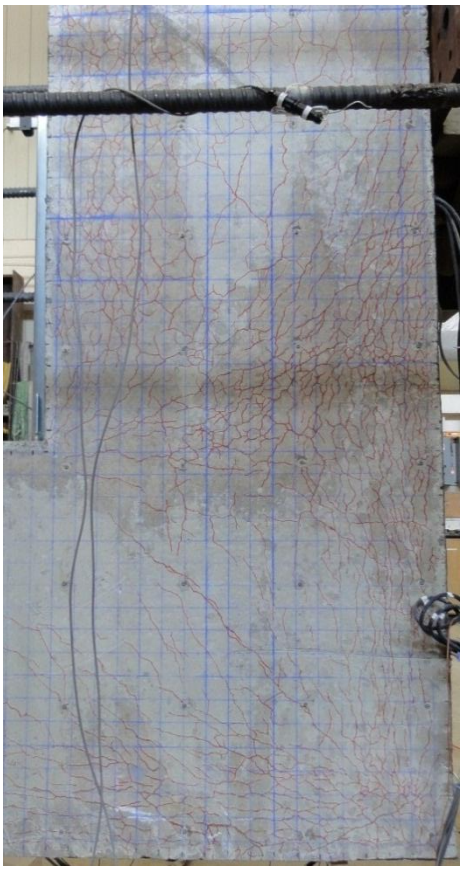

(b) Singly Reinforced Beam Region

Figure 5-11 Test of Specimen 4 – In-Service Load at 200 Kips

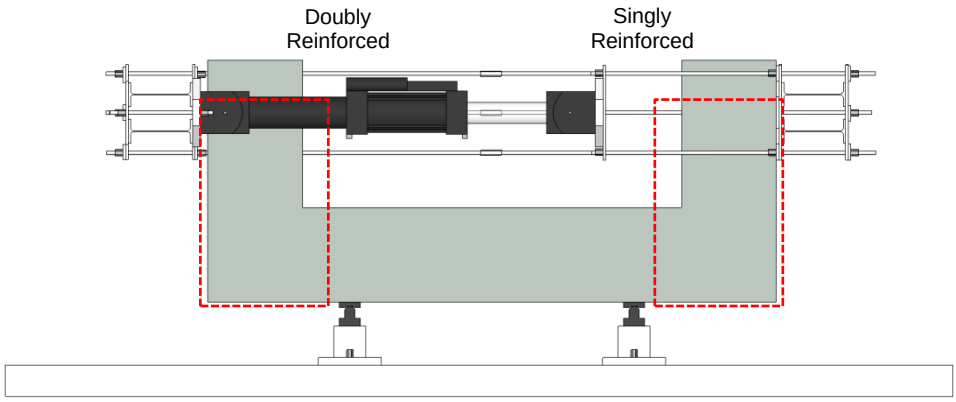

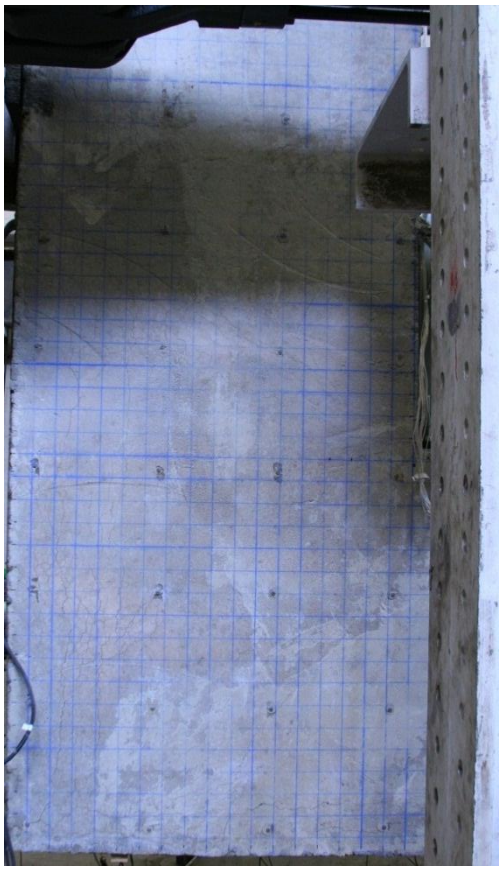

(a) Doubly Reinforced Beam Region

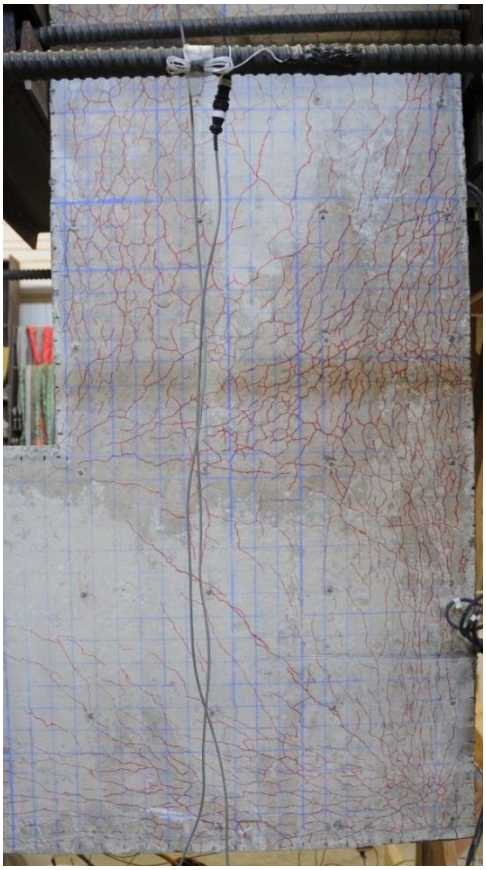

(b) Singly Reinforced Beam Region

Figure 5-12 Test of Specimen 4 – Load at 400 Kips

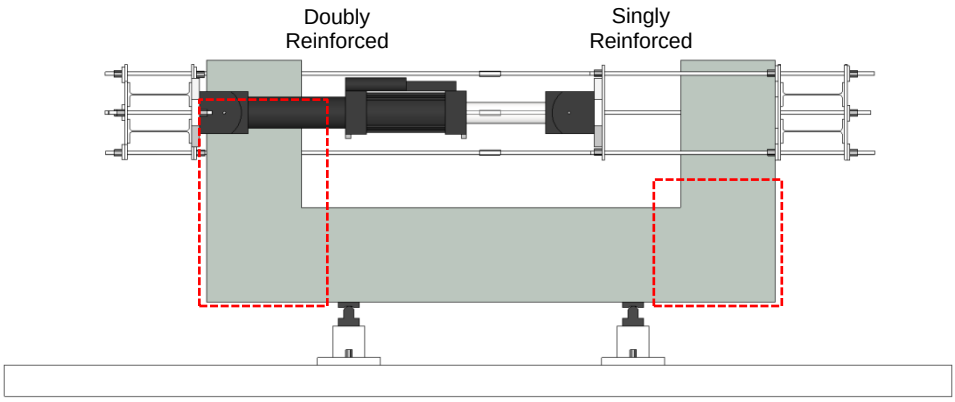

(a) Doubly Reinforced Beam Region

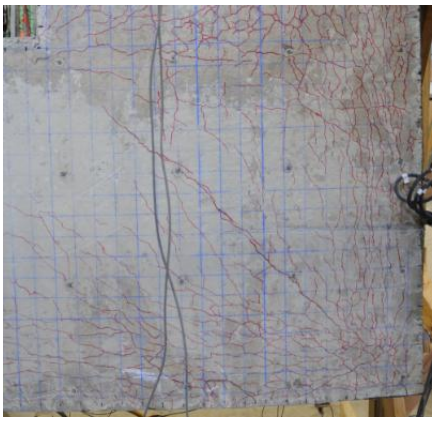

(b) Singly Reinforced Beam Region (before Failure)

(c) Singly Reinforced Beam Region (after Failure)

Figure 5-13 Test of Specimen 4 – Ultimate Load at 503 Kips

5.6 EXPERIMENTAL PERFORMANCE

In Test 1 of Specimen 1, the doubly reinforced beam region was protected using external post-tensioning and the singly reinforced beam region was the subject area of the test. In the unprotected singly reinforced beam region, flexural cracking in the critical bending regions of the beam was first observed at about 110 kips (489 kN), shortly followed by small flexural cracking throughout the column region of the specimen. Distinct diagonal cracking in the beam-column joint of the tested end was observed at approximately 170 kips (756 kN). Diagonal cracking through the beam region of the tested end from the loading point to the supporting column was observed at a load of about 200 kips (890 kN). Upon reloading, existing cracks in the beam region and beam-column joint propagated toward the inside corner of the joint, that is, CCC node in STM, with the largest crack width observed in the beam region of 0.050 inches (1.27 mm) at a load of 440 kips (1957 kN). In the protected doubly reinforced beam region, diagonal cracking in the beam-column joint propagating from the post-tensioning header beam to the inside corner of the joint was observed at about 120 kips (534 kN). A distinct diagonal crack formed in the beam region at a load of 360 kips (1601 kN) with a width of 0.020 inches (0.51 mm).

In Test 2 of Specimen 1, the singly reinforced beam region was protected by means of external post-tensioning and the doubly reinforced beam region was tested. Due to the pre-cracked state, existing cracks propagated with the formation of a few new cracks in the beam region and beam-column joint at higher loads. At 440 kips (1957 kN), the largest diagonal cracks in the beam region and beam-column joint were

approximately 0.025 inches (0.64 mm) and 0.035 inches (0.89 mm), respectively. The ultimate failure mechanism of the specimen occurred suddenly in the tested beam-column joint region along the main corner to corner diagonal (STM strut). This brittle failure was at the maximum applied load of about 474 kips (2108 kN). The applied post-tensioning at the other end of the specimen successfully protected the beam longitudinal reinforcement from yielding by offsetting the measured strains to approximately zero when the applied load was 200 kips (890 kN).

The specimens exposed in the field with supplemental watering were loaded to simulate the in-service gravity effect, as discussed in Section 4.2.2. The intention of the application of pre-loading was to ensure that the exposed specimens had a moderate amount of normal service cracking during their exposure phase. During this exposure phase, the load-induced cracks grew in both length and width over time. Significant amounts of new cracking also developed throughout the specimens as a result of the ASR/DEF expansion. Prior to shipping the specimens back to the structural testing laboratory for their experimental load testing, the prestress load that mimicked the in-service gravity load was released. An important observation made at that time was that the existing cracks in the exposed specimens did not fully close after releasing the prestress load. This inelastic response confirmed that certain amount of material property changes had occurred as a consequence of the concrete expansion in the exposed specimens due to ASR/DEF effects. Since the ASR/DEF effects on the exposed specimen's structural performance were unclear before the structural testing, only one test was conducted for each exposed specimen (Specimens 2 and 4).

Specimen 2 was slowly loaded to the ultimate failure load of about 500 kips (2224 kN) without unloading. In the singly reinforced bent, the largest measured crack widths of the diagonal cracking through the beam region were 0.013 inches (0.33 mm) and 0.016 inches (0.41 mm) at loads of 200 kips (890 kN) and 400 kips (1779 kN), respectively. In addition, the largest crack widths measured in the beam-column joint were 0.013 inches (0.33 mm) and 0.016 inches (0.41 mm) at the same loads of 200 kips (890 kN) and 400 kips (1779 kN). In the doubly reinforced bent, the largest measured crack widths of the diagonal cracking through the beam region were 0.016 inches (0.41 mm) and 0.030 inches (0.76 mm) at loads of 200 kips (890 kN) and 400 kips (1779 kN), respectively. Moreover, the largest crack widths measured in the beam-column joint were 0.010 inches (0.25 mm) and 0.016 inches (0.41 mm) at the same loads of 200 kips (890 kN) and 400 kips (1779 kN). Note that some large cracks parallel to the main tension reinforcing steel bars were observed at the outside corner of the beam-column joint during the exposure phase. The largest measured crack widths among these cracks were 0.035 inches (0.89 mm) and 0.040 (1.02 mm) at loads of 200 kips (890 kN) and 400 kips (1779 kN), respectively. For Specimen 4, to minimize pauses in the test, no crack width measurements were made during loading. Both Specimens 2 and 4 had a sudden brittle failure in the beam-column joint of the singly reinforced bent. The ultimate failure mechanism of Specimens 2 and 4 occurred in the beam-column joint along the STM strut as that of Specimen 1. The maximum applied loads of Specimens 2 and 4 were about 500 kips (2224 kN) and 503 kips (2237 kN), respectively.

5.7 FORCE-DISPLACEMENT BEHAVIOR

Figure 5-14 presents the measured force-displacement behavior for both the singly and doubly reinforced regions of Specimens 1, 2 and 4. Note that the tip displacement at the loading point was obtained by averaging the recorded displacements using the top and bottom string potentiometers (SPs) near the header beam at the loading point (Figure 5-14).

In terms of the ultimate peak load, Specimen 1 reached a peak load of 474 kips (2108 kN) and then failed shortly afterwards, while the peak loads for Specimens 2 and 4 were 500 kips (2224 kN) and 503 kips (2237 kN), respectively. Some levels of ductility were observed in Specimens 2 and 4 prior to failure that was not observed in Specimen 1. Despite ASR/DEF effects, Specimens 2 and 4 were 5% and 6% stronger, respectively, than Specimen 1 in terms of the ultimate peak load. In addition, the initial and overall general stiffness of both Specimens 2 and 4 were slightly greater than that of Specimen 1. The strength and stiffness increases were attributed to the beneficial prestressing and confining effects of the core concrete from the peripheral longitudinal and transverse reinforcement caused by concrete expansion due to ASR/DEF effects. Although significant map cracking on the concrete surface of the exposed specimens was evident as a result of ASR/DEF expansion, this cracking did not appear to impair the specimen structural performance.

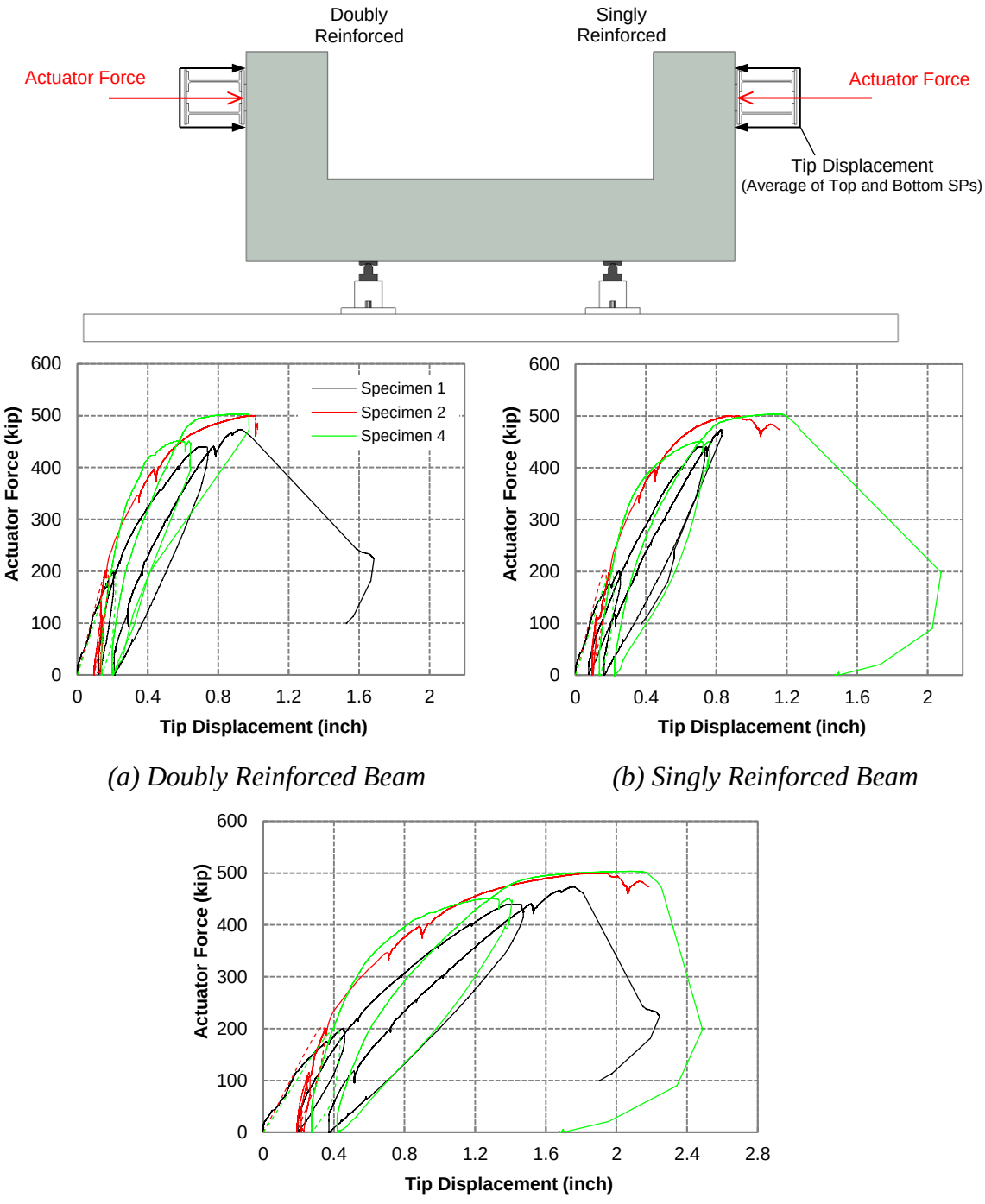

(a) Doubly Reinforced Beam

(b) Singly Reinforced Beam

(c) Total Tip Displacement

Figure 5-14 Force-Displacement Behavior of Specimens 1, 2 and 4

5.8 DISCUSSION

5.8.1 Failure Assessment

The ultimate failure mechanism in the control specimen (Specimen 1) and the two exposed specimens (Specimens 2 and 4) with varying levels of ASR/DEF expansion was common to all tested specimens. These failures may be classified as brittle shear failure through the beam-column joint region. This failure mechanism was triggered by the sudden concrete softening of the joint corner to corner diagonal STM strut and loss of support of the strut at the outside corner of the joint (STM CTT node). Immediately following the incipient failure mode, a redistribution of the joint forces to the reinforcement in the joint was necessary. However, because the reinforcement in the joint region had limited capacity, overall failure was sudden with a rapid drop in resistance. The brittle nature of the failure was attributed to the limited overlapping U-shaped reinforcement in the joint region within the plane of loading and also the lack of out-of-plane reinforcement along the column face of the joint region (Figure 5-15). The joint reinforcement, consisting of four sets of overlapping U-shaped steel bars and straight side face longitudinal distribution steel from the beam (skin reinforcement) and column (longitudinal column reinforcement), was not sufficient to confine the beam-column joint region. Overlapping U-shaped bars relied on bond strength in the spliced regions of the cover concrete to transfer the confining force. In the cracked cover sections, the bond strength may have been significantly reduced, resulting in insufficient confining force in the joint region. Moreover, the limited amount of joint reinforcement could not resist the redistributed forces from sudden concrete softening, leading to a

rapid brittle failure mechanism. The proposed additional U-shaped reinforcing steel bars would have helped confine the joint region in the out-of-plane direction and provide additional shear resistance in the joint (Figure 4-25).

Figure 5-16 shows the joint failure mechanism in the end of the doubly reinforced beam of Specimen 1 before and after removal of spalled concrete. Crushing of the cover concrete at the inside corner of the beam-column joint, that is, STM CCC node, was observed prior to the ultimate brittle failure at the outside corner of the joint (Figure 5-16c and d). Debonding was observed around the U-shaped steel bars and signs of pullout were evident from the direction of the steel ties as a result of spalling of cover concrete (Figure 5-16e). Moreover, the U-shaped steel bars bulged and bent due to the forces from the concrete strut in the joint region (Figure 5-16f). The bend of the tension longitudinal steel bars at the outside corner was pulled into concrete, leading to splitting and bursting in the concrete strut in the joint region. Out-of-plane splitting and bursting of the joint region was also observed as evidenced by the crack patterns on the column face and the out-of-plane bending of the longitudinal steel bars (Figure 5-16f).

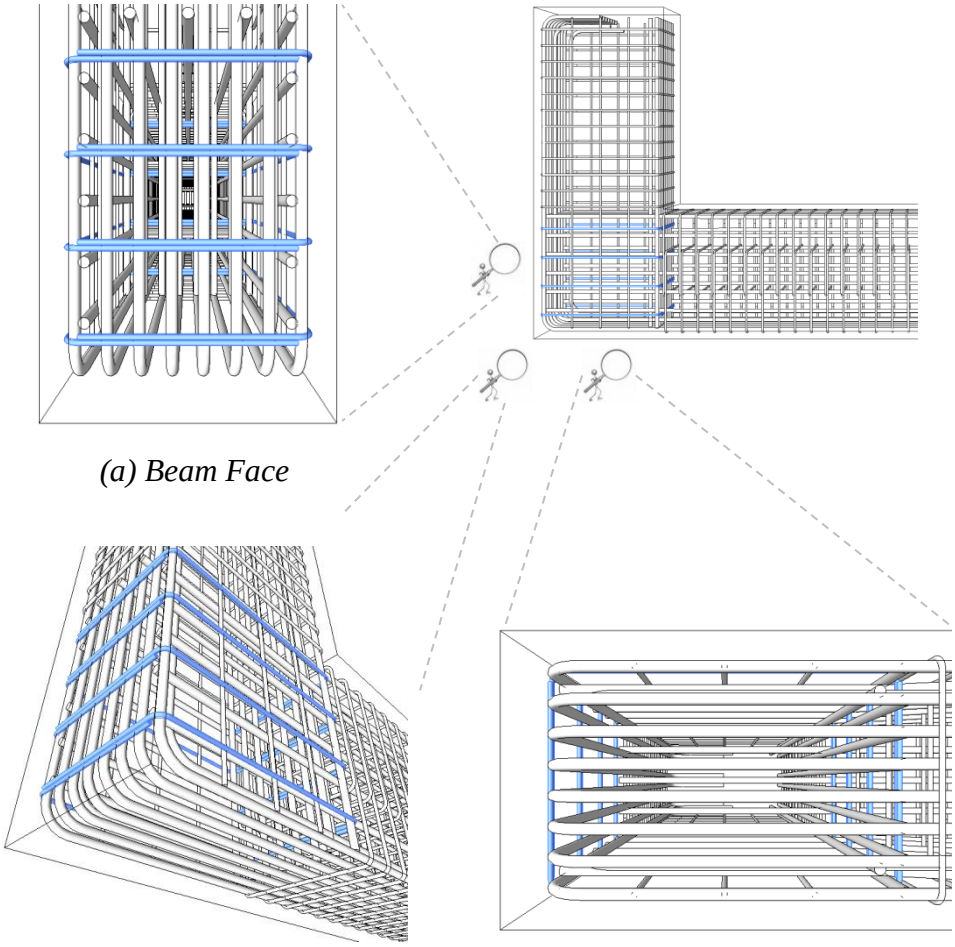

(a) Beam Face

(b) Outside Corner of Beam-Column Joint

(c) Column Face

Figure 5-15 Overlapping U-Shaped Reinforcement in Beam-Column Joint Region

(a) Failure at Outside Corner of Joint Region

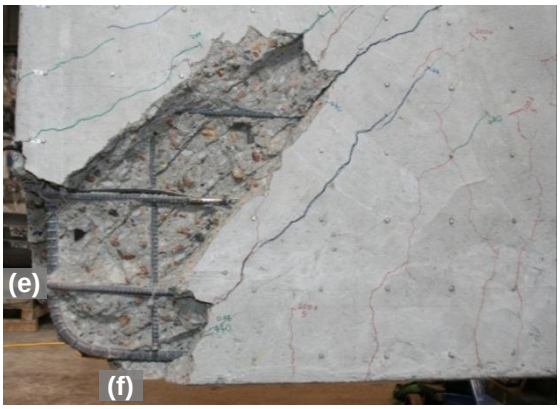

(b) After Removal of Spalled Concrete at Outside Corner of Joint Region

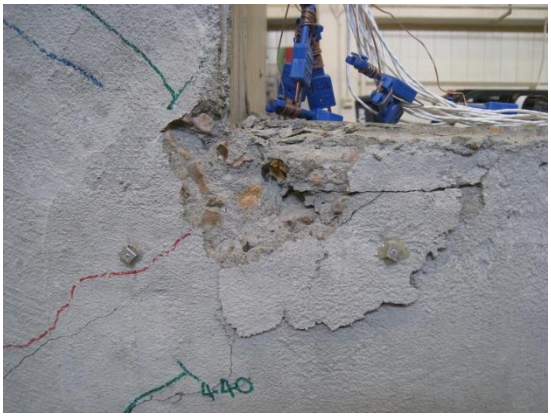

(c) Crushed Concrete at Inside Corner of Joint Region

(d) Crushed Concrete at Inside Corner of Joint Region

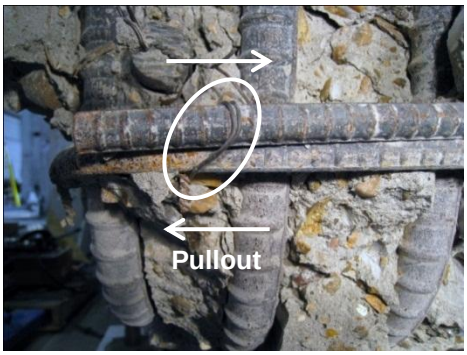

(e) Debonding of U-Shaped Steel Bars

(f) Bulging of U-Shaped Steel Bars and Out-of-Plane Bending of Longitudinal Steel Bars

Figure 5-16 Failure Mechanism of Specimen 1

The same failure mechanism was observed in the end of the singly reinforced beam of Specimens 2 and 4 (Figures 5-17 and 5-18). Note that only a single test was conducted for Specimens 2 and 4. The measured maximum displacement at the loading point at the end of the singly reinforced beam was greater than that at the end of the doubly reinforced beam (Figure 5-14a and b). Due to the lack of compression reinforcing steel that can slightly contribute to the stiffness of the beam, the singly reinforced side tended to fail prior to the doubly reinforced side. The cover concrete at the inside corner of the beam-column joint, that is, STM CCC node, for both Specimens 2 and 4 commenced crushing prior to the ultimate brittle failure at the outside corner and more spalling of concrete was observed compared to the testing of Specimen 1 due to ASR/DEF effects on the cover concrete (Figure 5-17c and d; Figure 5-18c and d), which was not observed in the testing of Specimen 1. At the outside corner of the joint, debonding, pullout, bulging of the U-shaped steel bars, and slicing into concrete at the bend of the tension longitudinal steel bars were observed, promoting out-of-plane bursting in the joint region (Figure 5-17e and f; Figure 5-18e and f). In addition, significant corrosion of the reinforcing steel bars of Specimen 4 was observed after removal of spalled concrete (Figure 5-18e and f). The reinforcing steel bars showed the commencement of significant corrosion over a 2 year exposure period to exterior weather conditions and supplemental watering. The severe surface concrete cracking due to ASR/DEF of Specimen 4 permitted more moisture ingress over time, leading to the steel corrosion. It is expected that this may become significantly worse over time and raise concerns of serviceability and durability of ASR/DEF affected structures.

(a) Failure at Outside Corner of Joint Region

(b) After removal of Spalled Concrete at Outside Corner of Joint Region

(c) Crushed Concrete at Inside Corner of Joint Region

(d) After removal of Spalled Concrete at Inside Corner of Joint Region

(e) Debonding of U-Shaped Steel Bars

(f) Bulging of U-Shaped Steel Bars and Out-of-Plane Bending of Longitudinal Steel Bars

Figure 5-17 Failure Mechanism of Specimen 2

(a) Failure at Outside Corner of Joint Region

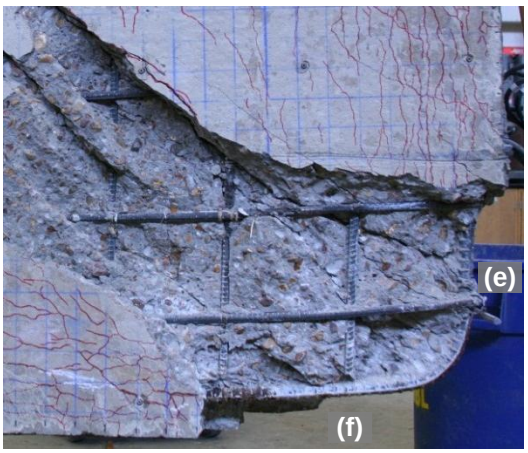

(b) After removal of Spalled Concrete at Outside Corner of Joint Region

(c) Crushed Concrete at Inside Corner of Joint Region

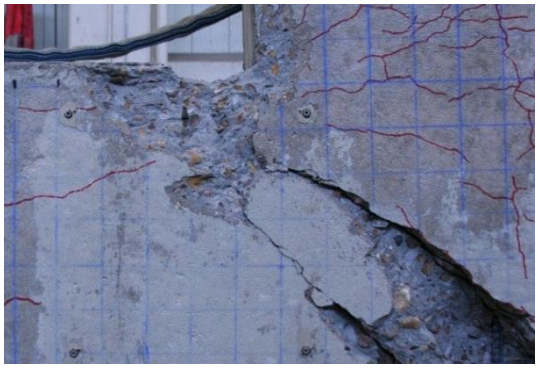

(d) After removal of Spalled Concrete at Inside Corner of Joint Region

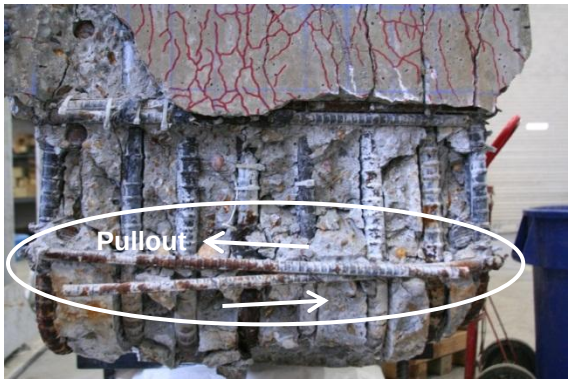

(e) Debonding of U-Shaped Steel Bars

(f) Bulging of U-Shaped Steel Bars, Out-of-Plane Bending of Longitudinal Steel Bars, and Steel Corrosion

Figure 5-18 Failure Mechanism of Specimen 4

5.8.2 Reinforcing Steel Behavior

Figures 5-19 and 5-20 present the longitudinal reinforcing steel behavior in the beam regions during the structural load testing of the specimens. Note that some strain gages failed prior to the load testing. For the exposed specimens (Specimens 2 and 4), some strain gage readings had significantly scattered behavior during specimen's exposure phase. However, as shown in Figures 5-19 and 5-20, it appeared that these gages were still able to capture reinforcing steel behavior during specimen's load testing.

For Specimen 1, two tests were conducted, that is, the doubly reinforced beam was protected and the singly reinforced beam was tested in Test 1, while the singly reinforced beam was protected and the doubly reinforced beam was tested to failure in Test 2. As shown in Figure 5-19b and Figure 5-20b, the external post-tensioning successfully protected the longitudinal tension steel in the protected beam from yielding. However, in Test 2 the longitudinal steel in the tested beam (doubly reinforced beam) yielded at the ultimate peak load of 474 kips (2108 kN), as shown in Figure 5-20.

For Specimens 2 and 4, the longitudinal steel strains prior to the structural load testing were due to the ASR/DEF effects during specimen's exposure phase and some of these strains scattered significantly over time. However, an amount of over 0.004 strain increment was observed in both the singly and doubly beams near the ultimate peak load, which evidently showed that the longitudinal reinforcing steel yielded prior to the failure of the specimens (Figure 5-19c and d; Figure 5-20c and d).

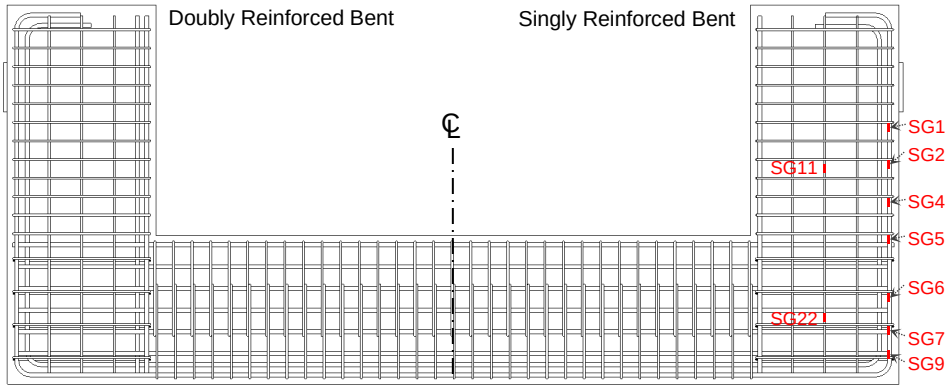

(a) Locations of Strain Gages Attached to Reinforcing Steel

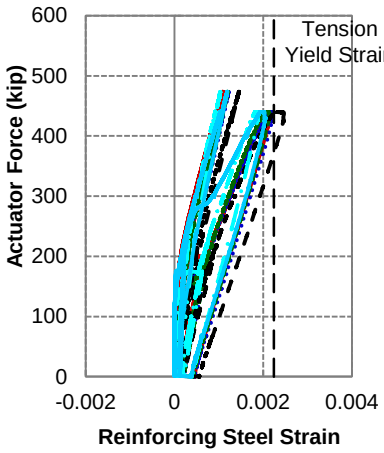

(b) Specimen 1

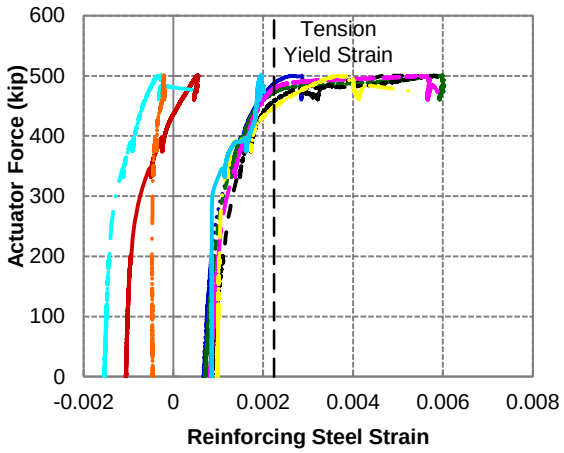

(c) Specimen 2

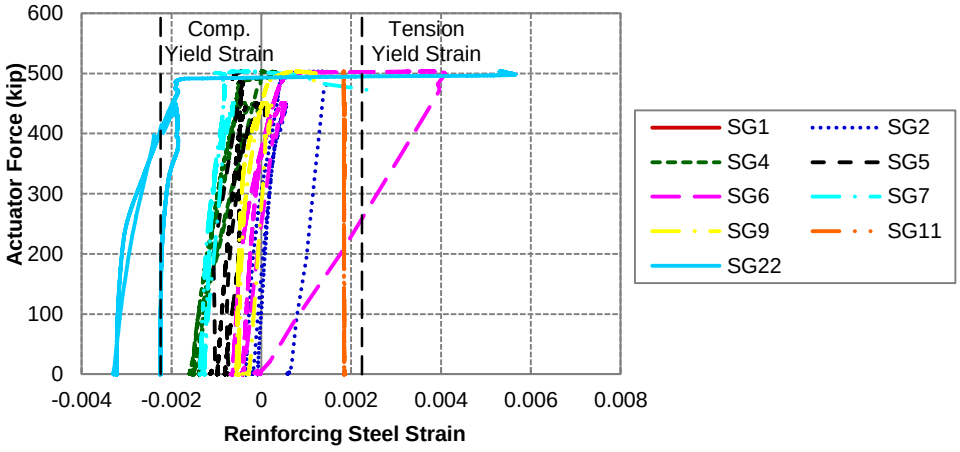

(d) Specimen 4

Figure 5-19 Longitudinal Reinforcing Steel Behavior of Singly Reinforced Beam during Structural Load Testing

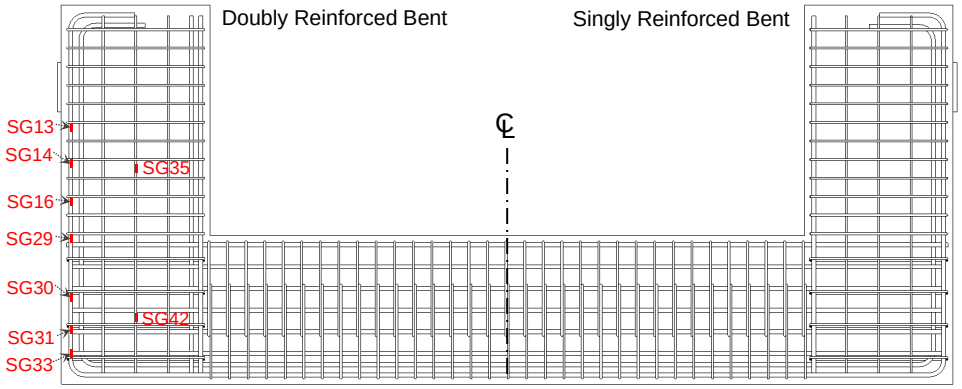

(a) Locations of Strain Gages Attached to Reinforcing Steel

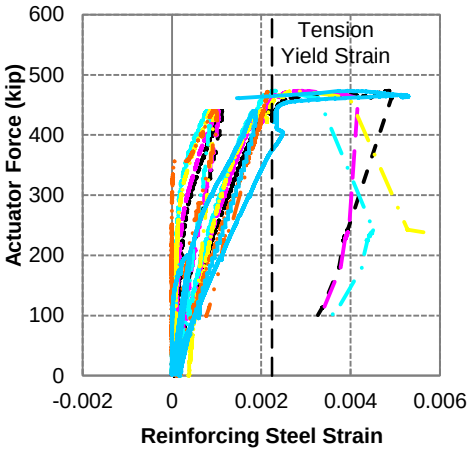

(b) Specimen 1

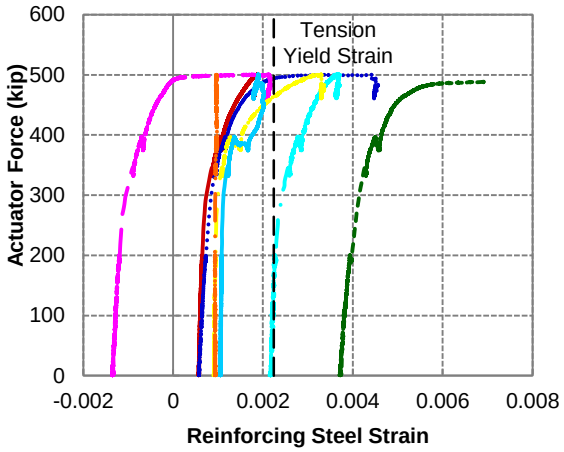

(c) Specimen 2

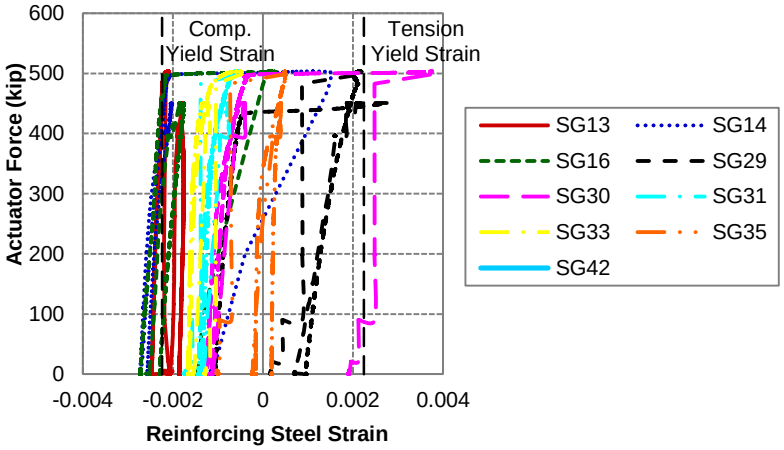

(d) Specimen 4

Figure 5-20 Longitudinal Reinforcing Steel Behavior of Doubly Reinforced Beam during Structural Load Testing

Figure 5-21 shows the longitudinal reinforcing steel strains in the column region during the structural load testing. For Specimen 1, the longitudinal steel in some locations reached the tension yield strain. For Specimens 2 and 4, the longitudinal steel strains gradually increased and the strain near the centerline of the specimen (SG51) in Specimen 2 exhibited more strain increases than the other locations. Note that SGs 49 and 51 in Specimen 4 failed prior to the structural load testing.

Figures 5-22 and 5-23 presents the behavior of the transverse reinforcing steel and U-shaped steel bars during specimen's structural load testing. For Test 2 of Specimen 1, the transverse hoops in the beam region (SGs 34 and 36) and the U-shaped steel bars in the beam-column joint (SG41) of the tested beam (doubly reinforced beam) reached yield strain (Figure 5-23b), indicating the out-of-plane bursting forces in STM struts. The U-shaped steel bars were insufficient to confine the joint region due to the debonding of the spliced regions, leading to the failure in the joint region. Some large strains in the transverse hoops of the beam regions were observed in Specimen 2 (Figure 5-22c and Figure 5-23c), while the U-shaped steel bars in the beam-column joints of Specimen 4 exhibited large amount of strain increases (Figure 5-22d and Figure 5-23d).

Minor changes of reinforcing steel strains in compression zones were observed during the structural load testing for all the tested specimens (Figure 5-24). The variations of these strains were within a strain of 0.002, which was less than the reinforcing steel yield strain.

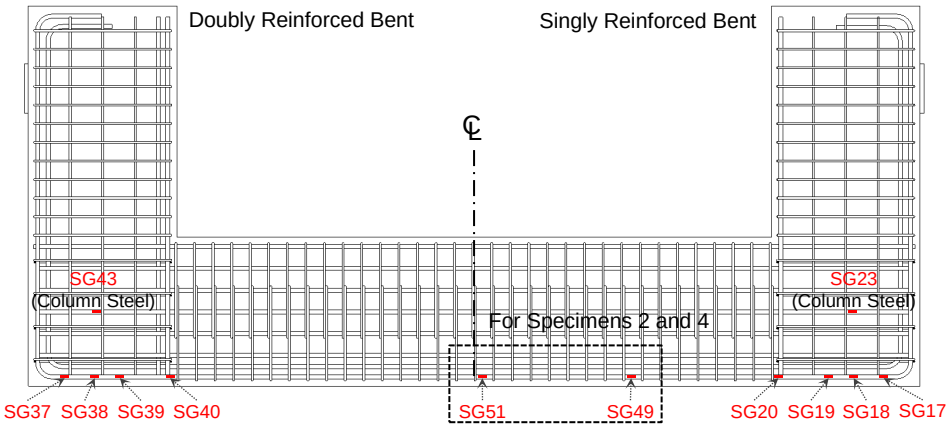

(a) Locations of Strain Gages Attached to Reinforcing Steel

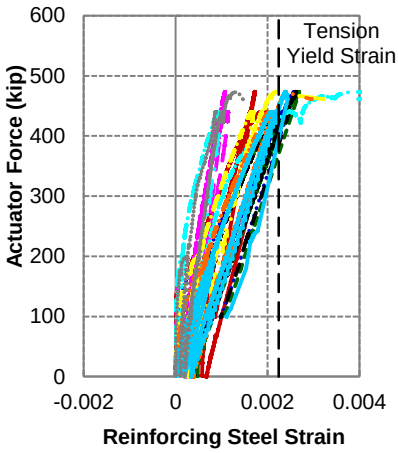

(b) Specimen 1

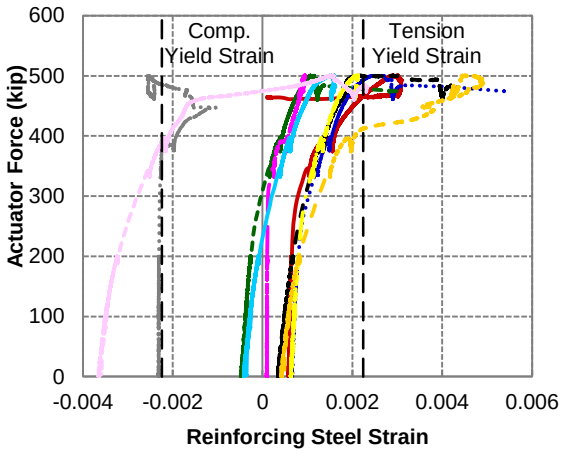

(c) Specimen 2

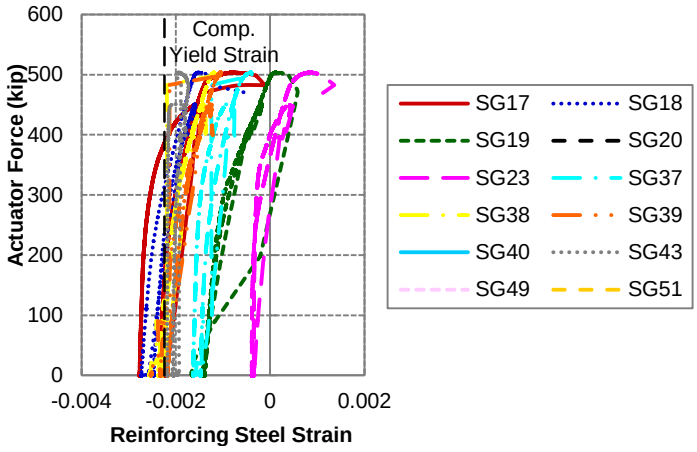

(d) Specimen 4

Figure 5-21 Longitudinal Reinforcing Steel Behavior of Column Region during Structural Load Testing

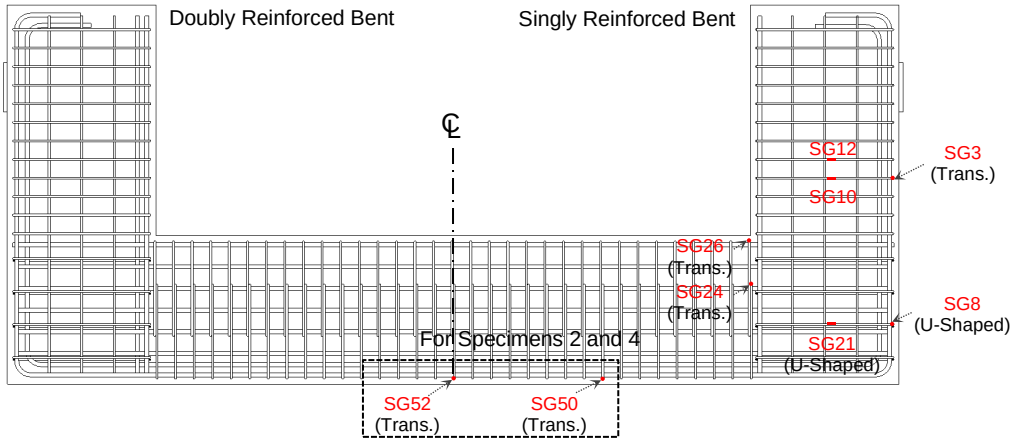

(a) Locations of Strain Gages Attached to Reinforcing Steel

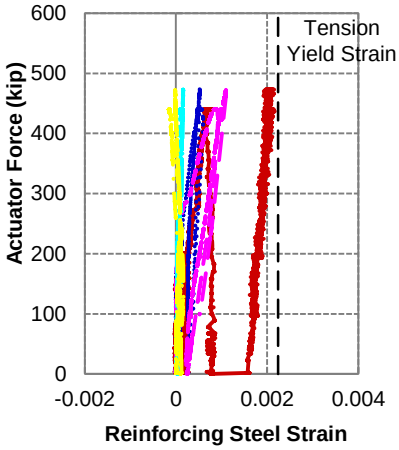

(b) Specimen 1

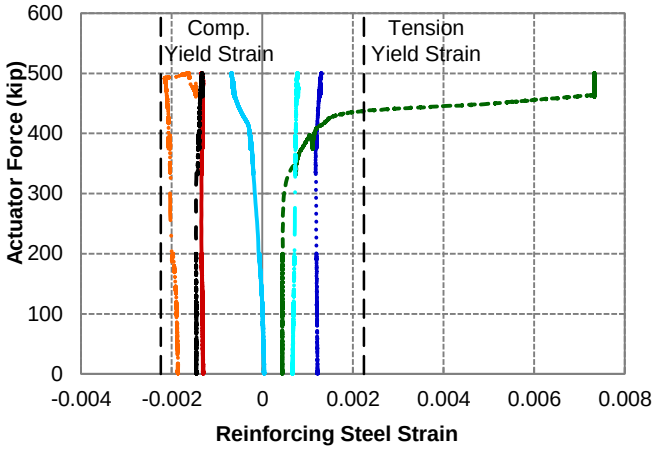

(c) Specimen 2

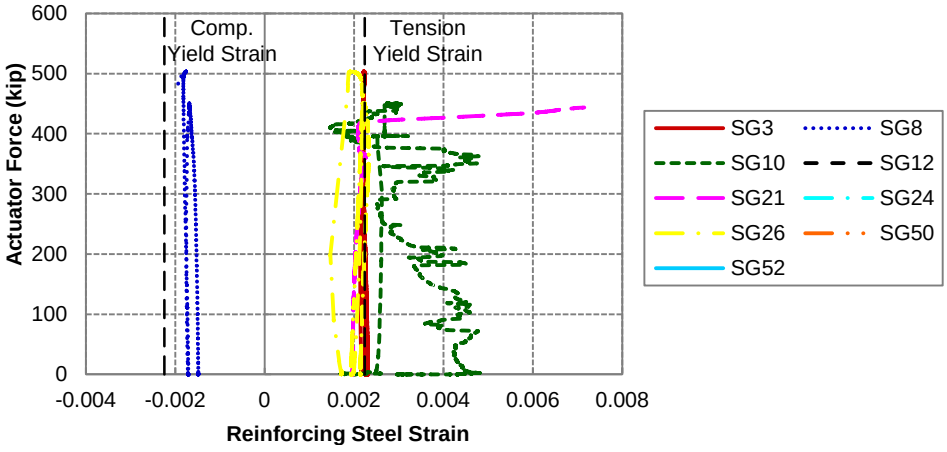

(d) Specimen 4

Figure 5-22 Behavior of Transverse Reinforcing Steel and U-Shaped Steel Bars of Singly Reinforced Beam and Column during Structural Load Testing

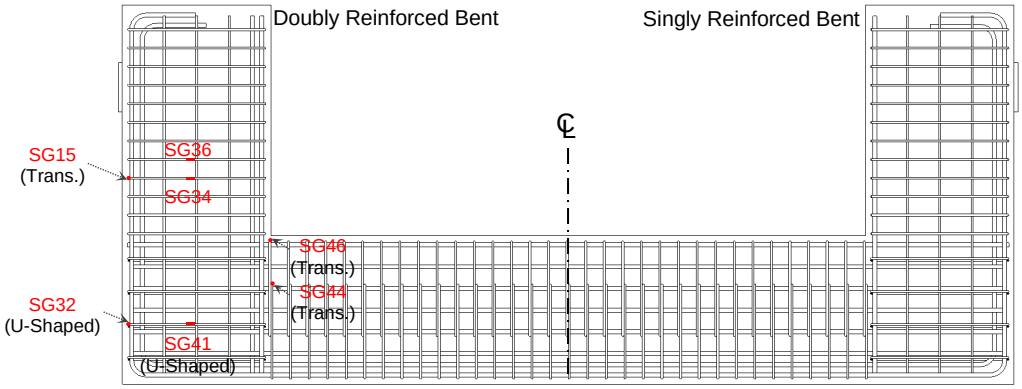

(a) Locations of Strain Gages Attached to Reinforcing Steel

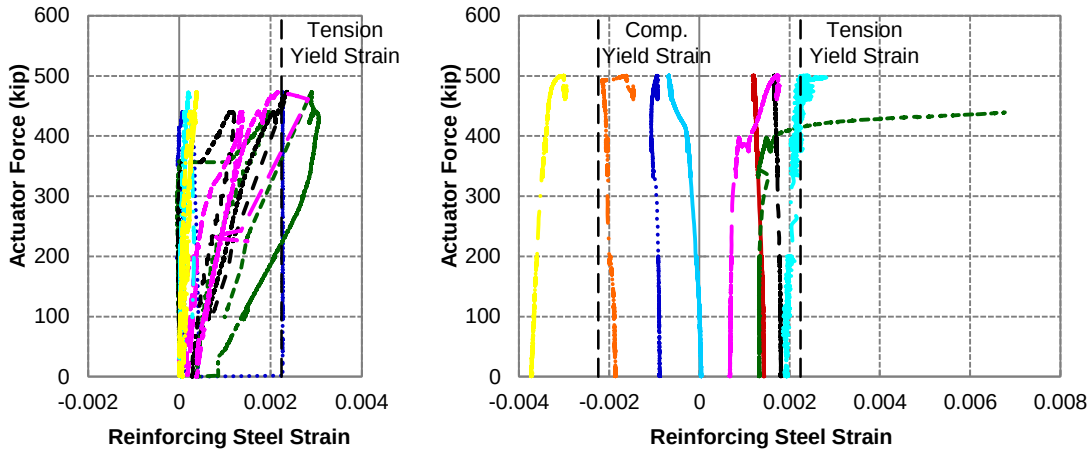

(b) Specimen 1

(c) Specimen 2

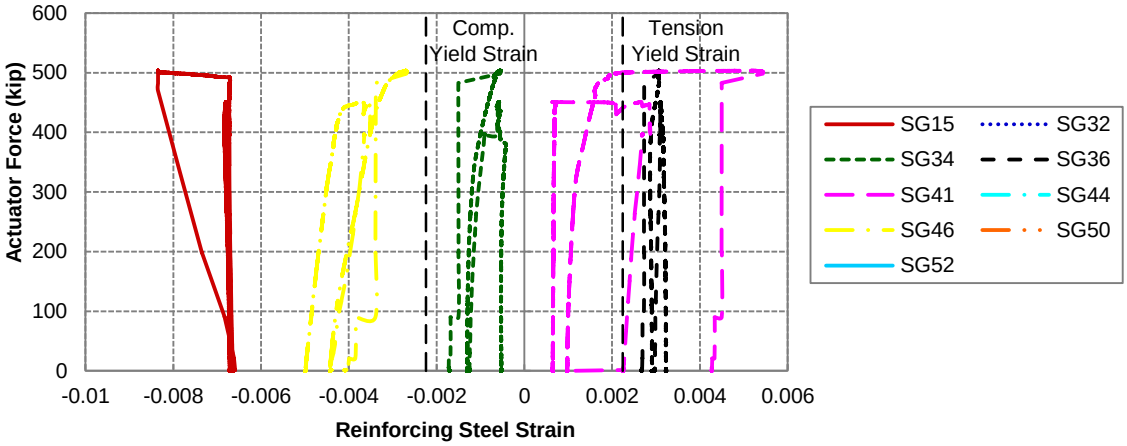

(d) Specimen 4

Figure 5-23 Behavior of Transverse Reinforcing Steel and U-Shaped Steel Bars of Doubly Reinforced Beam during Structural Load Testing

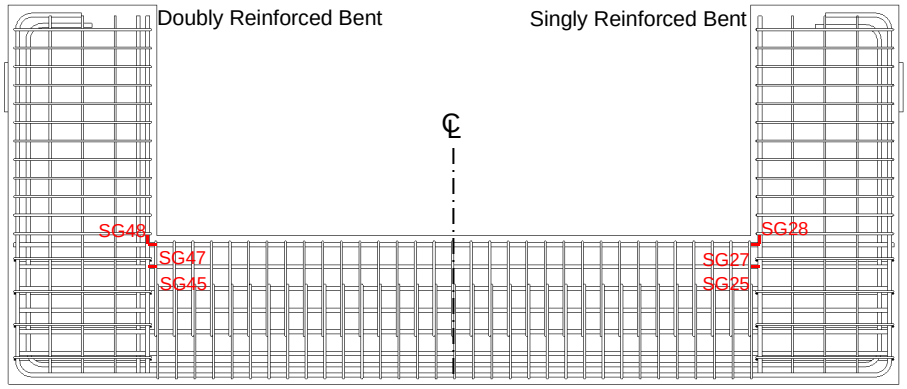

(a) Locations of Strain Gages Attached to Reinforcing Steel

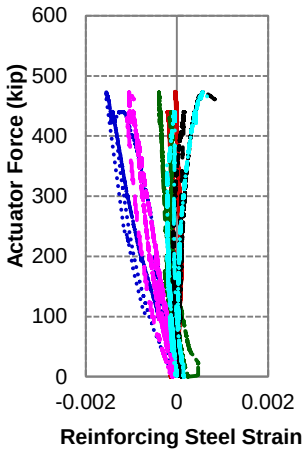

(b) Specimen 1

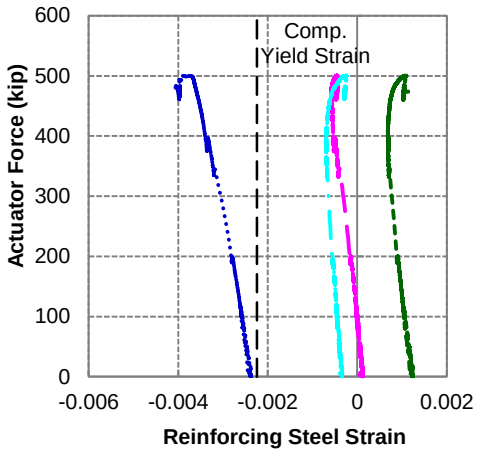

(c) Specimen 2

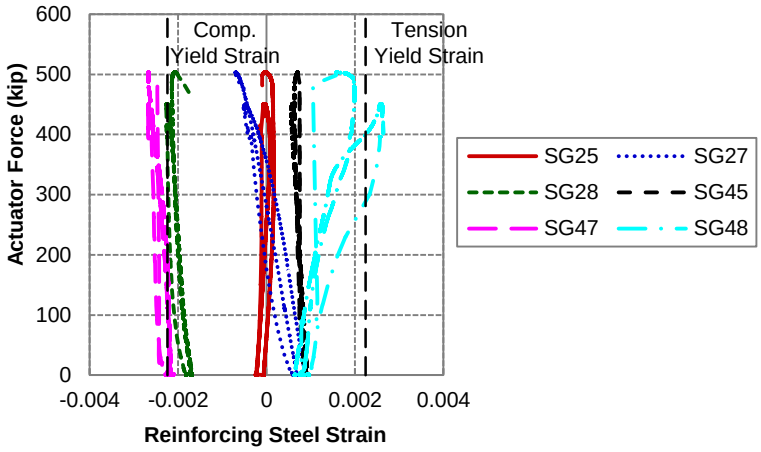

(d) Specimen 4

Figure 5-24 Reinforcing Steel Behavior of Compression Zone during Structural Load Testing

5.8.3 Core Concrete Behavior

Figures 5-25 and 5-26 present the behavior of the core concrete at mid-depth during the structural load testing. Note that some large strains in Specimens 2 and 4 were observed prior to their structural testing due to the ASR/DEF effects. In Test 2 of Specimen 1, a strain over 0.006 was observed in the direction perpendicular to STM strut (KM11) and the out-of-plane direction (KM12) in the failure beam-column joint (Figure 5-26b). For Specimens 2 and 4, large strains perpendicular to STM strut in the joints (KM5) were also observed prior to failure (Figure 5-25c and d). This showed the sign of concrete softening in the joint STM strut, which forced the redistribution of the joint forces to the joint reinforcement and suddenly resulted in ultimate joint failure.

5.8.4 Failure Joint Behavior

Figure 5-27 compares the behavior in the mid-depth core concrete and the reinforcing steel near the concrete cover region in the diagonal STM strut of the failure beam-column joint for each tested specimen. Evidently, the failure of each specimen was initiated by concrete softening of the corner to corner diagonal STM strut (Figure 5-27a, c and e). Then, a redistribution of the joint forces to the joint reinforcement was necessary. However, the reinforcement in the joint region was insufficient to resist the redistributed forces and to confine the bursting forces (Figure 5-27b, d and f), leading to the overall failure with a rapid drop in resistance due to the concrete softening in the concrete strut. In addition, the nodal support at the outside corner of the joint (STM CTT node) was also insufficient to resist the redistribution of the joint forces, leading to the failure near the nodal area.

(a) Orientations of Concrete Gages at Mid-Depth

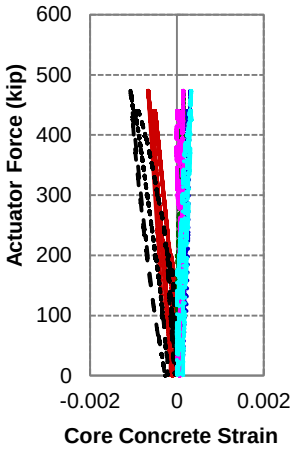

(b) Specimen 1

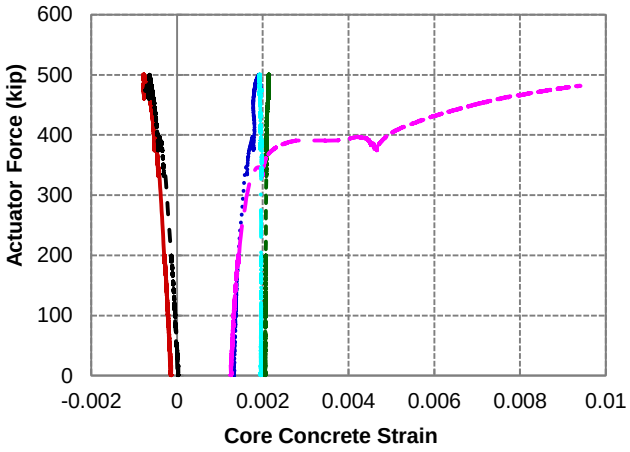

(c) Specimen 2

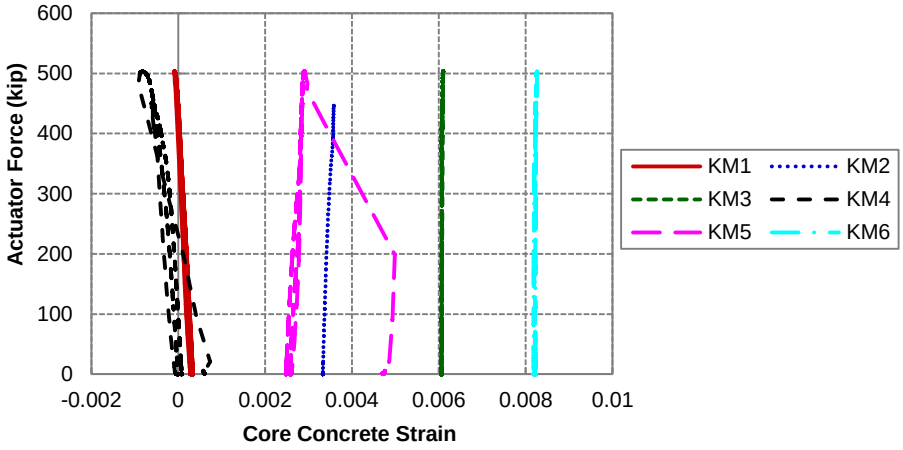

(d) Specimen 4

Figure 5-25 Mid-Depth Concrete Behavior of Singly Reinforced Bent during Structural Load Testing

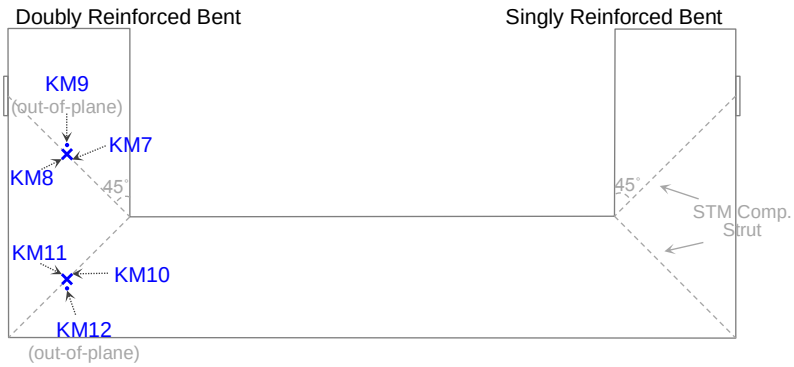

(a) Orientations of Concrete Gages at Mid-Depth

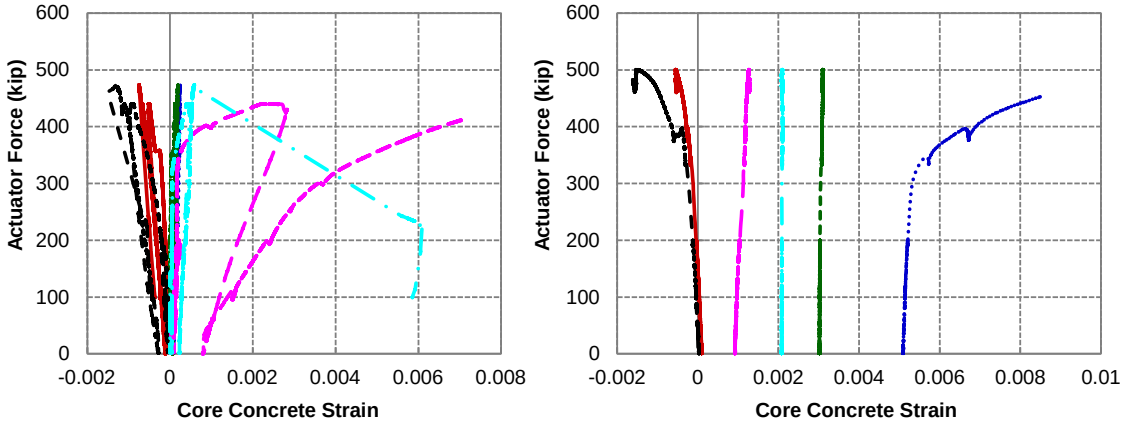

(b) Specimen 1

(c) Specimen 2

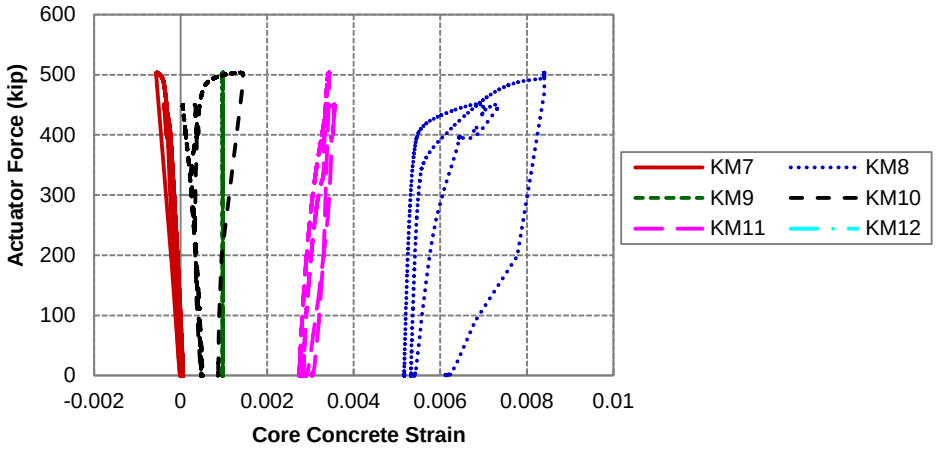

(d) Specimen 4

Figure 5-26 Mid-Depth Concrete Behavior of Doubly Reinforced Bent during Structural Load Testing

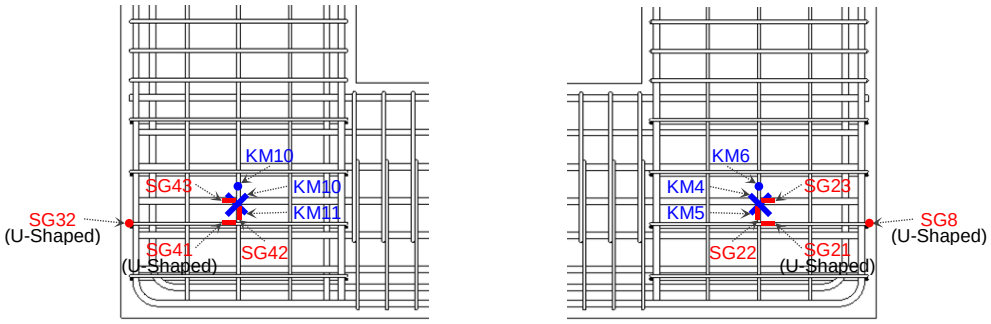

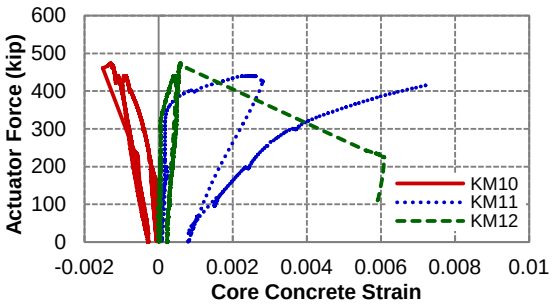

(a) Core Concrete – Specimen 1

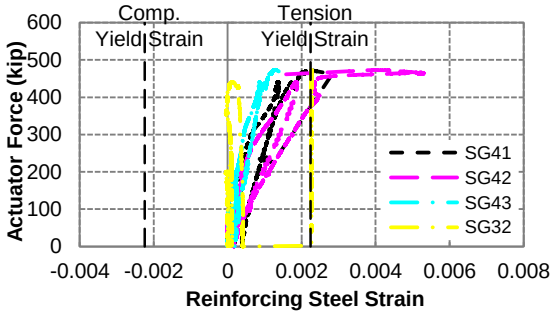

(b) Reinforcing Steel – Specimen 1

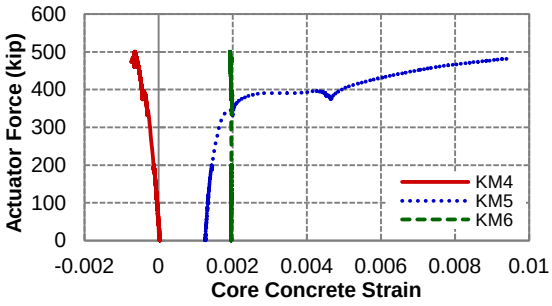

(c) Core Concrete – Specimen 2

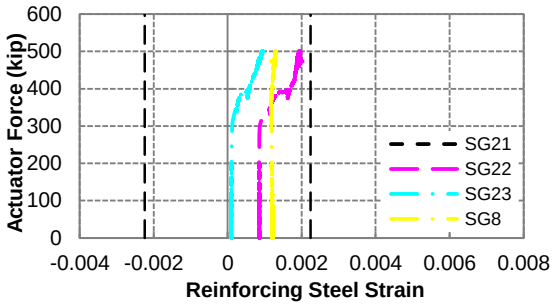

(d) Reinforcing Steel – Specimen 2

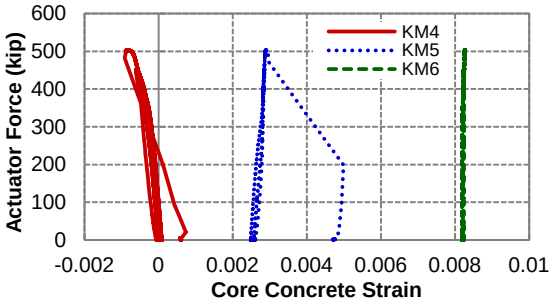

(e) Core Concrete – Specimen 4

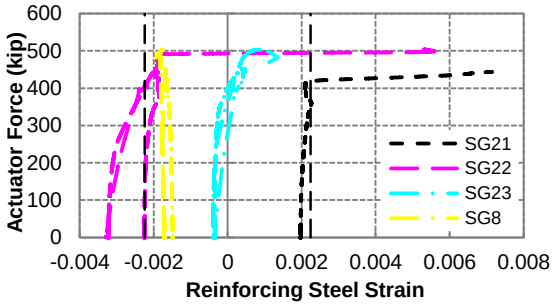

(f) Reinforcing Steel – Specimen 4

Figure 5-27 Comparison of Behavior of Mid-Depth Core Concrete and Reinforcing Steel in Failure Beam-Column Joint

5.8.5 Diagonal Strut Behavior

Figure 5-28 presents the strains parallel and perpendicular to the diagonal STM struts (cracks) calculated using LVDT readings in both beam-column joints and beam regions of the failure end for each tested specimen. Crack width increments perpendicular to the STM struts were measured by LVDTs mounted perpendicular to the struts (cracks) with a gage length of 9 inches (0.23m). Note that for Specimens 2 and 4, some pre-existing cracks across the gage were induced by the application of pre-loading to emulate the in-service gravity load effects and the later field exposure with supplemental water to accelerate the ASR/DEF mechanisms.

Evidently, the average strains perpendicular to the struts were significantly greater in the beam-column joints than in the beam regions. For Specimen 1, the average strain perpendicular to the strut across the gage length in the joint was greater than that in the beam region and increased significantly after the peak load due to the splitting forces in the joint strut (Figure 5-28a and b). Moreover, a significantly greater average strain increment perpendicular to the strut in the beam-column joint than in the beam region was observed for Specimens 2 and 4 (Figure 5-28c and d; Figure 5-28e and f). This also evidenced the overall joint failure as a consequence of the concrete softening of the STM strut in the joint region.

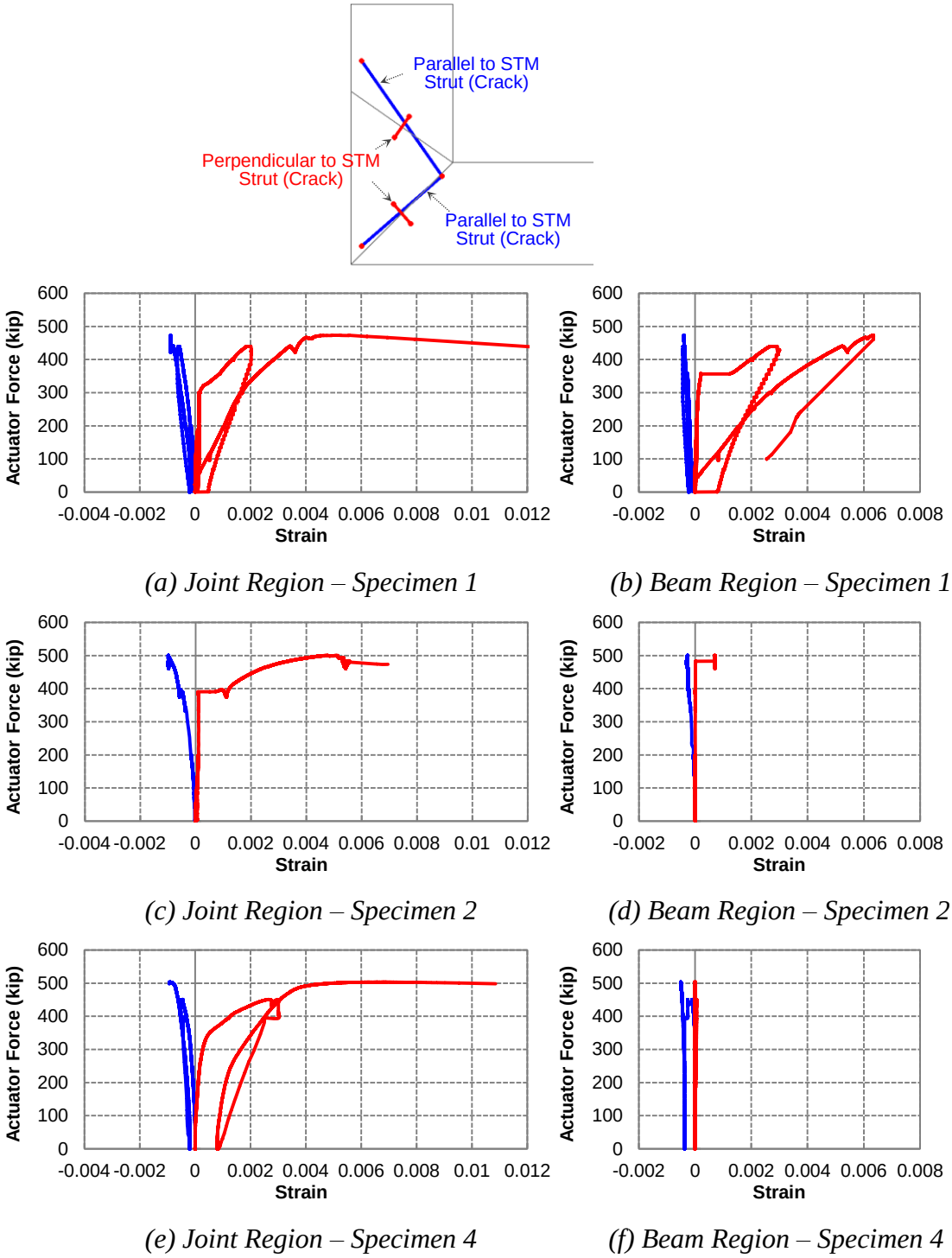

(a) Joint Region – Specimen 1

(b) Beam Region – Specimen 1

(c) Joint Region – Specimen 2

(d) Beam Region – Specimen 2

(e) Joint Region – Specimen 4

(f) Beam Region – Specimen 4

Figure 5-28 Comparison of Strains Parallel and Perpendicular to STM Struts in Beam-Column Joint and Beam Region of Failure End

5.8.6 Out-of-Plane Behavior

The failure mechanism of Specimen 1 drew attention to the out-of-plane bursting strains in the beam-column joint region. Therefore, for Specimens 2 and 4, out-of-plane strains at the outside corner of the beam-column joint were measured using LVDTs on the beam face at the first set of U-shaped steel bars (6 inches [0.15 m] from the corner) and the column face near the first set of longitudinal distribution steel (9 inches [0.23 m] from the corner) as shown in Figure 5-29. The out-of-plane strains of the failure beam-column joint in Specimens 2 and 4 were obtained by averaging the measured displacements over a 22-inch (0.56-m) span. Some strains were observed on both beam and column face and evidently supported the bursting behavior in the beam-column joint region (Figure 5-29a and b). Moreover, the observed out-of-plane strains on the column face were greater than the beam face for both Specimens 2 and 4.

5.9 SUMMARY AND CONCLUSIONS

In summary, the control specimen (Specimen 1) and two exposed specimens (Specimens 2 and 4 after eight months and two years of exposure, respectively) were structurally tested to failure. Compared to the control specimen, it was shown that the exposed specimens expanded considerably over time due to the ASR/DEF mechanisms, as discussed in Chapter IV. Consequently, this concrete swelling mechanism effectively activated the peripheral reinforcing steel, which prestressed and confined the core concrete. Based on the structural testing results, it can be concluded that these beneficial prestressing and confining effects offset the deleterious effects induced by ASR/DEF in terms of the ultimate peak load. Although significant cracking developed on the surface

due to ASR/DEF, the structural performance in terms of the strength, stiffness and ductility of the structure was not impaired up to this stage of ASR/DEF deterioration.

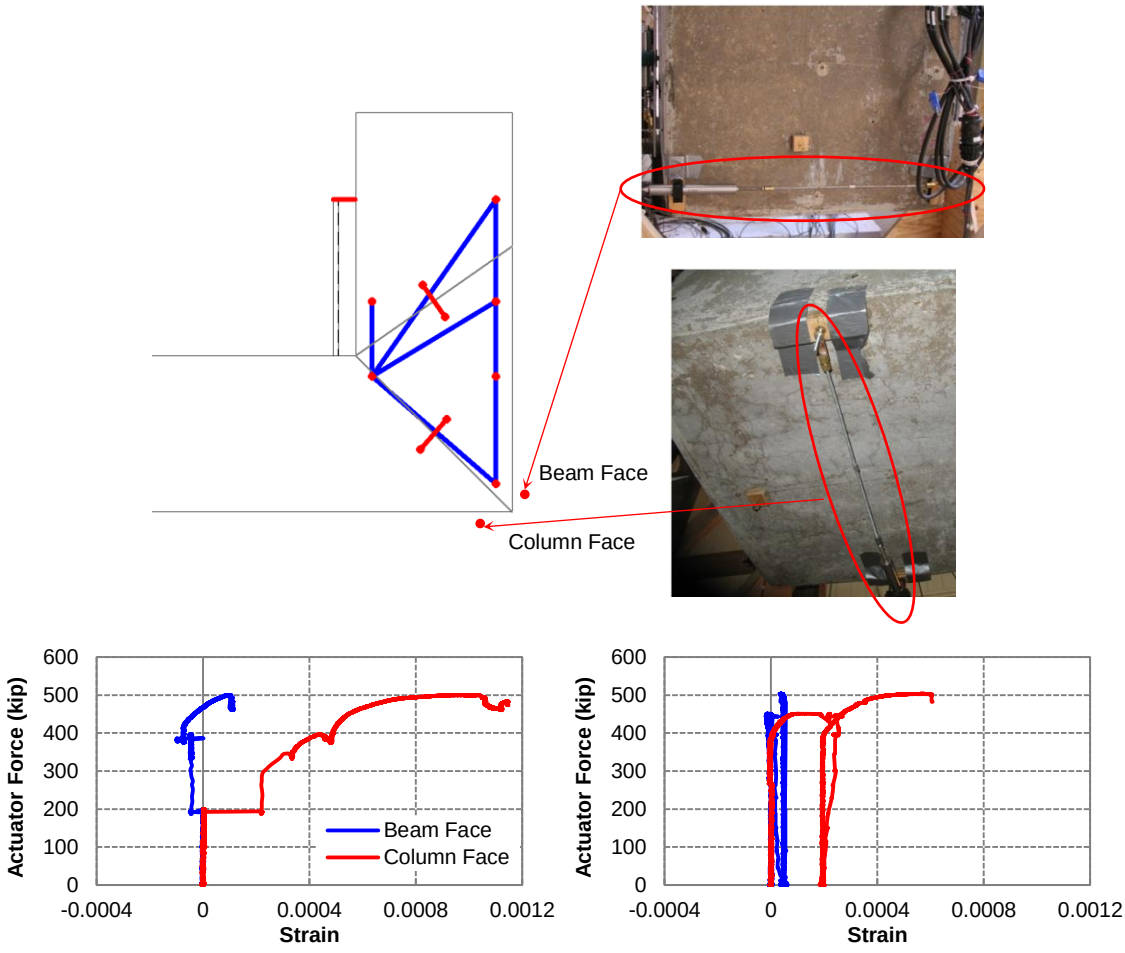

(a) Specimen 2 *(b) Specimen 4*

Figure 5-29 Out-of-Plane Behavior at Outside Corner of Failure Beam-Column Joint

Based on the experimental investigation where three specimens were tested to failure, the key findings are summarized as follows:

- In contrast to the control case (Specimen 1) when loaded to failure, the two exposed specimens with various levels of ASR/DEF (Specimens 2 and 4 after eight months and two years of exposure, respectively) and associated concrete swelling effects led to slightly greater stiffness, strength and ductility.
- Similar ultimate failure mechanisms in the control specimen and the two exposed specimens were observed. These failures may be classified as brittle joint failure within the beam-column joint region. This failure mechanism resulted from the concrete softening of the diagonal STM strut in the beam-column joint, the out-of-plane bursting forces of the joint without adequate confinement reinforcement, the limited capacity and insufficient bonding mechanism in the spliced regions of the overlapping U-shaped steel bars, and the lack of out-of-plane reinforcement along the column face of the beam-column joint region. The joint reinforcement consisted of four sets of overlapping U-shaped steel bars and straight side face longitudinal distribution steel from the beam (skin reinforcement) and column (longitudinal column reinforcement) that were not sufficient to confine the beam-column joint region. The proposed additional U-shaped reinforcing steel bars in the joint region would have helped better confine the joint region and provide additional shear resistance in the beam direction.
- Some corrosion of the reinforcing steel bars was observed in Specimen 4 which had two years of field exposure. Although in this case the deterioration from

ASR/DEF and corrosion did not appear to impair the structural performance in terms of structural performance, it is unknown whether more severe ASR/DEF deterioration and additional steel corrosion as a by-product of the ASR/DEF-induced cracking would affect the structural capacity over time. It is expected that corrosion of reinforcing steel may become significantly worse over time and raise concerns of serviceability and durability of ASR/DEF affected structures.

CHAPTER VI

ANALYTICAL PROGRAM — SECTIONAL ANALYSIS AND STRUT-AND-TIE MODELING

6.1 OVERVIEW

The strength of D-regions in reinforced concrete structures can be determined using various analytical techniques. These techniques are sometimes adopted by design codes and often have slightly different design criteria. This chapter presents the sectional analysis as per ACI 318-08 (2008) and AASHTO LRFD (2010), and the strut-and-tie modeling (STM) based on the provisions in ACI 318-08 (2008), AASHTO LRFD (2010) and the recommendations proposed by Birrcher et al. (2009) to evaluate the ultimate strength of the specimens in the experimental program.

6.2 EXPERIMENTAL SPECIMEN APPLICATION

6.2.1 Sectional Analysis

Sectional analysis of the experimental specimens includes the determination of the flexural and shear capacities based on the ACI 318-08 (2008) and AASHTO LRFD (2010). For computing the ultimate loading capability of the specimen for a given ultimate flexural capacity, the flexural capacity was divided by an assumed lever arm based on the critical section for flexure. For the shear capacity, the provisions in both ACI 318-08 (2008) and AASHTO LRFD (2010) were used. Figures 5-2 and 5-3 show the test setup in the experimental program where loading points were located at a distance of 3 feet (0.91 m) from the inside column face. For all analyses, the yield

strength of the reinforcement, f_y, was taken as 65 ksi (448 MPa) based on tensile coupon testing as discussed in Section 3.3. The compressive strength of the concrete, $f_c^{'}$, was taken as 5.4, 5.6, and 4.0 ksi (37.2, 38.6, and 27.6 MPa) for Specimens 1, 2, and 4, respectively, based on compression cylinder testing as discussed in Section 5.2.

Table 6-1 summarizes the sectional analysis and strut-and-tie modeling results, however the STM approach is discussed in the next section. The nominal flexural moment M_n of the singly and doubly reinforced beam sections was calculated as per Eqs. (2-1) and (2-4), respectively. The inside column face and one quarter of section depth from the inside column face were assumed as the critical sections. Thus, the lever arm from the loading point to the critical section *L* was 36 inches (0.91 m) and 45 inches (1.14 m), respectively. Then, the critical loading to develop flexural capacity for singly and doubly reinforced beam sections of each specimen was determined according to Eq. (2-5), as presented in Table 6-1. The critical loading of the singly and doubly reinforced beam sections in Specimen 1 (the unexposed specimen) was found to be 441 kips (1962 kN) and 445 kips (1979 kN) when 36 inches (0.91 m) was used as the lever arm, respectively. The critical loading of the singly and doubly beam sections in Specimen 2 was found to be 442 kips (1966 kN) and 446 kips (1984 kN) when the same lever arm was used, respectively. For Specimen 4, 433 kips (1926 kN) and 438 kips (1948 kN) was the critical loading for the singly and doubly reinforced beam sections when the same lever arm was used, respectively. It was found that when 36 inches was used as the lever arm, flexure analysis yielded relatively accurate results in terms of the peak experimental load, ranging from 86 to 94% of the experimental results.

Table 6-1 Sectional Analysis and Strut-and-Tie Modeling Results

Specimen				**Specimen 1**		**Specimen 2**		**Specimen 4**	
Experimental Peak Load				474 kips (2108 kN)		500 kips (2224 kN)		503 kips (2237 kN)	
Analysis Method				**Analysis Results [Analysis/Experiment Ratio]**					
Bent Reinforcement				*Singly*	*Doubly*	*Singly*	*Doubly*	*Singly*	*Doubly*
Flexure	M_n	kip-ft (kN-m)		1324 (1795)	1335 (1810)	1327 (1799)	1338 (1814)	1299 (1761)	1313 (1780)
	$\frac{M_n}{L}$	$L = 36"$	kips (kN)	441 (1962) [0.93]	445 (1979) [0.94]	442 (1966) [0.88]	446 (1984) [0.89]	433 (1926) [0.86]	438 (1948) [0.87]
		$L = 45"$		353 (1570) [0.74]	356 (1584) [0.75]	353 (1570) [0.71]	357 (1588) [0.71]	346 (1539) [0.69]	350 (1557) [0.70]
Shear	V_n	ACI 318	kips (kN)	309 (1375) [0.65]		312 (1388) [0.62]		293 (1303) [0.58]	
		AASHTO LRFD		358 (1592) [0.76]	357 (1588) [0.75]	361 (1606) [0.72]	360 (1601) [0.72]	339 (1508) [0.67]	339 (1508) [0.67]
STM	P_n	ACI 318	kips (kN)	210 (934) [0.44]		218 (970) [0.44]		154 (685) [0.31]	
		AASHTO LRFD		183 (814) [0.39]		189 (841) [0.38]		135 (601) [0.27]	
		Birrcher et al.		190 (845) [0.40]		194 (863) [0.39]		157 (698) [0.31]	

The shear strength V_n of the experimental specimen was determined based on the provisions of ACI 318-08 (2008) and AASHTO LRFD (2010) as per Eqs. (2-7) and (2-10), respectively. For Specimen 1, the shear strength was found to be 309 kips (1375 kN) based on ACI 318-08 (2008), while 358 kips (1592 kN) and 357 kips (1588 kN) were for the singly and doubly reinforced beams according to the AASHTO LRFD (2010), respectively. For Specimen 2, 312 kips (1388 kN) was found to be the shear strength based on ACI 318-08 (2008), while 361 kips (1606 kN) and 360 kips (1601 kN) were for the singly and doubly reinforced beams as per the AASHTO LRFD (2010). For Specimen 4, 293 kips (1303 kN) was obtained to be the shear strength according to the ACI 318-08, while 339 kips (1508 kN) was for both singly and doubly beams based on the AASHTO LRFD (2010). This analysis approach based on shear strength of the beam sections yielded conservative results ranging from 58 to 76% of the peak experimental load.

6.2.2 Strut-and-Tie Modeling

Figure 6-1 shows the strut-and-tie truss model developed for the specimen in the experimental program and the corresponding nodal geometries. The crack angle of the strut in the beam-column joint ϕ was assumed as 45˚, and that in the beam region θ was calculated according to Eq. (2-17), as specified in the provisions of the AASHTO LRFD (2010). The width of the back face of the CTT and CCT nodes was assumed to be two times the distance from the tension face to the centroid of the tension reinforcement, which was 5.5 inches (0.14 m). The width of the strut-to-node interface of the CTT

node, W_{CTT}^{j}, was based on the bar bend radius at the centerline of the tension reinforcing steel bars (typically 3.5 inches [89 mm] for #8 reinforcing steel bars) (Figure 6-1b). The width of the bottom face of the CCC node, W_{CCC}^{c}, was equal to the depth of compression zone of the column region as determined through Eq. (2-2). This width can be proportioned based on the equilibrium of the forces in the struts that intersected at the CCC node, as follows:

$$W_{CCC}^{c1} = W_{CCC}^{c} \times \frac{\tan\theta}{\tan\theta + \tan\phi} \tag{6-1}$$

$$W_{CCC}^{c2} = W_{CCC}^{c} \times \frac{\tan\phi}{\tan\theta + \tan\phi} \tag{6-2}$$

The height of the CCC node H_{CCC} was assumed to be the depth of the compression zone of the beam region which was defined by Eq. (2-2). Then, the width of the strut-to-node interface from the strut in the beam-column joint W_{CCC}^{j} and that in the beam region W_{CCC}^{b}, can be defined based on the geometry of the CCC node, as follows:

$$W_{CCC}^{b} = \sqrt{H_{CCC}{}^{2} + W_{CCC}^{c1\ 2}} \times \cos\left(\theta - \varphi_1\right) \tag{6-3}$$

$$W_{CCC}^{j} = \sqrt{H_{CCC}{}^{2} + W_{CCC}^{c2\ 2}} \times \cos\left(\phi - \varphi_2\right) \tag{6-4}$$

where

$$\varphi_1 = \tan^{-1}\left(\frac{W_{CCC}^{c1}}{H_{CCC}}\right) \tag{6-5}$$

$$\varphi_2 = \tan^{-1}\left(\frac{W_{CCC}^{c2}}{H_{CCC}}\right) \tag{6-6}$$

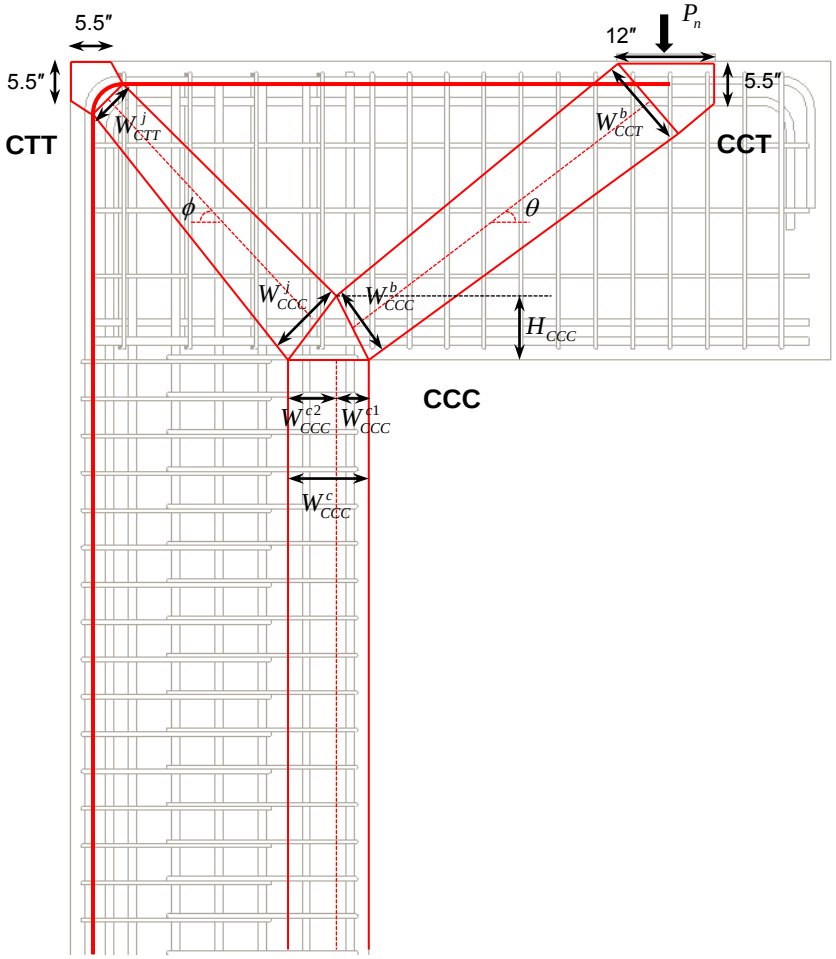

(a) Strut-and-Tie Model

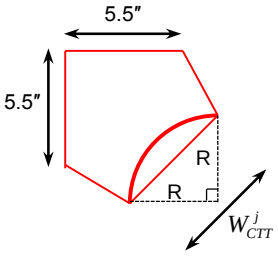

(b) CTT Node

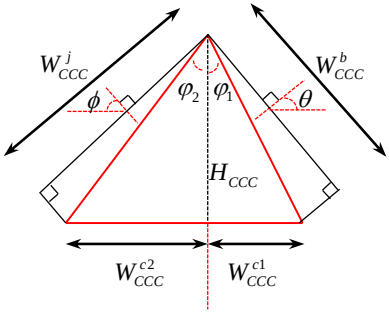

(c) CCC Node

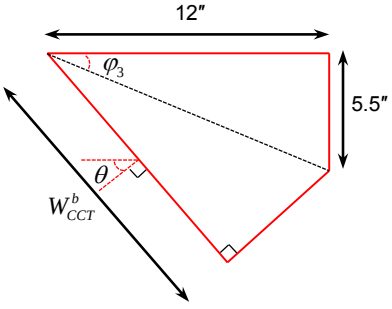

(d) CCT Node

Figure 6-1 Strut-and-Tie Model and Nodal Geometries

The width of the bearing face of the CCT node was determined to be the width of the bearing plate, that is, 12 inches (0.30 m). Then, the width of the strut-to-node interface of the CCT node, W_{CCT}^{b}, can be defined based on the geometry of the CCT node, as follows:

$$W_{CCT}^{b} = \sqrt{5.5^2 + 12^2} \times \cos\left(90° - \theta - \varphi_3\right) \tag{6-7}$$

where

$$\varphi_3 = \tan^{-1}\left(\frac{5.5}{12}\right) = 24.6° \tag{6-8}$$

The forces in the ties and struts can be determined based on the geometry of the truss model when subjected to a given external load P_n. The efficiency factor of each type of node based on the provisions of ACI 318-08 (2008) and AASHTO LRFD (2010) plus the recommendation of Birrcher et al. (2009) was discussed in Chapter II and summarized in Tables 2-3, 2-4 and 2-5. Note that the effective compressive strength of a strut was presented as the efficiency of the strut-to-node interface in a node intersected by such strut. That is, the strength of a strut was determined at the strut-to-node interface since the critical cross-sectional area of a strut coincided at such interface. Thus, only the nominal strength of the nodes in a given truss model was considered in the analysis.

The effective strength of each node with respect to different standards can be calculated based on Eq. (2-26). Table 6-2 summarized the applied external load, P_n, which developed the capacity of each node and the corresponding critical nodal face for the given STM truss model. The critical nodal face for each specimen was then found to

be the strut-to-node interface of the CTT node before the ties reached the yield strength of the reinforcing steel. The applied external load to yield the ties was found to be about 370 kips (1646 kN) for each specimen.

Table 6-2 External Load to Develop Capacity of Node and Corresponding Critical Nodal Face in STM Approach

Specimen		Specimen 1		Specimen 2		Specimen 4	
Analysis Standard	Node Type	External Load kips (kN)	Critical Nodal Face	External Load kips (kN)	Critical Nodal Face	External Load kips (kN)	Critical Nodal Face
ACI 318	CTT	210* (934)	Strut-Node Interface	218* (970)	Strut-Node Interface	154* (685)	Strut-Node Interface
	CCC	291 (1294)	Strut-Node Interface	297 (1321)	Strut-Node Interface	251 (1117)	Strut-Node Interface
	CCT	350 (1557)	Back Face	363 (1615)	Back Face	258 (1148)	Back Face
AASHTO LRFD	CTT	183* (814)	Strut-Node Interface	189* (841)	Strut-Node Interface	135* (601)	Strut-Node Interface
	CCC	363 (1615)	Bottom Face	371 (1650)	Bottom Face	303 (1348)	Bottom Face
	CCT	361 (1606)	Strut-Node Interface	374 (1664)	Strut-Node Interface	266 (1183)	Strut-Node Interface
Birrcher et al.	CTT	190* (845)	Strut-Node Interface	194* (863)	Strut-Node Interface	157* (698)	Strut-Node Interface
	CCC	264 (1174)	Strut-Node Interface	264 (1174)	Strut-Node Interface	255 (1134)	Strut-Node Interface
	CCT	360 (1601)	Back Face	374 (1664)	Back Face	265 (1179)	Back Face

* Critical loading was found to be at the strut-to-node interface of CTT node for each specimen.

6.3 DISCUSSION

For the experimental specimens, the singly reinforced bent cap had two #8 reinforcing steel bars on the compression side for construction purposes (typical in cantilevered bents), and the doubly reinforced bent cap (typical in straddle bents) in the other D-region had ten #8 reinforcing steel bars that served as compression steel. The amount of reinforcing steel on the compression side and the determination of the critical sections for flexure should be taken into account for the critical loading to develop the flexure capacity of the sections on both bent caps. The flexure capacities of the singly and doubly reinforced bent caps slightly differed from each other because of the different amount of steel bars on the compression side. Additionally, since the compressive strength of the concrete for each specimen was different, the flexure capacities of the bent caps were similar and had minor differences between the specimens. The critical loading to develop the flexure capacities of the specimens ranged from 433 kips (1926 kN) to 446 kips (1984 kN) when 36 inches (0.91 m) was used for the lever arm and varied from 346 kips (1539 kN) to 357 kips (1588 kN) when 45 inches (1.14 m) was used. The ratios of the analytical results to the experimental results ranged from 0.86 to 0.94 when 36 inches (0.91 m) was used, while those ranged from 0.69 to 0.65 when 45 inches (1.14 m) was used. Although this indicated flexure analysis yielded relatively accurate predictions in terms of the peak experimental load of the specimen when 36 inches (0.91 m) was used as the lever arm, this approach, which was based on beam theory, completely missed the joint failure mechanism in the experimental specimens of this research.

The shear capacities of the specimens based on ACI 318-08 (2008) were not affected by the amount of compression steel and ranged from 293 kips (1303 kN) to 312 kips (1388 kN) due to the different concrete compressive strengths of each specimen. The ratios of analytical results to the experimental results were within the range of 0.58 to 0.65. As discussed in Section 2.4.1, a different provision from the AASHTO LRFD (2010) was used for the sectional shear capacity, which led to minor differences between singly and doubly reinforced beam sections. The shear capacities based on the AASHTO LRFD (2010) varied from 339 kips (1508 kN) to 361 kips (1606 kN), and the ratios of these results to the experimental results were from 0.67 to 0.76. Note that the ASR/DEF effects were not considered in the present codes for sectional analysis. Moreover, sectional analysis may not be valid in D-regions such that the STM approach should be conducted for the experimental specimens in this research.

In STM approach, the CTT node was found to be the critical node and the strut-to-node interface of such node was the critical face for each specimen. That is, the critical region was the end of CTT node of the strut in the beam-column joint. This may indicate the strut failure near the CTT node once the strut-to-node interface loses the support for the forces in such strut, leading to a joint failure. However, STM significantly underestimated the ultimate load for each specimen. The critical loading of the truss model developed for the specimens in the experimental program with respect to the standards of the present code provisions and the recommendations from previous study ranged from 183 kips (814 kN) to 210 kips (934 kN) for Specimen 1. The critical loading for Specimen 2 ranged from 189 kips (841 kN) to 218 kips (970 kN) and that for

Specimen 4 varied from 135 kips (601 kN) to 157 kips (698 kN). Note that the effective strength of the nodes in STM is attributed to the compressive strength of the concrete. Thus, the critical loading for Specimen 4 ($f_c^{'} = 4$ ksi [27.6 MPa]) was found to be less than Specimens 1 ($f_c^{'} = 5.4$ ksi [37.2 MPa]) and 2 ($f_c^{'} = 5.6$ ksi [38.6 MPa]). The ratios of the analytical results to the experimental results of all specimens were from 0.27 to 0.44, indicating that STM significantly underestimated the ultimate load of the experimental specimen. In addition, the ASR/DEF effects were not taken into account in this STM approach.

It can then be concluded that for each specimen, the sectional analysis (except flexure analysis when 36 inches was used as the lever arm) and STM approach underestimated the ultimate strength of the specimens and yielded conservative results compared to the peak experimental load from the structural load tests. Figure 6-2 also compares the sectional analysis and STM results with the experimental results for each specimen, showing conservative results from both sectional analysis and STM approach.

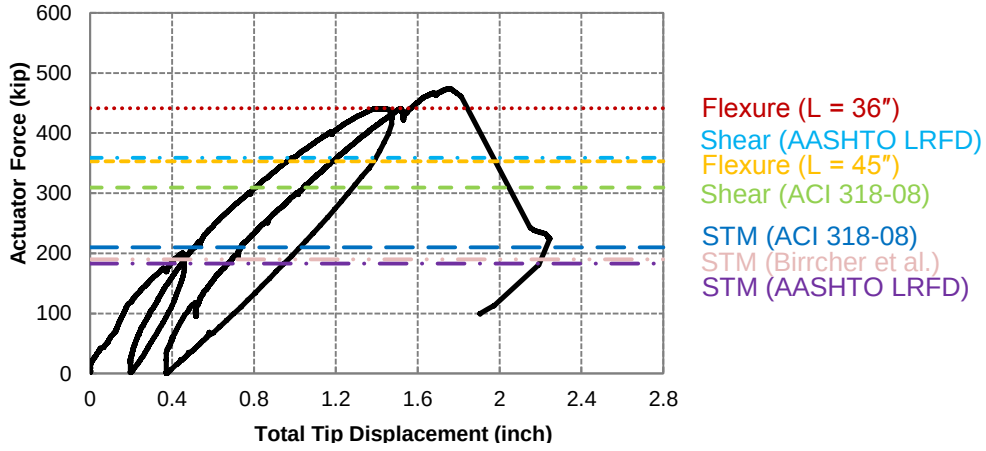

(a) Specimen 1

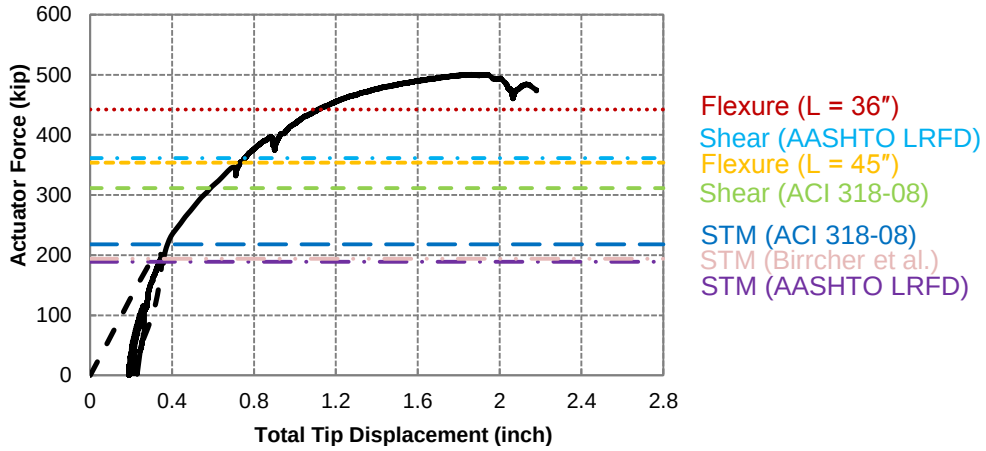

(b) Specimen 2

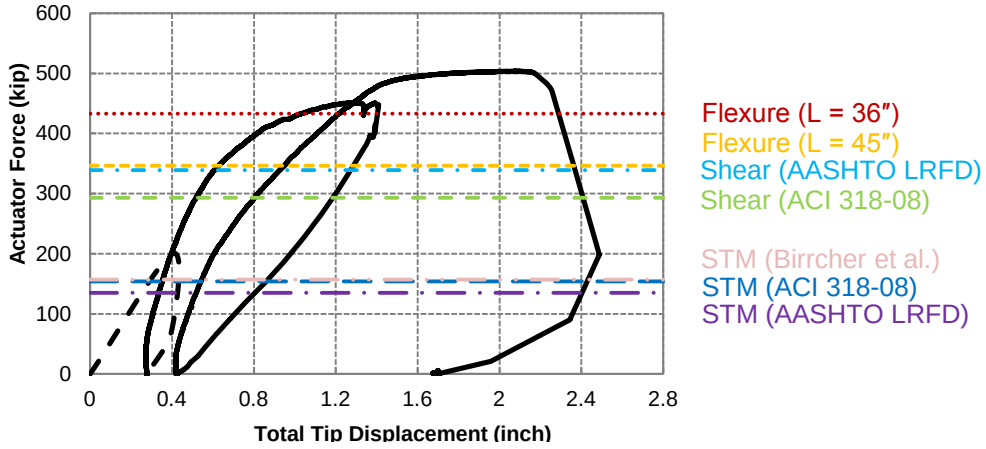

(c) Specimen 4

Figure 6-2 Comparisons of Sectional Analysis, Strut-and-Tie Modeling, and Experimental Results

6.4 SUMMARY

In summary, sectional analysis and STM approach were conducted to assess the ultimate strength of the D-regions for the specimens in the experimental program. Based on this analytical investigation, the key findings were summarized as follows:

- The ratios of the flexure sectional analysis to the peak experimental loads for all specimens that were tested to failure varied from 0.86 to 0.94 when the inside column face was assumed to be the critical section, which were accurate compared to the peak experimental loads, and conservatively ranged from 0.69 to 0.75 when one quarter of section depth from the inside column face was taken as the critical section. Although this indicated flexure analysis yielded relatively accurate predictions in terms of the peak experimental load of the specimen when the inside column face was assumed to be the critical section, this approach, which was based on beam theory, completely missed the joint failure mechanism in the experimental specimens of this research.
- The ratios of the shear capacities based on the ACI 318-08 (2008) and AASHTO LRFD (2010) to the peak experimental loads for all specimens that were tested to failure conservatively ranged from 0.58 to 0.76. That is, this analysis approach based on shear strength of the beam sections yielded conservative results.
- The ASR/DEF effects were not considered in the present codes for sectional analysis. Moreover, sectional analysis may not be valid in D-regions such that the STM approach should be conducted for the experimental specimens in this research.

- In STM approach, the critical face was found to be the strut-to-node interface of the CTT node at the outside corner of the beam-column joint. This may indicate the strut failure near the CTT node once the strut-to-node interface loses the support for the forces in such strut, leading to a joint failure. However, STM significantly underestimated the ultimate load for each specimen. The ratios of the critical loading obtained via STM approach to the ultimate peak load for all specimens that were tested to failure varied from 0.27 to 0.44 based on various standards. The analyses according to the provision of the ACI 318-08 (2008) yielded 44, 44 and 31% of the ultimate peak load from the tests of Specimens 1, 2 and 4, respectively. The critical loading from STM approach based on the provision of AASHTO LRFD (2010) was 39, 38 and 27% of the test results for Specimens 1, 2 and 4, respectively. As per the recommendations of Birrcher et al. (2009), the analysis results were 40, 39 and 31% of the ultimate peak load for Specimens 1, 2 and 4, respectively.

CHAPTER VII

ANALYTICAL PROGRAM — NONLINEAR FINITE ELEMENT MODELING

7.1 OVERVIEW

As discussed in Chapter VI, sectional analysis (except flexure analysis when the inside column face was used as the critical section) and strut-and-tie modeling approaches underestimated the strength of the D-region in the experimental specimens compared to ultimate peak load from the experimental results. In addition, these methods only yielded overall strengths and overlooked the force-deformation relations and out-of-plane behavior of the experimental specimens. Moreover, the ASR/DEF effects were not taken into account in such analytical approaches.

This chapter presents a three-dimensional nonlinear finite element analysis (FEA) approach to simulate the overall force-deformation behavior and out-of-plane behavior of the experimental specimens. The effects of varying concrete constitutive models in tension on overall structural performance are compared. Moreover, a method to take into account concrete expansion due to ASR/DEF mechanisms by applying various levels of equivalent thermal expansion within the member's depth is proposed and incorporated into the FEA approach. The comparisons between the analytical results and the experimental results are presented in the later sections.

7.2 STEEL CONSTITUTIVE MODEL

A bi-linear constitutive relation was used to model the reinforcing steel (Figure 7-1), as it is commonly used in the literature on finite element modeling of reinforced

concrete elements. The yield strength of the steel was taken as 65 ksi (448 MPa) based on coupon test results as discussed in Section 3.3, and the elastic modulus, E_s, was taken as 29,000 ksi (200 GPa). A strain hardening modulus, E_{sh}, of 3% of the elastic modulus was used to describe the post-yield behavior of the reinforcing steel.

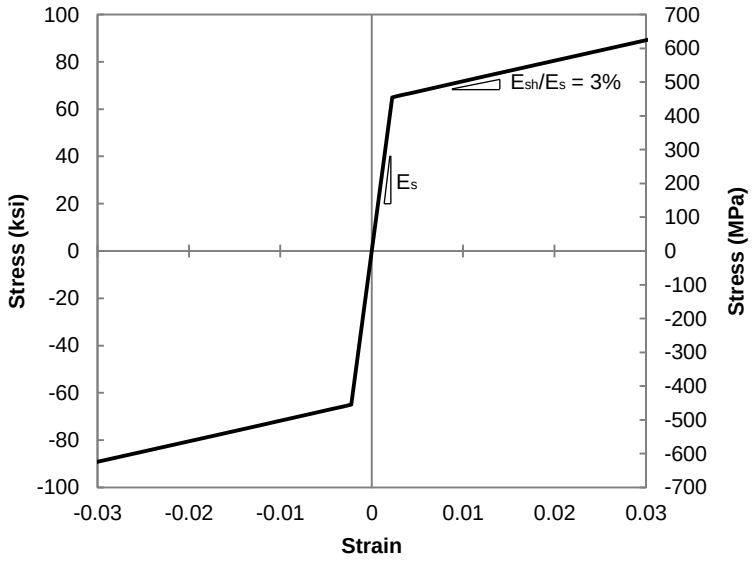

Figure 7-1 Steel Constitutive Relation

7.3 CONCRETE CONSTITUTIVE MODEL

Figure 7-2 shows the constitutive relations of the concrete in compression and tension that were used in the numerical models for each specimen based on the measured compressive strength in cylinders for each specimen that was tested to failure. The Popovics' empirical equation (Eq. [2-27]) was adopted to define the constitutive relation

of concrete in compression. For tension behavior, as discussed in Section 2.4.4, the MCFT takes into account the concrete tensile stresses after cracking due to the reinforcement's ability to transmit tension across the cracks (Eq. [2-33]) (Vecchio and Collins 1986), which is commonly termed tension stiffening. Based on this equation, the modified constitutive relation of concrete in tension proposed by Collins and Mitchell (1987) (Eq. [2-34]) to account for the tension stiffening effect and other relations from the literature were used and compared in the numerical models.

The compressive strength of the concrete, $f_c^{'}$, for each specimen was based on the concrete cylinder test results as summarized in Table 5-2. The elastic modulus of the concrete, E_c, and the tensile strength of the concrete, f_{cr} ($f_t^{'}$), for each specimen were calculated according to the empirical expressions from the provisions of the ACI 318-08 (2008), as follows:

$$E_c = 57,000\sqrt{f_c^{'}\left(psi\right)} \tag{7-1}$$

$$f_{cr} = f_t^{'} = 7.5\lambda\sqrt{f_c^{'}(psi)} \tag{7-2}$$

where $\lambda = 1.0$ for normal weight concrete.

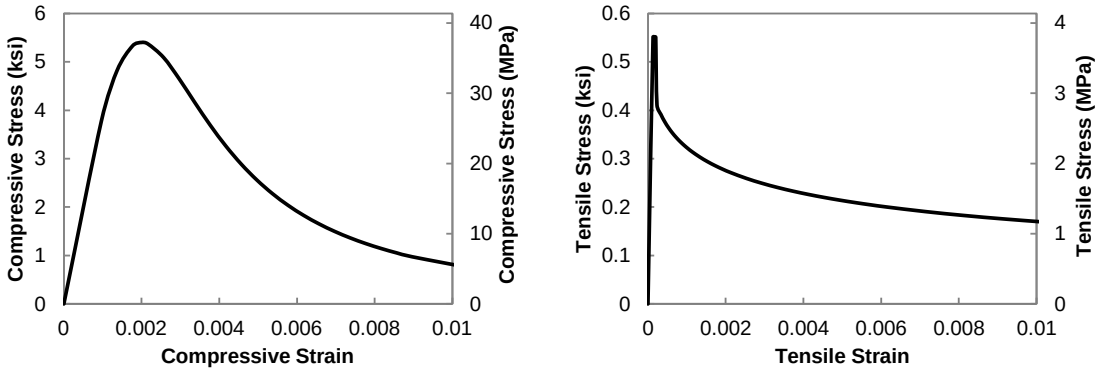

(a) Specimen 1

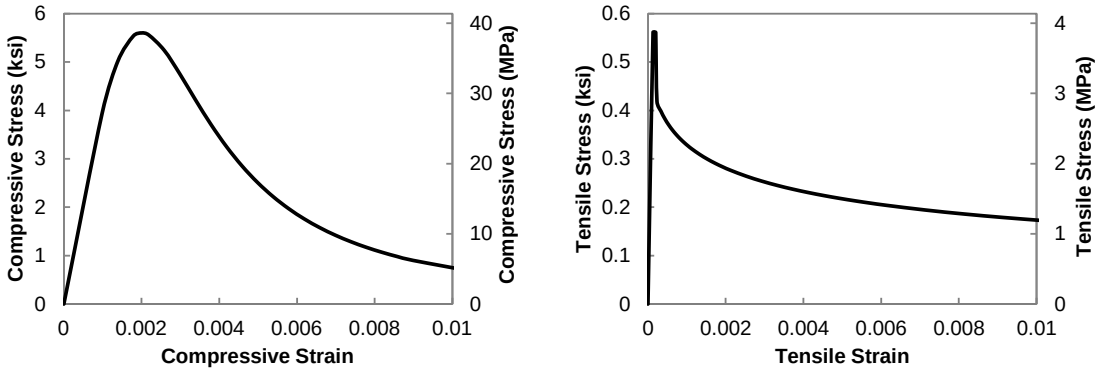

(b) Specimen 2

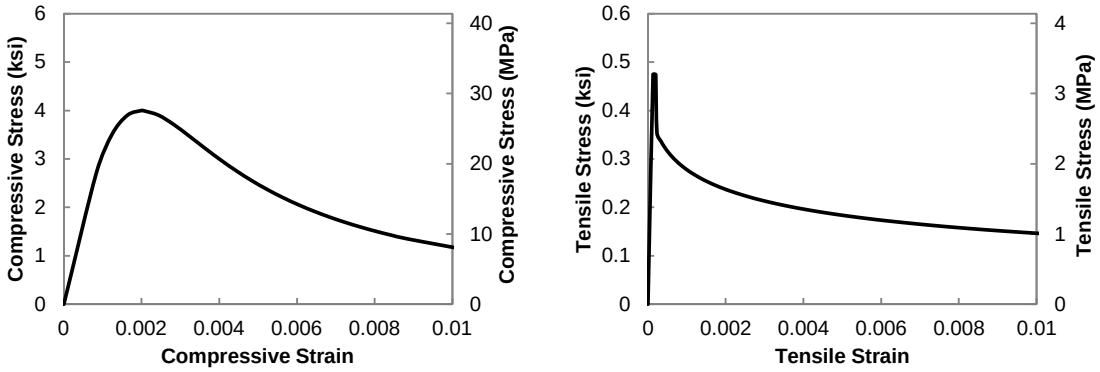

(c) Specimen 4

Figure 7-2 Concrete Constitutive Relations for Each Specimen

As discussed in Section 2.4.4, the available tensile stress-strain relations from literature were compared in the numerical models for Specimen 1. Figure 7-3 depicts the MCFT tension stiffening relation proposed by Vecchio and Collins (1986) (Eq. [2-33]) and the later modified form suggested by Collins and Mitchell (1987) (Eq. [2-34]) along with the equation proposed by Okamura et al. (1985) (Eq. [2-35]) using different powers in the expression, that is, $c = 0.4$ and $c = 0.2$, with respect to the concrete tensile strength for Specimen 1. The differences in the modeling equations are the sudden drop in the available concrete strength after first cracking and also the available concrete strength at strains beyond first cracking. The effects of these tension stress-strain relations on the overall force-deformation behavior are discussed in a later section.

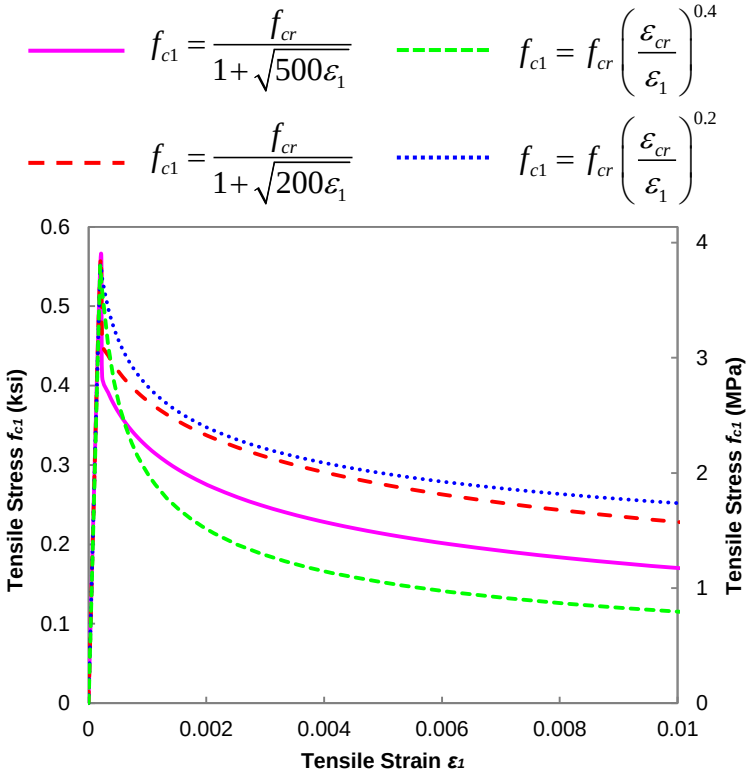

Figure 7-3 Tensile Stress-Strain Relations Adopted in Numerical Models for Specimen 1

7.4 FINITE ELEMENT MODEL FORMULATION

Numerical simulations were conducted using a general purpose finite element analysis commercial package, namely Abaqus 6.8 (2008). As discussed in Section 2.4.4, the heterogeneity nature of concrete makes it challenging to model in 3D applications. However, by applying user-defined constitutive relations of concrete in compression and tension, three built-in features are available to mimic concrete behavior in Abaqus 6.8 (2008): (i) Concrete Smeared Cracking; (ii) Cracking Model for Concrete; and (iii) Concrete Damaged Plasticity. However, each feature has limitations due to the compatibility and feasibility to mimic concrete behavior of a given structure.

The Concrete Smeared Cracking feature allows users to define the constitutive relations by applying stress-strain relations of concrete in compression and tension. However, it is only compatible with Abaqus/Standard solver, which is based on implicit methods in numerical analysis. In general, the implicit methods in numerical analysis find a solution through solving an equation consisting of both current and later state of analysis steps. As discussed in Section 2.4.4, the sudden drop in tensile strength after concrete cracking and the nonlinear behavior near peak compressive strength can cause singularity in the formation of the overall stiffness matrix (Figure 2-3). This complexity nature of concrete can also cause convergence problems in unstable regions, leading to numerical errors in such analysis, particularly when modeling RC structures with complex reinforcement details.

The Cracking Model for Concrete feature, on the other hand, is compatible with Abaqus/Explicit solver and is mainly utilized for structures that are dominated by tensile

cracking. The explicit methods in the numerical analysis derive a later state of the system based on the current state, hence potentially leading to reduction of computational costs and helping mitigate potential convergence problems. However, the compressive behavior of concrete in such a feature is assumed to be within the linear elastic region, that is, no concrete crushing is considered. This assumption can potentially overestimate the overall strength of a RC structure with local compression zones under structural loading, e.g., D-regions in RC structures.

The Concrete Damaged Plasticity feature is compatible with both Abaqus/Standard and Abaqus/Explicit solvers. This feature allows users to define the constitutive relations by applying stress-strain relations of concrete in both compression and tension. In addition, the inelastic behavior of concrete is taken into account via the concepts of isotropic damaged elasticity in both compression and tension to simulate the structural behavior under cyclic loading. Moreover, the concept of the yield surface of concrete based on the experimental results presented by Kupfer et al. (1969) is pre-implemented in this feature to determine the evolution of element strength under simultaneous compression and tension.

Since the objectives of this research is to mimic the overall force-deformation relation and out-of-plane behavior of the experimental specimens, a three-dimensional nonlinear FEA approach was conducted. Due to the complexity of the reinforcement details of the experimental specimen, the Concrete Damaged Plasticity feature was therefore applied to conduct the numerical analyses. However, the constitutive relations of damage elasticity of concrete are ambiguous and the experimental data to quantify

such material properties are limited. In addition, the structural behavior under cyclic loading is uncertain, which is beyond the scope of this analytical research. Thus, only plasticity of concrete in this feature was considered in the numerical analyses and the Abaqus/Explicit was selected to be the solver to avoid numerical errors and to minimize computational effort.

Figure 7-4 depicts the finite element analysis procedure of the experimental specimens. The geometry (mesh and element types), material properties, boundary conditions, and loading conditions are the essential components to construct a finite element model. As discussed in the previous sections, the material properties for steel and concrete were based on expressions from literature with respect to the material strengths of experimental specimens. The details of other components in constructing numerical models are discussed in the following sections. Moreover, a method to take into account ASR/DEF effects is proposed and incorporated into this analysis approach.

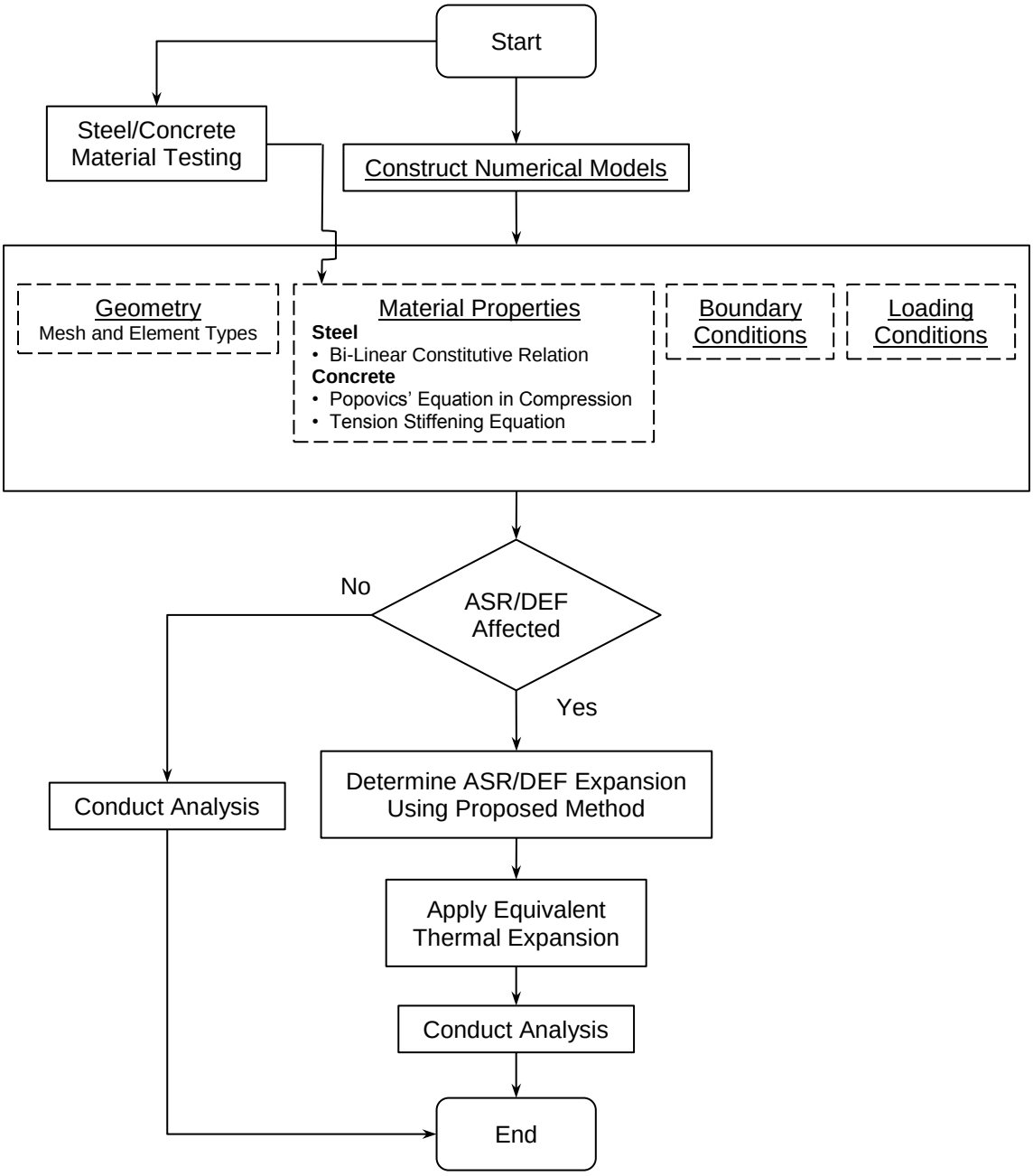

Figure 7-4 Flow Chart for Finite Element Analysis Procedure of Experimental Specimens

7.4.1 Geometry – Mesh and Element Types

The experimental structural performance of the singly and doubly reinforced ends of the bent specimens was found to be nearly identical as discussed in Chapter V. Therefore, to minimize computational costs in FEA approach, only half of the experimental C-shaped specimen was modeled in the analyses as shown in Figure 7-5. This mesh layout consisted of three-dimensional eight-node hex elements with reduced integration (type C3D8R elements), and three-dimensional six-node wedge elements in the STM CCC node region (type C3D6 elements) with a total of 7578 nodes and 6112 elements that represented concrete. This mesh configuration was found to be numerically efficient and demonstrated satisfactory results through a preliminary mesh convergence study. Moreover, this mesh configuration had better interaction with the reinforcement layout as presented in the later section (i.e. minimal stress/strain discontinuity).

As discussed in the previous section, the Concrete Damaged Plasticity feature in Abaqus 6.8 (2008) was selected to model the stress-strain behavior of concrete. This feature requires users to define the dilation angle of the concrete and allows users to assign eccentricity, ratio of initial equi-biaxial compressive yield stress to initial uniaxial compressive stress, and the viscosity parameter of the concrete. According to a previous study by Jankowiak and Łodygowski (2005), the dilation angle of the concrete was defined as 38 degrees. Due to the limited concrete material testing data, the default values for the other parameters pre-defined in Abaqus 6.8 (2008) were used.

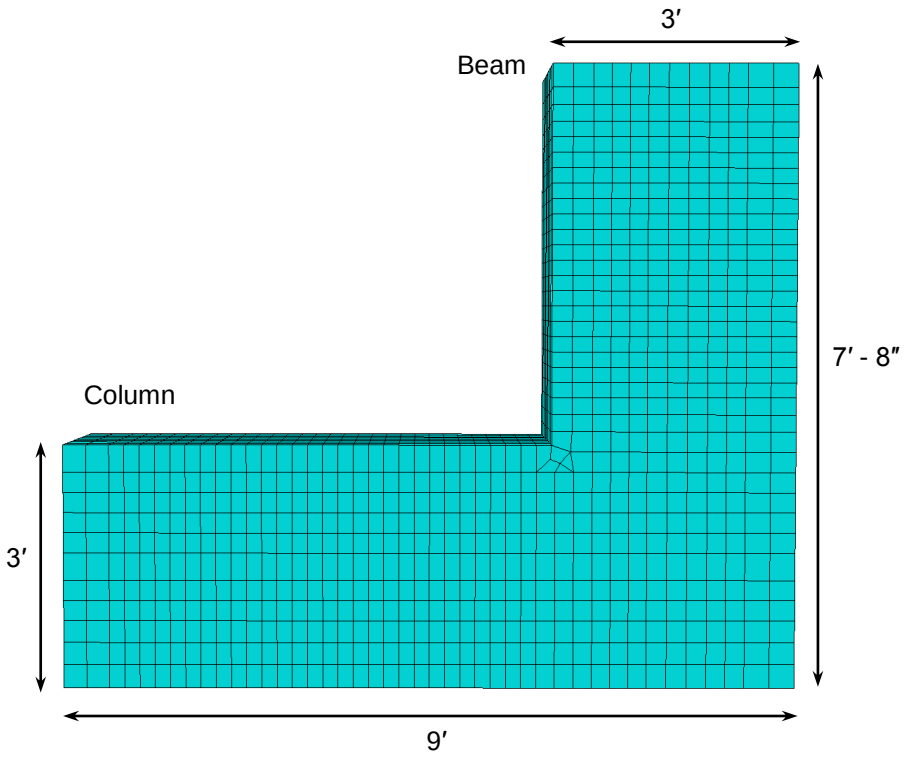

Figure 7-5 Finite Element Mesh of Concrete for Half of Experimental Specimen

Although Abaqus 6.8 (2008) has a built-in feature to account for the contribution of the steel bars, such built-in feature is not sufficient to model the prestressing and confining effects from the reinforcing steel on the concrete due to ASR/DEF expansion when modeling RC structures with intricate reinforcing details. In this built-in feature, the reinforcing steel is treated as a smeared layer that results in overall concrete strengthening and stiffening in a chosen direction. However, the local behavior of reinforcing steel, that is, stress/strain under a certain load, is neglected. Therefore, the finite element mesh for the reinforcing steel was constructed based on the reinforcing details of the specimen in the experimental program (Figure 7-6). This mesh layout consisted of three-dimensional two-node truss elements (type T3D2 elements) with a

total of 9763 nodes and 9722 elements for the singly reinforced specimen end (two #8 compression steel bars), and a total of 10453 nodes and 10410 elements for doubly reinforced specimen end (ten #8 compression steel bars). These truss elements that represented the reinforcing steel were attached to the hex and wedge concrete elements, thereby adopting a bonded condition between the reinforcing steel and the concrete; thus potential for bond-slip effects were neglected.

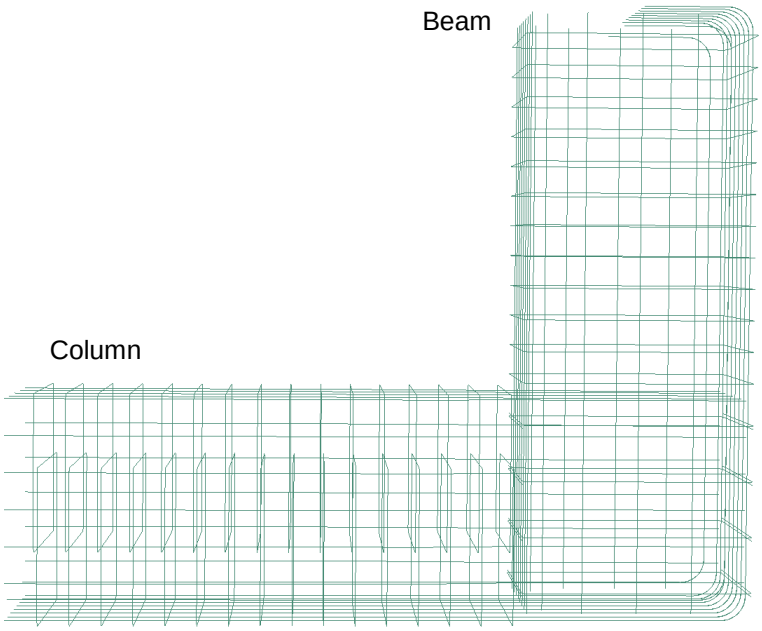

Figure 7-6 Finite Element Mesh of Reinforcing Steel for Half of Experimental Specimen

7.4.2 Boundary Conditions

As shown in Figures 5-2 and 5-3, the specimen was seated externally on two hinge supports located at a distance of 1.5 feet (0.46 m) from the inside beam face in the experimental setup. Thus, the vertical displacements of the nodes at such locations were

similarly constrained in the numerical models (Figure 7-7). Furthermore, the specimen was symmetric with respect to the centerline, that is, the horizontal displacements and the rotation degree of freedoms with respect to the vertical and out-of-plane axes were constrained at the centerline of the specimen.

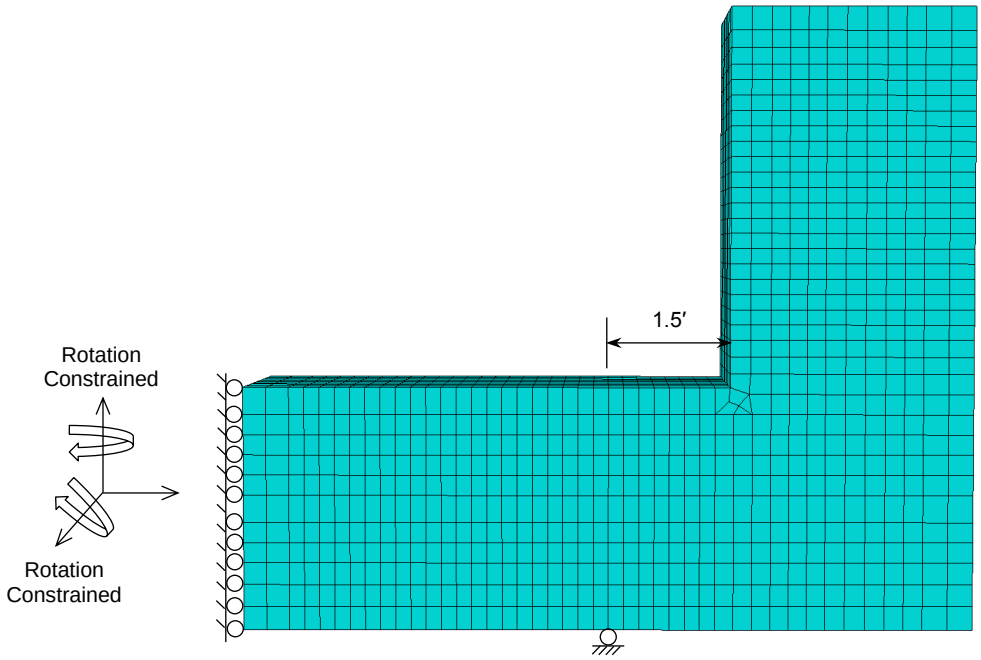

Figure 7-7 Boundary Conditions of Finite Element Model

7.4.3 Loading Conditions

As shown in Figures 5-2 and 5-3, 1 inch (25.4 mm) thick bearing plates were used at the loading points in the structural load testing that had a bearing area of 12 inches by 24 inches (0.30 m by 0.61 m). The loading points were located at a distance of 3 feet (0.91 m) from the inside column face. Thus, a two-dimensional rigid planar shell object was created in the numerical model and used for the loading bearing area (Figure 7-8). A velocity of 0.05 inch/sec (1.27 mm/sec) was applied to the center of the rigid

shell to simulate the actual experimental test setup and loading operated in incremental displacement control. The forces exerted on the rigid shell object were simultaneously recorded in the numerical analyses to provide the external force-deformation relations during loading. These analytical results and comparisons with experimental data are presented in the later sections.

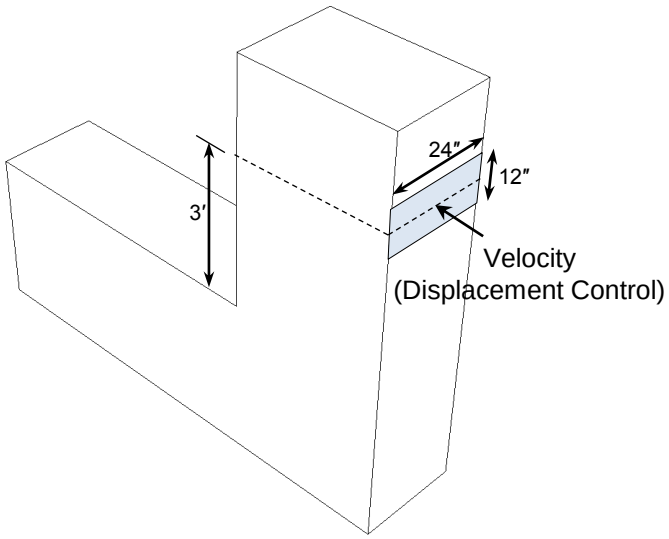

Figure 7-8 Loading Conditions of Finite Element Model

7.5 CONCRETE EXPANSION DUE TO ASR/DEF

A method to take into account concrete expansion due to ASR/DEF was developed and incorporated into the FEA approach. Figure 7-9 summarizes the analysis procedure of the proposed method, which is based on the analysis results of the specimen under in-service loading (prior to the exposure phase) and the exposure phase data from the ASR/DEF affected specimens. The amount of average concrete expansion in the exposed specimens was quantified from surface measurements and internal measurements within the specimens. To mimic these different levels of expansion in the

numerical models, various levels of equivalent thermal expansions were applied to the concrete elements within the depth of the specimen. Moreover, ranges of the average concrete expansion for different levels of concrete distress were proposed according to the core locations and the petrographic analysis results. In addition, an expression to quantify the average concrete expansion over time due to both ASR and DEF effects was proposed based on the previous studies. The details of the proposed method are discussed in the following sections.

7.5.1 Specimen under In-Service Load

As discussed in the previous sections, analyses of the experimental specimens prior to their exposure phase (without ASR/DEF effects) were conducted when the essential components for FEA were developed and defined, that is, the geometry, material properties, boundary conditions, and loading conditions. For the analysis of the specimen under in-service load (200 kips [890 kN]), the material properties of the control specimen (Specimen 1) were used, hence indicating the structural behavior without ASR/DEF effects.

Figures 7-10 and 7-11 show the maximum principal stress distributions of the numerical model under in-service load (200 kips [890 kN]) in the concrete cover region and in the middle of specimen width, respectively. From these analyses, it was found that the concrete region within about one-half of the member depth from the tension-most side (except the end of the beam region and the outside corner of the beam-column joint) experienced more than 25% of the concrete tensile strength (0.55 ksi [3.8 MPa]) in tension.

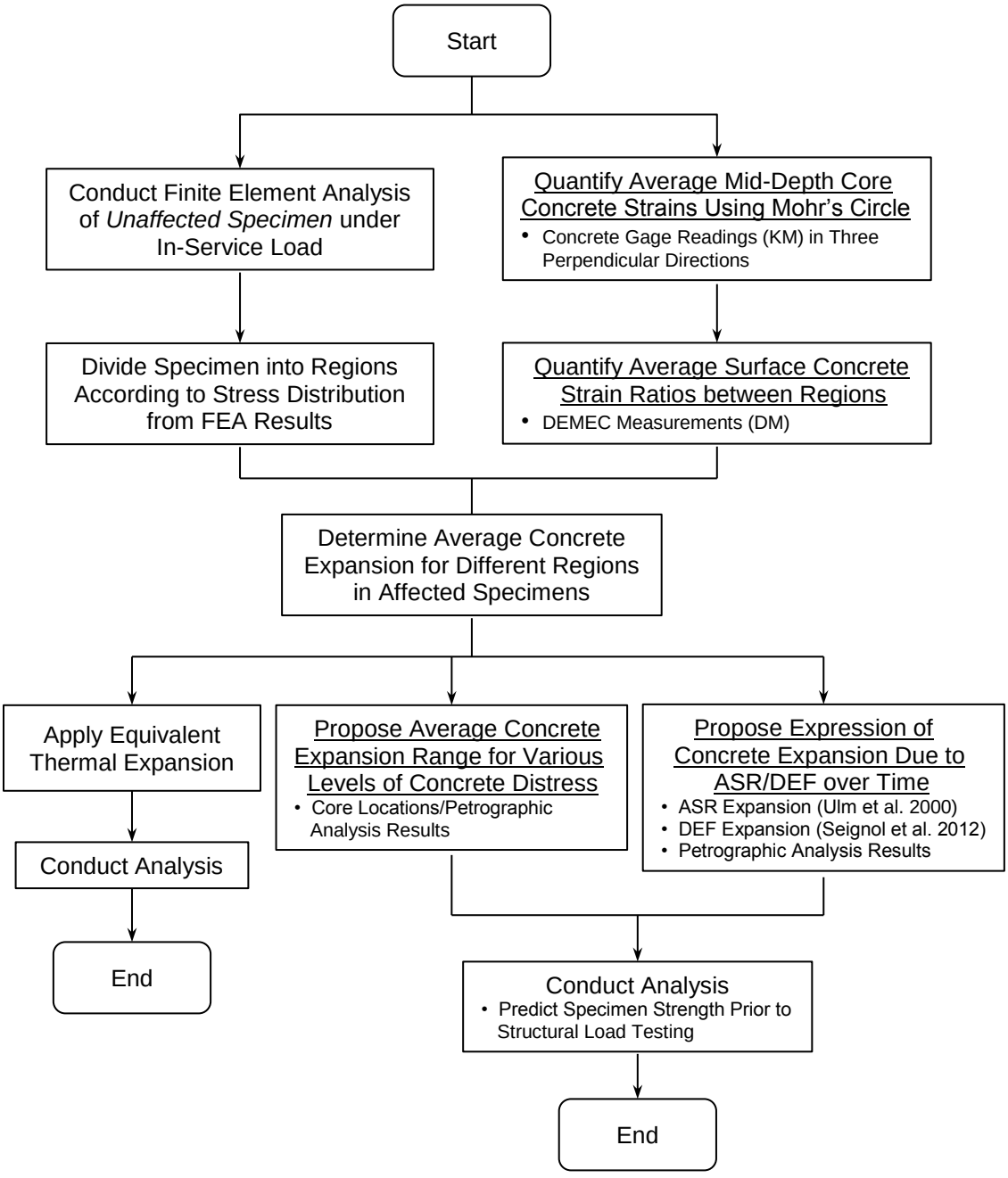

Figure 7-9 Proposed Method to Simulate ASR/DEF Expansion Effects in FEA

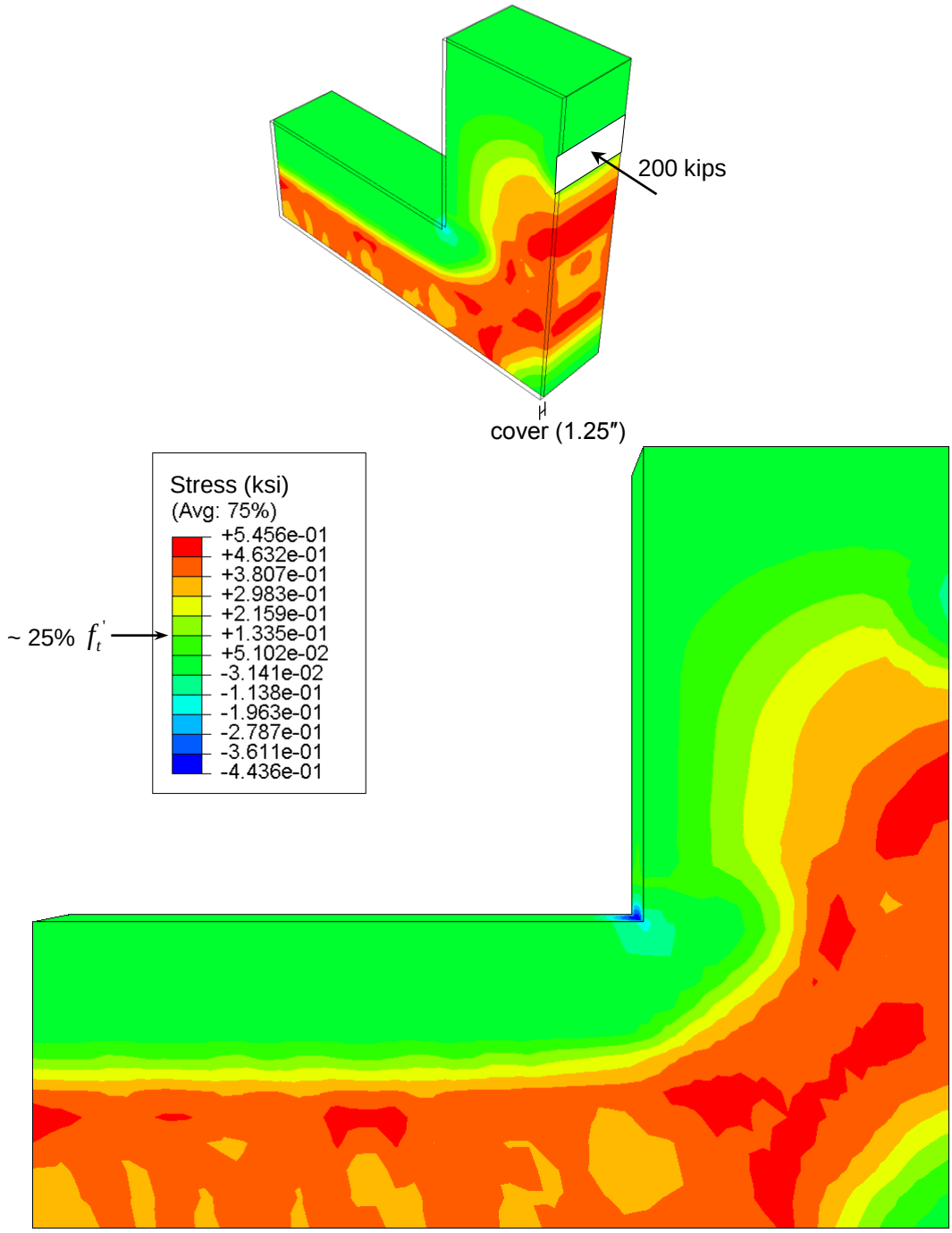

Figure 7-10 Maximum Principal Stress Distribution under In-Service Load in Concrete Cover Region

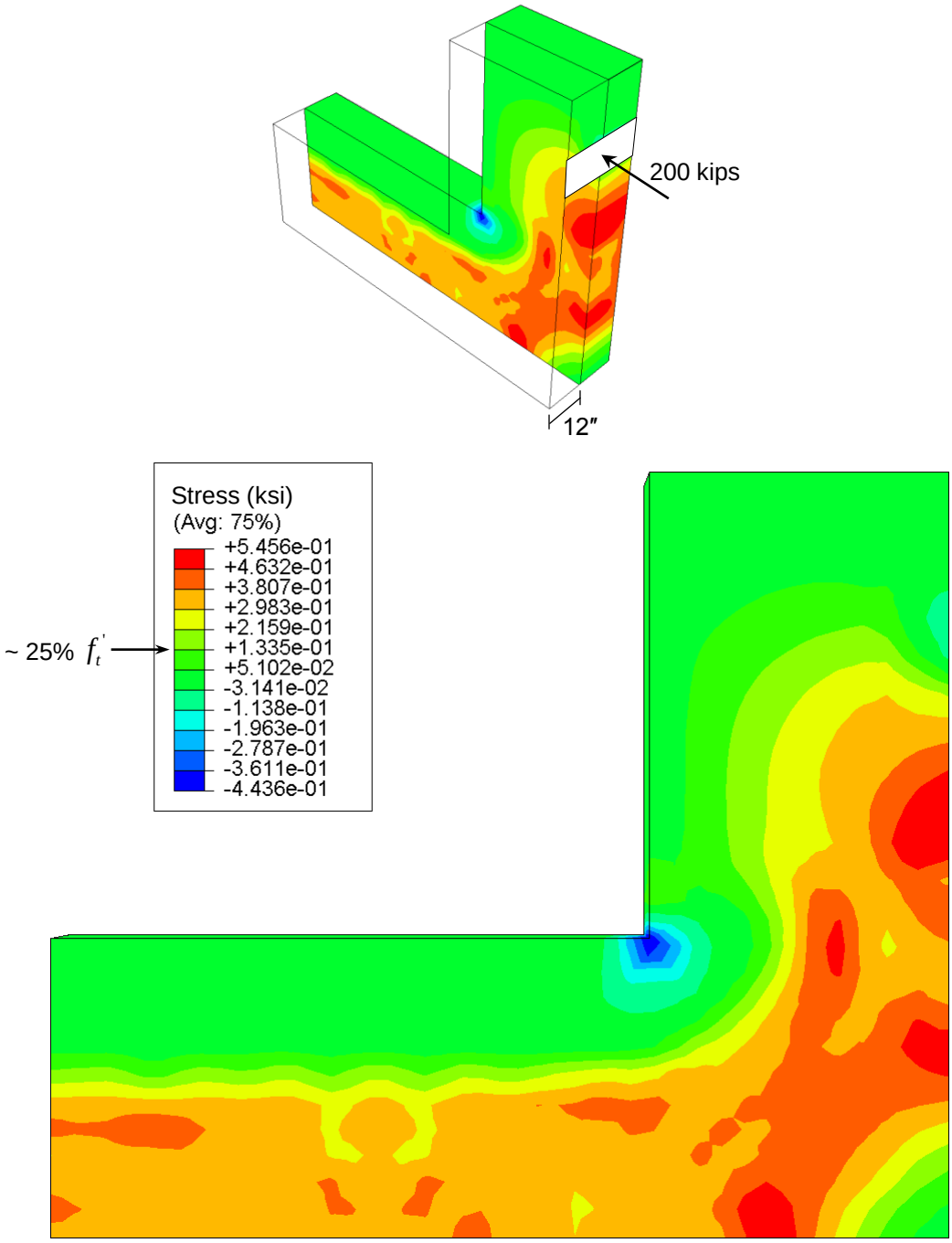

Figure 7-11 Maximum Principal Stress Distribution under In-Service Load in Middle of Specimen Width

Figures 7-12 and 7-13 present the minimum principal stress distributions of the numerical model under the same in-service load (200 kips [890 kN]) in the concrete cover region and the region in the middle of the specimen width, respectively. The results show that the concrete within approximately one-quarter of the member depth from the compression-most side in the column regions and the regions near the STM CCC node experienced more than 25% of the concrete compressive strength (5.4 ksi [37 MPa]) in compression under the in-service loading. These locations were used to characterize the interface of different regions for applying various levels of concrete expansion due to ASR/DEF in the later analyses.

As discussed in Chapter IV, the existing cracking on the tension side of the specimen due to the prestress load to simulate in-service load essentially permitted more water ingress, which led to significant ASR/DEF expansion and excessive cracking on the tension side. Based on the abovementioned observations from the analysis results, the numerical models were then divided into three characterized regions to apply different levels of expansion, hence mimicking the different levels of concrete expansion in ASR/DEF affected specimens (Figure 7-14). To minimize the stress discontinuities, which may lead to numerical errors, at the interfaces of each region, only three regions within the specimen were characterized to mimic concrete expansion due to ASR/DEF (Figure 7-14). The method to derive the amount of concrete expansion for each region is discussed in the following sections.

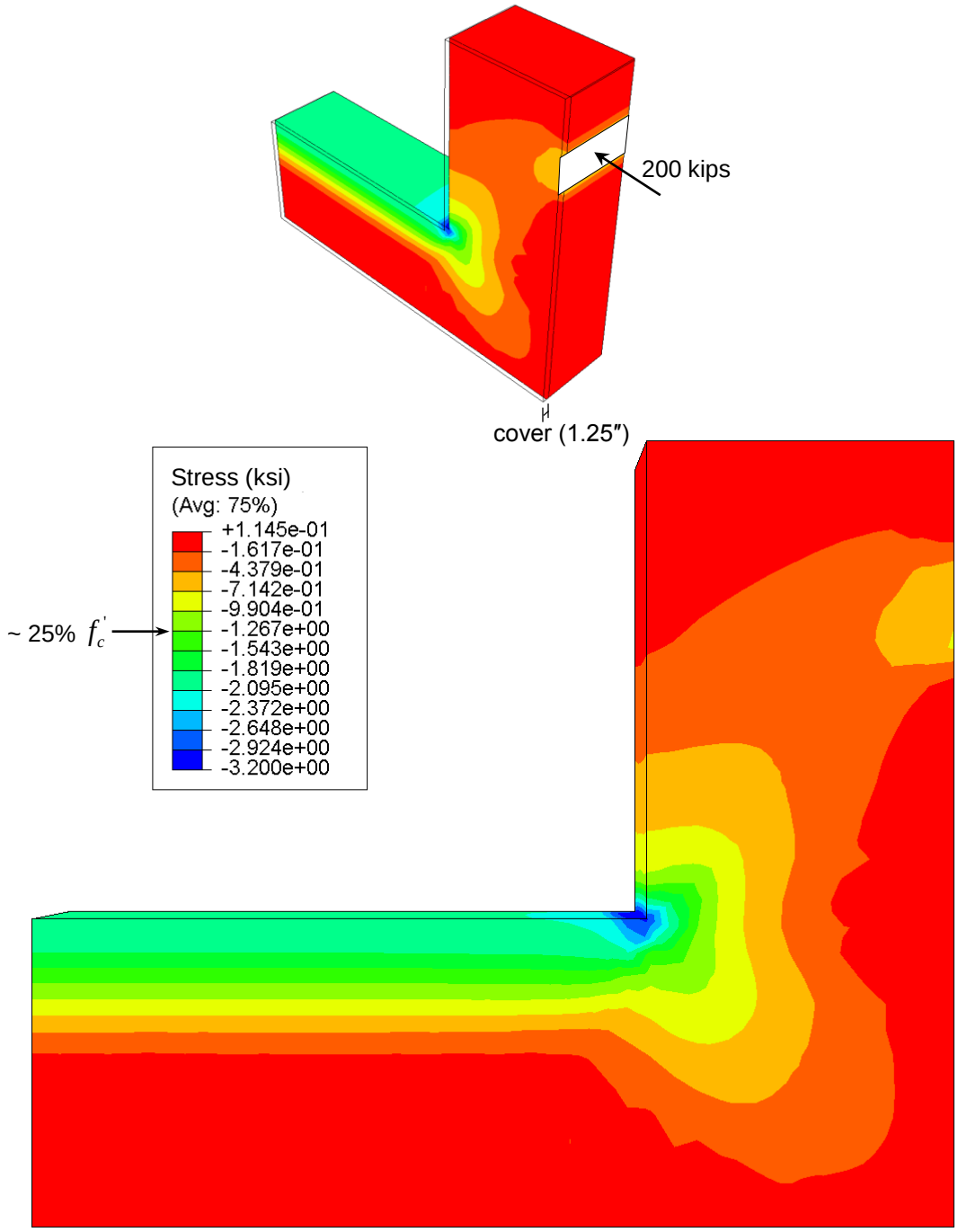

Figure 7-12 Minimum Principal Stress Distribution under In-Service Load in Concrete Cover region

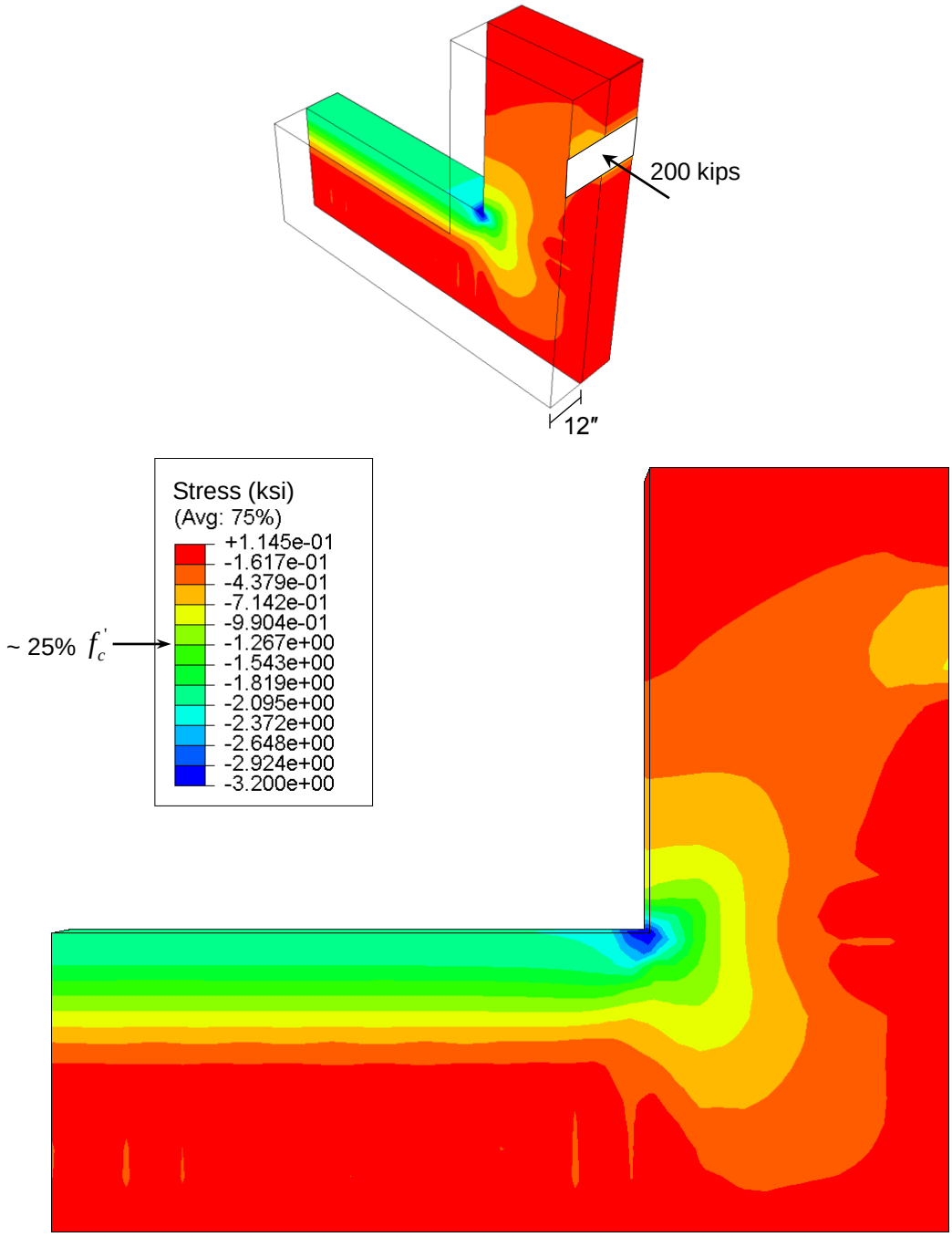

Figure 7-13 Minimum Principal Stress Distribution under In-Service Load in Middle of Specimen Width

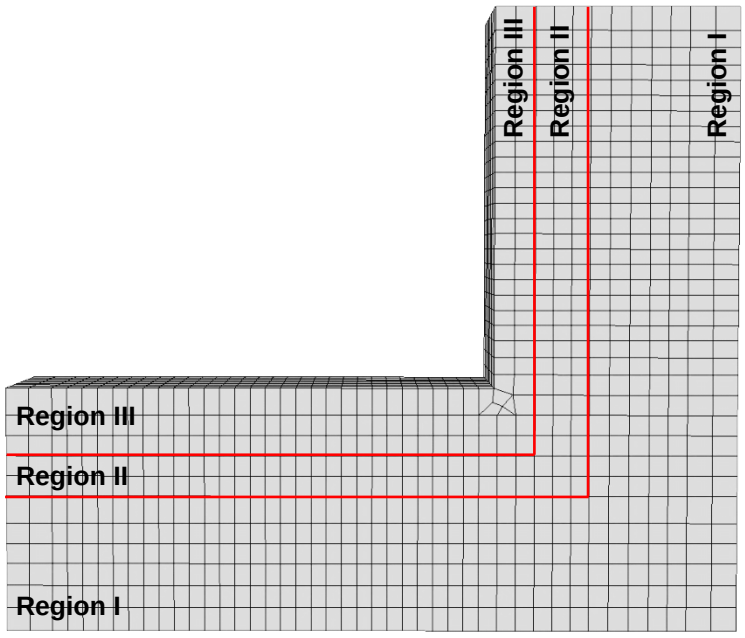

Figure 7-14 Characterized Regions for Applying Various Levels of Concrete Expansion Due to ASR/DEF

7.5.2 Average Volumetric Concrete Expansion

As discussed in Chapter IV, specimens experienced significant expansion in the in-plane and out-of-plane directions during their exposure phase, according to the surface concrete strain measurements (DMs) and mid-depth core concrete strain measurements (KMs) over time. Moreover, from observations of the mid-depth core concrete strains (KMs), greater amounts of expansion were observed in the directions perpendicular to cracks rather than in the directions parallel to cracks. This anisotropic nature of concrete expansion due to the ASR/DEF effects is difficult to model in numerical analyses. Therefore, to account for local ASR/DEF effects and to simplify the numerical models, the mid-depth core concrete strain increments over time in the three

perpendicular directions of the STM struts (KMs) were plotted on Mohr's circle to obtain the average volumetric concrete expansion due to ASR/DEF, $\varepsilon_{ASR/DEF}$, for later numerical analyses (Figure 7-15).

Table 7-1 summarizes the average strain increments in the three perpendicular directions of the mid-depth core concrete at STM struts over time and the corresponding average volumetric concrete expansions, $\varepsilon_{ASR/DEF}$, derived from Mohr's circle for both Specimens 2 and 4. To simplify the numerical models and to minimize the stress discontinuities, the mid-depth core concrete strain increments of the STM struts in the beam regions and beam-column joints for both singly and doubly reinforced ends of the specimen were averaged to derive an overall averaged amount of volumetric concrete expansion that represented the ASR/DEF effects in a single specimen. Since the locations of mid-depth core concrete strain measurements (KMs) were within Region I as defined in the previous section, this average volumetric concrete expansion, $\varepsilon_{ASR/DEF}$, was taken as the average volumetric concrete expansion for Region I to mimic the concrete expansion due to ASR/DEF for the later numerical analyses.

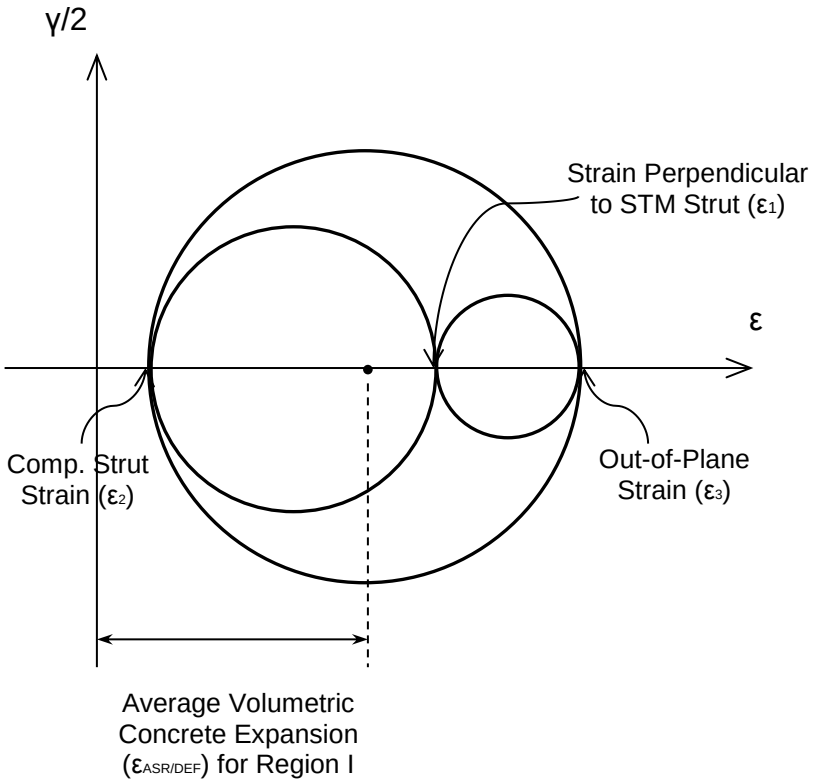

Figure 7-15 Mohr's Circle

Table 7-1 Average Strain Increments of Mid-Depth Core Concrete at STM Struts over Time and Corresponding Average Volumetric Concrete Expansions

Average Strain Increment	**Specimen 2** (252 days of Exposure)				**Specimen 4** (748 days of Exposure)			
	ε_1	ε_2	ε_3	Average Concrete Expansion ($\varepsilon_{ASR/DEF}$) for Region I*	ε_1	ε_2	ε_3	Average Concrete Expansion ($\varepsilon_{ASR/DEF}$) for Region I*
	0.0022	<0.0001	0.0021	0.0011	0.0033	0.0003	0.0054	0.0025

* The average concrete expansion, $\varepsilon_{ASR/DEF}$, was derived through plotting ε_1, ε_2 and ε_3 on Mohr's circle.

Due to the limited amount of embedded concrete gages (KMs) and the scattered reinforcing steel strains recorded by strain gages over time (SGs) during the exposure phase of the specimens as discussed in Chapter IV, the average volumetric concrete expansions for Regions II and III were obtained using the previously derived average volumetric concrete expansion for Region I and the ratios between the averaged longitudinal surface concrete strain increments from DEMEC measurements (DMs) at different depths of the specimen in Regions I, II and III.

The longitudinal surface concrete strain increments at different depths of the specimen were divided into four groups, denoted as DEPs 1 through 4 (Figure 7-16). An average longitudinal surface concrete strain increment over time was calculated for each group of each specimen. Then, the results of the DEPs 1 and 2 were averaged, that is, $(DEP1+DEP2)/2$, representing the longitudinal surface concrete increment for Region I. These calculated average longitudinal surface concrete strain increments for Specimens 2 and 4 are summarized in Table 7-2. Subsequently, the strain ratios of DEPs 3 and 4 to the longitudinal surface concrete strain increment of Region I, $(DEP1+DEP2)/2$, were calculated and summarized in Table 7-3.

Therefore, the average volumetric concrete expansions of Regions II and III for modeling various concrete expansions at such regions were estimated by dividing the average volumetric concrete strain ($\varepsilon_{ASR/DEF}$) for Region I by the strain ratios, as presented in Table 7-3. These estimated average volumetric concrete expansions for different characterized regions were later used for the numerical analyses.

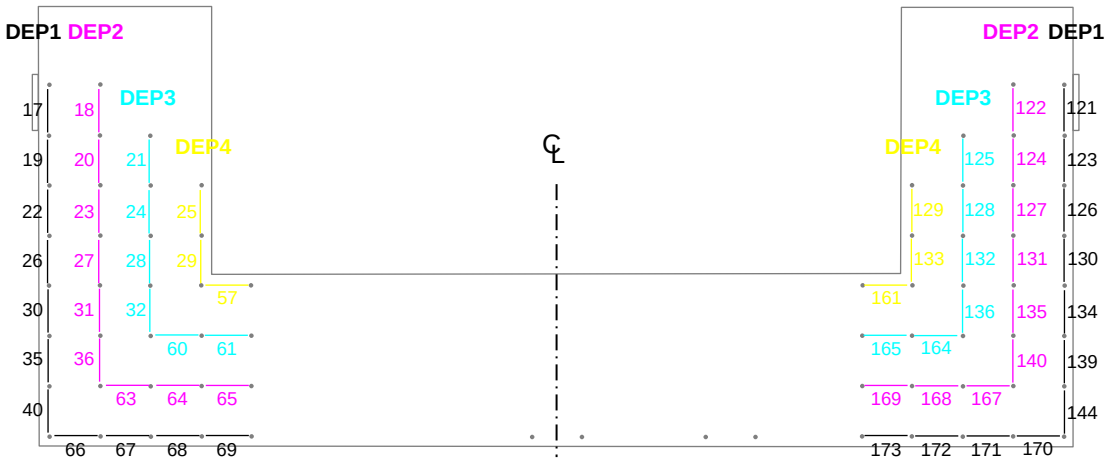

Figure 7-16 Grouped Average Longitudinal Surface Concrete Strains (DMs) at Different Depths (DEPs 1 through 4)

Table 7-2 Average Longitudinal Surface Concrete Strains at Different Depths of Specimen

Average Strain Increment	Specimen 2 (252 days of Exposure)			Specimen 4 (748 days of Exposure)		
	$\frac{(DEP1+DEP2)}{2}$	$DEP3$	$DEP4$	$\frac{(DEP1+DEP2)}{2}$	$DEP3$	$DEP4$
	0.0011	0.0009	0.0006	0.0018	0.0014	0.0010

Table 7-3 Strain Ratios at Different Depths of Specimen and Corresponding Average Volumetric Concrete Expansion

Strain Ratio	Specimen 2 (252 days of Exposure)		Specimen 4 (748 days of Exposure)	
	$(DEP1+DEP2)/2 \,/\, DEP3$	$(DEP1+DEP2)/2 \,/\, DEP4$	$(DEP1+DEP2)/2 \,/\, DEP3$	$(DEP1+DEP2)/2 \,/\, DEP4$
	1.24	1.85	1.26	1.74
$\varepsilon_{ASR/DEF}$	*Region II*	*Region III*	*Region II*	*Region III*
	0.0009	0.0006	0.0020	0.0014

7.5.3 Equivalent Thermal Expansion

As discussed in Section 2.4.4, ASR/DEF expansion in concrete can be modeled by applying an equivalent thermal load on the elements or by incorporating an empirical model. A method to quantify volumetric concrete expansions in the different characterized regions of the experimental specimen was proposed and discussed in the previous section. The objectives of this analytical research were to investigate the overall force-deformation relation and out-of-plane behavior of the specimens that were structurally tested to failure. Thus, the volumetric concrete expansions were taken into account in the numerical models by applying equivalent thermal expansions to selected elements of the three defined characterized regions as presented in the previous section. The pseudo thermal expansion coefficient, α, of the concrete was taken as 1×10^{-5}. Then, the pseudo temperature increment for each characterized region, ΔT, in the numerical models was determined by:

$$\Delta T = \frac{\varepsilon_{ASR/DEF}}{\alpha} \tag{7-3}$$

where $\varepsilon_{ASR/DEF}$ was the average volumetric concrete expansion in each characterized region. These temperature increments for the different regions were applied uniformly and slowly in the numerical models to prevent numerical errors prior to the structural loading application. Then, the constant velocity loading was subsequently applied at the loading point, representing displacement control loading as discussed in Section 7.4.3, to simulate the overall structural behavior of the exposed specimens that were structurally tested to failure. The analytical results are presented in the later sections.

7.5.4 Proposed Ranges of Average Volumetric Concrete Expansions for FEA Due to Various Levels of Primarily ASR Distress

As presented in Section 4.7, some concrete cores were taken from the specimens after they were structurally load tested to failure. The cores were intentionally drilled through longitudinal and transverse reinforcement, near locations with mild or no cracking, near locations with large cracks and severe map cracking, and near locations with white residue on the surface. Some of these cores were located on the tension side and the others were located on the compression side of the specimen with respect to the loading conditions (Figure 4-50a, Figure 4-51a and Figure 4-52a). Appendixes A, B and C show the complete petrographic analysis results of these cores for Specimens 1, 2 and 4, respectively. For Specimens 2 and 4, ASR was found to be the primary cause of the distress in concrete. Although accumulations of ettringite were observed in some locations, it was reported that the distribution of ettringite was not consistent with DEF.

Table 7-4 summarizes the levels of ASR distress of each core from the petrographic analysis results of Specimens 2 and 4 and the corresponding characterized regions as defined in the previous section. It was found that Region I experienced greater levels of distress than Regions II and III, hence leading to greater amounts of concrete expansion. Therefore, according to the average volumetric concrete expansion for each characterized region as derived using the proposed method presented in the previous sections and the locations of the cores in Specimens 2 and 4, selected ranges of the average volumetric concrete expansions for the FEA due to the various levels of ASR distress were proposed as presented in Table 7-5. These proposed ranges can be

used for further investigations to predict the overall structural behavior for Specimen 3 using FEA based on the petrographic results of the cores taken from Specimen 3 after its structural load testing.

Table 7-4 Summary of Levels of ASR Distress from Petrographic Analysis Results of Specimens 2 and 4 and Corresponding Characterized Regions

Core	**Specimen 2** (252 days of Exposure)		**Specimen 4** (748 days of Exposure)	
	Level of ASR Distress	Location w.r.t. Characterized Regions	Level of ASR Distress	Location w.r.t. Characterized Regions
1	Moderate to High	Region I	High	Region III
2	Moderate to High	Region I	Moderate to High	Region III
3	High	Region I	Extensive	Region I
4	High	Region I	Extensive	Region I
5	Moderate	Region II	Moderate to High	Region III
6	Low	Region III	Extensive	Region II
7	Low to Moderate	Region III	High	Region I
8	Low	Region III	High	Region I

Table 7-5 Proposed Ranges of Average Volumetric Concrete Expansion for FEA Due to Various Levels of ASR Distress

Level of ASR Distress	Extensive	High	Moderate	Low
Range of Average Concrete Expansion	> 0.0020	0.0010~0.0020	0.0005~0.0010	< 0.0005

7.5.5 Proposed Expression for ASR/DEF Expansion over Time

As discussed in Section 2.4.4, Ulm et al. (2000) proposed a numerical model for ASR expansion as a function of time based on experimental results (Eq. [2-43]). This expression successfully described the three periods of ASR expansion, that is, the incubation period, cracking period, and stabilized period (Mohammed et al. 2003). Seignol et al. (2012) modified this model and took into account the ability of continuous growth of DEF in a later age to depict DEF expansion over time (Eq. [2-44]). The comparison of these typical expressions of ASR and DEF expansions over time was presented in Section 2.4.4 (Figure 2-10). One objective of this research is to develop an approach to account for the formation of ASR and DEF in the specimens prior to structural load testing. As discussed in Chapter III and Chapter IV, a designed concrete mix with high alkali content, elevated curing temperatures, and later supplemental watering were applied to promote ASR/DEF formation. Thus, an expression combining ASR and DEF expansions over time based on the previous studies (Ulm et al. 2000; Seignol et al. 2012) was used for the experimental specimens in this research, as follows:

$$\begin{aligned}\varepsilon_{total}(t) &= \varepsilon_{ASR}(t) + \varepsilon_{DEF}(t) \\ &= \varepsilon_{ASR}(\infty)\frac{1-\exp\left(-t/\tau_C^{ASR}\right)}{1+\exp\left(-t/\tau_C^{ASR}+\tau_L^{ASR}/\tau_C^{ASR}\right)} \\ &\quad +\varepsilon_{DEF}(\infty)\frac{1-\exp\left(-t/\tau_C^{DEF}\right)}{1+\exp\left(-t/\tau_C^{DEF}+\tau_L^{DEF}/\tau_C^{DEF}\right)}\left(1-\frac{\phi}{\delta+t}\right)\end{aligned} \quad (7\text{-}4)$$

where $\varepsilon_{ASR}(\infty)$ and $\varepsilon_{DEF}(\infty)$ are potential expansions due to ASR and DEF, respectively; τ_L^{ASR} and τ_L^{DEF} are latency durations for ASR and DEF, respectively; τ_C^{ASR}

and τ_C^{DEF} are characteristic durations for ASR and DEF, respectively; ϕ and δ are two corrective durations where $0 < \phi < \delta$, to adjust the end of the DEF expansion expression. Figure 7-17 shows a representative concrete expansion curve which takes into account ASR and DEF effects, as described in Eq. (7-4).

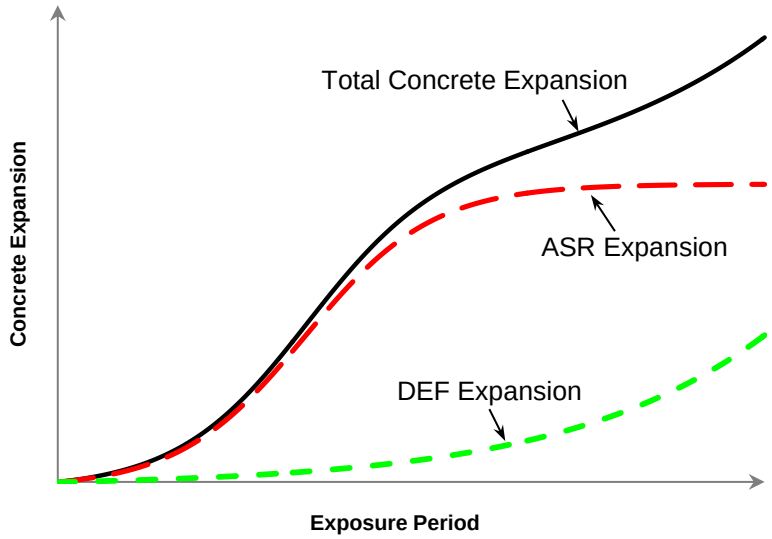

Figure 7-17 Concrete Expansion Curve Combining ASR and DEF Effects

As discussed in Section 2.2, it usually takes longer for DEF to occur than for ASR in field structures and the overall potential expansion induced by DEF can significantly exceed that by ASR. For the specimens in this research, the potential expansions of ASR and DEF should be determined based on the observations in the experimental and analytical programs of this research, since these expansion potentials will vary due to different concrete mix designs, reinforcement details, loading conditions, and exposure conditions. Fan and Hanson (1998a) conducted an

experimental program to investigate the concrete expansion due to ASR and recorded 0.4% length expansion in plain concrete but reduced expansion, 0.35% and 0.2% in transverse and longitudinal directions, respectively, in reinforced concrete prisms when 0.54% steel reinforcement ratio was added in longitudinal direction. Note that these prisms were not under any loading conditions. As presented in Section 3.3.1, the longitudinal tensile reinforcement ratio of the experimental specimen for this research was 0.91%. In the specimen's exposure phase, it was evident that the experimental specimens experienced more concrete expansion on the tension side due to the preloading than on the compression side as discussed in Chapter IV. This evidently indicated that the stress field may significantly affect the subsequent concrete expansion due to ASR/DEF. Although greater amounts of tensile longitudinal reinforcement was used as compared to those in the literature, the average volumetric concrete expansion in Region I of Specimen 4, where the concrete exhibited tensile stresses under prestress load, was calculated as 0.0025 (0.25%), as discussed in the previous sections. In addition, the petrographic report of Specimen 4 showed that concrete in such region experienced extensive level of ASR distress, that is, ASR formation was nearly exhausted. Therefore, the volumetric expansive potential due to ASR was assumed to be 0.0025 (0.25%) for Region I of the experimental specimen. For Regions II and III, where concrete stresses were either in minimal tension or compression, lower potential ASR/DEF volumetric expansions of concrete could be expected due to potentially less water ingress over time. In addition, the levels of ASR distress of these regions in Specimen 4 were reported to be from high to extensive. That is, ASR formation was

nearly completed for the concrete mix used in this research after 748 days of exposure. Hence, the derived average volumetric concrete expansions of Specimen 4 were assumed to be the volumetric expansive potential in such regions, that is, 0.0020 (0.20%) and 0.0014 (0.14%) for Regions II and III, respectively. Since DEF was not the cause of concrete distress for the specimens that were tested to failure, the maximum concrete expansion due to DEF (3.5%) observed by Barbarulo et al. (2005) was used as the volumetric expansive potential of DEF for all regions in this research, but of course this value will need to be further assessed at a later time when DEF is more prominent in Specimen 3.

The latency time and characteristic time for ASR were obtained by plotting the derived average concrete expansions of various regions in Specimens 2 and 4 with the proposed expression of total concrete expansions, as shown in Figure 7-18. The latency time for ASR was found to be about 250 days while the characteristic time for ASR was about 120 days for the experimental specimens in this research. Since DEF had only minimum effects after the first 748 days of exposure (Specimen 4), the latency time and characteristic time of DEF were assumed to be 5000 days and 770 days such that DEF expansion commenced approximately after 900 days of exposure (Figure 7-19), again these values will need to be assessed at a later time when DEF is more prominent in Specimen 3. Note again that these assumptions were only used to predict the concrete expansion for Specimen 3 and have not been experimentally measured to date. The effects of the two corrective durations, ϕ and δ, are more pronounced in the later stages

of DEF formation (Figure 2-10). Thus, such effects are not shown in Figure 7-19 and are beyond the available information from this research.

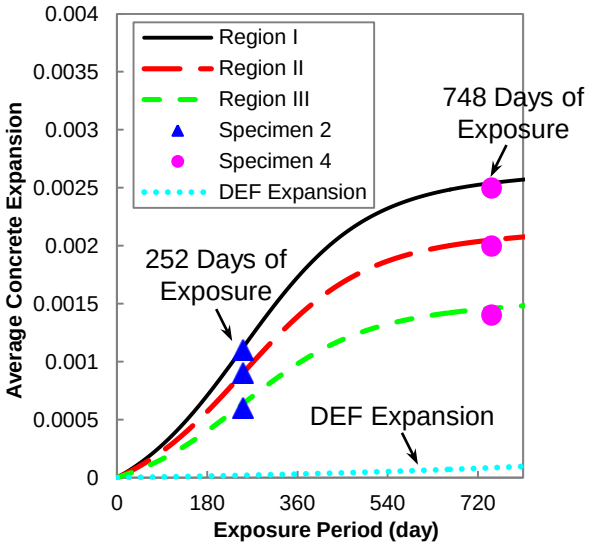

Figure 7-18 Volumetric Concrete Expansion Curves for Each Region of Experimental Specimen

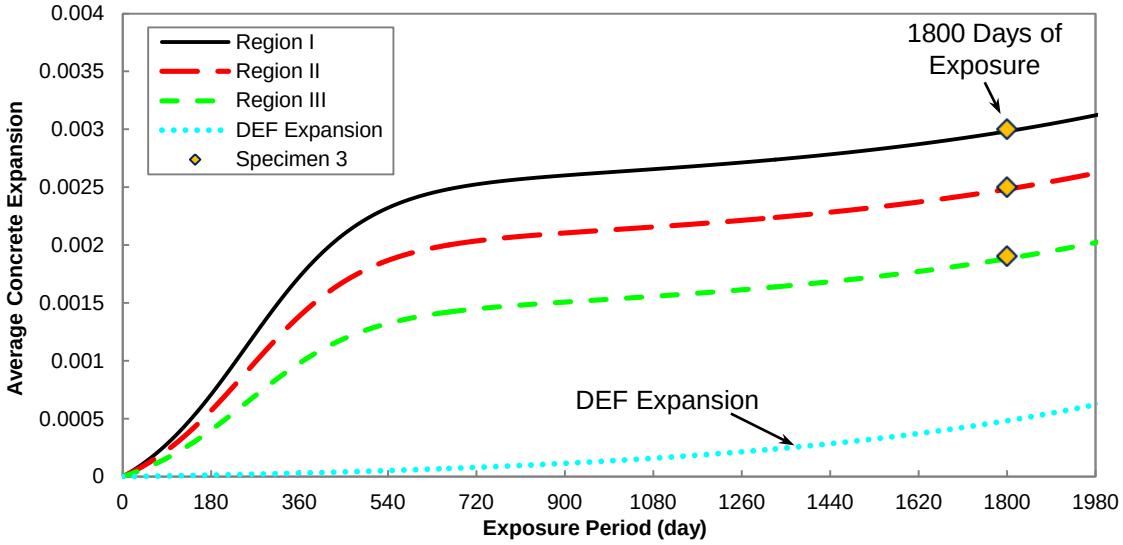

Figure 7-19 Prediction of Volumetric Concrete Expansion Curve for Each Region of Experimental Specimen

As discussed in Chapter IV and Chapter V, Specimen 3 remains in the field for additional exposure to hopefully develop further expansions from DEF. The amount of average concrete expansions in all regions for Specimen 3 after 1800 days of exposure can be estimated using the expression for total concrete expansion over time by Ulm et al. (2000) and Seignol et al. (2012) as described in Eq. (7-4) (Figure 7-19). Thus, these average concrete expansions along with assumed concrete compressive strength can be used to estimate the overall structural behavior of Specimen 3 after 1800 days of exposure once the compressive strength of concrete is determined through material testing.

7.6 ANALYTICAL RESULTS

This section presents results of the numerical simulations using the FEA approach. The force-deformation relation and the reinforcing steel strains from the numerical simulations in each specimen are compared with the experimental structural load test results. The effects of the varying concrete constitutive relations in tension on the overall structural performance of the doubly reinforced end of Specimen 1 are compared. The compressive stresses in the STM struts for both the singly and doubly reinforced ends in Specimen 1 are highlighted to further investigate the applicability of strut and tie modeling (STM). In addition, comparisons of the out-of-plane behavior along the specimen depth at various critical sections are made to examine the diverse performances in core and cover concrete regions.

7.6.1 Force-Deformation Behavior

The experimental failure end in each specimen, namely the doubly reinforced bent in Specimen 1 and the singly reinforced bent in Specimens 2 and 4, was individually modeled using the FEA approach, which incorporated the proposed method to take into account ASR/DEF effects for Specimens 2 and 4. Table 7-6 summarizes the overall specimen loading capability from the FEA approach and experimental results. For Specimen 1, the effects of the constitutive relations of the concrete in tension on specimen strength are compared. The ratio of the overall analytical strength to the experimental strength ranged from 0.85 to 0.93 (Table 7-6). In addition, the calculated strengths for Specimens 2 and 4 using the FEA approach yielded comparable results to the experimental peak loads (analysis/experiment ratio within 1.00 to 1.03), hence at least partially validating the proposed method for simulating the strength of the specimens that experienced ASR/DEF expansion.

Figure 7-20 compares the FEA and experimental results in terms of the force-deformation relations for the failure end of each specimen. The results of force-deformation relations for each specimen showed that the FEA approach simulated the overall behavior of each specimen reasonably well (Figure 7-20a, 7-20c and 7-20d), correspondingly demonstrating the applicability of the proposed method for mimicking ASR/DEF effects. To examine the near identical behavior of singly and doubly reinforced ends that was observed in the experimental program, the singly reinforced end of Specimen 1 was also simulated using the FEA approach. As observed in the

experimental program, comparable analytical results were obtained in the singly and doubly reinforced ends in terms of the force-deformation curves (Figure 7-20b).

As discussed in Section 5.5, two experimental tests were conducted for Specimen 1. In addition, both Specimens 1 and 4 experienced unloading during their structural load tests. However, the effect of the cyclic loading was beyond the objectives of this research and was not considered in the numerical simulations.

Table 7-6 Comparisons of Specimen Strengths from FEA Approach and Experimental Results

Specimen	**Specimen 1**	**Specimen 2**	**Specimen4**
Experimental Peak Load	474 kips (2108 kN)	500 kips (2224 kN)	503 kips (2237 kN)
Constitutive Model of Concrete in Tension	**Analysis Results, kips (kN) [Analysis/Experiment Ratio]**		
$f_{c1} = \frac{f_{cr}}{1+\sqrt{500\varepsilon_1}}$ (Eq. [2-34])	414 (1842) [0.87]	498 (2215) [1.00]	518 (2304) [1.03]
$f_{c1} = \frac{f_{cr}}{1+\sqrt{200\varepsilon_1}}$ (Eq. [2-33])	442 (1966) [0.93]	n/a	n/a
$f_{c1} = f_{cr}\left(\frac{\varepsilon_{cr}}{\varepsilon_1}\right)^{0.4}$ (Eq. [2-35])	405 (1802) [0.85]		
$f_{c1} = f_{cr}\left(\frac{\varepsilon_{cr}}{\varepsilon_1}\right)^{0.2}$ (Eq. [2-35])	442 (1966) [0.93]		

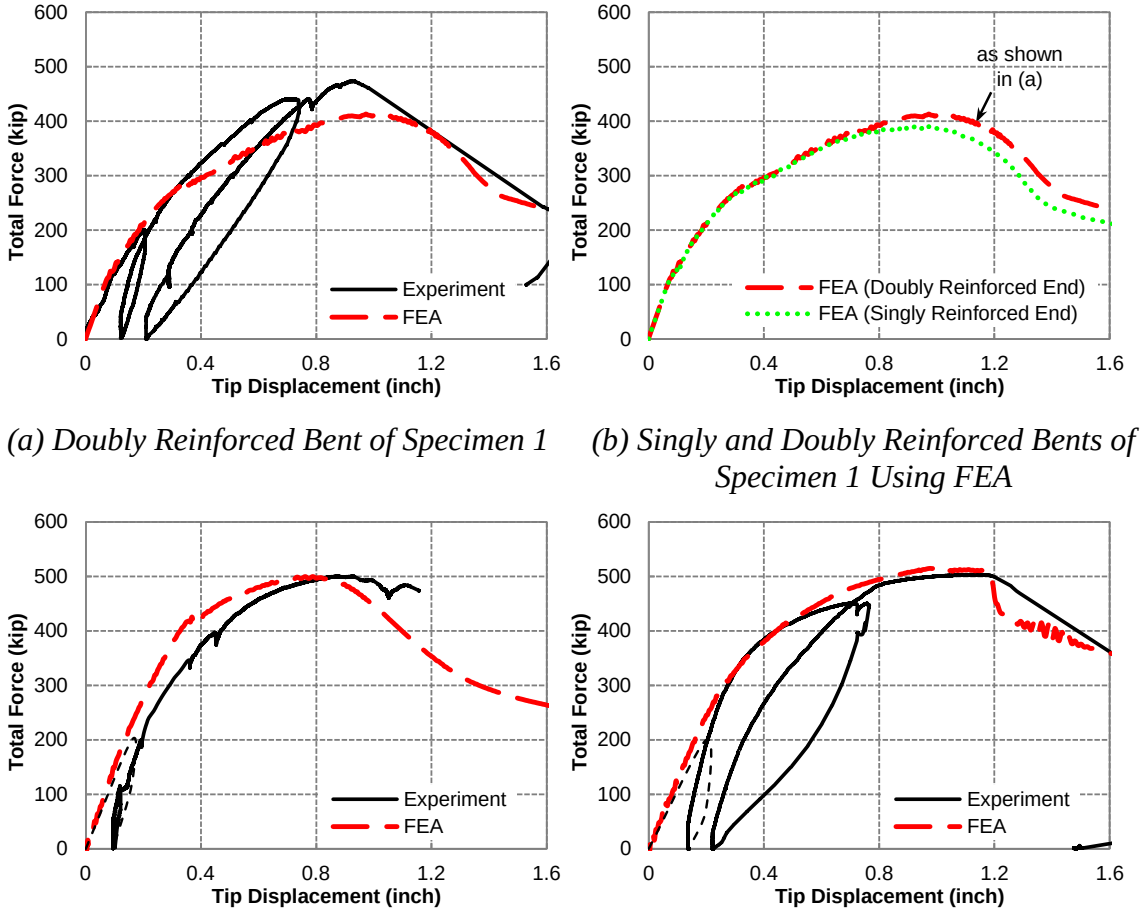

(a) Doubly Reinforced Bent of Specimen 1

(b) Singly and Doubly Reinforced Bents of Specimen 1 Using FEA

(c) Singly Reinforced Bent of Specimen 2

(d) Singly Reinforced Bent of Specimen 4

Figure 7-20 Comparisons of Force-Deformation Relations from FEA and Experimental Results

Figure 7-21 compares the effects of the various constitutive relations of concrete in tension on the force-deformation curves. The figure shows that the constitutive models of concrete in tension proposed by Vecchio and Collins (1986) and Okamura et al. (1985) using Eqs. (2-33) and (2-35) with $c = 0.2$, respectively, for welded wire meshes produced greater specimen strengths in the numerical models. Furthermore, the

results indicated that the applied constitutive relation of concrete in tension had a significant influence on the predicted specimen response. Note that these constitutive models from the literature were developed from concrete panel tests, as discussed in Section 2.4.4. The tension stiffening effects in reinforced concrete beam and column sections and those in beam-column joint D-regions are yet unclear. Thus, only the expression proposed by the MCFT for deformed reinforcing steel bars from Eq. (2-34) was used in the numerical simulations for Specimens 2 and 4.

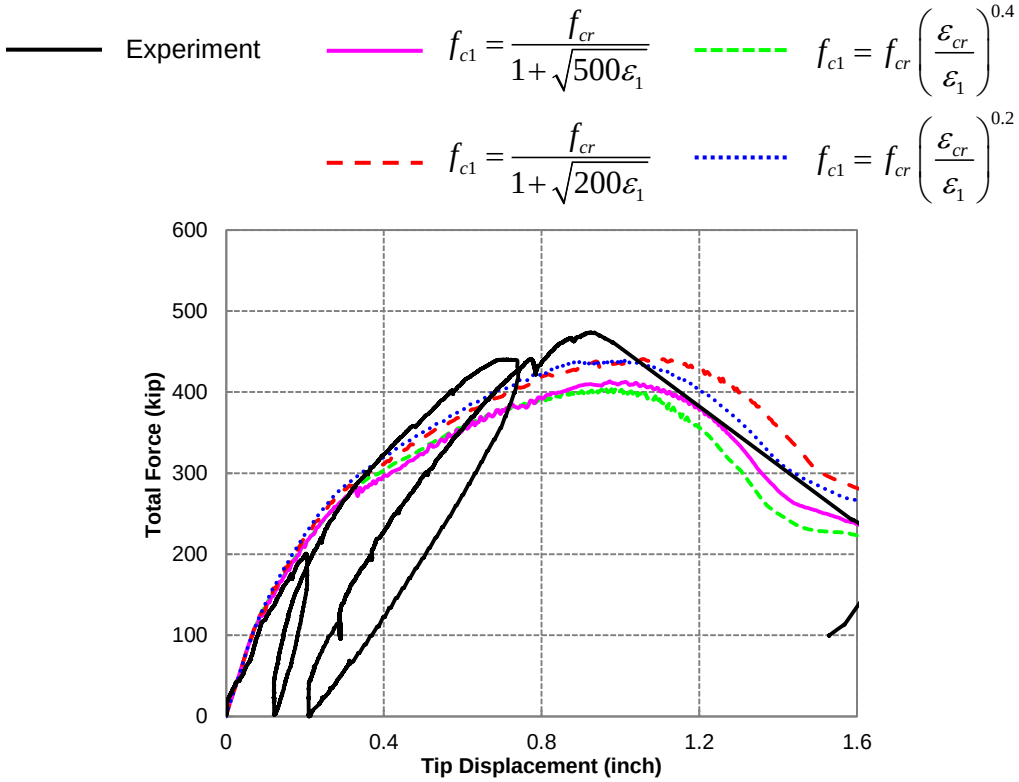

Figure 7-21 Effects of Various Constitutive Relations of Concrete in Tension on Force-Deformation Curves

7.6.2 Reinforcing Steel Strains

The reinforcing steel strains obtained from the numerical simulations are compared to the measured strain data from the embedded strain gages (SGs). Note that some strain gages failed after the concrete casting, during the exposure phase, and during structural load testing. Moreover, as discussed in Section 4.6, some scattered reinforcing steel strains were recorded in the ASR/DEF-affected specimens during the exposure phase, which might be attributed to the development of faulty gages due to ASR/DEF expansion over time. Thus, the initial readings for some of the reinforcing steel strains in the affected specimens (Specimens 2 and 4) may differ from those from the numerical simulations.

Figure 7-22 compares the reinforcing steel strains at the critical locations from the FEA and experimental results of the failure end in Specimen 1. The results showed that the FEA approach yielded comparable reinforcing steel behavior with the measured strain data obtained during the structural load tests. Note that the yield strain of the reinforcing steel used in this research was ± 0.0022 based on the coupon test results as discussed in Section 3.3.

For Specimen 1, the longitudinal tension reinforcement in beam region had a strain over 0.003 both in the experimentally measured data and in the analytical results from the FEA approach, which indicated that yielding in tension occurred at such locations (Figure 7-22a).

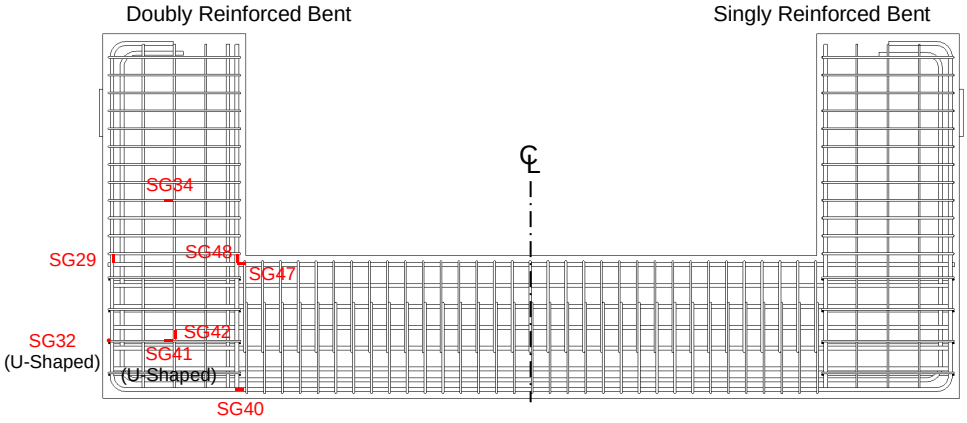

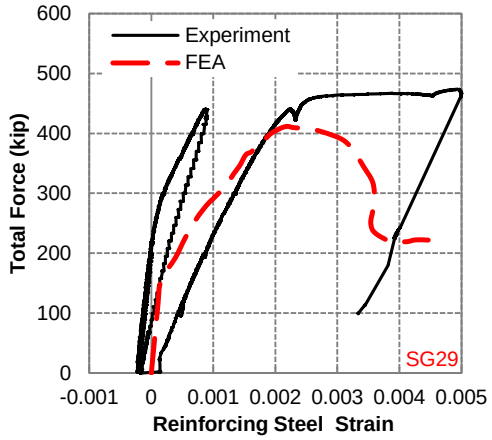

(a) Tension Reinforcement in Beam Region

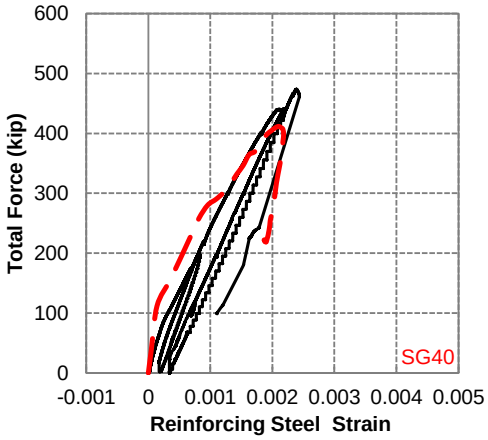

(b) Tension Reinforcement in Column Region

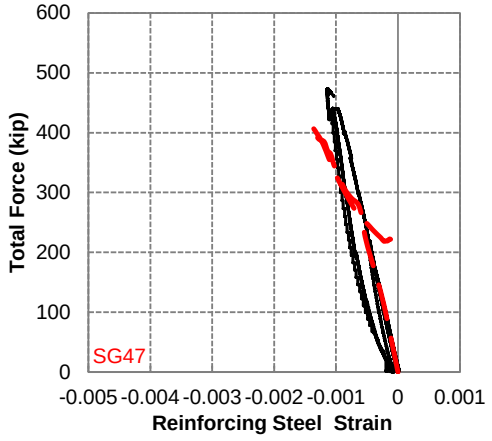

(c) Compression Reinforcement in Column Region

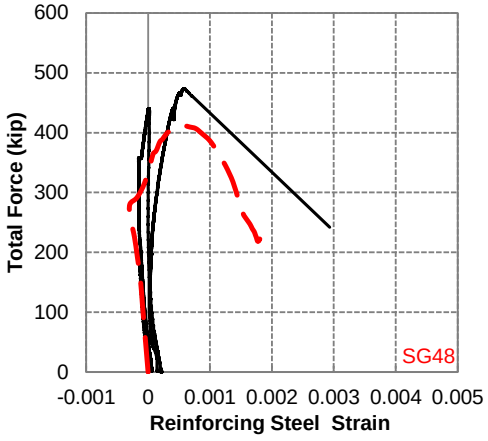

(d) Compression Reinforcement in Beam Region

Figure 7-22 Comparisons of Reinforcing Steel Strains from FEA and Experimental Results – Specimen 1

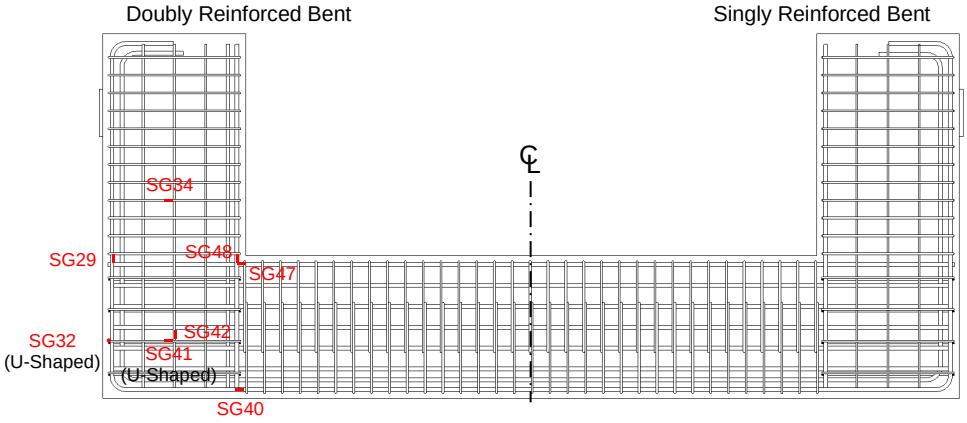

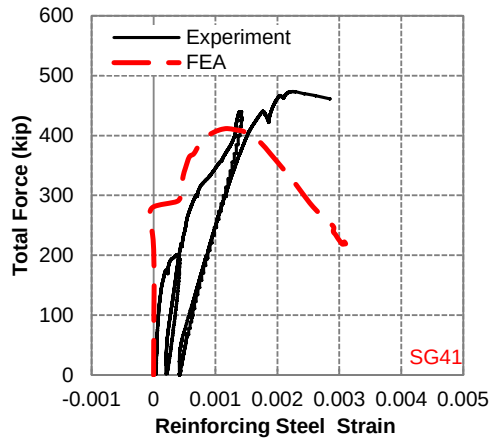

(e) U-Shaped Joint Reinforcing Steel

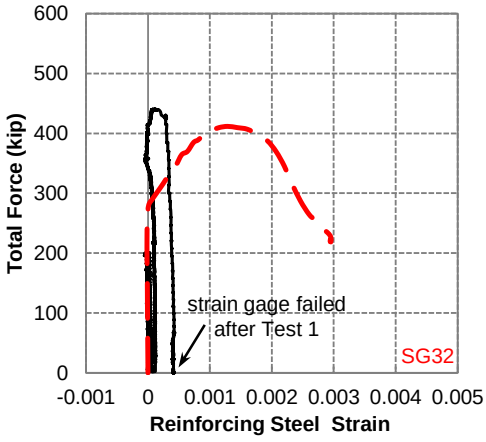

(f) U-Shaped Beam Face Reinforcing Steel

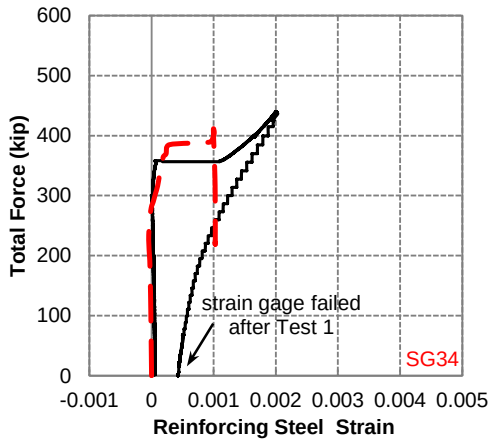

(g) Transverse Reinforcement in Beam Region

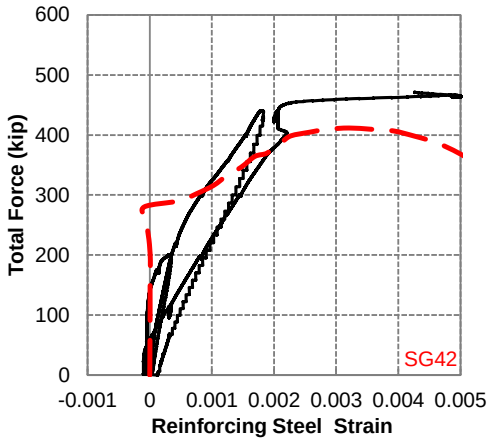

(h) Skin Reinforcement

Figure 7-22 Comparisons of Reinforcing Steel Strains from FEA and Experimental Results – Specimen 1(Continued)

Moreover, the strain of the longitudinal tension steel in the column region reached 0.002 from both the experimental data and analytical results, suggesting that incipient yielding had resulted prior to failure of the specimen (Figure 7-22b).

For both the experimental and analytical results, it was observed that the longitudinal column steel on the compression-most side remained in compression during the two tests conducted for Specimen 1, as shown in Figure 7-22c, while the longitudinal compression reinforcement in the beam region switched from compression to tension during the tests for both the experimentally measured data and analytical results (Figure 7-22d).

Note that the strain gage attached to the U-shaped steel bar on the beam end face, that is, SG32, failed after Test 1 of Specimen 1. However, the U-shaped steel within the joint region experienced strains beyond the yield strain before failure on both the side face and beam end face from analytical results (Figure 7-22e and f).

In addition, tensile strain was observed in the transverse reinforcement in the beam region for both the experimental and analytical results, indicating a potential of arch action at the center of the STM strut in such region (Figure 7-22g).

The skin reinforcement in the beam-column joint region experienced significant strains over 0.005 in tension from both the FEA and experimental results as shown in Figure 7-22h, which indicates the lack of sufficient shear resistance in this direction and confinement within the joint region.

Figure 7-23 depicts the strain distributions of the reinforcing steel in Specimen 1 under peak load in the numerical analysis. It was found that the main longitudinal tension reinforcement at some critical locations in the joint region reached the tensile yield strain under the loading capability. In addition, incipient yielding was observed in the longitudinal tension reinforcement in both the beam and column regions near the joint under peak load. Note again that the skin reinforcement in the beam-column joint region exceeded the tensile yield strain at peak load (Figure 7-23).

Figures 7-24 and 7-25 compare the reinforcing steel strains at the critical locations in Specimens 2 and 4 from the FEA approach and experimental results. Note that the initial steel strains from FEA approach are attributed to the preloading to simulate service loading and the ASR/DEF expansion.

Figure 7-26 shows that tensile strains develop in the longitudinal and transverse reinforcing steel as a result of the equivalent expansion due to ASR/DEF using the proposed method. These tensile strains effectively prestress and confine the core concrete, as shown in Figures 7-27.

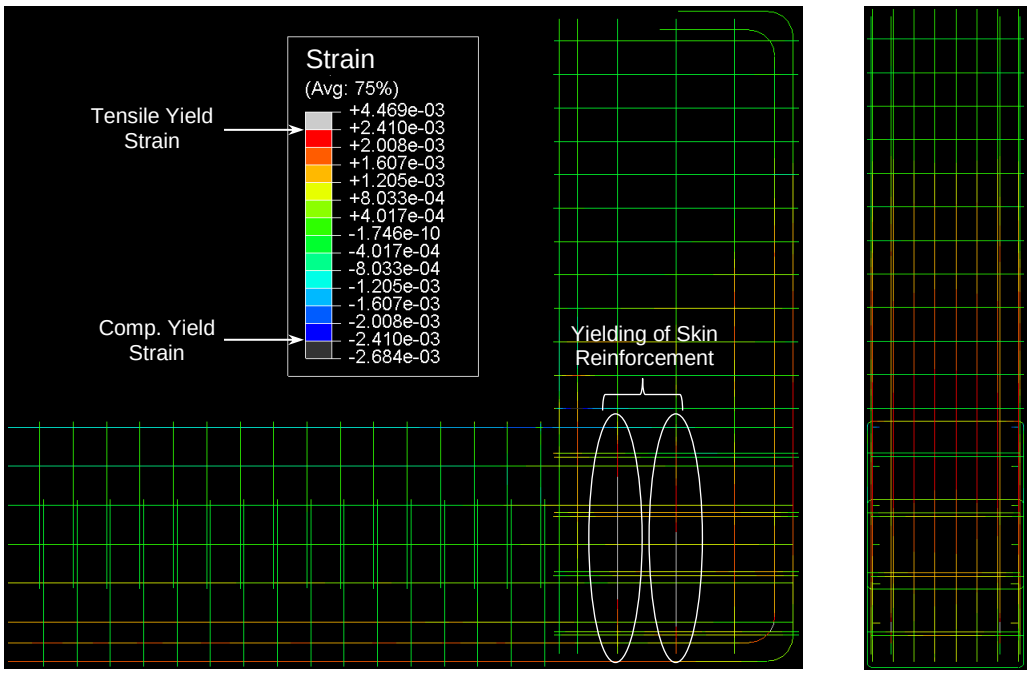

(a) Isometric View

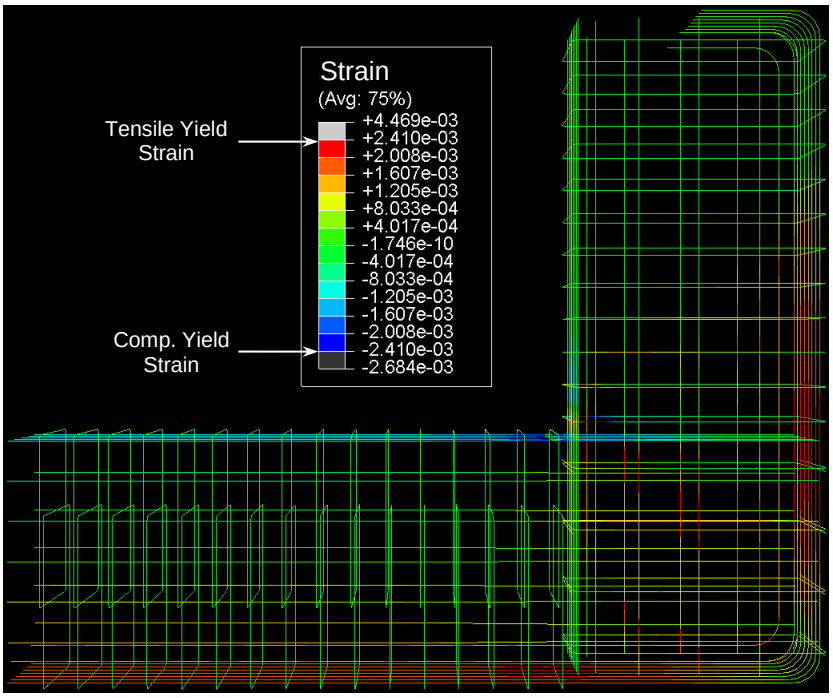

(b) Perspective View

Figure 7-23 Reinforcing Strains in Specimen 1 at Peak Load

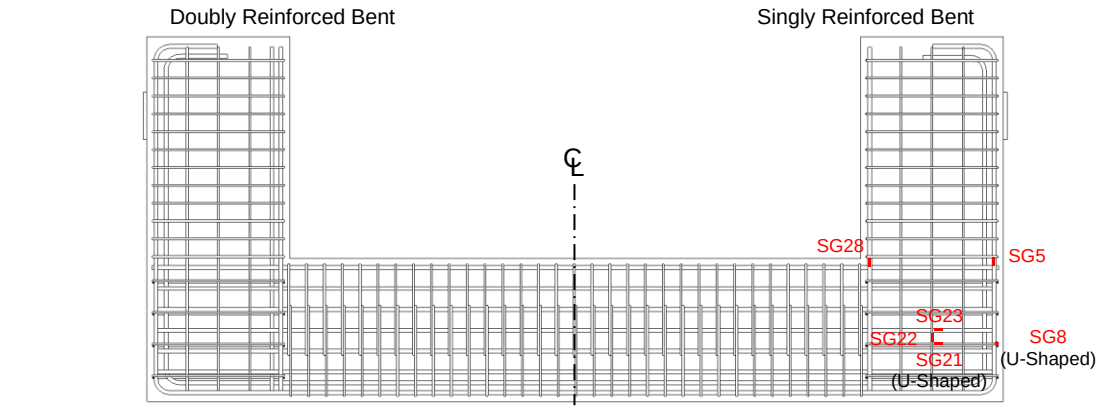

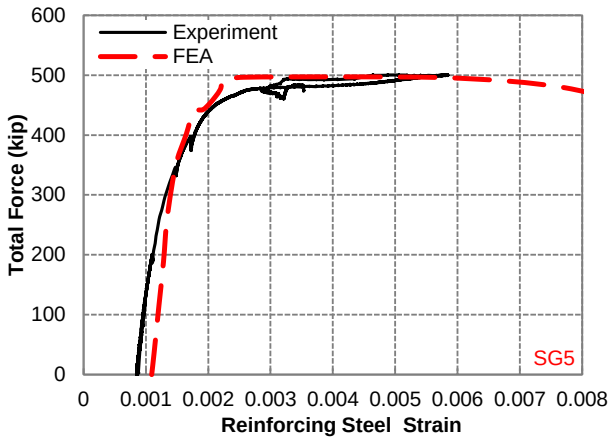

(a) Tension Reinforcement in Beam Region

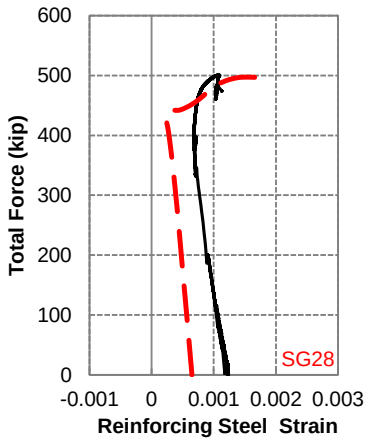

(b) Compression Reinforcement in Beam Region

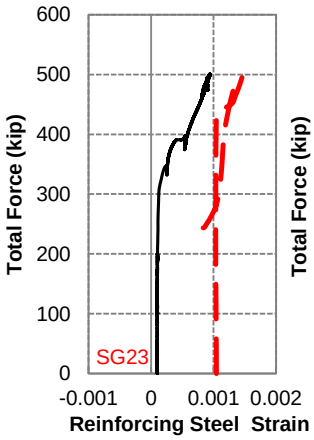

(c) Comp. Reinforcement in Column Region

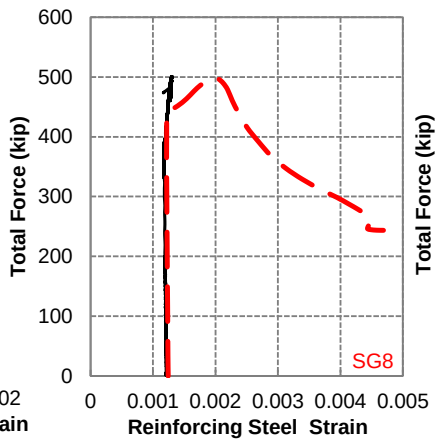

(d) U-Shaped Beam Face Reinforcing Steel

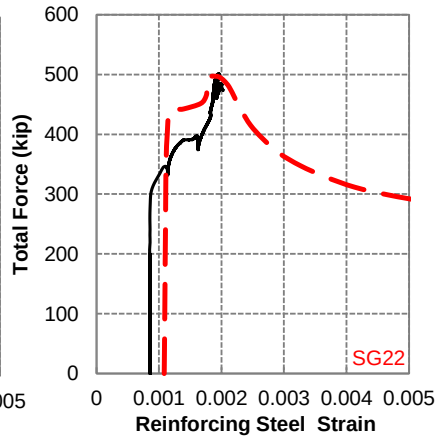

(e) Skin Reinforcement

Figure 7-24 Comparisons of Reinforcing Steel Strains from FEA and Experimental Results – Specimen 2

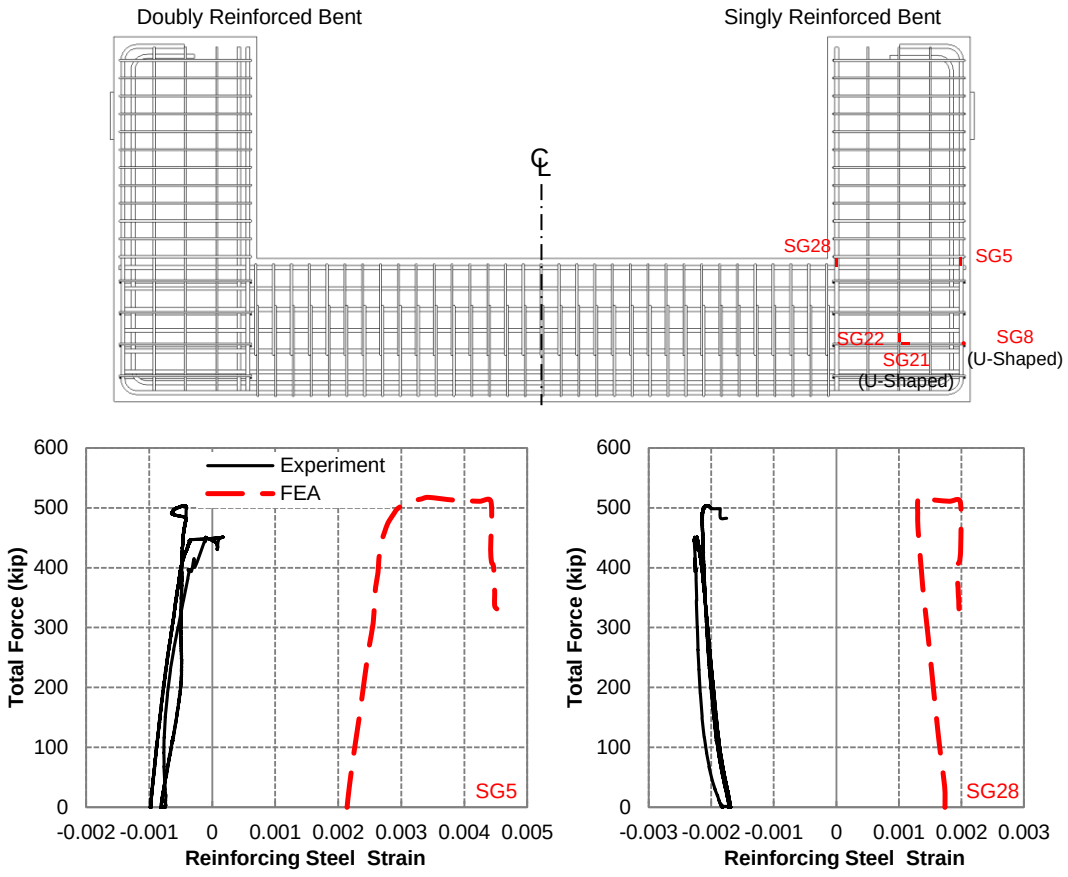

(a) Tension Reinforcement in Beam Region

(b) Compression Reinforcement in Beam Region

(c) U-Shaped Joint Reinforcing Steel

(d) U-Shaped Beam Face Reinforcing Steel

Figure 7-25 Comparisons of Reinforcing Steel Strains from FEA and Experimental Results – Specimen 4

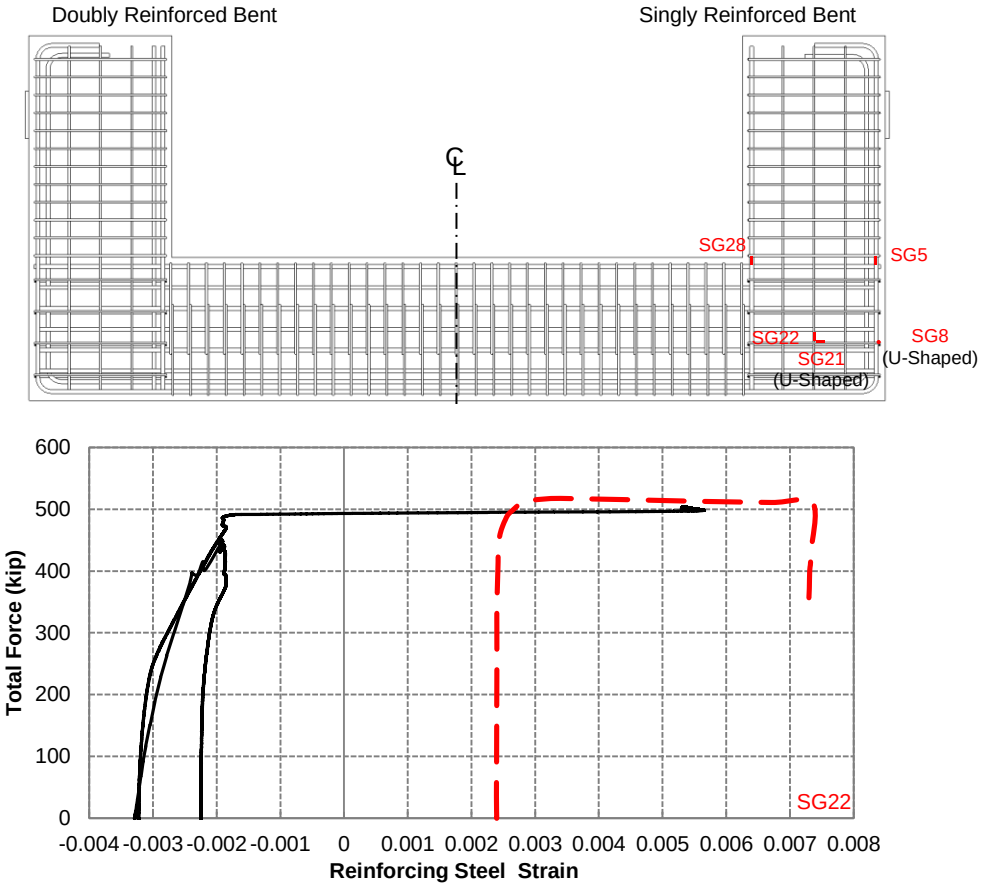

(e) Skin Reinforcement

Figure 7-25 Comparisons of Reinforcing Steel Strains from FEA and Experimental Results – Specimen 4 (Continued)

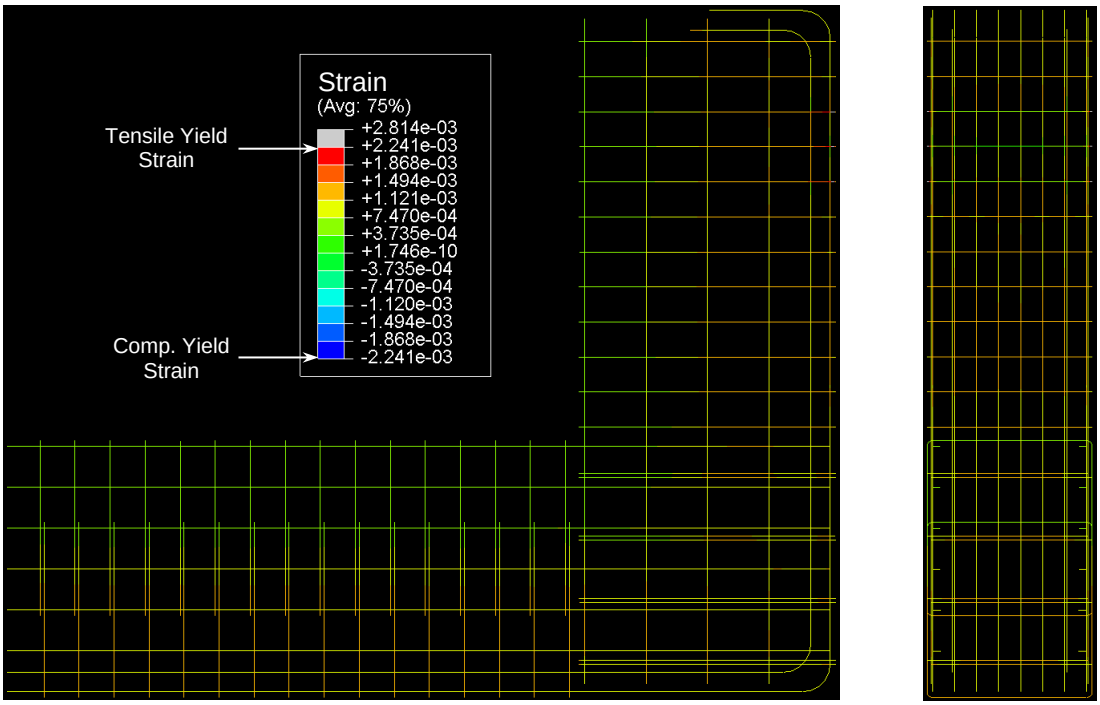

(a) Specimen 2

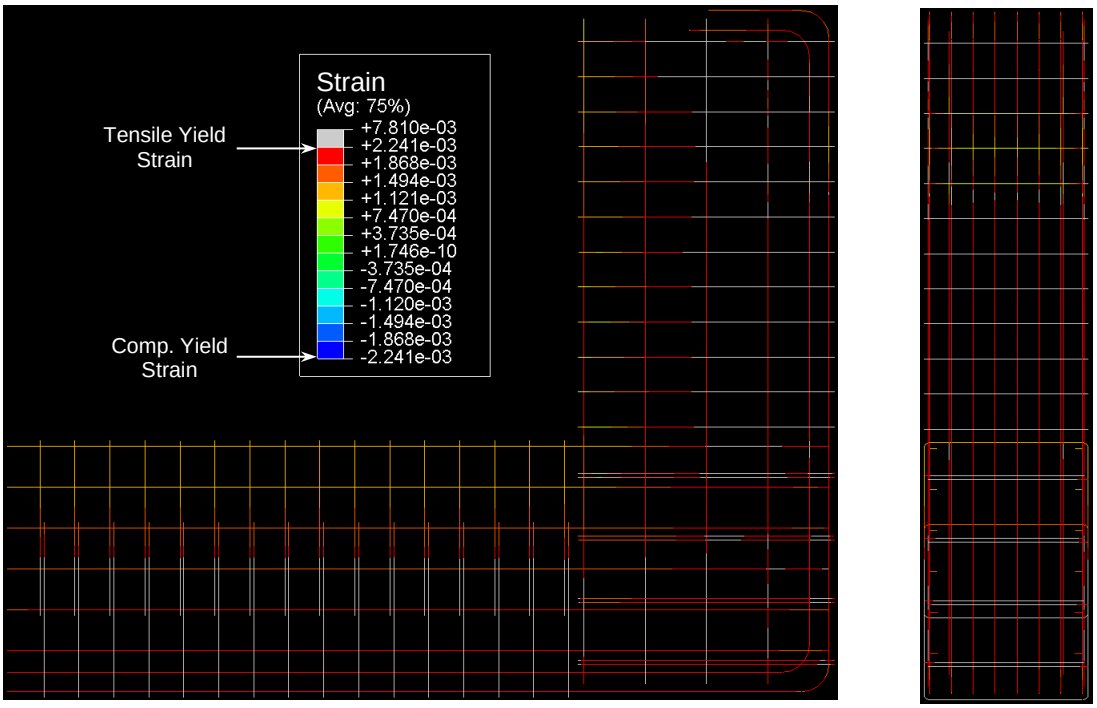

(b) Specimen 4

Figure 7-26 Prestressing and Confining Effects Due to ASR of Reinforcing Steel

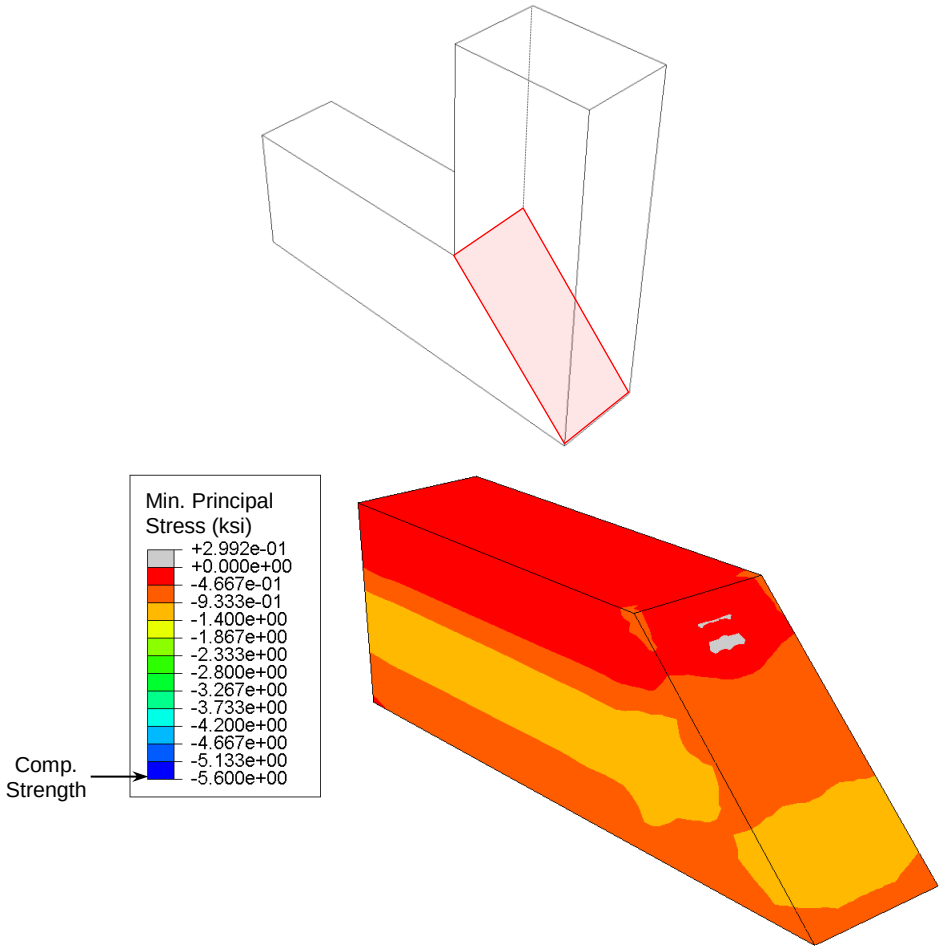

(a) Specimen 2

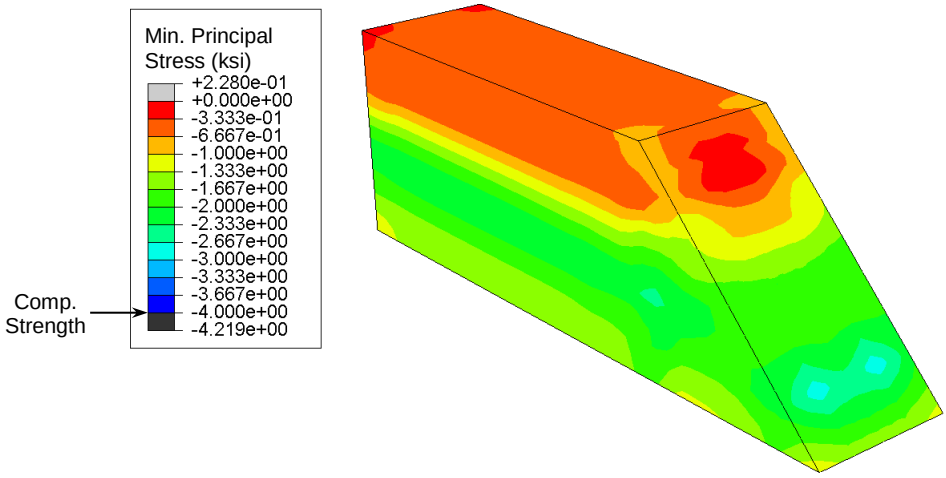

(b) Specimen 4

Figure 7-27 Prestressing and Confining Effects Due to ASR on Core Concrete

For Specimen 2, the longitudinal tension steel in the beam region reached 0.006 from both the experimental and analytical results before failure of the specimen occurred (Figure 7-24a). For the longitudinal compression reinforcement in the beam region, although the strain remained in tension during the overall loading for both the experimental test and numerical simulation, strain increases in compression were observed and followed by strain increases in tension after the load reached 400 kips (1779 kN) (Figure 7-24b). Note that the strain gage attached to the U-shaped steel bar on the side face (SG21) failed before specimen's load test. However, the strain in the longitudinal column steel next to such U-shaped steel bar slightly increased during loading from both the experimental measured data and analytical results (Figure 7-24c). The strain in the U-shaped steel bar on the beam end face approximately stayed unchanged during the experimental load test, yet that from the numerical analysis reached 0.002 at peak load (Figure 7-24d). As shown in Figure 7-24e, the strain in the skin reinforcement in the beam-column joint region reached 0.002 at peak load for both the experimental test and the numerical analysis, indicating incipient yielding of steel in tension.

For Specimen 4, strains in the longitudinal tension and compression reinforcement in the beam region slightly changed in the experimental load test, while the analysis results showed some ductile behavior (Figure 7-25a and b). The U-Shaped steel bar exhibited smaller changes in strain for both the analysis and experiment except the strain gage readings on the side face (SG21) from the experimental load test (Figure 7-25c and d). In addition, Figure 7-25e showed that the skin reinforcement experienced

a significant increase in strain for both the analysis and experiment, demonstrating lack of the shear resistance in such direction and confinement wihin the joint region.

7.6.3 Behavior in STM Struts

Figure 7-28 through Figure 7-30 compare the core concrete strains in the three perpendicular directions of the embedded concrete gages (KMs) at the center of the STM strut in the failure beam-column joint derived from the FEA approach and those measured by the embedded concrete gages (KMs). Note that the initial readings for the concrete gages before structural load testing for Specimens 2 and 4 were due to the preloading that mimicked service loading and the ASR/DEF expansion during specimen's exposure phase.

Generally, the measured compressive strain in the STM strut, that is, KM10 in Specimen 1 and KM4 in Specimens 2 and 4, unloaded near the peak loading, yet greater amounts of compressive strength and ductility were observed in the numerical results (Figure 7-28a, Figure 7-29a and Figure 7-30a). The FEA approach provided comparable tensile strains perpendicular to the STM strut, that is, KM11 in Specimen 1 and KM5 in Specimens 2 and 4 to the experimental results (Figure 7-28b, Figure 7-29b and Figure 7-30b). The strains in such direction of the failure joint in Specimens 1 and 2 had significant total strain increases of about 0.007 in tension for both the experimental measured data and analytical results. For Specimen 4, the total strain increases were about 0.002 in tension from both the experiment and analysis. Out-of-plane behavior at the failure beam-column joint was observed in the experimental load tests for all specimens as discussed in Section 5.8 and was validated by the recorded concrete gage

data from Specimen 1 (Figure 7-28c). The measured core concrete strain in this direction was nearly unchanged in Specimens 2 and 4 throughout the experimental load tests (Figure 7-29c and Figure 7-30c), which might be attributed to the development of faulty gages during specimens' exposure. Note that the FEA results showed strain increases in tension in the out-of-plane direction at such locations of the failure beam-column joint for all specimens (Figure 7-28c, Figure 7-29c and Figure 7-30c).

Comparable compressive stress distributions of the concrete under peak load were observed in each specimen in the FEA approach. Figures 7-31 and 7-32 present the FEA results of the concrete compressive stress distribution in the STM struts under peak load in the doubly reinforced end of Specimen 1 in the concrete cover region and in the middle of specimen width, respectively. As aforementioned, the overall structural behavior of the singly reinforced bent in Specimen 1 was also simulated using FEA approach. The compressive stress distribution of concrete in the STM struts under peak load for this case are shown in Figures 7-33 and 7-34, respectively, for the concrete cover region and the middle of specimen width. In general, for both doubly and singly reinforced ends of all specimens, the compressive stresses in the struts of the beam and column regions had comparable magnitudes and distribution patterns (Figure 7-31 through Figure 7-34).

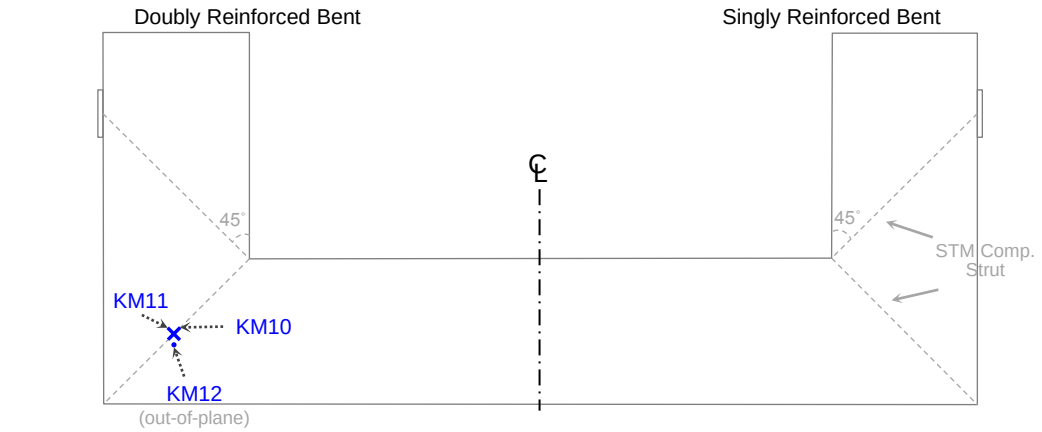

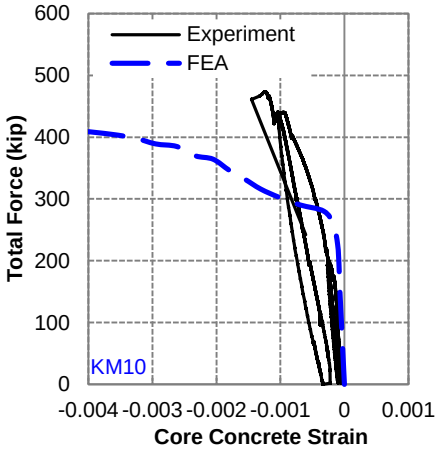

(a) Compression Strain in Strut

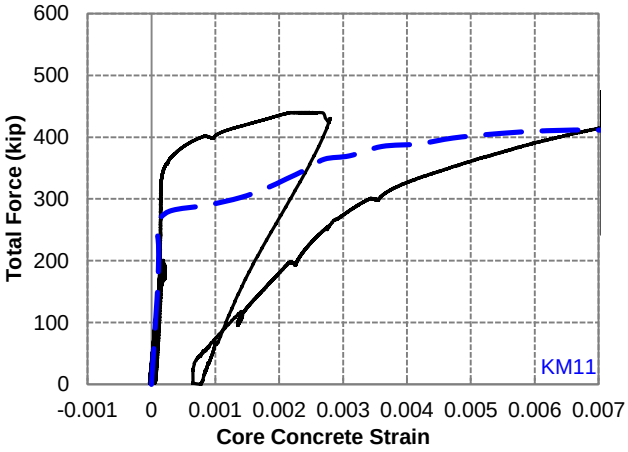

(b) Strain Perpendicular to Strut

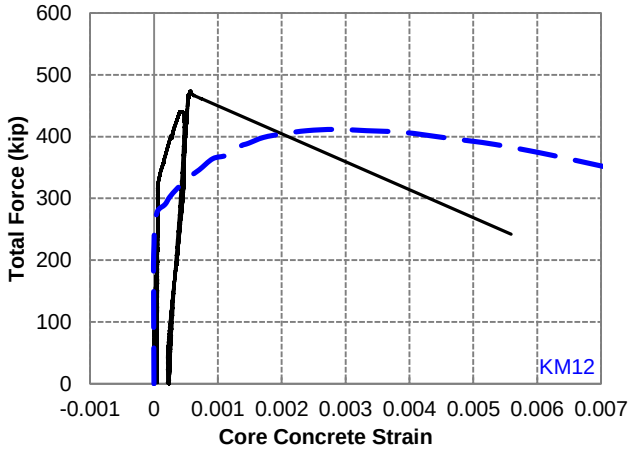

(c) Out-of-Plane Strain

Figure 7-28 Strains in STM Strut at Failure Beam-Column Joint – Specimen 1

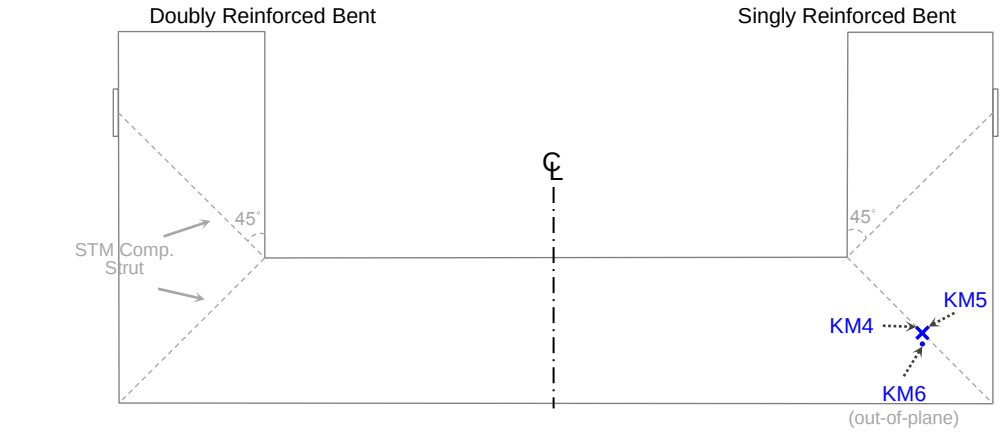

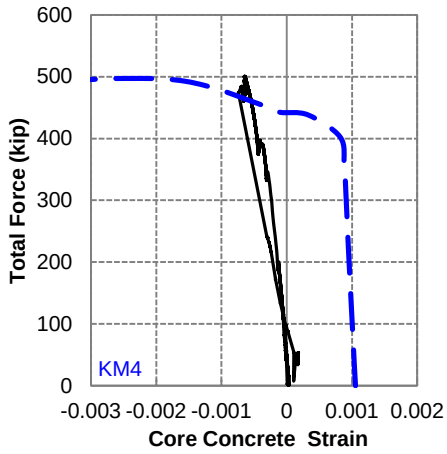

(a) Compression Strain in Strut

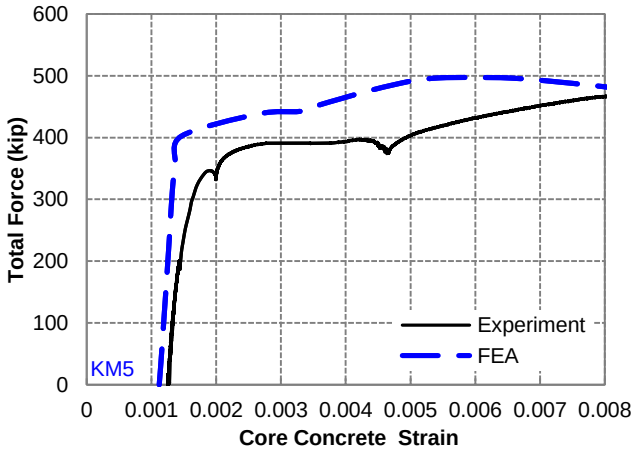

(b) Strain Perpendicular to Strut

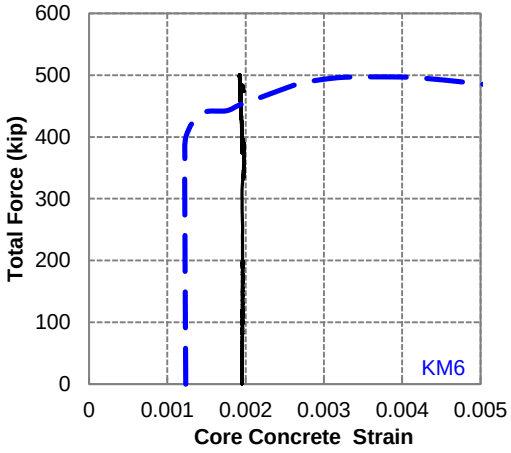

(c) Out-of-Plane Strain

Figure 7-29 Strains in STM Strut at Failure Beam-Column Joint – Specimen 2

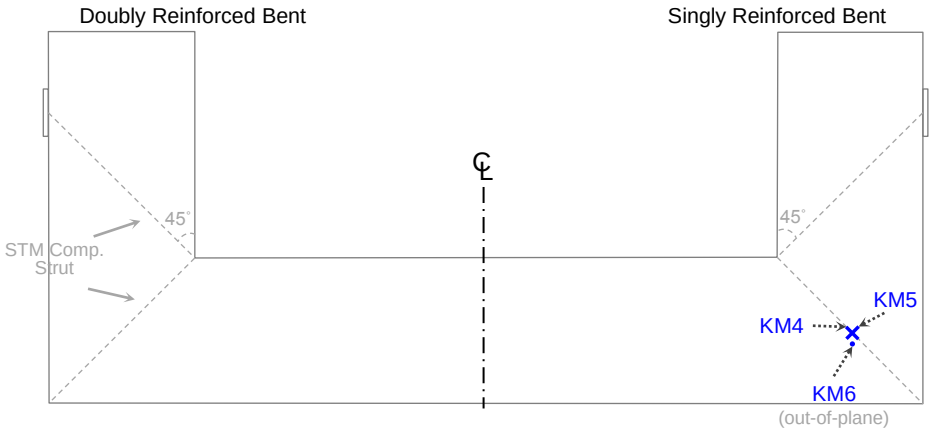

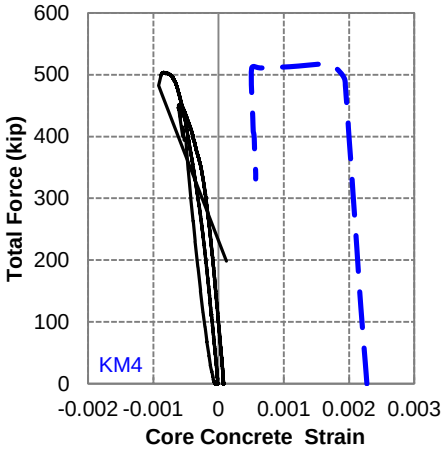

(a) Compression Strain in Strut

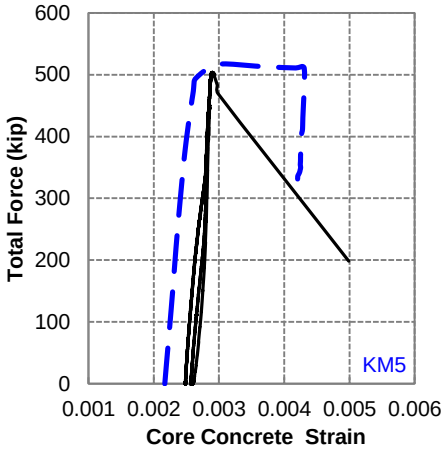

(b) Strain Perpendicular to Strut

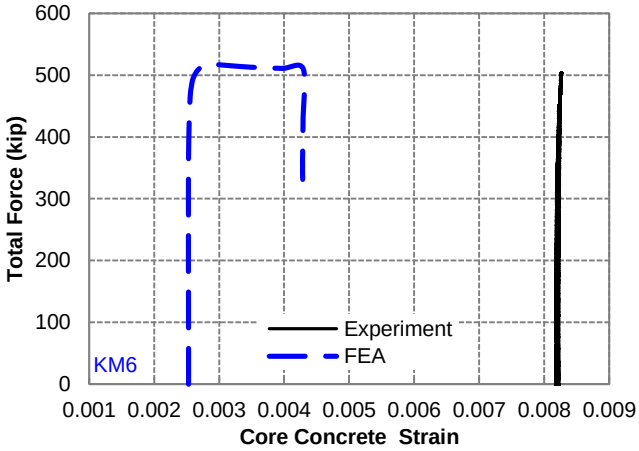

(c) Out-of-Plane Strain

Figure 7-30 Strains in STM Strut at Failure Beam-Column Joint – Specimen 4

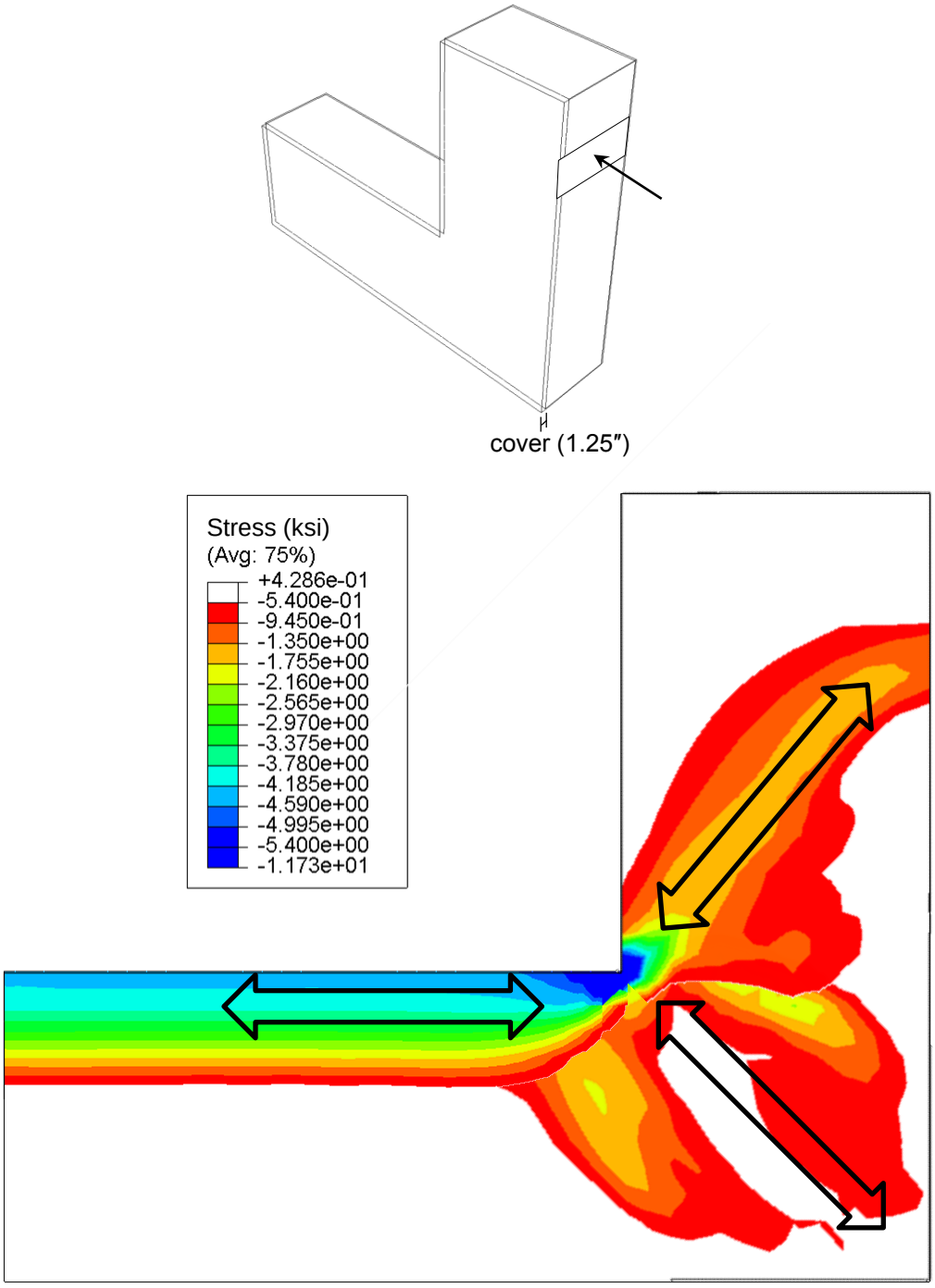

Figure 7-31 Compressive Stress Distribution in STM Struts under Peak Load in Doubly Reinforced End of Specimen 1 in Concrete Cover Region

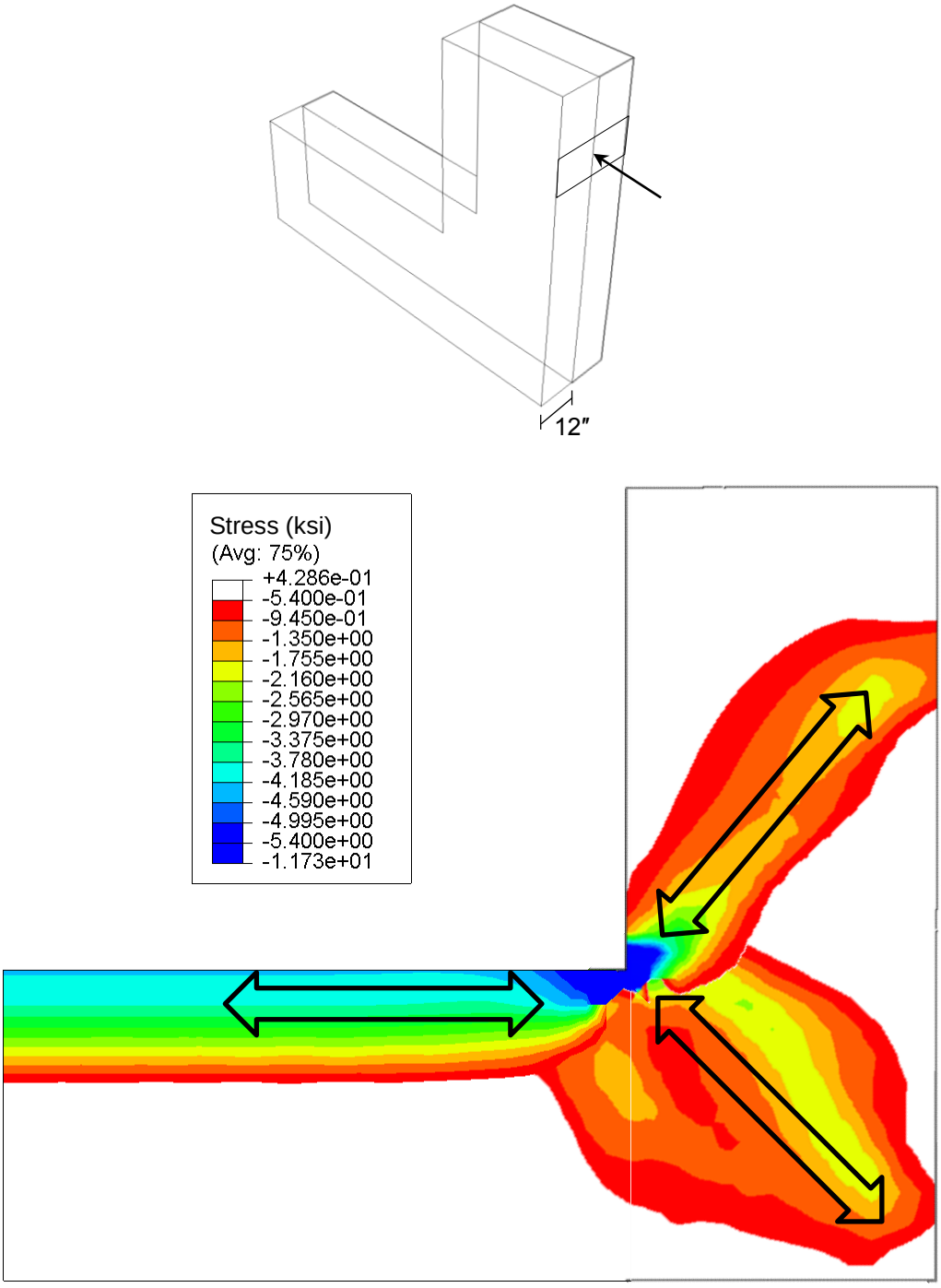

Figure 7-32 Compressive Stress Distribution in STM Struts under Peak Load in Doubly Reinforced End of Specimen 1 in Middle of Specimen Width

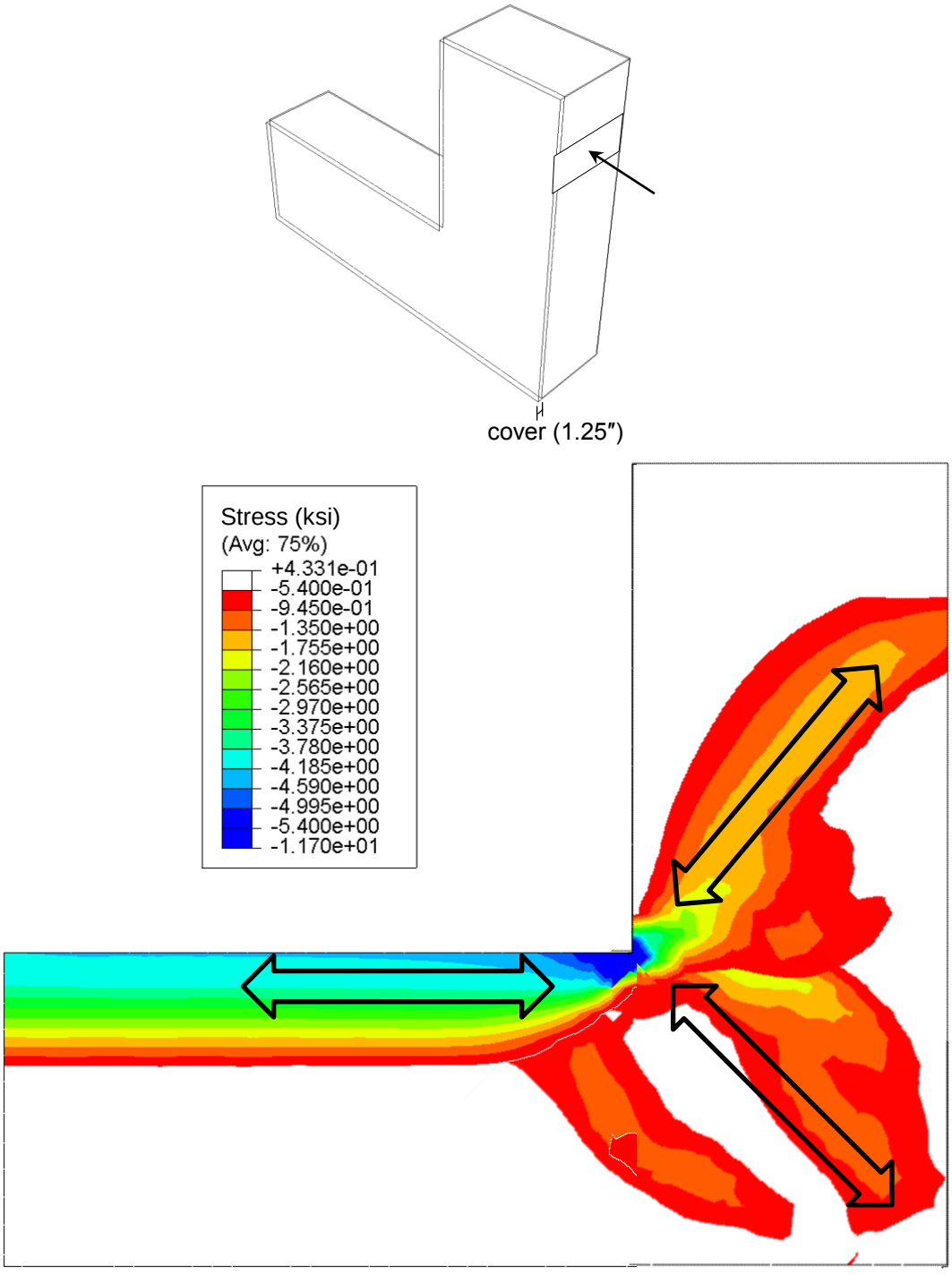

Figure 7-33 Compressive Stress Distribution in STM Struts under Peak Load in Singly Reinforced End of Specimen 1 in Concrete Cover Region

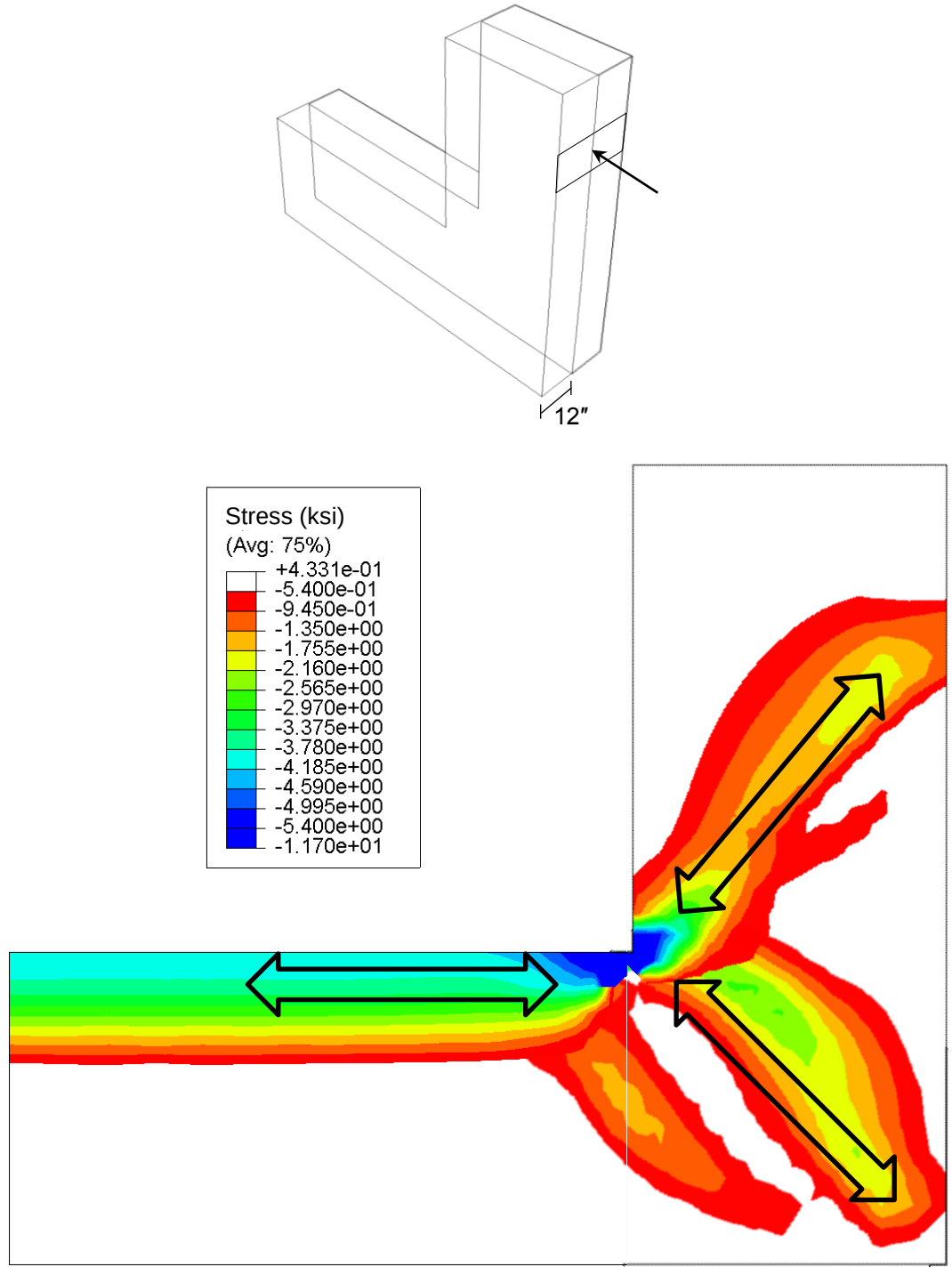

Figure 7-34 Compressive Stress Distribution in STM Struts under Peak Load in Singly Reinforced Bent of Specimen 1 in Middle of Specimen Width

For the singly reinforced end, greater magnitudes of compressive stresses were observed at the middle of specimen width than those at the cover region (Figures 7-33 and 7-34). Moreover, it was found that compressive stress flows in the strut at the joint region were separated into two groups (Figures 7-33 and 7-34). Similar compressive stress distribution pattern of the concrete in the strut region of the joint in the concrete cover region was found near the doubly reinforced end (Figure 7-31). Nevertheless, the compressive stress pattern of concrete in the middle of specimen width appeared to be more uniform (Figure 7-32). Moreover, the magnitudes of compressive stresses at such locations in the doubly reinforced end were generally less than those in the singly reinforced end. This may suggest that the greater amount of compression steel which continued through the joint region tended to distribute the strut load more uniformly throughout the joint width.

7.6.4 Out-of-Plane Behavior

As discussed in Section 5.8, out-of-plane behavior was observed in the beam-column joint through the structural load tests in all specimens that were tested to failure. Therefore, one of the objectives of the three-dimensional FEA conducted in this research was to investigate the influence of such behavior on the failure of the beam-column joint region.

Since comparable amounts of out-of-plane deformations under peak load were observed experimentally in each specimen tested to failure, analysis for Specimen 1, the doubly reinforced bent section, is used below.

Figures 7-35 and 7-36 present the out-of-plane strains at peak load in the doubly reinforced bent of Specimen 1 in the concrete cover region and middle region of the specimen width, respectively. The figures show that a significant amount of out-of-plane strains were concentrated in the beam-column joint region. In addition, the maximum out-of-plane strain at the middle of specimen width in the joint region was found to be approximately 25% greater than that in the cover region. The results also show that strains in the middle of specimen width were concentrated at the center of the beam-column joint, which differed from those in the cover region. Note that the strain concentration at the outside corner of the beam-column joint may imply the significant localized cracking of the concrete at this location, which may lead to the loss of support for the compression strut in the CTT node region, especially that carried by arch action from C-STM.

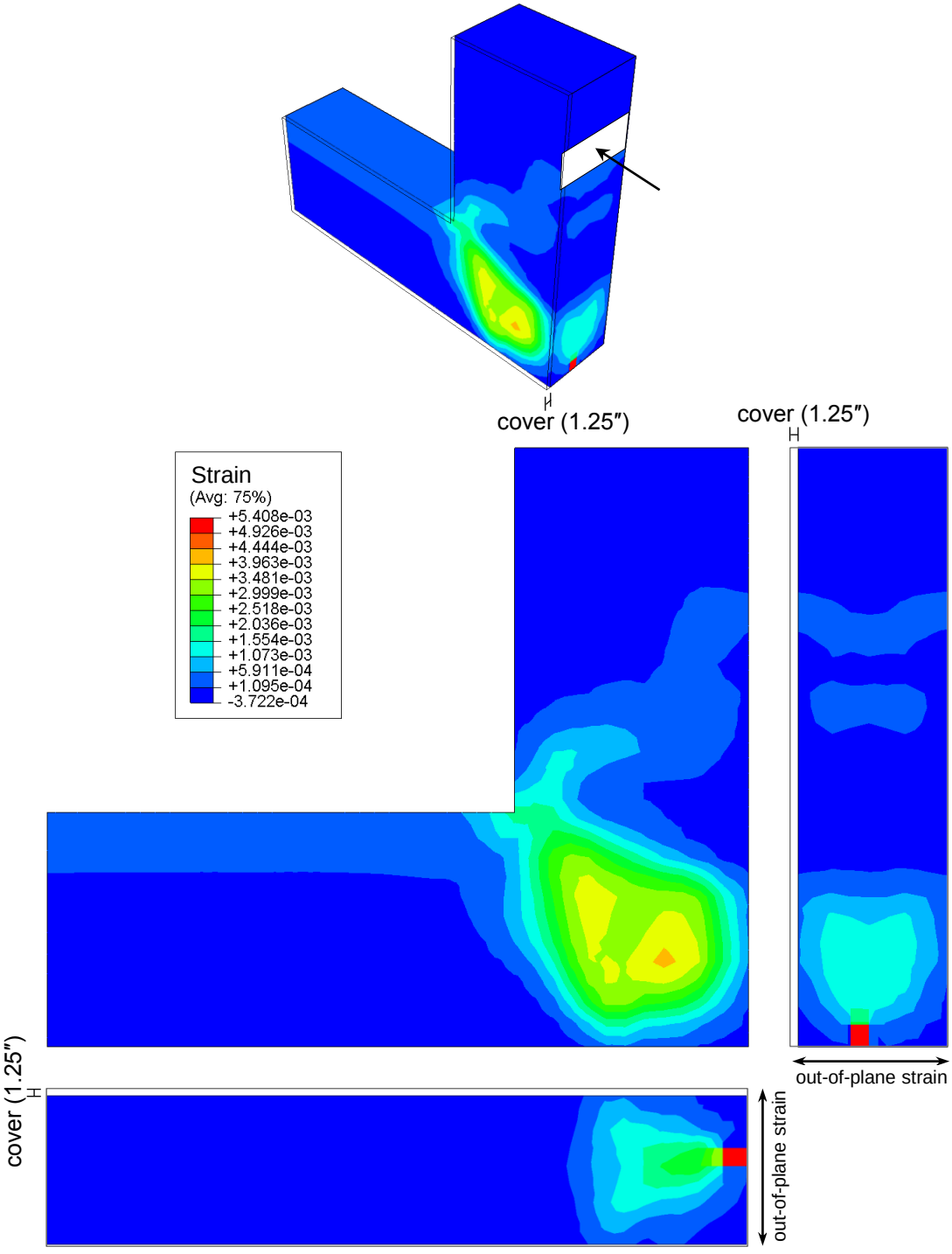

Figure 7-35 Out-of-Plane Strains of Concrete under Peak Load in Doubly Reinforced Bent of Specimen 1 in Concrete Cover Region

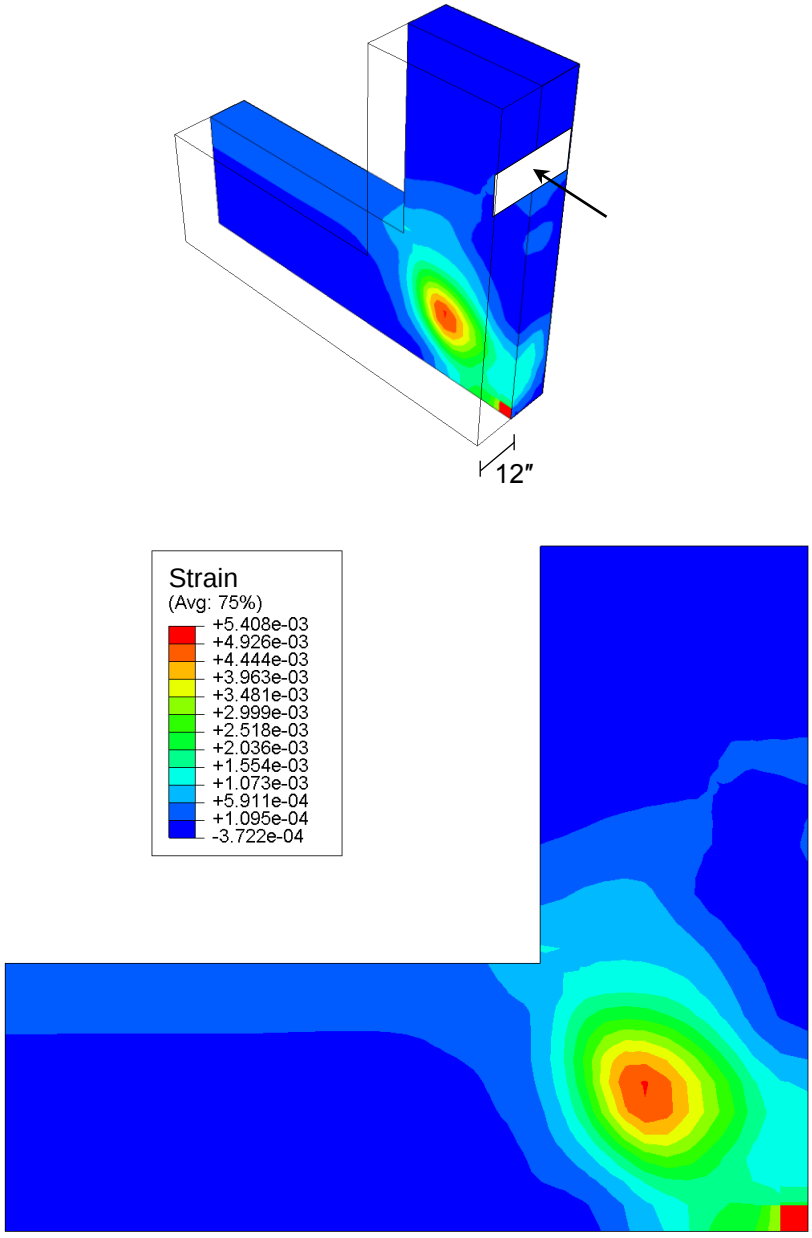

Figure 7-36 Out-of-Plane Strains of Concrete under Peak Load in Doubly Reinforced Bent of Specimen 1 in Middle of Specimen Width

Figure 7-37 shows the magnitudes of the out-of-plane strains of concrete under peak load obtained from the same numerical model in the concrete cover region and middle of specimen width. In the concrete cover region, the magnitudes of the out-of-plane strains were found to be approximately the same through the STM strut, while those at the middle of specimen width appeared to be in an arch-shaped distribution. These different types of behavior in the concrete cover region and middle of specimen width of the beam-column joint were also taken into account and referred to as truss and arch action in the C-STM approach, as discussed in Section 2.4.3 (Mander et al. 2012; Scott et al. 2012a and 2012b). Furthermore, the figure again shows that large out-of-plane strains were observed near the outside corner of the beam-column joint in the middle of specimen width.

Figure 7-38 shows the out-of-plane deformations of concrete under peak load in the doubly reinforced end of Specimen 1 at the concrete surface and at one-quarter of specimen width. The results show a large concentrated deformation in the out-of-plane direction at the center of the beam-column joint at the concrete surface and a less pronounced out-of-plane deformation at one-quarter of specimen width. The deformations gradually accumulate from the middle of specimen width toward the concrete surface at the center of the STM strut in the joint region. This mechanism numerically demonstrates the potential for out-of-plane bursting of the diagonal strut within the beam-column joint. This joint failure mode was observed in each of the specimens that were tested to failure as discussed in Section 5.8.

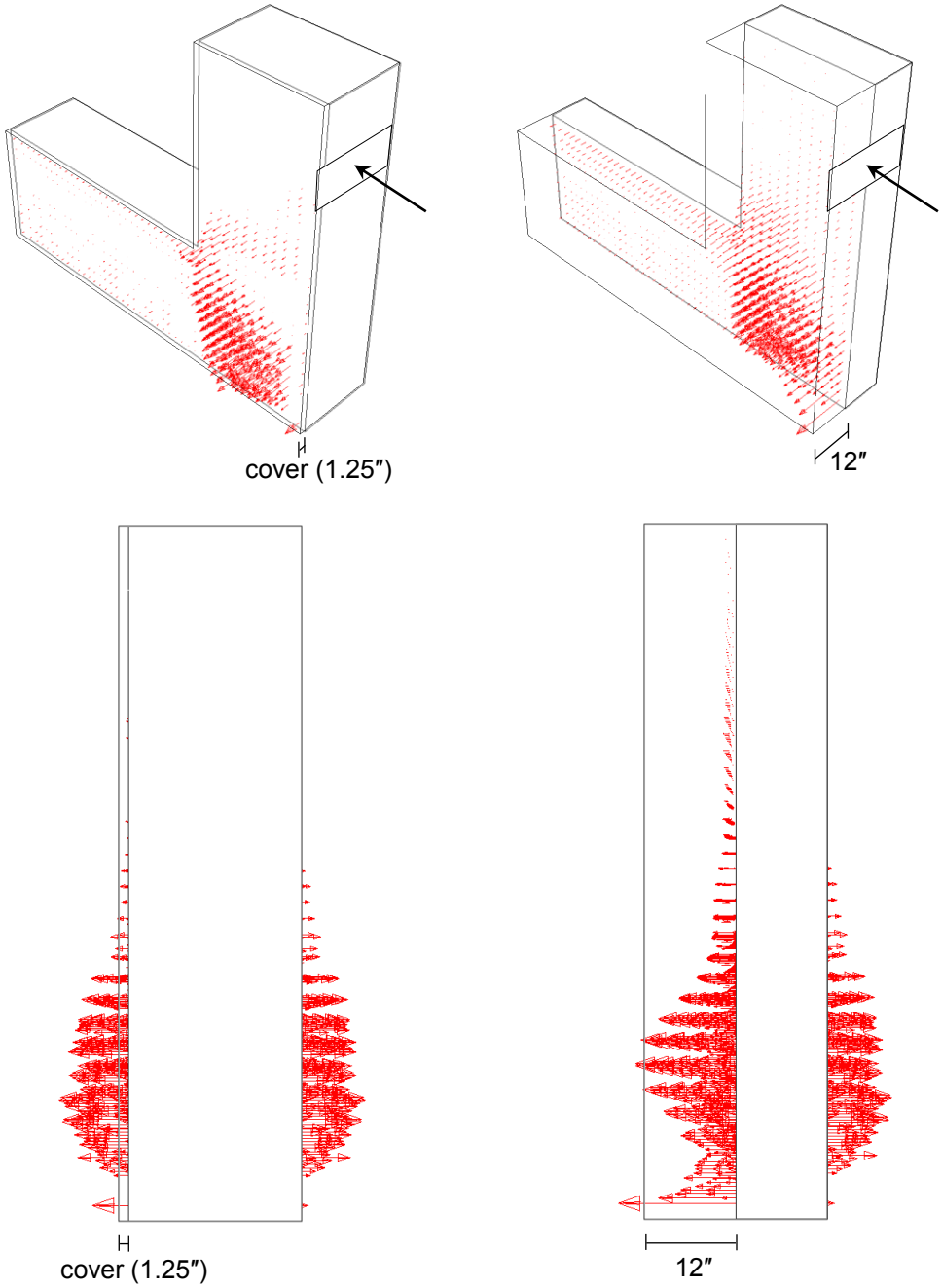

(a) Cover Region *(b) Middle of Specimen Width*

Figure 7-37 Magnitudes of Out-of-Plane Strains of Concrete under Peak Load in Doubly Reinforced End of Specimen 1 at Different Widths

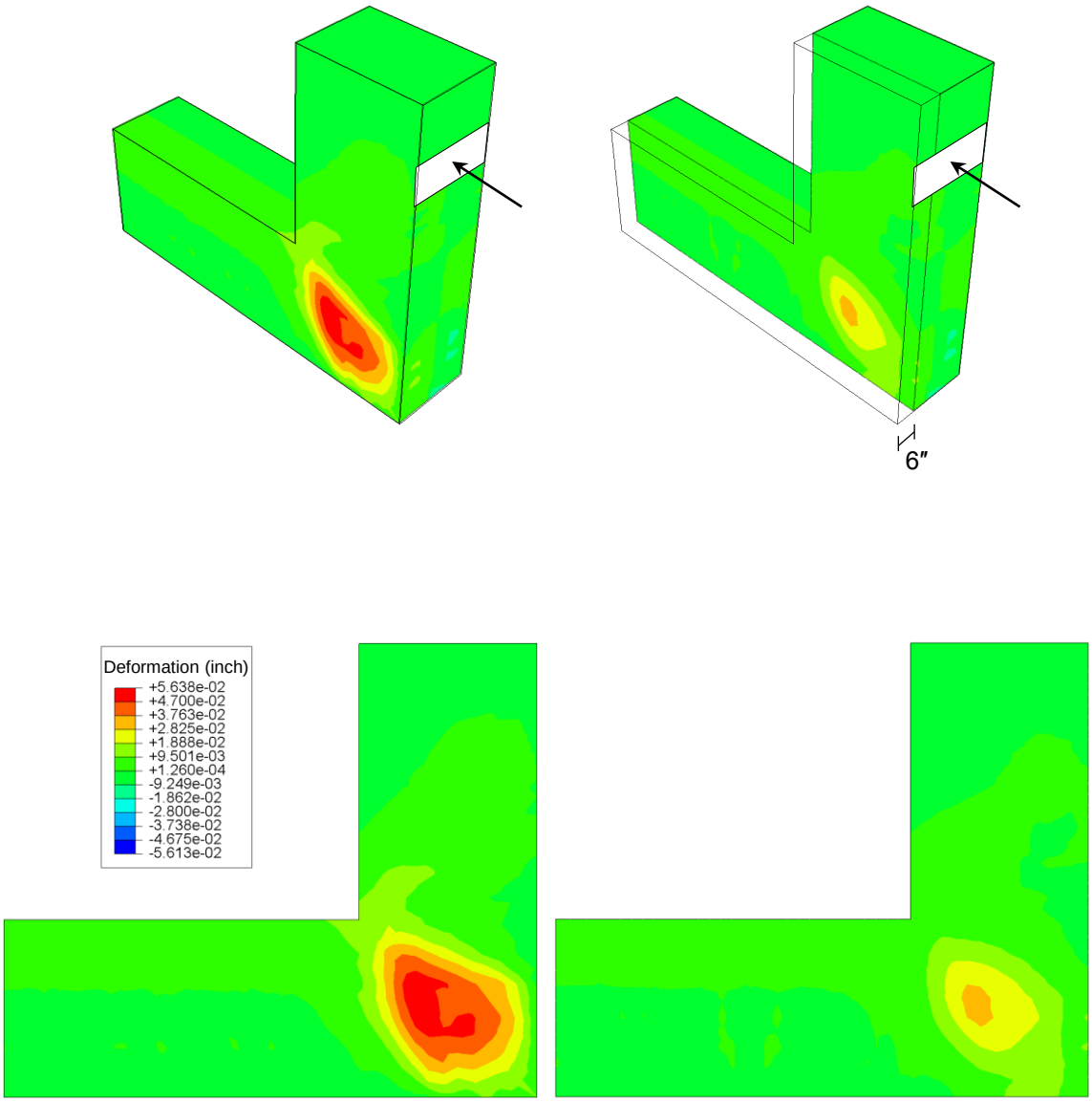

(a) Concrete Surface *(b) One-Quarter Specimen Depth*

Figure 7-38 Out-of-Plane Deformations of Concrete under Peak Load in Doubly Reinforced Bent of Specimen 1 at Different Widths

Additionally, the FEA numerical results of Specimens 2 and 4 show that out-of-plane strains developed on the beam and column faces in the joint region (Figure 7-39), which was validated by the experimental measured results as presented in Section 5.8. However, the out-of-plane strains on the column face of the joint region were significantly larger than the beam face. This can be attributed to the lack of sufficient restraint from the U-shaped joint reinforcing steel on the column face.

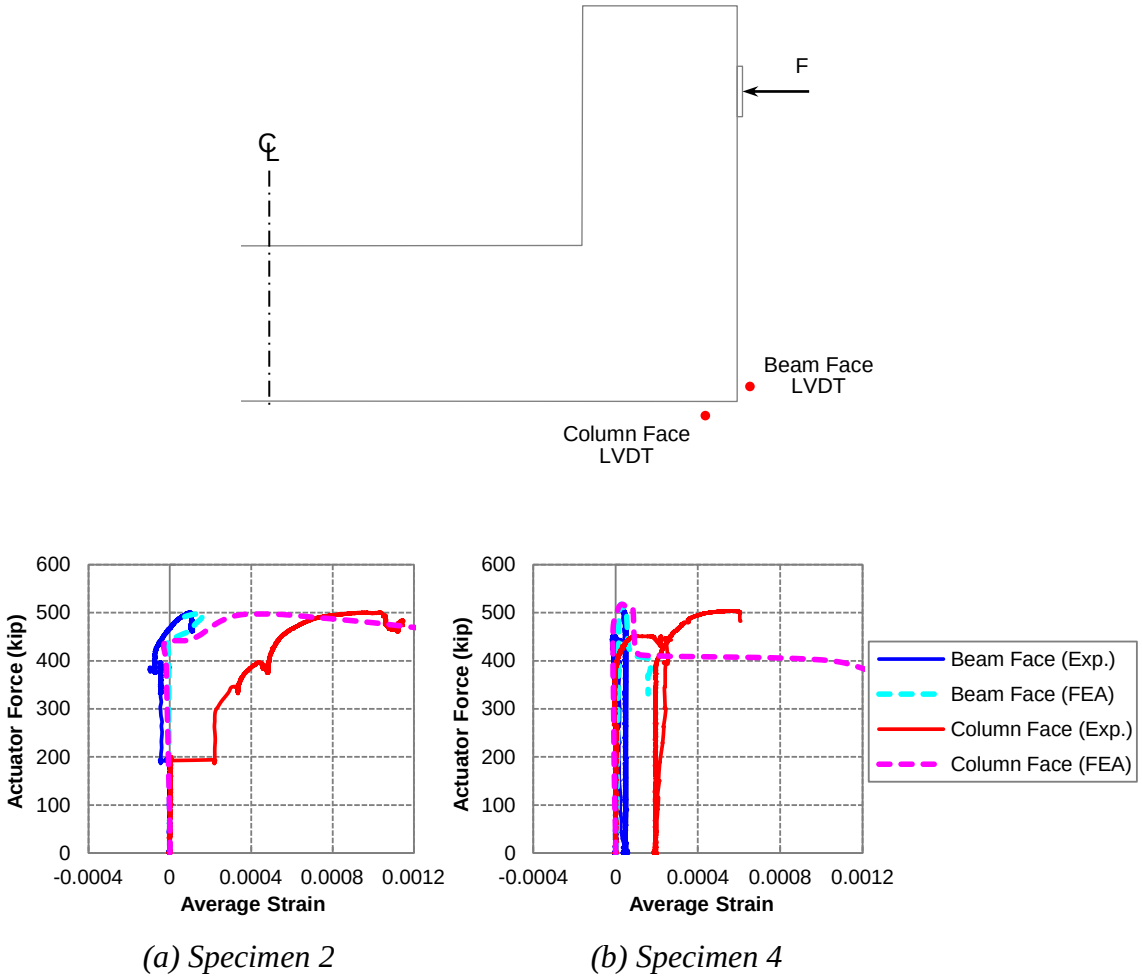

(a) Specimen 2 *(b) Specimen 4*

Figure 7-39 Comparisons of Out-of-Plane Strains at Joint Region from FEA and Experimental Results

7.7 DISCUSSION

7.7.1 Comparisons of FEA and STM

The compressive stress distribution under peak load at the middle of specimen width of the doubly reinforced end of Specimen 1 obtained from the FEA approach was compared to the idealized geometry of the strut-and-tie model that was used to assess the strength of the experimental specimen as discussed in Section 6.2.2 (Figure 7-40a).

In STM, the stress is idealized to be uniform on a given face of a node, as in this research the forces in the column strut were assumed to be uniformly distributed on the bottom face with the given width W_{CCC}^{c} in the CCC node. In the FEA, comparable compressive stress distributions near the CCC node were observed in both the doubly and singly reinforced bents, suggesting the same geometry for the CCC node regardless of the amount of compression steel (Figures 7-32 and 7-34). However, the results from the FEA approach show that larger stresses concentrate near the inside corner of the beam-column joint of the STM CCC node, which indicates that the strut forces are not uniformly distributed on the faces of the CCC node and the equivalent center of the CCC node is located closer to the inside column face compared to the STM approach. As a consequence of this mechanism, the difficulty to determine the geometry of the CCC node exists. In addition, this mechanism potentially results in crushing of the cover concrete at the inside corner of the joint region, which was observed and validated in the testing of all specimens as discussed in Section 5.8.1. However, the crushing of the cover concrete in such region was not the primary cause for the failure of the specimen since the specimen was able to redistribute the loading after the cover concrete crushed.

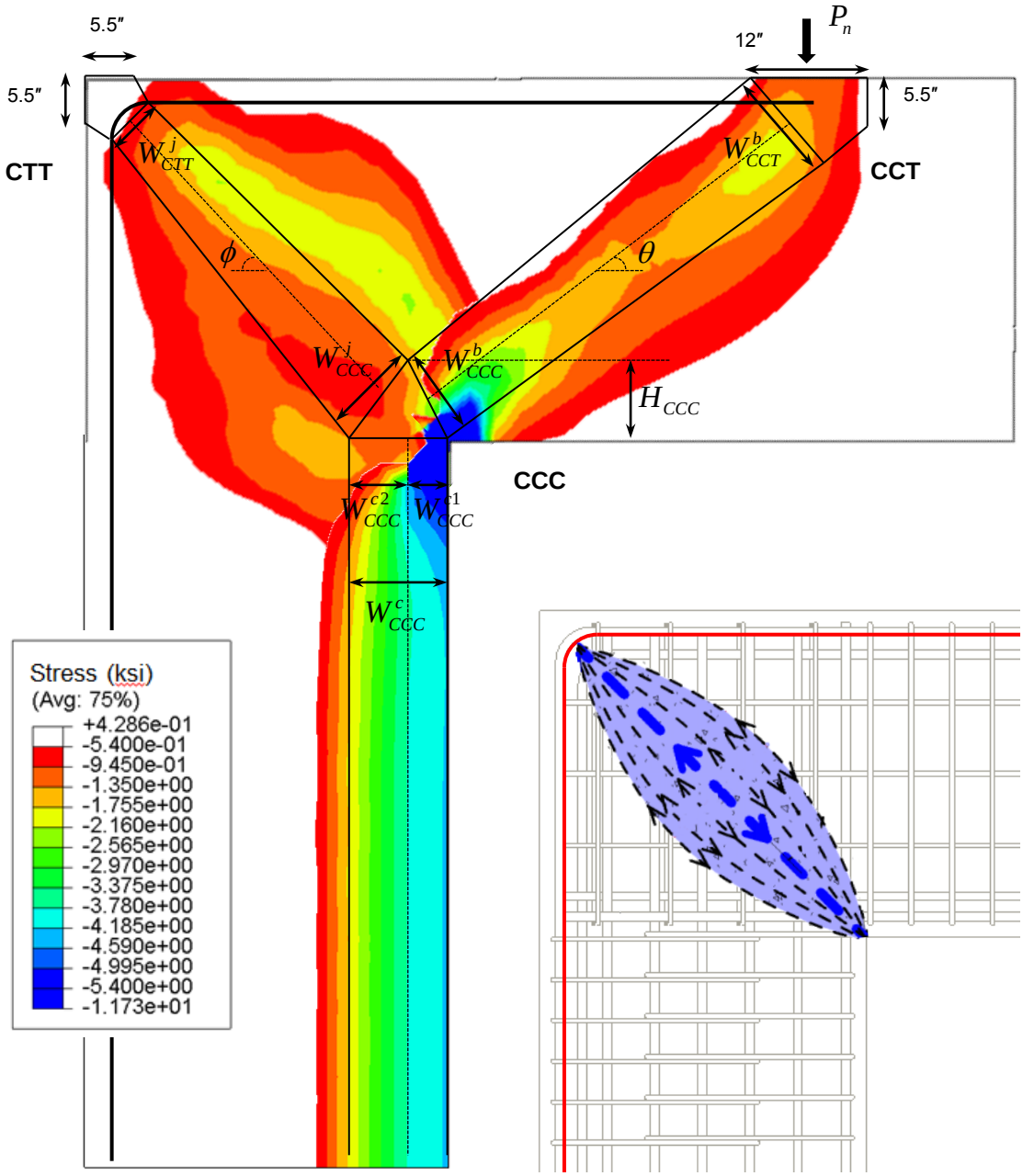

(a) Compressive Stress Distribution with Idealized Strut-and-Tie Model

(b) Arch Action in Beam-Column Joint

Figure 7-40 Comparisons of Compressive Stress Distribution of Concrete from FEA and Idealized Strut-and-Tie Model (Figure b Adapted from Mander et al. [2012])

A critical region of the specimen was near the CTT node, which relied on the bend radius of the continuing tension longitudinal reinforcing steel. It was observed that the load was not distributed to the cover concrete outside the reinforcing steel bend at the outside joint corner and the strut-to-node interface was the critical face for this node. Thus, if insufficient support of the CTT node is provided, this might cause sudden failure in the joint region due to the lack of support for the strut forces.

For the CCT node near the loading point, the nodal geometry used in STM was found to be comparable to the FEA results.

In general, the widths of the strut-to-node interfaces of each node and the bottom face of the CCC node were larger from the FEA results compared to the STM geometry used in this research. Note that the critical face of each node as per different design methods was typically the strut-to-node interface of each node and the bottom face of the CCC node for the model of the experimental specimen as discussed in Section 6.2 (Table 6-2). The larger widths of the critical face obtained from FEA indicated that the nodal strength was potentially higher than the code-based nodal strength. That is, the code-based calculations using STM yielded conservative results. However, as abovementioned, larger stresses were concentrated at the inside corner of the beam-column joint, implying that the nodal stresses are not uniform. For the beam region, the prismatic strut used in STM corresponded to the compressive stress distribution obtained from FEA quite well. However, in the beam-column joint, the distribution of compressive stresses in the strut appeared to be arch-shaped, which indicated arch action in such strut (Figure 7-40b).

As discussed in Section 2.4.2, ACI 318-08 (2008) provides different efficiency factors to assess the strength of a strut in STM according to the shape of the strut and the amount of reinforcement across such strut. Moreover, AASHTO LRFD (2010) incorporates the tensile strain in the direction of the tension tie and the angle between the compressive strut and adjoining tension ties to determine the efficiency factor of the strut in STM. However, the compressive strength of a strut is generally presented as the efficiency of the strut-to-node interface in a node intersected by the strut where the highest stress occurs. Thus, the mechanisms of cracking and splitting of a strut are rather unclear using STM.

7.7.2 Principal Strains

Figures 7-41 and 7-42 show the maximum principal strains of concrete at peak load in the doubly reinforced bent of Specimen 1 in the cover region and middle of specimen width, respectively. Comparable distribution patterns of the maximum principal strains are observed at the different depths. Note that some discontinuous distribution of maximum principal strains at the middle of specimen width is located at the interface between concrete elements in the joint region close to the outside column face. This may be caused by the nature of the constitutive relations of concrete in tension used for this case (Eq. [2-34]) which has a sudden drop in tensile strength after concrete cracking, leading to a discontinuity between the elements at local regions. Figure 7-43 depicts the directions of the maximum principal strains of concrete at the middle of specimen width and shows the opening directions of potential cracking for the same numerical model as aforementioned. For the constitutive relation of concrete in

tension used (Eq. [2-34]), the concrete cracking strain was calculated as 1.32×10^{-4} (Figure 7-2a). Although the effects of concrete cracking were smeared into the constitutive relation for the elements representing concrete in the numerical simulations, the results show the potential for significant cracking perpendicular to the STM strut in the joint region. Thus the STM strut forces must be redistributed throughout the joint or else the joint may fail by an out-of-plane splitting mechanism. Moreover in the experimental testing, some cracking was also observed in the beam and column regions. The cracking in the beam region was typically perpendicular to the diagonal STM strut, while that in the column region was primarily due to bending and aligned with the transverse hoops as shown in Figure 7-42. Note that some out-of-plane strains were also observed at the outside corner of the beam-column joint, indicating the potential opening of concrete that may further lead to losing support of the STM CTT node for the forces in the diagonal STM strut in the joint region. This mechanism was validated by the experimental observations in the load tests of all specimens, as discussed in Section 5.8.

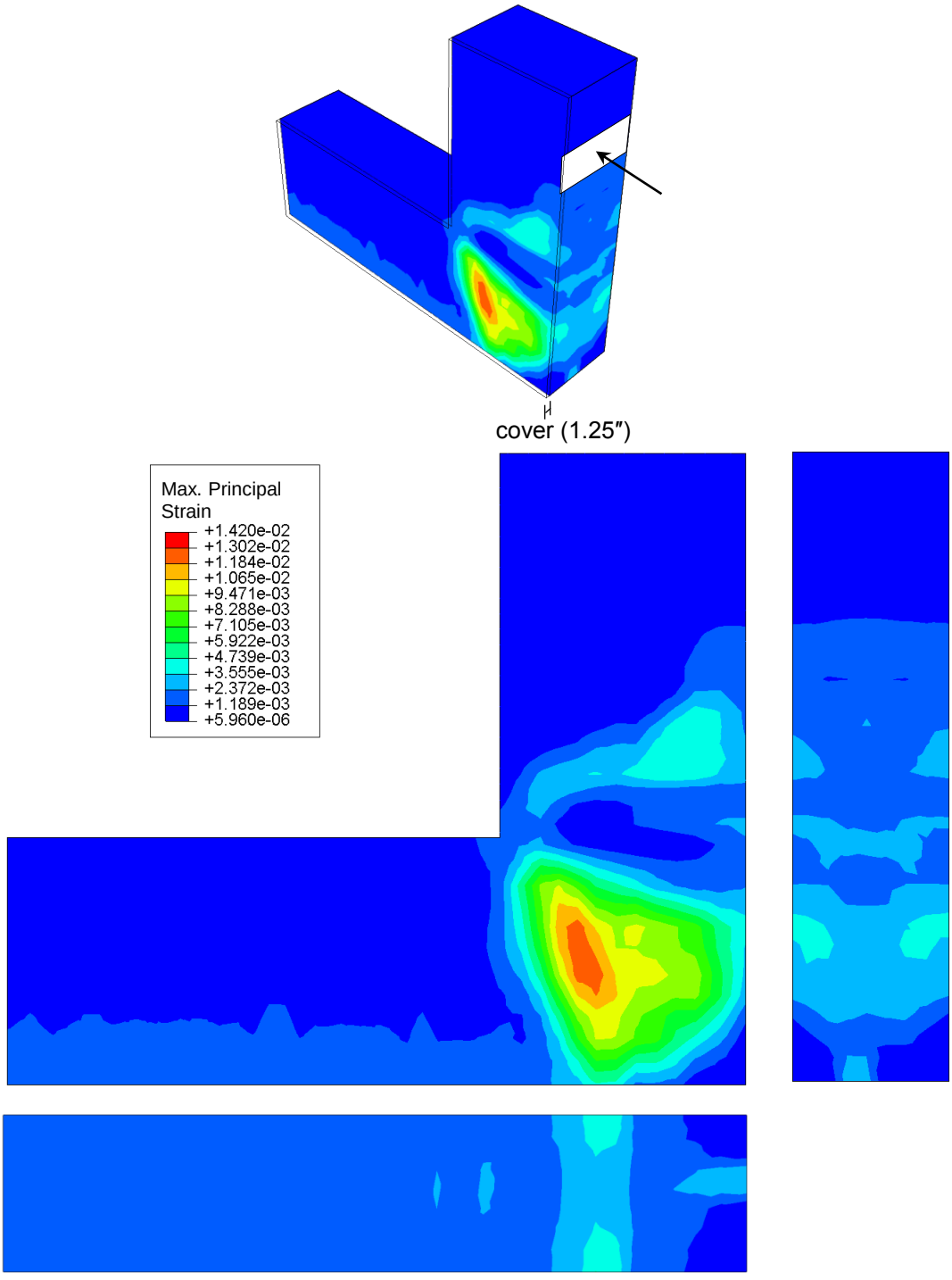

Figure 7-41 Maximum Principal Strains of Concrete under Peak Load in Doubly Reinforced Bent of Specimen 1 in Concrete Cover Region

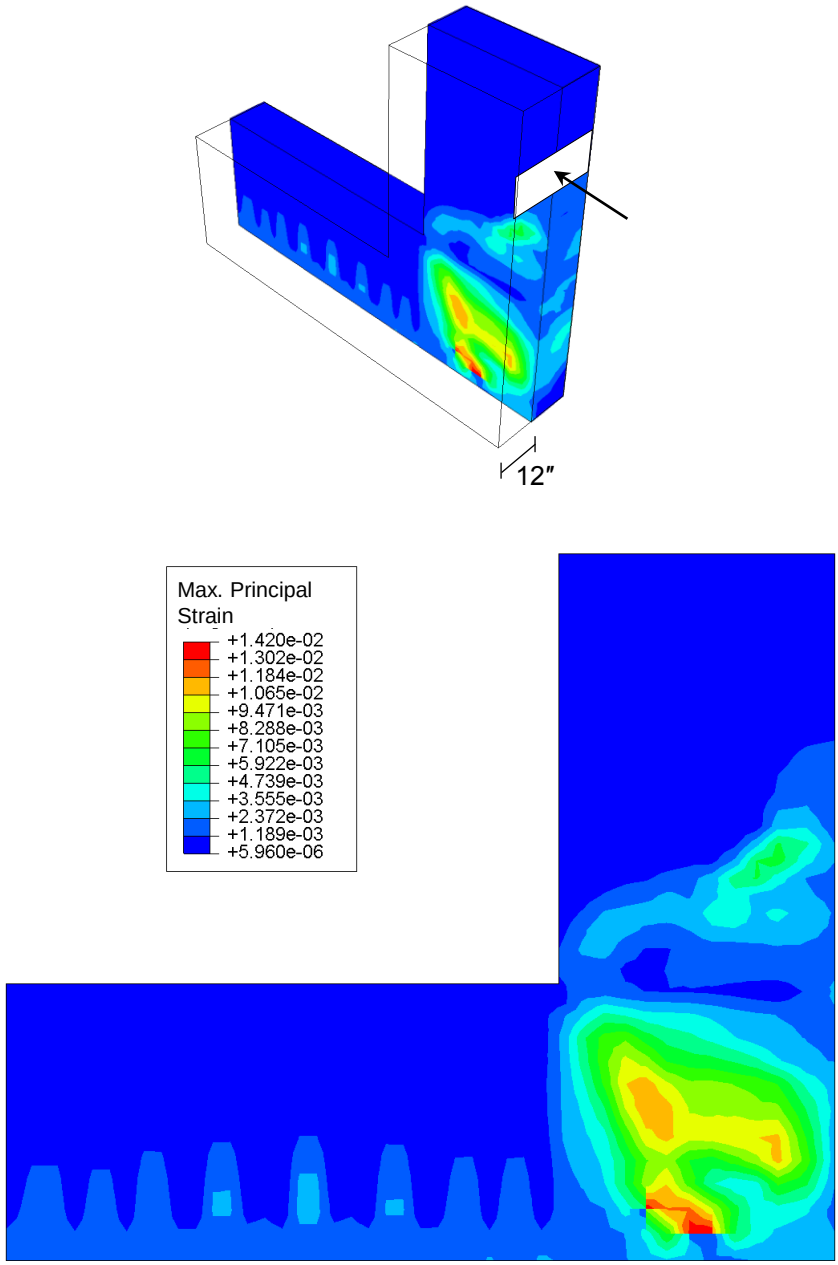

Figure 7-42 Maximum Principal Strains of Concrete under Peak Load in Doubly Reinforced Bent of Specimen 1 in Middle of Specimen Width

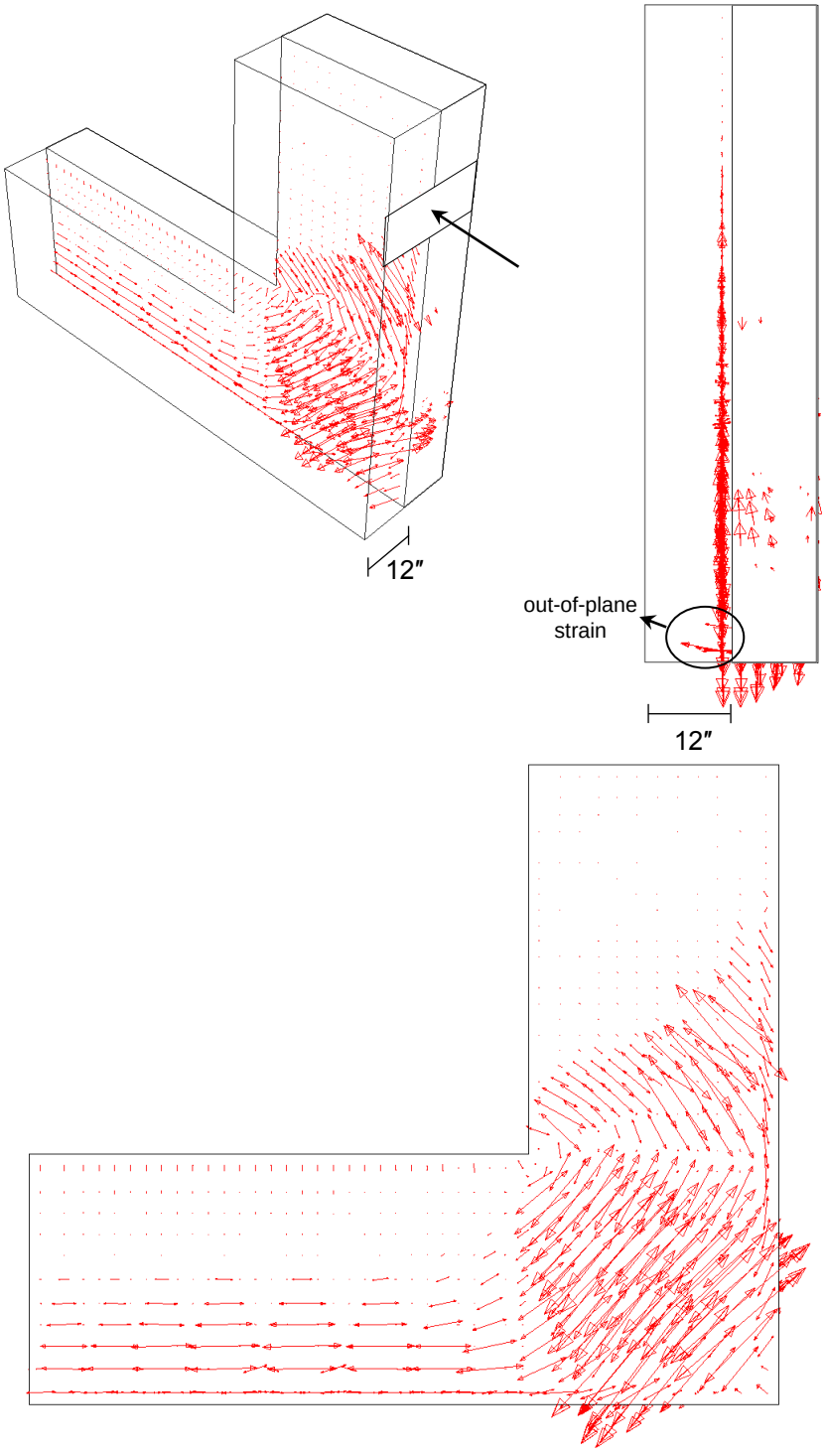

Figure 7-43 Directions of Maximum Principal Strains of Concrete under Peak Load in Doubly Reinforced Bent of Specimen 1 in Middle of Specimen Width

Figures 7-44 and 7-45 highlight the minimum principal strains of concrete under peak load of the doubly reinforced end of Specimen 1 in the concrete cover region and middle of specimen width, respectively. Comparable strain distribution patterns of the minimum principal strains are observed at different widths. Note that the strain at the concrete compressive strength (ε_{c0}) in the model was defined as -0.002 (negative value for compressive strain) (Figure 7-2a). The distribution of the minimum principal strains approximately aligned with the diagonal STM struts in both the beam and beam-column joint regions, but that in the joint region appeared to be arch-shaped. Moreover, concentrated compressive strains exceeded ε_{c0} at the center of the beam-column joint (center of the STM strut), regardless of depth. This may validate the bursting of the concrete strut in such regions that was observed in the load tests for all specimens as discussed in Section 5.8. Figure 7-46 shows the directions of the minimum principal strains of concrete in the middle of specimen width for the same numerical model and outlines the flow directions of the compressive stresses in the STM struts. The figure shows that the compressive stress distribution in the joint region is arch-shaped, thus demonstrating the arch action in the STM strut. Note that the compressive stresses in the struts intersected at the STM CCC node close to the inside column face where a stress concentration was observed, as shown in Figure 7-40. This demonstrates the difficulty to define the geometry of the CCC node in STM approaches.

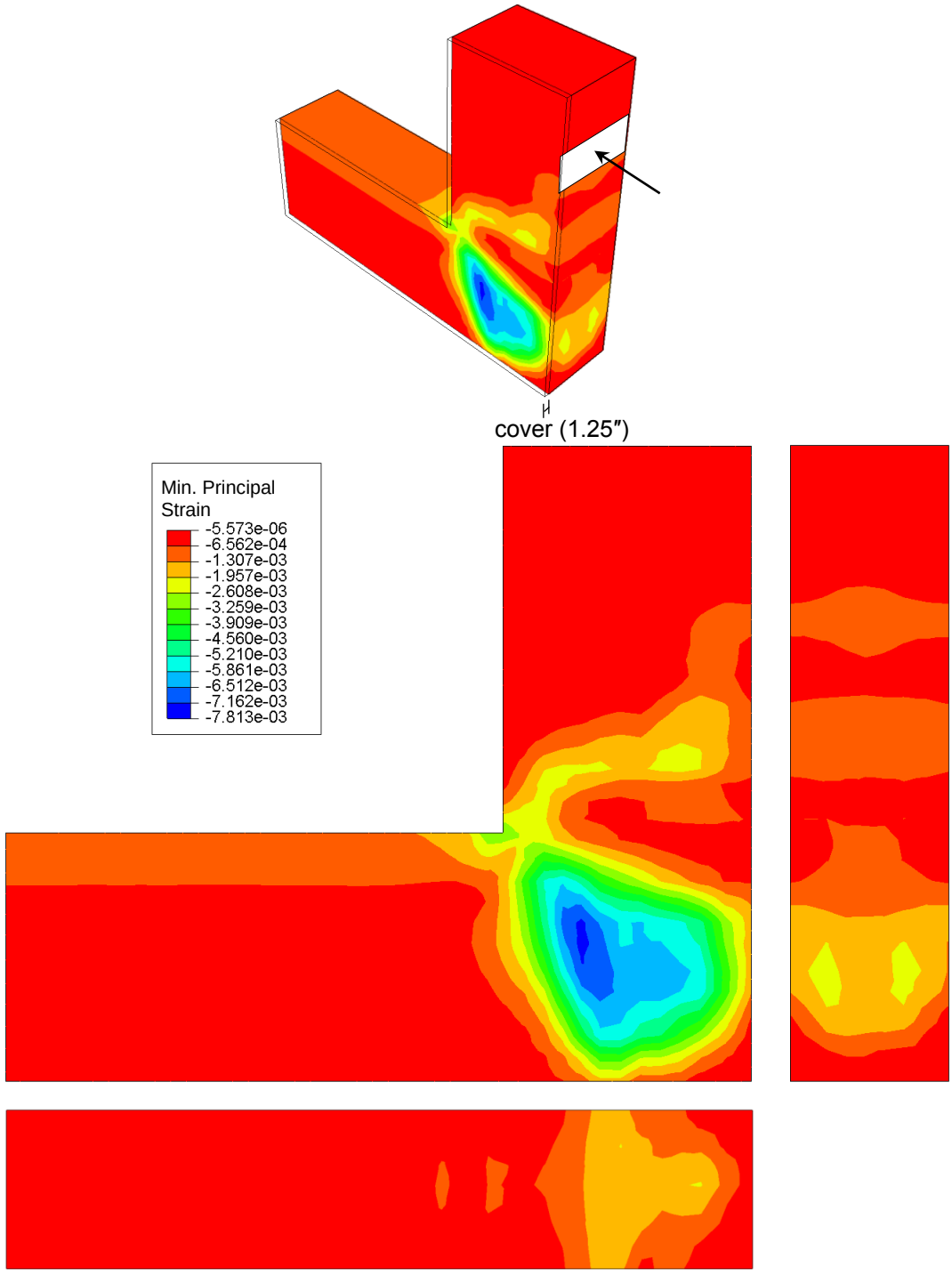

Figure 7-44 Minimum Principal Strains of Concrete under Peak Load in Doubly Reinforced Bent of Specimen 1 in Concrete Cover Region

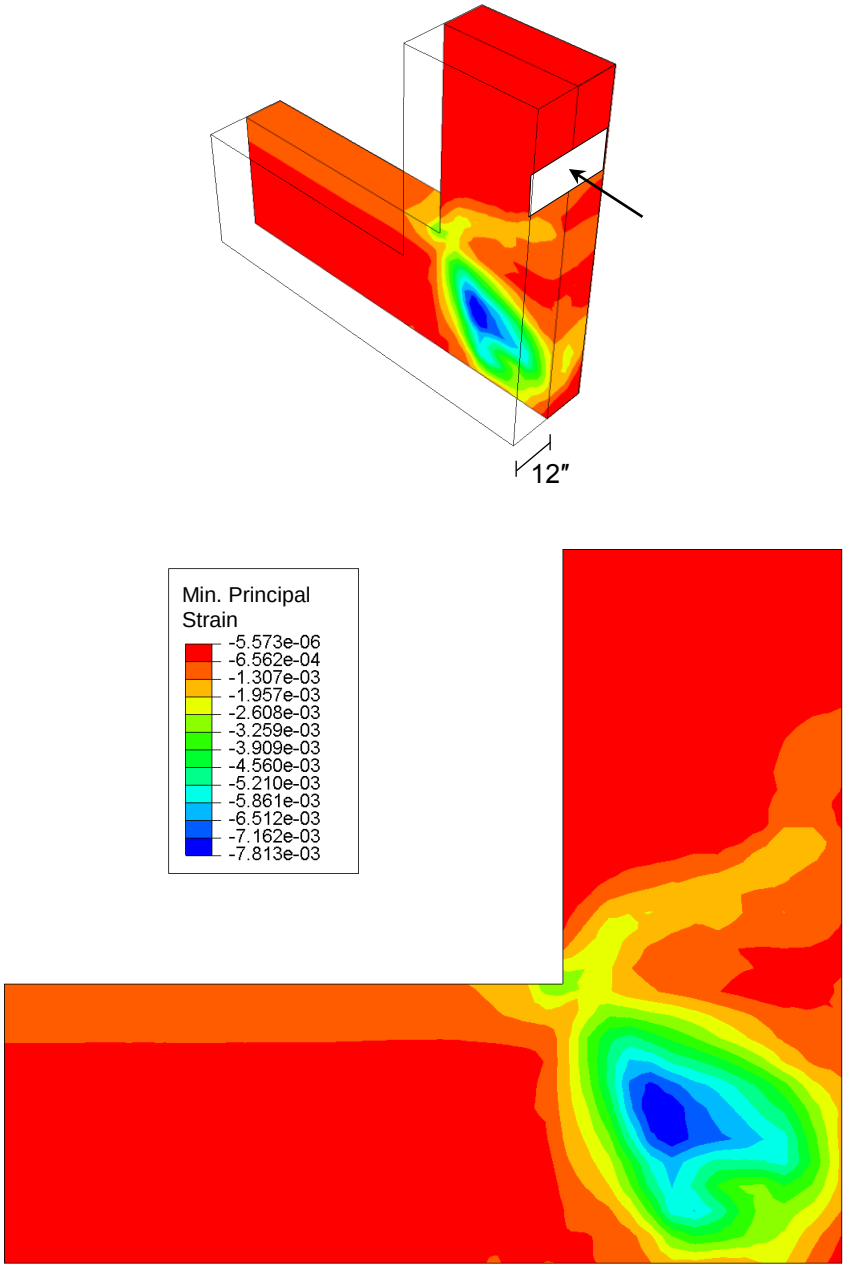

Figure 7-45 Minimum Principal Strains of Concrete under Peak Load in Doubly Reinforced Bent of Specimen 1 in Middle of Specimen Width

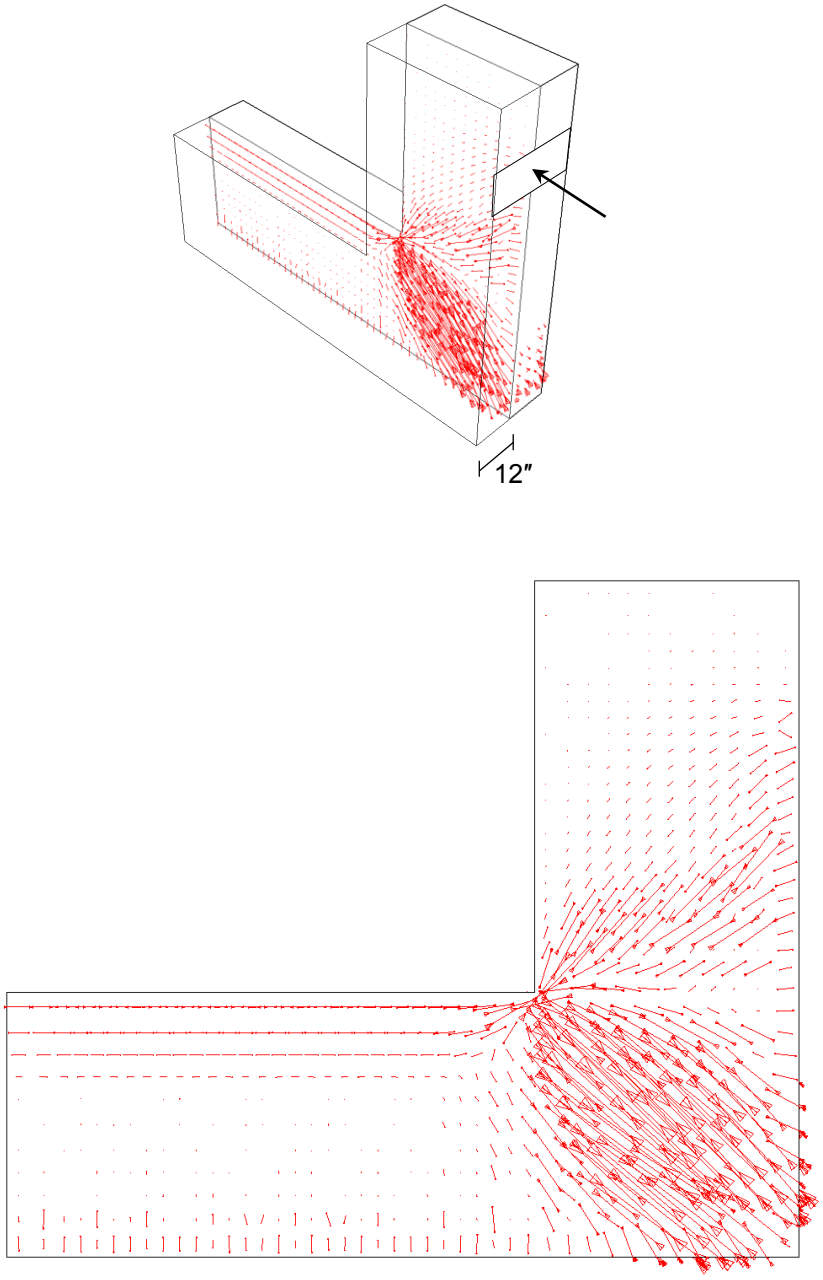

Figure 7-46 Directions of Minimum Principal Strains of Concrete under Peak Load in Doubly Reinforced Bent of Specimen 1 in Middle of Specimen Width

7.7.3 Comparisons of FEA and C-STM

As discussed in Section 2.4.3, compatibility-based strut-and-tie modeling (C-STM) consists of arch and truss actions (Mander et al. 2012; Scott et al. 2012a and 2012b). Arch action consists of a compressive stress field that forms the diagonal concrete strut, representing the center of the section (Figure 7-47a), while truss action engages the transverse reinforcement representing the remainder of the section outside the center region (Figure 7-47b). These two mechanisms work in parallel (Figure 7-47c) and displacement compatibility is taken into account at each node of the model (Figure 7-47d). To consider the ASR/DEF effects, prestressing forces were applied to the longitudinal and transverse reinforcement in the beam and column regions (Mander et al. 2012). Moreover, modified constitutive relations for the concrete (Mander et al. 1988) were utilized to take into account the confining effects of the transverse reinforcement due to the ASR/DEF expansion (Mander et al. 2012).

Figure 7-48 compares the analytical force-deformation relations obtained from FEA, C-STM, and experimental results. As discussed in Section 7.4.1 to minimize computational costs in FEA approach, only half of the experimental specimen was modeled in the numerical simulations in this research. Mander et al. (2012) constructed a compatibility strut and tie model of the entire C-shaped specimen and had the ability to investigate the overall structural behavior. However, it was found both experimentally and analytically that the overall behavior of the singly and doubly reinforced bent was nearly identical, as presented in Sections 5.7 and 7.6. Thus, the force-deformation

results from half of the specimen in C-STM were compared with the FEA and experimental results.

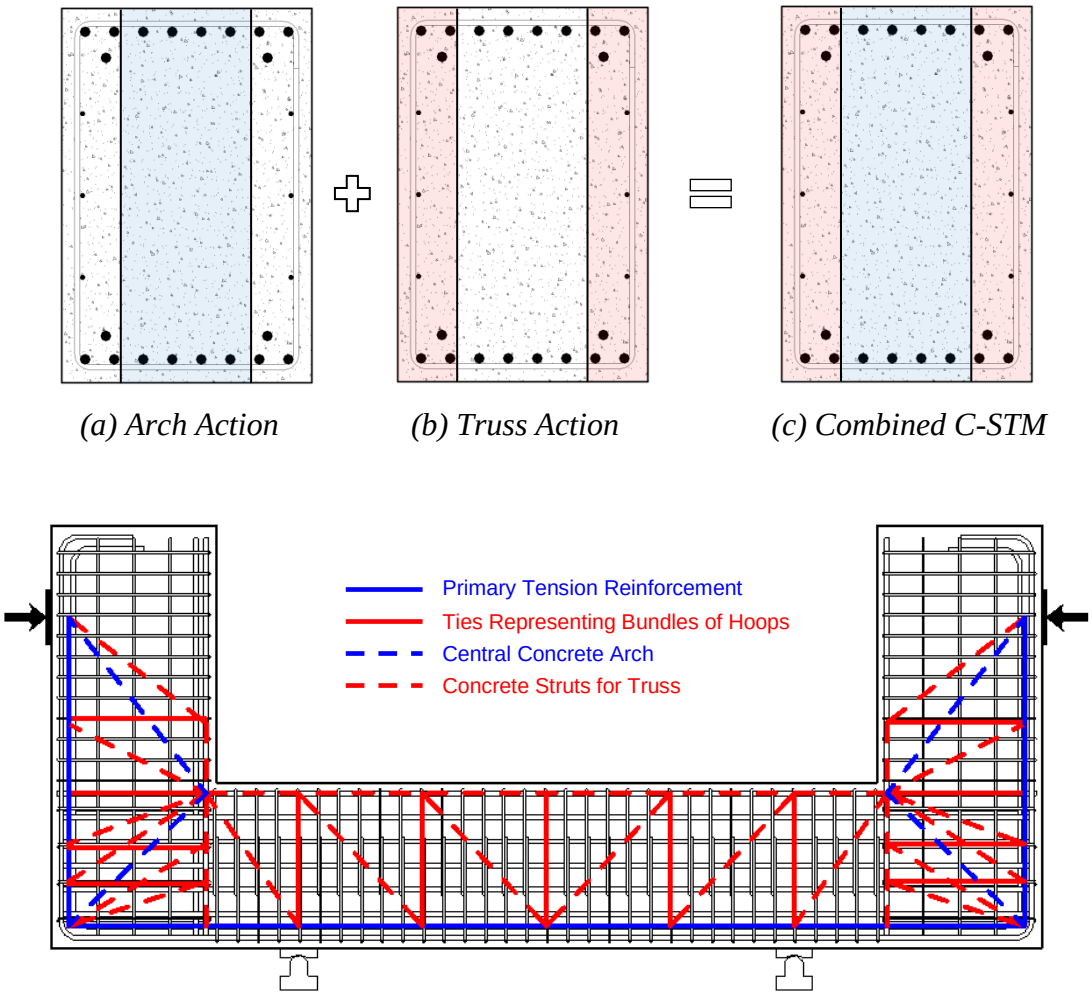

(a) Arch Action *(b) Truss Action* *(c) Combined C-STM*

(d) Compatibility Strut and Tie Model for Experimental Specimen

Figure 7-47 Composition of Arch and Truss Action and Compatibility Strut and Tie Model for Experimental Specimen (Adapted from Mander et al. [2012])

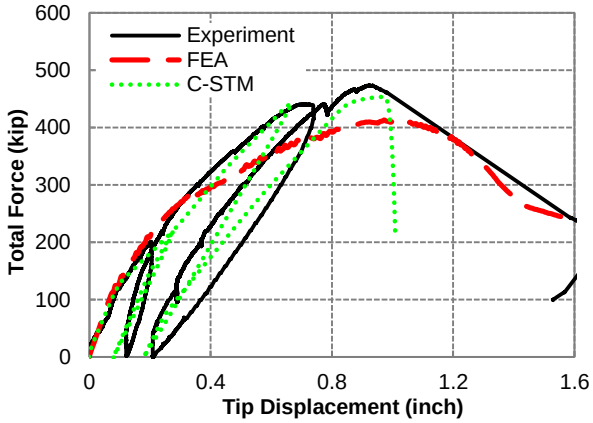

(a) Specimen 1

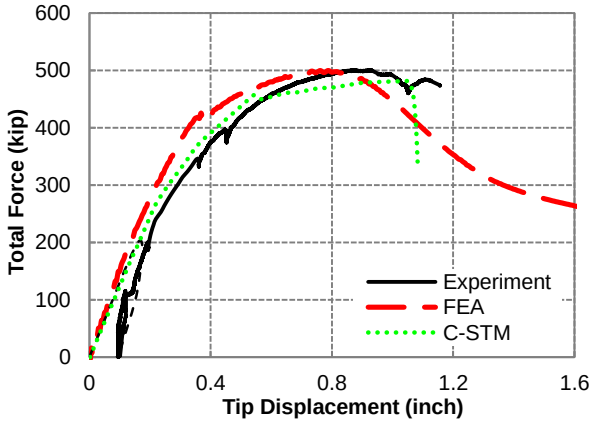

(b) Specimen 2

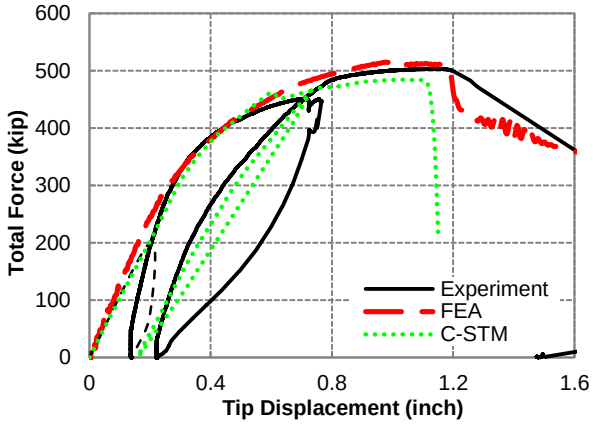

(c) Specimen 4

Figure 7-48 Comparisons of Force-Deformation Curves from FEA, C-STM and Experimental Results

Figure 7-48 shows that C-STM provided a reasonable agreement with the experimentally observed force-deformations in all specimens that were tested to failure. The unloading and reloading during the tests were also modeled in the C-STM approach and yielded satisfactory results. Moreover, the overall structural behavior was categorized by the main tension reinforcement, ties representing transverse hoops, concrete arch at the center of the section, and concrete struts for truss outside the center region (Figure 7-47d). Thus, failure of each component can be discretized in the analysis and the ultimate failure mechanism can be clearly determined.

The FEA approach also produced comparable force-deformation curves compared to the experimental results for all specimens (Figure 7-48). Although the force-deformation curve for Specimen 1 obtained using FEA diverged from the test results at approximately 70% of the peak load, the numerical model still satisfactorily yielded the ultimate peak loading (87% of the experimental value). Furthermore, the ASR/DEF expansion was successfully replicated via the proposed method that substantially applied equivalent thermal expansion in the numerical models. The prestressing and confining effects due to ASR/DEF expansion on reinforcing steel and concrete, respectively, were effectively applied into the numerical models (Figures 7-26 and 7-27). In the selected feature of Abaqus 6.8 (2008) for modeling concrete, the effects of cyclic loading were quantified using the concepts of isotropic damaged elasticity in both compression and tension. However, the constitutive relations of damage elasticity of concrete are ambiguous and the experimental data to quantify such material properties are limited. Additionally, the structural behavior under cyclic

loading was beyond the objectives of this research. Therefore, such effects were not considered in the numerical simulations from FEA approach.

The FEA analytical results confirm that the concept of using arch and truss representations in C-STM is governed in principle. The maximum and minimum principal strain distributions and the corresponding directions obtained from FEA validate the arch action in the joint region that was incorporated in C-STM. Moreover, the difference of the out-of-plane behavior at the center of the section and the cover region was identified, hence suggesting arch and truss action as applied in the C-STM. The failure mechanism of the joint region was also clarified by the FEA approach, which highlights the potential out-of-plane splitting and bursting of concrete in the STM strut at the joint region and demonstrates the potential opening of concrete at the outside corner of the beam-column joint, which were both observed in the experimental tests as discussed in Section 5.8.

7.7.4 Analysis of Proposed Reinforcement Detail at Joint Region

As discussed in Chapter IV and Chapter V, U-shaped reinforcing steel bars should be also used in the direction perpendicular to the existing U-shaped steel bars in the beam-column joint regions to better confine the joint region, especially along the column face of the joint region, to restrain the ASR/DEF expansion in the out-of-plane direction and also provide additional joint shear resistance. To validate the new joint detail, the proposed U-shaped steel bars in the joint region were incorporated into the numerical model of the doubly reinforced bent of Specimen 1 for further investigations using FEA.

Figure 7-49 compares the force-deformation relations for the numerical models consisting of the original reinforcement detail and the proposed reinforcement detail. As discussed in Section 7.6.1, the numerical model for the original reinforcement detail reached a peak load of 414 kips (1842 kN). However, a greater peak load of 436 kips (1939 kN) was achieved for the numerical model including the proposed U-shaped steel bars (Figure 7-49). However the strength loss after the peak load is greater in the case of the proposed reinforcing detail. The strength loss might be attributed to meshing in the FEA and more research is needed.

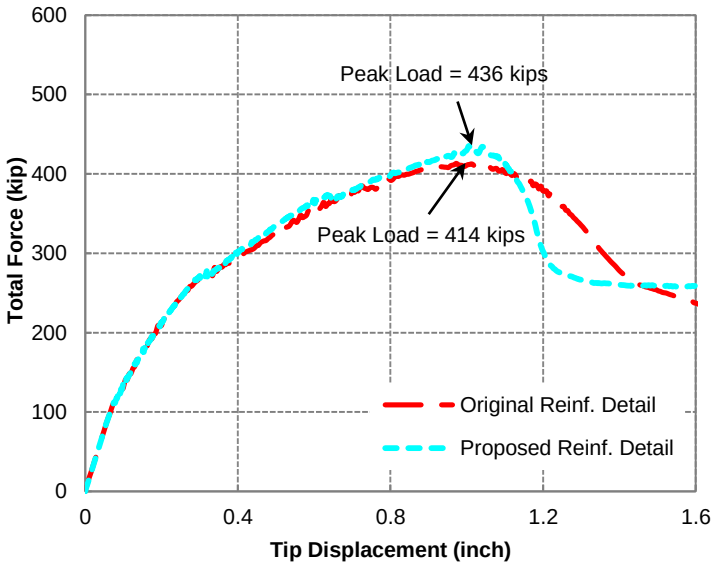

Figure 7-49 Comparisons of Force-Deformation Relations for Numerical Model Consisting of Original and Proposed Reinforcement Detail

Figure 7-50 depicts the reinforcing strains at peak load for the numerical model with the proposed reinforcement detail. As discussed in Section 7.6.2 for the original reinforcement detail, the continuing skin reinforcement at the joint region results in a significant tension strain over 0.005 due to the limited amount of reinforcement in such direction. Figure 7-50 shows that the additional reinforcement in the beam direction mitigates the strains in skin reinforcement and substantially increases the shear resistance in this direction. However, some incipient yielding of the transverse steel was observed in the beam region, indicating potential for a shear failure in this region.

Figure 7-51 shows the out-of-plane strains of concrete at peak load for the numerical model with the proposed reinforcement detail at different widths. The figure shows that the out-of-plane strains are reduced and more restraint is provided in the joint region because of the additional U-shaped steel bars. However, an equivalent amount of out-of-plane strain in the joint region was also observed in the beam region, indicating potential for a shear failure in the beam region.

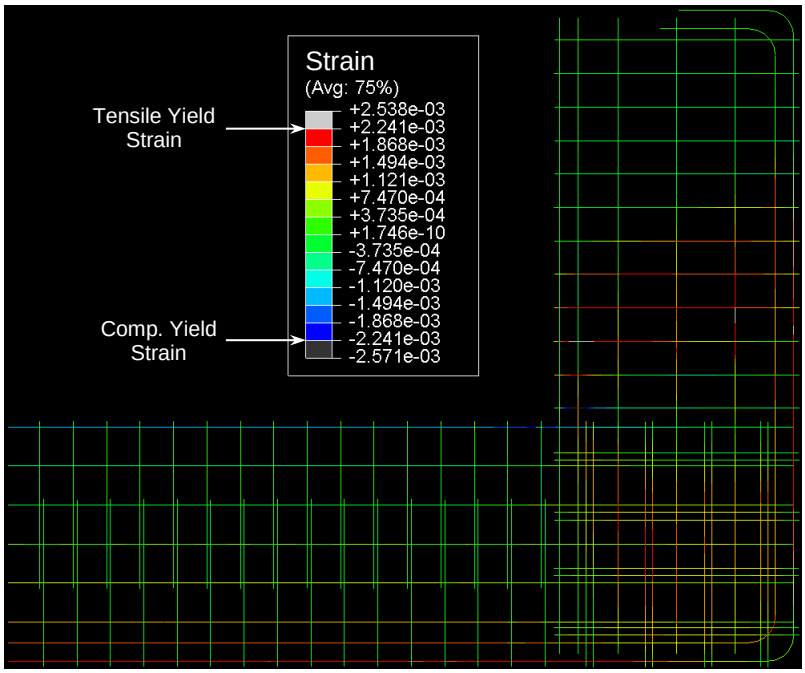

(a) Isometric View

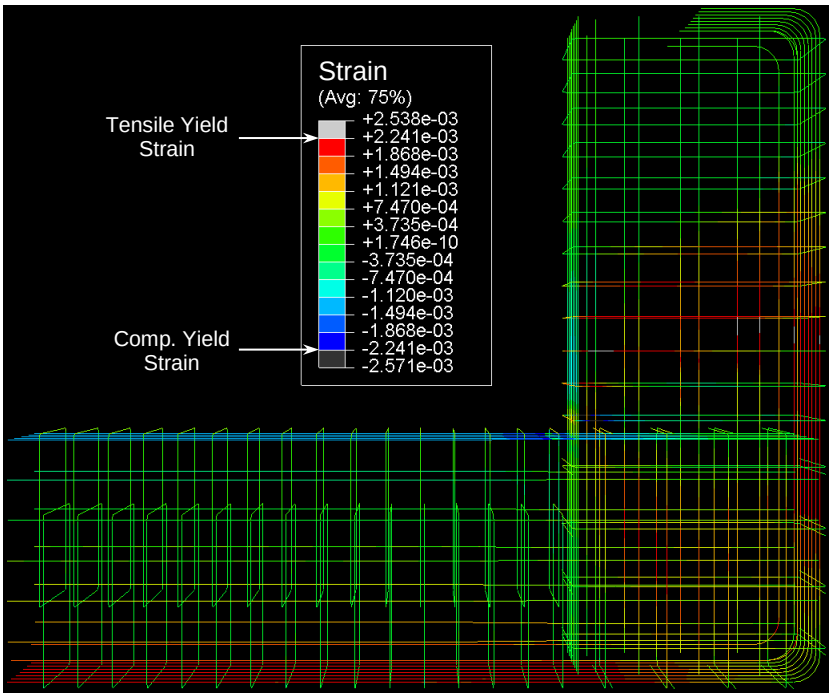

(b) Prospective View

Figure 7-50 Reinforcing Strains under Peak Load for Numerical Model Consisting of Proposed Reinforcement Detail

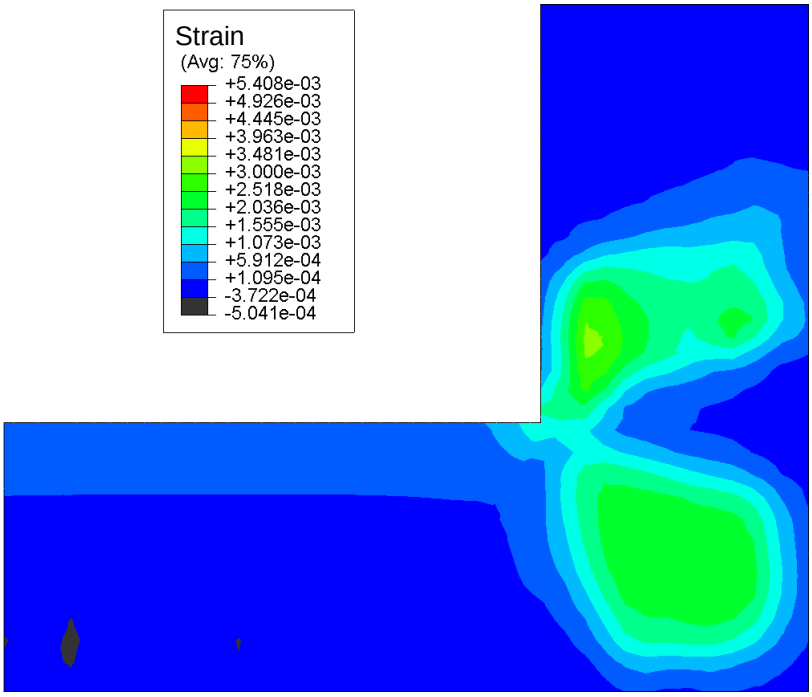

(a) Cover Region

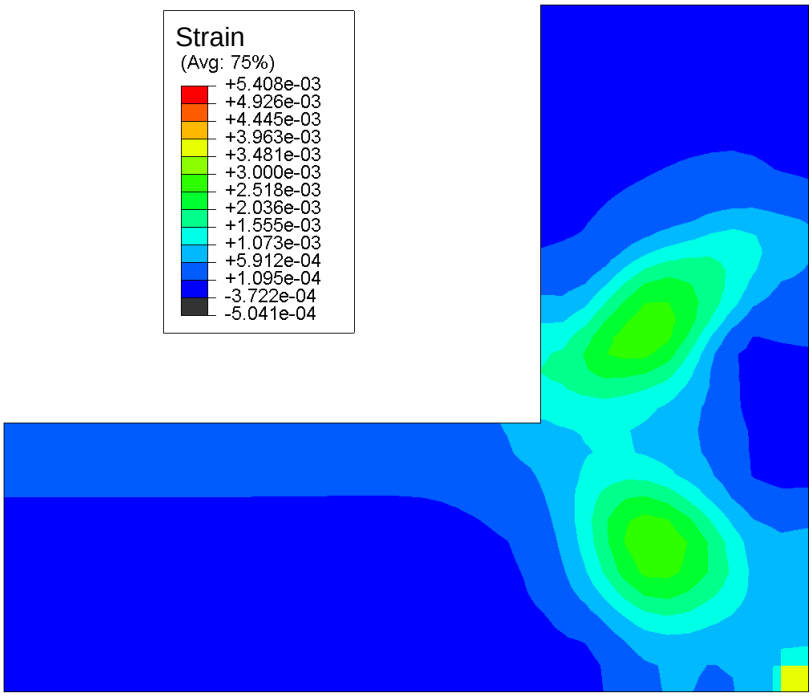

(b) Middle of Specimen Width

Figure 7-51 Out-of-Plane Strains of Concrete under Peak Load for Numerical Model Consisting of Proposed Reinforcement Detail

7.8 SUMMARY AND CONCLUSIONS

In summary, the control specimen (Specimen 1) and two exposed specimens (Specimens 2 and 4) were analytically simulated using the FEA approach. As discussed in Chapter IV, the exposed specimens expanded significantly over time due to primarily ASR mechanism. A method to numerically implement such mechanism in the FEA was proposed and validated by the experimental observations. Although significant cracking developed over time due to primarily ASR, the structural performance in terms of the strength of the structure was not impaired, as discussed in Chapter V. This was attributed to the additional prestressing and confining effects of reinforcing steel on the core concrete that developed due to the ASR expansion, which offset the detrimental effects of concrete cracking induced by ASR. By incorporating the proposed method into the FEA, the additional prestressing and confining effects due to ASR expansion were successfully employed in the numerical simulations.

The key findings from the analytical investigation are summarized below:

- Overall structural behavior of the control specimen and two exposed specimens with concrete expansion effects due to the ASR/DEF mechanisms were successfully replicated in the FEA. The concrete expansion due to ASR was successfully mimicked by applying equivalent thermal expansion to the concrete in three characterized regions of the specimen. This expansion essentially activated the longitudinal and transverse reinforcement in the model, which resulted in additional prestressing and confining of the core concrete. Comparable to the experimental observations, the analytical simulations also led

to greater stiffness and strength in the exposed specimens due to the concrete expansion from primarily ASR.

- Stress concentrations at the inside corner of the beam-column joint region (the STM CCC node) were observed, which indicated that the strut forces were not uniformly distributed on the faces of the CCC node. This may result in crushing of the cover concrete at the inside corner of the joint region, which was experimentally validated in the testing of the specimens. However, the overall widths of the strut-to-node interfaces of each STM node and the bottom face of the CCC node in the FEA were larger than those of the strut and tie model used in this research. This indicated the code-based calculations of the nodal strength using STM yielded conservative results.
- Arch action in the joint was visualized in the FEA by the distribution of principal strains of the concrete. The maximum principal strain distribution showed significant cracking potential perpendicular to the STM strut in the joint region, suggesting that a brittle joint splitting mechanism might form if the strut forces are not properly redistributed throughout the joint. The minimum principal strain distribution outlined the flow directions of the compressive stresses and highlighted the potential bursting of concrete in the STM struts at the CTT nodal region.
- Different distributions of out-of-plane behavior in the concrete cover region and middle of specimen width of the beam-column joint were observed, which demonstrate truss and arch actions in the joint region as per C-STM. Large

magnitude out-of-plane strains were noticed near the outside corner of the beam-column joint in the middle of specimen width, suggesting the potential opening of the concrete that can lead to loss of the support of the STM CTT node for the compression strut in the joint region.

- The proposed additional U-shaped reinforcing steel bars within the joint region were incorporated into numerical simulations and successfully evaluated. The additional U-shaped reinforcing steel bars provided additional shear resistance in the joint region and mitigated the strains in skin reinforcement. In addition, the out-of-plane strains were significantly reduced and more restraint in the joint region was provided.

CHAPTER VIII

SUMMARY, CONCLUSIONS, AND FUTURE WORK

8.1 SUMMARY

It has been observed that a significant amount of reinforced concrete (RC) bridge structures in Texas have experienced premature concrete deterioration (PCD) due to a variety of material degrading mechanisms such as alkali-silica reaction (ASR) and delayed ettringite formation (DEF). Both mechanisms lead to concrete expansion due to the development of ASR gel and the reformation of ettringite within the concrete, respectively. This concrete expansion can lead to excessive cracking of RC bridge structures. Therefore an assessment of the structural performance of structures in such conditions is required.

The structural assessment of D-regions in RC bridge bents exposed to various levels of ASR/DEF expansion was conducted using a combined large-scale experimental program and analytical program. The major objectives of this dissertation were to:

- Perform an experimental program which consists of the construction of large scale RC bridge bent specimens, the exposure of these specimens to supplemental water and outdoor weather condition for promoting concrete expansion due to ASR/DEF mechanisms, the observations of cracking and expansion at the surface concrete, mid-depth core concrete strains and reinforcing steel strains over time, and the structural testing of the exposed specimens and one control/unaffected specimen.

- Develop an analytical program which includes conventional code-based analyses (sectional analysis and strut-and-tie modeling [STM]) to estimate the strength capacity of the control specimen and three-dimensional nonlinear finite element analyses (FEA) to simulate the overall structural behavior, to visualize out-of-plane behavior of the control and the exposed specimens, and to mimic the ASR/DEF effects on the exposed specimens.

In summary, four large-scale RC specimens representative of bridge bents with D-regions in Texas were constructed. High reactive aggregates, along with Type III cement, and a mix dosage of sodium hydroxide solution were used in the concrete mix to accelerate both the ASR and DEF expansion mechanisms. Specimens were heated using electrical resistive wiring (ERW) during curing to maintain concrete temperatures above 170 ˚F (77 ˚C) for at least two days to promote the development of DEF. After construction, one of these specimens was stored in the climate-controlled structural laboratory without supplemental water, serving as the control specimen. The other three specimens were preloaded to simulate in-service load conditions and then transported to the Texas A&M University Riverside Campus for their exposure phase where they were exposed to wetting and drying cycles using supplemental watering system. Visual observations of surface concrete cracking, surface concrete expansion measurements, internal concrete expansion measurements, and reinforcing steel strain measurements were achieved throughout the specimens' exposure phase. The control and two exposed specimens, after eight months and two years of exposure, were structurally load tested to failure.

To estimate the strength capacity of the D-regions for the specimens in the experimental program, sectional analyses and STM approaches were conducted for the control specimen. To investigate the overall structural behavior and out-of-plane behavior for the control and two exposed specimens that were tested to failure, a three-dimensional nonlinear FEA approach was developed to account for ASR/DEF expansion by applying equivalent thermal expansion in three different characterized regions of the experimental specimen. The analytical and experimental results were then compared for further examination.

8.2 CONCLUSIONS

The conclusions and key findings from the experimental and analytical programs are presented in this section.

8.2.1 Experimental Program

8.2.1.1 Specimen Exposure Phase

The following highlights some of the findings derived from the specimen exposure phase in the experimental program:

- The exposed specimens successfully developed significant concrete expansion primarily due to ASR. Considerable growth of the preload-induced cracks and numerous new cracks were observed. Map cracking and cracks parallel to longitudinal reinforcing steel bars developed and grew significantly over time. The progression of cracks will allow bridge inspection engineers key evidence on

the effects of ASR on structures with D-regions during different stages of concrete expansion.

- The amount of compression steel in the beam (bent cap) significantly influenced the concrete expansion on the compression side of the beam region. The longitudinal surface concrete strain on the compression side in the doubly reinforced end was only 31% of that in the singly reinforced end of Specimen 3 over 40 months of exposure.
- The tension field on the tension side induced by pre-load to mimic service conditions significantly influenced the initiation and later growth of ASR/DEF-induced cracking, highlighting the significance of applied member stresses to the ASR/DEF expansion. Numerous new cracks and crack orientations were observed on the tension side of the specimens during the early stages of exposure.
- The transverse surface concrete strains were about five times larger than the longitudinal surface strains on the tension side of the beam region due to the longitudinal restraint provided by the longitudinal tension reinforcement as compared to the smaller amount of transverse reinforcement.
- The out-of-plane surface concrete strains on the beam/column face in the joint regions developed at a higher rate than that in the direction parallel to the main longitudinal reinforcing steel as a consequence of the lack of sufficient reinforcement in the joint region to restrain expansion in the out-of-plane direction.

- The specimens expanded at a higher rate during the warmer months (April through October), when the outside temperature exceeded about 80 ˚F (26.7 ˚C).

8.2.1.2 Structural Testing

The following highlights some of the findings derived from the structural testing of the control and two exposed specimens in the experimental program:

- Failure was observed in all specimens as a result of a brittle shear failure through the beam-column joint.
- The predominant ASR expansion of the concrete in the exposed specimens did not impair their structural performance. In contrast to the control specimen, the two exposed specimens and their associated concrete expansion effects resulted in slightly greater stiffness, strength, and ductility. This improved performance was attributed to the concrete expansion from ASR that activated the reinforcing steel and caused beneficial prestressing and confining effects on the core concrete.
- A brittle shear failure for all specimens resulted from the deterioration of the diagonal STM strut in the beam-column joint and CTT nodal failure that experienced significant out-of-plane bursting forces due to the lack of sufficient reinforcement at the CTT node and column face of the joint region in the out-of-plane direction.
- Some corrosion of the reinforcing steel was observed in Specimen 4 which had two years of exposure. This additional steel corrosion was a by-product of the

ASR/DEF-induced cracking. Although the corrosion in Specimen 4 did not lessen the structural performance of the specimen, the development of corrosion in structures affected by ASR/DEF expansion is concerning for life cycle assessments. The coupled effects of corrosion and ASR/DEF expansion on the structural performance are also important.

8.2.2 Analytical Program

8.2.2.1 Sectional Analysis and Strut-and-Tie Modeling

The following presents some of the findings derived from the sectional analyses and STM approach in the analytical program:

- The ratios of the flexure sectional analysis to the peak experimental loads for all specimens that were tested to failure ranged from 0.86 to 0.94 when the inside column face was assumed to be the critical section and were much smaller when critical sections within the joint were considered.
- The code-based shear capacities yielded conservative results compared to the ultimate peak load of the experimental specimens.
- In the STM approach, the critical face was found to be the strut-to-node interface of the CTT node at the outside corner of the joint region, which was a direct result of the code-provided bend radius of the longitudinal reinforcement for the beam and column within the joint region. This indicates that strut failure near the CTT node would occur once the strut-to-node interface loses support in the joint region. However, STM significantly underestimated the ultimate peak load for

the experimental specimens, which can be attributed to the conservative effective stresses in nodal zones and struts as required by the codes.

8.2.2.2 Nonlinear Finite Element Modeling

The following presents some of the findings derived from the three-dimensional FEA approach in the analytical program:

- The FEA approach, which incorporated a proposed method to account for primarily ASR expansion by applying equivalent thermal expansion in three different characterized regions in the experimental specimen was developed and validated by the large-scale experiments. Overall structural behavior of the control and two exposed specimens that were tested to failure were successfully replicated in the FEA approach.
- Stress concentrations at the inside corner of the beam-column joint region (the STM CCC node) were observed, indicating that the strut forces were not uniformly distributed on the faces of the CCC node as suggested by STM. This mechanism may result in crushing of the cover concrete at the inside corner of the joint region, which was observed in the experiments for all specimens that were tested to failure.
- The overall widths of the strut-to-node interfaces of each STM node and the bottom face of the CCC node were found to be larger than those of the strut and tie model used in the previous STM analysis. This indicated that the code-based calculations of the nodal strength using STM yielded conservative results.

- Arch and truss actions in the joint region for C-STM were justified by the distribution of principal strains of the concrete. In addition, different distributions of out-of-plane behavior in the concrete cover region and middle of specimen width of the beam-column joint were observed, which also demonstrate truss and arch actions in the joint region.
- The maximum principal strain distribution showed significant cracking potential perpendicular to the diagonal STM strut in the joint region, which indicated that a brittle joint splitting mechanism might form if the strut forces are not properly redistributed throughout the joint region. The minimum principal strain distribution outlined the compressive stress flow directions and highlighted the potential bursting of concrete in the STM struts.
- High magnitudes out-of-plane strains were observed near the outside corner of the beam-column joint in the middle of specimen width, which indicated the potential opening of the concrete that can lead to loss of the support of the STM CTT node for the diagonal strut in the joint region.
- Proposed additional U-shaped reinforcing steel bars within the joint region were evaluated using the FEA approach. The additional U-shaped reinforcing steel bars provided additional shear resistance in the joint region and the out-of-plane strains were significantly reduced along the column face of the joint region as compared to the performance with the original reinforcement detail.

8.3 FUTURE WORK

From the experimental program, some corrosion was observed in the exposed specimen that was tested after two years of exposure (Specimen 4). One experimental specimen (Specimen 3) remains in the field and has been exposed to outdoor weather conditions over 40 months. Additional corrosion along with more severe ASR/DEF expansion and cracking of the concrete may cause serious structural and durability concerns for field structures affected by ASR/DEF. The effects of corrosion and more ASR/DEF mechanisms on the structural performance are yet unknown. Further investigations are necessary and such effects will be elucidated once the remaining specimen (Specimen 3) is tested.

From the experimental and analytical investigations, the original reinforcement detail in the beam-column joint was found to be insufficient for sufficient deformability beyond peak load (ductility). Additional reinforcement in the out-of-plane direction on the column face of the joint region can reduce the surface concrete expansion due to ASR/DEF, hence deterring corrosion of the reinforcing steel at this region. Furthermore, additional reinforcement in the beam direction of the joint region could mitigate the strains in the skin reinforcement and provide additional shear resistance in the joint region. Therefore, additional U-shaped reinforcing steel bars perpendicular to the existing U-shaped steel bars were proposed. The effects of the additional U-shaped reinforcing steel bars and other detailing on restraining local ASR/DEF expansion and the overall structural performance needs to be further examined.

Due to the limited experimental data to define the constitutive relations of the damage elasticity of concrete for accounting for degraded elastic modulus after cracking/crushing, the effects of the cyclic loading were not considered in the FEA approach in this research. In addition, due to the complexity of the reinforcement detail of the experimental specimen, the bond-slip effects were neglected in the FEA approach in this research. These effects, especially with specimens exposed to more severe ASR and DEF deterioration, deserve further examinations to clarify local degradation of concrete and local bond-slip mechanism between reinforcing steel and concrete within the structural loading history.

REFERENCES

AASHTO. (2010). "LRFD Bridge Design Specifications." fifth edition, *American Association of State Highway and Transportation Officials*, Washington DC.

Abaqus Version 6.8 Documentation. (2008). *Dassault Systèmes Simulia Corp.*, Providence, Rhode Island.

ACI Committee 318. (2008). "Building Code Requirements for Structural Concrete (ACI 318-08) and Commentary." *American Concrete Institute*, Farmington Hills, Michigan.

Ahmed, T., Burley, E., and Rigden, S. (1998). "The Static and Fatigue Strength of Reinforced Concrete Beams Affected by Alkali-Silica Reaction." *ACI Mater. J.*, 95(4), 376-388.

Ahmed, T., Burley, E., and Rigden, S. (1999a). "Effect of Alkali-Silica Reaction on Tensile Bond Strength of Reinforcement in Concrete Tested under Static and Fatigue Loading." *ACI Mater. J.*, 96(4), 419-428.

Ahmed, T., Burley, E., and Rigden, S. (1999b). "Effect of Alkali-Silica Reaction on Bearing Capacity of Plain and Reinforced Concrete." *ACI Struct. J.*, 96(4), 557-570.

ASCE-ACI Committee 445 on Shear and Torsion. (1998). "Recent Approaches to Shear Design of Structural Concrete." *J. Struct. Eng., ASCE*, 124(12), 1375-1417.

ASTM C31. (2007). "Standard Practice for Making and Curing Concrete Test Specimens in the Field." *American Society for Testing and Materials, Annual Book of ASTM Standards, 04.02, Concrete and Aggregates*, West Conshohocken, Pennsylvania.

ASTM C39. (2007). "Standard Test Method for Compressive Strength of Cylindrical Concrete Specimens." *American Society for Testing and Materials, Annual Book of ASTM Standards, 04.02, Concrete and Aggregates*, West Conshohocken, Pennsylvania.

ASTM C496. (2007). "Standard Test Method for Splitting Tensile Strength of Cylindrical Concrete Specimens." *American Society for Testing and Materials, Annual Book of ASTM Standards, 04.02, Concrete and Aggregates*, West Conshohocken, Pennsylvania.

Bae, S., Bayrak, O., Jirsa, J. O., and Klingner, R. E. (2007). "Anchor Bolt Behavior in ASR/DEF-Damaged Drilled Shafts." *Rep. No. IAC 88-5DDIA004*, The University of Texas at Austin.

Barbarulo, R., Peycelon, H., Prené, S., and Marchand, J. (2005). "Delayed Ettringite Formation Symptoms on Mortars Induced by High Temperature Due to Cement Heat of Hydration or Late Thermal Cycle." *Cem. Concr. Res.*, 35(1), 125-131.

Barton, D. L., Anderson, R. B., Bouadi, A., Jirsa, J. O., and Breen, J. E. (1991). "An Investigation of Strut-and-Tie Models for Dapped Beam Details." *Rep. No. FHWA/TX-92+1127-1*, Center for Transportation Research, The University of Texas at Austin.

Bauer, S., Cornell, B., Figurski, D., Ley, T., Miralles, J., and Folliard, K. J. (2006). "Alkali-Silica Reaction and Delayed Ettringite Formation in Concrete: A Literature Review." *Rep. No. FHWA/TX-06/0-4085-1*, Center for Transportation Research, The University of Texas at Austin.

Bérubé, M.-A., Chouinard, D., Pigeon, M., Frenette, J., Boisvert, L., and Rivest, M. (2002). "Effectiveness of Sealers in Counteracting Alkali-Silica Reaction in Plain and Air-Entrained Laboratory Concretes Exposed to Wetting and Drying, Freezing and Thawing, and Salt Water." *Can. J. Civ. Eng.*, 29(2), 289-300.

Birrcher, D., Tuchscherer, R., Huizinga, M., Bayrak, O., Wood, S., and Jirsa, J. (2009). "Strength and Serviceability Design of Reinforced Concrete Deep Beams." *Rep. No. FHWA/TX-09/0-5253-1*, Center for Transportation Research, The University of Texas at Austin.

Bouzabata, H., Multon, S., Sellier, A., and Houari, H. (2012). "Swellings Due to Alkali-Silica Reaction and Delayed Ettringite Formation: Characterisation of Expansion Isotropy and Effect of Moisture Conditions." *Cem. Concr. Compos.*, 34(3), 349-356.

Bracci, J. M., Gardoni, P., Eck, M. K., and Trejo, D. (2012). "Performance of Lap Splices in Large-Scale Column Specimens Affected by ASR and/or DEF." *Rep. No. FHWA/TX-12/0-5722-1*, Texas Transportation Institute, The Texas A&M University System.

Burgher, B., Thibonnier, A., Folliard, K. J., Ley, T., and Thomas, M. D. A. (2008). "Investigation of the Internal Stresses Caused by Delayed Ettringite Formation in Concrete." *Rep. No. FHWA/TX-09/0-5218-1*, Center for Transportation Research, The University of Texas at Austin.

Carse, A., and Dux, P. F. (1990). "Measurement of Concrete Expansive Strains Due to Alkali-Silica Reaction in Australian Concrete Structures." *Cem. Concr. Res.,* 20(3), 376-384.

Chana, P. S., and Korobokis, G. A. (1991). "Structural Performance of Reinforced Concrete Affected by Alkali Silica Reaction: Phase I." *Rep. No. 267,* Transport and Road Research Laboratory, Department of Transport, Crowthorne, United Kingdom.

Chana, P. S., and Korobokis, G. A. (1992). "Structural Performance of Reinforced Concrete Affected by Alkali Silica Reaction: Phase II." *Rep. No. 311,* Transport and Road Research Laboratory, Department of Transport, Crowthorne, United Kingdom.

Claeson, C. (1998). "Finite Element Analysis of Confined Concrete Columns." Chalmers University of Technology, Göteborg, Sweden.

Collins, M. P. (1978). "Towards a Rational Theory for RC Members in Shear." *J. Struct. Div., ASCE,* 104(4), 649-666.

Collins, M. P., and Mitchell, D. (1987). "Prestressed Concrete Basics." *Canadian Prestressed Concrete Institute,* Ottawa, Canada.

Cook, W. D. (1987). "Studies of Reinforced Concrete Regions near Discontinuities". Ph.D. Dissertation, McGill University, Montreal, Canada.

Cook, W. D., and Mitchell, D. (1988). "Studies of Disturbed Regions near Discontinuities in Reinforced Concrete Members." *ACI Struct. J.,* 85(2), 206-216.

Courtier, R. H. (1990). "Assessment of ASR-Affected Structures." *Cem. Concr. Compos.,* 12(3), 191-201.

Dere, Y., and Dede, F. T. (2011). "Nonlinear Finite Element Analysis of an R/C Frame under Lateral Loading." *Math. Comput. Appl.,* 16(4), 947-958.

Deschenes, D. J., Bayrak, O., and Folliard, K. J. (2009). "ASR/DEF-Damaged Bent Caps: Shear Tests and Field Implications." *Rep. No. 12-8XXIA006,* Ferguson Structural Engineering Laboratory, The University of Texas at Austin.

Dunant, C. F., and Scrivener, K. L. (2010). "Micro-Mechanical Modelling of Alkali-Silica-Reaction-Induced Degradation Using the AMIE Framework." *Cem. Concr. Res.,* 40(4), 517-525.

Duthinh, D., and Carino, N. J. (1996). "Shear Design of High-Strength Concrete Beams: A Review of the State-of-the-Art." *Rep. No. NISTIR 5870,* Building and Fire Research Laboratory, National Institute of Standards and Technology, Gaithersburg, Maryland.

Fafitis, A., and Won, Y. H. (1994). "Nonlinear Finite Element Analysis of Concrete Deep Beams." *J. Struct. Eng., ASCE,* 120(4), 1202-1220.

Famy, C., and Taylor, H. F. W. (2001). "Ettringite in Hydration of Portland Cement Concrete and Its Occurrence in Mature Concretes." *ACI Mater. J.,* 98(4), 350-356.

Fan, S., and Hanson, J. M. (1998a). "Length Expansion and Cracking of Plain and Reinforced Concrete Prisms Due to Alkali-Silica Reaction." *ACI Mater. J.,* 95(4), 480-485.

Fan, S., and Hanson, J. M. (1998b). "Effect of Alkali Silica Reaction Expansion and Cracking on Structural Behavior of Reinforced Concrete Beams." *ACI Struct. J.,* 95(5), 488-495.

Farage, M. C. R., Alves, J. L. D., and Fairbairn, E. M. R. (2004). "Macroscopic Model of Concrete Subjected to Alkali-Aggregate Reaction." *Cem. Concr. Res.,* 34(3), 495-505.

Folliard, K. J., Barborak, R., Drimalas, T., Du, L., Garber, S., Ideker, J., Ley, T., Williams, S., Juenger, M., Fournier, B., and Thomas, M. D. A. (2006). "Preventing ASR/DEF in New Concrete: Final Report." *Rep. No. FHWA/TX-06/0-4085-5,* Center for Transportation Research, The University of Texas at Austin.

Fu, Y., Xie, P., Gu, P., and Beaudoin, J. J. (1994). "Effect of Temperature on Sulphate Adsorption/Desorption by Tricalcium Silicate Hydrates." *Cem. Concr. Res.,* 24(8), 1428-1432.

Giaccio, G., Zerbino, R., Ponce, J. M., and Batic, O. R. (2008). "Mechanical Behavior of Concretes Damaged by Alkali-Silica Reaction." *Cem. Concr. Res.,* 38(7), 993-1004.

Giaccio, G., Torrijos, M. C., Tobes, J. M., Batic, O. R., and Zerbino, R. (2009). "Development of Alkali-Silica Reaction under Compressive Loading and Its Effects on Concrete Behavior." *ACI Mater. J.,* 106(3), 223-230.

Grattan-Bellew, P. E., Beaudoin, J. J., and Vallée, V.-G. (1998). "Effect of Aggregate Particle Size and Composition on Expansion of Mortar Bars Due to Delayed Ettringite Formation." *Cem. Concr. Res.*, 28(8), 1147-1156.

Habuchi, T., and Torii, K. (2012). "Corrosion Characteristics of Reinforcement in Concrete Structures Subject to ASR and Seawater Attack in Marine Environment." *Proceedings of the 14th International Conference on Alkali-Aggregate Reactivity in Concrete,* Drimalas, T., Ideker J. H., and Fournier, B., Eds., Austin, Texas.

Heinz, D., and Ludwig, U. (1987). "Mechanism of Secondary Ettringite Formation in Motars and Concretes Subjected to Heat Treatment." *ACI Spec. Publ. (Concr. Durability)*, 100(105), 2059-2071.

Hime, W. G., and Marusin, S. L. (1999). "Delayed Ettringite Formation: Many Questions and Some Answers." *ACI Spec. Publ.*, 177(13), 199-206.

Hobbs, D. W. (1984). "Expansion of Concrete Due to Alkali-Silica Reaction." *Struct. Eng.*, 62 A(1), 26-34.

Hobbs, D. W. (1986). "Alkali-Silica Reaction in Concrete." *Struct. Eng.*, 64 A(12), 381-383.

Hobbs, D. W. (1999). "Expansion and Cracking in Concrete Associated with Delayed Ettringite Formation." *ACI Spec. Publ.*, 177(11), 159-182.

Inoue, S., Mikata, Y., Takahashi, Y., and Inamasu, K. (2012). "Residual Shear Capacity of ASR Damaged Reinforced Concrete Beams with Ruptured Stirrups." *Proceedings of the 14th International Conference on Alkali-Aggregate Reactivity in Concrete,* Drimalas, T., Ideker J. H., and Fournier, B., Eds., Austin, Texas.

Jankowiak, T., and Łodygowski, T. (2005). "Identification of Parameters of Concrete Damage Plasticity Constitutive Model." *Foundations of Civil and Environmental Engineering,* 5, House of Poznan University of Technology, Poznan.

Jensen, V. (2003). "Elgeseter Bridge in Trondheim Damaged by Alkali Silica Reaction: Microscopy, Expansion and Relative Humidity Measurements, Treatment with Mono Silanes and Repair." *9th Euroseminar on Microscopy Applied to Building Materials,* September 9-12, Trondheim, Norway.

Kelham, S. (1996). "The Effect of Cement Composition and Fineness on Expansion Associated with Delayed Ettringite Formation." *Cem. Concr. Compos.*, 18(3), 171-179.

Kim, J. H., and Mander, J. B. (1999). "Truss Modeling of Reinforced Concrete Shear-Flexure Behavior." *Rep. No. MCEER-99-0005,* The University at Buffalo, New York.

Kim, J. H., and Mander, J. B. (2007). "Influence of Transverse Reinforcement on Elastic Shear Stiffness of Cracked Concrete Elements." *Eng. Struct.,* 29(8), 1798-1807.

Kubo, Y., Iketomi, O., Nakashima, T., and Torii, K. (2003). "Experimental Study of Fracture of Reinforced Steel Bar in Concrete Structures Due to Alkali-Silica Expansion." *ACI Spec. Publ.,* 212(40), 637-652.

Kupfer, H., Hilsdorf, H. K., and Rusch, H. (1969). "Behavior of Concrete under Biaxial Stresses." *J. Am. Concr. Inst.,* 66(8), 656-666.

Mander, J. B., Priestley, M. J. N., and Park, R. (1988). "Theoretical Stress-Strain Model for Confined Concrete." *J. Struct. Eng., ASCE,* 114(8), 1804-1826.

Mander, J. B., Bracci, J. M., Hurlebaus, S., Grasley, Z., Karthik, M. M., Liu, S.-H., and Scott, R. M. (2012). "Structural Assessment of "D" Region Affected by Premature Concrete Deterioration: Technical Report." *Rep. No. FHWA/TX-12/0-5997-1,* Texas Transportation Institute, The Texas A&M University System.

Marti, P. (1985). "Basic Tools of Reinforced Concrete Beam Design." *J. Am. Concr. Inst.,* 82(1), 46-56.

Mitchell, D., and Collins, M. P. (1974). "Diagonal Compression Field Theory - A Rational Model for Structural Concrete in Pure Torsion." *J. Am. Concr. Inst.,* 71(8), 396-408.

Mohammed, T. U., Hamada, H., and Yamaji, T. (2003). "Alkali-Silica Reaction-Induced Strains over Concrete Surface and Steel Bars in Concrete." *ACI Mater. J.,* 100(2), 133-142.

Monette, L. J., Gardner, N. J., and Grattan-Bellew, P. E. (2002). "Residual Strength of Reinforced Concrete Beams Damaged by Alkali-Silica Reaction - Examination of Damage Rating Index Method." *ACI Mater. J.,* 99(1), 42-50.

Multon, S., Seignol, J.-F., and Toutlemonde, F. (2005). "Structural Behavior of Concrete Beams Affected by Alkali-Silica Reaction." *ACI Mater. J.,* 102(2), 67-76.

Multon, S., and Toutlemonde, F. (2010). "Effect of Moisture Conditions and Transfers on Alkali Silica Reaction Damaged Structures." *Cem. Concr. Res.,* 40(6), 924-934.

Odler, I., and Chen, Y. (1996). "On the Delayed Expansion of Heat Cured Portland Cement Pastes and Concretes." *Cem. Concr. Compos.*, 18(3), 181-185.

Okamura, H., Maekawa, K., and Sivasubramaniyam, S. (1985). "Verification of Modeling for Reinforced Concrete Finite Element." *Proceedings of Finite Element Analysis of Reinforced Concrete Structures, ASCE*, 528-543.

Pagnoni, T., Slater, J., Ameur-Moussa, R., and Buyukozturk, O. (1992). "A Nonlinear Three-Dimensional Analysis of Reinforced Concrete Based on a Bounding Surface Model." *Comput. Struct.*, 43(1), 1-12.

Park, R., and Paulay, T. (1975). *Reinforced Concrete Structures.* John Wiley and Sons, New York.

Pavoine, A., and Divet, L. (2003). "Delayed Ettringite Formation in Concrete: Tests Based on Drying and Wetting Cycles." *ACI Spec. Publ.*, 212(61), 989-1003.

Petrov, N., Thibault, M., and Tagnit-Hamou, A. (2006). "Expansion Due to DEF in Normally-Cured Concrete Heated by Cement Hydration." *ACI Spec. Publ.*, 234(16), 239-250.

Poole, A. B. (1992). "Introduction to Alkali-Aggregate Reaction in Concrete." *The Alkali-Silica Reaction in Concrete,* Swamy, R. N., Ed., Blackie; Van Nostrand Reinhold, Glasgow, New York.

Popovics, S. (1973). "A Numerical Approach to the Complete Stress-Strain Curve of Concrete." *Cem. Concr. Res.*, 3(5), 583-599.

Powanusorn, S. (2003). "Effect of Confinement on Shear Dominated Reinforced Concrete Elements". Ph.D. Dissertation, Texas A&M University, College Station, Texas.

Powanusorn, S., and Bracci, J. M. (2006). "Behavior of Reinforced Concrete Members Prone to Shear Deformations: Part I - Effect of Confinement." *ACI Struct. J.*, 103(5), 736-746.

Salem, H. M. M. (2002). "The Micro Truss Model: A New Rational Design Approach." *J. Eng. Appl. Sci.*, 49(2), 259-277.

Schlaich, J., Schäfer, K., and Jennewein, M. (1987). "Toward a Consistent Design of Structural Concrete." *PCI J.*, 32(3), 74-150.

Scott, R. M. (2010). "Experimentally Validated Compatibility Strut and Tie Modeling of Reinforced Concrete Bridge Piers." Master's Thesis, Texas A&M University, College Station, Texas.

Scott, R. M., Mander, J. B., and Bracci, J. M. (2012a). "Compatibility Strut and Tie Modeling: Part I - System Formulation." *ACI Struct. J.*, 109(5), 635-644.

Scott, R. M., Mander, J. B., and Bracci, J. M. (2012b). "Compatibility Strut and Tie Modeling: Part II- Implementation." *ACI Struct. J.*, 109(5), 645-654.

Scrivener, K., and Lewis, M. (1997). "A Microstructural and Microanalytical Study of Heat Cured Mortars and Delayed Ettringite Formation." *Proceedings of the 10th International Congress on the Chemistry of Cement*, Gothenburg, Sweden.

Seignol, J.-F., and Godart, B. (2012). "A Collective Effort to Propose Pratical Guidance on the Use of Numerical Models to Re-Assess AAR-Affected Structures." *Proceedings of the 14th International Conference on Alkali-Aggregate Reactivity in Concrete*, Drimalas, T., Ideker J. H., and Fournier, B., Eds., Austin, Texas.

Seignol, J.-F., Omikrine-Metalssi, O., Baghdadi, N., and Toutlemonde, F. (2012). "From AAR to DEF: Numerical Modeling of Structures Affected by Expansive Reactions in Concrete." *Proceedings of the 14th International Conference on Alkali-Aggregate Reactivity in Concrete*, Drimalas, T., Ideker J. H., and Fournier B., Eds., Austin, Texas.

Stanton, T. E. (1940). "Expansion of Concrete through Reaction between Cement and Aggregate." *Proc. Am. Soc. Civ. Eng.*, 66(10), 1781-1811.

Swamy, R. N., and Al-Asali, M. (1988). "Engineering Properties of Concrete Affected by Alkali-Silica Reaction." *ACI Mater. J.*, 85(5), 367-374.

Swamy, R. N., and Al-Asali, M. (1989). "Effect of Alkali-Silica Reaction on the Structural Behavior of Reinforced Concrete Beams." *ACI Struct. J.*, 86(4), 451-459.

Swamy, R. N. (1992). "Testing for Alkali-Silica Reaction." *The Alkali-Silica Reaction in Concrete*, Swamy, R. N., Ed., Blackie; Van Nostrand Reinhold, Glasgow, New York.

Thomas, M. D. A. (2001). "Delayed Ettringite Formation in Concrete: Recent Development and Future Directions." *Materials Science of Concrete VI*, J. S. S. Mindess, Ed., The American Ceramic Society, Westerville, Ohio, 435-481.

Torii, K., Yamato, H., Andrade, O., and Tarui, T. (2009). "Mechanisms of Fracture of Steel Bars in ASR-Affected Bridge Piers." *8th International Conference on Creep, Shrinkage and Durability Mechanics of Concrete and Concrete Structures, September 30, 2008 - October 2,* CRC Press, Ise-Shima, Japan, 1139-1145.

Ulm, F.-J., Coussy, O., Kefei, L., and Larive, C. (2000). "Thermo-Chemo-Mechanics of ASR Expansion in Concrete Structures." *J. Eng. Mech., ASCE,* 126(3), 233-242.

Vecchio, F. J., and Collins, M. P. (1986). "The Modified Compression-Field Theory for Reinforced Concrete Elements Subjected to Shear." *J. Am. Concr. Inst.,* 83(2), 219-231.

Vecchio, F. J. (1992). "Finite Element Modeling of Concrete Expansion and Confinement." *J. Struct. Eng., ASCE,* 118(9), 2390-2406.

Weather Underground. (2012). "Weather Underground, Inc." www.wunderground.com.

Williams, M. E., and Choudhuri, D. (2010). "Case Study in the Evaluation and Repair of ASR Deterioration in Concrete Bridge Beams." *ACI Spec. Publ.,* 277(10), 143-155.

Young, B. S., Bracci, J. M., Keating, P. B., and Hueste, H. M. B. D. (2002). "Cracking in Reinforced Concrete Bent Caps." *ACI Struct. J.,* 99(4), 488-498.

Zhang, Z., Olek, J., and Diamond, S. (2002). "Studies on Delayed Ettringite Formation in Early-Age, Heat-Cured Mortars: I. Expansion Measurements, Changes in Dynamic Modulus of Elasticity, and Weight Gains." *Cem. Concr. Res.,* 32(11), 1729-1736.

APPENDIX A

PETROGRAPHIC ANALYSIS REPORT – SPECIMEN 1

Petrographic Analysis

06/29/2010

Report:	TTI ASR DEF
Date Received:	04/12/2010
Structure Type:	Unknown
Sample Type:	Cores
Location:	Unknown
Coarse Aggregate Producer:	NA
Coarse Aggregate Type:	Siliceous Gravel
Fine Aggregate Producer:	NA
Fine Aggregate Type:	Siliceous Sand
Cement Producer:	NA
Cement Type:	NA

Comments:

This petrographic analysis was performed in response to a request from Dr. Joseph Bracci to assist the Texas A&M University in an ASR/DEF investigation of nine submitted cores. The following objectives were specified by Texas A&M:

- General observations on concrete quality. (Comments on placement, mixture proportions, water-cement ratio).
- Visual documentation of ASR and/or DEF micro structural damage. (Images depicting gel/ettringite locations, cracking and gapping of paste/aggregate interfaces).
- Qualitative study of damage severity in each sample. (Comparison of micro structural damage between all samples).
- Qualitative study of damage progression through the length of the sample. (Comparison of micro structural damage in surface and core concretes of each sample).

General observations on concrete quality (comments on placement, mixture proportions, water-cement ratio)

General Appearance
Four cores were submitted for analysis and were designated as: Core1, Core2, Core3 and Core4. The submitted cores were 3-3/4 inch in diameter and 3-5/8 inches in length. The cores had no surface cracking.

Water/Cement Ratio
None of the cores had abnormal or elevated w-c ratio. Based on appearance of the paste (color, ferrite distribution and granularity of the hydrates) estimates of w-c ratio for the eleven cores were consistent with the mix design.

Proportioning and types of aggregate
Based on point count data the paste volume indicate a high sack mix, low coarse aggregate factor and gap grading was noted in all the cores. Coarse aggregate consist of a siliceous gravel comprised of chert, agate and granite. Fine aggregate consist of quartz, agate, feldspar and chert. The following table summarizes the point count data:

Table A-1 Proportioning and Types of Aggregate

Core ID	Paste Volume	FA Volume	CA Volume	% Entrapped Air	% Entrained Air
Core2	27.06	39.24	30.50	0.49	2.58
Core4	29.49	44.52	22.5	0.68	2.81

Paste content and appearance
Paste content is indicative of a high sack mix and appearance is normal. No fly ash or other mineral admixtures were present in the mix.

Air Content
Non-Air Entrained.

Degree of Hydration
Normal.

Carbonation
Carbonation was noted at the exterior surface of all the cores. The following chart represents the depth of carbonation for each core.

Table A-2 Carbonation Depth

Core ID	Carbonation Depth From Exterior Surface of Core	Carbonation Depth Observed Along Surface Crack
Core1	None	NA
Core2	None	NA
Core3	None	NA
Core4	None	NA

Deleterious Reaction Mechanism

All the cores are producing some isolated sites of gel with very limited signs of distress. The primary ASR aggregate type in both the fine and coarse aggregate is a microcrystalline chert. ASR gel was noted in the cores; however, the amount was sparse. Gel in the cores was observed at the paste aggregate interfaces and oozing of small droplets from some of the aggregates. The gel consistency was extremely viscous and did not exhibit normal shrinkage cracking when dried indicating that the gel had not absorbed much water.

Microscopic documentation of ASR and/or DEF micro structural damage

(Images depicting ASR gel/ettringite formation, cracking and gapping at paste/aggregate interfaces)

ASR Related Evidence

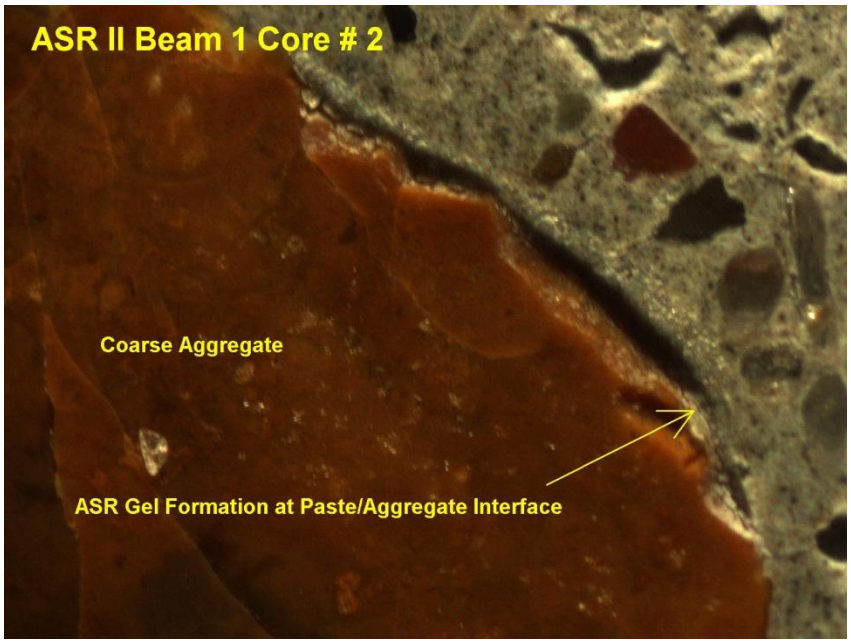

Figure A-1 Small Accumulation of ASR Gel near Paste/Aggregate Interface

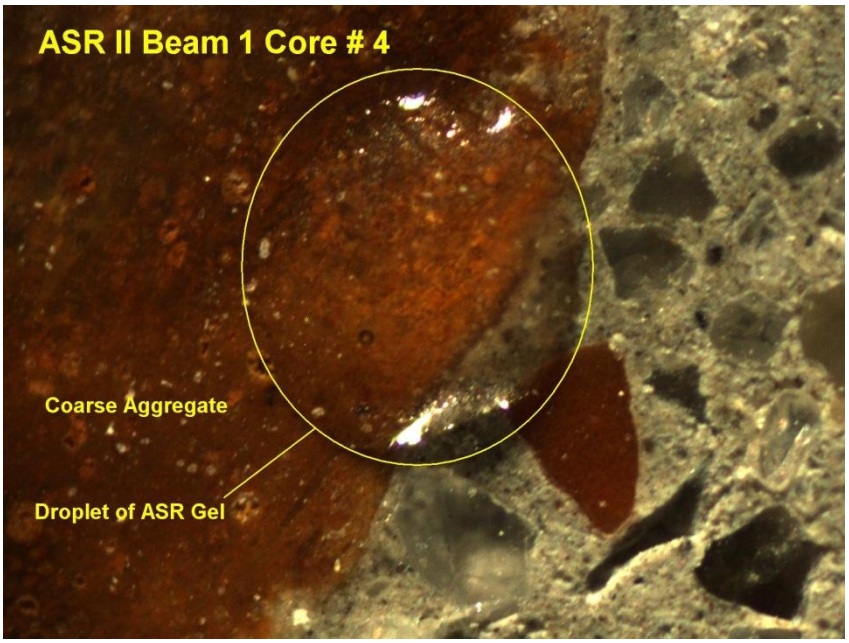

Figure A-2 Small Droplet of ASR Gel which Oozed Out of Aggregate after Cutting and Polishing

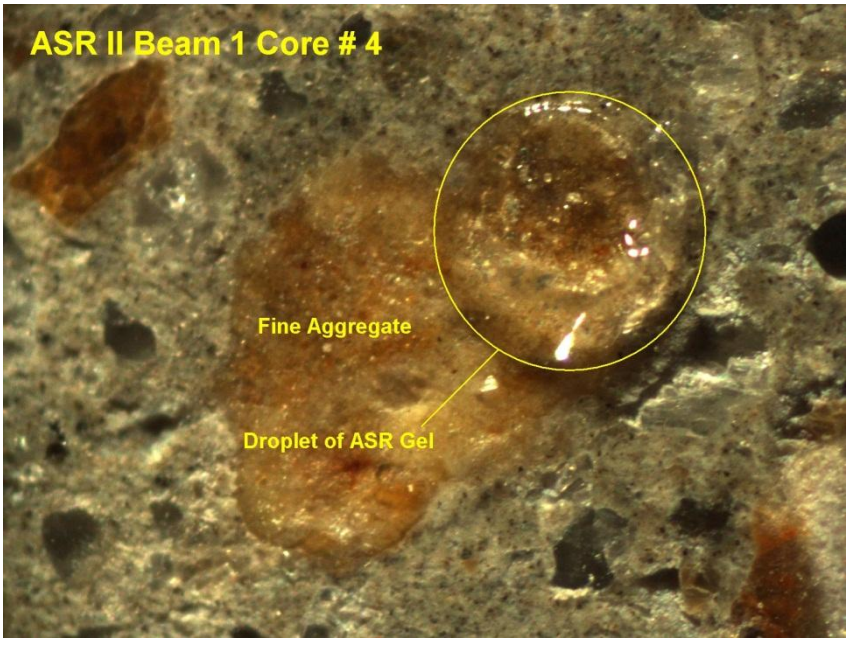

Figure A-3 Small Droplet of ASR Gel which Oozed Out of Fine Aggregate

Scanning Electron Microscope (SEM) Documentation

The SEM analysis was performed on a Hitachi brand 3200N variable pressure microscope with an Oxford EDS system. This tool was used to document and confirm the type of PCD responsible for the distressed concrete. EDS spectral analysis was used to verify reaction site chemistry and relationship to other phases in the mix (paste, aggregate). EDS elemental dot mapping was performed to document the location of reaction product within the mix. The following images document numerous ASR distressed aggregates and ettringite formation sites:

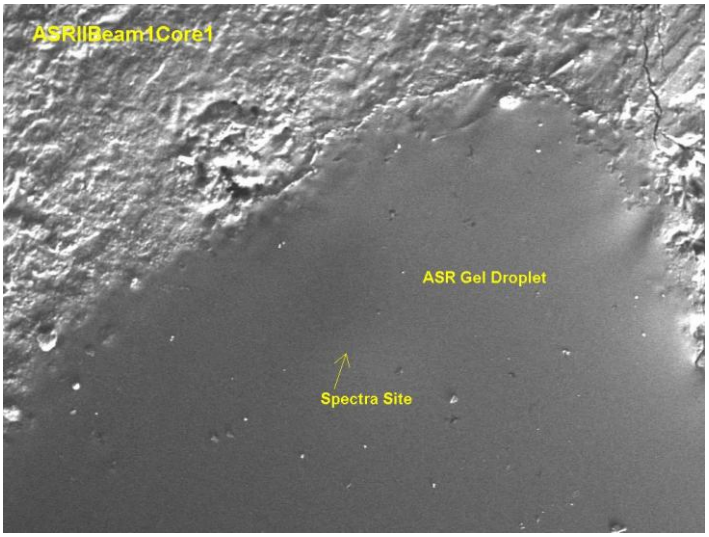

Figure A-4 Image Illustrating Droplet of Gel that Oozed Out of Aggregate

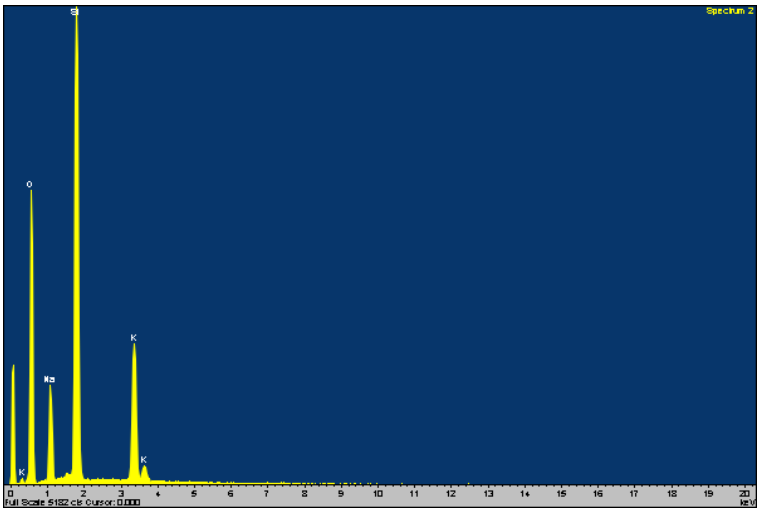

Figure A-5 Spectra Taken from Previous BSE Image Illustrating Gel Chemistry

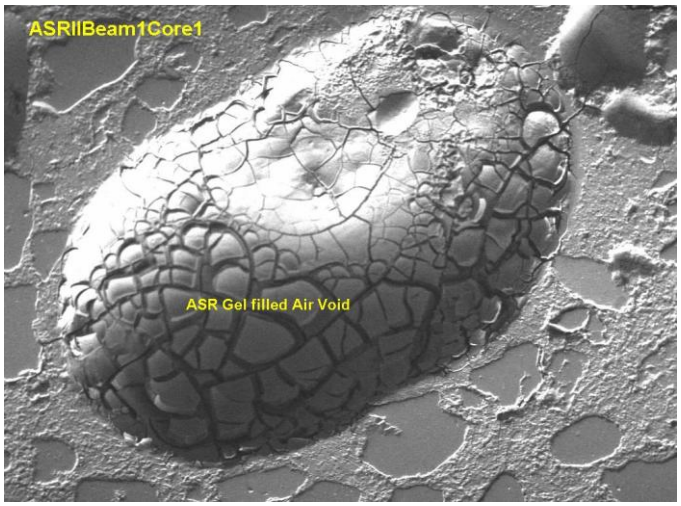

Figure A-6 ASR Gel Accumulation in Elongated Air Void

Table A-3 Qualitative Study of Damage Severity in Each Sample and Damage Progression through Length of Sample

Core ID (length)	Level of ASR Distress	Level of DEF Distress	Distress Characteristics and Crack Orientation
Core1 (3-5/8″)	Very early stage ASR	No Evidence	Very fine micro cracks at surface of core. Did not observe ASR distress crack on polished sections.
Core2 (3-5/8″)	Very early stage ASR	No Evidence	Very fine micro cracks at surface of core. Did not observe ASR distress crack on polished sections.
Core3 (3-5/8″)	Very early stage ASR	No Evidence	Very fine micro cracks at surface of core. Did not observe ASR distress crack on polished sections.
Core4 (3-5/8″)	Very early stage ASR	No Evidence	Very fine micro cracks at surface of core. Did not observe ASR distress crack on polished sections.

Conclusion

Although gel formation was observed in very sparse amount, the cores showed very little evidence of distress from ASR. With the aid of our stereomicroscope very fine surface cracks were observed in the cores.

APPENDIX B

PETROGRAPHIC ANALYSIS REPORT – SPECIMEN 2

Petrographic Analysis

02/09/2011

Report:	TTI ASR DEF
Date Received:	12/01/2010
Structure Type:	Unknown
Sample Type:	Cores
Location:	Unknown
Coarse Aggregate Producer:	NA
Coarse Aggregate Type:	Siliceous Gravel
Fine Aggregate Producer:	NA
Fine Aggregate Type:	Siliceous Sand
Cement Producer:	NA
Cement Type:	NA

Comments:

This petrographic analysis was performed in response to a request from Dr. Joseph Bracci to assist the Texas A&M University in an ASR/DEF investigation of nine submitted cores. The following objectives were specified by Texas A&M:

- General observations on concrete quality. (Comments on placement, mixture proportions, water-cement ratio).
- Visual documentation of ASR and/or DEF micro structural damage. (Images depicting gel/ettringite locations, cracking and gapping of paste/aggregate interfaces).
- Qualitative study of damage severity in each sample. (Comparison of micro structural damage between all samples).
- Qualitative study of damage progression through the length of the sample. (Comparison of micro structural damage in surface and core concretes of each sample).

General observations on concrete quality (comments on placement, mixture proportions, water-cement ratio)

General Appearance
Eight cores were submitted for analysis and were designated as: Core1, Core2, Core3, Core4, Core5, Core6, Core7 and Core8. The majority of the submitted cores were 3-3/4 inches in diameter and ranged from 1-3/4 to 9-1/2 inches in length except for Cores 1, 3, and 4 which were 6 inches in diameter. Most of the cores had obvious distress cracks on the surface of the core.

Water/Cement Ratio
None of the cores had abnormal or elevated w-c ratio. Based on appearance of the paste (color, ferrite distribution and granularity of the hydrates), estimates of w-c ratio for the cores were consistent with the mix design.

Proportioning and types of aggregate
Based on microscopic observations, the paste volume indicates a high sack mix, low coarse aggregate factor and gap grading was noted in all the cores. Coarse aggregate consist of siliceous gravel comprised of chert, agate, and granite. Fine aggregate consist of quartz, agate, feldspar, and chert. The following table summarizes the point count data.

Paste content and appearance
Paste content is indicative of a high sack mix and appearance is normal, except for the numerous fine micro cracking and reaction products. The reaction products consist of ASR gel and ettringite. No fly ash or other mineral admixtures were present in the mix.

Air Content
Non-Air Entrained.

Degree of Hydration
Normal.

Carbonation
Carbonation was noted at the exterior surface of all the cores. The following chart represents the depth of carbonation for each core.

Table B-1 Carbonation Depth

Core ID	Carbonation Depth from Exterior Surface of Core
Core 1	2 mm
Core 2	Minimal
Core 3	Minimal
Core 4	2.3 mm
Core 5	3 mm
Core 6	4 mm
Core 7	2 mm
Core 8	2 mm

Deleterious Reaction Mechanism

The primary distress mechanism in all the cores is attributed to ASR. Although ettringite was noted in various amounts within some of the samples, it is not believed to have contributed much to the overall distress of the specimens. The following table describes the various levels of distress observed in the cores.

Table B-2 Various Levels of Distress in Each Sample

Sample #	Surface Distress	Level of ASR Distress	Reactive Aggregate count/cross-sectional length	Evidence of DEF
Core 1	Mod–High (surface cracks to 14 mm deep from the surface)	Mod. to High (reactive particles noted near surface of core)	52 reactive particles counted in top 3-3/4 inches of core	Ettringite was noted within voids, cracks and at paste aggregate interfaces and as semi continuous coating on re bar imprint
Core 2	High (Surface cracks up to 11 mm deep)	Mod to High with reactive particles noted near top of core.	27 reactive particles counted in top 1-3/4 inches of the core	Ettringite was noted within voids, cracks and at paste aggregate interfaces
Core 3	Moderate (surface cracks tighter than previous cores, to 10 mm)	High	56 reactive particles counted in top 3-5/8 inches from the surface	Ettringite noted within voids, cracks and at paste aggregate interfaces
Core 4	High (surface crack traced from surface to re bar at 2-1/2 inches deep)	High	70 reactive particles counted in top 3-3/4 inches from the surface	Ettringite noted within voids, cracks, at paste aggregate interfaces and as semi-continuous coating at re bar imprint
Core 5	Low to Moderate (surface crack to 1-1/4 inch intersecting rebar)	Moderate	38 reactive particles counted in top 3-1/2 inches from the surface	Minor accumulations of ettringite

Table B-2 Various Levels of Distress in Each Sample (Continued)

Sample #	Surface Distress	Level of ASR Distress	Reactive Aggregate count/cross-sectional length	Evidence of DEF
Core 6	Low	Low to Moderate (more reactive particles near the bottom of this section)	Eight reactive particles counted in top 2 inches from the surface	Negligible accumulations
Core 7	Low to moderate	Moderate	34 reactive particles counted in top 3-7/8 inches from the surface	Negligible accumulations
Core 8	Low	Low (reactive particles were deeper in section)	Seven reactive particles counted in top 3-3/4 inches from the surface	Negligible accumulations

Microscopic documentation of ASR and/or DEF micro structural damage
(Images depicting ASR gel/ettringite formation, cracking and gapping at paste/aggregate interfaces)

ASR Related Evidence

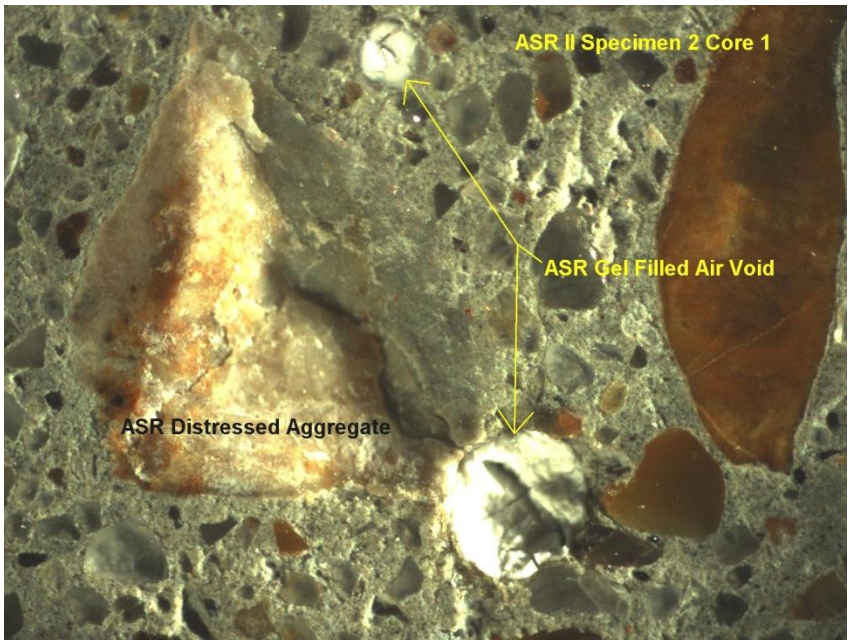

Figure B-1 ASR Filled Air Voids Adjacent To Reactive Particle

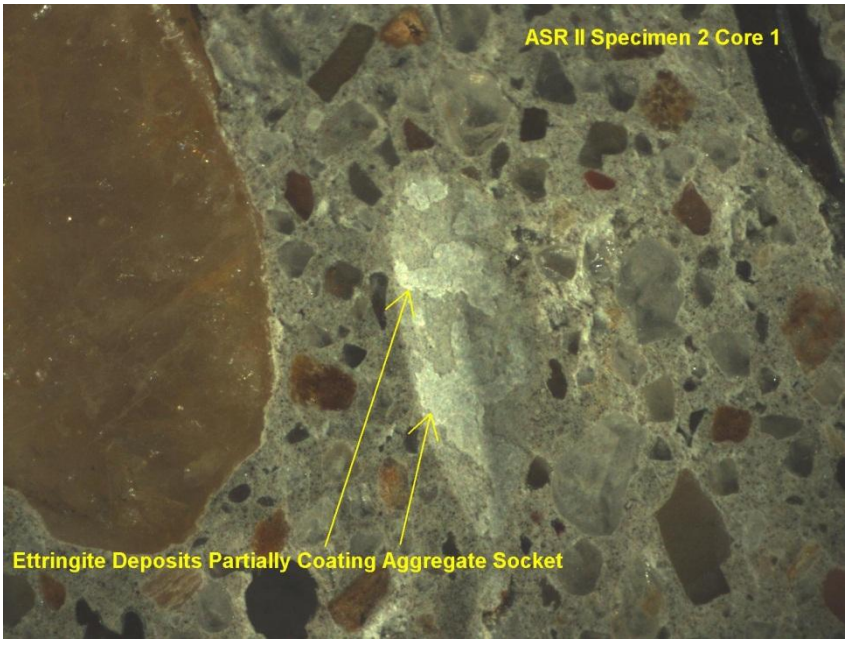

Figure B-2 Partial Coating of Ettringite within Aggregate Socket

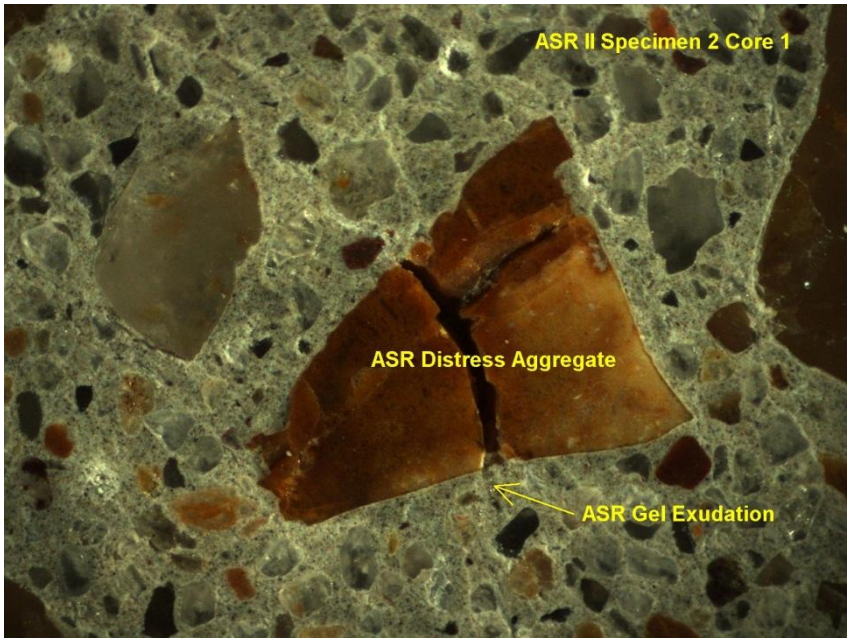

Figure B-3 ASR Gel Exudation Noted from Reactive Aggregate Particle

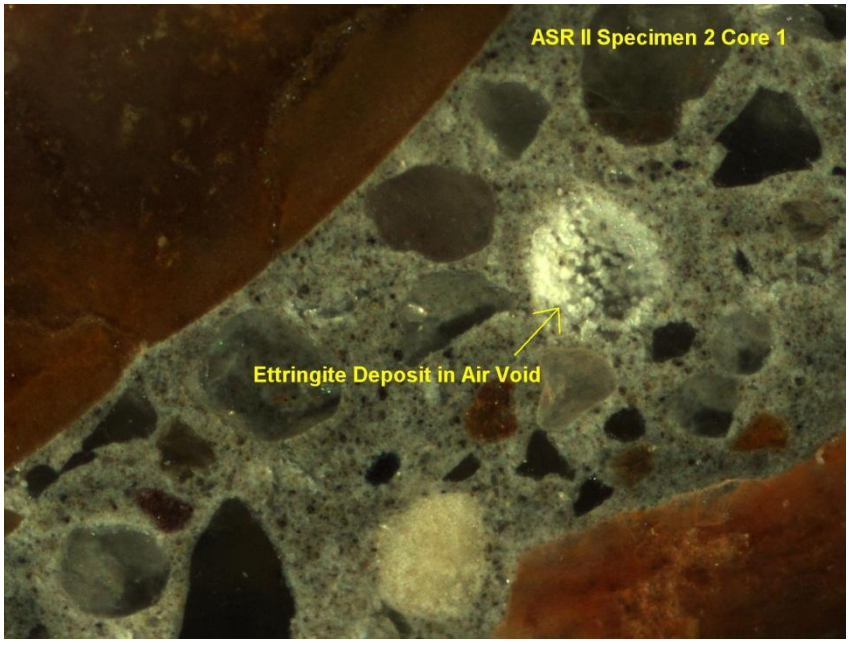

Figure B-4 Accumulation of Ettringite in Air Void

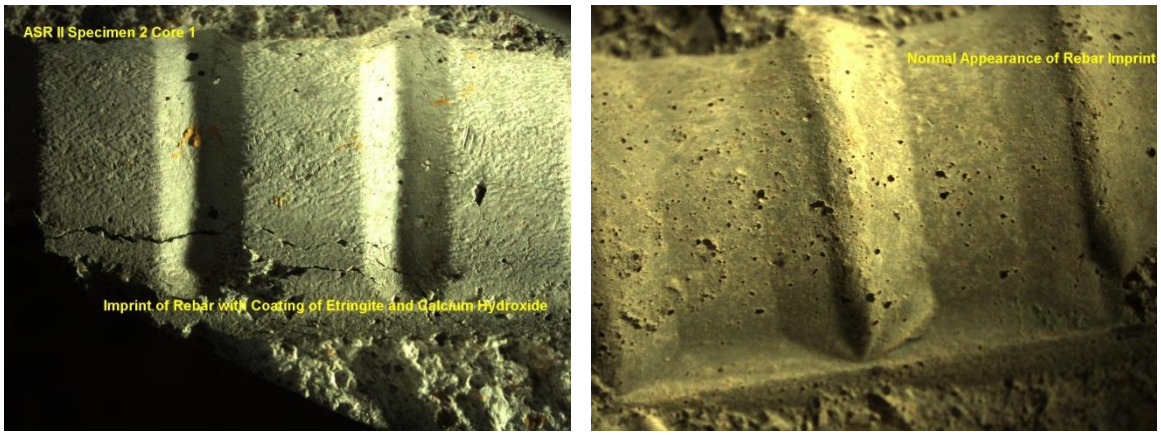

Figure B-5 Image on Left Illustrates Coating of Ettringite and Possible Calcium Hydroxide on Imprint of Rebar; Right Image Illustrates Normal Rebar Imprint without Coating

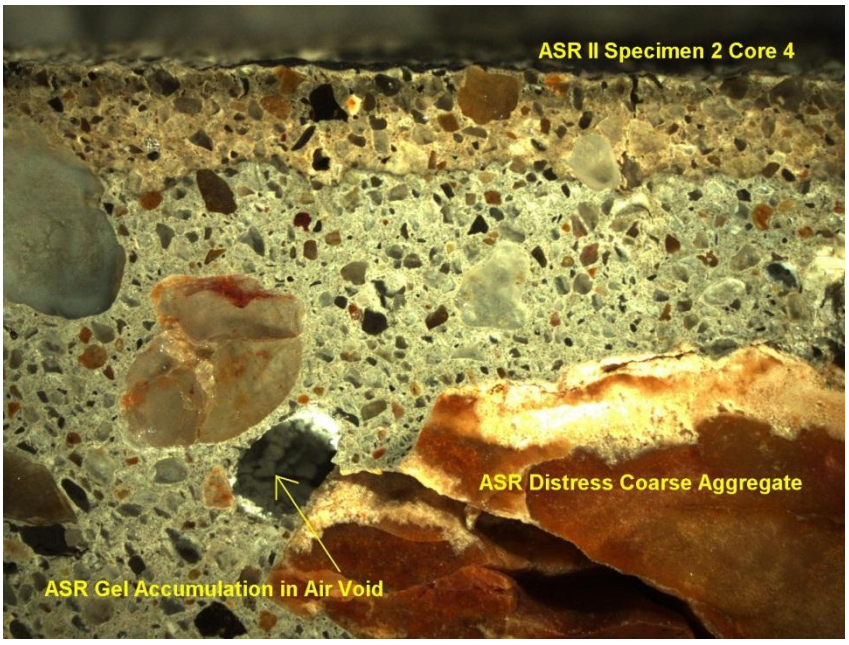

Figure B-6 Image Illustrating Carbonation Zone at Top of Core and Accumulation of ASR Gel within Air Void

Concluding Comments

Based on this analysis the primary cause for the distress concrete is related to ASR. As indicated by the above table, the degree of ASR distress varies from low to high degrees of reactivity. Although Ettringite is noted in numerous locations within some of the cores, it is not consistent with features (Ettringite filled gapped around aggregate, nest of ettringite in paste) associated with DEF; however, the Ettringite formation within some of the cores may have played a minor role in the distress. The ettringite deposits as coating on many of the rebar imprints does indicate that debonding had occurred.

APPENDIX C

PETROGRAPHIC ANALYSIS REPORT – SPECIMEN 4

Petrographic Analysis

07/31/2012

Report:	TTI ASR DEF
Date Received:	01/01/2012
Structure Type:	Unknown
Sample Type:	Cores
Location:	Unknown
Coarse Aggregate Producer:	NA
Coarse Aggregate Type:	Siliceous Gravel
Fine Aggregate Producer:	NA
Fine Aggregate Type:	Siliceous Sand
Cement Producer:	NA
Cement Type:	NA

Comments:

This petrographic analysis was performed in response to a request from Dr. Joseph Bracci to assist the Texas A&M University in an ASR/DEF investigation of six submitted cores. The following objectives were specified by Texas A&M:

- General observations on concrete quality. (Comments on placement, mixture proportions, water-cement ratio).
- Visual documentation of ASR and/or DEF micro structural damage. (Images depicting gel/ettringite locations, cracking and gapping of paste/aggregate interfaces).
- Qualitative study of damage severity in each sample. (Comparison of micro structural damage between all samples).
- Qualitative study of damage progression through the length of the sample. (Comparison of micro structural damage in surface and core concretes of each sample).

General observations on concrete quality (comments on placement, mixture proportions, water-cement ratio)

General Appearance

Eight cores and two pieces of concrete were submitted for analysis and were designated as: 1, 2, 3, 4, 5, 6, 7, 8 and A and B for the two small concrete specimens. The submitted cores were 3-3/4 inch in diameter and ranged from 1-1/2 to 11.0 inches in length. All of the cores had obvious distress cracks on the surface of the core. Reaction product was noted in voids and a coating on detached re-bar surfaces.

Water/Cement Ratio

None of the cores had abnormal or elevated w-c ratio. Based on appearance of the paste (color, ferrite distribution and granularity of the hydrates) estimates of w-c ratio for the six cores were consistent with the mix design.

Proportioning and types of aggregate

Based on microscopic observations the paste volume indicate a high sack mix, low coarse aggregate factor and gap grading was noted in all the cores. Coarse aggregate consist of siliceous gravel comprised of chert, agate, granite, feldspar and quartz aggregate. Fine aggregate consist of quartz, chert, agate, feldspar and rhyolite.

Paste content and appearance

Paste content is indicative of a high sack mix and appearance is normal except for the numerous fine micro cracking and reaction products. The reaction products consist of ASR gel and ettringite. No fly ash or other mineral admixtures were present in the mix.

Air Content

Non-Air Entrained.

Degree of Hydration

Normal.

Carbonation

Carbonation was noted at the exterior surface of all the cores. The following chart represents the depth of carbonation for each core.

Table C-1 Carbonation Depth

Core ID	Carbonation Depth From Exterior Surface of Core
1	3 mm
2	2 mm
3	1 mm
4	3 mm
5	2 mm
6	1.5 mm
7	2 mm
8	2 mm

Table C-1 Carbonation Depth (Continued)

Core ID	Carbonation Depth From Exterior Surface of Core
A	1.5 mm
B	2 mm

Deleterious Reaction Mechanism

The primary distress mechanism in all the cores is attributed to ASR. ASR gel was observed in air voids, within distress aggregate and as exudation from reactive particles. Although ettringite was noted in various amounts within some of the samples it is not believed to have contributed much to the overall distress of the specimens. Ettringite was noted in air voids, within micro cracks and as partial coating on surface of detached rebar.

Table C-2 Various Levels of Distress in Each Sample

Sample #	Surface Distress	Level of ASR Distress	Reactive Aggregate count/cross-sectional length	Evidence of DEF
1	Moderate (surface cracks oriented perpendicular to surface to 1 inch deep from the surface)	High with reactive particles noted throughout the core.) With depth cracking predominately parallel to sub-parallel to surface	66 reactive particles (rp) counted in top 3-1/8 inches of core. 59 reactive particles were count in next 2-7/8”	Ettringite was noted within voids, cracks and at paste aggregate interfaces.
2	Low (Fine tight surface cracks oriented perpendicular to surface one up to 5/8inch deep)	Moderate to high with reactive particles noted throughout the core. With depth cracking predominately parallel to sub-parallel to surface	61 rp counted in top 3-3/4 inches of the core. 80 rp counted in next 3-3/4 inches.	Ettringite was noted within voids, cracks and at paste aggregate interfaces
3	Severe (Surface cracks oriented perpendicular to surface, full depth of specimen)	Extensive, with reactive particles noted throughout the specimen. With depth cracking predominately parallel to sub-parallel to surface	20 rp counted in top 2-1/8”W x 1” L specimen.	Ettringite noted within voids, cracks and at paste aggregate interfaces and as semi continuous coating on fracture plane.

Table C-2 Various Levels of Distress in Each Sample (Continued)

Sample #	Surface Distress	Level of ASR Distress	Reactive Aggregate count/cross-sectional length	Evidence of DEF
4	Severe (several surface cracks oriented perpendicular to surface to 7/8 inches deep)	Extensive with reactive particles noted throughout the core. ASR gel was also noted on rebar imprint. With depth cracking predominately parallel to sub-parallel to surface	78 reactive particles counted in top 3-7/8 inches from the surface. 80 rp observed on next 3-3/4" section. 31 rp on next 1-7/8" x 2-1/2" section.	Ettringite noted within voids, cracks, at paste aggregate interfaces and as semi continuous coating at rebar imprint.
5	Moderate to high (surface crack oriented perpendicular to surface intersected steel rebar at 1-5/8")	Moderate to High with reactive particles noted throughout the core. With depth cracking predominately parallel to sub-parallel to surface	78 reactive particles counted in top 3-3/4 inches from the surface. 95 rp in next 3-1/2"	Ettringite was noted within voids, cracks and at paste aggregate interfaces
6	Severe Surface cracking oriented perpendicular to surface	Extensive with reactive particles noted throughout the core. With depth cracking predominately parallel to sub-parallel to surface	26 rp counted in top 1-58" x 2' section. 24 in next 1" x 3-1/4" section, 15 rp in next 1-1/4" x 1-5/8" section, 54 in next 2-3/8" x 3-1/2" section.	Ettringite noted within voids, cracks, at paste aggregate interfaces.
7	Moderate to high, with cracks oriented perpendicular to surface to 1" depth	High with reactive particles noted throughout the core. With depth cracking predominately parallel to sub-parallel to surface	39 rp counted in to 3-3/4" section, 103 rp in next 3-1/2" section, 39 rp in next 3-5/8" x 2" section.	Ettringite noted within voids, cracks and at paste aggregate interfaces.

Table C-2 Various Levels of Distress in Each Sample (Continued)

Sample #	Surface Distress	Level of ASR Distress	Reactive Aggregate count/cross-sectional length	Evidence of DEF
8	Moderate to High, one large crack oriented perpendicular to surface intersecting rebar at ¾" from the surface. Crack width up to 3mm	High with reactive particles noted throughout the core. ASR gel was also noted on rebar imprint. With depth cracking predominately parallel to sub-parallel to surface	77 rp counted in top 3-3/4" x 3-1/2" section, 106 rp counted in next 3-1/2 x 3-1/2" section, 36 rp counted in next 1-1/2" x 3-5/8" section	Ettringite noted within voids, cracks, at paste aggregate interfaces and as semi continuous coating at rebar imprint.
A	Severe Surface cracking, oriented perpendicular to surface	Extensive with reactive particles noted throughout the specimen. ASR gel was also noted on rebar imprint. With depth cracking predominately parallel to sub-parallel to surface	39 rp counted in 2-1/8" x 2-1/1" section	Ettringite noted within voids, cracks, at paste aggregate interfaces and as semi continuous coating at rebar imprint.
B	Severe Surface cracking, oriented perpendicular to surface	Extensive with reactive particles noted throughout the specimen. ASR gel was also noted on rebar imprint. With depth cracking predominately parallel to sub-parallel to surface	35 rp counted in 3-7/8" x 1-3/8" specimen	Ettringite noted within voids, cracks, at paste aggregate interfaces and as semi continuous coating at rebar imprint.

The following Stereoscopic, SEM/EDS and Fluorescent images illustrate distress features associated with the ASR degradation.

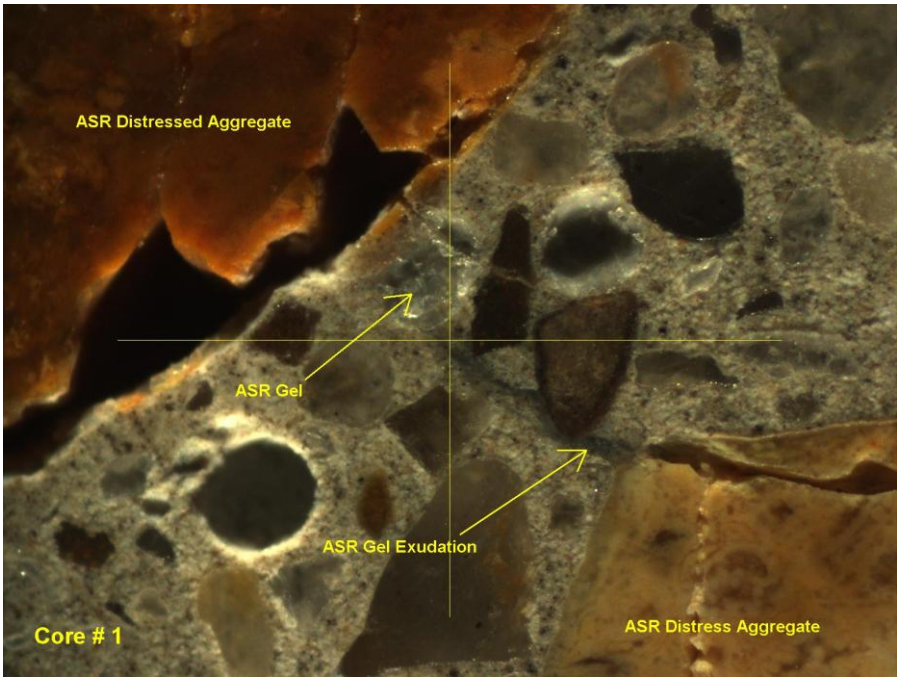

Figure C-1 Image Illustrating ASR Distressed Chert Aggregates and Gel Exudation

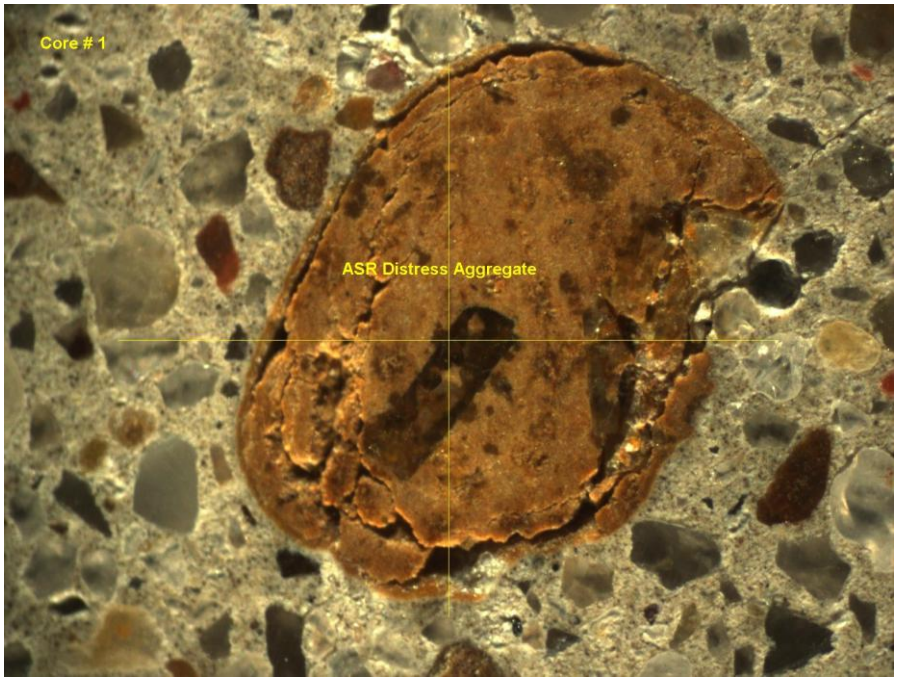

Figure C-2 Image Illustrating ASR Distressed Rhyolite Aggregate

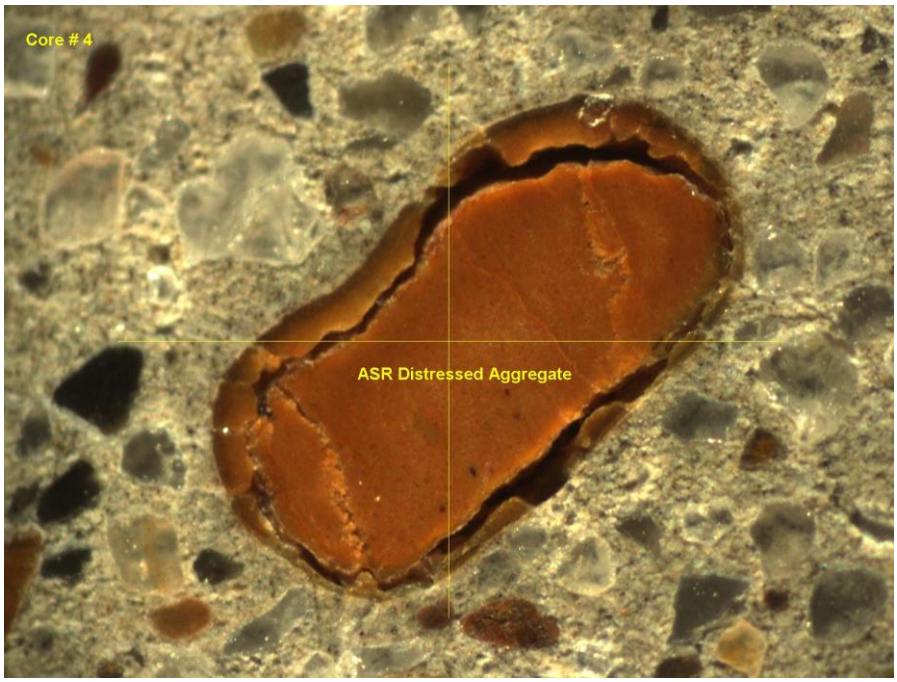

Figure C-3 Image Illustrating ASR Distressed Chert Particle

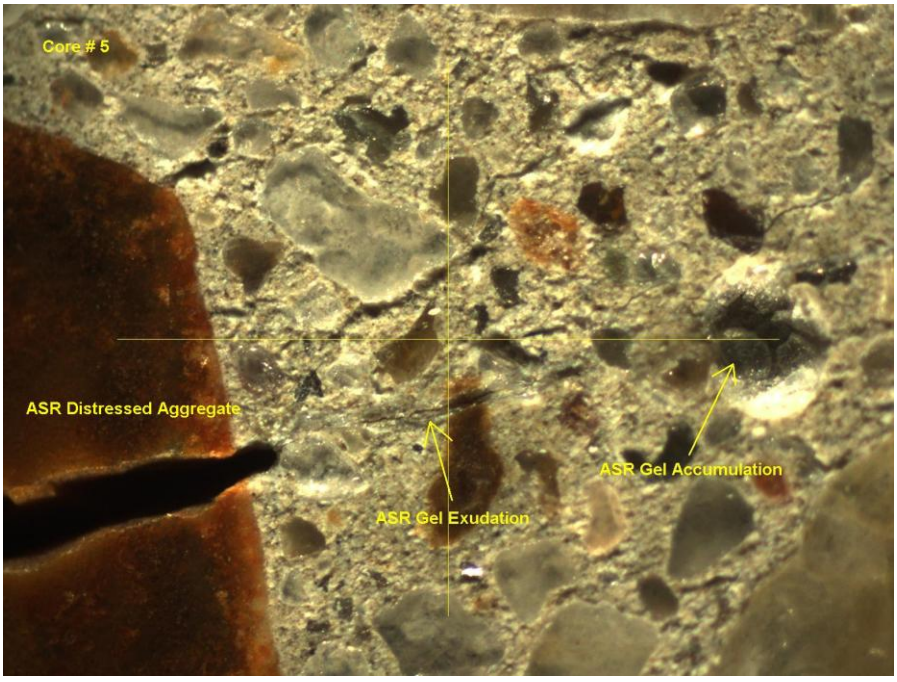

Figure C-4 ASR Distressed Chert Particle Exhibiting Gel Exudation

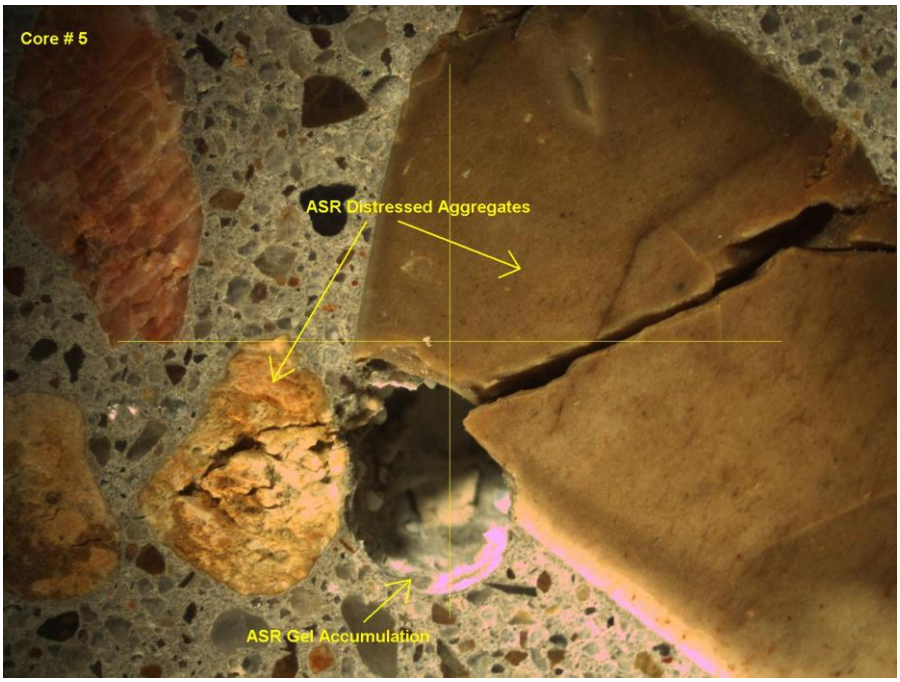

Figure C-5 ASR Distressed Aggregate with Adjacent Void Partially Filled with ASR Gel

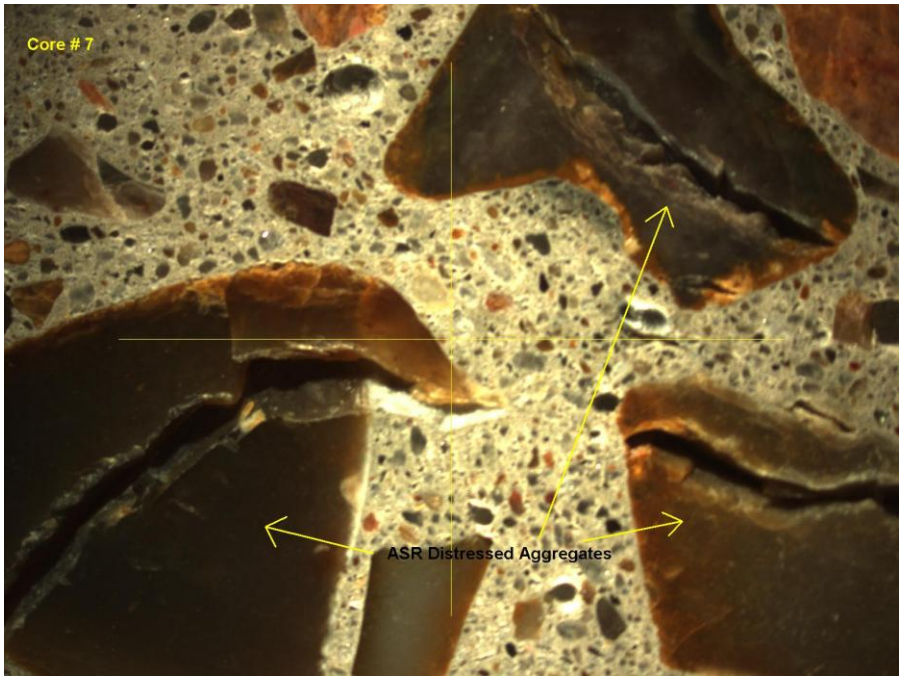

Figure C-6 Image Illustrating ASR Distressed Chert/Flint Particles

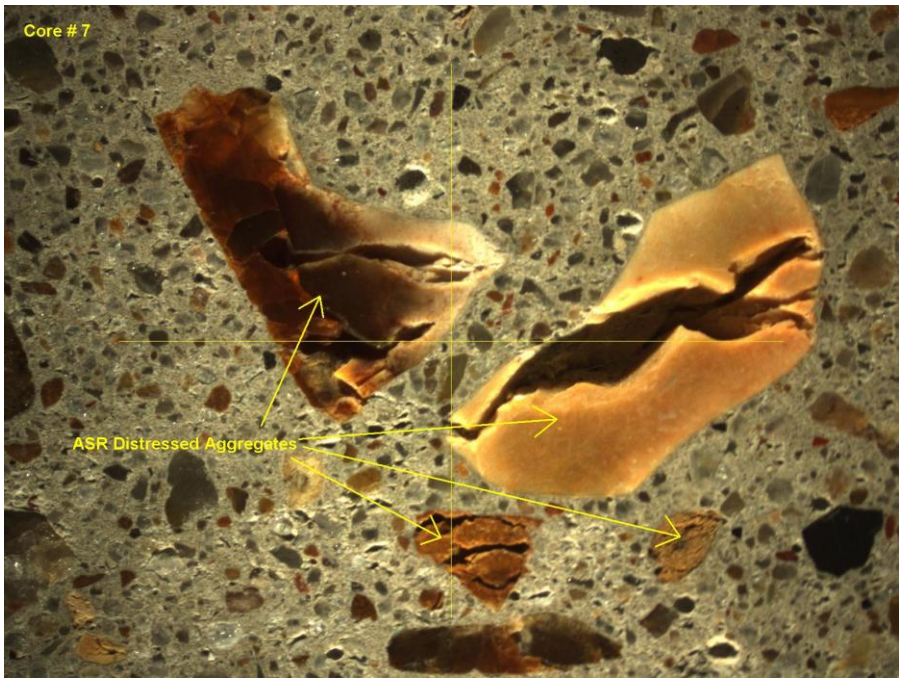

Figure C-7 Image Illustrating ASR Distressed Chert/Flint Particles

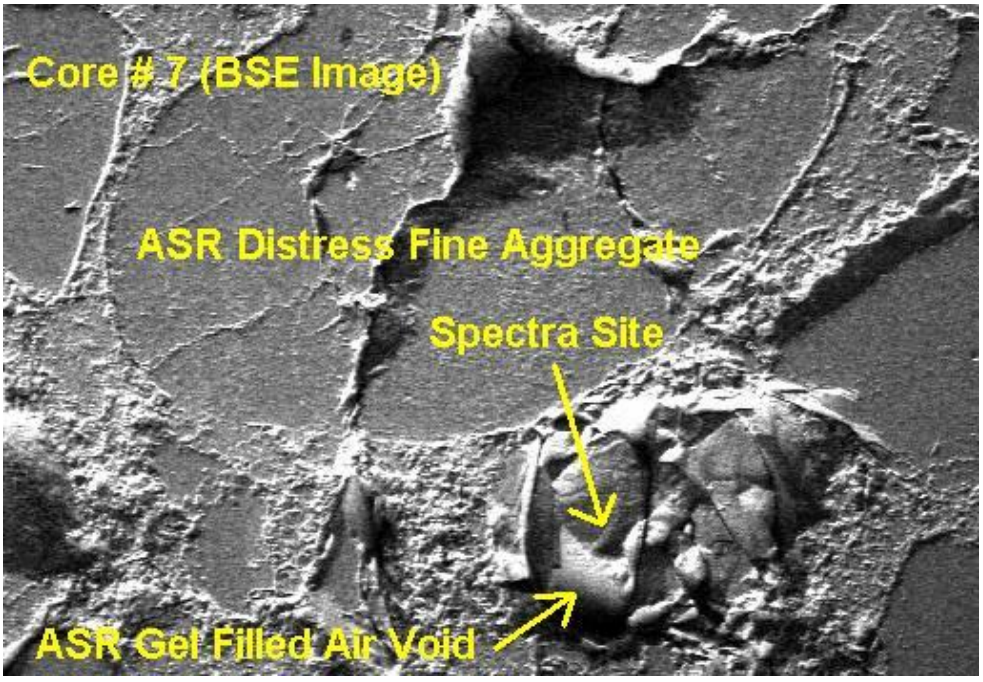

Figure C-8 SEM/BSE Image Illustrating Distressed Aggregate and Gel Accumulation

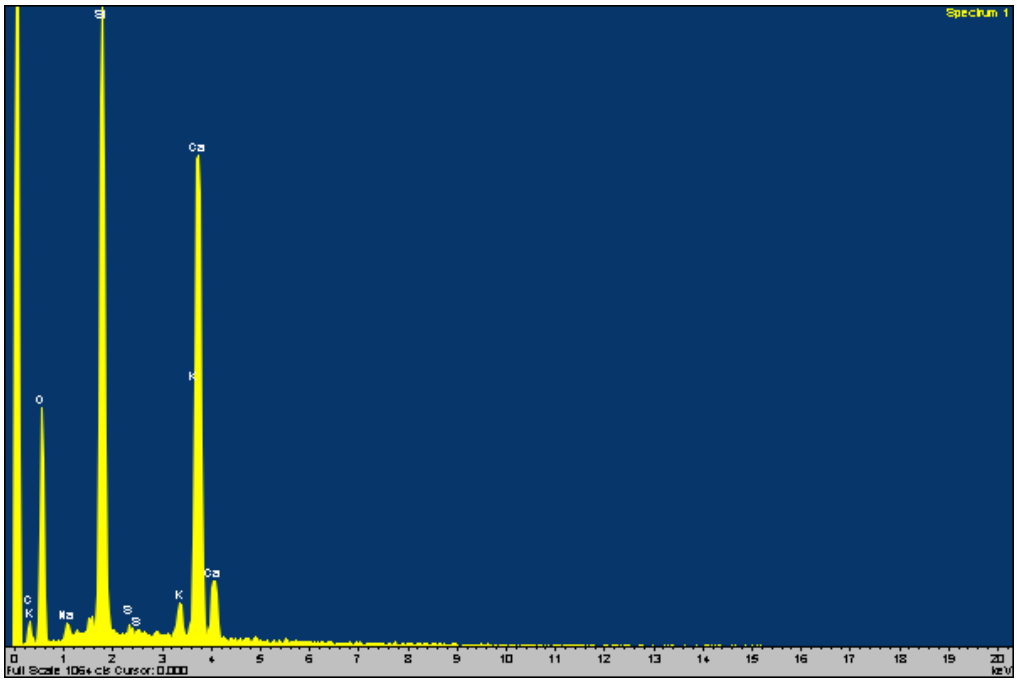

Figure C-9 EDS Spectra from Previous BSE Image Illustrating Gel Chemistry

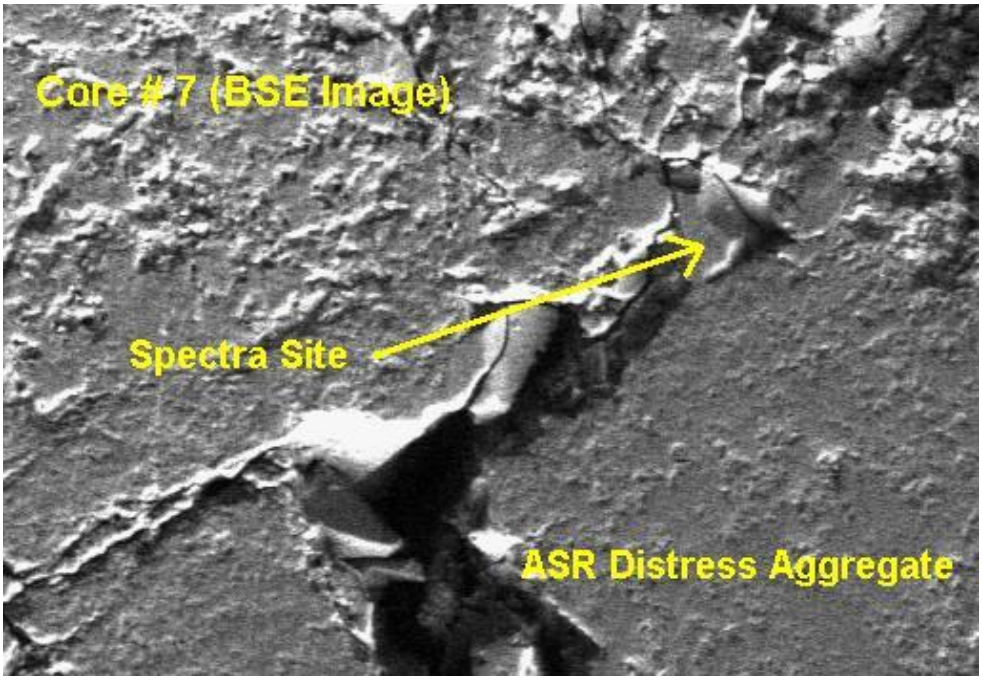

Figure C-10 SEM/BSE Image Illustrating ASR Distressed Aggregate and Gel Formation

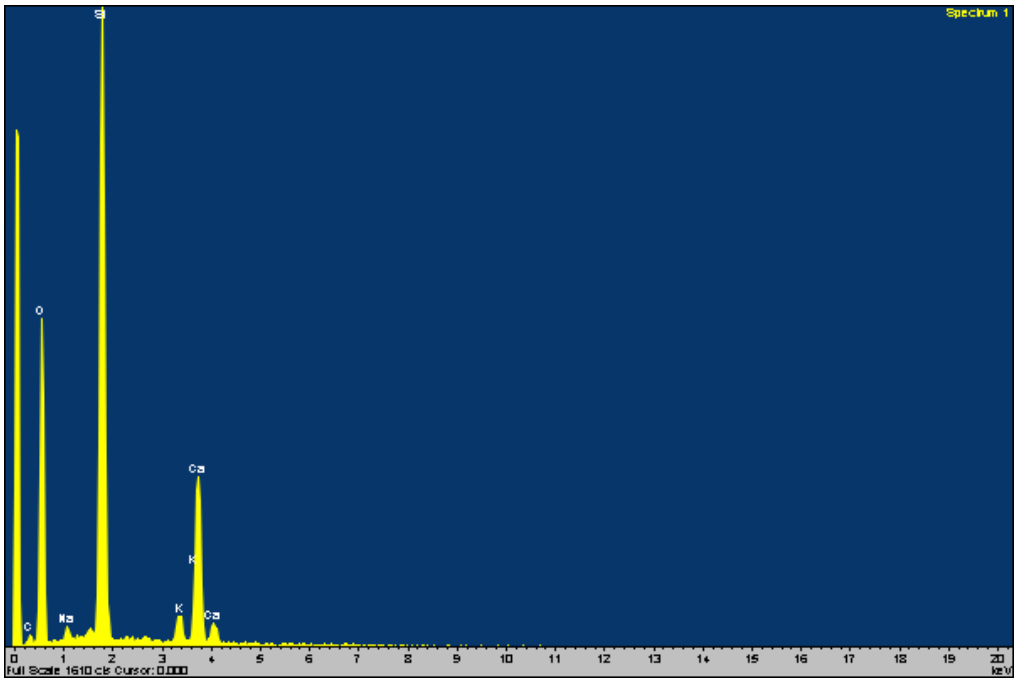

Figure C-11 EDS Spectra from Previous BSE Image Illustrating Gel Chemistry

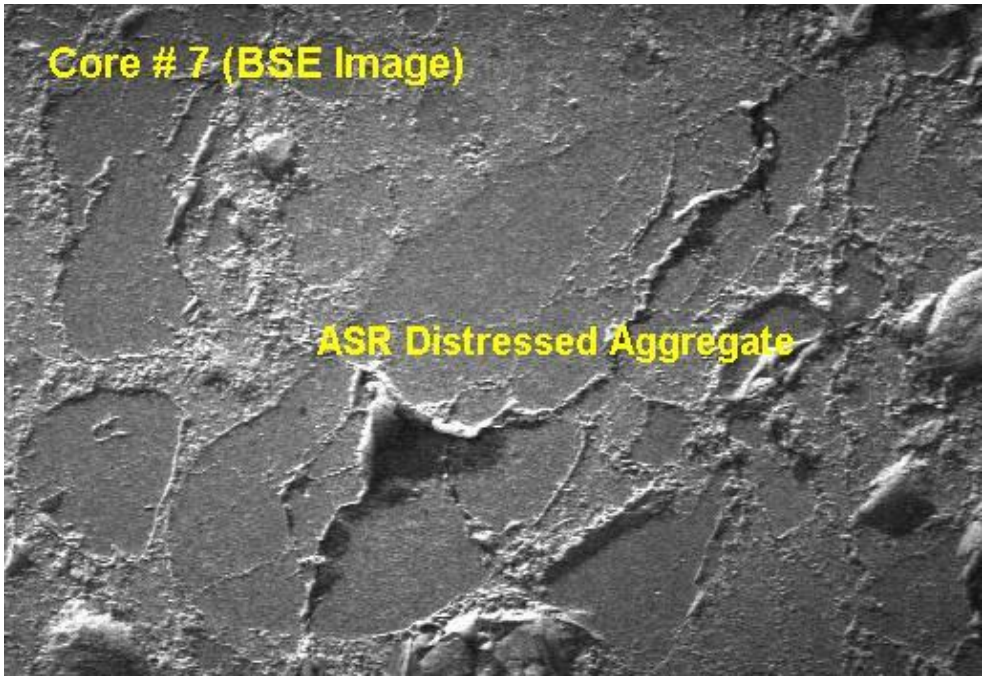

Figure C-12 SEM/BSE Image Illustrating ASR Distressed Aggregate

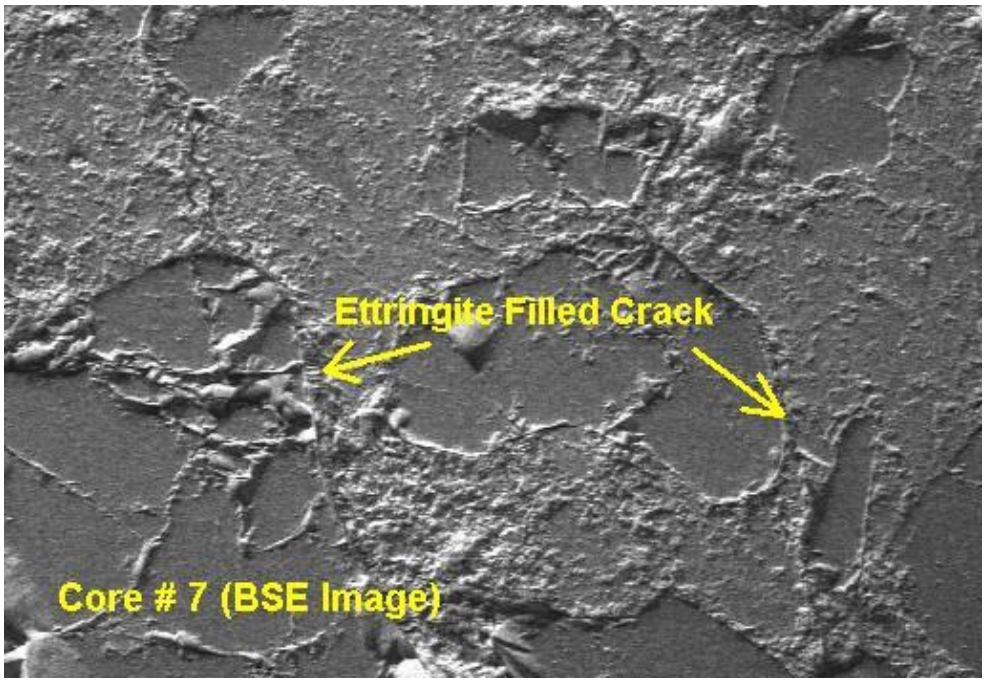

Figure C-13 SEM/BSE Image Illustrating Ettringite Filled Micro-Cracks

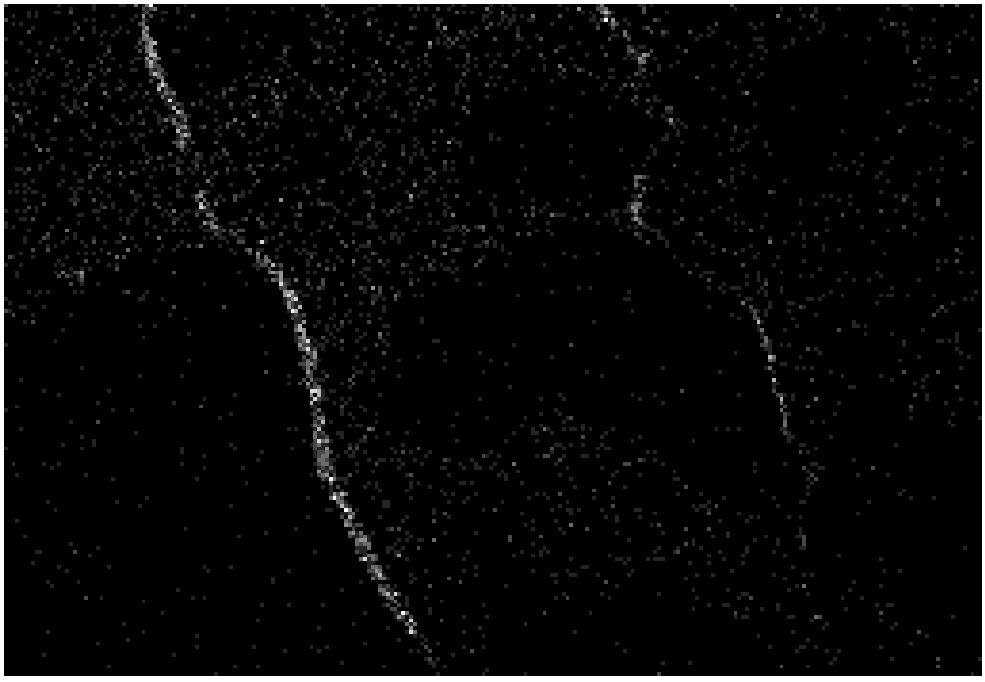

Figure C-14 EDS Sulfur Dot Map Illustrating Ettringite Concentration in Previous Image

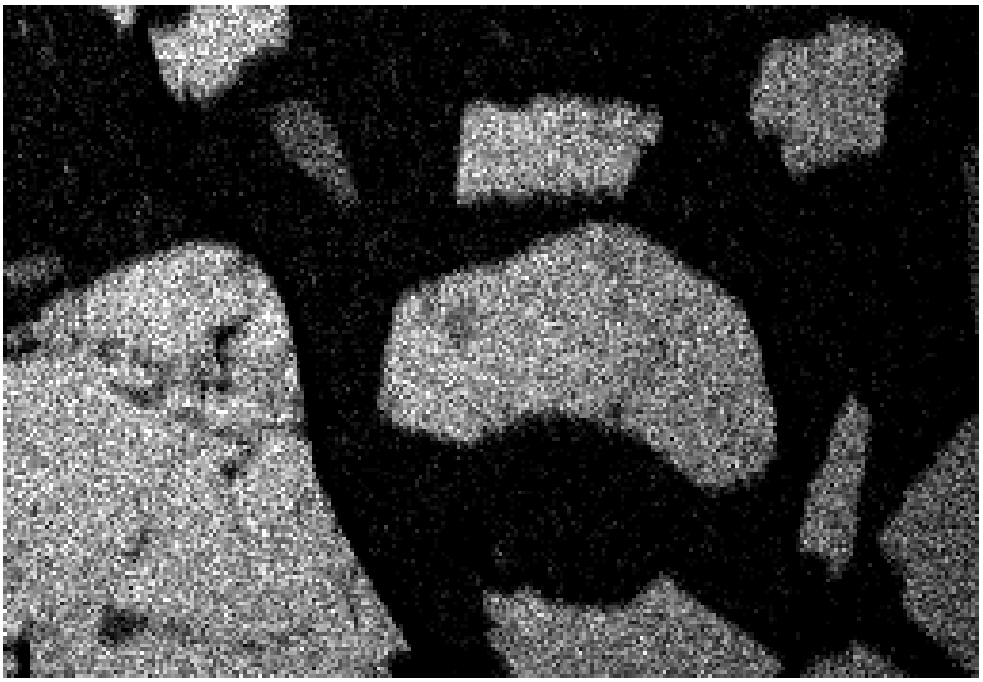

Figure C-15 EDS Silica Elemental Dot Map Illustrating Silica Rich Aggregates

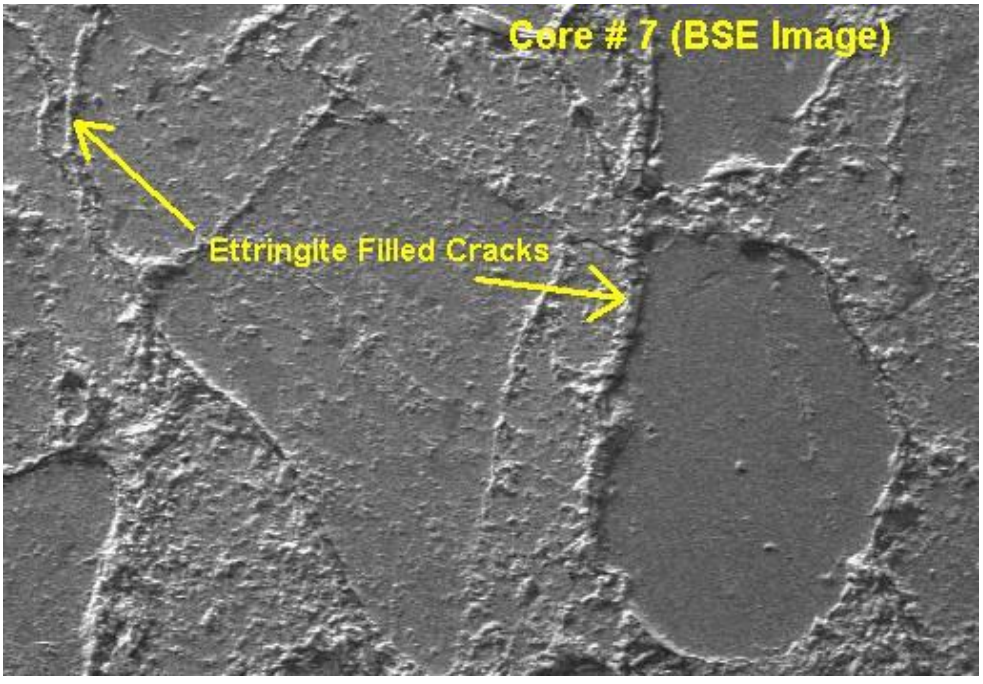

Figure C-16 SEM/BSE Image Illustrating Ettringite Filled Micro-Cracks

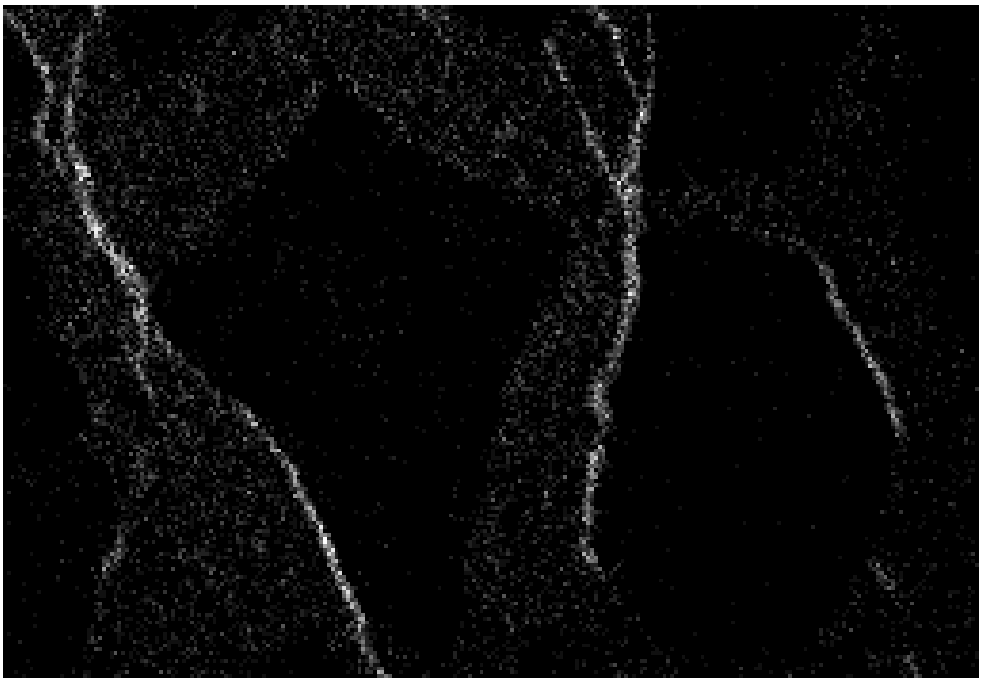

Figure C-17 EDS Sulfur Dot Map Illustrating Ettringite Concentration in Previous Image

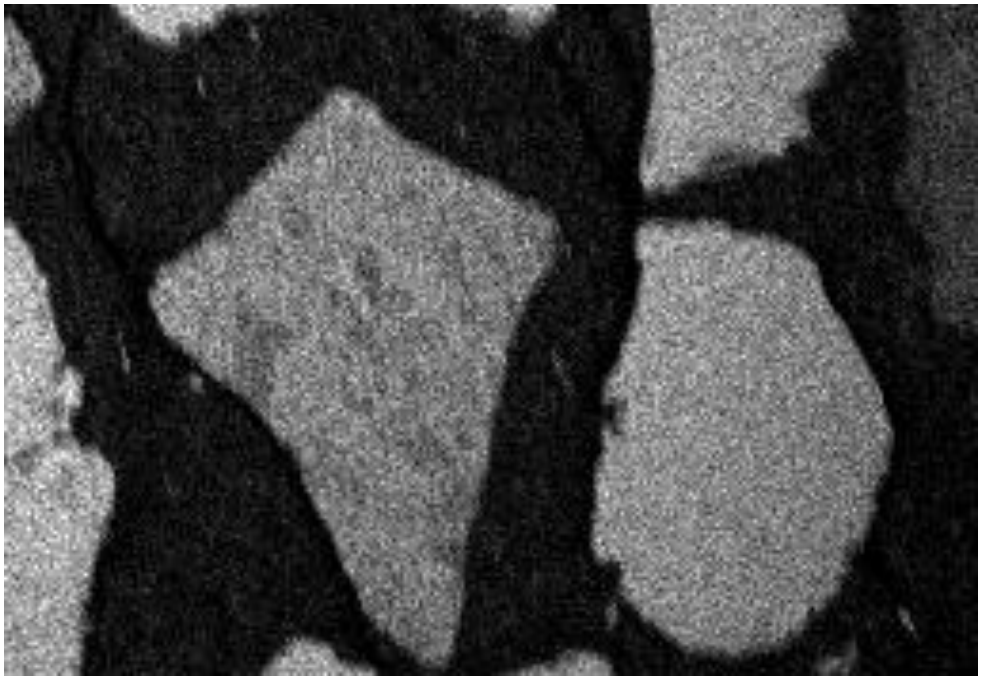

Figure C-18 EDS Silica Elemental Dot Map Illustrating Silica Rich Aggregates

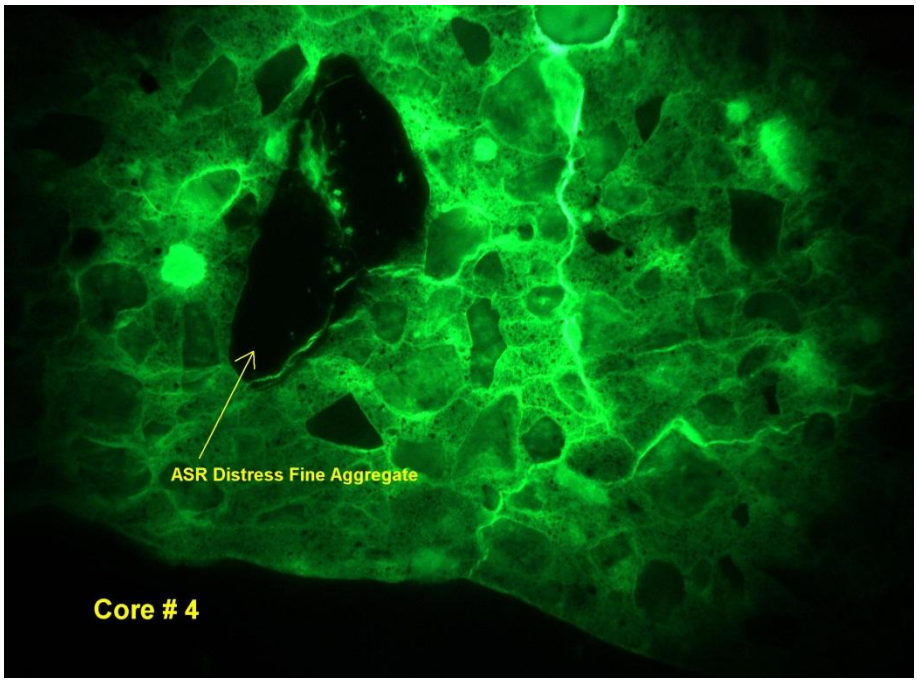

Figure C-19 Fluorescent Image Illustrating Fine Network of Micro-Cracking Associated with ASR

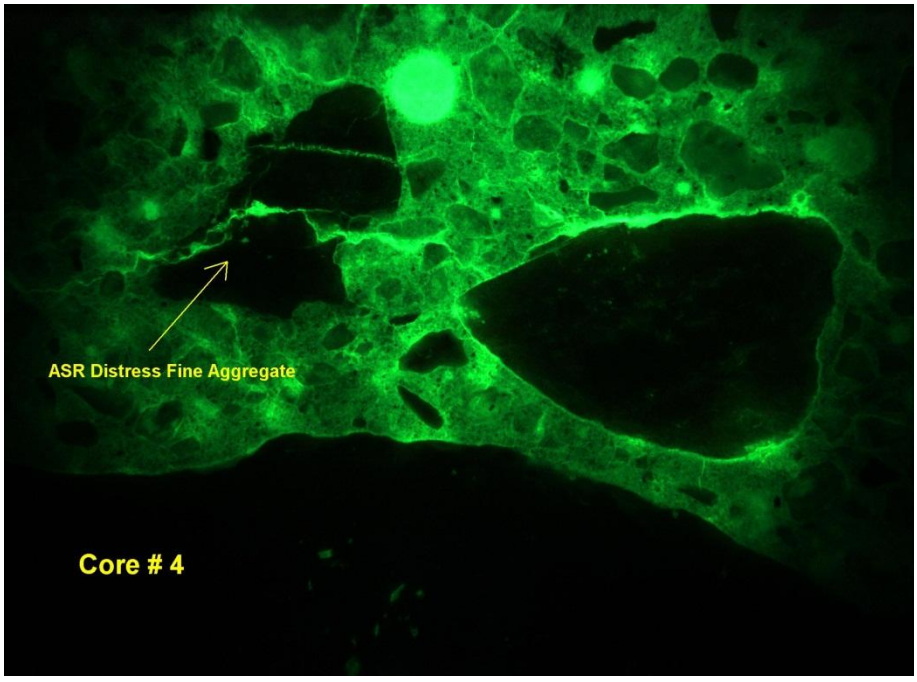

Figure C-20 Fluorescent Image Illustrating Fine Network of Micro-Cracking Associated with ASR

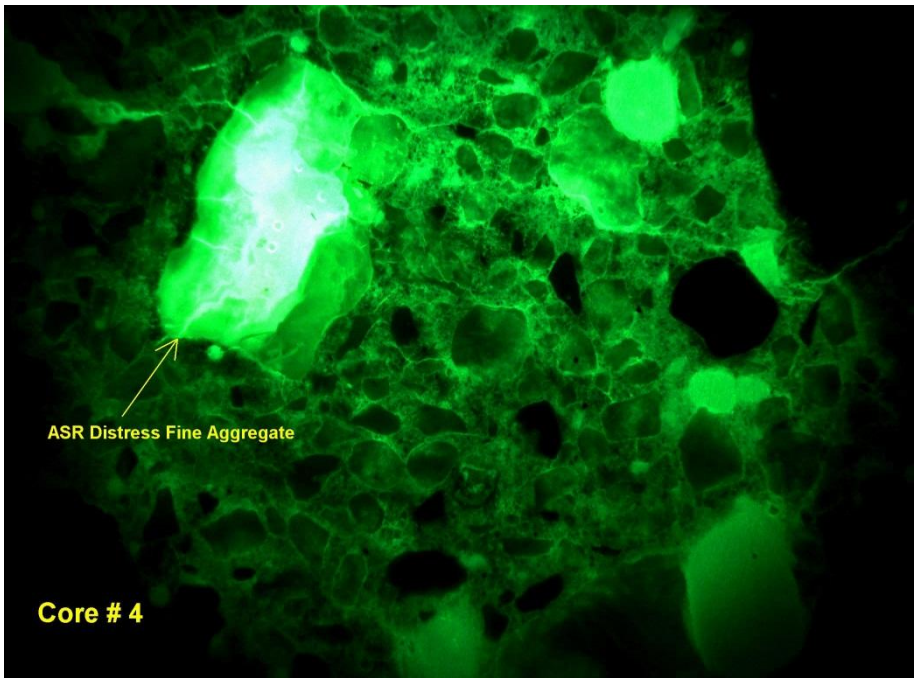

Figure C-21 Fluorescent Image Illustrating Fine Network of Micro-Cracking Associated with ASR

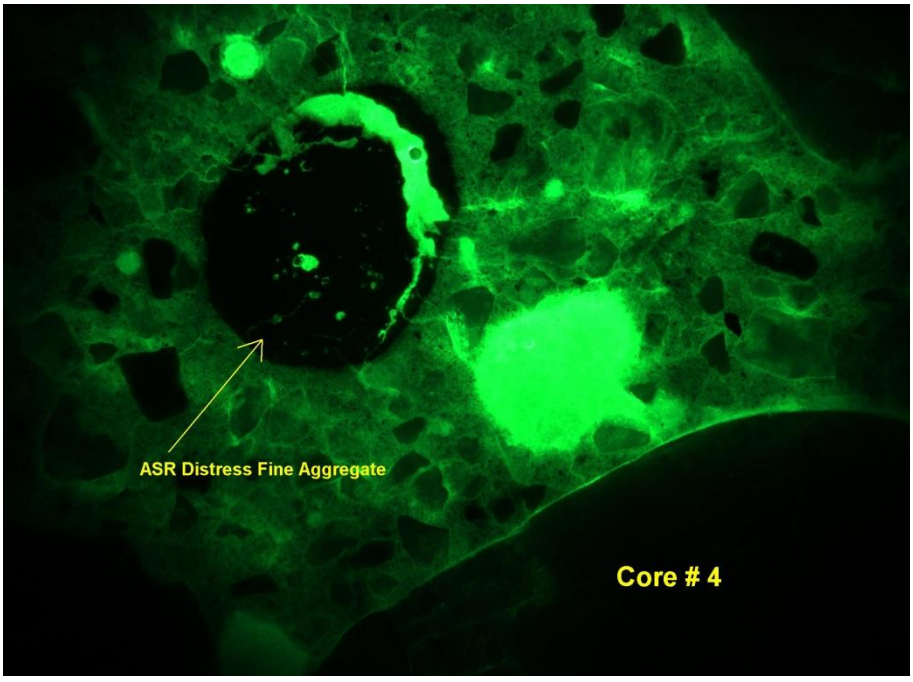

Figure C-22 Fluorescent Image Illustrating Fine Network of Micro-Cracking Associated with ASR

Concluding Comments

Based on this analysis all eight cores and two concrete specimens (A & B) are exhibiting moderate to extensive levels of ASR distress. Both the fine and coarse aggregates are experiencing ASR attack. The primary coarse aggregate lithology experiencing ASR attack is chert, flint and agate. The primary fine aggregate is chert, flint, agate and rhyolite. Although ettringite is apparent and observed in many air voids, fine network of micro cracking, partial coating of detached rebar and partial accumulation at paste aggregate interfaces the distribution is not consistent with delayed ettringite formation. Both ettringite and ASR gel accumulation was noted on the rebar imprints suggest partial to complete debonding had occurred between the paste and the steel.